

**AFRL-PR-WP-TP-2002-200, V1**

**ADVANCED LASER DIAGNOSTIC  
APPLICATIONS**

**Volume 1 of 3 (Pages 1 – 217)**

**Larry P. Goss, Ph.D.**

**Innovative Scientific Solutions, Inc.  
2766 Indian Ripple Road  
Dayton, OH 45440-3638**



**MARCH 2001**

**FINAL REPORT FOR 18 SEPTEMBER 1995 – 28 SEPTEMBER 2000**

**Approved for public release; distribution is unlimited.**

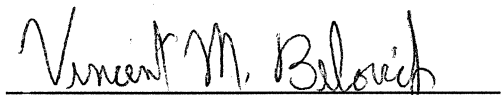
**PROPULSION DIRECTORATE  
AIR FORCE RESEARCH LABORATORY  
AIR FORCE MATERIEL COMMAND  
WRIGHT-PATTERSON AIR FORCE BASE, OH 45433-7251**

## NOTICE

USING GOVERNMENT DRAWINGS, SPECIFICATIONS, OR OTHER DATA INCLUDED IN THIS DOCUMENT FOR ANY PURPOSE OTHER THAN GOVERNMENT PROCUREMENT DOES NOT IN ANY WAY OBLIGATE THE U.S. GOVERNMENT. THE FACT THAT THE GOVERNMENT FORMULATED OR SUPPLIED THE DRAWINGS, SPECIFICATIONS, OR OTHER DATA DOES NOT LICENSE THE HOLDER OR ANY OTHER PERSON OR CORPORATION; OR CONVEY ANY RIGHTS OR PERMISSION TO MANUFACTURE, USE, OR SELL ANY PATENTED INVENTION THAT MAY RELATE TO THEM.

THIS REPORT IS RELEASABLE TO THE NATIONAL TECHNICAL INFORMATION SERVICE (NTIS). AT NTIS, IT WILL BE AVAILABLE TO THE GENERAL PUBLIC, INCLUDING FOREIGN NATIONS.

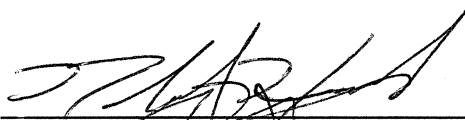
THIS TECHNICAL REPORT HAS BEEN REVIEWED AND IS APPROVED FOR PUBLICATION.



VINCENT M. BELOVICH, Ph.D.

Contract Monitor

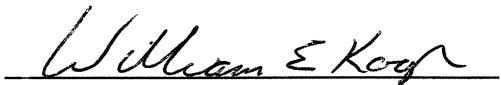
Combustion Science Branch (AFRL/PRTS)



ROBERT D. HANCOCK, Ph.D.

Chief

Combustion Science Branch, AFRL/PRTS



WILLIAM E. KOOP

Chief of Technology

Turbine Engine Division

Propulsion Directorate

Do not return copies of this report unless contractual obligations or notice on a specific document require its return.



<b>REPORT DOCUMENTATION PAGE</b>				<i>Form Approved</i> OMB No. 0704-0188				
The public reporting burden for this collection of information is estimated to average 1 hour per response, including the time for reviewing instructions, searching existing data sources, gathering and maintaining the data needed, and completing and reviewing the collection of information. Send comments regarding this burden estimate or any other aspect of this collection of information, including suggestions for reducing this burden, to Department of Defense, Washington Headquarters Services, Directorate for Information Operations and Reports (0704-0188), 1215 Jefferson Davis Highway, Suite 1204, Arlington, VA 22202-4302. Respondents should be aware that notwithstanding any other provision of law, no person shall be subject to any penalty for failing to comply with a collection of information if it does not display a currently valid OMB control number. <b>PLEASE DO NOT RETURN YOUR FORM TO THE ABOVE ADDRESS.</b>								
<b>1. REPORT DATE (DD-MM-YY)</b> March 2001		<b>2. REPORT TYPE</b> Final		<b>3. DATES COVERED (From - To)</b> 09/18/1995 – 09/28/2000				
<b>4. TITLE AND SUBTITLE</b> ADVANCED LASER DIAGNOSTIC APPLICATIONS Volume 1 of 3 (Pages 1 – 217)				<b>5a. CONTRACT NUMBER</b> F33615-95-C-2507				
				<b>5b. GRANT NUMBER</b>				
				<b>5c. PROGRAM ELEMENT NUMBER</b> 62203F				
<b>6. AUTHOR(S)</b> Larry P. Goss, Ph.D.				<b>5d. PROJECT NUMBER</b> 3048				
				<b>5e. TASK NUMBER</b> 04				
				<b>5f. WORK UNIT NUMBER</b> AI				
<b>7. PERFORMING ORGANIZATION NAME(S) AND ADDRESS(ES)</b> Innovative Scientific Solutions, Inc. 2766 Indian Ripple Road Dayton, OH 45440-3638				<b>8. PERFORMING ORGANIZATION REPORT NUMBER</b> 2507 Final				
<b>9. SPONSORING/MONITORING AGENCY NAME(S) AND ADDRESS(ES)</b> Propulsion Directorate Air Force Research Laboratory Air Force Materiel Command Wright-Patterson Air Force Base, OH 45433-7251				<b>10. SPONSORING/MONITORING AGENCY ACRONYM(S)</b> AFRL/PRTS				
				<b>11. SPONSORING/MONITORING AGENCY REPORT NUMBER(S)</b> AFRL-PR-WP-TP-2002-200, V1				
<b>12. DISTRIBUTION/AVAILABILITY STATEMENT</b> Approved for public release; distribution is unlimited.								
<b>13. SUPPLEMENTARY NOTES</b> This is Volume 1 of 3. See also AFRL-PR-WP-TP-2002-200, V2 and AFRL-PR-WP-TP-2002-200, V3. Report contains color. Report is comprised of numerous publications, such as journal articles and conference papers.								
<b>14. ABSTRACT</b> Reported are results of experimental and numerical investigations on gas turbine combustion and fuel processes, including: 1) Development, evaluation, and utilization of advanced laser diagnostic and analytical techniques for studying combustion and fuel processes important to current and future military aircraft; 2) Determination of cause and investigation of schemes to eliminate combustion and thermal-stability-related problems resulting from change from JP-4 to JP-8 fuel; 3) Proposal and evaluation of advanced combustor concepts and design characteristics to optimize tradeoffs in performance, visual observables, durability, and pollutants; 4) Investigation of methods for reducing emissions of carbon monoxide, hydrocarbons, oxides of nitrogen, and smoke in current and future gas turbine combustors; 5) Design and completion of experiments for establishing a database for developing and evaluating combustor and fuel-system-component design models; 6) Development of computational-fluid-dynamics (CFD) models for gas turbine combustor and fuel-system-component design; 7) Evaluation of additive and advanced thermally stable fuels that provide thermal stability up to 900 °F; 8) Evaluation of thermally stable and environmentally safe anti-icing additives for JP-8 and JP-900 fuels; 9) Investigation of methods of using fuel to cool hot engine components and determination of impact of fuel phase change on combustion, and 10) Investigation of new military and commercial applications for combustion and fuels technology developed in this program, including high-cycle fatigue and aging aircraft.								
<b>15. SUBJECT TERMS</b> Advanced laser diagnostics, fuel thermal stability, computational fluid dynamics with chemistry, vortex-flame interactions, pulse-detonation engines, trapped-vortex combustor, fuel additives, spray combustion								
<b>16. SECURITY CLASSIFICATION OF:</b> <table border="1" style="width: 100%; border-collapse: collapse;"> <tr> <td style="padding: 2px;"><b>a. REPORT</b> Unclassified</td> <td style="padding: 2px;"><b>b. ABSTRACT</b> Unclassified</td> <td style="padding: 2px;"><b>c. THIS PAGE</b> Unclassified</td> </tr> </table>			<b>a. REPORT</b> Unclassified	<b>b. ABSTRACT</b> Unclassified	<b>c. THIS PAGE</b> Unclassified	<b>17. LIMITATION OF ABSTRACT:</b> SAR		<b>18. NUMBER OF PAGES</b> 228
<b>a. REPORT</b> Unclassified	<b>b. ABSTRACT</b> Unclassified	<b>c. THIS PAGE</b> Unclassified						
<b>19a. NAME OF RESPONSIBLE PERSON (Monitor)</b> Vincent M. Belovich, Ph.D.			<b>19b. TELEPHONE NUMBER (Include Area Code)</b> (937) 255-4229					



## TABLE OF CONTENTS

<u>Section</u>		<u>Page</u>
1	INTRODUCTION .....	1
2	DIAGNOSTIC AND ANALYTICAL INSTRUMENTATION DEVELOPMENT .....	2
2.1	COMBUSTION DIAGNOSTICS .....	2
2.1.1	Overview .....	2
2.1.2	Two-Dimensional Flow-Visualization Technique .....	2
2.1.3	Three-Dimensional Flow-Visualization Technique .....	35
2.1.4	Ultrafast-Imaging Technique .....	56
2.1.5	Phase-Sensitive-Imaging Technique .....	71
2.1.6	Particle-Image-Velocimetry Technique .....	83
2.1.7	Pressure-Sensitive-Paint Technique .....	136
2.2	FUEL DIAGNOSTICS .....	179
2.2.1	Overview .....	179
2.2.2	Particle-Sizing, Oxygen-Concentration, and Mass- Deposition Methods .....	179
2.2.3	Picosecond Pump/Probe Diagnostics .....	196
2.2.4	Spectroscopic Techniques .....	213
3	DIAGNOSTIC APPLICATIONS .....	218
3.1	COMBUSTION STUDIES .....	218
3.1.1	Overview .....	218
3.1.2	Fundamental Combustion Studies .....	218
3.1.2.1	Jet Diffusion Flames .....	218
3.1.2.2	Counterflow Diffusion Flames .....	284
3.1.3	Large-Scale Combustion Studies .....	369
3.1.3.1	Trapped-Vortex Combustor .....	369
3.1.3.2	Lean Blowout and Emission .....	416
3.1.3.3	Combustor Design Trends .....	542
3.1.3.4	Active Combustion Control .....	571
3.1.3.5	Pulse Detonation Engines .....	623

## TABLE OF CONTENTS (CONTINUED)

<u>Section</u>	<u>Page</u>
3.2 FUEL STUDIES .....	644
3.2.1 Overview .....	644
3.2.2 Fuel Thermal Stability .....	644
3.2.2.1 Autoxidation of Jet-A Fuels .....	644
3.2.2.2 Kinetics .....	656
3.2.2.3 Fuel Blends .....	657
3.2.2.4 Fuel Recirculation .....	658
3.2.2.5 Fuel Pyrolysis .....	666
3.2.2.6 Lubricants .....	671
3.2.3 Effect of Additives on Fuel Thermal Stability .....	676
3.2.4 Icing Inhibitors .....	689
4 MODEL DEVELOPMENT .....	694
4.1 COMBUSTION MODELING .....	694
4.1.1 Overview .....	694
4.1.2 Jet Diffusion Flames .....	694
4.1.3 Opposing-Jet Diffusion Flames .....	913
4.1.4 Trapped-Vortex Combustor .....	941
4.1.5 Pulse Detonation Waves .....	981
4.1.6 Droplet and Two-Phase Flows .....	986
4.2 MODELING OF FUEL THERMAL STABILITY .....	1132
4.2.1 Overview .....	1132
4.2.2 Fuel Thermal Stability .....	1132
APPENDIX: Presentations, Publications, and Patents .....	1196

## PREPACE

This report was prepared by Dr. Larry P. Goss of Innovative Scientific Solutions, Inc., and covers work performed during the period 18 September 1995 through 28 September 2000 under Air Force Contract F33615-95-C-2507. The contract was administered under the direction of the Air Force Research Laboratory, Wright-Patterson Air Force Base, Ohio, with Captain Illari Vihinen and Dr. Vincent M. Belovich as Government project monitors.



## 1. INTRODUCTION

This report describes the results of experimental and numerical investigations on gas turbine combustion and fuel processes. Advanced laser-based diagnostic techniques were developed and applied to the experimental study of combustion and fuel-related issues. In addition, numerical computational-fluid-dynamics-with-chemistry (CFDC) models were developed to simulate real environments.

The objectives of this research program included:

- 1) Develop, evaluate, and utilize advanced laser diagnostic and analytical techniques in the study of combustion and fuel processes that are important to current and future military aircraft.
- 2) Determine the cause and investigate schemes to eliminate problems related to combustion and thermal stability that result from the change from JP-4 to JP-8 fuel.
- 3) Propose and evaluate advanced combustor concepts and design characteristics that optimize tradeoffs in performance, visual observables, durability, and pollutants.
- 4) Investigate methods for reducing emissions of carbon monoxide, hydrocarbons, oxides of nitrogen, and smoke in current and future gas turbine combustors.
- 5) Design and conduct experiments needed to establish a database for developing and evaluating models for combustor and fuel-system-component design.
- 6) Develop computational fluid dynamic (CFD) models for gas turbine combustor and fuel-system-component design.
- 7) Evaluate additives and advanced, thermally stable fuels that provide thermal stability up to 900 °F.
- 8) Evaluate thermally stable and environmentally safe anti-icing additives for JP-8 and JP-900 fuels.
- 9) Investigate methods of using fuel to cool hot engine components, and determine the impact of fuel phase changes on combustion.
- 10) Investigate new military and commercial applications for the combustion and fuels technology developed in this program, including high-cycle fatigue and aging aircraft.

The research conducted during this program resulted in more than 330 publications, presentations, and patents; a complete list can be found in the Appendix. In this report the research efforts are summarized in three sections. Section 2 details the development of diagnostic and analytical instrumentation for investigation of processes related to combustion and fuel. Section 3 describes the application of the diagnostic techniques to the study of combustion and fuel issues of importance to the military. Section 4 documents the development and evaluation of numerical models for simulating processes related to combustion and fuel. This report is a collection of reviewed papers published in technical journals and presentations published in conference proceedings. These papers are grouped in categories, each category being prefaced with an abstract summarizing the results of accomplishments in the field of study related to the reproduced source material.

## **2. DIAGNOSTIC AND ANALYTICAL INSTRUMENTATION DEVELOPMENT**

### **2.1 COMBUSTION DIAGNOSTICS**

#### **2.1.1 Overview**

The objective of this portion of the program was to continue and extend efforts that were initiated under previous Air Force contracts on the development of advanced laser diagnostic techniques for combustion research. The emphasis was placed on extending the capabilities of existing diagnostic techniques to achieve more accurate quantitative measurements and on developing new techniques that would aid in the development of advanced combustor concepts. Thus, the focus of the effort was on two- and three-dimensional techniques rather than on conventional pointwise approaches. Methods investigated included Reactive Mie Scattering (RMS), Holographic Flow Visualization (HFV), Ultrafast Imaging, Phase-Sensitive Imaging, Particle-Imaging Velocimetry (PIV), and Pressure-Sensitive Paint (PSP). Publications are included in this report to document the results of the development efforts in each of these areas.

#### **2.1.2 Two-Dimensional Flow-Visualization Technique**

RMS is a two-dimensional imaging technique that allows the structural dynamics of flow fields to be captured. Two important studies utilizing this technique were conducted during this program. The first is summarized in a review paper entitled "Dynamics of Propane Jet Diffusion Flames." This invited publication (see pp. 3-22) summarizes studies in which the dynamic structures associated with jet diffusion flames were captured with the RMS technique and compared with predictions from numerical simulations. The second study dealt with the nonreacting flow fields of coaxial nozzles. The paper entitled "Structure of Square Coaxial Nozzle Flows" (see pp. 23-34) reports visualization and flow-spectra results obtained on coaxial nozzles using the RMS technique.



*Atlas of*  
**VISUALIZATION**

---

*Edited by*  
**The Visualization Society of Japan**

**III**



CRC Press  
Boca Raton New York

Acquiring Editor: Joel Claypool  
Contact Editor: Ben Kato  
Associate Editor: Felicia Shapiro  
Project Editor: Jennifer Richardson  
Marketing Manager: Susie Carlisle  
Direct Mail Marketing Manager: Becky McEldowney  
Prepress: Gary Bennett  
Cover Designer: Denise Craig  
Manufacturing: Sheri Schwartz

Library of Congress Cataloging-in-Publication Data

Cataloging and ISSN number available from the Library of Congress.

This book contains information obtained from authentic and highly regarded sources. Reprinted material is quoted with permission, and sources are indicated. A wide variety of references are listed. Reasonable efforts have been made to publish reliable data and information, but the author and the publisher cannot assume responsibility for the validity of all materials or for the consequences of their use.

Neither this book nor any part may be reproduced or transmitted in any form or by any means, electronic or mechanical, including photocopying, microfilming, and recording, or by any information storage or retrieval system, without prior permission in writing from the publisher.

All rights reserved. Authorization to photocopy items for internal or personal use, or the personal or internal use of specific clients, may be granted by CRC Press LLC, provided that \$.50 per page photocopied is paid directly to Copyright Clearance Center, 27 Congress Street, Salem, MA 01970 USA. The fee code for users of the Transactional Reporting Service is ISBN 0-8493-2656-7/94/\$0.00+\$.50. The fee is subject to change without notice. For organizations that have been granted a photocopy license by the CCC, a separate system of payment has been arranged.

CRC Press LLC's consent does not extend to copying for general distribution, for promotion, for creating new works, or for resale. Specific permission must be obtained in writing from CRC Press LLC for such copying.

Direct all inquiries to CRC Press LLC 2000 Corporate Blvd., N.W., Boca Raton, Florida 33431.

© 1997 by CRC Press LLC      **PUBLISHED WITH PERMISSION**

No claim to original U.S. Government works

Printed in the United States of America 1 2 3 4 5 6 7 8 9 0

Printed on acid-free paper

## chapter twelve

---

# Dynamics of Propane Jet Diffusion Flames

V. R. Katta<sup>1</sup>, L. P. Goss<sup>1</sup>, W. M. Roquemore<sup>2</sup>, L.-D. Chen<sup>3</sup>

<sup>1</sup>Innovative Scientific Solutions, Inc., Dayton, Ohio

<sup>2</sup>Wright Laboratory, WL/POSC, Wright Patterson AFB, Ohio

<sup>3</sup>Department of Mechanical Engineering, The University of Iowa, Iowa City, Iowa

**Abstract**—Jet diffusion flames differ from corresponding cold jets in several aspects; for example, the flames have longer potential cores and undergo slower transition to turbulence. Understanding the processes that make the flames behave differently from the cold jets helps develop accurate mathematical models for practical combustors. By using reactive-Mie-scattering laser techniques details of the flow structures of both the combustions and cold flows are obtained. These flow-visualization images suggest that the vortices inside the flame remain coherent for a long time and undergo structural changes as they convect downstream. Using a third-order accurate, time-dependent, axisymmetric numerical code these flows are simulated and the code is tested for its ability to predict the differences observed between the reacting and the cold jets. Numerical experiments are performed to understand the mechanisms responsible for these differences. Based on the numerical results an explanation is provided for the longer coherence lengths for vortices in flames. Experiments and numerical simulations are also made for flames at higher jet velocities to investigate the turbulent structure of a jet diffusion flame.

## Introduction

The understanding of jet diffusion flames is important in many practical applications and for developing theories of combustion processes. Because of this, they have been actively studied since the classic works published in the *3rd Symposium on Combustion Flame and Explosion Phenomena* in 1949 (Wohl et al., 1949; Hottel and Hawthorne, 1949; Hawthorne et al., 1949; Wohl et al., 1949). Considerable data on statistical quantities such as time-averaged and rms values of velocity, temperature, and species concentrations have been obtained with single-point measurement techniques (Bilger, 1976; Eickhoff, 1982; Faeth and Samuelson, 1986). These data have formed the bases for understanding many of the processes occurring in jet diffusion flames. Because of the success of the statistical approach there is a tendency to think about combustion processes in terms of time-averaged parameters. For engineering applications, there is definite value and, in many cases, a necessity of thinking in terms of mean values of parameters. However, there is a danger to this line of thinking in that the mean and fluctuating quantities can, in many cases, mask

the physics and chemistry that are germane to understanding the fundamental processes that give rise to the statistical results. This is particularly true for near-laminar and transitional jet flames in which the impact of large-scale, organized, buoyancy-induced vortices on the air side of the flame and the Kelvin–Helmholtz-type vortex structures on the fuel side of the flame dominate the flame characteristics (Yule et al., 1981; Eickhoff and Winandy, 1985; Coats and Zhao, 1988; Roquemore et al., 1989; Davis et al., 1991). To gain an insight into these processes, it is helpful and perhaps essential to think in terms of the dynamic characteristics of jet flames.

This paper attempts to develop a qualitative view of the dynamic processes responsible for some of the important physics occurring in propane jet diffusion flames. The approach is to examine the structure of reacting and nonreacting jet flows experimentally and then to use a direct numerical simulation to probe the physics of the dynamic processes in these flows.

## Experimental Methods

### *Experimental Setup*

The experimental setup consists of vertically mounted coannular jets and is described in Chen and Roquemore (1986). Unless otherwise stated, the central fuel jet is a 25.4-mm-diameter tube which contracts to a 10-mm-diameter nozzle. The nozzle is designed to provide a flat mean velocity profile with low velocity fluctuations at the nozzle exit. The annulus air jet has a diameter of 245 mm. An air velocity of 0.15 m/s was found to be sufficient to reduce the room air disturbances in the first 15 diameters of the jet exit while not causing a significant effect on the visible flame structure.

### *Reactive-Mie-Scattering (RMS) Technique*

The RMS technique provides a more detailed view of the mixing processes than is normally obtained by the shadowgraph and smoke (performed particle) visualization techniques (Chen and Roquemore, 1986). It involves seeding both the fuel and the dry annulus air with  $\text{TiCl}_4$  vapor. The  $\text{TiCl}_4$  reacts spontaneously and nearly instantaneously and nearly isothermally with the water product of the flame to form micron-size  $\text{TiO}_2$  particles. The Mie scattering from these particles provides a view of where: (1) the water product is *molecularly* mixed with the air outside the flame surface, (2) the fuel is mixed with the water product inside the flame surface, and (3) the streakline pattern that results from the convection of the  $\text{TiO}_2$  product downstream.

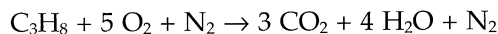
Both horizontal and vertical views of the flame were captured by the RMS technique. A camera positioned at right angles to a laser sheet passing through the center of the fuel jet provided a vertical view of the flame. The horizontal view was obtained by looking down at an angle of about  $75^\circ$  on a horizontal laser sheet. A pulsed Nd:YAG laser was used as a light source and was electronically triggered when the camera shutter was opened. Both the orange-colored blackbody radiation from the soot particles and the scattered green-colored laser light from  $\text{TiO}_2$  particles (Mie scattering) were recorded on the film. The flame luminosity was integrated over the 2-ms camera shutter speed, while the Mie scattered light was captured during the 15-ns duration of the laser pulse. The luminous yellow flame surface appears to be 2D in the photographs, which is a 3D surface superimposed on the 2D photograph. Using the color discrimination between the luminous flame and the 2D Mie scattered light, one can obtain a clear interpretation of the flame photographs.

## Mathematical Model

### Formulation

A time-dependent axisymmetric model which solves for axial- and radial-momentum equations, continuity, enthalpy, and species conservation equations is used to simulate the reacting and nonreacting flow fields associated with coannulus jets. The body-force term due to the gravitational field is included in the axial-momentum equation. Density is obtained by solving the state equation while the pressure field at every time step is determined from pressure Poisson equations. Even though all the governing equations are solved in an uncoupled manner and iteratively, the species conservation equations are coupled through the source terms during the solution process to improve the stability of the algorithm.

In the present analysis of reacting flows a simple global-chemical-kinetics model involving propane, oxygen, water, carbon dioxide, and nitrogen is used. The stoichiometry follows



and the specific reaction rate is written in Arrhenius form. In order to represent very fast chemical kinetics, an activation energy of 1 kcal/mol and a pre-exponential constant of  $1.0 \times 10^{19} \text{ m}^6/\text{mol}^2/\text{s}$  is used.

An orthogonal, staggered grid system with varying cell sizes in both the  $z$  and  $r$  directions is utilized. The momentum equations are integrated using an implicit QUICK-EST (quadratic upstream interpolation for convective kinematics with estimated streaming terms) numerical scheme (e.g., see Katta et al., 1994; Leonard, 1979) which is third-order accurate in both space and time and has a very low numerical diffusion error. The species equations, which have relatively large source terms, are integrated using a second-order upwind scheme. By rearranging the terms, the finite-difference form of each governing equation at all grid points is written as a system of algebraic equations which is then solved by using the alternative direction implicit (ADI) technique. The time increment,  $\Delta t$ , is determined from the stability constraint and maintained as a constant during the entire calculation. The pressure field at every time step is accurately calculated by simultaneously solving the system of algebraic pressure Poisson equations at all grid points using the LU (lower-upper) decomposition technique.

Temperature- and species-dependent thermodynamic and transport properties are used in present formulation. The enthalpy of each species is calculated from polynomial curve-fits, while the viscosity, thermal conductivity, and diffusion coefficients of the species are estimated from the Lennard-Jones potentials.

### Boundary Conditions

The flow field considered in the present study has vortical structures of two different scales. Small-scale vortices develop on the fuel side of the flame (stoichiometric) surface along the shear layer of the fuel jet and larger-scale vortices are formed on the air side of the flame surface. The computational domain and the boundary conditions employed to capture these vortical structures are shown in Figure 1. The outer boundaries II and IV (cf. Figure 1) of the computational domain are located 40 and 15 nozzle diameters from the nozzle exit and the centerline, respectively, which are sufficiently far to minimize the propagation of disturbances into the region of interest. Flat velocity profiles are used at the fuel and air inflow boundaries. The outflow boundary in these flows is difficult to treat

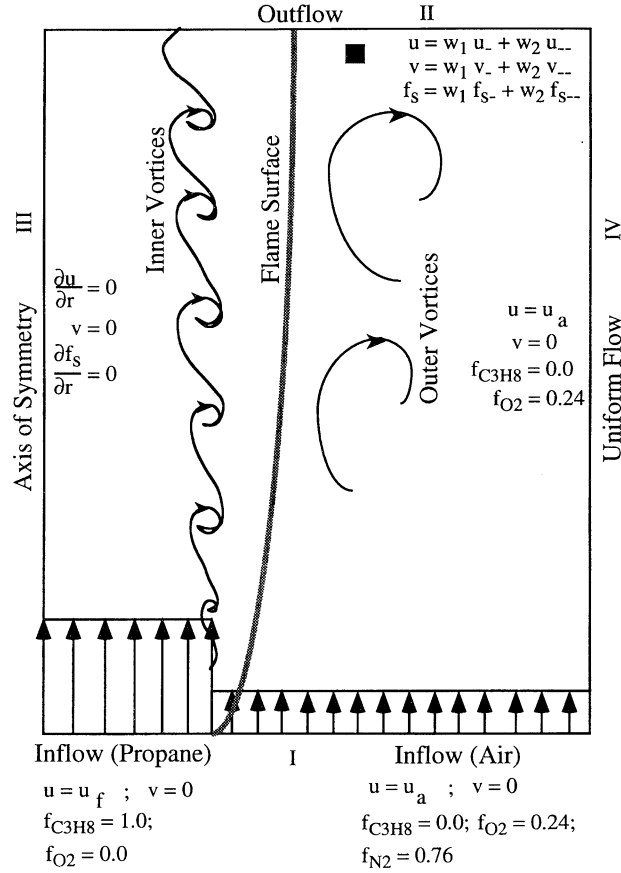


**Figure 1** Computational domain and boundary conditions used in the numerical simulations.

because the flow leaving this boundary continuously evolves in time as the large outside and small inside vortices cross this boundary. A simple extrapolation procedure with weighted zero- and first-order terms is used to estimate the flow variables on the boundary. The weighting functions,  $w_1$  and  $w_2$  (cf. Figure 1), are selected by the trial-and-error approach; the main criterion used is that the vortices crossing the outflow boundary should leave smoothly without being distorted.

## Results and Discussion

### Vortical Structures

Several investigators have observed that jet diffusion flames possess longer potential cores and undergo slower transition to turbulence than the corresponding nonreacting cold jets (Yule et al., 1981; Eickhoff and Winandy, 1985; Coats and Zhao, 1988; Roquemore et al., 1989). These experiments indicate that the vortical structures in flames of low or transitional Reynolds numbers remain coherent for many nozzle diameters downstream. Typical flow fields representing cold and combusting jets are obtained using RMS technique and are shown in Figures 2(a) and 2(b), respectively. A long, straight tube with exit diameter of 11 mm was used in both experiments. Propane fuel was issued from the tube with a mass-averaged velocity of 2.0 m/s which corresponds to a Reynolds number of 3600 into a low-speed coannulus air flow. Since  $TiCl_4$  was added only in the fuel jet of Figure 2(a), jet spreading and potential core may be identified from the outer and inner edges of



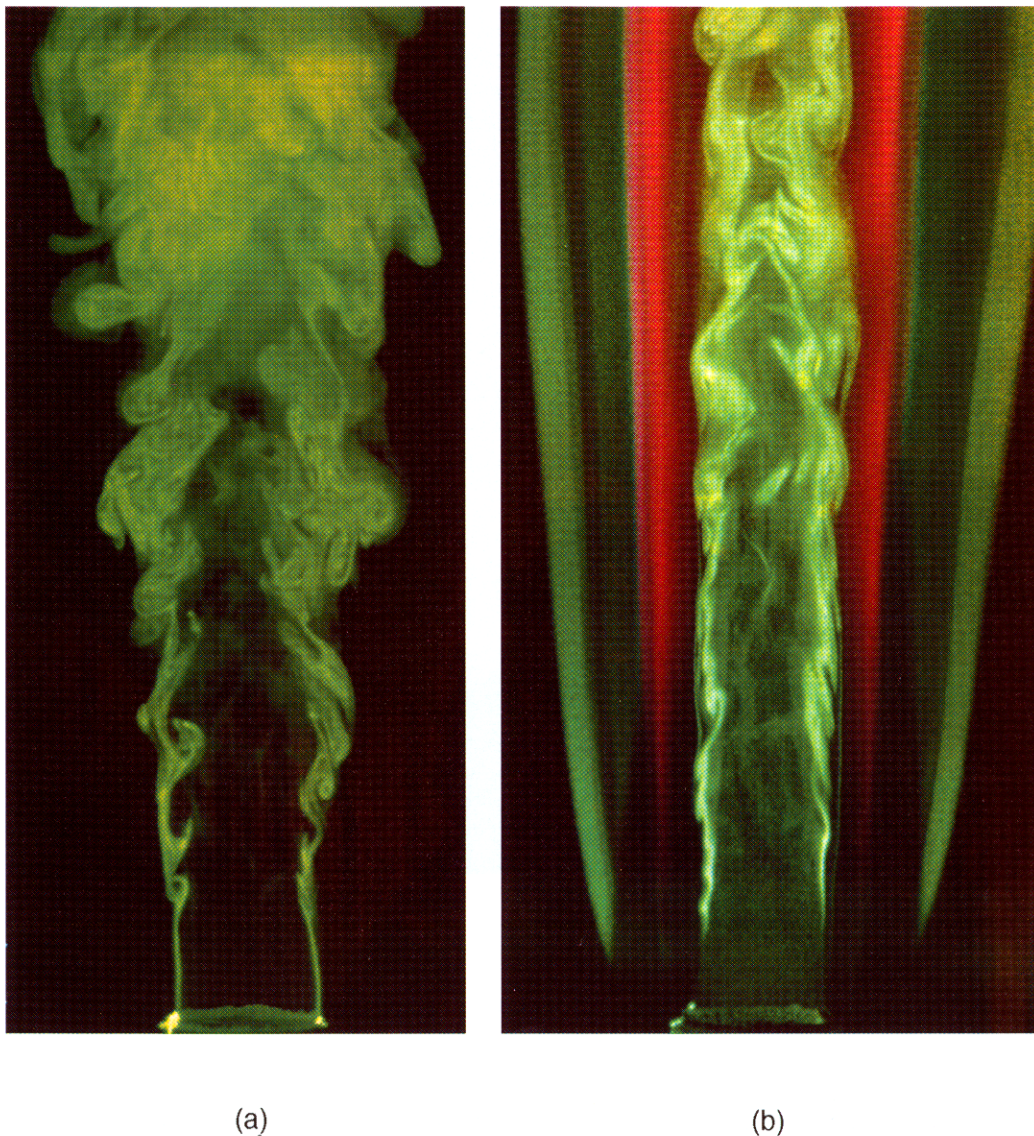


**Figure 2** Propane jets emanating from 11-mm-diameter tube into low-speed coannulus air flow. Flow visualization is made using RMS laser-sheet-light technique. (a) Nonreacting (cold) flow at  $Re = 3626$ ; (b) reacting (flame) flow at  $Re = 3988$ . Orange color represents the flame zone.

the green color, respectively. On the other hand, in the case of flame (Figure 2[b]), the potential core may still be identified in the same way; however, due to destruction of  $TiO_2$  at flame temperatures, jet spreading may be obtained by locating the outer edge of the high-temperature or orange-color region. As expected, the spreading of fuel jet is much slower and potential core is longer in flame. However, the vortical structures in both the cold flow and flame are random and diffusive and do not exhibit coherence nature.

It is known that flow in a long, straight tube becomes turbulent for Reynolds numbers greater than 2000. Because the Reynolds number of the flows (3600) in Figure 2 has exceeded the transitional Reynolds number of the pipe flow, the fuel jet exiting from the central tube might have become turbulent which, in turn, effects the natural growth process of instabilities (or vortices) in the jet shear layer. To investigate the effect of combustion on jet spreading, the turbulence in the fuel flow at the burner exit was



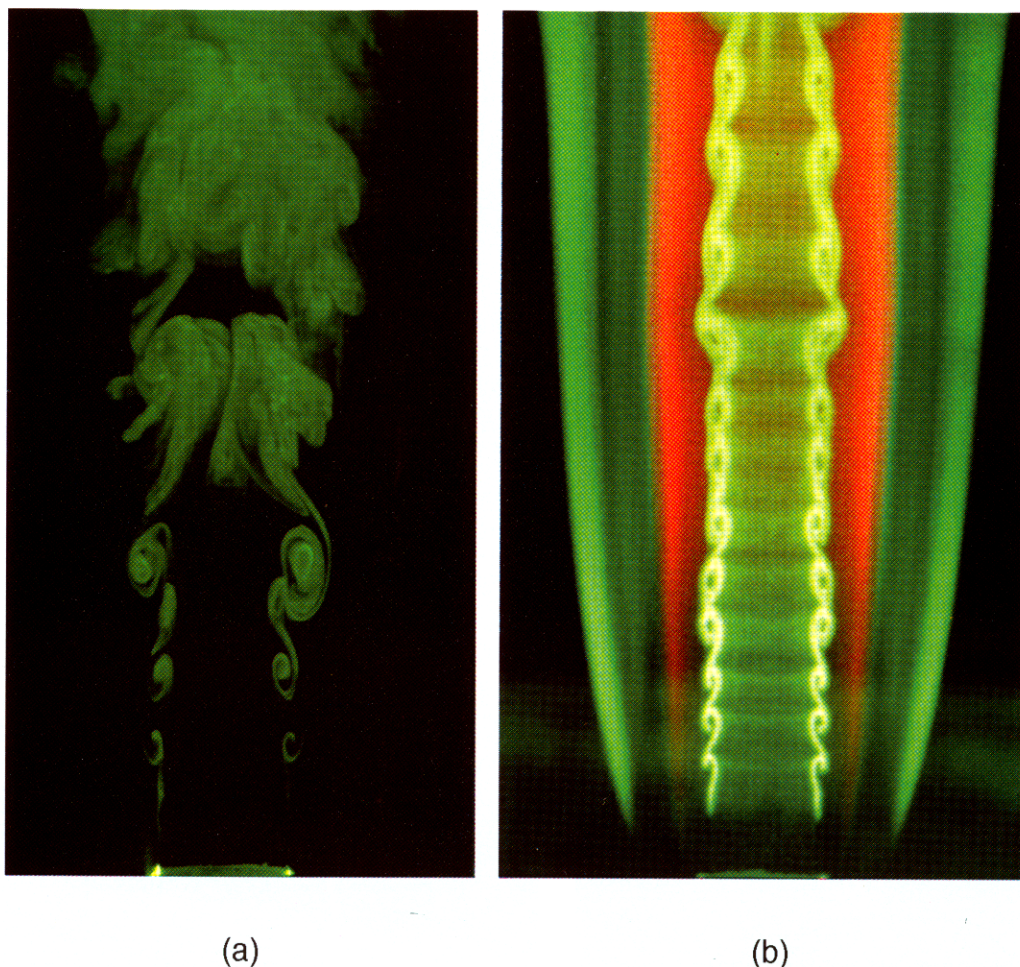


**Figure 3** Visualization of vortical structures using RMS technique in (a) cold flow at  $Re = 3988$ , and (b) flame at  $Re = 3988$ . Burner consists of 10-mm-diameter contoured nozzle and 150-mm-diameter annulus duct.

reduced significantly by replacing the long, straight tube with a larger diameter tube and a contoured nozzle. The structures of the cold and combusting flows obtained with contoured nozzle for a slightly different flow rate ( $Re = 4000$ ) are shown in Figures 3(a) and 3(b), respectively. Velocity measurements at the nozzle exit indicate that the fluctuations are less than 1% of mean velocity. Similar to the observations made with tube flows (Figure 2) the contoured nozzle also results in less jet spreading and longer potential core for the flame (Figure 3[b]) compared to those for the cold flow (Figure 3[a]). However, in contrast, the contoured-nozzle flows yielded well-defined vortical structures in the shear layer. The coherence of vortices in cold flow is lost when vortex merging occurs at about two nozzle diameters downstream of the jet exit. The merged vortex pair remained intact while moving downstream for another three nozzle diameters before the vortex pair broke down into smaller fluid elements and the fluid elements exhibited a random and diffusive nature. However, in the case of combustion flow, no vortex merging was observed. The vortices remain coherent over a long distance and the vortex size also remains nearly unchanged.

In order to better understand the experimentally observed differences in the growth process of vortical structures in cold and combustion environments, these flows are numerically simulated using the time-dependent code discussed earlier. Numerical



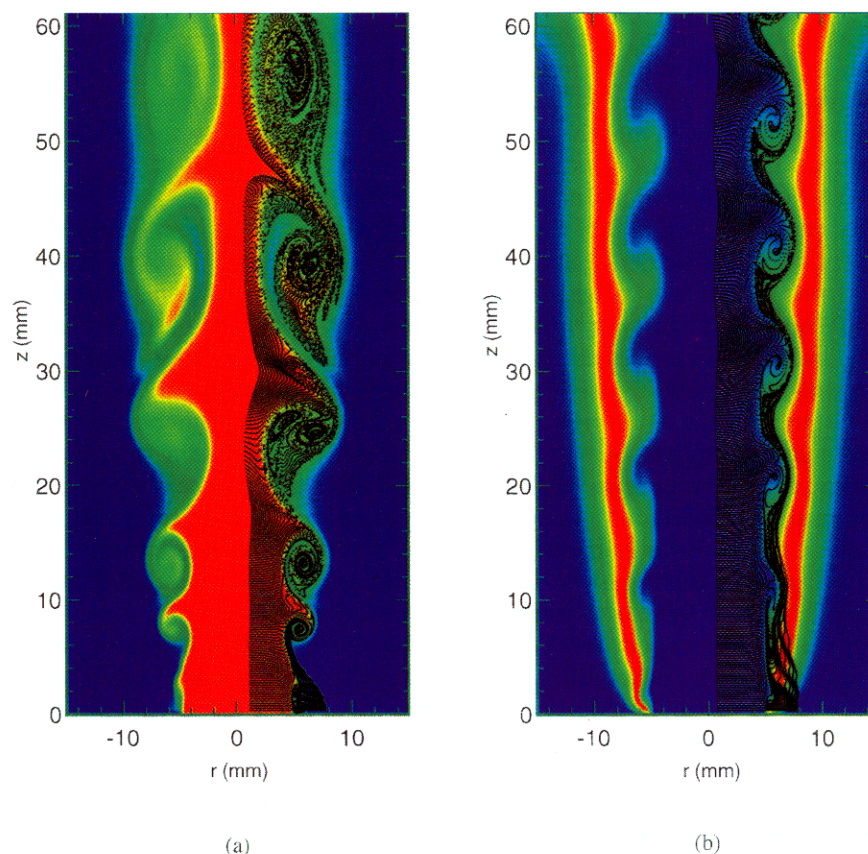


**Figure 4** Numerical results obtained for cases shown in Figure 2 using axisymmetric, time-dependent model. (a) Iso-mass-fraction contours of propane in cold flow; (b) iso-temperature contours in flame. Instantaneous locations of particles injected at nozzle exit are superimposed with black dots on right half of each image.

simulations were carried out using flat velocity profiles at the exits of the nozzle and the annulus duct which correspond to the respective mass flow rates used in the experiment. As the shear-layer vortices in experiments manifest from the small disturbances that are normally present in the incoming jets, a small, forced perturbation is needed in the calculations for triggering the instabilities. Previous studies have indicated that perturbations provided in different variables such as velocity or pressure result in similar shear-layer structures. Therefore, in the present study, a perturbation of 0.3% in the axial velocity was introduced in the shear layer formed between the fuel and air jets. Inviscid stability analysis suggests that the most amplified frequency for the co-annular jet shear layer considered is about 400 Hz, using a Strouhal number of 0.2 with nozzle diameter and mass-averaged jet exit velocity being the length and velocity scales. In actual calculations, the perturbations introduced at this frequency did not travel beyond 0.08 m. The reason for this could be due to the viscosity of the fluid and the numerical dissipation inherent in the model which becomes increasingly significant at downstream locations where coarse meshes were employed. In order to account for these differences, the most amplified frequency in the simulations was determined by virtually repeating several calculations by varying the perturbation frequency. At 180 Hz the disturbances traveled farther downstream. Computed instantaneous cold flow and flame are shown in Figures 4(a) and 4(b), respectively. Cold flow is visualized in Figure 4(a) by plotting the fuel mass-fraction contours color coded between red and blue with these two limiting colors representing the

pure fuel and no fuel, respectively. Instantaneous iso-temperature contours of the flame are shown in Figure 4(b) with red and blue colors representing maximum and room temperatures, respectively. In both figures, instantaneous locations of the massless particles that were introduced into the shear layer at exit of the nozzle are superimposed over the contour plots with black dots.

Similar to the observations made from experimental flow images, calculations also predict that the spreading rate of fuel jet is higher in the case of cold flow and the length of the potential core is longer in the flame case. Merging of two vortices in the cold flow is evident from the particle traces plot at about two nozzle diameters downstream of the exit ( $z = 20$  mm). This merging location matches well with that observed in the experiments. The individual vortices that are involved in pairing kept their identity for another four nozzle diameters downstream ( $20 \text{ mm} < z < 60 \text{ mm}$ ) before the pair got involved in another merging process at about  $z = 70$  mm. Even though experiments also show pattern for the convective motion of the paired vortices, results obtained with the present axisymmetric model become more skeptical soon after merging takes place. It is known that the azimuthal instabilities also become amplified during merging process of toroidal vortices and it results in three-dimensional flow. On the other hand, merging of vortices is not occurring in the flame case of Figure 4(b) and model predicted that these shear-layer vortices exhibit a high level of coherence and grow very slowly.

Larger view of the experimental flame in Figure 4(a) up to a height of about 180 mm is shown in Figure 5(a). The jet diffusion flame depicted in this figure exhibits two distinct vortical structures — one inside and the other outside the flame surface (orange-color region). While the smaller-scale inner vortices present in the jet shear layer lead to the development of turbulence in flames at higher jet velocities, the slowly moving outer vortices are associated with the low-frequency flame-flickering phenomenon first observed by Chamberlin and Rose (1928). As the jet shear layer is neither laminar nor turbulent, these flames are commonly referred to as transitional flames. The double-vortex structure of such transitional jet diffusion flame was first reported by Yule et al. (1981) and subsequently by Eickhoff (1982), Eickhoff and Winandy (1985), and Chen and Roquemore (1986).

The outer vortex structures of the flame in Figure 5 are the dominant characteristic of laminar and transitional jet diffusion flames. These slowly moving toroidal-vortex structures interact strongly with the flame and create outward bulges in the flame surface. The flickering appearance of the flame is the result of the upward convective motion of the flame bulge. Buckmaster and Peters (1986) were the first to recognize that buoyancy is responsible for the low-frequency instability associated with flame flicker. They argued that the natural convection of the flame and the forced convection of the jet are decoupled because the stoichiometric flame surface is located outside the shear layer of the jet; thus, the buoyancy-induced instability is nearly independent of jet characteristics such as fuel-jet exit velocity, nozzle diameter, and fuel type. By including buoyancy in the calculations they performed a linear instability analysis on a two-dimensional infinite candle flame. Their calculations resulted in a flicker frequency that was in good agreement with experiments. Recently, direct numerical simulations of buoyant jet flames have provided support and given additional insight into the findings of Buckmaster and Peters. By adopting a flame-sheet model, Davis et al. (1991) successfully simulated the dynamic structure of a 0.12-m/s buoyant propane jet diffusion flame established with a 22-mm-diameter tube. They showed that the flame is stationary and has no outside vortices when  $g$  was set to zero. In the presence of buoyancy, the outer vortex structures develop, and their upward convective motion is shown to be responsible for the 13-Hz flicker frequency associated with the flame bulge. Ellzey et al. (1991) successfully simulated a transitional hydrogen-nitrogen jet diffusion flame established by a 5-mm contoured nozzle having an exit velocity



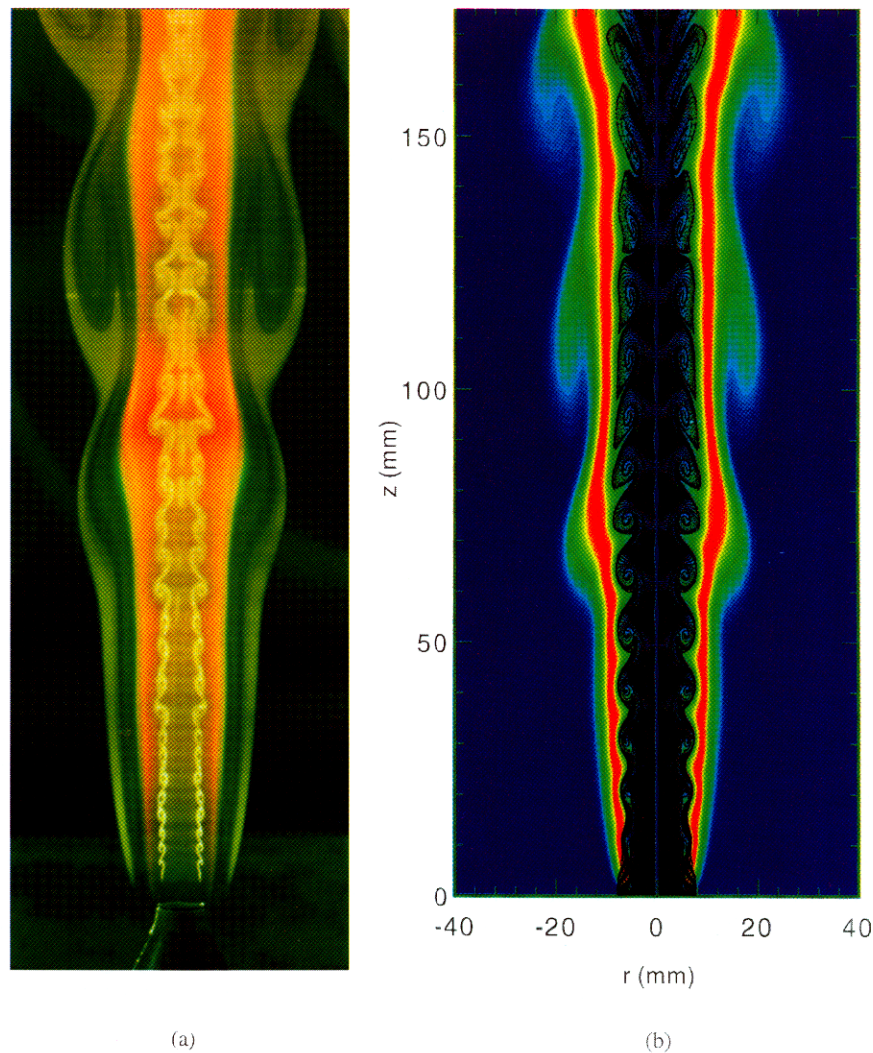


**Figure 5** Comparison between (a) experimental and (b) predicted flame. Vortical structures and flame surface are visualized in experiment using RMS laser light and direct light, respectively. Particle traces and temperature contours show the computed inner and outer vortices, respectively. Red-color zone represents flame region.

of 10 m/s. They also showed that the convective motion of the outside vortex structures is responsible for flame flicker and that buoyancy is required to produce these structures.

The computed results obtained for the flame shown in Figure 5(a) are depicted in Figure 5(b). These results, in fact, represent a larger view of those shown in Figure 4(b). Because of the buoyancy term in the axial-momentum equation, vortices outside the flame surface (red-color region) developed as part of the solution. A comparison of experimental (Figure 5[a]) and computed (Figure 5[b]) flames indicates that the present calculations have captured the important details of a transitional flame.

A good agreement was obtained between the calculated and measured flame-flicker frequency. At 80 mm above the nozzle, a 15.8-Hz frequency was obtained from the computed temperature fluctuations, while the frequency was observed to be approximately 15 Hz in the experiments. The instantaneous iso-temperature color plot of the computed flame in Figure 5(b) is at a phase very near that of the experimental flame in

Figure 5(a). These instantaneous images show that the bulging and squeezing of the computed flame surface occur at heights that are slightly upstream of the corresponding processes on the experimental flame. It should also be noted that the computed flame has three outer vortices, while the experimental image shows only two and one half vortices. The flat velocity profile used in the calculations at the exit of the annulus duct could account for this difference. The rapidly converging nozzle in the experiment is believed to generate a significantly thick boundary layer (approximately 5 mm) for the annulus air flow. This reduction in velocity outside the flame surface could be responsible for the slightly lower frequency and larger-size vortices observed in the experiment.

The vortices inside transitional jet diffusion flame of Figure 5(a) maintained their coherence for long distances downstream. Comparison of Figures 5(a) and 5(b) shows that the model has captured this important feature. Even the coherence lengths in the calculated and measured flames are about the same. The inner (or shear-layer) structures of the experimental flame are weakened at  $z = 165$  mm and completely dissipated at a height of approximately 210 mm. This weakening of the inner vortices appears to be associated with the third flame bulge. A change in the direction of rotation of the inner vortices may be seen in both the experimental and computed flames at a height of 150 mm and this process seems to be related to the second outward flame bulge.

The longer coherence length for the inner (or shear-layer) vortices in the case of combusting flow was conveniently explained by many authors (Eickhoff, 1982; Yule et al., 1981; Eickhoff and Winandy, 1985; Coats and Zhao, 1988) by the fact that the effective Reynolds number decreases due to the increase in viscosity. Chen et al. (1991) suggested that the vorticity destruction inside the flame due to the baroclinicity and volumetric expansion laminarizes the flame. Recent calculations of Katta and Roquemore (1993) further indicate that the buoyant acceleration of the hot gases also plays a significant role in retarding the transition to turbulence and in sustaining the orderliness of the inner structures. The influence of viscosity and gravity on the inner vortices is illustrated in the numerical experiments of Katta and Roquemore (1993).

In a flame, combustion of fuel and oxidizer results in formation of products and heat release, which, in turn, effect the fluid dynamics of the flow by changing the density (or volumetric expansion), the transport properties, and the body forces due to buoyancy. When all these three changes are *absent*, the resulting flow will be identical to the cold flow as shown in Figure 4(a). Therefore, the noted differences in the growth of vortical structures in cold and combustion environments should be resulting from the changes in density, transport properties, and body forces. To investigate their role on vortex dynamics two additional calculations were made; one by not considering the changes in density and body forces and in another only the body forces were neglected. The effects of these three on the vortex dynamics are studied in the first two simulations. Color contours of instantaneous mixture fraction obtained for a flame with  $g = 0$  and zero volumetric expansion are shown in Figure 6(a). The latter effect was simulated by maintaining the density of the fluid constant (incompressible) while allowing the viscosity, diffusion, and other transport properties of the flow to change with the calculated temperature. The solid circles represent the contour of the stoichiometric-mixture-fraction surface. Results obtained for the flame calculation with  $g = 0$  are shown in the form of instantaneous-mixture-fraction color contours in Figure 6(b). Transport property calculations made in this simulation are identical to the ones made for the flame in Figure 6(a). Finally, the flame in Figure 6(c) is the mixture-fraction contour visualization of the flame in Figure 5(b). The green lines in this figure are the iso-temperature contours plotted only on the air side of the stoichiometric surface to visualize the outer vortical structures.

As described earlier, Figure 6(a) examines the effects of the temperature dependence of the viscosity and other diffusion coefficients, neglecting volumetric expansion. The stoichiometric surface moves away from the shear layer due to increased diffusion, and the



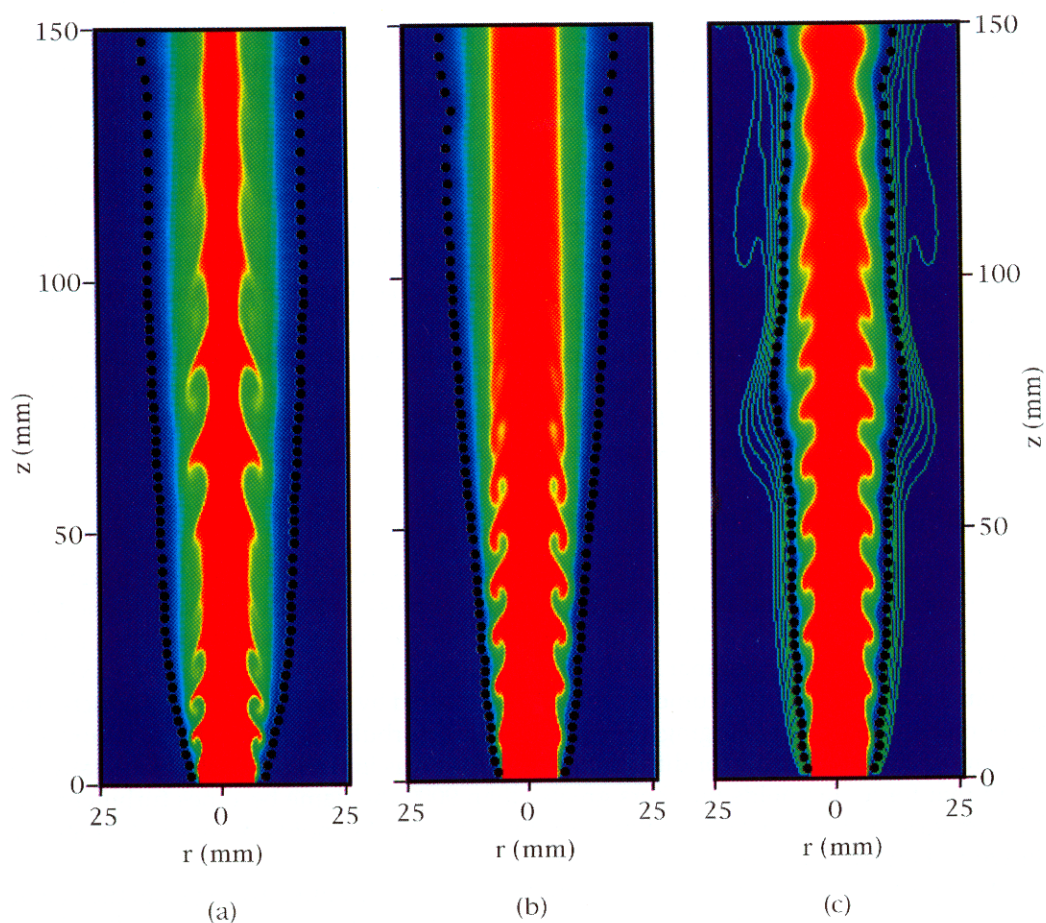


**Figure 6** Iso-mass-fraction contours of propane obtained with different assumptions on combustion products. (a) Volumetric expansion is neglected; (b) gravitational force is neglected; (c) same as the flame shown in Figure 5(b).

viscous layer along the stoichiometric surface appears to damp the growth of the inner vortices (cf., Figures 4[a] and 6[a]). The first vortex-merging in this case takes place at a location between two and three nozzle diameters downstream. Since the viscous layer surrounding the shear layer acts as a shield to the shear-layer vortices, these vortices are stretched axially more than radially.

When heat release was also added to the calculations (Figure 6[b]), the inner vortices did not grow significantly and were completely dissipated at approximately 100 mm above the nozzle. The reason for this is that the volumetric expansion moves the stoichiometric surface closer to the shear layer, and viscous fluid near the flame surface is entrained into the vortices, leading to their dissipation. When buoyancy is added to the computation (Figure 6[c]), the flame surface moves even closer to the shear layer and one might expect the inner structures to decay more quickly than for the condition in Figure 6(b) because more viscous fluid is expected to be entrained into the vortices. Instead, the inner vortices in Figure 6(c) travel farther downstream with only a small growth rate. Therefore, a comparison of Figures 6(b) and 6(c) suggests that buoyancy is a major factor in maintaining the long coherence length of the inner vortices since it must overcome the dissipative effects of viscosity and volumetric expansion due to heat release.

Referring to Figure 4(b) it may be noted that the inner vortices are located in the blue region where temperature is low at a radial position between 4 and 7 mm. The

high-temperature region (red color) is separated from the vortices. The acceleration of high-temperature fluid by buoyancy force entrains fluid from neighboring regions on both sides. Therefore, the amount of viscous fluid that is entrained into the vortices is reduced; the damping of vortices is reduced. The acceleration of fluid in the flame zone also reduces the velocity gradient in the shear layer which, in turn, reduces the entrainment of neighboring viscous fluid into the shear-layer vortices. In the case of cold jets, the axial-velocity gradient which is responsible for the formation of the shear-layer vortices is also responsible for their destruction as the higher velocity gradient leads to higher entrainment of the lower speed fluid into the vortices. Thus, the transitional jet flame and the cold jet differ in several important ways. In the flame case, fluid is entrained into the hot buoyant accelerated flame rather than into the inner vortices. The buoyant acceleration reduces the axial-velocity gradient of the jet shear layer, which reduces the tendency of fluid to be entrained into the inner vortices. In a cold jet significant entrainment of the low-speed fluid into the vortices leads to the loss of coherence of the vortices.

### *Vortical Structures of High-Speed Flows*

As seen from Figure 2(a), a laminar jet flow becomes turbulent when the shear-layer vortices grow rapidly and involve in the merging process. When a diffusion flame forms in the neighborhood of the shear layer the growth of the vortices will be retarded and the jet flow tends to become laminar. However, at higher jet velocities, the growth of vortices in a flame is expected to overcome the dissipation caused by the combustion products. This phenomenon results in merging of vortices and a turbulent flame. The structure of a propane jet diffusion flame for different jet velocities was investigated experimentally and found that for jet Reynolds numbers greater than 9000 the flame becomes turbulent. The RMS images of the cold and combustion flows at a jet Reynolds number of 22,600 are shown in Figures 7(a) and 7(b), respectively.

As expected, the cold flow became turbulent very quickly after exiting from the nozzle. The vortices are quite small and do not exhibit any coherent behavior. A close look at lower and higher Reynolds number cold flows (Figures 2[a] and 7[a]) suggests the following important features of a turbulent jet flow: (1) at higher Reynolds number the jet shear layer becomes turbulent well before the entire jet does, (2) small-scale structures dominating the high-speed turbulent jet in which presence of large-scale structures is also evident, and (3) height of the potential core is more or less the same (about five nozzle diameters) for both the Reynolds-number cases.

The turbulent flame shown in Figure 7(b) is partially lifted and has an interesting pattern near the flame-base region. Due to the minor differences in the construction of the nozzle and outer duct, the jet flow is not perfectly symmetric about its axis. As the jet velocity of 9.8 m/s is very close to the lift off velocity for propane jet diffusion flames, the asymmetry in the burner geometry caused the flame to lift off on the left half (Figure 7[b]) and attached on the right half. Note, in the reacting flow experiments, only fuel jet was doped with  $\text{TiCl}_4$  and the annulus air was dried to remove the moisture. The  $\text{TiO}_2$  particles, which are marked by the green-colored scattered light, will form only when  $\text{H}_2\text{O}$  is present as a reaction product. Therefore, in the absence of flame (or combustion) in the left half of jet near the flame base,  $\text{TiO}_2$  particle did not form and the shear-layer structures became invisible. As seen from the start of the green color, the lifted portion of the flame is anchored at an axial location of about two and a half nozzle diameters downstream of the nozzle exit. On the other hand, coherent (or organized) vortical structures have developed near the exit of the nozzle on the right half where the flame is attached to the nozzle. However, these vortices start losing coherence when merging of vortices begins to happen at about one nozzle diameter downstream of the exit and, subsequently, the shear layer became turbulent. Because of the cold conditions on the left half of the flame base, it is



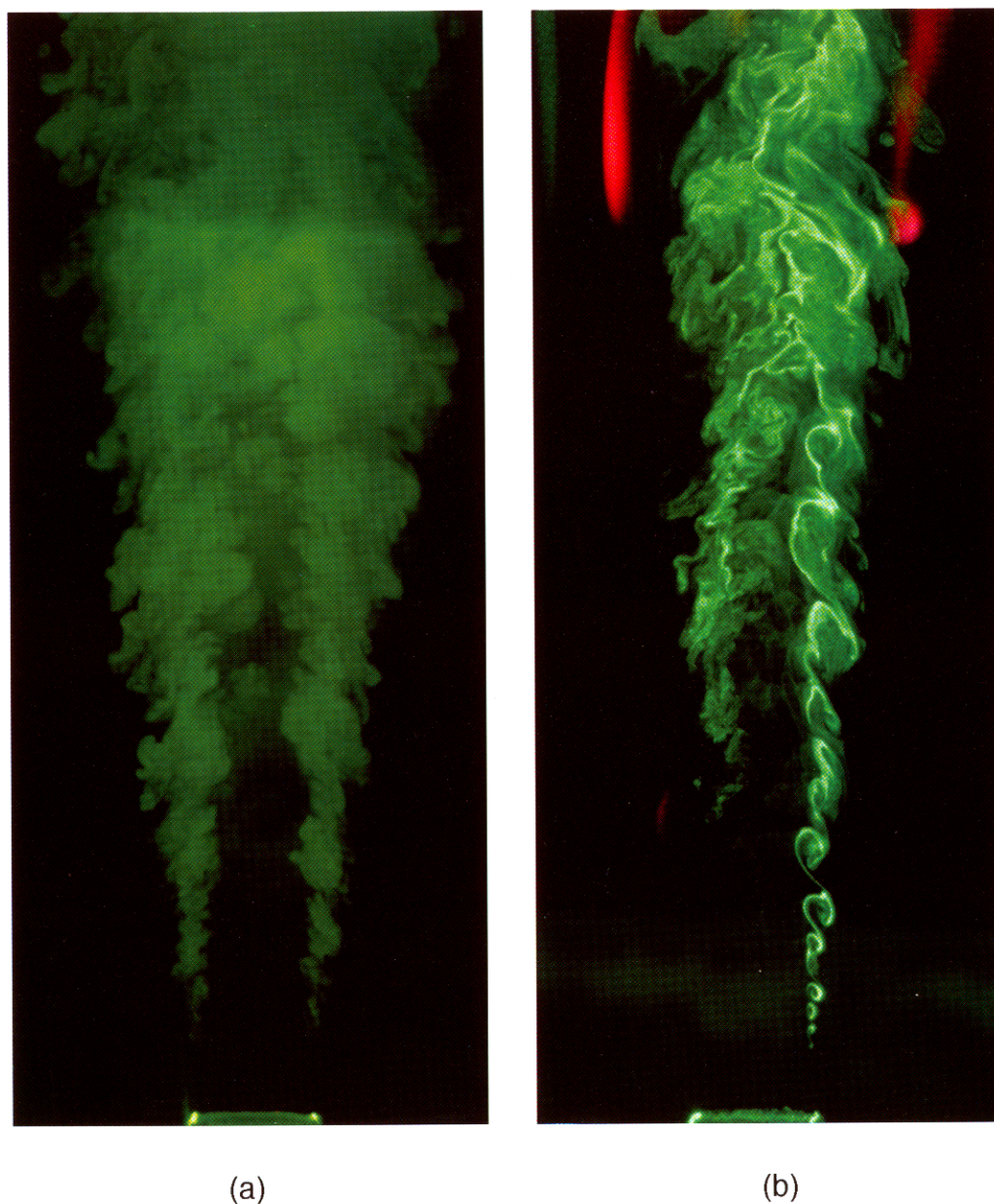


**Figure 7** Visualization of high-speed flows using RMS technique. (a) Cold flow at  $Re = 21,270$ ; (b) flame at  $Re = 22,600$ . Burner consists of 10-mm-diameter contoured nozzle and 150-mm-diameter annulus duct.

believed that the shear layer became turbulent quite early similar to that observed in a cold jet (Figure 7[a]) and overall the flow on the left half seems to be more turbulent than that on the right half.

Using the axisymmetric mathematical model described earlier, calculations were made for the high-speed reacting flow case shown in Figure 7(b). Unlike the fixed-frequency perturbation used for driving the shear layer of the low-speed jet (Figure 4[a]), a random noise was introduced in the shear layer of the high-speed jet to allow the calculations to respond to the most amplified frequency naturally. The random perturbation was applied to a region of about ten grid points within two-grid-point radius at the nozzle exit. No



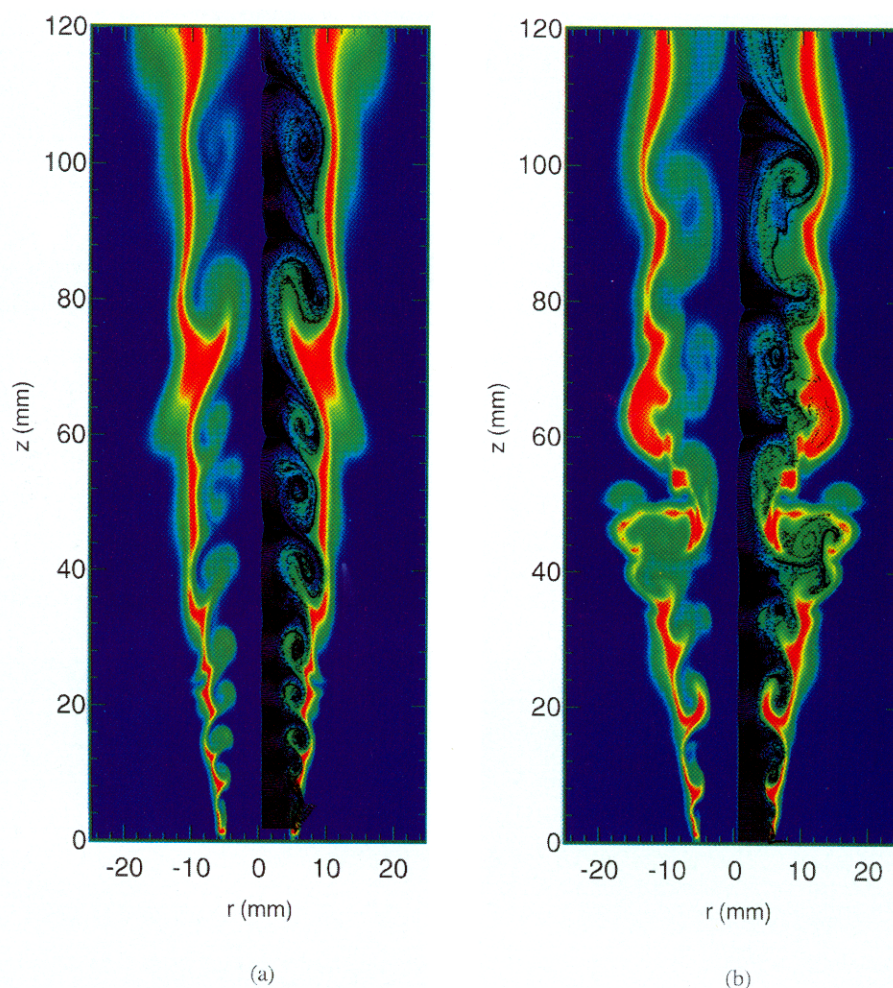


**Figure 8** Predictions made for flame shown in Figure 8(b) using two levels of perturbations. (a) 0.3%; (b) 0.6% of axial velocity. Instantaneous locations of particles superimposed over iso-temperature contours.

other perturbation was used, nor was another portion of the jet perturbed. Two calculations were made with different driving amplitudes to understand the effect of inlet turbulence on the flame structure. Instantaneous results for both cases are plotted in Figure 8 in the form of colored iso-temperature contours with locations of the particles superimposed with black dots. Figure 8(a) represents the results obtained for a driving amplitude of 0.3% of the axial velocity and Figure 8(b) represents those for a driving amplitude of 0.6%. For both cases, the perturbation of shear layer resulted in vortices with an initial crossing frequency of 1800 Hz. However, as seen from Figures 8(a) and 8(b), vortices grew rapidly and got involved in the merging process at about one nozzle diameter downstream of the exit and reduced the vortex crossing frequency to a value much lower than 1800 Hz. Even though the results obtained with an axisymmetric model might become skeptical once the vortices participate in a merging process, the data shown in Figure 8 depict some fundamental characteristics of a turbulent flame shown in Figure 7(b). When a small-magnitude perturbation (which represents a low-level initial turbulence) was used, the shapes of the shear-layer vortices (Figure 8[a]) were modified but not destroyed to an extent noted in the stronger-perturbation (which represents a high-level initial turbulence)



case (Figure 8[b]). The overall structure of the flame in the former case matches with that observed in experiments conducted with contoured nozzles (Figure 7[b]), and the flame structure obtained with 0.6% driving resembles that obtained in tube experiments (not shown here). In neither case, the lift-off at the flame base was predicted as the model was constructed based on very fast chemical kinetics. In both cases of perturbations, puffs of fluid were found to eject out from the shear layer during the vortex-merging processes. Such fluid elements are experimentally observed by several investigators in the studies of turbulent jet flames (Takahashi and Goss, 1992) and are believed to play a significant role in stretching and creating localized holes on the flame surface.

### *Cross Sections of the Vortical Structures*

To investigate the nature of the azimuthal instability in jet diffusion flames experiments were conducted by passing an additional laser sheet light across the flame surface. The RMS images obtained for a tube flow and for contoured-nozzle flows at different jet velocities are shown in Figure 9. These images depict both the longitudinal and azimuthal views of the shear-layer vortices. As seen from Figure 9(a), the azimuthal instabilities have grown to streamwise vortices within one nozzle diameter downstream of the exit. Similar to the toroidal (or ring) vortices that are visualized in the longitudinal section, these streamwise vortices also do not exhibit coherent behavior. Interestingly, the outer ring (green color) seen in the cross-sectional view is also asymmetric — indicating the three-dimensionality of the outer vortices that are developed due to gravitational force. As a very low speed (around 0.1 m/s) annulus flow was used in these experiments irrespective of whether a tube or contoured nozzle was used, the annulus air flow will be laminar. Therefore, it is speculated that the three-dimensionality observed for the outer vortices is a result of the rapid growth of the azimuthal instability of the inner vortices. This speculation may be confirmed by looking at the cross-sectional view of the flow structure obtained for the contoured nozzle at a moderate jet velocity (Figure 9[b]). In this case, the inner shear layer is laminar and the outer ring is quite symmetric even at an axial location of one and a half nozzle diameters downstream.

At transitional jet velocity a train of inner vortices has developed in the shear layer (Figure 9[c]). The cross-sectional view at an axial location of one and a half nozzle diameters downstream indicates that the inner shear layer lost its symmetry with the development of azimuthal instabilities; however, the outer flow remains to be symmetric. Since the inner vortices have not involved in any merging process, shear layer is dominated by the inner toroidal vortices that are nearly symmetric about the jet axis. Combining the observations made from the cross-sectional views of the inner- and outer-flow structures it may be argued that an axisymmetric mathematical model could be used for their prediction as long as the toroidal vortices keep their coherence and do not participate in a merging process. A three-dimensional model, however, should be used for the accurate prediction of flames in which merging of vortices takes place.

### *Conclusions*

The dynamic characteristics of a propane jet diffusion flame for different jet velocities are investigated. To understand the role of combustion on the flame dynamics, cold (nonreacting) flows under identical conditions are also studied. First, the major differences are identified by dissecting the reacting and cold flows with RMS laser-sheet-lighting technique. Then, both of the reacting and cold flows are simulated by using a third-order accurate, time-dependent numerical code. Finally, numerical experiments are performed to gain further insight into the physical processes responsible for the observed dynamic characteristics.

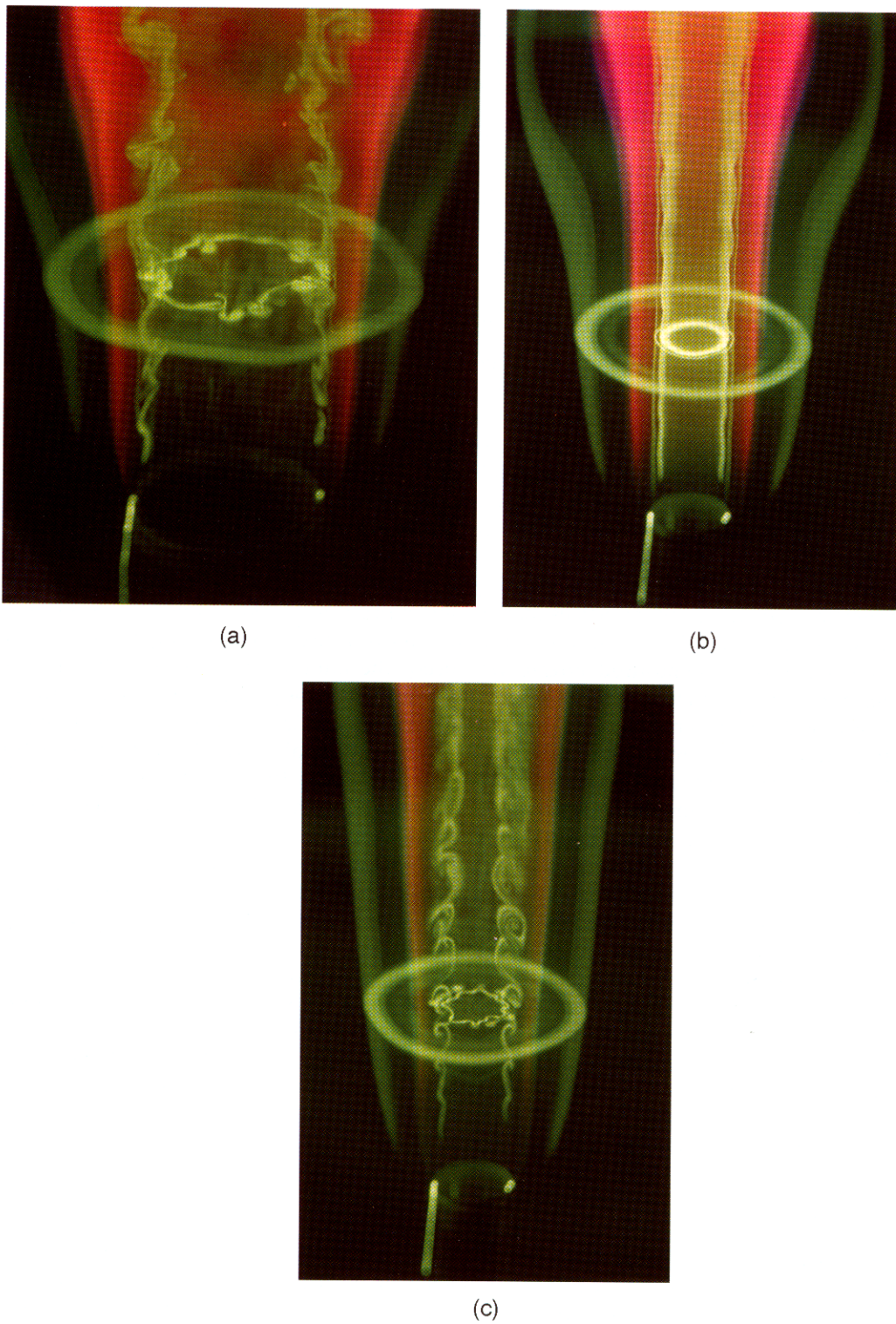


**Figure 9** Visualization of streamwise vortices using a pair of perpendicular laser sheets. (a) Tube flow; (b) nozzle flow at low speed; (c) nozzle flow at transitional speed.

It was observed from the experiments conducted with straight tubes and contoured nozzles that the jet spreading rate is lower and potential core is longer for the jet diffusion flames compared to the nonreacting flows with identical flow conditions. Numerical simulations performed for these conditions also predicted the similar differences between the jet flame and the nonreacting jets. Numerical simulations showed that viscosity, volumetric expansion, and body force due to buoyancy associated with the combustion products are responsible for making the flames less turbulent. Particularly, buoyant acceleration of hot products restrains the vortices from entrainment, resulting in slowly growing vortices with longer coherence lengths. At higher jet velocities the shear-layer vortices inside the flame grow rapidly, involve in the merging process, and become turbulent similar to the scenario noted for the cold jets at lower jet velocities. The growth characteristics of the streamwise vortices resulting from the azimuthal instability of the shear layer are also investigated.

## Acknowledgment

This work was supported in part by the Aerospace Sciences Division of Air Force Office of Scientific Research.

## References

- Bilger, R.W., Turbulent Jet Diffusion Flames, *Prog. Energy Combust. Sci.*, 1, 87, 1976.
- Buckmaster, J. and Peters, N., The Infinite Candle and its Stability — A Paradigm for Flickering Diffusion Flames, in *21st Symp. (Int.) on Combust.*, Combustion Institute, Pittsburgh, 1986, 1829.
- Chamberlin, D.S. and Rose, A., The Flicker of Luminous Flames, *Ind. Eng. Chem.*, 20, 1013, 1928.
- Chen, L.-D. and Roquemore, W.M., Visualization of Jet Flames, *Combust. Flame*, 66, 81, 1986.
- Chen, L.-D., Seaba, J.P., Roquemore, W.M., and Goss, L.P., Buoyant Diffusion Flames, in *22nd Symp. (Int.) on Combust.*, Combustion Institute, Pittsburgh, 1988, 677.
- Chen, L.-D., Roquemore, W.M., Goss, L.P., and Vilimpoc, V., Vorticity Generation in Jet Diffusion Flames, *Combust. Sci. Technol.*, 77, 41, 1991.
- Coats, C.M. and Zhao, H., Transition and Stability of Turbulent Jet Diffusion Flames, in *22nd Symp. (Int.) on Combust.*, Combustion Institute, Pittsburgh, 1988, 685.
- Davis, R.W., Moore, E.F., Roquemore, W.M., Chen, L.-D., Vilimpoc, V., and Goss, L.P., Preliminary Results of a Numerical-Experimental Study of the Dynamic Structure of a Buoyant Jet Diffusion Flame, *Combust. Flame*, 83, 263, 1991.
- Eickhoff, H., *Recent Contributions to Fluid Mechanics*, Springer-Verlag, New York, 1982.
- Eickhoff, H., Turbulent Hydrocarbon Jet Flames, *Prog. Energy Combust. Sci.*, 8, 159, 1982.
- Eickhoff, H. and Winandy, A., Visualization of Vortex Formation in Jet Diffusion Flames, *Combust. Flame*, 60, 99, 1985.
- Ellzey, J.L., Laskey, K.J., and Oran, E.S., A Study of Confined Diffusion Flames, *Combust. Flame*, 84, 249, 1991.
- Faeth, G.M. and Samuelson, G.S., Fast Reaction Nonpremixed Combustion, *Prog. Energy Combust. Sci.*, 12, 305, 1986.
- Hawthorne, W.R., Weddell, D. S., and Hottel, H. C., Mixing and Combustion in Turbulent Gas Jets, in *3rd Symp. on Combustion, Flame and Explosion Phenomena*, Combustion Institute, Pittsburgh, 1949, 266.
- Hottel, H.C. and Hawthorne, W.R., Diffusion in Laminar Flame Jets, in *3rd Symp. on Combustion, Flame and Explosion Phenomena*, Combustion Institute, Pittsburgh, 1949, 254.
- Katta, V.R. and Roquemore, W.M., Role of Inner and Outer Structures in a Transitional Diffusion Flame, *Combust. Flame*, 92, 274, 1993.
- Katta, V.R., Goss, L.P., and Roquemore, W.M., Effects of Nonunity Lewis Number and Finite-Rate Chemistry on the Dynamics of a Hydrogen-Air Jet Diffusion Flame, *Combust. Flame*, 96, 60, 1994.

- Leonard, B.P., A Stable and Accurate Convective Modelling Procedure Based on Quadratic Upstream Interpolation, *Comput. Methods Appl. Mech. Eng.*, 19, 59, 1979.
- Roquemore, W.M., Chen, L.-D., Goss, L.P., and Lynn, W.F., Structure of Jet Diffusion Flames, in *Turbulent Reactive Flows, Lecture Notes in Engineering, Vol. 40*, Borghi, R. and Murthy, S. N. B., Eds., Springer-Verlag, New York, 1989, 49.
- Takahashi, F. and Goss, L. P., Near-Field Turbulent Structures and the Local Extinction of Jet Diffusion Flames, in *24th Symp. (Int.) on Combust.*, Combustion Institute, Pittsburgh, 1992, 351.
- Wohl, K., Gazley, C., and Kapp, N.M., Diffusion Flames, in *3rd Symp. on Combustion, Flame and Explosion Phenomena*, Combustion Institute, Pittsburgh, 1949, 288.
- Wohl, K., Kapp, N.M., and Gazley, C., The Stability of Open Flames, in *3rd Symp. on Combustion, Flame and Explosion Phenomena*, Combustion Institute, Pittsburgh, 1949, 3.
- Yule, A.J., Chigier, N.A., Ralph, S., Boulderstone, R., and Ventura, J., Combustion-Transition Interaction in a Jet Flame, *AIAA J.*, 19(6), 752, 1981.



**AIAA 98-2917**

## **Structure of Square Coaxial Nozzle Flows**

Jason W. Bitting,  
Dimitris E. Nikitopoulos,  
Ephraim J. Gutmark  
Mechanical Engineering Department  
Louisiana State University  
Baton Rouge, LA

Sivaram Gogineni  
Innovative Scientific Solutions Inc.  
Dayton, OH

**29th AIAA Fluid Dynamics Conference**  
**June 15-18, 1998 / Albuquerque, NM**

## STRUCTURE OF SQUARE COAXIAL NOZZLE FLOWS

Jason W. Bitting  
 Dimitris E. Nikitopoulos\*  
 Ephraim J. Gutmark  
 Mechanical Engineering Department  
 Louisiana State University  
 Baton Rouge, LA 70803

Sivaram Gogineni  
 Innovative Scientific Solutions Inc.  
 Dayton, OH 45430

### ABSTRACT

Flow visualization and measurement results are presented for flows in square coaxial nozzles with parallel sides, and the corresponding geometry of axisymmetric coaxial nozzles, at a co-flow-jet Reynolds number of 19,000 and at two inner-to-outer jet velocity ratio values (0.22 to 0.3). The presence of large-scale periodic structures is evident near the origin of the shear layers, although not as clear as in lower Reynolds number flows. The internal unmixed regions are reduced in size with decreasing velocity ratio. Visualizations and local measurements have indicated mixing enhancement when square nozzles are used compared to the axisymmetric ones. This is largely attributed to the difference in initial velocity profiles between these two configurations. The existence of axis-switching, a phenomenon observed in single non-axisymmetric nozzles, is not clearly evident from visualizations and measurements in the square coaxial nozzle. Four distinct regions in the development of the coaxial nozzle flows have been identified on the basis of the measured trends. Scaling of mean velocity and turbulence profiles has also been examined for the three shear layers formed in the near field of axisymmetric and square coaxial flows.

### INTRODUCTION

Coaxial nozzles are an integral part of many engineering systems where mixing of different fluid streams is required. They are used to provide mixing between fuel and oxidizer in combustors of propulsion systems and power producing gas turbine systems as

well as waste combustion and incineration systems. Single non-circular nozzles have been shown to have better mixing characteristics than their axisymmetric counterparts. Therefore, combinations of such nozzles into coaxial configurations is promising. The present work aims at investigating the flow structure of square coaxial nozzles and evaluate their potential to produce improved mixing between two coaxial flows.

Numerous studies have been performed on single planar circular jets. These jet configurations are well understood and pose little difficulty to current numerical simulations available to design engineers. Of more importance are coaxial circular jets which have complex vortices produced as the jet develops and the inner and outer shear layers interact. The vortices help produce the necessary large-scale mixing and small scale enhancement which are both needed for efficient combustion of a fuel. Work done by Ko and Kwan<sup>1</sup> (1976) provides information about the velocity and turbulence fields of coaxial jets with different inner to annular air velocity ratios,  $\lambda$ . Subsequent work by Ko and Au<sup>2</sup> (1985) has examined mean flow and turbulence scaling for the same flows. A thorough flow visualization study by Dahm et al<sup>3</sup> (1992) nicely shows the large-scale vortical structures and their interactions for various  $\lambda$  at low Reynolds numbers. Tang and Ko<sup>4</sup> (1993) have performed a studied forced coaxial jets for a velocity ratio of 0.3, and showed that the initial region of the jet plays an important role in the downstream development of large-scale structures.

Regarding non-circular nozzles, several configurations have been researched to date for a single jet, including: Rectangular/Square, Triangular, Lobed, and Elliptic.

---

\* Author to whom all correspondence should be directed.  
 Copyright © 1998 by the American Institute of  
 Aeronautics and Astronautics, Inc. All rights reserved.  
 REPRINTED WITH PERMISSION



The rectangular and square nozzles produce non-circular vortex rings at the exit which then deform and under certain conditions can lead to a switching of the jet axis. The axis switching is due largely to deformation and self-induction produced by the sharp corners of the nozzle and depends on the initial velocity profile characteristics. Early studies by Sforza et al<sup>5</sup> (1966), Trentacoste and Sforza<sup>6</sup> (1976), and duPlessis et al<sup>7</sup> (1974) investigated square jets but no insight was given to the underlying fundamental behavior of the square jet vortical interactions. Quinn and Militzer<sup>8</sup> (1988) showed that for a square jet of the same hydraulic diameter as a circular jet, the square jet had a faster spreading rate at similar distances from the jet exit as compared to the circular jet. A detailed numerical simulation by Grinstein et al<sup>9</sup> 1995 followed by experimental investigation illustrated that the axis switching is due to self-induction governed by the Biot-Savart Law with hairpin vortices developing along the diagonals of the square jets. Off-center velocity peaks have been observed by Quinn<sup>10</sup> (1992) for a square slot orifice exit.

The triangular jet has also been investigated by Schadow et al<sup>11</sup> (1988). The process of self-induction in the corners of the triangle produced enhanced mixing in that region. The flow results were different for triangular orifice exits or pipe/nozzle emphasizing the importance of initial conditions. A numerical and experimental study by Koshigoe et al<sup>12</sup> (1988) explained the differences and formulated conditions for which axis switching occurs. Enhancement in the fine scale mixing and combustion stability in the corner regions of the triangular jet were verified by Schadow et al<sup>13</sup> (1990). Large scale mixing was accomplished on the flat sides with reduced pressure oscillations as compared to the circular jet.

Elliptic jets have also been studied, and have exhibited the same axis switching and self-induction as found in triangular and rectangular jets. Gutmark and Ho<sup>14</sup> (1986) studied the elliptic jet. Axis switching was observed, resulting in entrainment rate of 8 times higher than a circular jet.

Although single non-circular nozzles have been shown to be promising in terms of improved mixing, coaxial configurations of such nozzles have hardly been studied. Recently Bitting et al.<sup>15,16</sup> (1997) presented flow visualization results for various combinations of non-circular (square, triangular, lobed) and axisymmetric coaxial nozzles for various intermediate Reynolds numbers and low velocity ratios. In this paper we have studied the flow structure of a square coaxial nozzle at a single co-flow Reynolds number and two inner-jet velocity ratios, and have compared the results with the corresponding axisymmetric coaxial jet flows.

## EXPERIMENTAL SETUP AND METHODS

The test facility used for this study incorporates a modular design that allows easy exchange of inner and outer nozzles with different lip geometries. The test facility uses two independent air flow supplies. Four, 1" lines provide air to the inner nozzle while eight 1/4" lines provide air to the outer nozzle. On each main supply line an orifice flow meter is used to determine the air flow rate. Valved, bypass ports allow the use of part of the metered air streams for seeding purposes. The inner jet flow passes through a flow-straightening honeycomb screen prior to entering the jet contraction with a contraction ratio of approximately 19:1. The outer jet flow reaches the outer jet through an annular passage with a contraction ratio of approximately 8:1.

A circular coaxial nozzle with an inner diameter of 0.6 inches and an outer diameter of 1.5 inches has been used as the baseline nozzle for the square, coaxial nozzle flow study. With the above dimensions, the hydraulic (effective) diameter of the inner jet and outer jet is 0.6 inches and 0.75 inches respectively. For the square nozzles, the hydraulic diameters are the same as for the circular jet for proper comparisons between the two nozzles. The inner-to-outer area ratio is preserved at 0.213. A top view of the axisymmetric and square nozzles is shown in Figure 1.

Visualizations have been carried out using a pulsed laser sheet and seeding with  $\text{TiCl}_4$ , which upon reaction with moisture produces fine sub-micron  $\text{TiO}_2$  particles. Several seeding strategies have been used to visualize the shear layers in the near field of the nozzles. Flow visualization of the inner and outer shear layers has been performed using  $\text{TiCl}_4$  as seed in the dry co-flow air, with water vapor in the inner jet air. The inner shear layer has been isolated by reversing the seeding of the streams, and the outer shear layer by removing the moisture from the inner nozzle. Instantaneous and time averaged cuts have been made with a laser sheet from a Nd-YAG laser pulsing at 10 Hz. Visualizations on a horizontal plane (perpendicular to the jet axis) have also been carried out at various distances from the jet exit. These were achieved by using a horizontal laser sheet and a mirror positioned above the laser-sheet plane at an angle of  $45^\circ$  with respect to the jet axis. Thus the top-view image was reflected horizontally into the receiving camera lens. The distance between the mirror and the exit of the jet was adequately large to avoid interference with the flow. Short (10nsec) exposures have been taken with a high-resolution Kodak CCD array (3000x2000) camera, to visualize the instantaneous structure of the jets, while long exposures (2 sec) have been used to provide a 20-realization average of the mixing regions.

Constant-Temperature Anemometry (CTA) measurements were carried out using a properly

calibrated single-film probe. The sensor was oriented parallel to the direction of traverse and perpendicular to the dominant direction of the air flow. The directions of the traverses used to determine velocity profiles across the jets are shown in Figure 2. Data from the probe was collected using the TSI IFA300 system with a sampling rate of 10,000Hz, a filter cutoff of 5,000Hz, and a sample size of 10,000 points.

## **RESULTS AND DISCUSSION**

The visualization results to be presented here are from axisymmetric and square coaxial nozzle flows at an outer flow  $Re_o=19,000$ . This Reynolds number is based on the outer nozzle hydraulic diameter and average velocity. Two inner-to-outer jet average velocity ratios,  $\lambda$ , were investigated through visualization (0.22 and 0.3). Local quantitative measurements were carried out for  $Re_o=19,000$  and  $\lambda=0.3$ , conditions for which the flow was investigated more extensively.

Instantaneous planar flow visualizations along the center-plane of the square coaxial nozzle are shown in Figure 3 for velocity ratios of 0.22 and 0.3. These visualizations were achieved by seeding the co-flow with  $TiCl_4$  and the inner jet with moisture. At the low velocity ratio the beginning of the existence of a local re-circulating region is evident at the end of the unmixed core of the inner jet. This is manifested through the presence of two pulsating mushroom vortices the signatures of which are visible in Figure 3a. This feature is not observed at the higher velocity ratio and the unmixed core of the inner jet is considerably longer than the low velocity ratio case. The visualizations of Figure 3 also reveal the fine structure of the shear layers due to the highly turbulent three-dimensional flow field. Evidence of a somewhat organized large-scale structure, obscured by smaller scale eddies, can be observed in the shear layers of the near-field. Many, well-defined, apparently three-dimensional, vortical structures are seen to be injected into the ambient air, which is an indication of strong intermittent character of the mixing process. Similar features were observed for the axisymmetric coaxial nozzle, the visualizations of which are not shown here for brevity.

In Figures 4, planar cuts perpendicular to the jet axis, taken under the same seeding conditions as in Figure 3 and for  $\lambda=0.3$ , visually show the variation of the jet shear-layer cross sections with distance from the jet-exit. Both instantaneous and time-averaged realizations are shown. The axisymmetric jet exhibits, on average, an axisymmetric flow pattern (Figure 4Cb, 4Cd, and 4Cf). Intense intermittency, manifested by injections of three-dimensional vortical structures of various scales, is evident at the edges of both the inner

and outer shear layers, as also seen in the axial laser sheet cuts. The injected structures often penetrate from one mixing layer to the other, across the outer jet unmixed region as evidenced, for example, in Figures 4Cc, 4Sa and 4Sc. The perpendicular cuts of the square jet in Figure 4 (Sa to Sf) show that the shear layers retain the geometrical shape of their origin for several outer hydraulic diameters. However, at the farthest location from the jet exit (Figure 4Sc and 4Sf) the tendency towards axisymmetric shape of the mixing region is evident). A region of interaction between the inner and outer shear layers of the co-flow is observed in the middle of the sides of the outer shear layer. This indicates strong interaction between the inner and outer shear layers in the square jet which was not observed in the axisymmetric jet until further downstream, and is indicative of the faster merging of the outer and inner mixing regions in the case of the square nozzle geometry. The horizontal planar visualizations of Figure 4 also show that the symmetries of the averaged flow expected on the basis of the nozzle geometry are present. No visual evidence of axis switching is present in the visualizations of the square jets in the near field.

Figure 5 presents instantaneous visualizations of the outer shear layer (5a, 5c, and 5e) and inner jet (5b, 5d, and 5f) separately for the square (5a-5d) and axisymmetric (5e, 5f) coaxial nozzles at  $\lambda=0.3$ . The outer shear layer was visualized by seeding the co-flow with  $TiCl_4$  and using dry air for the inner-jet. The inner shear layer and jet visualization was achieved by seeding the inner jet with  $TiCl_4$  and the co-flow jet with moisture. Two planar visualization cuts are shown for the square nozzle, one perpendicular to the square side through the centerline (5a and 5b) and one on the diagonal plane (5c and 5d). Only half of each jet field is shown. Figures 5b, 5d and 5f indicate that the inner jet flow is rapidly mixed with the co-flow air, as seen by the brighter areas at the end of the jet unmixed core. As expected because of the higher co-flow velocity, the "outwards" transport is limited as shown by the tracer pattern. The mixing boundary between the co-flow and inner-jet flow exhibits fine-scale, "wispy", structures that seem to be more stretched. This observation is also evident from the outer shear layer visualizations of Figures 5a, 5c and 5e. The instantaneous realizations of the outer shear layer bear evidence of large-scale structures obscured by smaller scales. A stream-wise instability of the inner jet is also outlined by the stream-wise wavering of the inner jet column. The outer shear layer appears thickest across the side of the square nozzle (Figure 5a) and is thinner along the diagonal (Figure 5c) as for the axisymmetric nozzle (Figure 5e). Intermittent presence of the tracer in the central region of the jet in Figures 5a, 5c, and 5e, indicates that transport from the outer shear layers has started. It is evident from these three Figures, that such transport is



considerably delayed in the axisymmetric case compared to the square. The outer shear layer inwards growth is more rapid for the square nozzle in the near field.

The visualizations presented thus far have given a qualitative picture of the coaxial flows under study and the differences between the axisymmetric and square coaxial nozzle flows. Quantitative measurements using Constant Temperature Anemometry have been carried out in order to obtain quantitative information. Axial mean velocity and velocity fluctuation profiles have been obtained across the jets at various downstream locations from the jet origin covering the near field of the coaxial jets. Samples of these profiles are shown in Figure 6 superimposed on time-averaged visualizations of the flow. Two profiles are given for the square nozzle case; one parallel to the square jet sides along the plane of symmetry (SS in Figure 2), and one along the diagonal (SDSD in Figure 2), as is customary in single square jet investigations. The velocities are scaled with the arithmetic average of the maximum velocities of the inner and co-flow streams at the exit of the coaxial jets. The difference between these average velocity scales between the axisymmetric and square cases is less than 3%, so this scaling does not produce a misleading picture. All lengths are scaled with the outer jet hydraulic diameter  $D_o$ .

The stream-wise development of the shear layers existing in the near field of the axisymmetric and square coaxial jets examined, is also shown in Figure 6. At the onset of the jets, three shear layers are identified; the *inner shear layer* of the inner jet, a *middle shear layer* on the inside of the co-flow jet, and the *outer shear layer* of the co-flow jet. The middle and inner shear layers form the wake of the inner nozzle lip. The development of the shear layers is tracked by recording the "radial" location ( $y_{0.5}/D_o$ ) of the point which has a velocity equal to 50% of the maximum velocity difference across each shear region.

A defining factor in the downstream development of a jet is the initial condition at the exit. The shape and details of the initial mean velocity and the turbulence intensity profiles are of critical importance in interpreting the observed differences in the development of the axisymmetric and square coaxial nozzles. It is observed here from Figure 6, that the initial mean profiles ( $x/D_o=0$ ) of the axisymmetric and square (SS scan) nozzles are almost identical in the inner nozzle region and the wake created after the inner nozzle lip. The core of the inner jet is uniform and the fluctuation level low (fraction of a percent) with a small peak inside the inner shear layer near the inner jet wall. However, a considerable difference exists between the mean profiles in the core of the co-flow region. The axisymmetric co-flow jet core is considerably more uniform than its square counterpart which has the shape

of a simple shear flow. In both cases the maximum velocity occurs closer to the inner wall. The difference between the axial fluctuation profiles in this region is more substantial. The maximum fluctuation level is observed near the middle of the co-flow core for the square nozzle case with secondary peaks inside the two bounding shear layers; the middle shear layer near the inner wall of the outer jet and the outer shear layer of the outer jet. No such peak is present in the core of the axisymmetric co-flow and the highest fluctuation levels are observed inside the bounding shear layers. Contrary to the square-jet side scan (SS), the shapes of the initial mean and fluctuation profiles along the square-jet diagonal scan (SD) are almost exactly similar to those of the axisymmetric jet, and the fluctuation levels are of the same magnitude.

On the basis of the measured profiles and with the aid of the time-averaged visualization, the coaxial jets can be divided into distinct regions, in a manner similar to Ko and Au<sup>2</sup> (1985). The first region is the one immediately downstream of the jet exit (approximately  $0 < x/D_o < 0.5$ ), where the inner jet core decelerates rapidly as shown in Figure 7a. At the end of this region the wake of the inner jet has completely disappeared as the inner and middle mixing layers merge, as evidenced in Figure 6. In the second region (approximately  $0.5 < x/D_o < 1.6$ ) the potential core of the inner jet persists at a fixed centerline velocity. At the end of this second region this potential core disappears and the middle shear regions merge. This is evident in Figure 6 from the time averaged visualization and the velocity profiles at  $x/D_o=1.6$ . The potential core of the inner jet disappears somewhat faster in the case of the axisymmetric nozzle. The relative shapes of the co-flow-jet core profiles are preserved in these two regions, while the peak mean velocity remains more or less fixed. By the end of the second region the original middle peak in fluctuation intensity has disappeared and the highest fluctuation intensity is observed inside the outer co-flow shear layer thereafter. In the same neighborhood the visualization (Figure 6) indicates that outer and middle shear layers merge. This occurs earlier for the square nozzle across its sides (SS scans in Figure 6a). The fluctuation level in the core of the square-jet co-flow is initially considerably higher (by more than a factor of 2) than that observed in the same region of the axisymmetric jet. The significant differences observed in the initial region profiles between the axisymmetric and square (SS scan) jet co-flows explain the higher mixing and inwards spread of the outer co-flow shear layer qualitatively documented by the visualizations of Figures 4, 5 and 6. Such growth was not observed along the diagonal of the square jet where the initial profile of the co-flow mean velocity is more uniform, fluctuation level lower and the profile shapes similar to the axisymmetric ones. The turbulence

intensity along the centerline increases steadily within both initial regions described above much like as in a single jet (Figure 7b).

The process of gradual merging of the opposite middle shear layers takes place within the third region of the coaxial jet (approximately  $1.6 < x/D_o < 8$ ) as seen in Figure 6. The centerline velocity minimum increases gradually (Figure 7a) until it becomes an absolute maximum at the end of the region. As the middle shear layers weaken the corresponding maximum in turbulence intensity is eliminated until only one peak remains at the end of this region corresponding to the outer shear layer. The centerline turbulence intensity reaches a peak in the beginning of this third region and gradually decays to a plateau at the end of the region (near  $x/D_o=8$  as seen in Figure 7b). It is seen from Figure 6 that, after the middle shear layer growth has completely overwhelmed the core of the inner jet (near  $x/D_o=2.4$ ), the axisymmetric and square (SS scan) jet mean and fluctuation profiles become very nearly identical in magnitude and shape. The fourth region beyond  $x/D_o=8$  displays the characteristics of a "single jet" with a single centerline maximum of the mean velocity and a single off-center peak in turbulence intensity associated with the outer shear layer (see Figure 6). In this region the centerline turbulence intensity remains approximately constant as the centerline velocity begins to decay. It should be noted that, upon superposition, the square-jet diagonal profiles (SD scan) collapse onto the those obtained from the SS scan and the axisymmetric nozzle case in the beginning of this fourth region. This indicates that the memory of the geometrical origin of the jet is being lost or it could be construed as weak evidence of an "axis-switching" phenomenon in progress.

Figure 6 also indicates that the middle shear layer development is nearly identical between the axisymmetric and square (SS-scan) jets. This is in agreement with the fact that the mean and fluctuation profiles are nearly identical between the two jets within the middle shear layer. The middle shear layer on the diagonal of the square jet exhibits a much faster inward growth than that in the SS direction. The inward growth of the middle shear layers is slowed down considerably past the end of the second region, where the inner jet is completely overwhelmed and the mean shear is diminished. The middle shear layer for the axisymmetric nozzle and the SS direction of the square nozzle ceases to exist around  $x/D_o=8$ . However, it persists past that point on the diagonal as also insinuated by the visualization in Figure 4Sd. The growth of the outer shear layer is distinctly different between the axisymmetric and square nozzle in the SS direction. The initial location of the half-velocity point is also different as a consequence of the difference in the initial profiles. As observed qualitatively in the

visualizations of Figure 6 the near-field growth of the outer shear layer for the square nozzle in the SS direction is somewhat faster than that in the axisymmetric case. This is again explained by virtue of the difference in the corresponding initial profiles. The growth of the outer shear layer on the diagonal is quite different. It is seen in Figure 6b that, after a short period of no growth a local contraction of the outer shear layer is documented followed by a second region of growth. The visualization along the diagonal plane, in the same Figure, qualitatively confirm this trend. The distance between the half-velocity points for the outer shear layers in the SS and SD directions diminishes downstream and is a possible indication of a weak tendency towards axis switching. However, in the absence of strong visualization and quantitative evidence we can not conclude that this phenomenon actually takes place. This is not surprising given that it has been shown in single non-circular jets that axis switching is very sensitive to the initial conditions.

Scaled velocity and turbulence intensity profiles from the three shear layers of the coaxial flow are presented in Figure 8. Scaling typically used in shear layers has been employed, following the example of Ko and Au<sup>2</sup> (1985). The trends of their scaled data from axisymmetric coaxial nozzles at various velocity ratios less than unity, have been used for comparisons, and to put the present data into perspective. Best fits of the scaled mean velocity profiles with typical hyperbolic tangent profiles are also included in Figure 6 (a-c). It is evident from Figure 6 that the scaled mean profiles from both axisymmetric and square (SS and SDSD scans) nozzle flows collapse on a single trend to a very satisfactory extent for all shear layers. This is more so for the middle and inner shear layers. The outer shear layer displays a higher degree of scatter. This is so primarily because the outer shear layer is less cleanly defined at the onset of the co-flow jet flow as discussed previously. The agreement with Ko and Au<sup>2</sup> (1985) is also very good. The scaling of the turbulence intensity is somewhat less clean. In the case of the outer layer, the scaling is good, while some deviations are observed primarily for the SS scans of the square nozzles. It is speculated that this is so for the same reason that causes the higher scatter in the mean scaled profiles. The agreement with Ko and Au<sup>2</sup> (1985) is reasonable considering that their turbulence profiles also displayed some scatter and that fewer downstream locations were included in their scaling. The turbulence intensity scaling is also good for the middle shear layer. In fact, it is very good to the left of the turbulence peak while it breaks down for the SS scan of the square nozzle to the right of the peak, for the same reason discussed previously. The comparison to Ko and Au<sup>2</sup> (1985) is quite good considering the difference in co-flow initial conditions between our study and theirs.

## CONCLUSIONS

The visualizations and local measurements presented have indicated mixing enhancement for square coaxial nozzles compared to axisymmetric ones under the same bulk flow conditions at velocity ratios less than unity. This was largely attributed to the difference in initial velocity profiles between these two configurations. The existence of axis-switching is not clearly evident from the visualizations and the measurements in the square coaxial nozzle. The presence of large-scale periodic structures was evident near the origin of the shear layers for both jets, although not as clear as in lower Reynolds number flows. The internal unmixed regions were reduced in size with decreasing velocity ratio. Four distinct regions in the development of the coaxial nozzle flows have been identified on the basis of the measured trends. Typical shear-layer scaling of mean velocity and turbulence profiles has also been successfully performed for the three shear layers formed in the near field of the axisymmetric and square coaxial flows. Additional work is necessary to determine to what extent mixing enhancement, other than the geometrical increase of the area subjected to shear, can be produced using square coaxial nozzles as opposed to axisymmetric ones. Variation of the jet initial conditions as well as active forcing could answer this question as well as reveal if axis switching in non-circular coaxial nozzle flows is possible.

## ACKNOWLEDGEMENTS

This work is supported by NASA the Louisiana Board of Regents LEQSF, and the AFOSR GSRP. The guidance and help of Dr. W. M. Roquemore of Wright Laboratory is also gratefully acknowledged.

## REFERENCES

- <sup>1</sup>Ko, N.W.M., and Kwan, A.S.H. (1976) "The Initial Region of Subsonic Coaxial Jets," *Journal of Fluid Mechanics*, Vol. 73, pp. 305-332.
- <sup>2</sup>Ko, N.W.M., and Au, H. (1985) "Coaxial Jets of Different Mean Velocity Ratios," *Journal of Sound and Vibration*, Vol. 100, No. 2, pp. 211-212.
- <sup>3</sup>Dahm, W.J.A., Frieler, C.E., and Tryggvason, G. (1992) "Vortex Structure and Dynamics in the Near Field of a Coaxial Jet," *Journal of Fluid Mechanics*, Vol. 241, pp. 371-402.
- <sup>4</sup>Tang, D.K., and Ko, N.W.M. (1993) "Coherent Structure Interactions in Excited Coaxial Jet of Mean Velocity Ratio of 0.3," *AIAA Journal*, Vol. 31, No. 8, pp. 1521-1524.
- <sup>5</sup>Sforza, P.M., Steiger, M.H., and Trentacoste, N. (1966) "Studies on Three-Dimensional Viscous Jets," *AIAA Journal*, Vol. 4, No. 5, pp. 800-806.
- <sup>6</sup>Trentacoste, N. and Sforza, P. (1967) "Further Experimental Results for Three-Dimensional Free Jets," *AIAA Journal*, Vol. 5, No. 5, pp. 885-891.
- <sup>7</sup>duPlessis, M.P., Wang, R.L., and Kahawita, R. (1974) "Investigation of the Near-Region of a Square Jet," *Transactions of the ASME, Journal of Fluids Engineering*, September 1974, pp. 247-251.
- <sup>8</sup>Quinn, W.R. and Militzer, J., (1988) "Experimental and Numerical Study of a Turbulent Free Square Jet," *Physics of Fluids*, Vol. 31, No. 5, pp. 1017-1025.
- <sup>9</sup>Grinstein, F. F., E. Gutmark, and T. Parr, (1995) "Near Field Dynamics of Subsonic Free Square Jets. A Computational and Experimental Study," *Physics of Fluids*, Vol. 7, No. 6, pp. 1483-1497.
- <sup>10</sup>Quinn, W.R. (1992) "Streamwise Evolution of a Square Jet Cross Section," *AIAA Journal*, Vol. 30, No. 12, pp. 2852-2857.
- <sup>11</sup>Schadow, K.C., Gutmark, E., Parr, D.M., and Wilson, K.J. (1988) "Selective Control of Flow Coherence in Triangular Jets," *Experiments in Fluids*, Vol. 6, pp. 129-135.
- <sup>12</sup>Koshigoe, S., Gutmark, E., Schadow, K.C., and Tubis, A. (1988) "Wave Structures in Jets of Arbitrary Shape. III. Triangular Jets," *Physics of Fluids*, Vol. 31, No. 6, pp. 1410-1419.
- <sup>13</sup>Schadow, K.C., Gutmark, E., Wilson, K.J. and Smith, R.A. (1990) "Noncircular Inlet Duct Cross-Section to Reduce Combustion Instabilities," *Combustion Science and Technology*, Vol. 73, pp. 537-553.
- <sup>14</sup>Gutmark, E. and Ho, C. (1986) "Visualization of a Forced Elliptic Jet," *AIAA Journal*, Vol. 24, No. 4, pp. 684-685.
- <sup>15</sup>Bitting J. W., Nikitopoulos D. E., Gogineni S. P., and Gutmark E. J., (1997) "Visualization of Non-Circular, Coaxial Nozzle Flow Structure", *Bulletin of the American Physical Society*, Vol. 42, 50th Annual Meeting of the American Physical Society, San Francisco, CA, November 23-25, 1997.
- <sup>16</sup>Bitting J. W., Nikitopoulos D. E., (1997), "Visualization and two-color digital PIV measurements in circular and square coaxial nozzles", Final Report, AFOSR GSRP, Wright Laboratory, Wright-Patterson AFB, August 1997.

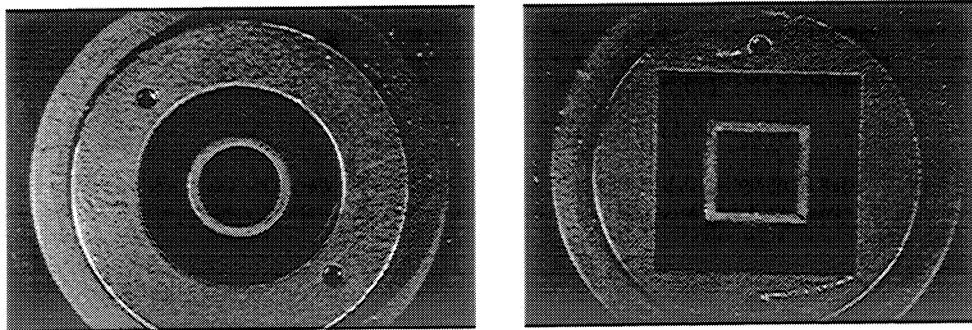


Figure 1: Axisymmetric and Square Coaxial Nozzles

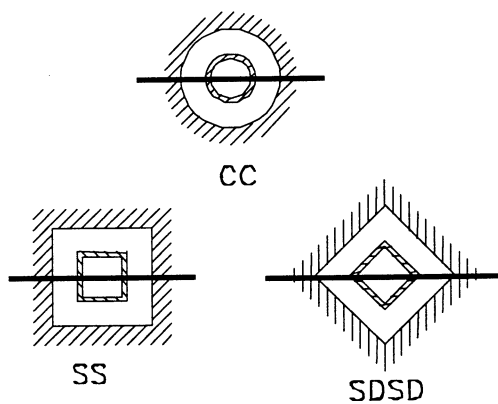


Figure 2: Laser Sheet Cuts

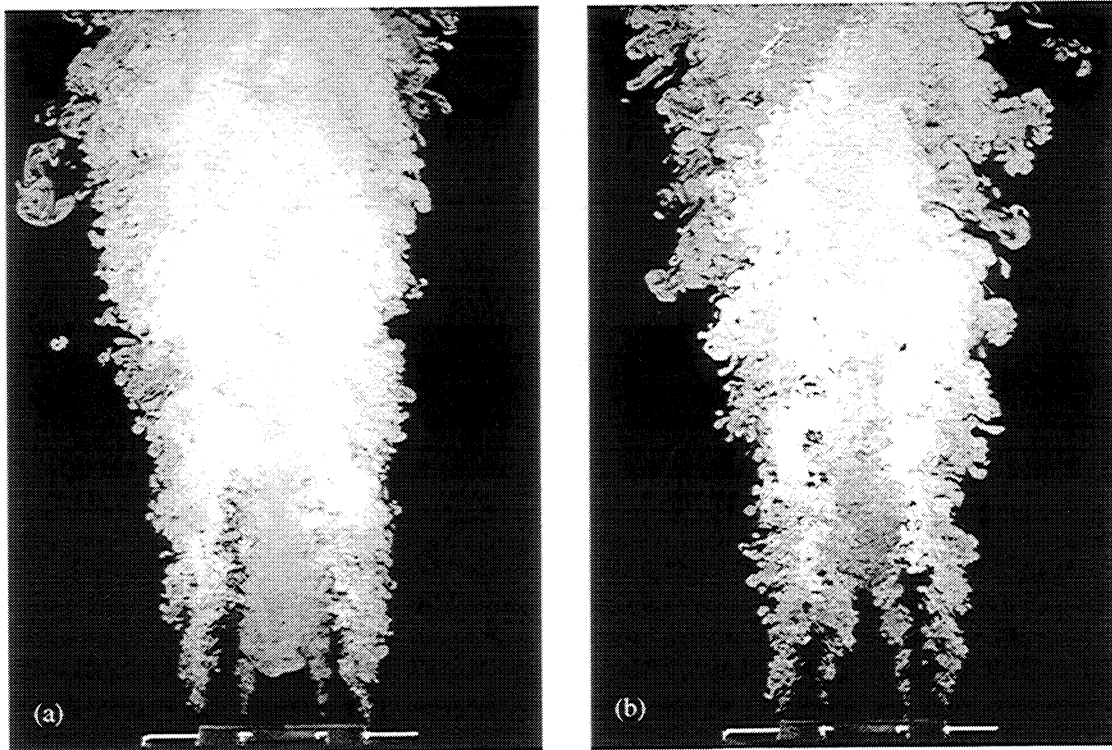


Figure 3: Instantaneous visualizations of a coaxial Square Jet ( $Re_o=19,000$ , (a)  $\lambda=0.22$  (b)  $\lambda=0.3$ ).

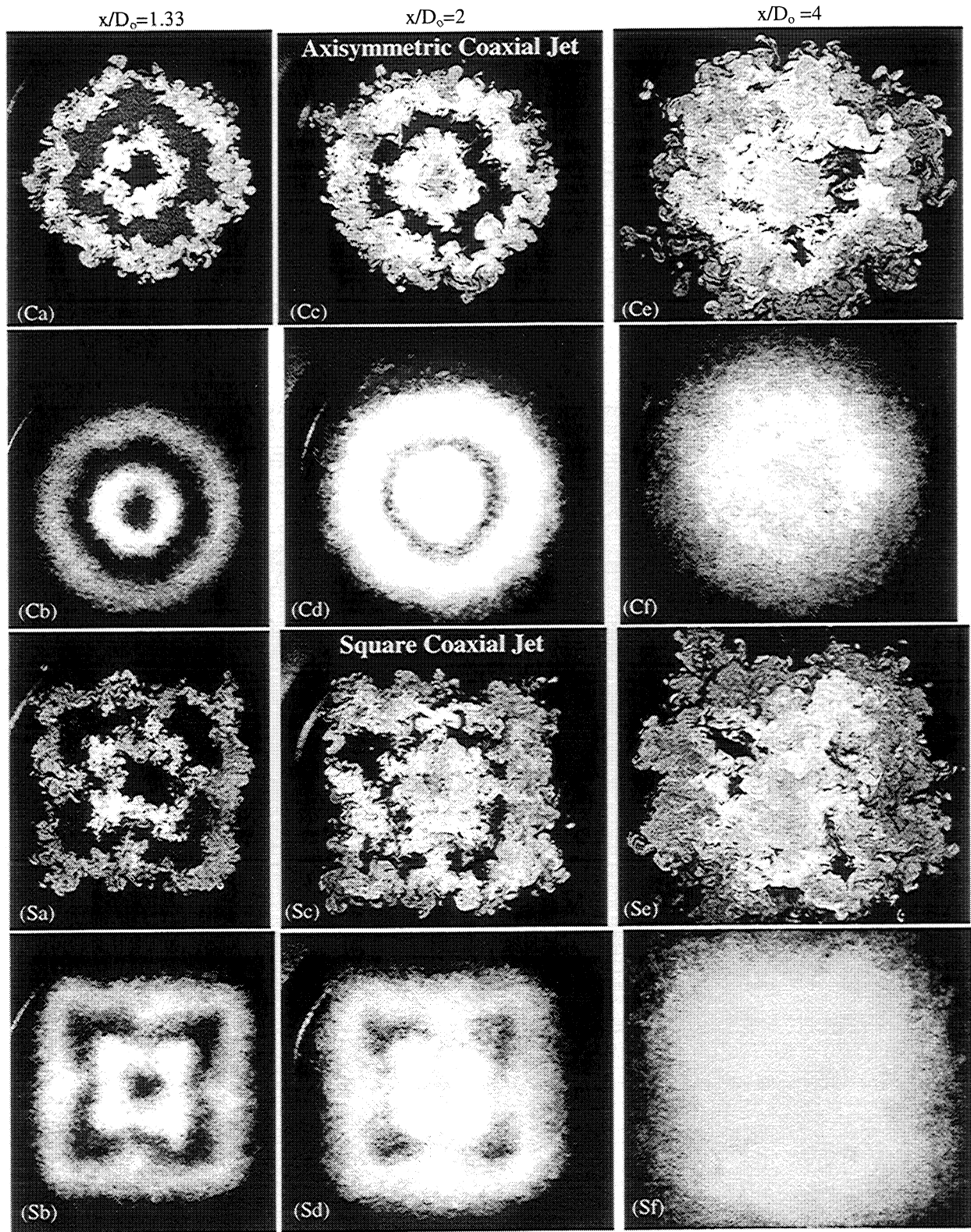


Figure 4: Horizontal Laser Sheet Visualizations ( $Re_o=19,000$ ,  $\lambda=0.3$ ): Instantaneous Images (Ca), (Cc), (Ce), (Sa), (Sc), and (Se); Time Averaged Images (Cb), (Cd), (Cf), (Sb), (Sd), and (Sf);



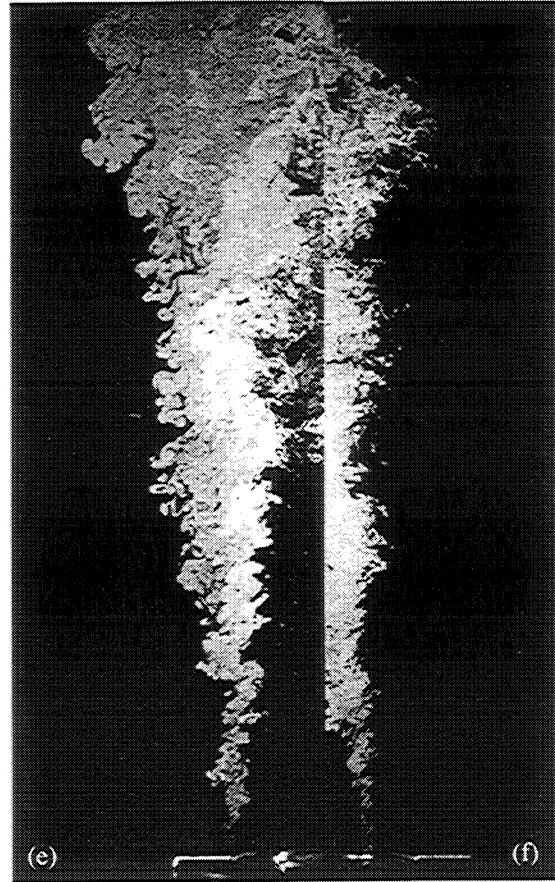
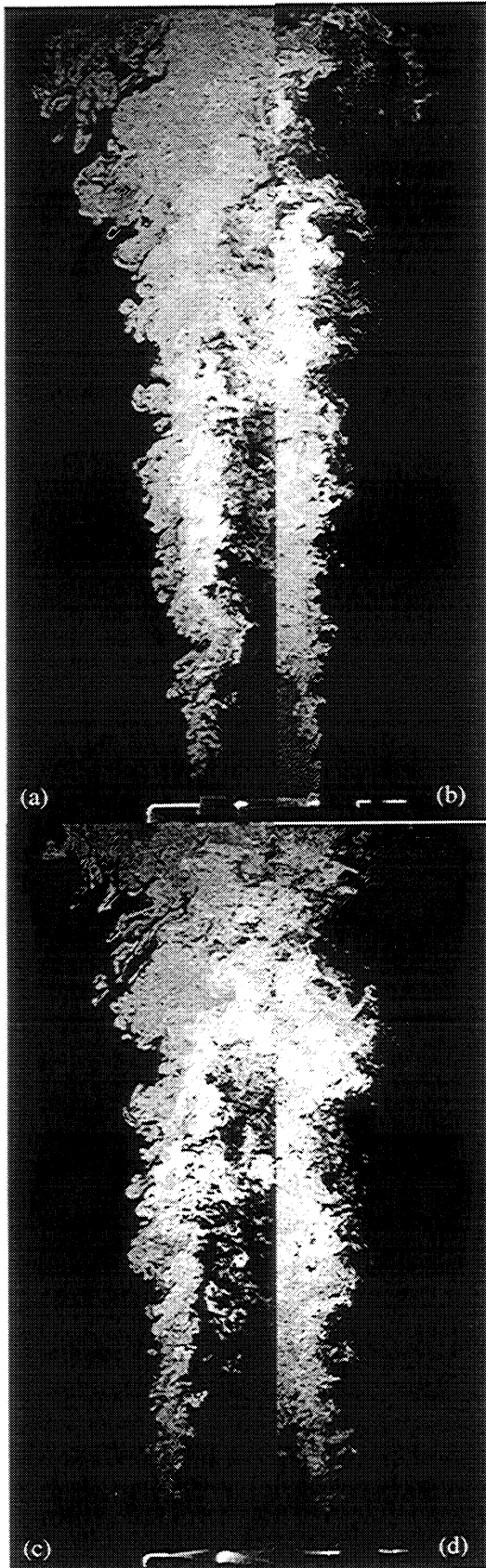


Figure 5: Instantaneous co-axial jet-flow visualizations ( $Re_0=19,000$ ,  $\lambda=0.3$ ):

- (a) Square Side, Outer Mixing Region,
- (b) Square Side, Inner Mixing Region,
- (c) Square Diagonal, Outer Mixing Region,
- (d) Square Diagonal, Inner Mixing Region,
- (e) Axisymmetric, Outer Mixing Region,
- (f) Axisymmetric, Inner Mixing Region.

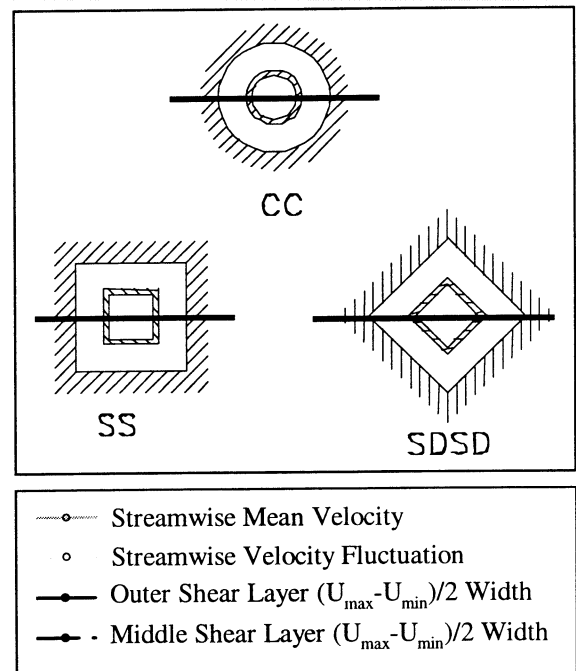
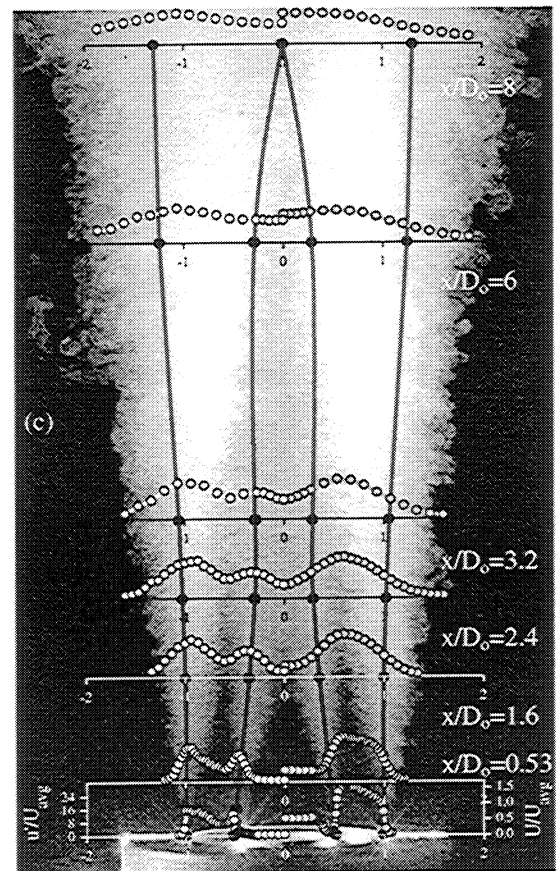
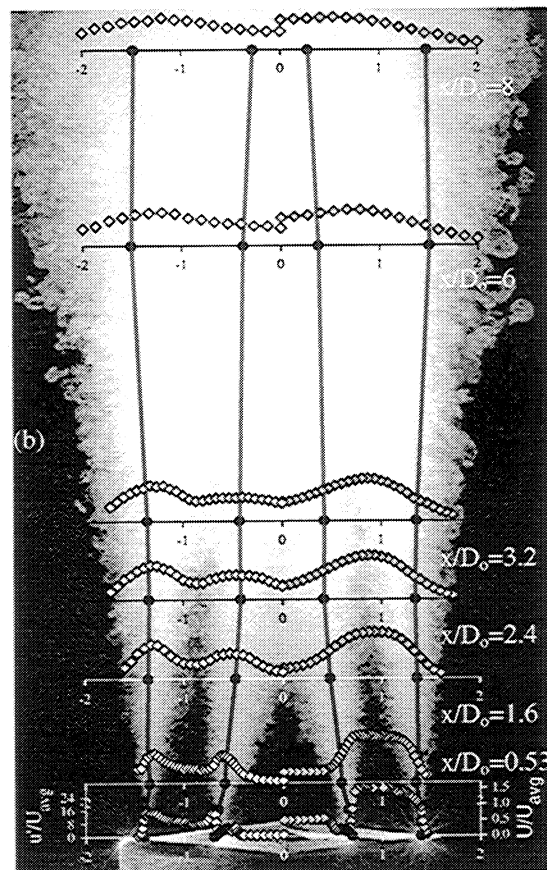
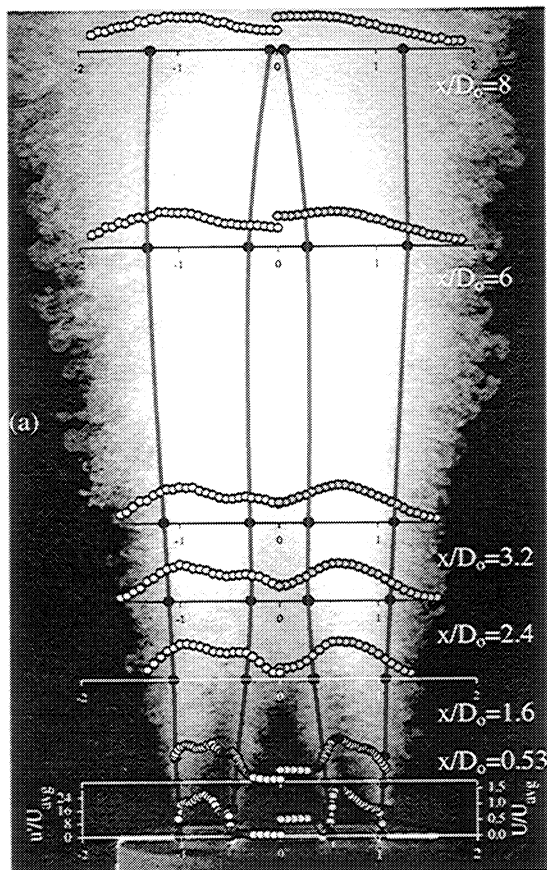


Figure 6: Visualization and measurement of the flow evolution in coaxial nozzles at  $Re=19,000$ ,  $\lambda=0.3$ : (a) square SS-plane, (b) square SDSD-plane, and (c) axisymmetric CC-plane.

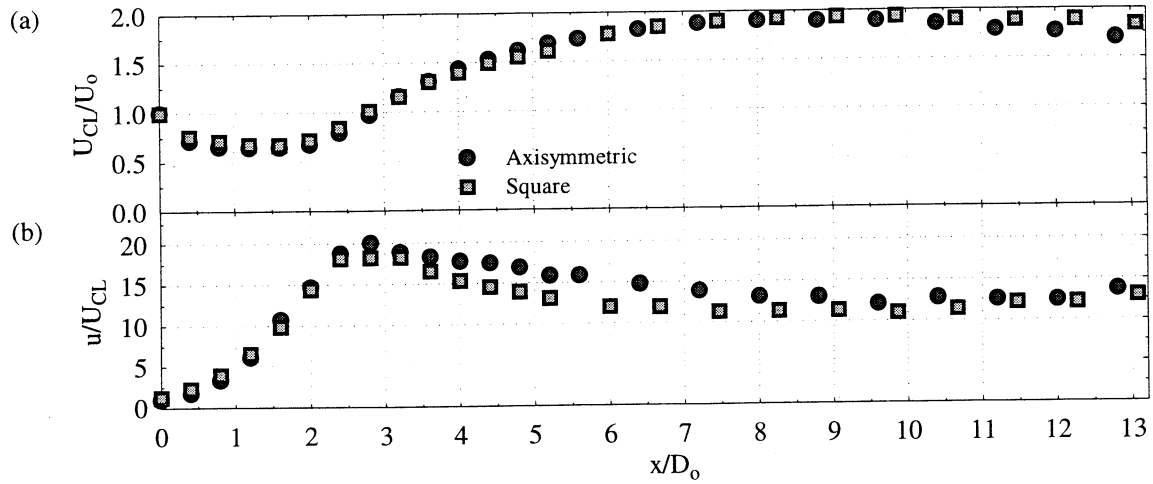


Figure 7: Centerline mean and fluctuation velocity development

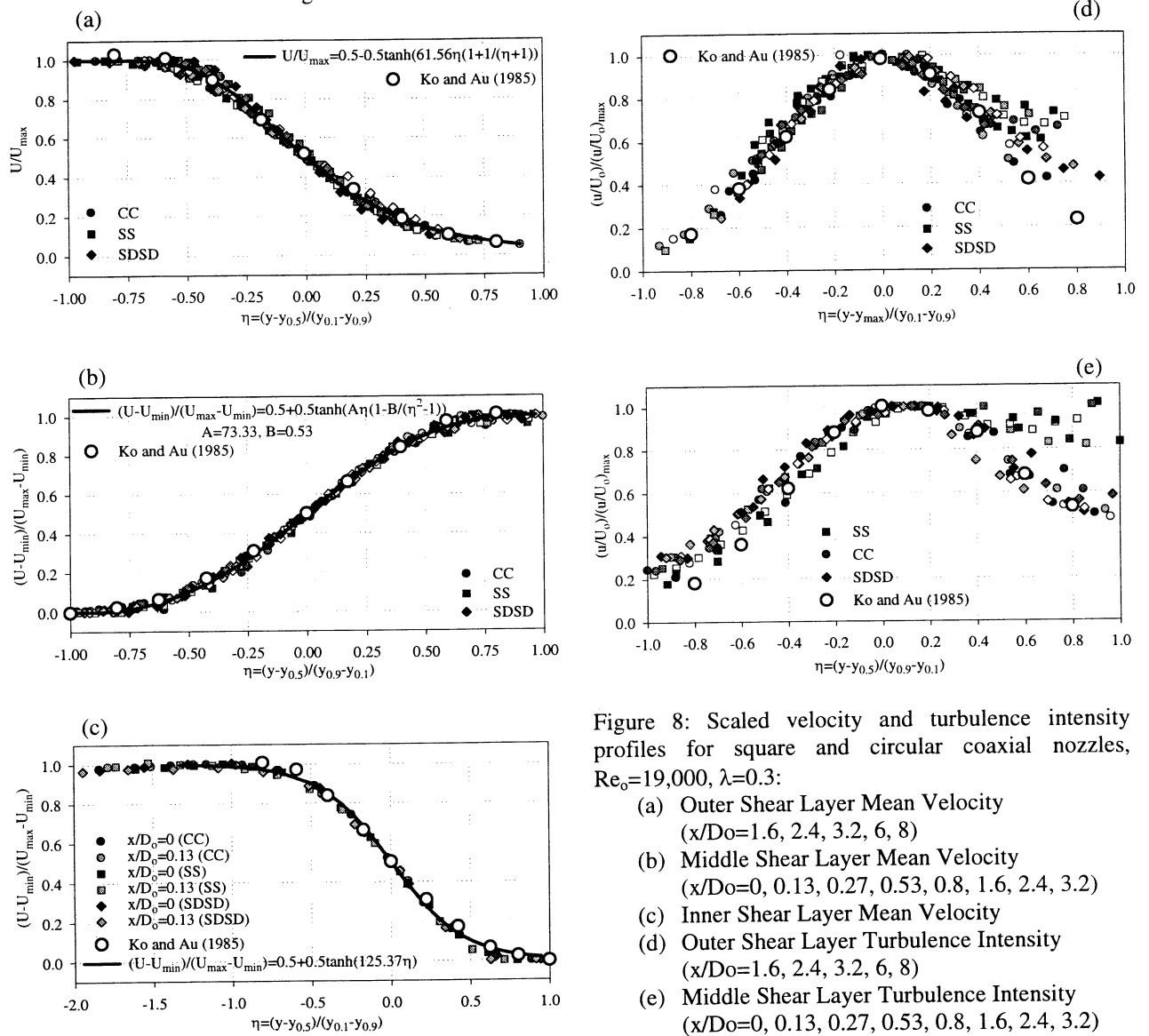


Figure 8: Scaled velocity and turbulence intensity profiles for square and circular coaxial nozzles,  $Re_0=19,000$ ,  $\lambda=0.3$ :

- (a) Outer Shear Layer Mean Velocity ( $x/D_0=1.6, 2.4, 3.2, 6, 8$ )
- (b) Middle Shear Layer Mean Velocity ( $x/D_0=0, 0.13, 0.27, 0.53, 0.8, 1.6, 2.4, 3.2$ )
- (c) Inner Shear Layer Mean Velocity
- (d) Outer Shear Layer Turbulence Intensity ( $x/D_0=1.6, 2.4, 3.2, 6, 8$ )
- (e) Middle Shear Layer Turbulence Intensity ( $x/D_0=0, 0.13, 0.27, 0.53, 0.8, 1.6, 2.4, 3.2$ )

### **2.1.3 Three-Dimensional Flow-Visualization Technique**

Holography can be used to obtain a three-dimensional representation of spatial objects such as fluid interfaces and particle ensembles. Based on this, a three-dimensional flow-visualization tool, HFV, was developed and utilized for flowfield studies. The results of this effort are summarized in two publications: “Investigation of Jet Diffusion Flames Using Holographic Flow Visualization (HFV) and Holographic PIV (HPIV) Techniques” (see pp. 36-43) and “Holographic Flow Visualization as a Tool for Studying Three-Dimensional Coherent Structures and Instabilities” (see pp. 44-55).

## Investigation of Jet Diffusion Flames Using Holographic Flow Visualization (HFV) and Holographic PIV (HPIV) Techniques

S. Gogineni,<sup>1</sup> J. Estevadeordal,<sup>1</sup> H. Meng,<sup>2</sup> and L. Goss<sup>1</sup>

<sup>1</sup>Innovative Scientific Solutions, Inc., 2786 Indian Ripple Road, Dayton, OH, USA 45440-3638

<sup>2</sup>Dept. of Mechanical Engineering, Kansas State University, Manhattan, KS, USA 66506-5106

### Abstract

The application of the simple In-line Recording and Off-axis Viewing (IROV) holographic technique to air and combusting flows was explored based on the successful implementation of this technique in a water flow. For combusting flows, we demonstrated its limitations which result from the distortion of the reference beam by temperature and density gradients and the presence of large amounts of speckle noise. An alternative to this technique, an off-axis-based holographic recording and reconstruction system that can perform both Holographic Flow Visualization (HFV) and Holographic Particle Image Velocimetry (HPIV), was developed. This system was successfully applied to both reacting and non-reacting propane jet flows in the presence and absence of a co-flowing air stream. Several seeding methods were implemented to identify the flame boundaries and to aid the understanding of the dynamics of jet diffusion flames, vortex-flame interactions, and the mechanism governing flame lift-off. The flow field seeded with preformed titanium-dioxide ( $TiO_2$ ) particles (dense scalar field) provided images suitable for high-quality 3D flow visualization and that seeded with aluminum-oxide ( $Al_2O_3$ ) particles (moderate scalar field) provided images suitable for both qualitative and quantitative (3D velocity) measurements.

### 1. Introduction

Over the past fifty years, considerable research has been performed on jet diffusion flames because of their practical applications. For example, Roquemore et al. [1] systematically investigated jet diffusion flames under conditions ranging from attached to lifted (0.16 to 17 m/sec) using Reactive-Mie-Scattering (RMS) flow visualization and Coherent Anti-Stokes Raman Spectroscopy (CARS) techniques; their objectives were to determine the influence of large toroidal vortices (present outside the visible flame zone) on the dynamic structure of free jet diffusion flames and to understand the mechanism governing flame lift-off. Katta et al. [2] examined the structure of reacting and non-reacting propane jet flows under identical conditions using experimental methods and probed the physics of the dynamic processes in these flows using numerical simulations. They observed from experiments that the jet spreading rate was lower and the potential core longer for reacting flows. Numerical simulations revealed that viscosity, volumetric expansion, and body force due to buoyancy associated with the combustion products were responsible for the flames being less turbulent. In efforts to gain further understanding of the dynamics of jet diffusion flames, vortex-flame interactions, and the mechanism governing flame lift-off and to validate the CFD codes, we resorted to a 3D diagnostic technique using holography.



Holographic imaging, which is capable of instantaneous 3D representation of spatial objects including particle ensembles, holds great promise as a 3D diagnostic tool—both qualitative and quantitative—for spatially and temporally evolving complex flow structures. Holographic flow visualization has been used in the past for visualizing particles in different types of flows [3]. Most recently holography has been used successfully to measure 3D velocity fields [4-7] in water and air flows. However, the power of holography as a scalar-based 3D flow-visualization tool has not been fully explored. We developed a unique, flexible holographic recording and reconstruction system where in-line and off-axis recording configurations can be interchanged without major modifications and both Holographic Flow Visualization (HFV) and Holographic PIV (HPIV) can be performed. This system was successfully applied to different types of flows and preliminary results were reported in ref. [8]. In the present paper, results pertaining to reacting and non-reacting propane jet flows undergoing external excitation in the presence and absence of a co-flowing air stream are presented.

## 2. Experimental Setup and Procedures

A schematic diagram of the experimental facility along with the holographic recording system is shown in Fig. 1(a). Two types of fuel tubes were used: 1) a 7-mm-dia. straight tube and 2) a 10-mm-exit-dia. jet having in a co-flowing air stream. The diameter of the annular jet was 150 mm, and the velocity of the co-flowing air stream was  $\sim 0.5$  m/sec. The propane jet was excited using a loud speaker which was attached below the fuel tube. The jet flow was seeded with preformed titanium-dioxide ( $\text{TiO}_2$ ) particles [formed from a reaction of titanium-tetrachloride ( $\text{TiCl}_4$ ) and water vapor] for 3D flow-visualization and  $1\text{-}5\text{ }\mu\text{m}$   $\text{Al}_2\text{O}_3$  particles for both visualization and 3D velocity (HPIV) measurements.

The holographic recording system [(Fig. 1(a))] uses two frequency-doubled, injection-seeded Nd:YAG lasers that can provide a coherence length  $> 1$  m. Use of a custom-designed shutter allowed only one pulse from each laser. The single pulse from each laser was directed to a pinhole for spatial filtering. The laser beams were expanded using collimators to illuminate a cylindrical volume in the test section. The interference waves from the reference beam and the object beam were recorded on a holographic plate. The two lasers were synchronized, and the time delay between them was monitored by a photo-diode.

The reconstruction of the holograms [Fig. 1(b)] was performed using a continuous-wave (Millennia, Spectra-Physics) Nd:YVO<sub>4</sub> laser that produces coherent light of the same wavelength (532 nm) as the recording Nd:YAG lasers. The reconstructed images were 3D replicas of the real flow at the time of exposure. These images were viewed from many directions, and the flow features were photographed with different magnifications and in different planes using a high-resolution digital color camera (3060 x 2036 pixel).

## 3. Results and Discussion

Flow visualization has been a major experimental tool for studying complex problems involved in fluid mechanics and combustion and is responsible for many of the most exciting discoveries in these fields. The invention of the laser, the speed and accessibility of the computer, and the introduction of high-resolution digital cameras have revolutionized this research tool in such a way that quantitative information including velocity and temperature can be obtained. Despite their contributions, current flow-visualization techniques are

basically limited either to a 2D slice of a flow illuminated by a laser light sheet or to a 2D field resulting from integration of a 3D density field along the path of a laser beam; thus, these techniques do not provide full visualization of the 3D information. For capturing the details of the complex 3D flow structures, we developed a 3D diagnostic tool using holography. One of the simplest holographic configurations available is IROV which uses a single beam for both reference and illumination. Since this technique was successfully applied to the measurement of 3D velocities in water flow [5], we adopted it and explored its possible extension to reacting and non-reacting jet flows.

Initial tests were conducted in a cylindrical jet with propane as the fuel. The reacting and non-reacting propane jets were first seeded with  $\text{Al}_2\text{O}_3$  particles and then with preformed  $\text{T}_1\text{O}_2$  particles and the images recorded on a hologram. The real images from the holograms were reconstructed using the procedure described in Sect. 2 and photographed with a high-resolution digital camera. Typical reconstructed images of non-reacting and reacting propane jets are shown in Figs. 2(a) and 2(b). Also shown for reference are the corresponding holographic plates, on which the shadowgraph pattern and footprints of the flow can be observed. The nozzle and the flow features near the jet exit can be clearly seen in the reconstructed image of the cold propane jet but not in the reconstructed image of the reacting jet. This can be attributed primarily to the wavefront distortion caused by temperature and density gradients in the flame and, to a much lesser extent, radiation of the flame onto the plate. Although the latter effect can be minimized by placing the holographic plate farther from the test section or by placing a shutter in front of the holographic plate, the presence of temperature and density gradients in the flame is unavoidable. These gradients distort the reference beam and, in turn, cause excessive speckle noise. This limits the application of the IROV technique for reacting flows.

As an alternative to the IROV technique, an off-axis recording and reconstruction system was developed for reacting flows. Although such configurations were used in earlier studies for water and air flows, their potential for flow visualization in conjunction with quantitative measurements has not been explored. In the present investigation we implemented several seeding methods and demonstrated that this technique could be used both for 3D visualization and for 3D velocity measurements. First, the technique was implemented for visualizing cylindrical jet flows with propane as the fuel. It was determined that high-quality flow visualizations could be obtained by seeding the jet flow with  $\text{T}_1\text{O}_2$  particles preformed from a mixture of  $\text{T}_1\text{Cl}_4$  and water vapor. This type of seeding produces the dense scalar field which is suitable for the visualization of vortical structures and vortex-flame interactions. Figures 3(a) and 3(b) are photographs of the reconstructed images of the reacting propane jet under lifted and attached flame conditions, respectively. The reconstructed holographic images contain both the flame and the vortical structures (which could be viewed with the naked eye during recording); however, since it is difficult for the viewer/reader to identify these flame boundaries, we obtained the 2D laser-sheet flow visualizations shown on the left side of Figs. 3(a) and 3(b). Although the flow conditions of 2D laser-sheet visualizations and of the reconstructed holograms are not identical, the type of flame and the flame boundaries are approximately the same. The reconstructed image in Fig. 3(a) corresponds to an unforced turbulent propane reacting jet and reveals that the flame is lifted at  $\sim 0.5$  dia. downstream of the exit and has five lobes or flamelets. The reconstructed

image in Fig. 3(b) corresponds to a forced jet and shows the organized 3D toroidal vortical structures. Both of the recorded holograms contain many different views, and the reconstructed images can be photographed with different magnifications (not shown) to aid the understanding of the vortex-flame interactions and the mechanism governing flame lift-off. The above seeding method was further implemented in a cold propane forced jet to demonstrate its potential for the exploration of complex flow features that exist near the jet exit such as waviness, bulging, and roll-up of the shear-layer instability into vortical structures (Fig. 4).

Although the above-mentioned seeding method provided high-quality 3D flow visualizations, quantitative information could not be obtained because of the "small" size of the seeding particles (believed to be on the order of  $0.1\text{ }\mu\text{m}$  or less). For obtaining 3D quantitative measurements, the propane jet was seeded with  $\text{Al}_2\text{O}_3$  particles ( $1\text{--}5\text{ }\mu\text{m}$ ) and microballoons. After several tests of the seeding density, it was determined that moderate seeding of the jet with either microballoons or  $\text{Al}_2\text{O}_3$  particles produces reconstructed images that are comparable to those of 2D PIV images, in terms of both flow visualization and measurement of velocities. A typical reconstructed image of the cold propane jet issuing into a co-flowing air stream is shown in Fig. 5. In this image, only the jet flow was seeded with  $5\text{-}\mu\text{m}$  microballoons. The velocities of the co-flowing air and the propane jet were  $0.5\text{ m/sec}$  and  $2.0\text{ m/sec}$ , respectively. The propane jet was forced using a loud speaker attached at the bottom of the fuel tube, and the forcing frequency was  $30\text{ Hz}$ . This figure displays a uniform flow at the exit and the formation of a 'bubble' or vortex-ring-shaped structure at  $\sim 3.5\text{ dia.}$  downstream of the exit. This image not only provides qualitative features but also contains many particle-image pairs in several planes which are useful for measuring velocity. This type of seeding was further implemented in another forced ( $150\text{-Hz}$ ) propane jet issuing into a co-flowing air stream that contains several organized vortical structures. Holograms were recorded under both cold and reacting conditions; in addition, a 2D laser-sheet visualization was obtained to aid the viewer/reader in identifying the flame boundaries. Analysis of the reconstructed image for the reacting condition is incomplete at present. However, the reconstructed image of the cold propane jet and the corresponding 2D laser-sheet visualization of the reacting condition are shown in Figs. 6(b) and 6(a), respectively. The main advantage of a 3D reconstructed image over a 2D slice counterpart is the larger angle of viewing and the flexibility of focusing at different depths. Figure 6(b), of course, is only a 2D photograph of the 3D object being reconstructed. These images display the generation and convection of the coherent vortical structures that can aid the further understanding of vortex-flame interactions.

Finally, Figs. 7(a) and 7(b) show typical double-exposed particle images from the reconstructed holograms of the non-reacting and reacting propane jets, respectively; velocity distributions can be obtained from these images. The viewing area in these figures is  $\sim 3 \times 2\text{ mm}$ , and they display both in-plane and out-of-plane particle pairs. The software for extracting the 3D velocity distribution from these reconstructed images is under development.

#### 4. Conclusions

An attempt was made to extend the application of the IROV holographic technique in water flows to different media—especially to combustng flows—and to demonstrate its limitation resulting from the distortion of the reference beam by the temperature and density gradients

and the presence of large amounts of speckle noise. As an alternative to this technique, an off-axis-based holographic recording and reconstruction system that can perform both HFV and HPIV was developed. This system was successfully applied to both reacting and non-reacting propane jet flows in the presence and absence of a co-flowing air stream. Several seeding techniques were implemented to explore the seeding densities necessary for flow visualization as well as for quantitative measurements. The flow field seeded with preformed  $TiO_2$  particles (dense scalar field) provided images suitable for high-quality 3D flow visualization and that seeded with  $Al_2O_3$  particles (moderate scalar field) provided images suitable for both qualitative and quantitative (3D velocity) measurements. This system holds great promise for elucidating vortex-flame interactions and the mechanism governing flame lift-off and for validating CFD codes. In future work, several off-axis configurations will be implemented for further improving the quality of the recorded holograms, and software will be developed for extracting the velocity field from the particle pairs.

### Acknowledgments

The authors gratefully acknowledge Drs. M. Roquemore and R. Hancock of Wright Laboratory for support and help during the design of the experiment and Dr. G. Sturgess of ISSI for valuable discussions. The editorial assistance of Mrs. M. Whitaker (ISSI) is appreciated. This work was supported by AFOSR and USAF Contract F33615-95-C-2507. Dr. H. Meng acknowledges support from the AFOSR Summer Research Program.

### References

- [1] Roquemore, W. M., Chen, L. D., Goss, L. P., Lynn, W. F., 1989: "Structure of Jet Diffusion Flames in Turbulent Reactive Flows," Lecture Notes in Engineering, Vol. 40, Borghi, R. and Murthy, S. N. B., Eds., Springer-Verlag, New York, pp. 49-62
- [2] Katta, V. R., Goss, L. P., Roquemore, W. M., Chen, L. D., 1997: "Dynamics of Propane Jet Diffusion Flames," Atlas of Flow Visualization, The Visualization Society of Japan, Vol. III, pp. 181-197
- [3] Vikram, C. S., Thompson, B. J., 1990: "Selected Papers on Holographic Particle Diagnostics," SPIE Milestone Series, Vol. MS 21
- [4] Meng, H., Hussain, F., 1991: "Holographic Particle Velocimetry, a 3D Measurement Technique for Vortex Interactions, Coherent Structures and Turbulence," Fluid Dynamics Research, 8, pp. 33-52
- [5] Meng, H., Hussain, F., 1995: "In-line Recording and Off-axis Viewing Technique for Holographic Particle Velocimetry," Applied Optics, 34, pp. 1827-1840
- [6] Barnhart, D. H., Adrian, R. J., Papen, G. C., 1994: "Phase-Conjugate Holographic System for High-Resolution Particle-Image Velocimetry," Applied Optics, 33(30), pp. 7159-7170
- [7] Zhang, J., Tao, B., Katz, J., 1996: "Three Dimensional Velocity Measurements Using Hybrid HPIV," Proceedings of the 8th International Symposium on Applications of Laser Techniques to Fluid Mechanics, Lisbon, Portugal, pp. 4.3.1-4.3.8
- [8] Estevadeordal, J., Meng, H., Gogineni, S., Goss, L., Trump, D., Sarka, B., 1997: "Investigation of Holographic Visualization and Holographic PIV Techniques for Fluid Flows," Experimental and Numerical Flow Visualization, ASME Fluids Engineering Division Summer Meeting, Vancouver, B. C., Canada, June 22-26

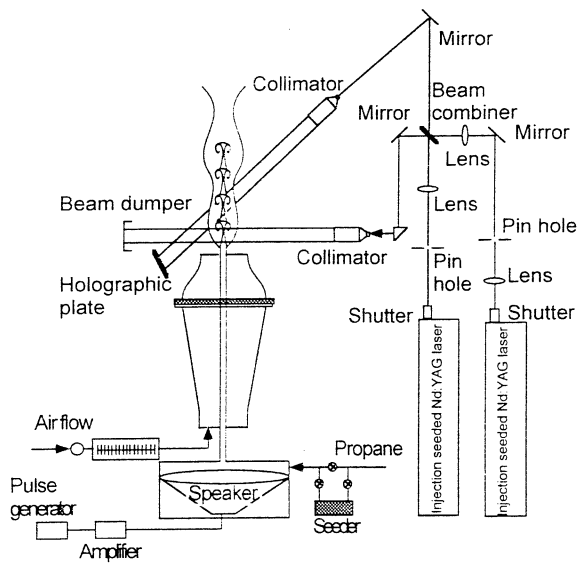


Fig. 1(a) Holographic recording system

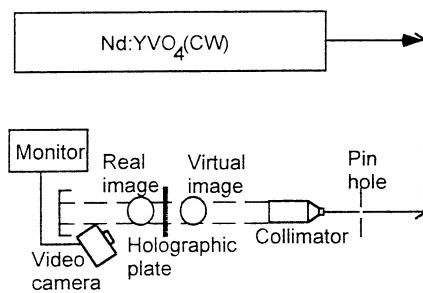
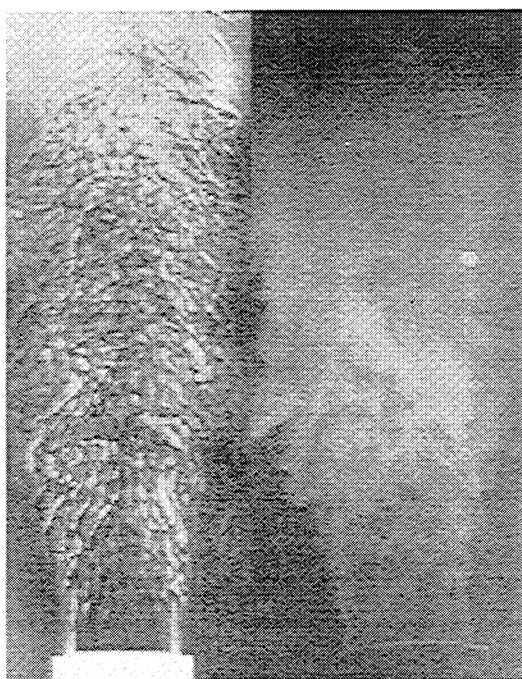


Fig. 1(b) Holographic reconstruction system



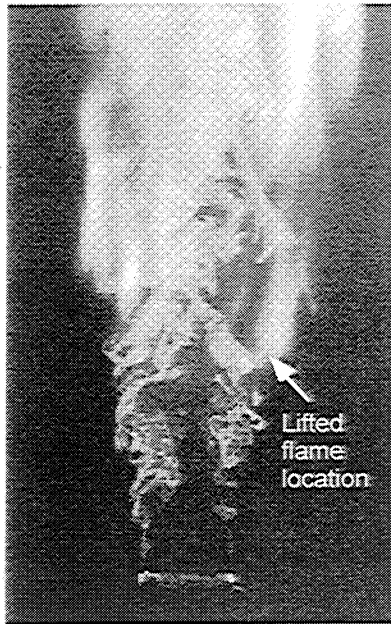
Holographic plate Reconstructed image  
a) Cold propane jet



Holographic plate Reconstructed image  
b) Reacting propane jet

Fig. 2 Photographs of the holographic plates and the reconstructed images (in-line recording)





2D Laser sheet visualization



Reconstructed image from a hologram

a) Lifted flame condition



2D Laser sheet visualization



Reconstructed image from a hologram

b) Attached flame condition

Fig. 3 Vortex-flame interactions in jet diffusion flames

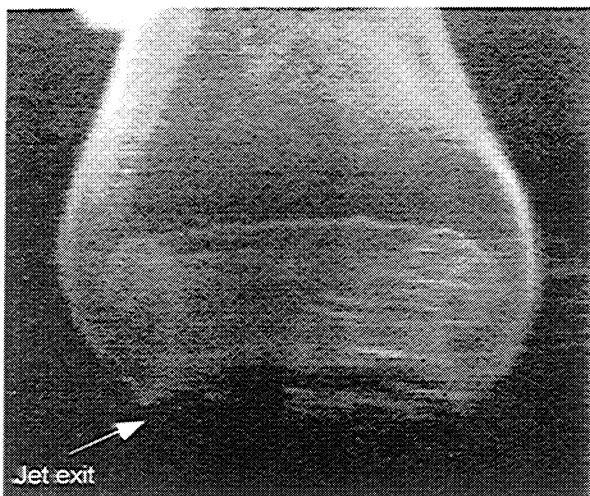


Fig. 4 Reconstructed image of cold propane jet

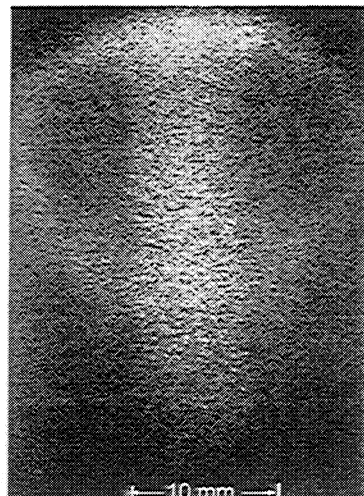
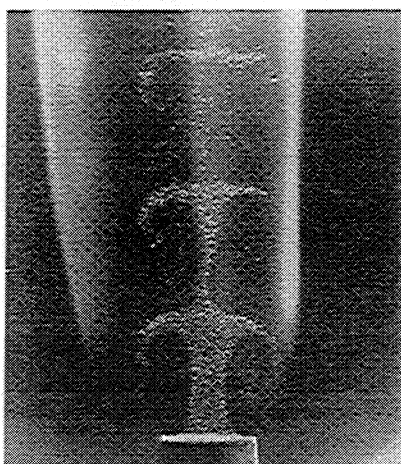
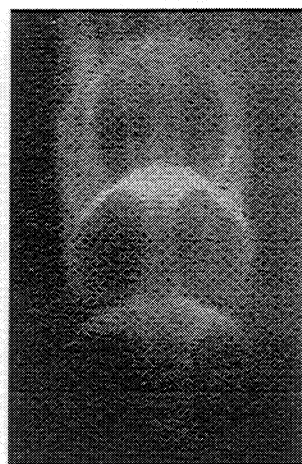


Fig. 5 Reconstructed image of cold propane jet issuing into co-flowing air

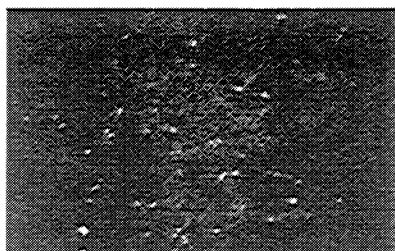


a) 2D laser sheet visualization of reacting propane jet

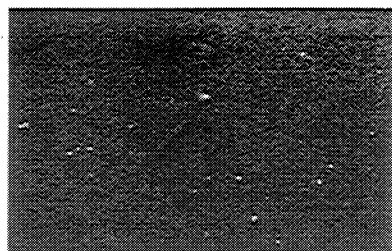


b) Reconstructed image of cold propane jet

Fig. 6 Photographs of the 2D laser sheet visualization and the reconstructed image obtained under identical flow conditions



a) Non-reacting propane jet



b) Reacting propane jet

Fig. 7 Double-exposed particle images suitable for obtaining velocity distribution

# Holographic Flow Visualization as a Tool for Studying Three-dimensional Coherent Structures and Instabilities

Meng, H.\*<sup>1</sup>, Estevadeordal, J.\*<sup>2</sup>, Gogineni, S.\*<sup>2</sup>, Goss, L.\*<sup>2</sup> and Roquemore, W. M.\*<sup>3</sup>

\*<sup>1</sup> Department of Mechanical & Nuclear Engineering, Kansas State University, Manhattan, KS 66506-5106, U.S.A.

\*<sup>2</sup> Innovative Scientific Solutions, Inc., 2786 Indian Ripple, Dayton, Ohio 45440-3638, U.S.A.

\*<sup>3</sup> Air Force Research Laboratory, Wright-Patterson AFB, Ohio 45433-7103, U.S.A.

Received 24 March 1998.

Revised 19 June 1998.

**Abstract:** Holography is capable of three-dimensional (3D) representation of spatial objects such as fluid interfaces and particle ensembles. Based on this, we adapt it into a 3D flow visualization tool called Holographic Flow Visualization (HFV). This technique provides a novel means of studying spatially and temporally evolving complex fluid flow structures marked by a disperse phase or interfaces of different fluids. This paper demonstrates that HFV is a straightforward technique, especially when the In-line Recording Off-axis Viewing (IROV) configuration is used. The technique can be applied either as a stand-alone experimental tool for studying scalar-based coherent structures, flow instabilities, interactions of different fluids driven by fluid dynamics, interfacial phenomena, or as a precursor to volumetric 3D velocity vector field measurement of complex transient flow dynamics. Experimental results in several complex fluid flows and flames demonstrate the effectiveness of HFV. Different methods are used to mark flow structures undergoing different instabilities: 1) a vortex ring grown out of a drop of polymer suspension falling in water, 2) cascade of a bag-shaped drop of milk in water, and 3) internal flow structures of a jet diffusion flame.

**Keywords:** holographic flow visualization, holographic PIV, particle-laden flows, jet diffusion flame, flame-vortex interaction, vortex cascade, vortex ring instability, drop instability.

## 1. Introduction

Flow visualization has been employed as an experimental tool in fluid mechanics for decades (Merzkirch, 1980; Lauterborn and Vogel, 1984). Based on light scattering of smoke, fluorescence of dye, visualization of fluid density variation, image of hydrogen bubbles or other types of flow markers, flow visualization has been widely applied to observe flow patterns and fluid fields. Numerous examples can be given in which flow visualization has been extremely insightful (a good source book is provided by Van Dyke, 1982). It reveals important flow physics, guides intuition into complex phenomena, inspires formulation of theories, and provides valuable feedback for engineering designs. For example, the notion of coherent structures – organized structures underlying transitional and turbulent flows – was born as a result of flow visualization of the plane mixing layer (Brown and Roshko, 1971). The coherent structure approach is key to understanding flow mechanisms and offers an effective means of flow control (Hussain, 1986). Much of the early development in the coherent structure approach can be attributed to flow visualization (Fiedler, 1988), which was later complemented by quantitative flow-field descriptions such as phased-locked measurements using hot-wire anemometry (Zaman and Hussain, 1981; Tung and Kleis, 1996), Direct Numerical Simulation (DNS) (Metcalf et al., 1987) and Particle Image Velocimetry (PIV) (Adrian 1986). Also noteworthy are the 3D reconstructions of coherent structures such as those of Lasheras et al. (1988), Jiménez

et al. (1985), and Agüí and Hesselink (1988).

Despite its enormous contributions in the past, flow visualization has been primarily limited to two-dimensional (2D) representations of three-dimensional phenomena. It normally functions in one of the following scenarios:

- (i) Flow structures seen within the depth of field of an imaging lens (or eyes), where the imaging process is 2D.
- (ii) A 2D slice of a flow structure illuminated by a light sheet.
- (iii) Integration of a 3D density field along the path of a laser beam.

In this sense, common visualization techniques based on photography, shadowgraphy, Schlieren, laser-induced fluorescence, laser-induced scattering (Rayleigh, Raman, Mie), interferometry and holographic interferometry (integration of a density field) are all 2D in nature. These techniques do not provide full 3D instantaneous visualization. Since most complex fluid flows are essentially 3D, many critical details of these flows require 3D visualization tools to capture. Although a flow field can be scanned using a light sheet, it is rather difficult to record details of the 3D structures when the flow is highly transient.

Holographic imaging is capable of instantaneous 3D representation of spatial objects including fluid interfaces and particle ensembles. It holds great promise as a 3D diagnostic tool – both qualitative and quantitative – for spatially and temporally evolving complex flow structures. Holography has been used for diagnosis of particles or aerosols in different types of flows and in combustion (Lee and Kim, 1986; Vikram, 1990). It has also been recently used in Holographic Particle Image Velocimetry (Holographic PIV or HPIV) to measure instantaneous full-field 3D velocity fields (Meng and Hussain, 1991; Barnhart et al., 1994; Meng and Hussain, 1995a, b; Pu et al., 1998). On the other hand, however, the power of holography as a scalar-based 3D flow-visualization tool has not yet been fully investigated.

This paper introduces a 3D flow-visualization method based on holographic imaging. Referred to as Holographic Flow Visualization (HFV), this method can instantaneously and three-dimensionally capture transient flow structures that are properly marked by a dense disperse phase. Since it allows time-resolved experimental study of detailed 3D topology of structures, HFV has great potential for providing insight into vortex dynamics, 3D instabilities, particulate flows and interfacial phenomena. In what follows we will discuss methods of recording the 3D holograms using relatively simple optical arrangements and methods of taking advantage of the three-dimensionality of holographic imaging to study the reconstructed flow structures.

## 2. Marking the Flow Structures

To be recorded by a hologram, the subject flow structure must scatter laser light elastically so that it produces an object wave that is coherent with a reference wave from the same laser. Fluids having different refractive indices can produce the desired elastic scattering on their interfaces. So can the disperse phase in a multiphase flow and tracer particles seeded in a single-phase flow. Ideally, the most faithful tracer for a continuous-phase flow is the fluid molecules, but elastic scattering from molecules (Rayleigh scattering) is generally too weak to be recorded on a hologram. On the other hand, particles of sizes comparable to or larger than the laser wavelength (which is usually a fraction of a micrometer) produce much more intense scattering called Mie scattering. A flow structure marked by a disperse phase (at high concentrations) is therefore suitable for holographic visualization.

We have investigated two scenarios where the flow structures are marked for light scattering in HFV:

- 1) flow structures formed and marked by milk or a dense polymer-sphere suspension, evolving in water and
- 2) flow structures of a jet traced by small solid particles, evolving in air, with or without the presence of a flame.

In the first case, the visualized physical phenomena are results of hydrodynamic interaction of a particle-laden fluid (emulsion or dense polymer-sphere suspension) with water. Here the flow “marker” is the subject of study. In the second case, light-scattering particles are introduced artificially as tracers of the air flow. Here it is desirable to use small particles to minimize their inertia and gravity effects; yet the preferential dispersion dominated by coherent structures (Squires and Eaton, 1991) is actually helpful to mark the structure boundaries. In any case, HFV visualizes structures through markers, and care must always be exercised when interpreting the hydrodynamic significance of the visualization results. Depending on its properties, the flow marker itself may strongly influence the structure through density-sensitive instabilities and particle-flow interactions.

In the area of turbulence and vortex dynamics, although the use of scalars as a basis for *defining* coherent structures is debatable, *visualization* of scalar structures has provided and will continue to provide valuable insight into coherent structures. It should be noted however, that the dynamics of coherent structures based on a scalar

field differs from that based on the flow vorticity field. Not only do the rates of diffusion of scalar and vorticity differ from one another when Schmidt number is non-unity, but scalar dynamics does not include vortex stretching, which is an important mechanism of vortex dynamics (Meng and Hussain, 1991). In the context of this paper, HFV implies visualization of scalar-based structures. Visualization of the vorticity-based structures is much more challenging and is possible only through high-spatial-resolution 3D velocimetry techniques such as Holographic PIV (HPIV), where particle displacements and hence velocities are measured (Meng and Hussain, 1995a, b; Pu et al., 1998). In fact, it is conceivable to build a holographic instrument that performs both HFV and HPIV, which was the motivation of this research (Esteveordal et al., 1997a). This paper will only focus on HFV — the relatively simple method — and not on HPIV.

### 3. Holographic Flow Visualization Principle

Holography consists of two phases: 1) Recording, where the object wave (the laser light scattered off an object) is mixed with a coherent reference wave to produce interference fringes, which are recorded on the holographic plate, and 2) Reconstruction, where the object wave is reconstructed from the developed hologram, forming a real image and a virtual image on separate sides of the hologram. This process is illustrated in Fig. 1(a), which (without loss of generality) shows an in-line configuration using the same collimated beam to serve as the reference wave and to illuminate the object. The two phases can share the same laser source. For fluid flows, however, the recording laser generally should be pulsed to freeze transient flow motions, while a continuous-wave (cw) laser may be more convenient for reconstruction and observation. The recording laser shown in Fig. 1(a) is a Nd:YAG laser with pulse duration of a few nanoseconds. The reconstructed-image size  $l'$  compared with the actual-object size  $l$  scales with  $\lambda_2 / n\lambda_1$ :

$$l'/l = \lambda_2 / n\lambda_1$$

where  $\lambda_1$  and  $\lambda_2$  are the wavelengths of recording and reconstruction lasers, respectively, and  $n$  is the refractive index of the ambient fluid of the flow structure to be imaged. For structures in water, for example,  $n=1.33$ . A holographic movie is produced by a series of laser pulses, each producing a single hologram on a film. The movie allows studying the dynamics of the flow structures.

Holographic imaging of flow structures is made possible through dense particle seeding of the structures. A three-dimensional image of a continuous 3D surface of structures, marked by a collection of particles, is sought rather than individual particle images. HFV therefore operates at much higher particle seeding densities than Holographic PIV. A major obstacle in the HPIV technique, namely speckle noise resulting from superposition of scattered light waves from different particles, is not a problem in HFV. Instead such speckle is used constructively to visualize the flow structure. Typically, particles will not be uniformly distributed in the flow (e.g., less particles are present in vortex cores), and thus speckle will not be uniform over the entire flow region. This actually helps the visualization by providing different tones.

For imaging non-transparent spatial objects, off-axis holography configuration has been widely used. Since HFV is used to image extended flow structures marked by densely seeded particles, off-axis holography is appropriate. It employs a separate reference beam to interfere with the object beam. However, another much simpler, novel configuration, namely the In-line Recording Off-axis Viewing (IROV) method, can be used for HFV. This method was originally developed as a configuration for Holographic PIV (Meng and Hussain, 1995a, b). It has the distinction of using only one laser beam for hologram recording. Since no separate reference beam is needed, a laser with a short coherence length ( $\sim$  centimeters) and low pulse energy ( $\sim$  10 mJ) is sufficient. Any laser that is adequate for regular planar PIV can be used for 3D HFV, whereby only a single laser rather than dual lasers is needed since double exposure is not required. A copper-vapor laser could even be used for HFV with the advantage of high pulse repetition rate (tens of kHz) for high-speed holographic movie (Meng and Hussain, 1991). The optical arrangement of IROV is rather simple as illustrated in Fig. 1(a). A detailed analysis of the IROV technique is given by Meng and Hussain (1995a). To image flow fields with temperature gradients such as those in flames or combustion chambers, IROV holography is not suitable and one must resort to off-axis holography. There, a laser with a much longer coherence length (tens of centimeters) and higher pulse energy ( $>100$  mJ) is required for off-axis hologram recording. Often, the coherence length of a pulsed Nd:YAG laser is achieved by providing the laser with injection seeding.

The methods for observing the reconstructed 3D flow structure are very versatile. A hologram reconstructs,



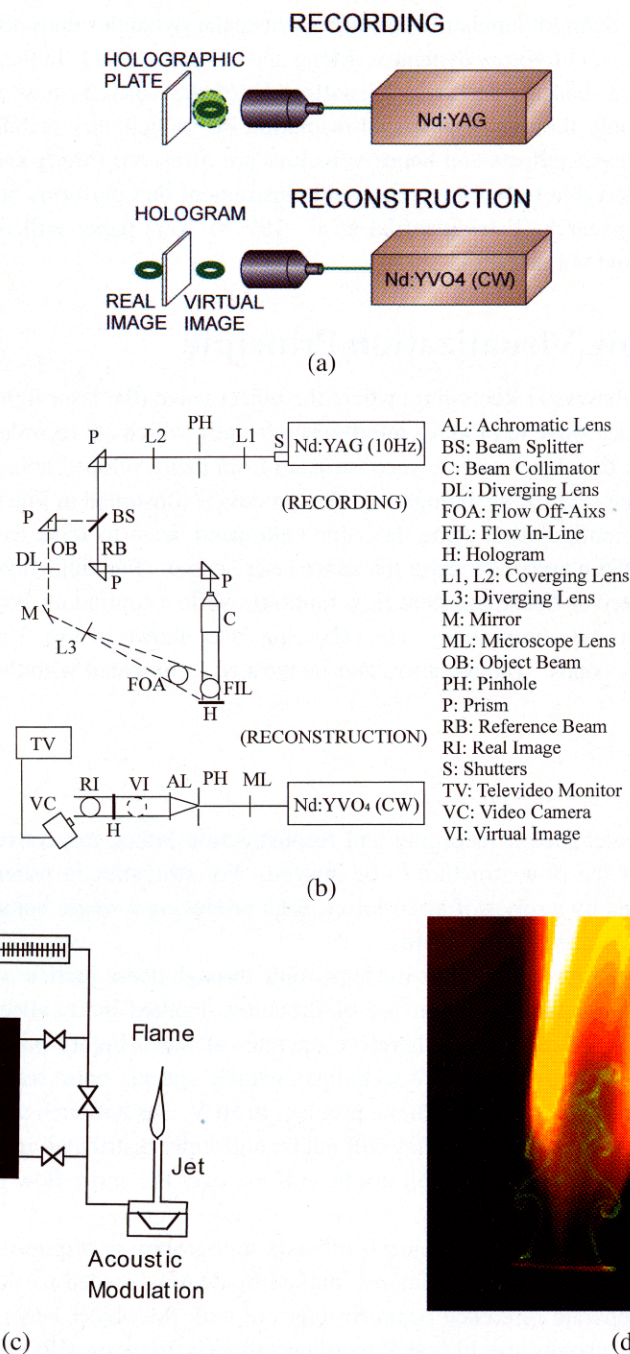


Fig. 1. Experimental setups:

- (a) Holographic recording and reconstruction principle, illustrated using the IROV scheme implemented in this work.
- (b) HFV experiment layout. The recording setup can be switched between IROV mode and off-axis mode. In IROV mode, flow test section is placed at FIL (Flow In-line), RB serves as both reference beam and object illumination beam, and OB is blocked. In off-axis mode, flow test section is placed at FOA (Flow Off-Axis), OB is used to illuminate the object field, and RB remains as reference beam. The reconstruction setup is the same for both modes.
- (c) Schematic of vortex-flame system used for HFV experiments of flames.
- (d) A typical vortex-flame picture (both flame and vortex structures) generated from the forced jet, illustrated two-dimensionally using a laser sheet.

in 3D space, a real image field and a virtual image field located on either side of the hologram. Either image field can be used for visualization. With the IROV method, the direction of observation must be at an angle to the hologram axis to avoid the directly transmitted illumination beam and the twin image. The three dimensionality of the reconstructed flow structure can be explored by changing the viewing angle and focusing at different distances on the 3D image. Different flow scales and details can be analyzed by changing the magnification.

## 4. Visualization Experiments

In the present study, the IROV and off-axis techniques are used for single-exposure holographic flow visualization for a drop of fluid falling into water and a jet-diffusion flame in air. The results are used to demonstrate the effectiveness of HFV in flows with three types of seeding undergoing different instabilities: 1) a vortex ring generated by a falling drop of polymer suspension in water, 2) cascade of a bag-shaped drop of milk in water, and 3) internal flow structures of a jet diffusion flame seeded with  $\text{TiCl}_4$  particles premixed with water (which produce particles  $\text{TiO}_2$  particles).

A holographic imaging system was set up using a 10Hz pulsed Quanta-Ray Nd:YAG laser (Spectra-Physics) at a wavelength of 532 nm and pulse duration of 10 ns, as shown schematically in Fig. 1(b). To make the recording of off-axis holograms easier, the laser was injection-seeded to provide a coherence length greater than 1 m. This laser was joined with a second laser to produce double exposures needed for Holographic PIV. But for the purpose of HFV the second laser was not used and hence not shown in the figure. The laser beam was split into two by a beamsplitter BS: the reference beam (RB) and the object beam (OB), where RB was collimated and projected to the hologram perpendicularly. When IROV holograms were recorded, only RB was used, both as reference beam and object illumination beam. When off-axis holograms were recorded, OB was used to illuminate the object field, while RB remains as reference beam. Hence the recording setup can be switched between the IROV mode (with the flow test section being placed at FIL) and the off-axis mode (with the flow test section being placed at FOA). For reconstruction, we used a cw laser – Millennia Nd:YVO<sub>4</sub> laser (Spectra-Physics) to produce a collimated beam like RB with the same wavelength, 532 nm. The setup for reconstruction is the same for both IROV and off-axis modes.

Initial tests of the technique were conducted in water. Holographic visualization was tested with drops of milk and aqueous suspensions of polymer microspheres (with specific gravity of 1.05 and diameter of  $14.5\ \mu\text{m}$ ) injected into a water tank ( $7.62 \times 10.16 \times 27.94\ \text{cm}^3$ ). The drops, with a typical size of 3.5 mm, were manually injected into the water with a drop counter and were allowed to fall freely (gravitational momentum) from a distance of 1 cm above the water surface.

The feasibility of holography for flame studies was explored in a combustor cylindrical jet forced with acoustic modulation (through a chamber with a speaker to perturb the propane line at a known frequency), as shown schematically in Fig. 1(c). The purpose of the acoustic excitation was to provide a reproducible vortex-flame system (Chen and Roquemore, 1986). The driving frequency was chosen to be a multiple of the Nd:YAG laser frequency, 10 Hz, to provide a strobe effect. A typical vortex-flame system (both flame and vortex structures) generated from the forced jet is shown in Fig. 1(d) using standard 2D laser-sheet visualization. The dense pre-formed seeds are submicron-size  $\text{TiO}_2$  particles produced by premixing  $\text{TiCl}_4$  particles with water. This seeding method produces a dense scalar field appropriate for the visualization of the inner coherent structures in the jet diffusion flame. Preliminary tests of HFV in flames revealed the effects of distortion of the reference beam by temperature and density gradients, and of the need to increase particle seeding density.

The flow structure images from HFV can be observed with the naked eye in most cases. The images are the 3D replicas of the real flow at the time of exposure and can be viewed from different sides and angles (top and bottom, inside and outside, etc.). To demonstrate this feature, photographs were taken with a video camera from different angles, using different magnifications, and focused at different parts of the 3D images.

## 5. Results and Discussion

It is our common experience that the best way to observe a 3D image is to view it with naked eye with the freedom of changing perspective. Since it is not convenient to allow such direct observation in this communication, we show two to three photographs for each 3D image reconstructed from our holograms so that the reader can get a glimpse of the three-dimensionality of the holographic images. It must be clarified that a holographic image is three-dimensional; its depth of focus is the depth of the entire 3D object. A photograph (2D) taken from a



reconstructed 3D holographic image, however, does have a finite depth of focus determined by the camera lens setting. The photographs shown in this paper will appear like regular photographs of some 3D objects—only that these are not real objects but the holographic reconstruction of them. Like frozen sculptures, they no longer move or change with time. We sometimes deliberately choose a small depth of focus on the camera lens to illustrate the freedom offered by the hologram for us (and for our cameras) to focus on different details of the reconstructed 3D flow structures.

### 5.1 HFV of Drops of Two-phase Fluid into Water

The HFV instabilities of a drop of two-phase fluid falling into water will be discussed first. Figures 2-4 show photographs of reconstructed images from IROV holograms. Figure 2 shows different stages of a drop of polymer-sphere suspension falling in water, while the drops falling in water shown in Figs. 3 and 4 are made of milk. Evidently, the drop of polymer-sphere suspension (Fig. 2) initially assumes a donut shape, while the drop of milk (Fig. 3) takes on a bag shape. Both leave behind a wake and a surface wave. In each figure, different stages of the flow evolution are demonstrated including the initial drop-water interaction, instability and subsequent cascading. Each group of photographs demonstrates different aspects of the same 3D holographic image viewed from different angles or focused on different regions.

It is evident from Fig. 2 that the polymer-suspension drop behaves like an impulsive jet flow that is unstable and evolves into a vortex ring. The holographic reconstruction allows different views of the initial ring as shown in Figs. 2(a)-(c). Holograms recorded after the ring formation show that the flow undergoes more complex evolution characterized by a cascade process. The ring is susceptible to 3D instabilities and breaks down into smaller droplets, which now behave as mini-jets and generate smaller rings or “ringlets”. This breakdown is shown from three different angles in Figs. 2(d)-(f). The cascade develops on smaller and smaller scales, producing many generations until diffusion processes dominate the fine-scale mixing of the suspension and water. Details of cascade on a smaller scale are shown in the three photographs of Figs. 2(g)-(i), which are produced from one hologram.

Figure 3, showing a milk drop in water, reveals that a drop falling into a fluid can be susceptible to other instabilities such as the “bag” instability (Craig, 1984; Pilch and Erdman, 1987), whereby a nearly spherical drop changes its shape into a surface resembling a bag. The bag develops a concave or convex shape depending on its Weber number. Two views of the bag are shown in Figs. 3(a), (b). This bag subsequently breaks up into droplets on the rim because of secondary instabilities. The resulting flow is shown in Figs. 3(c)-(e) from different perspectives. The bag-shaped instability occurs more often for milk drops than for the polymer-sphere suspension drops (Estevadeordal et al., 1997b).

It is observed that characteristics of the drop instability and cascade depend on factors such as the initial momentum of the falling drop, the viscosity and density of the fluid of the drop, the surface tension and capillary effects. These factors determine not only the initial shape of the drop, but also differences between generations. For example, as the droplets become smaller, surface tension becomes more important, and hence newer breakdowns assume different characteristics.

It can be seen from Figs. 2 and 3 that, among other common features both drops develop a localized defect that appears to be a preferred site for initiation of the cascade. A symmetrical breakdown (such as a perfect “crown” around the rim) is expected to occur only in ideal situations; in practice, some asymmetries will develop as a result of upstream perturbations (e.g., defect in the injector nozzle). It is noteworthy that each droplet has a trailing “wakelet” shared by the neighboring droplets. These “wakelets” remain connected to each other, giving the cascade a 3D arcade structure that is readily observed in the holographic visualizations. Some viewing angles of the reconstructed image (not shown here) allow observation of the reflection of the drop on the water surface.

Figure 4 shows holographic images of a milk drop injected with high momentum into water at an initial stage (Fig. 4(a)) and its downstream breakdown (Figs. 4(b), (c)). Although the initial stage (Fig. 4(a)) has footprint of a ring or bag shape, the drop quickly evolves into turbulent-like states (Figs. 4(b), (c)). This particular rapid flow shows different labyrinthic structures and chaotic connections not seen in the slower cascades in Fig. 3. This demonstrates the power of the HFV technique's ability to freeze the instantaneous 3D flow features and allow detailed analysis of them.



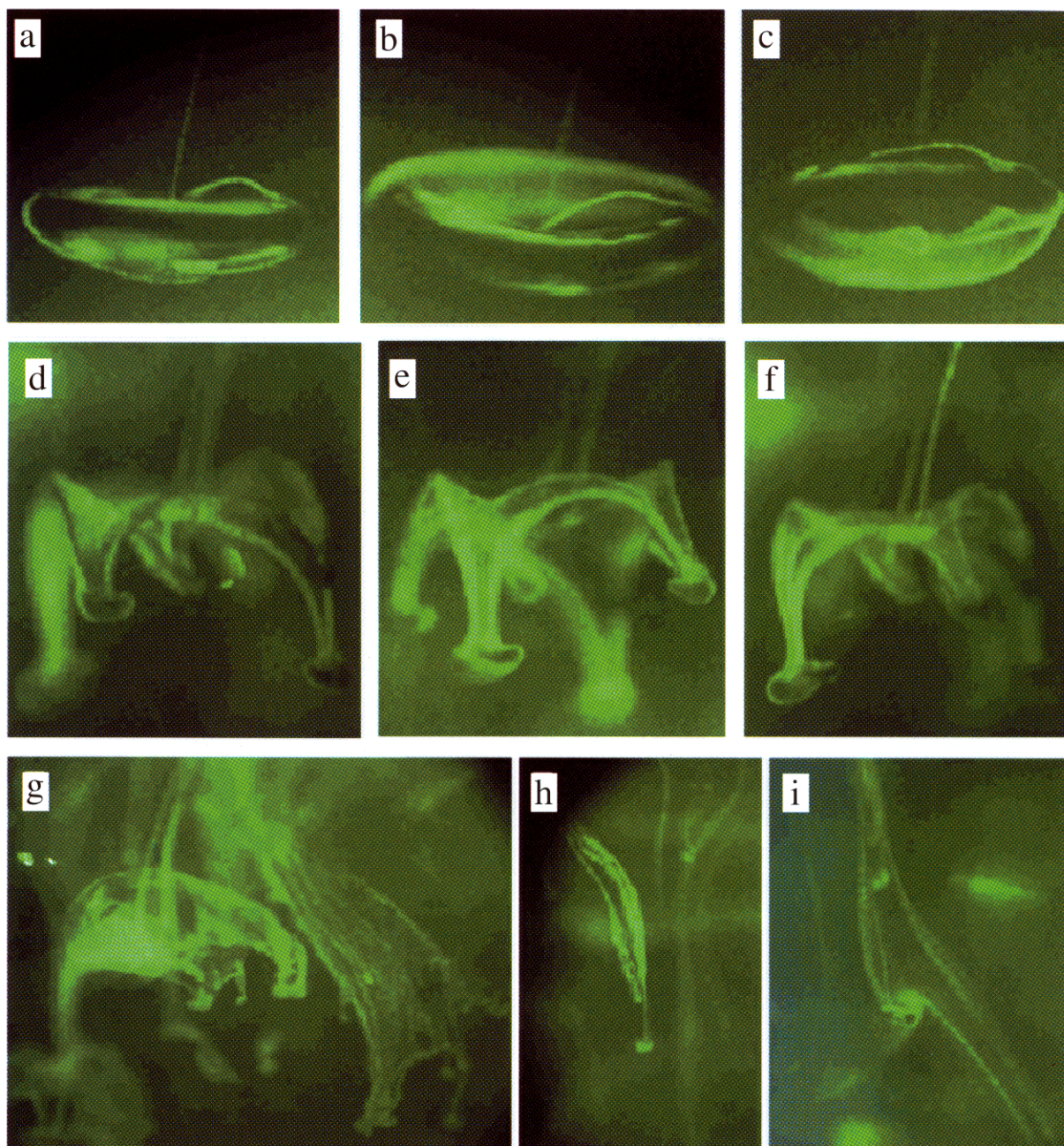


Fig. 2. Holographic images of polymer-suspension drop falling in water undergoing vortex-ring instability, photographed from 3D images reconstructed from IROV holograms:

- (a)-(c) Initial vortex ring evolved from the falling drop, photographed from different angles with respect to the normal of hologram. All are  $20^\circ$  horizontally; a)  $0^\circ$  vertically; b)  $20^\circ$  vertically; c)  $-20^\circ$  vertically.
- (d)-(f) Breakdown of the ring into smaller droplets forming a crown, shown from three different angles with respect to the normal of hologram. All are  $0^\circ$  vertically; d)  $20^\circ$  horizontally; e)  $-20^\circ$  horizontally; f)  $-10^\circ$  horizontally.
- (g-i)s Details of further cascade on a smaller scale, photographed from one hologram from different angles and focused at various distances.



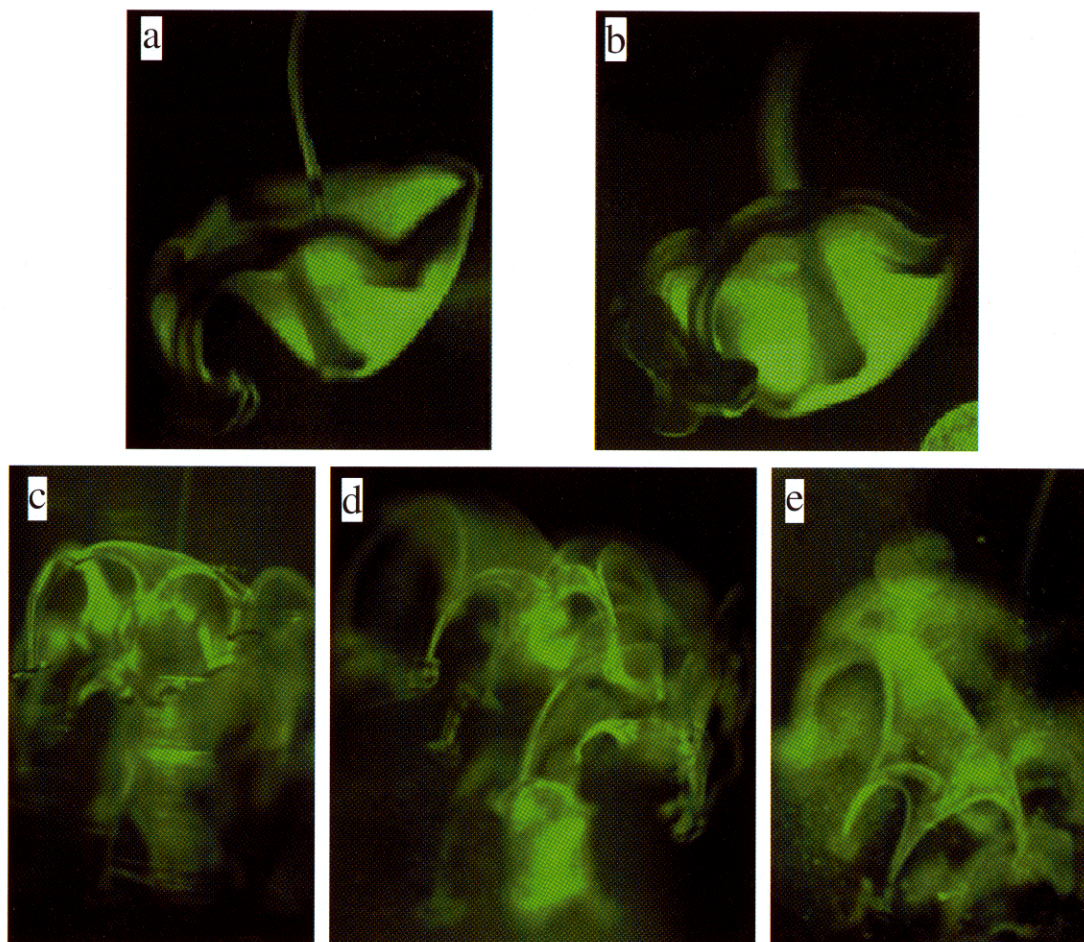


Fig. 3. Holographic images of a milk drop falling in water undergoing bag instability, photographed from 3D images reconstructed from IROV holograms:

- (a),(b) Initial bag evolved from the drop, photographed from different angles with respect to the normal of hologram. Both are  $20^\circ$  horizontally; a)  $20^\circ$  vertically; b)  $0^\circ$  vertically.
- (c)-(e) Downstream cascade of the bag, photographed from different angles with respect to the normal of hologram and focused at various distances. c)  $-20^\circ$  horizontally and  $0^\circ$  vertically, d)  $20^\circ$  horizontally and  $0^\circ$  vertically, e)  $20^\circ$  horizontally and  $40^\circ$  vertically.

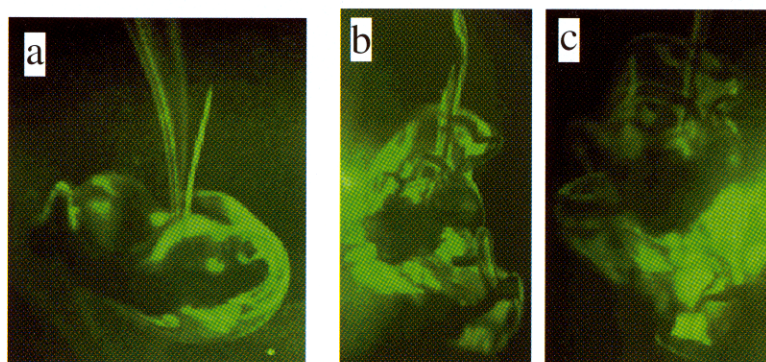


Fig. 4. Holographic images of a turbulent milk drop injected with high momentum into water, photographed from 3D images reconstructed from IROV holograms:

- (a) Initial structure of the drop.
- (b),(c) Downstream breakdown of the drop, photographed from different horizontal angles with respect to the normal of hologram. b)  $20^\circ$ ; c)  $-20^\circ$ .



## 5.2. HFV of Jet Diffusion Flames

3D holographic visualization of propane jet diffusion flames is discussed next. A typical vortex-flame system is shown in Fig. 1(d) using standard 2D laser-sheet visualization, which shows only one plane (sheet). The jet coherent structures are vortex rings generated through shear-layer instability at the nozzle exit. They undergo various hydrodynamic instabilities as they are convected downstream. The flow evolution is changed by the presence of the flame, whose behavior is also affected by the flow.

Holographic visualization relies on light scattering from markers, and thus the structures captured by the hologram are those marked by the collection of particles. The existence of temperature gradients in the presence of flame brings about the so called thermophoresis forces: forces that push particles away from the flame front (Song et al., 1993). Hence, the flame front itself often cannot be recorded by the hologram for lack of particles. However, flow structures can be traced by particles reasonably well even in the presence of flame, and flame-vortex interactions are readily observed. In high temperature regions, we found that we had to increase the particle seeding density.

The main challenge for HFV in presence of flames is the strong density/temperature gradients in the flow field. For in-line recording, the reference beam, which is also the illumination beam, passes through the temperature and density gradients of the flame. These gradients destroy the reference beam wavefront. As a result, flame holograms obtained with IROV contains a large amount of speckle noise resulting from the reference beam destruction by the flame. In this case the off-axis configuration should be used with the reference beam separate from the illumination beam.

Three different jet-diffusion flames were studied using off-axis holography based HFV. The 3D holographic reconstruction of the flow structures is shown in Figs. 5(a)-(c). Each pair of pictures was photographed by focusing at two different distances and from two slightly different angles. The first two cases correspond to forced jets (under different conditions) and the third one, an unforced turbulent jet. The maximum allowed viewing angle from the holographic image, based on this off-axis setup, was not as wide as that based on the IROV configuration. This is because the object was placed farther away from the hologram. However, characteristics of 3D structures are obvious from the pictures. Toroidal 3D structures are clearly visible in Fig. 5(a) and Fig. 5(b), where the vortex rings are evidently connected in contrast to planar flow visualization where each ring is only represented by a cross-section (Fig. 1 (d)).

An interesting phenomenon was observed from holographic visualization of case (c). Notice from Fig. 5(c) that after the jet exit (visible from the pictures), not many structures are present, but after about one jet diameter down stream, a vortex ring with 'bulges' or 'protuberances' can be seen. About five bulges (known in the jet community as 'lobes') are counted, consistent with prediction by Widnall instability (Widnall et al., 1974). These bulges grow in amplitude, generate streamwise vortices, and eventually undergo transition to turbulence. On the other hand, as the experiment was conducted, we clearly observed that the flame was not located at the jet exit, but was lifted up by 1 jet diameter. Therefore, we postulate that the flame was attached to the vortex ring that was undergoing the first instability. This postulation was confirmed with repeated experiments. Most of the lifted flames in this experiment had the common feature of being attached to the first vortex instability, usually with five lobes, which further generated five flamelets.

## 6. Conclusions and Discussions

Holographic Flow Visualization (HFV) techniques have been investigated as a unique 3D visualization tool for flow structures that are marked by densely seeded, light scattering particles. Preliminary experiments were conducted to study the feasibility of using this technique in the diagnosis of coherent structures, flow instabilities, flames, and hydrodynamic interactions of different fluids. Three-dimensional visualization was accomplished using IROV and off-axis holographic configurations. In all cases HFV results yielded good agreement with the expected flow and flame characteristics. The IROV configuration has simpler optical geometry. However, when the flow field includes significant density and/or temperature gradients (such as in flames), the off-axis configuration is preferred. It has been demonstrated that holographic imaging, which has the capability of instantaneous 3D representation of spatial objects including fluid interfaces and particle ensembles, holds great promise as a 3D diagnostic tool – both qualitative and quantitative – for spatially and temporally evolving complex fluid flow structures.

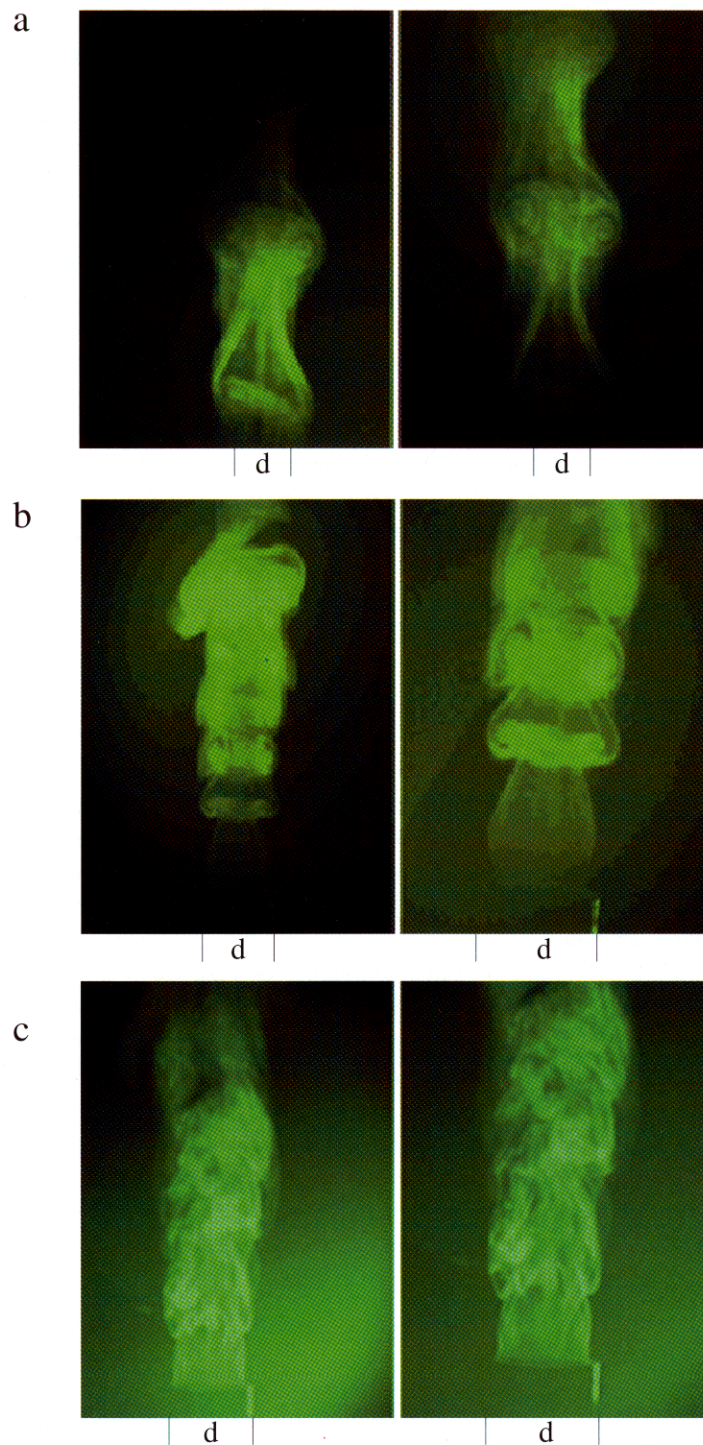


Fig. 5. Holographic images of three vortex-flame systems, photographed from 3D images reconstructed from off-axis holograms. The flame is not visible from these images. Nozzle location and diameter ( $d = 1$  cm) are marked as reference:

- (a) A forced jet, photographed from two horizontal angles with respect to the normal of hologram (Left:  $-5^\circ$ , Right:  $5^\circ$ ).
- (b) A forced jet, photographed using two different magnifications. Toroidal 3D structures are clearly visible.
- (c) An unforced forced jet, photographed using two different magnifications. About 1 jet diameter down stream, a vortex ring with 'bulges' or 'protuberances' can be seen. It was found that the flame was lifted and attached to this unstable vortex ring.

The limitations of the HFV technique include the need for a disperse phase (particles) or interfaces of fluids with different refractive indices. The reason as already discussed, is that in order to produce a hologram of the flow structure, elastic light scattering on flow markers needs to be produced to interfere with the reference laser beam. Like in PIV and HPIV, the introduction of seeds into the flow may not always be desirable or possible, especially because the seeding density required for HFV is generally higher than those for PIV and HPIV. This could prevent the HFV technique from being applied to some flow problems. Two other issues we would like to address are related to the limitation of the current HFV experiments. First, we did not perform quantitative analysis of the 3D images. This can be done with a CCD camera, a traverse, and a computer data acquisition system. Since the 3D holographic images are "frozen" during reconstruction, they are ready to be scanned by a CCD camera and input into a computer. Second, we did not perform time-resolved study of the flow structures. Again, this can be done in a more sophisticated study. Based on a continuously pulsing laser (like the 10Hz pulsed YAG laser used in this study or a chopped cw laser), temporal HFV requires sequential recording of a series of holograms. They can be implemented by a roll of holographic film, multiple holographic plates, or multiplexed onto one hologram. The current investigation has shown the feasibility and application potential of the holographic flow visualization technique, and its capabilities should further expand to include quantitative and time-resolved analyses.

### Acknowledgments

The authors gratefully acknowledge discussion with of R. Hancock on flame experiments and editorial assistance of M. Whitaker and Y. Pu. This work was supported by AFOSR and USAF Contract F33615-96-C-2507. H. Meng gratefully acknowledges support from the AFOSR Summer Research Program, a National Science Foundation grant, and the Program for Complex Fluid Flows at the Kansas State University.

### References

- Adrian, R. J., Particle-imaging Techniques for Experimental Fluid Mechanics, *Ann. Rev. Fluid Mech.*, 23 (1991), 261-304.
- Agüí, J. C. and Hesselink, L., Flow Visualization and Numerical Analysis of a Coflowing Jet: A Three-Dimensional Approach, *Journal of Fluid Mechanics*, 191 (1988) 19-45.
- Barnhart, D. H., Adrian, R. J. and Papen, G. C., Phase-Conjugate Holographic System for High-Resolution Particle-Image Velocimetry, *Applied Optics*, 33 (1994), 7159-7170.
- Brown, G. L. and Roshko, A., The Effect of Density Difference on the Turbulent Mixing Layer, *Turbulent Shear Flows*, (1971) AGARD-CP-93, 23-1.
- Chen, L. D. and Roquemore, W. M., Visualization of Jet Flames, *Combustion and Flame*, 66 (1986), 81-86.
- Craig, J. E., Conventional and Liquid Metal Droplet Breakup in Aerodynamic Nozzle Contractions, AIAA-84-0201, (1984) Reno, NV.
- Esteveordal, J., Meng, H., Gogineni, S., Goss, L., Trump, D. and Sarka, B. (1997a), Investigation of Holographic Visualization and Holographic PIV for Fluid Flows and Flames, *Proceedings of ASME Fluids Engineering Division Summer Meeting, FEDSM97-3093*, Vancouver, BC, June 22-26, 1997.
- Esteveordal, J., Meng, H., Gogineni, S., Goss, L., and Roquemore, M. (1997b), "3D Visualization of Vortex-Ring and Bag-Shaped Instabilities Using Holography, *Physics of Fluids (Gallery of Fluid Motion)*, 9 (1997), No. 9, S5.
- Fiedler, H. E., Coherent Structures in Turbulent Flows," *Progress in Aerospace Science*, 25 (1988), 231-269.
- Hussain, A. K. M. F., Coherent Structures and Turbulence, *Journal of Fluid Mechanics*, 173 (1986), 303-356.
- Jiménez, J., Cogollos, M. and Bernal, L. P., A Perspective View of the Plane Mixing Layer, *Journal of Fluid Mechanics*, 152 (1985), 125-143.
- Lasheras, J. C., Cho, J. S. and Maxworthy, T., On the Origin and Evolution of Streamwise Vortical Structures in a Plane, Free Shear Layer, *Journal of Fluid Mechanics*, 172 (1986), 231-248.
- Lauterborn, W. and Vogel, A., Modern Optical Techniques in Fluid Mechanics, *Annual Review of Fluid Mechanics*, 16 (1984), 223.
- Lee, Y. J. and Kim, J. H., A Review of Holography Applications in Multiphase Flow Visualization Study, *Journal of Fluid Engineering*, 108 (1986), 279-287.
- Lugt, H. J., *Vortex Flow in Nature and Technology*, (1983), John Wiley, New York.
- Meng, H. and Hussain, F., Holographic Particle Velocimetry, a 3D Measurement Technique for Vortex Interactions, Coherent Structures and Turbulence, *Fluid Dynamics Research*, 8 (1991), 33-52.
- Meng, H. and Hussain, F. (1995a), In-line Recording and Off-Axis Viewing Technique for Holographic Particle Velocimetry, *Applied Optics*, 34 (1995), 1827-1840.
- Meng, H. and Hussain, F. (1995b), Instantaneous Flow Field in an Unstable Vortex Ring Measured by Holographic Particle Velocimetry, *Physics of Fluids*, 7 (1995), 9-11.
- Merzkirch, W., *Flow Visualization* (2nd Edition), (1987), Academic Press, Orlando, FL.
- Metcalfe, R. W., Orzag, S. A., Brachet, M. E., Menon, S. and Riley, J. J., Secondary Instability of a Temporally Growing Mixing Layer, *Journal of Fluid Mechanics*, 184 (1987), 207-247.
- Pilch, M. and Erdman, C. A., Use of Breakup Time Data and Velocity History Data to Predict the Maximum Size of Stable Fragments for Acceleration-Induced Breakup of a Liquid Drop, *Journal of Multiphase Flow*, 13 (1987), 741-757.
- Pu, Y., Huang, Z. and Meng, H., An Advanced Off-axis Holographic Particle Image Velocimetry (HPIV) System, *The 9th Int'l Symposium for Applications of Laser Techniques to Fluid Mechanics*, Lisbon, Portugal, July 13-16, 1998.
- Squires, K. D. and Eaton, J. K., Preferential Concentration of Particles by Turbulence, *Phys. Fluids A* 3 (1991), 1169-1178.
- Sung, C. J., Law, C. K. and Axelbaul, R. L., Effect of Thermophoresis on Seeding Particles in LDV Measurements of Flames", *Proceedings of*

Eastern States Comb. Meeting (1993), San Antonio, TX, 354-357.

Tung, S. and Kleis, S. J., Initial Streamwise Vorticity Formation in a Two-stream Mixing Layer, *Journal of Fluid Mechanics*, 319 (1996), 251-279.

Van Dyke, M., *An Album of Fluid Motion*, (1982), Parabolic Press, Stanford, CA.

Vikram, C. S., *Particle Field Holography*, (1992), Cambridge University Press, U.K.

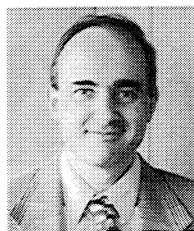
Widnall, S. E., Bliss, D. B. and Tsai, C.-Y., The Instability of Short Waves on a Vortex Ring, *Journal of Fluid Mechanics*, 66 (1974), 35-47.

Zaman, K. B. M. Q. and Hussain, A. K. M. F., Taylor Hypothesis and Large-Scale Coherent Structures, *Journal of Fluid Mechanics*, 112 (1981), 379-396.

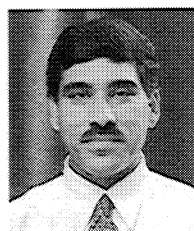
## Authors' Profiles



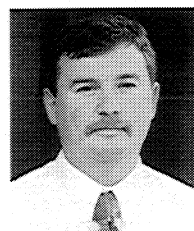
Hui Meng: She received her MS degree in Optical Engineering in 1987 from Zhejiang University and her Ph.D. degree in Mechanical Engineering from University of Houston in 1994. As a DAAD Scholar she conducted research in Applied Physics at the Technical University of Berlin from 1987 to 1990. In 1995 she became an Assistant Professor in Mechanical Engineering at Kansas State University. She is leading the Laser Flow Diagnostics Laboratory to develop holographic particle image velocimetry (HPIV) techniques. Her current research also involves application of PIV and other optical diagnostic techniques to studying turbulence, vortex dynamics, mixing, and CFD validation. In summer 1996 she worked at the Air Force Research Laboratory to help developing HPIV and holographic flow visualization for combustion.



Jordi Esteveordal: He received his Ph.D. degree in Mechanical Engineering in 1996 from the University of Houston. His current research efforts involve the development and application of DPIV for transonic turbomachinery flows and evaluation of MEMS for hypersonic flows. He is also involved in the development and application of innovative Holographic Flow Visualization (HFV) and Holographic PIV techniques for both reacting and non-reacting flows. Previously, he investigated two-stream flow transition to turbulence in a large wind-tunnel facility using hot-wire anemometry and provided the first detailed experimental studies of the complex evolution of spanwise and secondary vortices in a plane mixing layer.



Sivaram Gogineni: He received his Ph.D. degree in Mechanical Engineering in 1993 from Florida State University. He is presently the Principal Investigator on several projects involving digital particle-image velocimetry (DPIV) development for transonic turbomachinery flows and evaluation of MEMS for film-cooling flows and hypersonic flows. He is actively involved in the extension of DPIV to large-scale wind-tunnel facilities and supersonic flows. His high-resolution PIV data were used to develop 3D DNS simulations of transitional wall jets and numerical simulations of vortex-flame interactions. He was instrumental in the development of innovative Holographic Flow Visualization (HFV) and Holographic PIV techniques for both reacting and non-reacting flows.



Larry Goss: He received his Ph.D. degree in Physical Chemistry in 1978 from the University of Georgia. He is Founder/President of Innovative Scientific Solutions, Inc. His current research involves the development and application of advanced laser-based diagnostic techniques for the study of combustion and fuel degradation and the development of pressure- and temperature-sensitive-paint technology. Previously he developed two-dimensional diagnostic techniques for flow visualization and for velocity, temperature, and species-concentration measurements in combustion and aerodynamic environments. These techniques include planar laser-induced fluorescence, reactive Mie scattering, planar Raleigh scattering, particle-imaging velocimetry, thin-filament pyrometry, and pressure-sensitive paint. Prior to these efforts he conducted research utilizing Coherent Anti-Stokes Raman Spectroscopy (CARS) and a combined CARS/Laser Doppler Velocimetry system for spatially and temporally resolved measurements of various gas species in combustion environments.



William Melvyn Roquemore: He received his BS Degree in Physics in 1963 from Auburn University. After graduation, he started working at the Air Force Aero Propulsion Laboratory. He received an MS in Physics in 1969 from the University of Dayton, and a Ph.D. in Physics from the University of Cincinnati as part of an Air Force Long Term Training Program. He is currently a Senior Scientist at the Propulsion Directorate of the Air Force Research Laboratory. He directs experimental and computational research involving fundamental combustion processes and advanced combustor concepts.

#### **2.1.4 Ultrafast-Imaging Technique**

To characterize transient flow-field events such as those associated with advanced ignition systems, several laser-based diagnostic techniques were developed. These techniques were designed to exploit an ultrafast framing camera [charge-coupled device (CCD)] and high-repetition-rate laser sources for capturing high-speed transient events. The results of this diagnostic development effort are summarized in two papers: “Imaging Strategies for the Study of Gas Turbine Spark Ignition” (see pp. 57-66) and “Ultrafast Imaging of a Gas Turbine Spark Igniter” (see pp. 67-70).



## Imaging strategies for the study of gas turbine spark ignition

James R. Gord,<sup>\*a</sup> Charles Tyler,<sup>a</sup> Keith D. Grinstead, Jr.,<sup>b</sup>  
Gregory J. Fiechtner,<sup>b</sup> Michael J. Cochran,<sup>c</sup> and John R. Frus<sup>c</sup>

<sup>a</sup>Air Force Research Laboratory, Wright-Patterson Air Force Base, OH 45433-7103

<sup>b</sup>Innovative Scientific Solutions, Inc., 2766 Indian Ripple Road, Dayton, OH 45440-3638

<sup>c</sup>Unison Industries, 7575 Baymeadows Way, Jacksonville, FL 32256

### ABSTRACT

Spark-ignition systems play a critical role in the performance of essentially all gas turbine engines. These devices are responsible for initiating the combustion process that sustains engine operation. Demanding applications such as cold start and high-altitude relight require continued enhancement of ignition systems. To characterize advanced ignition systems, we have developed a number of laser-based diagnostic techniques configured for ultrafast imaging of spark parameters including emission, density, temperature, and species concentration. These diagnostics have been designed to exploit an ultrafast-framing charge-coupled-device (CCD) camera and high-repetition-rate laser sources including modelocked Ti:sapphire oscillators and regenerative amplifiers. Spontaneous-emission and laser-schlieren measurements have been accomplished with this instrumentation and the results applied to the study of a novel Unison Industries spark igniter that shows great promise for improved cold-start and high-altitude-relight capability as compared to that of igniters currently in use throughout military and commercial fleets. Phase-locked and ultrafast real-time imaging strategies are explored, and details of the imaging instrumentation, particularly the CCD camera and laser sources, are discussed.

**Keywords:** Visualization, Imaging, Ultrafast Lasers, CCD Cameras, Vortex-Flame Interactions, Spark Ignition

### 1. INTRODUCTION

Experimental and computational techniques for the visualization of fluid flows have emerged as essential tools for increasing our understanding of the physics and chemistry of these flows. Indeed, many—if not most—of the breakthroughs in fluid mechanics and dynamics can be attributed to the understanding achieved through imaging of the various multidimensional structures in fluid flow. Flow visualization has played a powerful role in the process of validating computational models through comparisons of experiment and theory. For example, the development and validation of the UNsteady Ignition and COMbustion with Reactions (UNICORN) code at Wright-Patterson Air Force Base have been achieved through continuous improvement and refinement based on comparisons with experimental flow-visualization data.<sup>1</sup> The literature is replete with reviews and primers describing the practice and theory of both experimental and computational flow-visualization techniques.

The diagrams in Figure 1 capture two methodologies that can be applied to the acquisition of experimental flow-visualization data. In both cases, the goal is to resolve the temporal and spatial scales required to achieve an understanding of the flowfield. These diagrams represent scenarios in which an optical excitation source and detector are employed to capture the dynamics associated with the flowfield under study. In many instances, no excitation source is required, and the flow is imaged directly using an appropriate detector; however, such instances are not the focus of the current work. Rather this paper addresses those cases where optical excitation is applied to produce the flowfield signal for subsequent detection.

In the first case, the time-evolving dynamics characteristic of the flowfield under study are explored through careful control of the relative phase between excitation/detection and the fluid-dynamic event. This approach, which is often referred to as phase-locked imaging, relies upon the reproducibility of the phenomena under study. Time-evolving data are obtained by repeating an experiment many times while incrementing the phase delay between the excitation/detection and fluid-dynamic events in a controlled fashion with each new experiment. In this manner, a sequence of images is constructed over time, and each image represents the features of the flowfield under study at a precise phase delay. Through post processing, the sequence of images can be joined to produce an animation or movie that reveals the phase-resolved—and, therefore, time-resolved—behavior of the flowfield. This phase-locked approach demands that the fluid dynamics under study occur in each experiment with a very high degree of reproducibility. Any differences in these events from experiment to experiment will be realized as random, uncorrelated structures in the final phase-resolved animation. Because of this reproducibility

\*Correspondence: E-Mail: james.gord@pr.wpafb.af.mil; Telephone: 937 255 7431; Fax: 937 656 4570

requirement, externally driven or forced flows and naturally periodic flows are those most often studied via phase-locked imaging techniques.

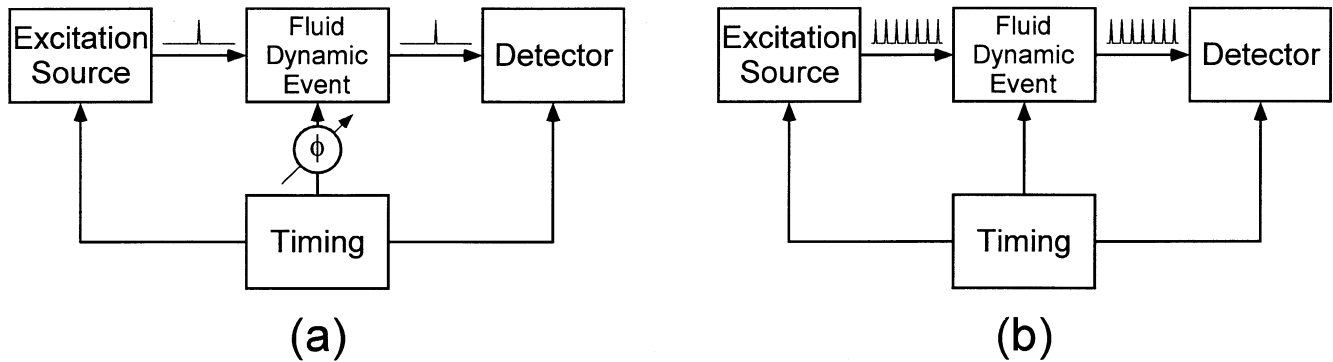


Figure 1. Experimental methodologies for flow visualization. (a) Phase-locked approach in which the excitation and detection events are synchronized in time while the phase of the fluid-dynamic event is varied with respect to excitation/detection. (b) Ultrafast real-time approach in which a high-repetition-rate excitation source and an ultrafast-framing detector are utilized to capture the time dynamics of a single transient fluid-dynamic event.

While phase-locked imaging has been used extensively to reveal the detailed time dynamics of many interesting flows, these techniques cannot be applied to many important flows that lack the required periodic characteristics and phase-resolved reproducibility. These flows involve fluid dynamics that are truly transient in nature, occurring only once or occurring repeatedly with decidedly different time-evolving structures in each instance. A partial list of such phenomena includes fully developed turbulence, ignition and extinction of combusting flowfields, and detonation events. Studying the time dynamics of these important flowfields requires a visualization approach that can capture an entire sequence of time-resolved images on the time scale of the event under study (i.e., in real time). Such an approach places demanding requirements on the imaging hardware and software employed. Experimental tools must provide sufficient bandwidth to resolve the temporal evolution of the structures of interest. Furthermore, the excitation source and the detector must supply sufficient spectral brightness (in the case of the source) and sensitivity (in the case of the detector) to record the signals of interest in a single pass, given that signal-to-noise enhancement through repetitive sampling is not possible for these types of flowfield studies.

In this paper, recent experiments performed through phase-locked imaging and ultrafast real-time imaging, are described to compare and contrast the relative merits of the two approaches. Visualization of vortex-flame interactions has been achieved in a reproducible opposed-jet burner; the data and experimental methodology are presented as examples of the phase-locked approach. The real-time behavior of a gas turbine spark igniter has been explored through the use of a high-repetition-rate laser source and an ultrafast-framing camera. The design of these experiments and the data obtained are presented as examples of the ultrafast real-time imaging methodology.

## 2. BACKGROUND

The hardware and software necessary to accomplish phase-locked imaging have been available and employed experimentally for quite some time. A pulsed excitation source (e.g., a flashlamp or a pulsed laser), a two-dimensional array detector (e.g., a film camera, a photodiode array, or a CCD), and a means of synchronizing the experimental events and controlling the associated phase (e.g., a digital delay generator) are required. On the other hand, the tools for achieving ultrafast real-time imaging with the bandwidth required to resolve fluid-dynamic timescales of interest have been difficult to develop and acquire. Ultrafast real-time imaging methodologies have evolved continuously with the development of increasingly capable hardware and software that yield higher repetition rates for excitation and increased data-acquisition bandwidths and storage capability.

Early developments in real-time imaging based on flashlamp-pumped sources and modelocked lasers coupled with analog recording devices have been reviewed by Sklizkov.<sup>2</sup> Many of the schemes described involve streaking the high-bandwidth signal across an appropriate detector through the use of rotating mirrors, etc.

Hanson and coworkers<sup>3-6</sup> have exploited the latest available technology to achieve time-evolving two-dimensional visualization of important flowfields as well as three-dimensional realizations of complex flows. In early work, the Stanford team accomplished instantaneous three-dimensional visualization of combustor flowfields by sweeping a single high-energy laser sheet through the flow using a scanning mirror and capturing a sequence of planar slices using a fast-framing camera system. Laser excitation was provided by a single 1.5-2- $\mu$ s-wide pulse from a Candela SLL-8000 coaxial flashlamp-pumped dye laser. Pulse energies from 1-5 J were achieved with Rhodamine 590 laser dye. Images of the laser profile as well as planar Mie scattering from soot particles were achieved using a camera system based on the Hadland 790 Imacon image converter that frames at 10 MHz. Sequences of eight to twenty images were generated by the Imacon phosphor and subsequently recorded using photographic film or a CCD camera. By frequency doubling the dye-laser output to 285 nm, pulse energies of 300 mJ/pulse were available for planar laser-induced fluorescence (PLIF) imaging of acetone-seeded flows.

More recently, Ben-Yakar and Hanson<sup>7</sup> have developed an ultra-high-speed schlieren system to study cavity flameholders for ignition and flame stabilization in scramjets. Signals are generated using a Hadland Model 20/50 xenon flashlamp that provides a 200- $\mu$ s excitation pulse. Schlieren images are recorded using a Hadland Imacon 468 digital camera. This camera employs a beamsplitter to direct the input signal to eight separate 576x384-pixel intensified CCD arrays. Interframing times as short as 10 ns can be achieved with this system.

Long and coworkers<sup>8-10</sup> explored high-speed digital imaging of turbulent flows, recording time-evolving digital images of gas concentrations and instantaneous three-dimensional fuel-concentration profiles through Mie scattering and biacetyl-fluorescence techniques. Excitation sources included an acousto-optically modulated argon-ion laser and a 6-kHz-pulsed copper-vapor laser; detectors included a silicon-intensified target (SIT) vidicon, a Reticon MC9128 photodiode array, and Spin Physics SP2000 high-speed video recording system.

Lempert, Wu, and Miles<sup>11,12</sup> recently developed a megahertz-rate, pulse-burst laser system based on Nd:YAG technology that is designed to deliver bursts of pulses at 532 nm with pulse durations between 10 and 100 ns, interpulse periods as short as 1  $\mu$ s, and pulse energies up to 1 mJ. This excitation source is complemented by a Princeton Scientific Instruments (PSI) ultrafast-framing camera designed to accomplish the acquisition of 30 frames of data at framing rates up to 1 MHz. (A second-generation PSI device described below was utilized in the spark-ignition studies that are the subject of the current paper.) This laser and camera have been employed to study supersonic shock-wave/boundary-layer interactions through images obtained via filtered Rayleigh scattering.

At the Lund Institute of Technology, Kaminski and coworkers<sup>13</sup> have accomplished high-speed visualization of spark ignition through the use of a Q-switched Nd:YAG-based laser source and the Hadland eight-frame camera described above. The outputs of four double-pulsed Q-switched lasers are doubled to 532 nm and beam combined to pump a single dye laser and yield a frequency-tunable burst of eight laser pulses. The effects of turbulence on spark-kernel evolution have been explored with these instruments through PLIF measurements.

The behavior of a spark igniter represents an ideal case study for the demonstration of ultrafast real-time imaging. Our experiments have been designed to exploit laser schlieren for visualizing refractive-index gradients in the flowfield produced during firing of the spark igniter. These simple schlieren experiments are straightforward to implement and require only a high-repetition-rate laser source for generation of the signal. The spatial variation in spark location from event to event limits the applicability of techniques that utilize a two-dimensional light sheet for illumination. Schlieren yields a line-of-sight image that captures the spark despite variations in position and morphology. Furthermore, the spark characteristics are of great practical interest. Concerns over engine cold start and high-altitude relight are driving research and development of advanced ignition systems that incorporate lasers and microwave plasmas, for example, in addition to enhancements of traditional spark-based systems. Through continuing laboratory experiments, the ultrafast real-time imaging techniques described in this paper are currently being applied to the characterization and improvement of the spark-ignition process.

An in-depth description of the phase-locked and ultrafast real-time imaging methodologies follows. Applications to the study of vortex-flame interactions and gas turbine spark ignition are explored. The balance of the paper includes phase/time-resolved data achieved in each case, with some conclusions and recommendations for further study.

### 3. PHASE-LOCKED IMAGING (VORTEX-FLAME INTERACTIONS)<sup>14</sup>

#### 3.1 Rolon Opposed-Jet Burner

Recent studies of vortex-flame interactions achieved using the Rolon opposed-jet burner exemplify the phase-locked approach to flow visualization. A picture (a) and diagram (b) of the Rolon burner are shown in Figure 2. The flame is supported between upper and lower nozzles separated by 40 mm, each with an exit diameter of 25 mm. The fuel consists of hydrogen diluted with nitrogen and flows from the upper nozzle. Air flows from the lower nozzle. Unique to this type of apparatus is a tube with 5-mm inner diameter that is installed concentrically within the lower nozzle. This tube is attached to a cylinder that contains a piston which, in turn, is attached to an actuator. Feeding an appropriate current to the actuator causes a solenoid to force the piston upward abruptly, resulting in the emergence of a vortex from the tube. The vortex travels upward within the surrounding oxidizer flow. A flow of air is supplied to the vortex tube such that in the absence of a vortex, the exit velocity matches the velocity of the air from the surrounding nozzle. To minimize the impact of room-air disturbances, upper and lower guard flows of nitrogen are supported through outer nozzles, which are concentric with the respective upper and lower inner nozzles that support the flame.

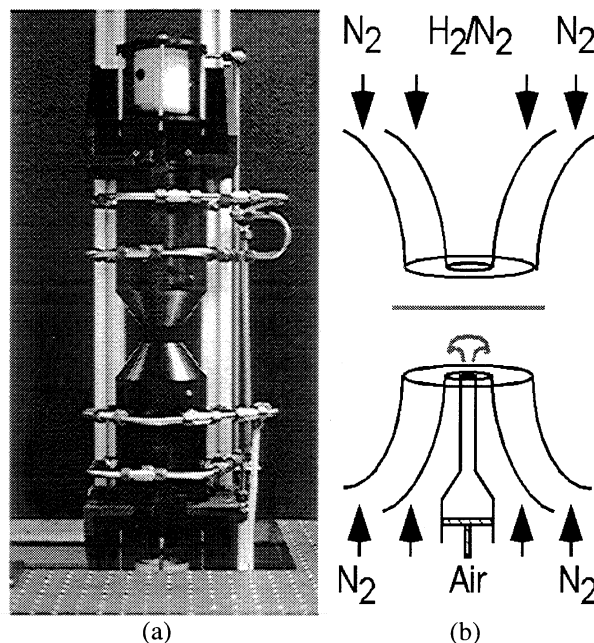


Figure 2. (a) Digital photograph of the opposed-jet burner. (b) Cross-sectional diagram of burner nozzles and piston.

#### 3.2 PLIF Hardware

The PLIF system contains a frequency-doubled, Q-switched Nd:YAG laser that is used to pump a dye laser which, in turn, is frequency doubled. The UV radiation is directed through a telescope that is adjusted to produce a light sheet with a height that matches as nearly as possible the 40-mm burner separation. The resulting beam thickness is  $\sim 300 \mu\text{m}$ , which corresponds to the full width (defined as the distance between the locations of the 25% peak intensity points).

Hydroxyl radicals absorb the laser radiation at 281.3414 nm via the  $R_1(8)$  transition of the (1,0) band in the A-X system. Fluorescence from the A-X (1,1) and (0,0) bands is detected at right angles through WG-295 and UG-11 colored-glass filters, using a 105-mm-focal-length f/4.5 UV lens. The resulting light is recorded on an intensified CCD camera with an intensifier gate width of 100 ns.

#### 3.3 Synchronization and Timing

Precise synchronization of several experimental events is required, including vortex generation and propagation, production of laser pulses, and activation of the camera shutter or intensifier. Figure 3 contains a block diagram of the synchronization scheme. (Note that a number of elements in this figure are employed to accomplish particle-image velocimetry and planar Rayleigh scattering in addition to the PLIF measurements described above.)

The scheme depicted in Figure 3 provides precise control of the relative timing between the laser diagnostics and the vortex-flame event. To explore the temporal evolution of the event, data are captured utilizing the following phase-locked timing sequence: 1) an image is recorded, 2) the delay between vortex production and the laser/camera events is adjusted, and 3) another vortex is initiated and a second image recorded. This process is repeated to acquire numerous images, obtained at increasing delays; then an animation is created by assembling the individual images in temporal order. Effective temporal separation between images is selected between 10 and 200  $\mu\text{s}$ , depending on the timescale of the event under study. The resulting animations are a testament to the high degree of repeatability achievable with this apparatus. Typical phase-locked OH PLIF images are depicted in Figure 4.

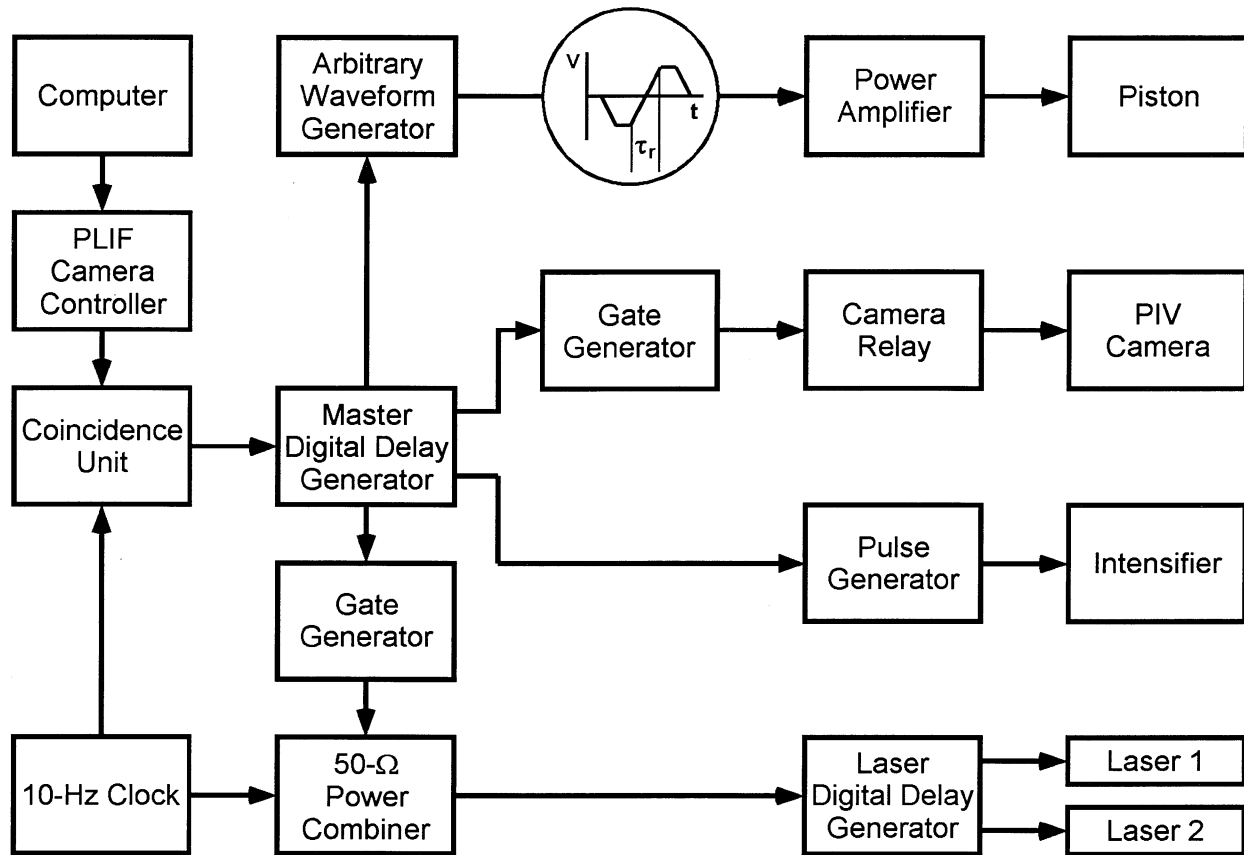


Figure 3. Diagram of electronic timing connections for phase-locked OH PLIF measurements.

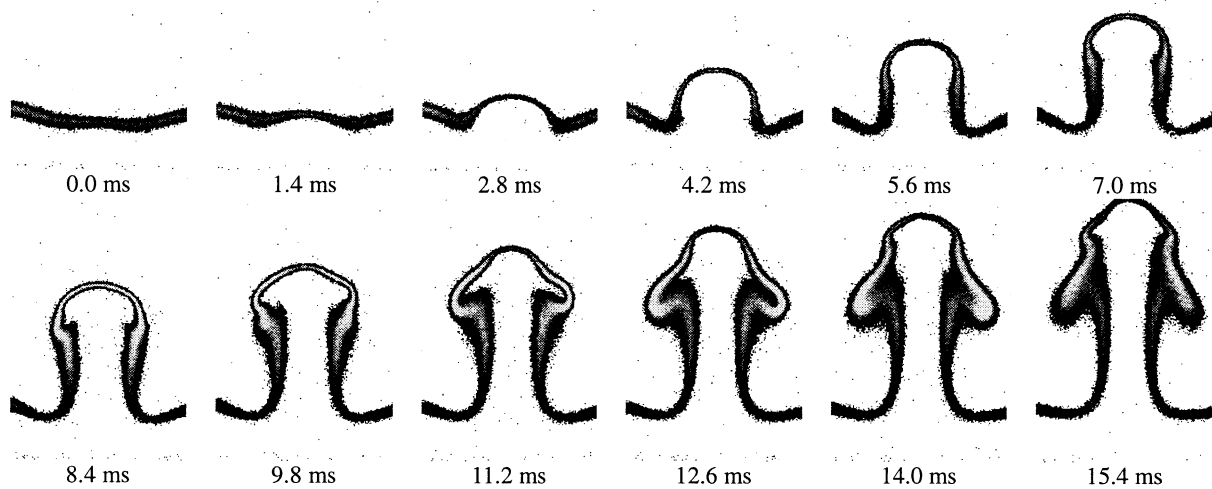


Figure 4. Phase-locked OH PLIF images depicting vortex-flame interactions in the Rolon burner.



## **4. ULTRAFAST REAL-TIME IMAGING (GAS TURBINE SPARK IGNITER)**

### **4.1 Gas Turbine Spark Igniter**

Spark events produced by a Unison Industries Vision spark-ignition system were visualized using the ultrafast real-time imaging system to be described in detail below. The Vision system, which is utilized in both military and commercial aviation, is designed to produce a tailored ignition spark at the tip of the igniter plug through delivery of a pulse (nominal energy 4-12 J) from the Vision-system igniter box. The plug tip is composed of a ring electrode encompassing a center electrode. Upon delivery of the igniter-box pulse, an arc occurs across the center-electrode/ring-electrode gap. Because the location and physical characteristics (morphology, etc.) of this arc can vary from shot to shot, an ultrafast real-time imaging system is required to capture the detailed time-dynamics of the process. If the spark event were highly reproducible from shot to shot, phase-locked imaging could be applied rather than the real-time approach described below.

### **4.2 High-Repetition-Rate Sources**

Laser schlieren techniques were employed to visualize propagation of the shock produced during firing of the Unison Industries Vision system spark igniter. The characteristics of the spark event demand high temporal resolution and ultrafast real-time imaging for capture of the physics of interest. To accomplish the required temporal resolution, two different high-repetition-rate laser sources were considered. The first is the Spectra-Physics "Merlin" intracavity-frequency-doubled Nd:YLF laser, and the second is the Spectra-Physics "Tsunami" modelocked Ti:sapphire laser. Characteristics and system-specific applications of the two laser systems are addressed below.

### **4.3 Q-switched Nd:YLF laser**

The Merlin laser is a Q-switched Nd:YLF laser that operates at kilohertz repetition rates. The device installed at Wright-Patterson Air Force Base is configured for 50-kHz operation and produces a 13-W pulsetrain (260  $\mu$ J/pulse) at 527 nm through intracavity doubling of the Nd:YLF fundamental in lithium triborate (LBO). The multi-mode output beam provides a uniform spatial beam profile ideal for flow-visualization applications. While the Merlin's high spectral brightness and mode characteristics proved to be excellent for studies of the spark igniter, its repetition rate proved to be insufficient for resolving the shock phenomena of interest. This situation motivated a series of studies that employed the pulse-selected Tsunami as an excitation source.

### **4.4 Pulse-Selected Ti:Sapphire Laser**

The Tsunami modelocked Ti:sapphire laser employed in these studies is configured to produce an 82-MHz pulsetrain, spectrally tunable over the wavelength range 800-900 nm. Experiments were accomplished at 850 nm for all cases described here. When pumped by the 5-W, 532-nm output of a Spectra-Physics Millennia V intracavity-doubled (LBO) Nd:YVO<sub>4</sub> laser, the Tsunami provides ~1 W output power (12 nJ/pulse). The 82-MHz repetition rate is excessive for imaging the spark igniter while using the 1-MHz ultrafast framing camera described below; therefore, the repetition rate of the modelocked Ti:sapphire laser is reduced using a Spectra-Physics Model 3980 pulse selector. This device employs a TeO<sub>2</sub> acousto-optic modulator to select subsets of pulses from the full 82-MHz output pulsetrain. Losses in the pulse selector reduce the laser energy to 8 nJ/pulse.

### **4.5 Ultrafast-Framing Camera**

Laser-schlieren images of the Unison Industries spark igniter were captured using a PSI ultrafast framing camera. This device features a CCD image sensor that can be exposed at rates up to 1 MHz and provides an on-chip storage array for 32 images. The array associated with the camera employed in these experiments is 180x90 pixels.

### **4.6 Synchronization and Timing**

A number of configurations for experimental visualization of the spark igniter via ultrafast real-time imaging were explored. Preliminary experiments were designed to capture the spontaneous emission produced during firing of the spark igniter. Synchronization and timing of the various experimental events were achieved easily during these experiments. The camera was configured with an appropriate lens and placed to view the tip of the spark-igniter plug. In addition, a photodiode was arranged to collect light from the spark-ignition event. The camera was configured in the pre-trigger mode in which data

frames are acquired continuously and processed through the on-chip storage array in a first-in-first-out (FIFO) arrangement. The spark igniter was fired via user-entered commands to a personal computer that was driving the Unison exciter box and the spark plug itself. The signal produced at the photodiode was employed to trigger the camera, terminating data acquisition in the pre-trigger mode and capturing the spark-igniter-image data in the on-chip storage array.

Laser-based schlieren studies of the spark igniter required a more sophisticated experimental arrangement, with greater attention to the details of synchronization and timing. Three unique strategies for schlieren-data acquisition were explored. In the first approach, the Merlin Q-switched Nd:YLF laser provided light for the schlieren measurements, and the 50-kHz laser served as the master oscillator for the experiment. The ultrafast framing camera was configured in the “multi” external trigger mode, with triggers being supplied by the spark-igniter event and the laser. Under these conditions, 32 frames of camera data were acquired in synchrony with the laser during the 640- $\mu$ s period spanning the spark event. This approach provided tremendous optical energies and saturating signals at the camera; therefore, neutral-density filters were inserted into the optical path to attenuate the laser beam. Unfortunately, the 50-kHz repetition rate of the laser proved insufficient to resolve the progress of the spark-initiated shock wave adequately.

This situation prompted experiments conducted via the second approach in which the pulse-selected Tsunami Ti:sapphire laser was utilized for production of the schlieren signal. As in the previous experiments, the laser served as the master oscillator, and the camera was slaved to the laser and the spark event via the “multi” external trigger mode. This arrangement permitted the acquisition of image data at framing rates up to 800 kHz, improving the temporal resolution over that achieved in the Merlin experiments by a factor of sixteen.

The third and final approach, however, produced the optimum visualization and enabled spark imaging at the full 1-MHz data-acquisition bandwidth of the camera. For these experiments, the camera served as the master oscillator, and the pulse selector—and, therefore, the laser—were slaved to the camera. A block diagram of the experimental apparatus is depicted in Figure 5. The Millennia/Tsunami/pulse selector provide the laser pulse for schlieren measurements. The output pulsetrain is expanded to a nominal diameter of  $\sim 32$  mm through two 4x telescopes. The collimated, expanded laser beam traverses a sample region in which the spark-igniter plug is suspended. A lens collects the transmitted light, which is focused to a point where a knife edge is inserted. Light traveling past the knife edge is imaged through a neutral-density filter (ND=1) and an interference filter (center frequency=850nm, bandwidth=10 nm) onto the ultrafast framing camera using a Nikon lens.

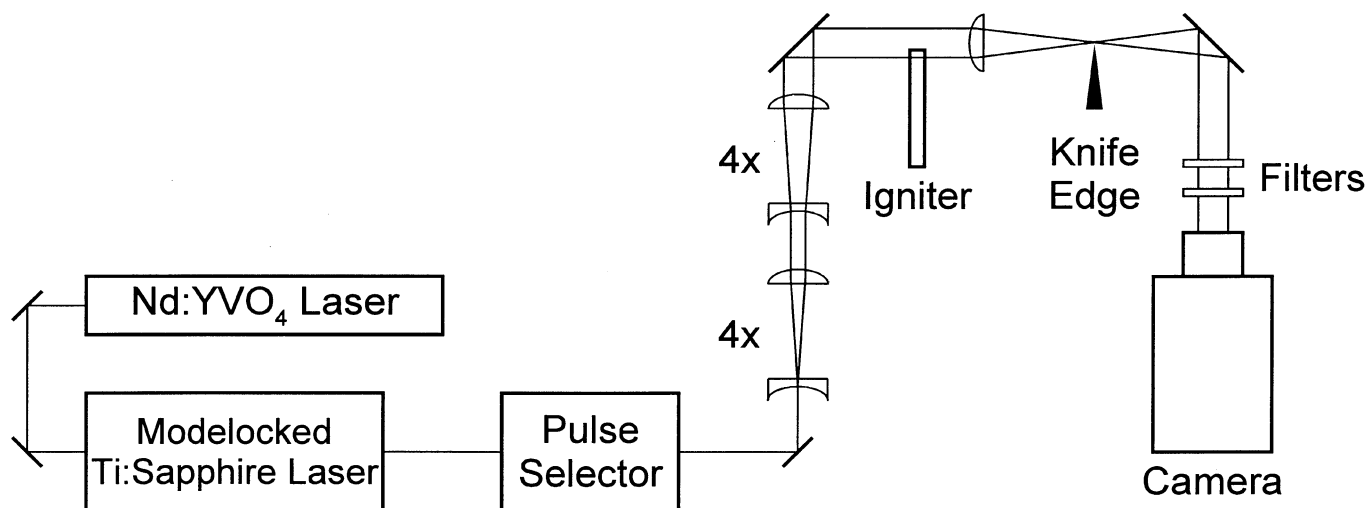


Figure 5. Experimental apparatus for ultrafast real-time laser-schlieren imaging of a Unison Industries spark igniter.

Details of the synchronization and timing are presented schematically in Figure 6. The ultrafast framing camera is configured in the post-trigger mode and, therefore, acquires images continuously until a spark event occurs. The spark event is initiated by the experimenter through entry of commands at the personal computer. These commands trigger the Unison exciter box, firing the spark plug and producing a trigger via the remote module that drives a digital delay generator (DDG). This DDG triggers the camera. Once the camera is triggered, it acquires and stores the 32 images that comprise the final data set. Trigger delays are carefully adjusted to ensure that the frames are acquired during the spark event. Once triggered, the camera is responsible for driving the pulse selector and synchronizing the laser with the image-acquisition process. The

camera is configured to record images at its full 1-MHz acquisition rate. During each frame, the camera generates a vertical-strobe pulse that drives the pulse selector. This strobe pulse is shaped and further processed with a pulse generator and then mixed with the  $\sim 41$ -MHz signal from the Ti:sapphire modelocker. This process ensures that a single laser pulse is selected from the 82-MHz pulsetrain during the exposure time associated with each of the 32 camera frames. The vertical-strobe-driven pulse generator can be adjusted to select an envelope of pulses from the 82-MHz train during each framing event. For example, experiments were accomplished with 10 and 100 laser pulses per frame; however, the data presented in this paper were achieved with a single pulse for each frame. Those data, depicting the propagation of the spark-initiated shock, are presented in Figure 8.

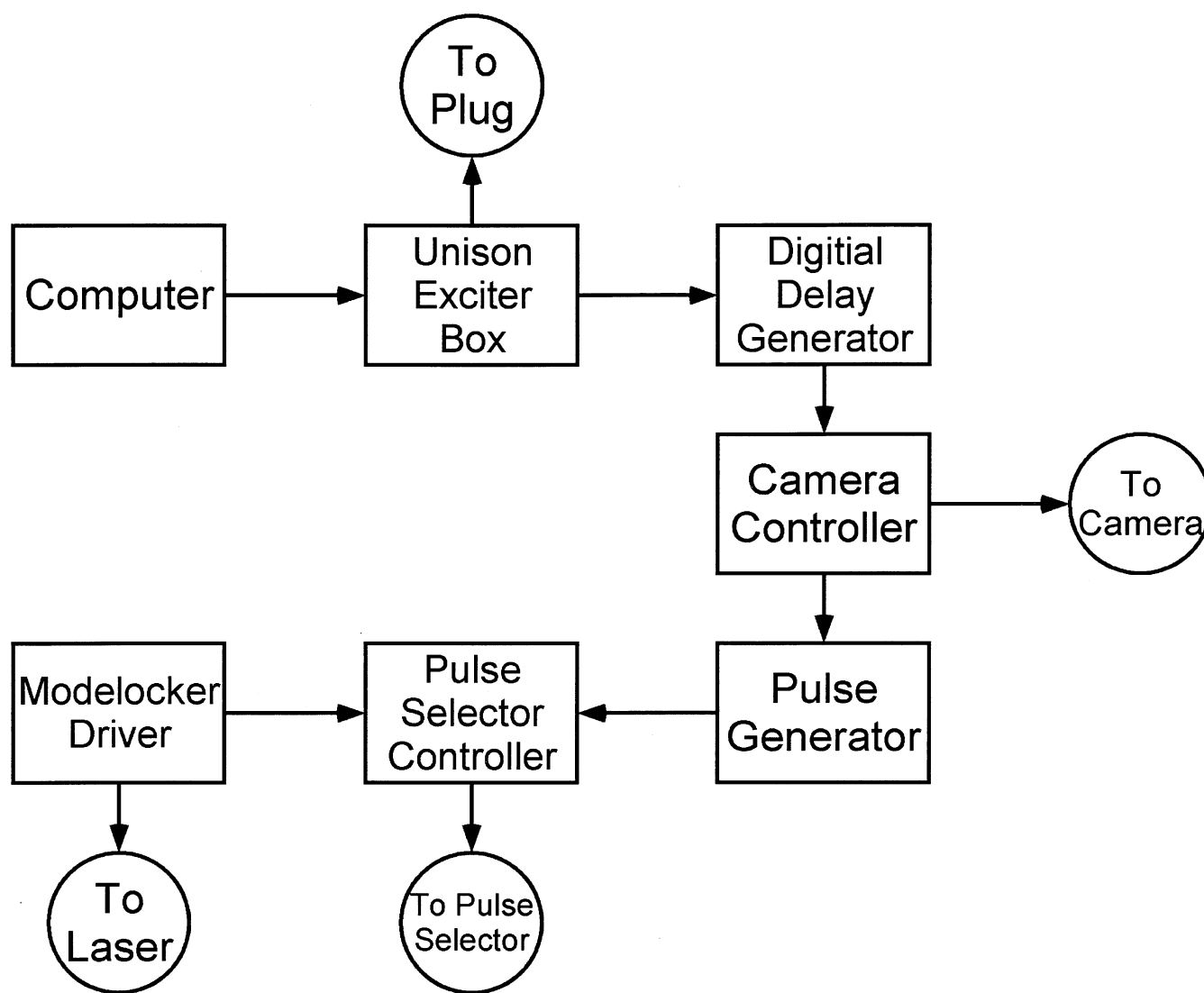


Figure 7. Diagram of electronic timing connections for ultrafast real-time laser-schlieren measurements.

## 5. CONCLUSIONS

Ultrafast real-time imaging of the shock structure produced by a Unison Industries spark igniter has been accomplished. Spontaneous-emission and laser-schlieren techniques have been demonstrated in conjunction with a number of high-repetition-rate laser sources (50-kHz, Q-switched Nd:YLF laser; pulse-selected, 82-MHz modelocked Ti:sapphire laser) and an ultrafast-framing CCD camera (framing rates up to 1 MHz). The methodology employed in accomplishing these ultrafast real-time imaging experiments has been compared to that recently utilized to generate phase-locked animations of vortex-

flame interactions in the Rolon opposed-jet burner. Future activity will be focused on applying the ultrafast methodology to measurements of other key spark parameters through the use of various advanced laser-based diagnostics including PLIF and planar Rayleigh scattering.

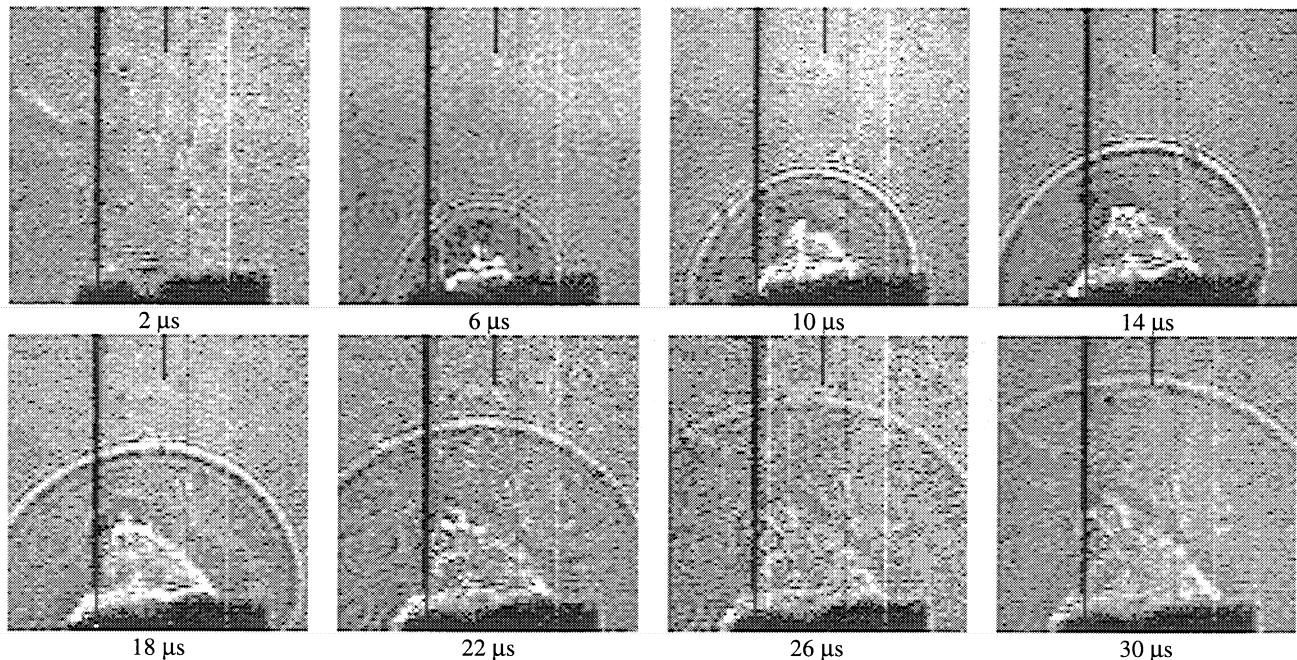


Figure 8. A selection of laser-schlieren images acquired at 1-MHz framing rate that depicts propagation of the shock produced during firing of the Unison Industries spark igniter.

## ACKNOWLEDGMENTS

The authors gratefully acknowledge the expert editorial assistance of Ms. M. M. Whitaker. This work is supported by research funding from the Air Force Office of Scientific Research (Dr. Julian Tishkoff, Program Manager) and U.S. Air Force Contract F33615-95-C-2507.

## REFERENCES

1. W. M. Roquemore and V. R. Katta, "Role of Visualization in the Development of UNICORN," presented at the International Conference on Optical Technology and Image Processing in Fluid, Thermal, and Combustion Flow, 6-10 December 1998, Yokohama, Japan, and published in the Proceedings.
2. G. V. Sklizkov, "Lasers in High-Speed Photography," in *Laser Handbook*, F. T. Arecchi and E. O. Schulz-Dubois, eds., Vol. 2, pp. 1545-1577, North-Holland, Amsterdam, 1972.
3. J. M. Seitzman, B. J. Patrie, P. H. Paul, and R. K. Hanson, "Instantaneous 3-D and Temporal Evolution Measurements by Rapid Acquisition of Planar Images," AIAA 91-0178 presented at the 29<sup>th</sup> AIAA Aerospace Sciences Meeting, Reno, Nevada, 1991.
4. B. J. Patrie, J. M. Seitzman, and R. K. Hanson, "Planar Imaging at High Framing Rates: System Characterization and Measurements," AIAA 92-0584 presented at the 30<sup>th</sup> AIAA Aerospace Sciences Meeting, Reno, Nevada, 1992.
5. B. J. Patrie, J. M. Seitzman, and R. K. Hanson, "Planar Imaging for 3-D Flow Visualization," 22<sup>nd</sup> International Congress on High Speed Photography and Photonics, SPIE Vol. 1801, 1992.
6. B. J. Patrie, J. M. Seitzman, and R. K. Hanson, "Planar Imaging at High Framing Rates: System Characterization and Measurements, II," AIAA 93-0364 presented at the 31<sup>st</sup> AIAA Aerospace Sciences Meeting, Reno, Nevada, 1993.
7. A. Ben-Yakar and R. K. Hanson, "Cavity Flameholders for Ignition and Flame Stabilization in Scramjets: Review and Experimental Study," AIAA 98-3122 presented at the 34<sup>th</sup> AIAA/ASME/SAE/ASEE Joint Propulsion Conference, Cleveland, Ohio, 1998.
8. M. Winter, J. K. Lam, and M. B. Long, "Techniques for High-Speed Digital Imaging of Gas Concentrations in Turbulent Flows," *Exp. Fluids* 5, pp. 177-183, 1987.

9. M. B. Long and B. Yip, "Measurement of Three-Dimensional Concentrations in Turbulent Jets and Flames," *Twenty-Second Symposium (International) on Combustion*, pp. 701-709, The Combustion Institute, Pittsburgh, 1988.
10. B. Yip, R. L. Schmitt, and M. B. Long, "Instantaneous Three Dimensional Concentration Measurements in Turbulent Jets and Flames," *Opt. Lett.* **13**, pp. 96-98, 1987.
11. W. R. Lempert, P.-F. Wu, B. Zhang, R. B. Miles, J. L. Lowrance, V. Mastrocola, and W. F. Kosonocky, "Pulse-Burst Laser System for High-Speed Flow Diagnostics," AIAA 96-0179 presented at the 34<sup>th</sup> AIAA Aerospace Sciences Meeting, Reno, 1996.
12. W. R. Lempert, P.-F. Wu, and R. B. Miles, "Filtered Rayleigh Scattering Measurements Using a MHz Rate Pulse-Burst Laser System," AIAA 97-0500 presented at the 35<sup>th</sup> AIAA Aerospace Sciences Meeting, Reno, 1997.
13. C. F. Kaminski, A. Franke, J. Hult, M. Alden, and R. B. Williams, "Applications of a Multiple-Pulse YAG Laser/Framing Camera System for Ultrafast Visualization of Combustion Processes," Work-in-Progress poster presented at the 27<sup>th</sup> Symposium (International) on Combustion, Boulder, 1998.
14. G. J. Fiechtner, P.-H. Renard, J. R. Gord, K. D. Grinstead, Jr., C. D. Carter, and J. C. Rolon, "Application of Imaging Techniques to the Study of Vortex-Flame Interactions," presented at the SPIE Conference on Optical Diagnostics for Fluids/Heat/Combustion and Photomechanics for Solids, Denver, 1999.



## Ultrafast Imaging of a Gas Turbine Spark Igniter

James R. Gord,<sup>\*a</sup> Gregory J. Fiechtner,<sup>b</sup> Keith D. Grinstead, Jr.,<sup>b</sup>  
Michael J. Cochran,<sup>c</sup> and John R. Frus<sup>c</sup>

<sup>a</sup>Air Force Research Laboratory, Propulsion Directorate, WPAFB, OH 45433-7103

<sup>b</sup>Innovative Scientific Solutions, Inc., 2766 Indian Ripple Road, Dayton, OH 45440-3638

<sup>c</sup>Unison Industries, 7575 Baymeadows Way, Jacksonville, FL 32256

### 1. Introduction

Experimental and computational techniques for the visualization of fluid flows have emerged as essential tools for increasing our understanding of the physics and chemistry of these flows. Indeed, many—if not most—of the breakthroughs in fluid mechanics and dynamics can be attributed to the understanding achieved through imaging of the various multidimensional structures in fluid flow. Flow visualization has played a powerful role in the process of validating computational models through comparisons of experiment and theory. For example, the development and validation of the UNsteady Ignition and COmbustion with Reactions (UNICORN) code at Wright-Patterson Air Force Base have been achieved through continuous improvement and refinement based on comparisons with experimental flow-visualization data.<sup>1</sup>

Spark-ignition systems play a critical role in the performance of essentially all gas turbine engines. Demanding applications such as cold start and high-altitude relight require continued enhancement of ignition systems. To characterize advanced ignition systems, we have developed a number of laser-based diagnostic techniques designed to exploit an ultrafast-framing charge-coupled-device (CCD) camera and high-repetition-rate laser sources including modelocked Ti:sapphire oscillators. Spontaneous-emission and laser-schlieren measurements have been accomplished with this instrumentation and the results applied to the study of a novel Unison Industries spark igniter that shows great promise for improved cold-start and high-altitude-relight capability as compared to that of igniters currently in use throughout military and commercial fleets.

The behavior of a spark igniter represents an ideal case study for the demonstration of ultrafast real-time imaging. Our experiments have been designed to exploit laser schlieren for visualizing refractive-index gradients in the flowfield produced during firing of the spark igniter. These simple schlieren experiments are straightforward to implement and require only a high-repetition-rate laser source for generation of the signal. The spatial variation in spark location from event to event limits the applicability of techniques that utilize a two-dimensional light sheet for illumination. Schlieren yields a line-of-sight image that captures the spark despite variations in position and morphology.

Early developments in real-time imaging based on flashlamp-pumped sources and modelocked lasers coupled with analog recording devices have been reviewed by Sklizkov.<sup>2</sup> Hanson and coworkers<sup>3-6</sup> accomplished instantaneous three-dimensional visualization of combustor flowfields by sweeping a single high-energy laser sheet through the flow using a scanning mirror and capturing a sequence of planar slices using a fast-framing camera system. More recently, Ben-Yakar and Hanson<sup>7</sup> developed an ultra-high-speed schlieren system to study cavity flameholders for ignition and flame stabilization in scramjets. Long and coworkers<sup>8-10</sup> explored high-speed digital imaging of turbulent flows, recording time-evolving digital images of gas concentrations and instantaneous three-dimensional fuel-concentration profiles through Mie scattering and biacetyl-fluorescence techniques. Lempert, Wu, and Miles<sup>11,12</sup> recently applied a megahertz-rate, pulse-burst laser system and a Princeton Scientific Instruments (PSI) ultrafast-framing camera to study supersonic shock-wave/boundary-layer interactions through images obtained via filtered Rayleigh scattering. Finally, at the Lund Institute of Technology, Kaminski and coworkers<sup>13</sup> have utilized high-speed visualization to study the effects of turbulence on spark-kernel evolution through PLIF measurements.

### 2. Experimental Apparatus

Spark events produced by a Unison Industries Vision spark-ignition system were visualized using an ultrafast real-time imaging system. The Vision system, which is utilized in both military and commercial aviation, is designed to produce a tailored ignition spark at the tip of the igniter plug through delivery of a pulse (nominal en-

\*Correspondence: E-Mail: james.gord@pr.wpafb.af.mil; Telephone: 937 255 7431; Fax: 937 656 4570

ergy 4-12 J) from the Vision-system igniter box. The plug tip is composed of a ring electrode encompassing a center electrode. Upon delivery of the igniter-box pulse, an arc occurs across the center-electrode/ring-electrode gap. Because the location and physical characteristics (morphology, etc.) of this arc can vary from shot to shot, an ultrafast real-time imaging system is required to capture the detailed time-dynamics of the process. If the spark event were highly reproducible from shot to shot, phase-locked imaging could be applied rather than the real-time approach described below.

Laser-schlieren techniques were employed to visualize propagation of the shock produced during firing of the Unison Industries Vision-system spark igniter. The characteristics of the spark event demand high temporal resolution and ultrafast real-time imaging for capture of the physics of interest. To accomplish the required temporal resolution, two different high-repetition-rate laser sources were considered. The first is the Spectra-Physics "Merlin" intracavity-frequency-doubled Nd:YLF laser, and the second is the Spectra-Physics "Tsunami" modelocked Ti:sapphire laser.

The Merlin laser is a Q-switched Nd:YLF laser that operates at kilohertz repetition rates. The device installed at Wright-Patterson Air Force Base is configured for 50-kHz operation and produces a 13-W pulsetrain (260  $\mu$ J/pulse) at 527 nm through intracavity doubling of the Nd:YLF fundamental in lithium triborate (LBO). The multi-mode output beam provides a uniform spatial beam profile ideal for flow-visualization applications. While the Merlin's high spectral brightness and mode characteristics proved to be excellent for studies of the spark igniter, its repetition rate proved to be insufficient for resolving the shock phenomena of interest. This situation motivated a series of studies that employed the pulse-selected Tsunami as an excitation source.

The Tsunami modelocked Ti:sapphire laser employed in these studies is configured to produce an 82-MHz pulsetrain, spectrally tunable over the wavelength range 800-900 nm. Experiments were accomplished at 850 nm for all cases described here. When pumped by the 5-W, 532-nm output of a Spectra-Physics Millennia V intracavity-doubled (LBO) Nd:YVO<sub>4</sub> laser, the Tsunami provides  $\sim$ 1 W output power (12 nJ/pulse). The 82-MHz repetition rate is excessive for imaging the spark igniter while using the 1-MHz ultrafast framing camera described below; therefore, the repetition rate of the modelocked Ti:sapphire laser is reduced using a Spectra-Physics Model 3980 pulse selector. This device employs a TeO<sub>2</sub> acousto-optic modulator to select subsets of pulses from the full 82-MHz output pulsetrain. Losses in the pulse selector reduce the laser energy to 8 nJ/pulse.

Laser-schlieren images of the Unison Industries spark igniter were captured using a PSI ultrafast framing camera. This device features a CCD image sensor that can be exposed at rates up to 1 MHz and provides an on-chip storage array for 32 images. The array associated with the camera employed in these experiments is 180x90 pixels.

### 3. Data-Acquisition Strategies and Results

A number of configurations for experimental visualization of the spark igniter via ultrafast real-time imaging were explored. Preliminary experiments were designed to capture the spontaneous emission produced during firing of the spark igniter. Synchronization and timing of the various experimental events were achieved easily during these experiments. The camera was configured with an appropriate lens and placed to view the tip of the spark-igniter plug. In addition, a photodiode was arranged to collect light from the spark-ignition event. The camera was configured in the pre-trigger mode in which data frames are acquired continuously and processed through the on-chip storage array in a first-in-first-out (FIFO) arrangement. The spark igniter was fired via user-entered commands to a personal computer that was driving the Unison exciter box and the spark plug itself. The signal produced at the photodiode was employed to trigger the camera, terminating data acquisition in the pre-trigger mode and capturing the spark-igniter-image data in the on-chip storage array.

Laser-based schlieren studies of the spark igniter required a more sophisticated experimental arrangement, with greater attention to the details of synchronization and timing. Three unique strategies for schlieren-data acquisition were explored. In the first approach, the Merlin Q-switched Nd:YLF laser provided light for the schlieren measurements, and the 50-kHz laser served as the master oscillator for the experiment. The ultrafast framing camera was configured in the "multi" external trigger mode, with triggers being supplied by the spark-igniter event and the laser. Under these conditions, 32 frames of camera data were acquired in synchrony with the laser during the 640- $\mu$ s period spanning the spark event. This approach provided tremendous optical energies and saturating signals at the camera; therefore, neutral-density filters were inserted into the optical path to attenuate the laser beam. Unfortunately, the 50-kHz repetition rate of the laser proved insufficient to resolve the progress of the spark-initiated shock wave adequately.

This situation prompted experiments conducted via the second approach in which the pulse-selected Tsunami Ti:sapphire laser was utilized for production of the schlieren signal. As in the previous experiments, the laser served as the master oscillator, and the camera was slaved to the laser and the spark event via the “multi” external trigger mode. This arrangement permitted the acquisition of image data at framing rates up to 800 kHz, improving the temporal resolution over that achieved in the Merlin experiments by a factor of sixteen.

The third and final approach, however, produced the optimum visualization and enabled spark imaging at the full 1-MHz data-acquisition bandwidth of the camera. For these experiments, the camera served as the master oscillator, and the pulse selector—and, therefore, the laser—were slaved to the camera. A block diagram of the experimental apparatus is depicted in Figure 1. The Millennia/Tsunami/pulse selector provide the laser pulse for schlieren measurements. The output pulsetrain is expanded to a nominal diameter of ~32 mm through two 4x telescopes. The collimated, expanded laser beam traverses a sample region in which the spark-igniter plug is suspended. A lens collects the transmitted light, which is focused to a point where a knife edge is inserted. Light

traveling past the knife edge is imaged through a neutral-density filter (ND=1) and an interference filter (center frequency=850nm, bandwidth=10 nm) onto the ultrafast framing camera using a Nikon lens.

Details of the synchronization and timing are presented schematically in Figure 2. The ultrafast framing camera is configured in the post-trigger mode and, therefore, acquires images continuously until a spark event occurs. The spark event is initiated by the experimenter through entry of commands at the personal computer. These commands

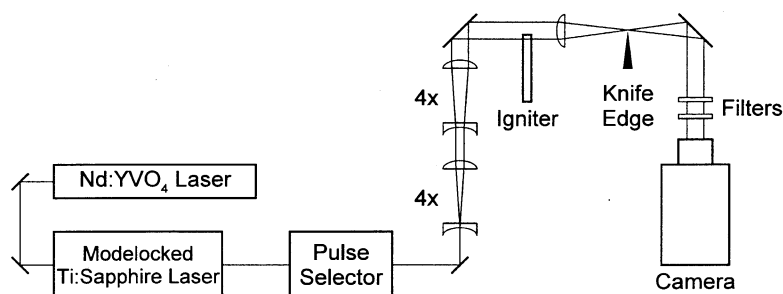


Figure 1. Experimental apparatus for ultrafast real-time laser-schlieren imaging of a Unison Industries spark igniter.

trigger the Unison exciter box, firing the spark plug and producing a trigger via the remote module that drives a digital delay generator (DDG). This DDG triggers the camera. Once the camera is triggered, it acquires and stores the 32 images that comprise the final data set. Trigger delays are carefully adjusted to ensure that the frames are acquired during the spark event. Once triggered, the camera is responsible for driving the pulse selector

and synchronizing the laser with the image-acquisition process. The camera is configured to record images at its full 1-MHz acquisition rate. During each frame, the camera generates a vertical-strobe pulse that drives the pulse selector. This strobe pulse is shaped and further processed with a pulse generator and then mixed with the ~41-MHz signal from the Ti:sapphire modelocker. This process ensures that a single laser pulse is selected from the 82-MHz pulsetrain during the exposure time associated with each of the 32 camera frames. The vertical-strobe-driven pulse generator can be adjusted to select an envelope of pulses from the 82-MHz train during each framing event. For example, experiments were accomplished with 10 and 100 laser pulses per frame; however, the data presented in this paper were achieved with a single pulse for each frame. Those data, depicting the propagation of the spark-initiated shock, are presented in Figure 3.

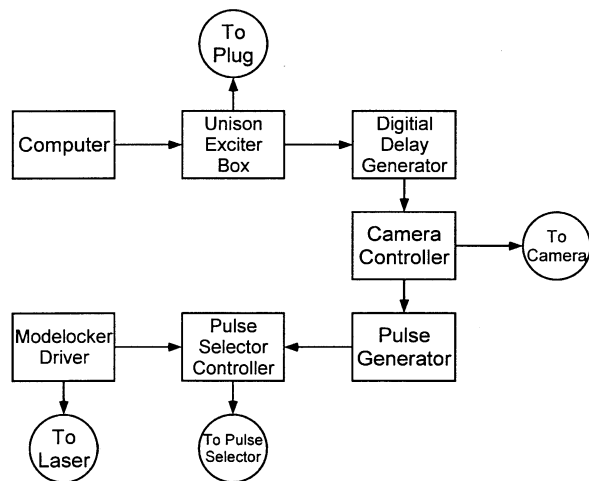


Figure 2. Diagram of electronic timing connections for ultrafast real-time laser-schlieren measurements.

#### 4. Conclusions

Ultrafast real-time imaging of the shock structure produced by a Unison Industries spark igniter has been accomplished. Spontaneous-emission and laser-schlieren techniques have been demonstrated in conjunction with a number of high-repetition-rate laser sources (50-kHz, Q-switched Nd:YLF laser; pulse-selected, 82-MHz modelocked Ti:sapphire laser) and an ultrafast-framing CCD camera (framing rates up to 1 MHz). Future activity will be focused on applying the ultrafast methodology to measurements of other key spark parameters through the use of various advanced laser-based diagnostics including PLIF and planar Rayleigh scattering.

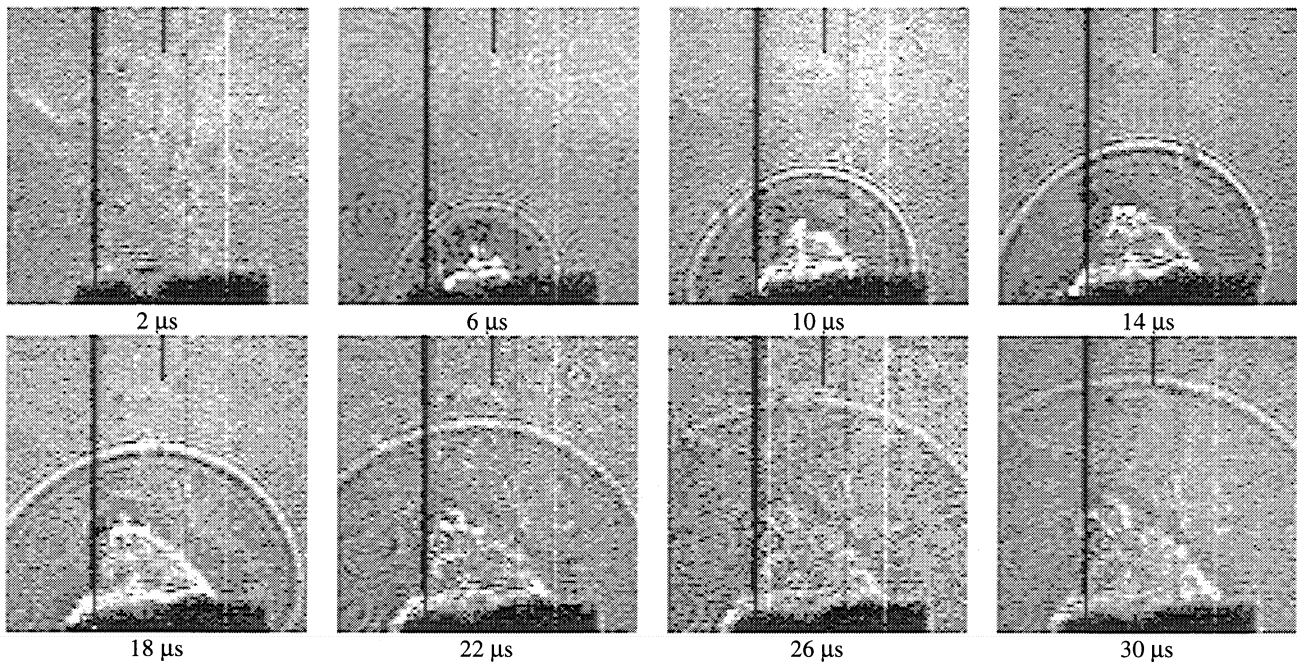


Figure 3. A selection of laser-schlieren images acquired at 1-MHz framing rate that depicts propagation of the shock produced during firing of the Unison Industries spark igniter.

### Acknowledgments

The authors gratefully acknowledge the expert editorial assistance of Ms. M. M. Whitaker. This work is supported by research funding from the Air Force Office of Scientific Research (Dr. Julian Tishkoff, Program Manager) and U.S. Air Force Contract F33615-95-C-2507.

### References

1. W. M. Roquemore and V. R. Katta, "Role of Visualization in the Development of UNICORN," presented at the International Conference on Optical Technology and Image Processing in Fluid, Thermal, and Combustion Flow, 6-10 December 1998, Yokohama, Japan, and published in the Proceedings.
2. G. V. Sklizkov, "Lasers in High-Speed Photography," in *Laser Handbook*, F. T. Arecchi and E. O. Schulz-Dubois, eds., Vol. 2, pp. 1545-1577, North-Holland, Amsterdam, 1972.
3. J. M. Seitzman, B. J. Patrie, P. H. Paul, and R. K. Hanson, "Instantaneous 3-D and Temporal Evolution Measurements by Rapid Acquisition of Planar Images," AIAA 91-0178 presented at the 29<sup>th</sup> AIAA Aerospace Sciences Meeting, Reno, Nevada, 1991.
4. B. J. Patrie, J. M. Seitzman, and R. K. Hanson, "Planar Imaging at High Framing Rates: System Characterization and Measurements," AIAA 92-0584 presented at the 30<sup>th</sup> AIAA Aerospace Sciences Meeting, Reno, Nevada, 1992.
5. B. J. Patrie, J. M. Seitzman, and R. K. Hanson, "Planar Imaging for 3-D Flow Visualization," 22<sup>nd</sup> International Congress on High Speed Photography and Photonics, SPIE Vol. 1801, 1992.
6. B. J. Patrie, J. M. Seitzman, and R. K. Hanson, "Planar Imaging at High Framing Rates: System Characterization and Measurements, II," AIAA 93-0364 presented at the 31<sup>st</sup> AIAA Aerospace Sciences Meeting, Reno, Nevada, 1993.
7. A. Ben-Yakar and R. K. Hanson, "Cavity Flameholders for Ignition and Flame Stabilization in Scramjets: Review and Experimental Study," AIAA 98-3122 presented at the 34<sup>th</sup> AIAA/ASME/SAE/ASEE Joint Propulsion Conference, Cleveland, Ohio, 1998.
8. M. Winter, J. K. Lam, and M. B. Long, "Techniques for High-Speed Digital Imaging of Gas Concentrations in Turbulent Flows," *Exp. Fluids* 5, pp. 177-183, 1987.
9. M. B. Long and B. Yip, "Measurement of Three-Dimensional Concentrations in Turbulent Jets and Flames," *Twenty-Second Symposium (International) on Combustion*, pp. 701-709, The Combustion Institute, Pittsburgh, 1988.
10. B. Yip, R. L. Schmitt, and M. B. Long, "Instantaneous Three Dimensional Concentration Measurements in Turbulent Jets and Flames," *Opt. Lett.* 13, pp. 96-98, 1987.
11. W. R. Lempert, P.-F. Wu, B. Zhang, R. B. Miles, J. L. Lowrance, V. Mastrocola, and W. F. Kosonocky, "Pulse-Burst Laser System for High-Speed Flow Diagnostics," AIAA 96-0179 presented at the 34<sup>th</sup> AIAA Aerospace Sciences Meeting, Reno, 1996.
12. W. R. Lempert, P.-F. Wu, and R. B. Miles, "Filtered Rayleigh Scattering Measurements Using a MHz Rate Pulse-Burst Laser System," AIAA 97-0500 presented at the 35<sup>th</sup> AIAA Aerospace Sciences Meeting, Reno, 1997.
13. C. F. Kaminski, A. Franke, J. Hult, M. Alden, and R. B. Williams, "Applications of a Multiple-Pulse YAG Laser/Framing Camera System for Ultrafast Visualization of Combustion Processes," Work-in-Progress poster presented at the 27<sup>th</sup> Symposium (International) on Combustion, Boulder, 1998.

### **2.1.5 Phase-Sensitive-Imaging Technique**

A commercially available imaging system employing a 1030 by 1300 pixel interline-transfer CCD was modified to produce a phase-sensitive-imaging device that is also capable of reducing the level of integrated background light. The camera is capable of extracting a weakly modulated signal that carries useful information from a large amount of background intensity, or dc offset. The results of this effort are summarized in the paper entitled "Phase Sensitive Imaging in Flows" (see pp. 72-82).



AIAA 99-0771

PHASE SENSITIVE IMAGING IN  
FLOWS

C.W. Fisher, M.A. Linne, and N.T. Middleton  
Center for Commercial Applications of Combustion in  
Space,  
Colorado School of Mines, Golden, CO 80401  
Gregory Fiechtner  
Innovative Scientific Solutions Inc., Dayton, OH  
James Gord  
Propulsion Directorate, Air Force Research Laboratory,  
Wright Patterson AFB, OH

37th AIAA Aerospace Sciences Meeting and Exhibit  
January 11-14, 1999/Reno, NV



# PHASE SENSITIVE IMAGING IN FLOWS

C.W. Fisher, M.A. Linne, and N.T. Middleton  
*Center for Commercial Applications of Combustion in Space,  
Colorado School of Mines, Golden, CO 80401*

Gregory Fiechtner  
*Innovative Scientific Solutions Inc., Dayton, OH*

James Gord  
*Propulsion Directorate, Air Force Research Laboratory,  
Wright Patterson AFB, OH*

## Abstract

A commercially available imaging system, using a 1030 x 1300 pixel, interline transfer CCD, is modified to produce a phase sensitive imaging device that is also capable of reducing the level of integrated background light. The camera is able to extract a weakly modulated signal, that carries useful information, from a large amount of background intensity, or dc offset. Based on initial results, the imaging system can reduce the integrated dc offset by an order of magnitude and detect a modulation depth of  $10^{-4}$ .

## Introduction

Two-dimensional imaging of radical species concentrations in reacting flows (e.g. OH, CH, NO etc.) has yielded a large amount of useful information. As one example, Planar Laser Induced Fluorescence (PLIF) has become the technique of choice for turbulent flame studies.<sup>1</sup> While PLIF has proven invaluable, there are a number of data manipulations required in order to make the measurement quantitative, such as a system calibration and the collisional quenching correction. In non-premixed, turbulent flames it is difficult to quantify the collisional environment within each pixel area in the flow. This has proven to be a significant limitation to the PLIF technique.

We have demonstrated a Pump/Probe diagnostic technique based upon picosecond, mode-locked Ti:sapphire lasers.<sup>2</sup> The principal advantages of this technique include:

1. Pump/Probe spectroscopy is a spatially resolved absorption-based diagnostic - even species with poor fluorescence yields can be observed;
2. The Pump/Probe technique offers a determination of absolute number density, free of corrections and without the need for calibration; and

3. Picosecond Pump/Probe spectroscopy is not expected to be strongly affected by the collisional environment.

While Pump/Probe techniques offer significant advantages, it is not a background-free technique. With respect to Laser Induced Fluorescence (LIF), Pump/Probe spectroscopy is somewhat more complex to set up and has not been as well proven. LIF is a very well known, simpler approach which is background-free, but is subject to corrections and calibrations.

While there are trade-off's to each diagnostic, either one could be used with the imaging system described herein. Our principal goal has been to develop a camera that will take advantage of the attributes associated with a Pump/Probe diagnostic system. This required that we overcome the challenge posed by a dc-offset problem.

A phase sensitive imaging system could be used with other diagnostic techniques as well. For example, the system could be applied to a modulated filtered Rayleigh scattering experiment to measure velocity cross sections and two-dimensional velocity profiles. Modulated filtered Rayleigh scattering using solid state diode lasers has been demonstrated as a technique for making single point velocity measurements.<sup>3</sup> When the laser beam traverses a flow, the Rayleigh scattered light is Doppler shifted. Velocity fluctuations are converted to intensity fluctuations bypassing the scattered light through an atomic line filter.

To improve detectability the solid-state laser is modulated and a heterodyne detection system is utilized. The laser source is modulated at a frequency of 50 kHz and the laser frequency is scanned repetitively by a 10 Hz triangle wave, which provides a 10.5 GHz tuning bandwidth. Ambient light interference can be a problem because the Rayleigh signal is weak, particularly when using a cw, solid-state laser. An intensifier would need to be used with this diagnostic technique, however, the intensifier would not be gated. The intensifier

would be set in a constant, minimum noise, gain state and the phase sensitive detection would be performed on the CCD chip. Consecutive in and out of phase demodulated images, at the same laser frequency, can be subtracted to remove steady state and low frequency noise, resulting in multidimensional velocity and mass flow information.

In what follows, we describe the development and testing of a phase sensitive imaging system. The concepts implemented in this imaging system were introduced in an earlier paper.<sup>4</sup>

## Demodulation Imaging

In initial demodulating array research,<sup>5</sup> we used a liquid crystal mounted in front of a normal CCD camera to modulate optical gain (similar to the mixer in a lock-in amplifier). That approach had several problems but it proved sufficient for a proof-of-concept demonstration. Similar ideas have been demonstrated in the field of phase fluorometry for medical imaging. In phase fluorometry, photocathode or mcp gain is modulated in front of the camera and this serves as the mixer<sup>6</sup> and the references found therein). The principal difference between the two approaches is that the liquid crystal modulates loss and the image intensifier modulates gain. Both systems suffer from a large dc background problem, and this limits the performance of such camera systems.

### Phase Sensitive Detection

Phase sensitive detection, or heterodyne detection, is a process used to detect a modulated signal. Heterodyning means the translating or shifting in frequency. In a heterodyne receiver the incoming modulated signal is translated in frequency, thus occupying equal bandwidth centered about a new frequency. If the heterodyne detection or the phase sensitive detection is performed at the same frequency of the incoming modulated signal, then the modulated signal will be shifted to the baseband.

Let  $f(t)$  be a bandlimited signal that is amplitude modulated by  $m(t)$ , shown in equation 1.

$$m(t) = a(t) \cos[\omega_c t + \gamma(t)] \quad (1)$$

In equation 1,  $a(t)$  is the carrier signal gain, or envelope, and  $\omega_c$  is the carrier frequency. In amplitude modulation, the phase term,  $\gamma(t)$ , is zero, or a constant value. This characteristic allows us to use a phase sensitive detection system, to recover the information signal, since the phase is fixed. If we assume the envelope  $a(t)$  is proportional to  $f(t)$ , then we obtain the amplitude modulated signal  $\phi(t)$ .

$$\phi(t) = f(t) \cos \omega_c t \quad (2)$$

The frequency spectrum of the modulated signal,  $\phi(t)$ , shows us that the complete spectral shape of  $f(t)$  is

shifted in frequency by  $\pm\omega_c$ . Low frequency noise, below  $\omega_c$  minus the bandwidth of  $f(t)$ , will at this point not effect the spectral content of  $f(t)$ .

To detect the original signal  $f(t)$ , we use the modulation property of the Fourier Transform for demodulation. Convolving the modulated signal, in frequency space, with a signal equal to (same frequency and phase) the original carrier signal, is the same as multiplying by the signal  $d(t)$  in time, if  $d(t)$  is set equal to  $m(t)$ . To demodulate a signal, this multiplication is literally performed, by electronic devices, as described below. Multiplying the modulated signal,  $\phi(t)$ , by  $d(t)$  gives us equation 3.

$$\phi(t).d(t) = f(t) \cos^2 \omega_c t \quad (3)$$

Which, using a trigonometric identity can be rewritten as equation 4.

$$\phi(t).d(t) = \frac{1}{2} f(t) + \frac{1}{2} f(t) \cos 2\omega_c t \quad (4)$$

The frequency spectrum of the demodulated signal, in equation 5, shows us that the spectral content of  $f(t)$  is shifted again in frequency to  $\pm 2\omega_c$  and to its original baseband state.

$$F[\phi(t).d(t)] = \frac{1}{2} F(\omega) + \frac{1}{4} F(\omega + 2\omega_c) + \frac{1}{4} F(\omega - 2\omega_c) \quad (5)$$

If the Nyquist sampling rate is satisfied, then a low-pass filter can be used, following detection, to filter out the double-frequency terms from the original spectral components.

Both the correct phase and frequency of the modulated signal must be known to perform synchronous or phase sensitive detection. A phase error in the detection system will cause a variable gain factor in the recovered signal that is proportional to the cosine of the phase error. Small phase errors are tolerable, however, the signal is wiped out when the error approaches  $\pm 90^\circ$ . On the other hand, if there is a frequency error, the signal  $f(t)$  is multiplied by a low frequency sinusoid producing unacceptable distortion.<sup>7</sup>

### Imaging Issues

Mixers themselves can be thought of as simple amplifiers, in which the amplifier gain is synchronously modulated at the reference phase and frequency. The amplifier output is the linear product of the input and the gain (now modulated). Thus, a mixer can demodulate an incoming signal by multiplying it with its carrier as described in 3. For imaging, it is possible to accomplish a similar task using optical loss (e.g. by polarization modulation, using liquid crystals for example) or gain (e.g. by use of an mcp or photocathode) directly in front of the camera. It can also be accomplished by clocking photo-electronic charge within the

camera architecture, as described herein. Since the objective is to develop a system that can be utilized with background intensive diagnostics, the camera's architecture is attractive because it will provide us with a way to reject some of the dc background.

An important characteristic of a phase sensitive imaging systems using loss or gain is that the optical demodulator is capable of reducing the light level to zero and then driving it up to some maximum level characteristic of the system. The optical signal will not go negative. Thus, the input and the synchronously detected signal are square waves with a dc offset as described by equation 6. In this equation,  $T_c$  is the carrier period and  $\tau_c$  is the width of the pulse in time. The duty cycle is then the ratio of  $\tau_c$  to  $T_c$ . The amplitude of each pulse is defined as  $a$ .

$$p(t) = \sum \frac{a\tau_c}{T_c} Sa(n\pi \frac{\tau_c}{T_c}) e^{j2\pi n \frac{t}{T_c}} \quad (6)$$

The frequency spectrum of equation 6, in Figure 1, shows that the dc value of the signal accounts for 50% of the signal power. The dc magnitude is a function of the diagnostic technique used. At worst, the modulated portion of the signal is carried directly within a laser beam that is from  $10^4$  to  $10^7$  larger. Laser extinction in a particle-laden flow is one example. For scattering measurements (elastic and inelastic), the background is much lower, caused by flame emission and noise in the camera (including the mcp if one is used).

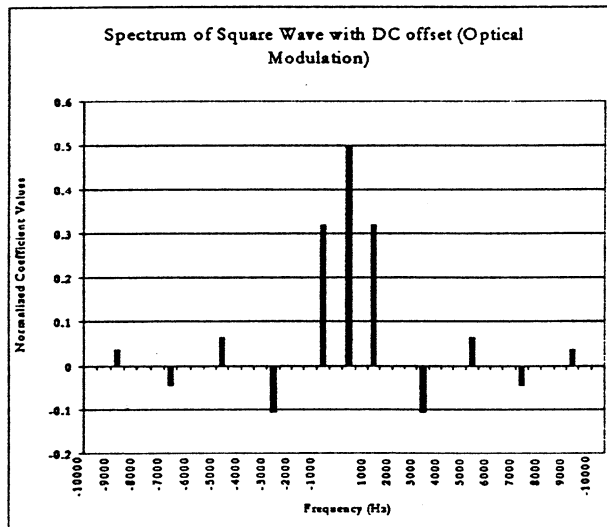


Fig. 1 Frequency Spectrum of Pulse Train

The dc magnitude can severely limit the minimum modulation depth detected by the camera, unless we can reduce it at the sensor. The problem manifests in one of two limiting electronic areas. First, the charge storage wells in a CCD camera have a finite limit, which is 20,000 electrons for the system we are using. In an ideal detector, the minimum modulation depth is obtained when the electron well fills with

background (dc) to the point where the modulated portion of the signal occupies the last two photoelectron sites. In practice, the situation is much worse because electronic and optical noise will also fill a portion of the well, which requires the modulated signal be larger than the noise level by a measurable amount. In a real (e.g. noisy) detector, therefore, the minimum modulation depth is given by  $(2 \times \text{noise}) / (\text{total electron well depth})$ . Commercially available cameras are then limited to modulation depths on the order of  $10^{-3}$  to  $10^{-5}$ .  $10^{-3}$  is a useful level of performance, but some applications will need to detect smaller modulation depths.

The second limiting factor in most imaging systems is the analog to digital converter (ADC) resolution. For example, an 8-bit ADC has 48dB of dynamic range, which results in a minimum modulation depth of 0.4 %, which is much too large to be useful. The resolution of the ADC used in our phase sensitive imaging system is 16-bit, giving us 96dB of dynamic range.

## Imaging System Development

Modifications have been made to a CCD camera system, model RTE/CCD-1300-Y manufactured by Roper Scientific (Princeton Instruments, Inc.), to provide gated integration control at the imaging chip level. The modifications and additions have been made in the camera controller logic, and the camera head circuitry and logic. The changes allow us to perform phase sensitive detection of a modulated light source, given that the modulation frequency and phase are known *a priori*.

Essentially, there are two unusual characteristics incorporated in the phase sensitive imaging system. The first is the ability to synchronously detect a modulated two-dimensional signal, by synchronizing to the modulated signal's frequency and phase. The second unusual characteristic is the imaging system's ability to sample a representative portion of the total integrated signal per integration period.

## Phase Sensitive Detection

In order to perform phase sensitive detection imaging, we must synchronize charge shifting and storage, in the CCD, with the incoming modulated information signal. Thus, we must have adequate control over the Read Out Gate (ROG) and the Overflow Drain (OFD) in the interline transfer CCD architecture, shown in Figure 2. The ROG and OFD control the flow of charge from the photo sensors to the vertical register and to the substrate respectively.<sup>8,9</sup> The vertical register is masked by an aluminum shield that prevents direct entry of photoelectrons. Photoelectrons integrated and stored in the sensor can either be dumped into the vertical register or discarded in the substrate. This is better illustrated in Figure 3. Charge in the sensor will migrate to the vertical register, under the

Al mask, when the Read Out Gate voltage is increased (voltage potential increases in the downward direction). Charge in the sensor will also migrate to, and be discarded in, the substrate when the Overflow Drain voltage is raised. Electronic shuttering is, thus, accomplished and controlled with the voltage applied to the OFD.

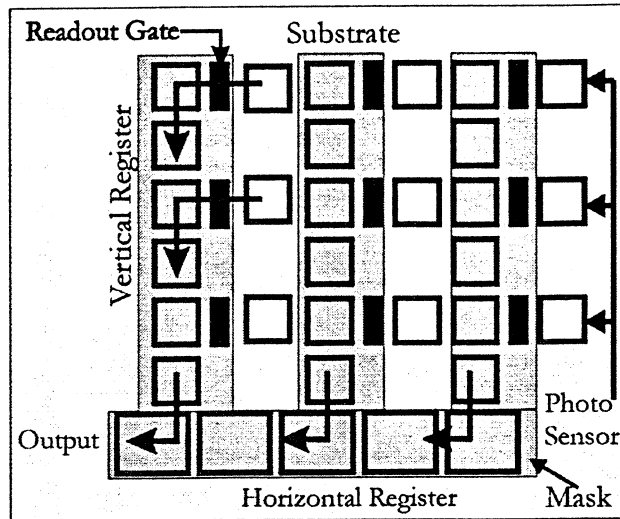


Fig. 2 Interline Transfer CCD Architecture

The ROG and OFD allow us to control the integration of the signal, to the extent that the signal is either integrated or not integrated. Assuming then that we are interested in detecting a laser source that is mechanically chopped, we can synchronize the imaging system to the chopper. Incorporating the phase lead or lag time with respect to the chopper 'sync' signal allows us to detect the signal when it is present and dump any noise when the signal is not present. As previously shown in Figure 3, the in-phase signal is integrated into the vertical register by raising the ROG voltage and lowering the OFD voltage. Then, as shown in Figure 4, the out-of-phase light is dumped to the substrate by raising the OFD voltage and lowering the ROG voltage. This synchronous process shifts the signal modulated at  $\omega_c$  back down to the baseband, by mixing it with the same detection frequency of  $\omega_c$ , as described earlier. The vertical register then performs lowpass filtering on the rectified signals, since multiple integrations are summed in the vertical register prior to reading out the image. The bandwidth of the lowpass filter depends on the number of integrations performed prior to readout.

As an aside, it is also possible to capture two separate images on the CCD chip prior to readout. A set of separate, high resolution images can be integrated on the CCD with a minimum temporal separation of  $1\mu s$ . If a pulsed diagnostic is used, such as Planar Laser Induced Fluorescence (PLIF) or Partial Imaging Velocimetry (PIV), then the first image can be directly integrated and stored in the vertical register and a

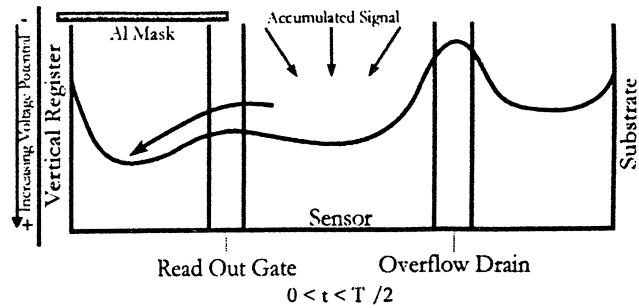


Fig. 3 Charge Flow Diagram (In-Phase)

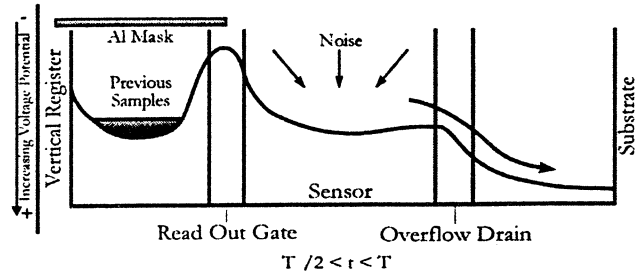


Fig. 4 Charge Flow Diagram (180° Out-of-Phase)

separate second image can be integrated and stored in the sensor area. Capturing two separate images is performed by lowering the voltage on the ROG after the first image is integrated, which prevents the second image from migrating to the vertical register, causing the second image to be stored in the sensor area. The two images can then be read out of the CCD separately. The double image feature has been used with a PLIF diagnostic in recent investigations.<sup>10</sup>

#### Integration Threshold

The second unusual characteristic incorporated into the imaging system is the ability to reduce the amount of stored photoelectrons per integration. A Pump/Probe type of diagnostic will quickly saturate the CCD with its large dc value, after only a few or one integration period. Since we know that the signal has a consistent dc offset intensity, in which the modulated signal resides, we would like to only sample the signal above a certain threshold. We would like to increase the number of integrations performed by reducing the overall magnitude at each integration. This is accomplished in the CCD with a non-linear integration threshold value associated with the Read Out Gate.

To better explain the idea of dc reduction with an integration threshold parameter, we will first briefly look at the 'normal' operation of an interline transfer CCD in block form, as shown in Figure 5. The well depth of the CCD is determined by the charge storage capacity of the sensor. After an image is integrated in the sensor, the accumulated charge is quickly dumped, via the ROG, to the vertical register for readout. The OFD controls the electronic shutter and the anti-blooming functions. Applying a high voltage to

the OFD will activate the electronic shutter function and send any charge in the sensor directly to the substrate. In a lower potential state, the OFD allows the sensor to store charge up to a certain integration level, which is the well depth of the sensor. Once the sensor is saturated, any additional charge will 'overflow' to the substrate, so that CCD blooming is eliminated.

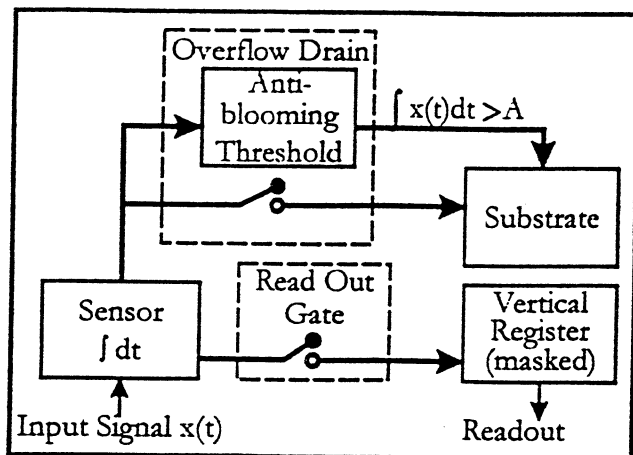


Fig. 5 Charge flow of normal CCD With Anti-blooming

Now, referring to Figure 6, we are using the ROG, instead of the OFD, to set the integration threshold on the sensor. Then, as long as the potential on the OFD is less than the potential on the ROG, relative to the sensor, additional charge, exceeding the integration threshold, will migrate to the vertical register, where it is stored. The OFD is now used as a switch to dump the charge built up in the sensor after an integration period. This process is performed by setting an 8 bit digital to analog converter (DAC), with the serial inter-integrated circuit ( $I^2C$ ) protocol, prior to imaging. The DAC output sets the ROG level during an integration period through an analog switch. The ROG level can be set from 12.75 V to 0 V, during integration, with a resolution of 50 mV. Future studies will relate the ROG level to the dc reduction level.

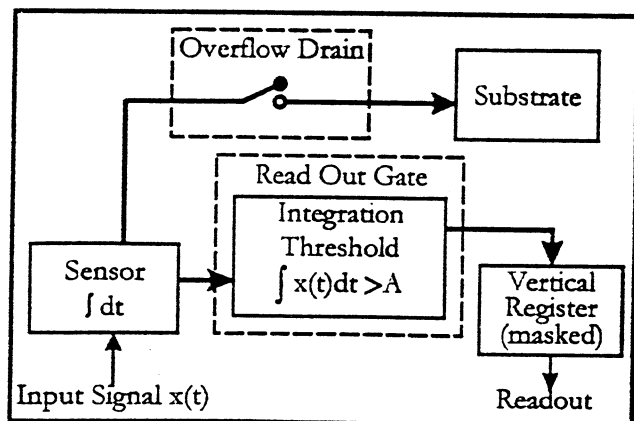


Fig. 6 Charge Flow of CCD with Integration Threshold

## Imaging System

Putting the two characteristics, the phase sensitive detection and the integration threshold, together, the imaging system functions as shown in Figures 7, 8, and 9. At the the first synchronous trigger, the imaging system performs the first integration by lowering the OFD to its minimum potential and raising the ROG to a voltage level proportional to the DAC (In Figures 7, 8, and 9, increasing voltage potential is as shown on the left hand side of the figures, thus increasing voltage lowers the gate threshold.). Once the integration threshold is exceed by charge in the sensor, additional integrated charge will migrate to and be stored in the vertical register. Once the exposure time for that integration period has elapsed, the ROG is lower to its minimum to prevent any further migration of charge from the sensor to the vertical register, and the OFD is set to its maximum to dump the charge from the sensor to the substrate (Figure 8). During this time, when no signal is present, the ROG and OFD remain as shown in Figure 8, activating the electronic shutter and dumping the steady state background, which includes noise, to the substrate. During the next, and the  $n^{th}$ , integration period, the ROG and the OFD are set as shown in Figure 9, summing each integrated signal period in the vertical register. In other words, lowpass filtering the integrations in phase with the signal.

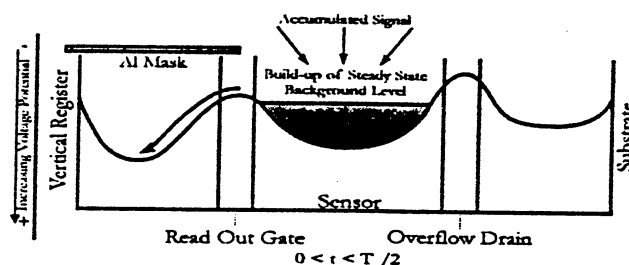


Fig. 7 Charge flow Diagram (In-Phase Integration)

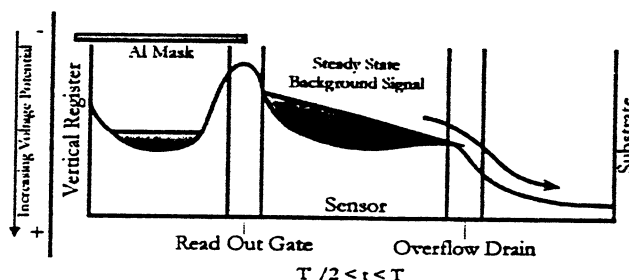


Fig. 8 Charge Flow Diagram (Not Sampling When Out-of-Phase)

## Established Instrument Comparison

The phase sensitive imaging system can be compared to two established and commonly used instruments, which are the Lock-in Amplifier and the Boxcar Integrator. The imaging system can be compared to a



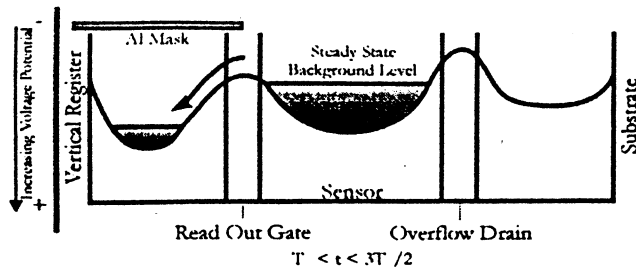


Fig. 9 Charge Flow Diagram (In-Phase [Nth] Integration)

Lock-in Amplifier, in the sense that it synchronously rectifies the signal of interest. A Lock-in Amplifier, however, has an advantage over the imaging system in its demodulation process. A Lock-in Amplifier mixes the signal of interest with a sinusoidal signal, with zero dc offset, which prevents the signal's power spectrum from mixing with the dc value and into low frequency noise. Also, either a bandpass filter, prior to demodulation, or a lowpass filter, after demodulation, is used in a Lock-in amplifier, to eliminate any noise outside the power spectrum of the information signal. The imaging system can only mix the modulated signal with a positive square wave, thus, convolving the power spectrum of the information signal with the dc and low frequency noise spectrum. The advantage of the imaging system, however, is that detection occurs in two dimensions and the Lock-in Amplifier is only capable of single point processing.

The imaging system is probably more comparable to a boxcar integrator. A boxcar integrator is a more appropriate instrument for measuring a train of short pulses that are separated by relatively long durations of zero information, which is the case when the duty cycle is  $\ll 50\%$ . A boxcar integrator greatly improves the SNR by detecting the signal only when it is present and not detecting anything when there is nothing but noise. The detection is performed simply by switching, or gating, the signal input, to an amplifier, ON and OFF. Significant amplification of the gated signal, on the order of  $10^8$ , is possible, to detect small amplitude signals. The time-pulse information is then fed into a lowpass filter, which integrates all of the 'ON' gates. Thus, the boxcar integrator is essentially a gated lowpass filter. The final signal value on the filter (which is the sum of the contributions from all the members of the Fourier series) is equal to the average value of the signal pulse over the ON interval of the gate. The SNR is improved by reducing the noise bandwidth and patiently gathering information, which is spread out over time.

The phase sensitive imaging system operates in much the same manner. The signal is gated, by the Read Out Gate, either ON or OFF. The time-pulse information is stored in the vertical register, which performs the lowpass filtering function, as described

in the boxcar integrator. Unlike a typical boxcar integrator, the imaging system is not capable of amplifying the signal prior to lowpass filtering the gated signal. In fact, there is actually a slight loss in signal due to the quantum efficiency of the detector. However, as previously stated, the phase sensitive imaging system captures two-dimensional data, which is not possible with a boxcar integrator.<sup>11</sup>

## Experimental Results

### Experimental Setup

The phase sensitive detection imaging system uses a Sony 1300 x 1030 Interline Transfer CCD. Each pixel in the array is  $6.7\mu\text{m}$  square and have microlenses to improve the fill factor. The system uses a 16 bit ADC with a clock speed of 1 MHz. The minimum integration time is on the order of  $10\mu\text{s}$ , resulting in a maximum signal modulation frequency of 100 kHz. Currently the number of integrations per image can be set from 1 to 255. A region of interest (ROI), a specified subsection of the entire CCD array, was used in the results presented here. The images shown are 301 x 301 pixels, which are captured at a framing rate of 11 Hz or less depending on the number of integrations and integration period. The analog to digital conversion rate limits the maximum framing rate speed. The charge in the CCD can be clocked out at a much faster rate than the ADC rate. Princeton Instruments, Inc. now offers a 5 MHz, 12 bit system, that uses the same CCD.

In order to test the phase sensitive imaging system, we set up a simple scattering experiment, shown in the Appendix as Figure 15. The basic objective of the experimental setup is to combine an intense, steady state beam of light, with a weak, modulated beam of light. The imaging system then extracts the weak modulated light from the intense steady state, background light. As shown in Figure 15, the beam is first split by a beam splitter. Thirty percent of the beam passes through a neutral density filter, is modulated with a mechanical chopper, and then recombined with the steady state beam at the second beam splitter. A lens expands the beam so that it completely covers the object of interest, which in this case is simply an integrated circuit (IC) package. Scattering from the object is then collected by the CCD camera. An image of the IC package is shown in Figure 10, which was taken under ambient light conditions to show the resolution of the camera.

A 1 kHz modulation frequency was applied to the chopper, and a photodiode was first used to determine the phase lead or lag time between the chopper sync output and the modulated beam. The sync output from the chopper was used as an external trigger to a Stanford Research Systems Inc., DG535, delay generator. The imaging system was then triggered by the rising edge of a  $20\mu\text{s}$  pulse from the DG535, which al-

lowed us to control the phase delay setting, based on the chopper sync signal.

### Initial Results

The first imaging experiment was set for a  $100\mu\text{s}$  exposure time per integration (duty cycle = 10%) and 255 integrations per image. Also worth mentioning, the camera system is thermo-electrically cooled and was set at  $-10^\circ\text{C}$ . Also, to perform dc reduction, the 8 bit DAC was set to 165 (maximum setting is 255), which reduced the maximum Read Out Gate voltage during integration by 30%. This is only a measurement of the voltage applied to the Read Out Gate and not a measure of the integration threshold. Further study is needed to completely characterize the integration threshold and the camera's ability to reduce the background intensity.

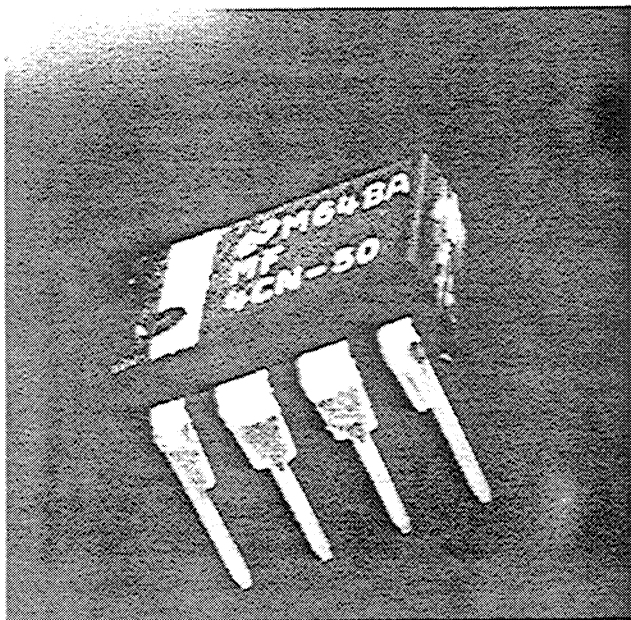


Fig. 10 IC Package Image

The power of the two beams, the steady state beam and the modulated beam, was measured with a Spectra Physics 404 power meter. The steady state beam power, for the first test, was measured at  $1.6\text{mW}$ , and the modulated beam power was found to be  $8\mu\text{W}$ . Thus, the steady state beam power is 200 times larger than the modulated beam power. If we define 'modulation depth' as the ratio between the modulated beam power and the steady state beam power, then the modulation depth for the first test is  $5 \times 10^{-3}$ .

The results of the first test are shown in Figures 11 and 12. Figure 11 shows the in-phase integrated image and Figure 12 shows the result of integrating  $180^\circ$  out-of-phase. A mask bleed-through image (not shown) was also captured by setting the integration threshold DAC to zero. The aluminum mask on the CCD is not perfect and some small portion of the image 'bleeds' through the mask and into the vertical register. Thus, by setting the DAC to zero, no integration is performed

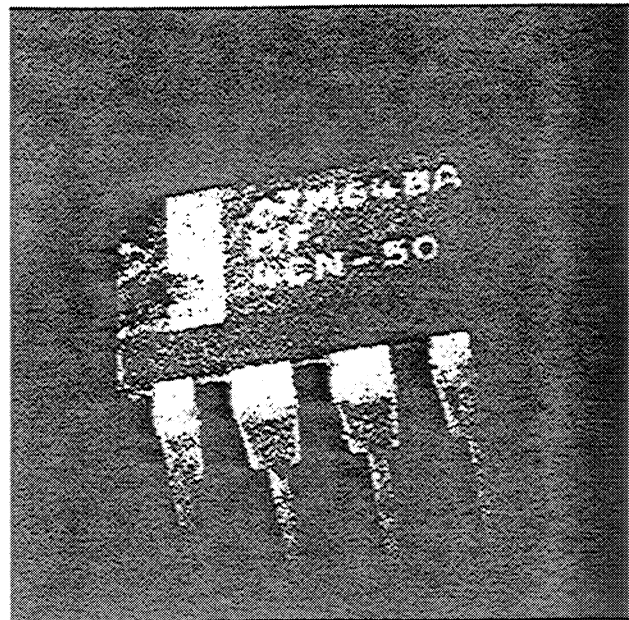


Fig. 11 In-Phase Image (Includes Modulation)

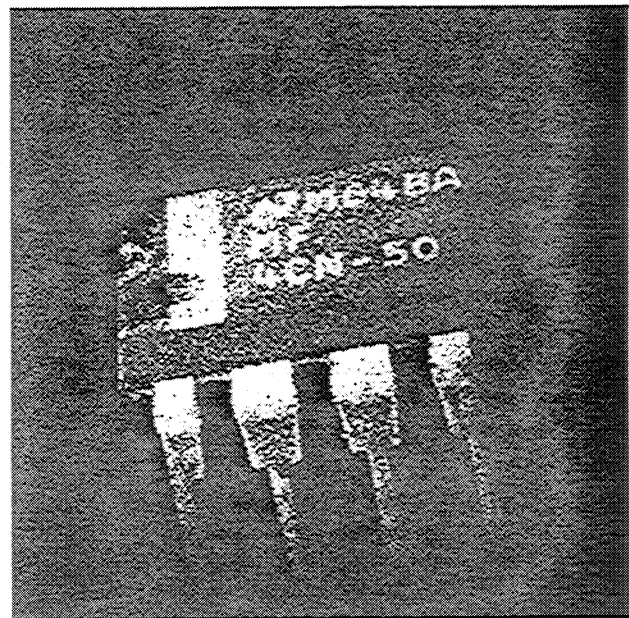
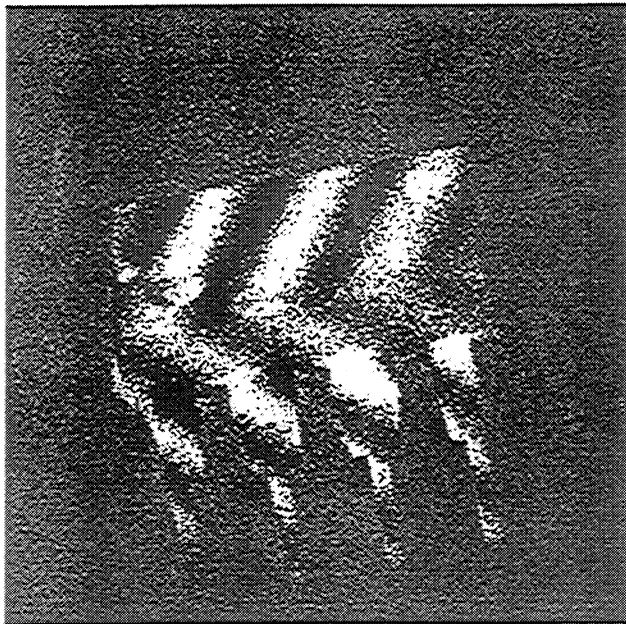


Fig. 12 Out-of-Phase Image (Modulation Absent)

over the total time it takes to capture the image and a mask bleed-through image is obtained. The in-phase and out-of-phase images are initially corrected by subtracting the mask bleed-through image from them. Then the 'corrected' in-phase and out-of-phase images are subtracted from each other. By subtracting the out-of-phase image, which contains only steady state beam intensity, from the in-phase image, which contains both modulated beam intensity and steady state beam intensity, we obtain an image that contains only modulated beam intensity. The result obtained from subtracting the image in Figure 12 from the image in Figure 11 is shown in Figure 13.

The resulting image in Figure 13 shows that the

phase sensitive imaging system is capable of detecting a modulation depth on the order of  $10^{-3}$ . There are some interesting characteristics seen in Figure 13. The interference pattern between the steady state beam and the modulated beam is definitely apparent and is an expected result. Also, the area around the chip, in the image, is canceled out since in-phase scattering only occurs in the small focal length volume of the object, creating very defining edges.



**Fig. 13 Image Detected at  $10^{-3}$  Modulation Depth**

A second imaging test was then performed at a smaller modulation depth. The steady state beam was set at 2.88mW and the modulated beam was attenuated to  $0.92\mu\text{W}$  with a neutral density filter. This resulted in a modulation depth of  $3.2 \times 10^{-4}$  for this test. The exposure time per integration was lowered to  $50\mu\text{s}$  and the integration threshold DAC was set at 180. The integrations per image remained at 255. Again, an in-phase image and an out-of-phase image were obtained and corrected for mask bleed-through. The result from subtracting the out-of-phase image from the in-phase image is shown in Figure 14. The signal to noise ratio of Figure 14 is approximately 2 to 3. This image shows that the system is capable of detecting a minimum modulation depth on the order of  $10^{-4}$ , which is an exciting and promising result.

#### Future Phase Sensitive Imaging System Research

In the near future, the imaging system will be utilized with both background free and background intensive diagnostics. Initially, we plan to image acetone seeded flows with Pump/Probe techniques. The imaging system will be carefully characterized in terms of the dc reduction capability and absolute detection limits. Future work will also include studies on image enhancement with image processing techniques.

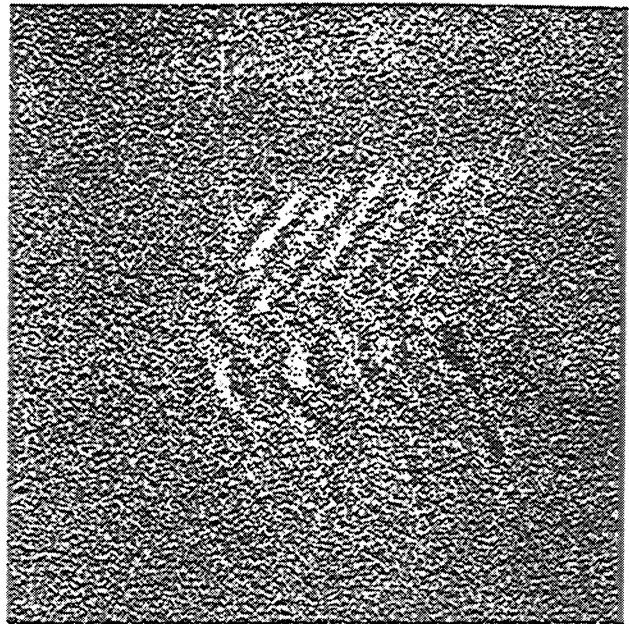


**Fig. 14 Image Detected at  $10^{-4}$  Modulation Depth**

#### Future Detection System Development

The offset level, or dc reduction process described in the phase sensitive camera systems does not remove all of the dc signal entering the detector. In imaging, the dc level, or background intensity, is, for example, the largest undesirable attribute in a pump/probe diagnostic setup. Thus, minimizing the background intensity would greatly improve the signal to noise ratio of the detection system and improve on the minimum detectable modulation depth. Background noise elimination can be accomplished by bandpass filtering the signal at a center frequency near the carrier frequency, prior to demodulation. The bandpass filter will allow the modulated signal to pass unattenuated, but greatly attenuate the dc level that is outside the bandwidth of the filter. This would require that continuous signal processing be done at the photo site prior to demodulation, integration, and image readout.

CCD's are limited in their signal conditioning capabilities. Charge in a CCD can be transferred, dumped, or summed. Active pixel sensors (APS) designed with CMOS technology are now finding their way into more and more applications. The active pixel sensors are providing attractive alternatives to CCD devices by incorporating processing blocks that are impossible in CCD devices. Based on initial studies, we are initiating the development a CMOS imaging device that incorporates temporal filtering at the pixel level. Signal processing at the pixel level will greatly improve the detector performance and detectable modulation depth.

To test the concept of temporally bandpass filtering the signal, prior to demodulation, we setup a test circuit using discrete components. An LED, driven by a summing amplifier, which allowed us to add various

levels of dc, modulation, and noise to the signal, was set directly in front of a photodiode. The signal from the photodiode was converted to a voltage, amplified, and then passed into a CMOS, switched capacitor, bandpass filter. A switched capacitor filter was used since it is developed with CMOS processes (which is, therefore, compatible with APS technology) and the center frequency of the filter is adjusted with a clock input. The signal from the bandpass filter was analyzed with an Hewlett-Packard HP89410 vector signal analyzer. Based on the individual dc and modulation power applied to the LED, the test circuit showed that by temporally filtering the signal, prior to demodulation, a modulation depth of  $10^{-5}$  is obtainable.

## Conclusions

A commercially available CCD camera has been modified, resulting in a phase sensitive two-dimensional detection system. The imaging system improves the signal to noise ratio by synchronously detecting the information signal, by detecting the signal only when it is present, and by integrating multiple exposures into one image, which lowpass filters the signal. Thus, the imaging system can be related to a two-dimensional boxcar integration system. Also, the maximum intensity accumulated in the pixels is reduced by sampling each exposure with the same integration threshold, which is set prior to capturing an image. This allows the CCD to acquire a greater number of integrations per image and keeps the CCD from becoming saturated.

Using a simple scattering experiment, the data shows that the imaging system is capable of detecting a minimum modulation depth on the order of  $10^{-4}$ . Further studies will be pursued to determine the system's absolute detection ability, and improve detectability through post-processing. The phase sensitive imaging system will be used with background intensive and background free diagnostic techniques to acquire useful flow field information. Finally, the lessons learned and experiences gained through the development of this system will be applied to new detector designs intended to greatly improve detection limits and increase the obtainable signal to noise ratio.

## Acknowledgments

This work has been supported by The National Aeronautics and Space Administration through the Center for Commercial Applications of Combustion in Space under Cooperative Agreement Number NCCW-0096; The National Science Foundation MRI grant CTS-9711889; The Air Force Wright Laboratories under contracts F33615-96-C-2632 and F33615-98-C-2859; and Roper Scientific (Princeton Instruments, Inc.) Princeton, NJ.

## References

- <sup>1</sup>R.K. Hanson, "Combustion Diagnostics: Planar Imaging Techniques", *Twenty-first Symposium (International) on Combustion / The Combustion Institute*, Pittsburgh, PA, pp. 1677-1691, 1986.
- <sup>2</sup>G.J. Fiechtner and M.A. Linne, "Absolute Concentrations of Potassium by Picosecond Pump/Probe Absorption in Fluctuating, Atmospheric Flames", *Combustion Science and Technology*, Vol. 100, pp. 11-27, 1994.
- <sup>3</sup>J.J. Mach and P.L. Varghese, "Velocity Measurements Using Filtered Rayleigh Scattering of Near-IR Diode Lasers", *36th AIAA Aerospace Sciences Meeting & Exhibit*, Reno, NV, AIAA-98-0510, 1998.
- <sup>4</sup>T. Settersten, C. Fisher, N. Middleton, and M. Linne, (Colorado School of Mines); J. Gord (USAF, Research Laboratory, Wright-Patterson AFB); P. Paul and G. Fiechtner (Sandia National Labs., Livermore, CA), "Demodulating Camera System for Picosecond Pump/Probe Imaging", *35th AIAA Aerospace Sciences Meeting & Exhibit*, Reno, NV, AIAA-97-0158, 1997.
- <sup>5</sup>M.A. Linne, D.C. Morse, J.L. Skilowitz, G.J. Fiechtner, and J.R. Gord, "Two-dimensional Pump/Probe Imaging in Reacting Flows", *Opt. Lett.*, Vol. 20, No. 23, pp. 2414-2416, 1995.
- <sup>6</sup>T.E. French, "The Development of Fluorescence Lifetime Imaging and An Application in Immunology", Ph.D. Thesis, University of Illinois at Urbana-Champaign, 1996.
- <sup>7</sup>F.G. Stremler, "Introduction to Communication Systems", Third ed., Reading, MA: Addison-Wesley Publishing Company, Inc., 1990, Chapter 5.
- <sup>8</sup>Personal Communication with Jim Paton, Design Engineer, Roper Scientific (Princeton Instruments, Inc.), 1998
- <sup>9</sup>Personal Communication with A. Paterson, Product Operational Support Center, Business & Industrial Systems, Sony, Montvale, NJ, 1996
- <sup>10</sup>M.C. Thurber, R.K. Hanson, "Simultaneous imaging of temperature and mole fraction using acetone planar laser-induced fluorescence", submitted for publication to *Experiments in Fluids*, 1999.
- <sup>11</sup>American Dynamics Corporation, "Lock In The Devil, Feed Him To The Cat, Or Take Him For The Last Ride In A Boxcar?", *Tek Talk*, Vol. 6, No. 1.

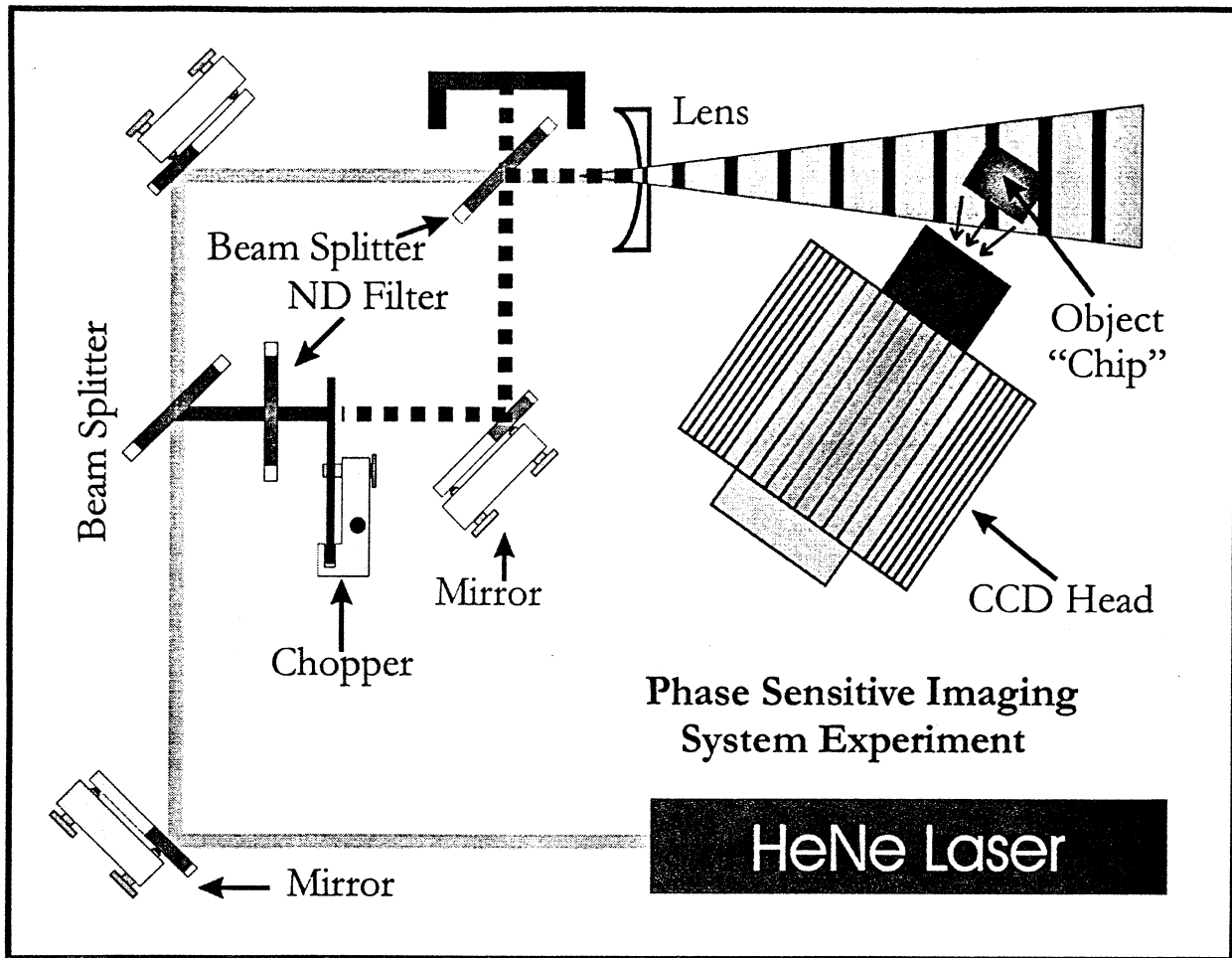


Fig. 15 Experiment Setup



### **2.1.6 Particle-Image-Velocimetry Technique**

The development, evolution, and application of the PIV technique were emphasized during this five-year program. Efforts on the development of a two-color PIV system are summarized in the paper entitled “Quantitative Visualization of Flowfields Using Two-Color PIV” (see pp. 84-88a). Application of this technique to studies of turbine film cooling is discussed in the publication entitled “The Unsteady Structure of Simulated Turbine Film Cooling Flows from PIV” (see pp. 89-101). The experimental investigation of wall jets is summarized in the paper entitled “Experimental Investigation of the Unsteady Structure of a Transitional Plane Wall Jet” (see pp. 102-110). The study of coaxial jet flows is discussed in the publication entitled “Visualization and DPIV Measurements of Non-Circular Coaxial Jet Flows” (see pp. 111-116). Vortex-flame interactions in a hydrogen jet diffusion flame were investigated with the two-color PIV method, and the resulting data are compared with predictions from direct numerical simulations in the paper entitled “Vortex-Flame Interactions in Hydrogen Jet Diffusion Flames: A DPIV and DNS Investigation” (see pp. 117-124). The study of a supersonic turbulent boundary layer with the PIV technique was summarized in the publication entitled “Structure of a Compressible Boundary Layer over a Curved Wall” (see pp. 125-135).

## QUANTITATIVE VISUALIZATION OF FLOWFIELDS USING TWO-COLOR PIV

S. Gogineni, L. Goss, G. Fiechtner, and C. Carter  
Innovative Scientific Solutions, Inc.  
2766 Indian Ripple Road  
Dayton, OH 45440-3638

F. Schauer, J. Gord, and J. Donbar  
Propulsion Directorate  
Air Force Research Laboratory  
Wright-Patterson AFB, OH 45433

### Abstract

The evolution, development, and application of two-color PIV to a wide variety of complex flowfields are discussed, including jet-in-a-crossflow, a supersonic turbulent boundary layer with pressure gradients, flow over a delta wing in a large-scale facility, and vortex-flame interactions. The high-resolution images obtained from these flowfields provide valuable insight concerning the instantaneous nature of the flow and quantitative data that are valuable for developing CFD and combustion models. Two-color PIV is also used simultaneously with planar laser-induced fluorescence (PLIF) imaging for understanding turbulent flame structure.

### Introduction

Particle Image Velocimetry (PIV) has been used for a number of years to measure velocity distributions in planar cross sections of aerodynamic flowfields (Adrian, 1991). One of the difficulties involved in implementing this velocimetry technique is the 180-degree directional ambiguity that results from the inability to determine the temporal sequence of the particle pairs. Several techniques have been developed to resolve this ambiguity problem; most involve imposing a shift between consecutive image exposures by means of a scanning or rotating mirror, pulse tagging, a calcite crystal, a polarizing beam splitter, a cross-correlation camera, and color coding of the particles.

The two-color system was originally developed by Goss et al. (1991) for combustion applications and has the following advantages: 1) resolving the directional ambiguity is inherent in the system, 2) higher data yields and signal-to-noise levels are attainable, and 3) the system is suitable for harsh environments and hypersonic flows. In this system two lasers were used--one for producing the green beam (532 nm) and the other for pumping the dye laser to produce the red beam (~ 605 nm); the two beams were combined by a

dichroic beam splitter and directed through a set of spherical and cylindrical lenses to generate a laser sheet. The particle images of the flowfield were recorded on 35-mm color film, and the images were analyzed by digitizing the film and using a particle-tracking approach. This technique was applied to several flowfields by Post et al. (1993, 1994) using pulsed lasers as well as a single argon-ion laser. The system was extended to cross-correlation-based PIV (Gogineni et al., 1995) and was applied to a jet-in-a-crossflow flowfield using several seeding strategies.

Unlike single-color PIV systems, extension of the two-color PIV technique from a film-based to a digital-based version was hampered by the lack of commercially available color CCD camera systems. Because of recent developments in color cameras, the difficulty in utilizing color CCD cameras for two-color PIV has decreased significantly. Gogineni et al. (1998) extended film-based two-color PIV to the digital version by recording the color images onto a single, high-resolution, digital (3060 x 2036 pixel) color CCD camera. This digital system was applied to a wide variety of fluid flows such as simulated turbine-film-cooling flows, vortex-flame interactions, turbo-machinery flows, a supersonic turbulent boundary layer with pressure gradients, flow over a delta wing in a large-scale facility, and hypersonic flows. Unlike conventional flow-visualization methods, two-color PIV provided images that were useful in analyzing flow structures both qualitatively and quantitatively. These images were also valuable in developing CFD codes. In addition, this system was used for simultaneous velocity and scalar (OH and CH) measurements in turbulent flames (Donbar et al., 1998a and 1998b) and vortex-flame interactions (Fiechtner et al., 1999). Spatial resolution, uncertainty, and sensor performance of this system as compared to color film and Kodak ES 1.0 CCD sensors were also evaluated (Gogineni et al., 1998a, 1999).

## Applications

### 1. Jet-in-a-Crossflow

For understanding the mixing and interaction of jet and crossflow fluids, an experiment was conducted by placing the square jet normal to the crossflow (Gogineni et al., 1995). The Reynolds number based on the side of the square jet and the exit velocity of the jet is  $\sim 600$ , and the crossflow Reynolds number based on the jet location downstream of the flat-plate leading edge is 9,000. The nominal blowing ratio, defined as the ratio of jet velocity to crossflow velocity, is 1.0. In this experiment a novel approach of seeding the jet and crossflow fluids with different-size particles was used to distinguish the jet fluid from the crossflow fluid.

Figures 1(a) - 1(c) show typical double-exposed two-color PIV images of the jet in a crossflow in the  $x$ - $y$  plane  $z = 0$ . Figure 1(a) where only the crossflow was seeded with submicron-size smoke particles, shows the entrainment of the crossflow fluid into the wake region and into jet-shear-layer vortical structures. Figure 1(b), where only the jet flow was seeded with  $1\text{-}\mu\text{m}$   $\text{Al}_2\text{O}_3$  particles, shows the jet penetration into the crossflow and jet fluid entering the wake region. Although these two images were taken at different instants, they have the same appearance because of the quasi-periodic nature of the flow. In Fig. 1(c) the jet fluid was seeded with  $1\text{-}\mu\text{m}$   $\text{Al}_2\text{O}_3$  particles, and the crossflow fluid was seeded simultaneously with submicron-size smoke particles in an attempt to understand the interaction of the two fluids. This image enables one to distinguish the jet from the crossflow fluid through the intensity levels of the scattered light (e.g., the bright region corresponds to the jet-flow region, and the dark region corresponds to the crossflow region). These images were processed using cross-correlation procedures, and the resulting velocity distribution for the image of Fig. 1(c) is shown in Fig. 1(d). The vorticity distribution computed from the velocity field was superposed in Fig. 1(d) and clearly shows the shear-layer structures emanating from both the upstream and the downstream lip of the jet. Further details of this study have been reported previously by Gogineni et al. (1998b).

### 2. Supersonic Turbulent Boundary Layer With Pressure Gradients

A two-color digital PIV (DPIV) system was developed and applied to analyze the structure of a supersonic turbulent boundary layer distorted by wall-curvature-driven streamwise pressure gradients. These tests were performed in a supersonic wind tunnel located at Wright-Patterson AFB. The free-stream Mach number was 2.8 at the measurement location. In this experiment the red laser beam was obtained by passing the green laser beam through a Princeton Optics Model

RC1000 Raman cell that contained  $\text{N}_2$  and He at a pressure of 65.6 Mpa. Two-color PIV images of the flowfield were recorded using a Kodak DCS 460 CCD camera ( $3\text{k} \times 2\text{k}$  pixel array). The performance of this sensor was evaluated by Gogineni et al. (1998a, 1999) using simulated displacements, and the data were found to be in excellent agreement with the corresponding film data and the Kodak ES1.0 data.

Figures 2(a) and 2(b) correspond to zero-pressure-gradient (ZPG) and favorable-pressure-gradient (FPG) conditions. The ZPG boundary-layer structures had an inclination angle of  $45^\circ$  -  $60^\circ$  and spanned approximately one-half the boundary-layer thickness. The FPG boundary layer grew in the streamwise direction, as expected. In addition, a higher population of small-scale structures was evident near the FPG boundary-layer edge, which is consistent with the theory that a FPG promotes the dissociation of large-scale structures into small-scale structures. These images were processed; the mean velocity of the FPG data was compared with the corresponding LDV data obtained in an earlier experiment and found to be in good agreement [Fig. 2(c)]. Further details on this study have been reported by Wier et al. (1999).

### 3. Flow Over a Delta Wing in a Large-Scale Wind-Tunnel Facility

Several challenges are involved in the transition from small- to large-scale facilities. These challenges include particle illumination and seeding over large regions and recording the particle scattering from a distance far from the selected plane. The ISSI team conducted experiments on the crossflow planes of a delta-wing model (with and without vertical tails) in the Subsonic Aerodynamics Research Laboratory (SARL) wind-tunnel facility at Wright-Patterson AFB. The model was tested at a 23-deg. angle of attack, a Mach number of 0.2, and a Reynolds number of  $1.87 \times 10^6$  (based on root chord).

Figure 3 shows a two-color PIV image of the flow over a delta wing with tails. The laser-sheet location was at 114.3% root chord. The flowfield was seeded with submicron-size smoke particles. The recording optics was placed 4 m from and at angle of  $69^\circ$  to the illuminated plane. The flow in this case is highly unsteady because of the vortex-bursting phenomenon. The number of secondary structures on the periphery of the primary vortex is higher than that for the flow condition without tails. Figure 3(b) shows the average velocity distribution from eight instantaneous images. These data reveal a counterclockwise vortex motion on the inboard side of the tail. On the outboard side, the velocity vectors mainly follow the direction of the primary vortex motion. The implementation issues regarding this experiment were discussed by Gogineni et al. (1999).

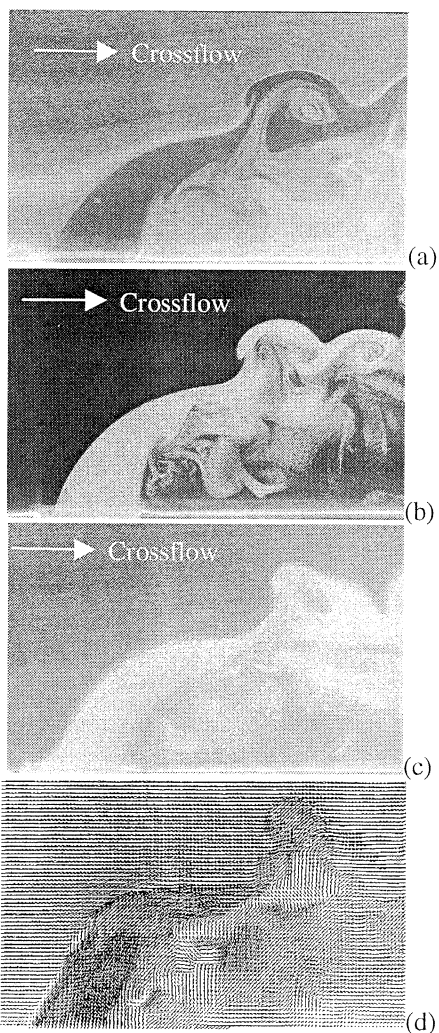


Fig.1. Flowfield of jet-in-a-crossflow  
 (a) Only crossflow seeded  
 (b) Only jet flow seeded  
 (c) Two seeded simultaneously  
 (d) Velocity and vorticity distributions

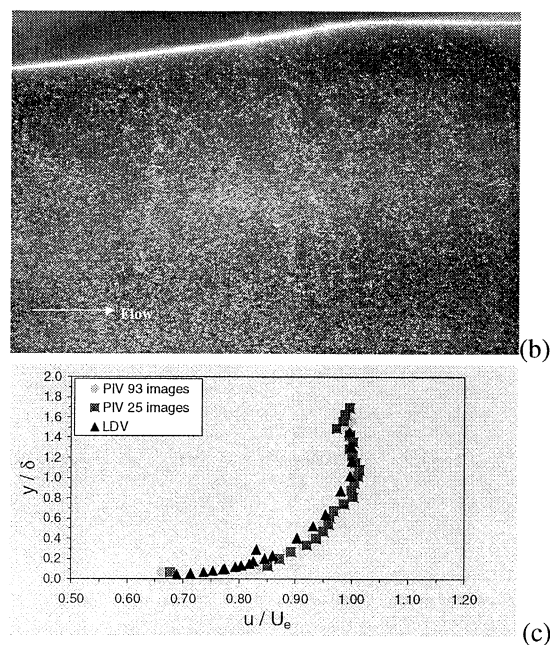
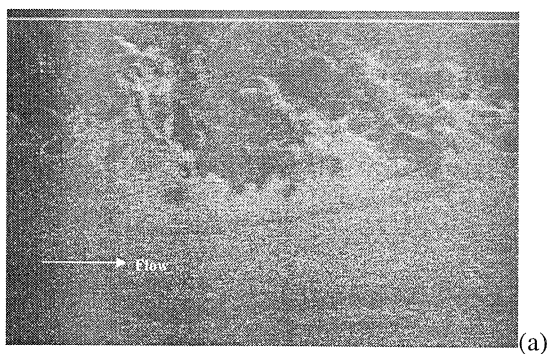


Fig. 2 Flowfield of supersonic turbulent boundary layer  
 (a) Zero Pressure Gradient (ZPG)  
 (b) Favorable Pressure Gradient (FPG)  
 (c) Comparison of DPIV and LDV data for FPG

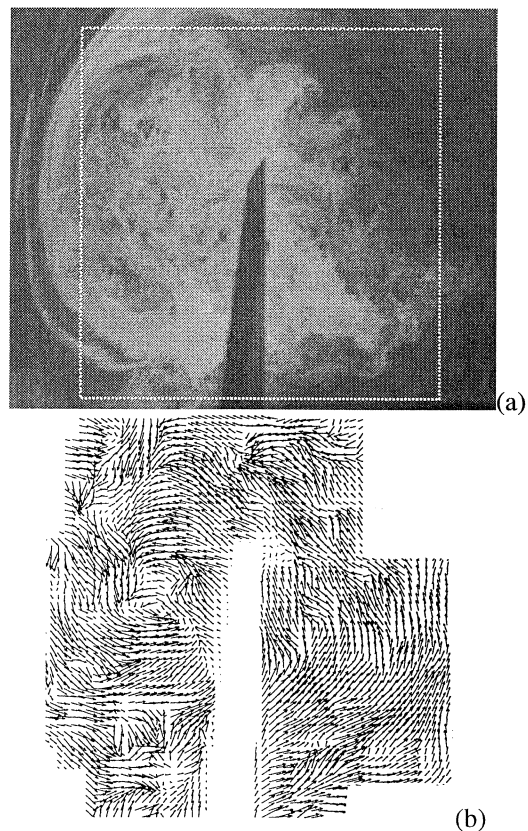


Fig. 3 Flow over delta wing with vertical tails  
 (a) PIV image  
 (b) Average velocity distribution

#### 4. Vortex-Flame Interactions

Vortex-flame interactions in a hydrogen jet diffusion flame were investigated with two-color DPIV and the results used to develop combustion models. Driven-jet vortex-flame interactions are of particular interest because they are reproducible turbulent-like events that can be investigated comprehensively to gain insight into turbulent combustion. Previously, temperature and species-concentration measurements were made in this flame (Hancock, 1996), but a complete understanding of the vortex-flame interactions could not be gained without additional information concerning the flowfield. The vortex structure of the combustng flow could not be reproduced using hot-wire velocity data from cold flows. When the jet-exit velocities from DPIV measurements were used as the driving profile for the DNS code, the resulting computations produced a vortex that matched the experimental vortex (Schauer et al., 1998).

By seeding both the jet flow and the co-flow, Figs. 4(a) and 4(b) were captured for visualizing the entire burner, co-flow, and flame. Figure 4(a) reveals the inner driven fuel-side vortex, the flame-zone where the seed density is low, and the larger flame zone structures above the fuel jet which are produced both by buoyancy and by the periodically driven vortices. It is also evident that the co-flow is effective in producing laminar flow.

In contrast to the driven flame, the steady undriven flame [Fig. 4(b)] has no inner vortex structure. Figure 4(b) shows a classic jet diffusion flame. Although buoyant structure is evident in this image, it is much different from that in the driven flame of Fig. 4(a), which contains large structures in the flame zone that are much nearer the nozzle. Although not clearly visible in Figs 4(a) and 4(b), a bulge in the flame zone is observed in the driven flame near the inner vortex. The contrasting images show the dramatic effect of the vortex-flame interaction on the overall flame structure.

Figure 5(a) shows a typical DPIV image corresponding to the square region of Fig. 4(a), and Fig. 5(b) displays the velocity and vorticity distributions. The cold-flow image under the same flow conditions is shown in Fig. 6. The difference in vortex structure is attributable to heat-release effects and demonstrates the importance of performing the velocity measurements under reacting conditions for developing combustion models. Figure 7 is a split experimental and computational image of the driven hydrogen jet diffusion flame. The left half is the DPIV image, and the right half is an image from the computational model. The DNS vortex is indicated by theoretical particle traces, and the peak-flame-temperature locations are represented by dots. From Fig. 7 it is evident that the vortex is generated when the faster moving fuel encounters the slower moving fuel, forcing

the fuel outward radially and causing a bulge in the flame zone. Similar results are shown in Fig. 8, which displays the DPIV and DNS images of the cold flow.

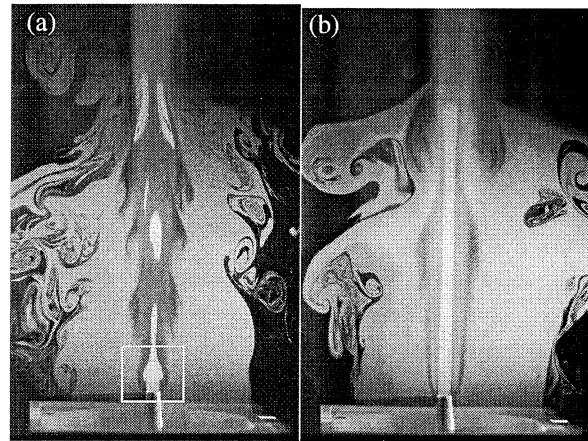


Fig. 4 Flow visualization of (a) driven and (b) undriven hydrogen jet diffusion flame

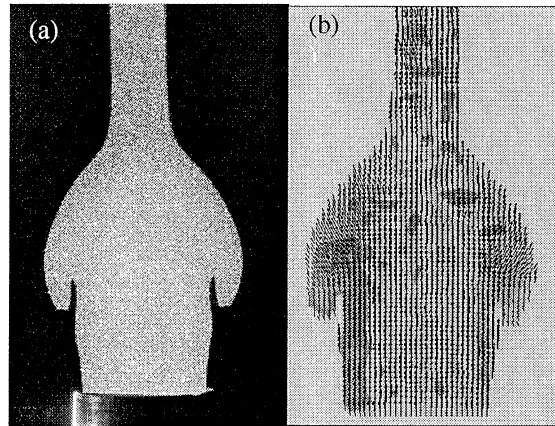


Fig. 5 Flow structure near jet exit (reacting): (a) DPIV image, (b) Velocity superposed with vorticity

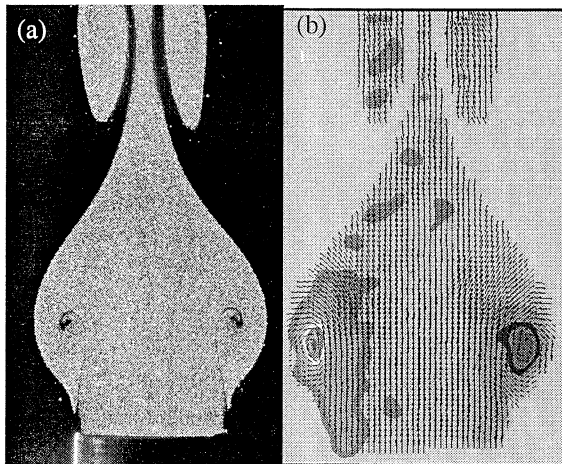


Fig. 6 Flow structure near jet exit (non-reacting): (a) DPIV image, (b) Velocity superposed with vorticity



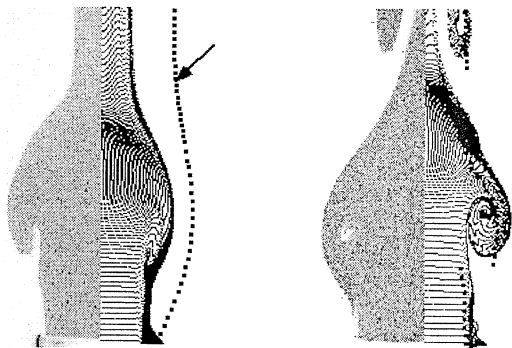


Fig. 7 Split computational and experimental images: (a) Reacting, (b) Non-reacting

The two-color DPIV instrument has also been valuable during recent studies of the interaction of a vortex and a nonpremixed hydrogen-air flame. The vortex was injected into the flame zone of an opposed-jet burner. The images of Fig. 8 were taken using simultaneous planar laser-induced fluorescence (PLIF) of OH (lower half of the figure) and DPIV (upper half of the figure) (Fiechtner et al., 1999). Superimposed on both images is the instantaneous velocity field which, in this case, indicates that the vortex travels upward at 4 m/s. The distinct annular break in the OH layer agrees closely with previous numerical computations of Katta, validating the utility of his CFD code (Katta et al., 1998).

### 5. Turbulent Flames (Simultaneous Velocity-Scalar Measurements)

Donbar et al. (1998a) addressed the question of whether the chemical-reaction zone within a turbulent, high-Reynolds-number jet flame is thin and can be modeled using strained, wrinkled, laminar flamelet theory or thick and must be modeled using distributed-reaction-zone theory. The region near the wrinkled, instantaneous stoichiometric contour was identified using CH PLIF imaging, and the strain on this interface was measured simultaneously using DPIV. A typical CH PLIF image of a methane flame with overlaid vectors is shown in Fig. 9. To visualize the vortical structures, 75% of the mean centerline velocity was subtracted from all vectors; thus, vectors on the low-speed coflow side are pointing downward. Several features of velocity field/CH layer interactions are noticeable, particularly the large structure deforming the top right and the small vortex distorting the middle of the right-hand side of the flame. The upper left-hand side shows a relatively weak CH region that is being influenced by two small vortical structures—one from the jet fluid and the other from the oxidizer. The relative position of the reaction zone and the shear layer is evidenced by the close proximity of the downward-pointing vectors to the CH layer.

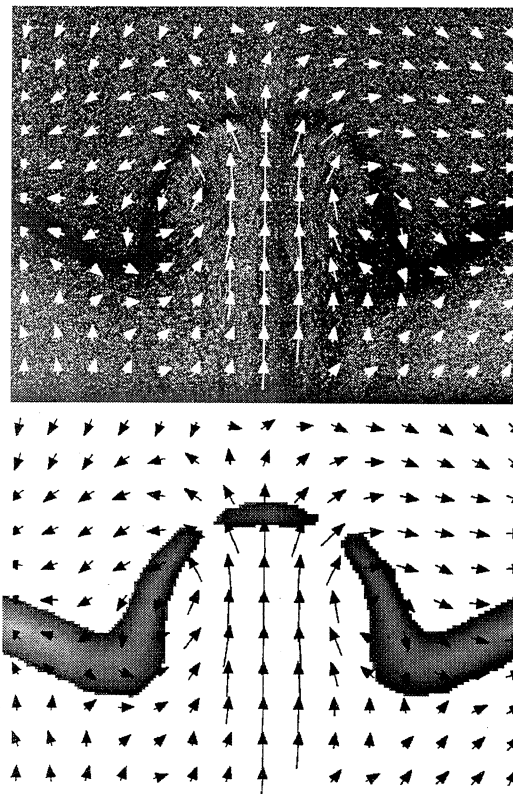


Fig. 8 Interaction of vortex with nonpremixed hydrogen-air flame: (a) DPIV image with velocity vectors, (b) OH PLIF image with velocity vectors

Donbal et al. (1998b) also implemented the simultaneous OH PLIF/PIV technique for characterizing a methane flame diluted with nitrogen, surrounded by a coflowing mixture of oxygen and nitrogen with swirl. Figure 10 shows the realization of the simultaneous OH PLIF/PIV field downstream of the attached diffusion flame. At this position, the flame-front location and structure vary greatly from image to image. This figure shows an unbroken flame, with the velocity field showing little reverse flow in the core region. Near the image center is a vortical structure that has apparently thickened the OH layer in this region. Meanwhile, the flow pattern near the swirl region (lower right edge) has almost wrapped the OH layer back onto itself.

### 6. Summary

Several complex flowfields were investigated using two-color PIV. The technique proved to be valuable in providing high-quality, high-resolution images. Many of these images were used to develop combustion models and CFD codes. Implementation of this technique for transonic turbomachinery flows and hypersonic flows is currently underway.

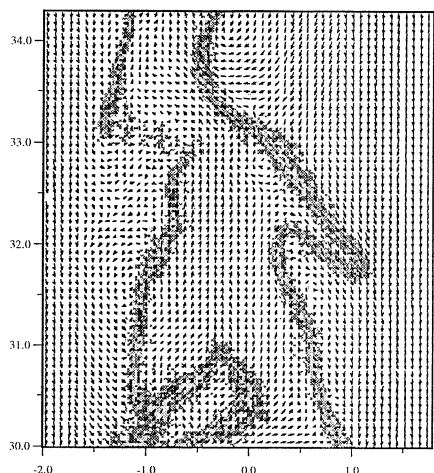


Fig. 9 Simultaneous CH PLIF/PIV image (75% of mean centerline velocity was subtracted from all vectors)

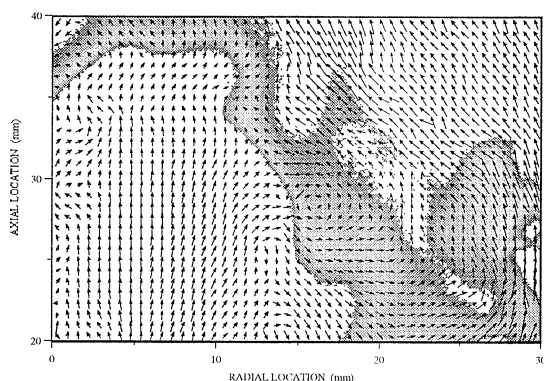


Fig. 10 Simultaneous OH PLIF/PIV image in downstream region of attached diffusion flame

### Acknowledgments

This work was supported by the U.S. Air Force Research Laboratory, Propulsion Directorate, Wright-Patterson AFB (WPAFB), OH. The authors would like to thank M. Roquemore, R. Hancock (WPAFB), T. Beutner (AFOSR), R. Bowersox (University of Alabama), and J. Estevadeordal (ISSI) for, experimental assistance and valuable suggestions at various stages of the work. The editorial assistance of M. Whitaker is greatly appreciated.

### References

- Adrian RJ** (1991) Particle imaging techniques for experimental fluid mechanics. *Ann Rev Fluid Mech* 23: 261-304.
- Donbar JM; Driscoll J; Carter, CD** (1998a): Simultaneous CH planar laser induced fluorescence and particle imaging velocimetry in turbulent flames.

AIAA-98-0151, 36<sup>th</sup> Aerospace Sciences Meeting and Exhibit, Reno, NV.

**Donbar JM; Carter CD; Ratner A; Driscoll J; Dahm J** (1998b) Simultaneous velocity-scalar measurements within intensely turbulent non-premixed flames. Fall Technical Meeting, Western States Section of the Combustion Institute, Seattle, WA.

**Fiechtner GJ; Renard PH; Carter CD; Gord JR; Rolon JC** (1999) Vortex-flame interactions: experimental observation of the annular extinction predicted by Katta. Submitted to *Combust Flame*.

**Gogineni S; Goss L; Sutkus D; Glezer A** (1995) Investigation of a jet in a crossflow using PIV. AIAA Paper No. 95-0790, AIAA 33rd Aerospace Sciences Meeting and Exhibit, Reno, NV.

**Gogineni S; Goss L; Pestian D; Rivir R** (1998a) Two-color digital PIV employing a single CCD camera. *Exp Fluids* 25: 320-328

**Gogineni; Goss L; Roquemore M** (1998b) Manipulation of a jet in a cross flow. *Exp Thermal Fluid Sci* 16: 208-219.

**Gogineni S; Goss L; Beutner T** (1999) Application of two-color PIV in a large-scale wind tunnel facility. AIAA Paper No. 99-0269, AIAA 37th Aerospace Sciences Meeting and Exhibit, Reno, NV.

**Goss LP; Post, ME; Trump DD; Sarka B** (1991) Two-color particle-image velocimetry. *J Laser Appl* 3: 36-42.

**Hancock RD** (1996) Laser diagnostic investigation of the structure of steady and driven hydrogen jet diffusion flames. Ph.D. Dissertation, University of Illinois, Urbana-Champaign, IL.

**Katta VR; Carter CD; Fiechtner GJ; Roquemore WM; Gord JR; Rolon JC** (1998) Interaction of a vortex with a flat flame formed between opposing jets of hydrogen and air. Twenty-Second Symposium (International) on Combustion, The Combustion Institute, Pittsburgh, PA, pp 587-594.

**Post ME; Goss LP** (1993) Two-color particle imaging velocimetry in vortex structures. AIAA-93-0412, 31<sup>st</sup> Aerospace Sciences Meeting and Exhibit, Reno, NV.

**Post ME; Trump DD; Goss LP; Hancock RD** (1994) Two-color particle imaging velocimetry using a single argon-ion laser. *Exp Fluids* 16: 263-272.

**Wier R; Bowersox R; Glawe D; Gogineni S** (1999) Structure of compressible boundary layer over a curved wall. Submitted to *J Prop Power*.

**Schauer F; Hancock R; Gogineni S; Lucht R** (1999) Vortex-flame interactions in hydrogen jet diffusion flames. Submitted to *Exp Fluids*.

Original version of this material was first published by AGARD/NATO in CP-598 - Advanced Non-Intrusive Instrumentation for Propulsion Engines in May 1998. PUBLISHED WITH PERMISSION

## The Unsteady Structure of Simulated Turbine Film Cooling Flows from PIV

Richard B. Rivir

Aero Propulsion and Power Directorate, Wright Laboratory/POTT  
Wright-Patterson Air Force Base, OH 45433 - 7251, USA

Sivaram P. Gogineni and Larry P. Goss

Innovative Scientific Solutions Inc., 2786 Indian Ripple Road  
Beavercreek, OH 45430, USA

David J. Pestian

University of Dayton Research Institute  
Dayton, OH 45469, USA

### 1. SUMMARY

Unsteady turbine film cooling flows are subjected to free stream disturbances which exceed those of a fully turbulent boundary layer. Hot wires, cold wires, and thermocouples have in the past been used to obtain local, time resolved point measurements of velocity, temperature and mixing. The structure of the flow and its interaction with free stream structures remains largely hidden. Two-color, double pulsed, PIV (Particle Image Velocimetry) was used to investigate simulated turbine film-cooling flows with high free stream turbulence and wake passing. High resolution (3000x2000 pixels), instantaneous, velocity distributions obtained by CCD camera have been compared against those obtained from 35mm film digitized at 2700 ppi resulted in realizations with similar spatial resolution. Averages of 1 to 30 instantaneous PIV velocity measurements have been compared against simulated turbine film cooling flow velocity profiles measured by hot wire. The resulting PIV velocity profile measurements were mostly within the envelope of the mean and rms velocity measurements of the hot wire. The PIV images allow instantaneous estimates of the shear layer development, vertical cooling jet film spread, turning, and interactions with the free stream turbulence. Instantaneous vorticity, and dissipation distributions have also been obtained. The lateral jet spread of the film at the wall was measured with liquid crystals and thermocouples and compared with the vertical PIV spread. The centerline vertical film jet spread, turning angle, and shear layer growth has been characterized from the PIV realizations as a function of blowing ratio, Reynolds number, periodic forcing amplitude, frequency, and free stream turbulence.

### NOMENCLATURE

A	Film foot print with Tu or forcing, (cm <sup>2</sup> )
A <sub>o</sub>	Film foot print with Tu = 1% (cm <sup>2</sup> )
c <sub>r</sub>	Constant f (accuracy of software determination of particle displacement, 1-10%)

d <sub>i</sub>	Recorded image diameter (mm)
d	Film-cooling-hole diameter (1.905 cm)
DVR	Dynamic Velocity Range = M <sub>o</sub> Δp <sub>max</sub> / c <sub>r</sub> d <sub>i</sub>
M <sub>o</sub>	Magnification factor
Δp <sub>max</sub>	Maximum velocity displacement (μm)
R	coolant blowing (mass-flux) ratio (ρ <sub>c</sub> U <sub>c</sub> /ρ <sub>f</sub> U <sub>f</sub> )
Re	Reynolds number based on film-cooling-hole diameter
Tu	Turbulence intensity (u'/U)
U	Mean local streamwise velocity (m/s)
x	Streamwise distance measured from the downstream lip of the injection hole (cm)
y	Vertical distance from the injection surface (cm)
f	Forcing frequency (Hz)
ω	Vorticity, 1/2((V/(x-(U/(y)) (1/s)
Ω	Reduced frequency (free stream velocity/coolant-hole diameter/oscillation frequency, U/d f)

### 2. INTRODUCTION

PIV has been explored as an initial step for the measurement of unsteady flow phenomena associated with the film cooling of turbine components. Recent trends in aircraft gas-turbine combustor designs have resulted in short, high-temperature combustors which produce highly turbulent exit flows. These flows are further complicated by stator wake interactions, non steady passage vortices, end wall horseshoe vortices, along with non-steady up stream cooling flows. As the exit temperature of the combustors is raised to increase engine-cycle efficiency, effective film cooling of the turbine components downstream of the combustor becomes increasingly important. Modeling of turbine film cooling flows computationally requires extensive meshes and intersection of meshes of different densities such that experimental verification of film effectiveness and heat transfer coefficient is still required for code verification. The instantaneous

realizations of velocity obtainable from PIV can provide a detailed understanding of many of these unsteady flow features.

Bons et al. (1994, 1995) investigated the effect of unsteadiness and high free stream turbulence on film-cooling effectiveness using physical probes including hot wires and thermocouples. Physical probes, however, are hampered by their intrusive nature, limited spatial resolution from point wise measurements, and spatial averaging over sparse arrays of measurement points. Liquid Crystals and IR measurements have been made of the surface temperature distributions but quantitative simultaneous spatially and temporally resolved measurements of the film flow are still lacking. This study provides instantaneous realizations of the film cooling hole centerline vector flow fields for a range of conditions encountered in turbine flows and summarizes results from several of our current PIV investigations of turbine film cooling flows.

### 3. EXPERIMENTAL SETUP AND PROCEDURES

#### 3.1 Facility description

The open-loop film-cooling wind tunnel, as shown in figure 1, has been described in detail by Bons et al. (1994, 1995). The main flow passes through a conditioning plenum containing perforated plates, honeycomb, screens, and a circular-to-rectangular transition nozzle. Downstream of the transition nozzle, at the film cooling station, free stream turbulence levels of 0.7% ( $\pm 0.05$ ) can be achieved, with velocity and temperature profiles uniform to within 1%. A single row of 1.905-cm film-cooling holes at an injection angle of 35 deg. to the primary flow was investigated. The length-to-diameter ratio of the film-cooling holes evaluated was 2.4. The ratio of integral turbulence scale to film-hole diameter is in the range 2.88 - 4.23, depending on the turbulence level and turbulence generation mechanism. The ratio of momentum thickness to hole diameter typically is 0.05. The ratio of micro scale to film-hole diameter is in the range 0.1 - 0.39. The ratio of temperature or density of the film flow to primary flow is typically, 1.07 - 1.09. The variation in blowing ratios ( $R = 0.5 - 1.5$ ) is achieved by varying the ratio of the film flow velocity to the primary flow velocity. For simulation of the vane-wake effects, the film cooling jet flow is modulated with a speaker located in the side wall of the coolant supply plenum at an appropriate reduced frequency  $\Omega$ .

#### 3.2 Range of Experimental Parameters Investigated

Film-cooling air is injected through rows of typically 0.5 - 0.8 mm diameter holes in the blade surface. The jet injection hole was scaled up by a factor of 35 to study the flow characteristics of a turbine-blade film-cooling hole. The cooling air is supplied from the compressor exit bleed flow and is maintained at essentially constant pressure. Typical engine Reynolds numbers for film cooling holes are in the range of 20,000. The Reynolds numbers ( $Re$  - based on the coolant-hole diameter of 1.905 cm) which were investigated for the unforced flow in this investigation were 10,000, 20,000 and 40,000. The effect of free stream turbulence was investigated for turbulence levels of 1%, 6%, 12% and 17% for the blowing ratios of 0.5, 0.7, 1.0,

and 1.5 at a Reynolds number of 20,000. The effect of Reynolds numbers of the film at 10,000, 20,000, and 40,000 was investigated for blowing ratios of 0.5, 0.7, 1.0, and 1.5 at turbulence levels of 1% and 17%. The two-color PIV technique was used to examine the region around the film-cooling hole for 3 diameters downstream, to document the penetration of the film jet into the free stream, to determine the shear-layer characteristics, and to determine the film jet spread.

The effect of vane wake on rotor film cooling flow was simulated by periodic forcing of the film-cooling flows at the typical rotor blade passing reduced frequency  $\Omega$ . Phase-locked measurements at 45-deg. increments of the periodic film forcing for free stream turbulence levels ( $Tu$ ) of 1 and 17% were obtained for frequencies of 5 and 20 Hz.

#### 3.3 Two-color PIV System

PIV has been used for a number of years to measure velocity distributions in planar cross sections of aerodynamic flow fields (Adrian 1991, Lourenco et al. 1989). The two-color PIV system uses color for temporal marking of the seed particles in the flow field which also results in higher data yields and signal-to-noise levels than are attainable with single color systems by eliminating any uncertainty in particle direction. The green (532-nm) laser output from a frequency-doubled Nd:YAG laser and the red (640-nm) laser output from a Nd:YAG-pumped dye laser (DCM dye) are combined by a dichroic beam splitter and directed through sheet-forming optics. The laser-sheet energy is typically 20 mJ/pulse, with a sheet thickness of  $< 1$  mm at the test section. The temporal delay between the two lasers is dependent upon the flow velocity, optical magnification, and interrogation spot size. It is set at  $\sim 12 \mu s$  for a  $Re = 20,000$  film flow velocity. A 105-mm micro lens with an f-number of 5.6 was used to record the images. The same lens was used for CCD and the 35mm film realizations.

The implementation and selection of the seeding is an important factor in PIV measurements in complex three-dimensional flows. The seed particles must be small (typically  $< 1 \mu m$ ) to track accelerations in the fluid effectively. In the present experiment sub-micron size particles are introduced into the film cooling flow in the film plenum.

One of the problems in the use of film for mean PIV measurements is the inability to maintain the absolute coordinates of the recorded features during the digitization process while multiple frames are averaged. This occurs because the film cannot be consistently loaded into the film-scanner to the degree required for reproducibility. This problem is eliminated when using a digital color CCD since no film digitization is required. The high-resolution Kodak DCS 460 CCD system extends two-color PIV by recording the color images onto a single high-resolution color CCD camera, thus eliminating the processing time and subsequent digitization time of color film and the complexities associated with conventional image-shifting techniques. The DCS 460 has  $3060 \times 2036$  pixels, with each pixel being  $9 \mu m^2$ . The CCD camera has a built-in 12-bit analog-to-digital converter for

increased dynamic range and a frame rate of 1 frame/sec. It also features a PC-MCIA storage drive which delivers about 26 exposures, with each PIV image occupying ~ 6 Mbytes. The color response of the DCS 460 CCD array is accomplished by overlaying the individual pixels of the camera with a series of red, green, and blue color filters. The chosen green and red laser wavelengths were situated near the peak of the transmission of the green and red camera filters, respectively. Because the camera was built to respond, as a human eye to color, most of the pixels are green-sensitive. The relative percentages of green, blue, and red pixels are 50%, 25%, and 25% respectively. The distribution of the red and blue pixels is random for minimizing straight-edge effects. The output from the camera controller to the computer is a 24-bit RGB tiff image; thus, the 12-bit A/D camera output must be mapped into three 8-bit colors, each having a spatial resolution equivalent to the chip size (3060 x 2036). This is accomplished through proprietary software developed by Kodak which involves some form of interpolation to increase the spatial resolution of the camera. Because of the proprietary nature of this interpolation software, it was not known how the resulting resolution of the color camera would compare with 35 mm film or if it would be useful for accurate PIV measurements. The CCD camera allowed on line optimization of the seed density and intensity of the sheet illumination.

The software for data reduction uses the correlation of 5-8 particles to compute the velocity vector at a single point. The cross-correlation technique is based on intensity maps of the red and green images of scattered light. The intensity distributions of the red and green images  $r(x,y)$  and  $g(x,y)$  and their corresponding Fourier transforms are  $R(a,b)$  and  $G(a,b)$ . The two-dimensional cross-correlation function

$$\begin{aligned} h(x,y) &= \int_R \int_R r(\alpha,\beta) g(x+\alpha, y+\beta) d\alpha d\beta \\ &= F^{-1}[F(r(x,y)) F(g^*(x,y))] \\ &= F^{-1}[R(\alpha,\beta) G^*(\alpha,\beta)] \end{aligned} \quad (1)$$

is employed to determine the magnitude and direction of the average velocity over the interrogation area. Note that unlike processing methodologies that are based on auto correlation, the direction of the velocity vectors is uniquely determined.

The correlation function (1) is calculated over small segments (interrogation domains) of the PIV image. In order to process the digitized PIV image, it is dissected into small sub regions. The dimensions of each interrogation domain depend on the particle density, estimated local velocity gradients, particle image size, and the desired spatial resolution. The maximum displacement of each particle must be less than half of the interrogation spot. In the present experiments, the interrogation domain measures 64 x 64 pixels and corresponds to 1.4 x 1.4 mm area in the measured flow. In order to enhance the overall resolution, the interrogation domains are overlapped by one-half the domain size. The peak of the correlation map

calculated by Eq. (1) corresponds to the average velocity within the interrogation spot. An intensity weighted peak searching routine is used to determine the exact location of the peak to a sub-pixel accuracy. The number of particle pairs that are necessary to ensure a desirable signal to noise ratio is reduced to four or five pairs when this cross-correlation analysis is employed.

### 3.4 PIV Calibration

A comparison of the resolution and accuracy of 35 mm film against the CCD camera was performed using a disk rotating at a constant rpm. The measurement of the rotating velocity vector is illustrated in figure 2a and the calibrations obtained for film and CCD are compared in figure 2b illustrating that similar accuracy and resolution is achieved for film and CCD (Gogineni et al. 1996a). Figure 2a also illustrates the direction resolving capability of this configuration. Since the PIV measurements are instantaneous realizations, some sort of averaging is required to compare against mean and rms hot wire measurements. Figure 3a illustrates a film boundary layer comparison of 30 PIV realizations and a hot wire traverse of the same flow. The bars indicate the spread in an average of 5, 10, 20, and 30 PIV realizations at each data point for unforced flow conditions ( $x/d = 1$ ,  $Re = 20,000$ ,  $R = 0.7$ , and  $Tu = 1$ , (Gogineni et al. 1996d). The wide scatter is due to the high Reynolds number, high turbulence levels, and the large-scale turbulent structures of the film-cooling flow. Since only the film-cooling flow was seeded in this experiment, the velocities obtained in the interface region of the unseeded high-speed free stream and the seeded slower-speed film-cooling flow would be expected to deviate from those obtained with a hot-wire probe which cannot distinguish between the two flows. The rms fluctuation was measured at a constant flow condition, and the results show that the rms deviation approaches 20% as the number of samples is increased. The PIV images do however represent the instantaneous flow structures with fidelity. In the present experiment 30 images is of course not sufficient for accurate determination of the mean velocity and rms velocities.

Gogineni et al. (1997) has examined the sensitivity of particle size to the accuracy of the mean and rms errors for a variable particle size as well as the variable displacement error for a fixed particle size. A particle size which records as 2.5 - 4 pixels results in an rms error of 0.017 to 0.06 pixels in position. A fixed particle size of 4 pixels results in an error of 2.5% at a 2 pixel pair displacement and 1.3% at a 20 pixel pair displacement as is illustrated by the plot of this relationship in figure 3b. Adrain's (1996) Dynamic Velocity Range (DVR) for the Kodak CCD camera results in a useful range of velocity measurement of nearly 70 for this configuration.

## 4. RESULTS AND APPLICATION OF PIV TO SIMULATED TURBINE FILM COOLING FLOWS

Turbine-blade film cooling takes place in a very hostile, unsteady environment where velocity and temperature disturbances exceed 20%. The free stream and film cooling boundary layer wall conditions in these flows exceed those encountered in classical fully turbulent boundary layers. Parameters of interest in this problem include jet spread or film



effectiveness,  $R$ ,  $Re$ ,  $Tu$ , and  $\Omega$ . Accurate modeling of these flows has proved difficult due to the high level of unsteadiness. Nominally 10 - 30 instantaneous images were obtained for a given flow condition to capture the essence of the flow features.

#### 4.1 Liquid Crystal and Thermocouple Measurements of Mean Jet Spread and Film Effectiveness

Liquid crystals were also used to measure wall surface temperatures allowing calculation of  $\eta$ , and  $h$ . Figure 4 shows liquid crystal measured temperature contours on the wall for turbulence intensities of 1%, 6%, 11%, and 17%. The green liquid crystal line is nominally 0.4°C wide. Figure 4 shows an increased spread angle with  $Tu$  for the same constant temperature contour. The film has virtually disappeared by a  $x/d = 6$  in figure 4. Figure 5 shows the spread half angle of the film coolant obtained by digitizing the temperature contours of figure 4. Figure 5 indicates the film spread angle to be nearly linear with  $Tu$ .

Direct measurement of the film cooling effectiveness was obtained from thermocouples on the adiabatic test section wall. An array of 84 thermocouples provided the wall surface temperature distribution. Figure 6 illustrates the centerline film cooling effectiveness measurements for  $Tu=0.9\%$ , 6.5%, 11.5%, and 17%. These measurements, which extended to large values of  $x/d$ , indicated a 50% attenuation in effectiveness over the low turbulence case at  $x/d=6$ , and an attenuation of 70% at  $x/d=22$ .

The liquid crystal measured lateral jet spread, figure 4, is compared with the measured thermocouple centerline vertical attenuation or spread, figure 5, in Table 1 at  $x/d = 6.7$ . Table 1 indicates similar jet spreads with turbulence from the two measurements

**Table 1 Comparison of Film Spread to  $Tu=1\%$   
Spread Area**

$Tu$ in %	$Ao/A$ Liquid Crystal	$Ao/A$ CI thermocouple
6	0.76	0.75
12	0.60	0.67
17	0.44	0.44

The film cooling effectiveness drops rapidly as the pair of counter rotating vortices, formed by the interaction of the free stream horseshoe vortex with the film jet, pull free stream fluid under the film and the center of the film flow lifts off the surface. The free stream contributes significantly to the rapid mixing out of the coolant temperature. The cylindrical film hole results in symmetric spread with the maximum film effectiveness moving away from the wall as a result of the vertical lifting of the film.

#### 4.2 PIV Measurements

The two-color PIV technique was used to measure the penetration of the film jet, the shear-layer characteristics (scale, frequency and angle of spread), vorticity, and the jet spread angles. Figure 7 compares centerline flows from PIV

realizations at  $Re = 20,000$  as the turbulence level is increased from 1% to 17%. One can see that increasing the turbulence from 1% to 17% more than doubles the vertical film spread for  $R = 0.7$ . The resulting vector velocity fields are shown below the corresponding PIV realization in figure 7. The slope of the shear layer over the film cooling hole and after the film cooling hole in figure 7 indicates different interactions take place over and after the film hole with the primary flow.

The resulting angles of the film coolant flow have been plotted in figure 8 for  $R=0.5, 0.7, 1.0, 1.5$ , and  $Tu=1, 6, 12, 17\%$  (Gogineni et al. 1996b). Figure 8 shows a linear relationship between the jet-exit slopes with both  $Tu$  and  $R$ , for  $R < 1.0$ . Different slopes of the linear relationship are observed for the spread angle over and after the film hole. There is a decrease in jet spread for  $R=1.5$ , however, the spread angle remains appreciable. Increased jet spread results in more rapid mixing out of the film cooling flow.

Figure 9a illustrates CCD images obtained at a Reynolds number of 40,000, at free stream  $Tu$  levels of 1% and 17% for  $R = 0.7$  and 1.5. The increase in  $Re$  has proportionally increased the frequency or reduced the scale of the shear layer over the film cooling hole, while after the film hole the blowing ratio and the free stream turbulence control the shear layer scales or frequency. When  $Tu$  was increased from 1 to 17% for  $R = 0.7$ , no appreciable change was observed in the eddy sizes in the shear layer after the film-cooling hole. A significant change however took place at  $Re=40,000$  for  $R = 1.5$ . When  $R$  was increased from 0.7 to 1.5 at a free stream  $Tu$  level of 17%, the roll-up frequency for the shear layer after the film-cooling hole decreases. In the shear layer over the film hole, a second parallel shear layer can be detected (figure 9a, which may be associated with a separation from the back side entrance of the film-cooling hole. When  $R < 1.0$ , it is observed that the shear-layer roll up is the reverse of what would normally be expected. This reverse roll up is attributed to the film-cooling wall boundary layer.

Figure 9b shows the vorticity distribution  $\Gamma$ , computed by central differencing of the velocity field. The solid lines indicate positive vorticity, and the dashed lines indicate negative vorticity. As expected, high values of vorticity are found in the shear layer and in the film layer at lower  $R$ . When  $R$  is increased to 1.5 and  $Tu$  to 17%, the vorticity is concentrated in the shear layer far from the surface. The vorticity distribution from the CCD data showed a significant improvement over that from the 35-mm, film data. This can be attributed to the presence of the more valid vectors and on line optimization of seeding and laser sheet intensity.

#### 4.3 Periodically Forced Film Measurements

The passage of the stator-wake was simulated by periodic forcing of the film-cooling flow at the appropriate reduced frequency,  $\Omega$ . Scaling up the film cooling holes on a turbine blade results in frequencies of interest for these simulated film cooling flows in the range of 5 to 50 Hz. The average  $\eta$  and average  $h$  resulting from periodically forced disturbances at 5, 10, and 20 Hz was compared to that from random turbulence in

Bons et al., 1995 using thermocouples with either a constant heat flux surface or an adiabatic wall. The mean film cooling effectiveness at large  $x/d$  ( $>20$ ) from the adiabatic wall measurements shows that the attenuation was the same for a periodically forced film flow as that of continuous free stream turbulence of the same amplitude. Adiabatic wall measurements of these flows forced at 5, 10, and 20 Hz showed little difference between the 10 and 20 Hz cases. A preferential amplification of a low forcing frequency (5 Hz) was observed near the film hole so 5 and 20 Hz cases were chosen for the PIV investigation.

PIV was used to examine the flow field for film flows forced at 5 and 20 Hz for preferential frequency response, flow structure, interaction with the free stream, and jet spread angle. PIV exposures were phase locked to the film-coolant driving frequency, and data recorded at phase-angle increments of 45 degrees of the forcing cycle (Gogineni et al. 1996c). The blowing ratios of 0.5, 0.7, 1.0, and 1.5 were investigated at a Reynolds number of 20,000. Figure 10 shows a typical double-exposed PIV image and the corresponding instantaneous velocity distribution at a phase angle of 180 degrees for  $R = 0.5$ ,  $Re = 20,000$ , and  $Tu = 17\%$  with periodic forcing at 5 Hz and 20 Hz. These realizations illustrate the double shear layer at the leading edge of the film hole, a reverse roll up of the shear layer, the two characteristic scales (one over the film hole and one after the film hole), and a preferential amplification of the low forcing frequency (this amplification was also observed with hot wire measurements).

It was previously indicated that jet spread (angle of the film) was indicative of the mixed film temperature. The film flow angles for the shear layers and the film jet were obtained from the instantaneous PIV realizations. Typical results for the phase locked spread angle over the film cooling hole and after the film cooling hole are summarized in figures 11 and 12. According to these results free stream turbulence of 17% contributed very little additional spread to the periodically forced flow. Periodic forcing of the film cooling flow resulted in forced film flows with twice the forcing frequency and average spread angles which were between those observed for the 1% and 17% free stream turbulence cases. Although the amplitude of the forced with or without  $Tu$  versus the 17% continuous case are similar, the average instantaneous spread angle for the periodically forced with or without  $Tu$  film is 57% less than the 17% continuous free stream case. An average of the phase averaged measurements should of course be investigated to see if this could be used to reduce film cooling mass flows. Table 2 presents the average spread angles for the periodically forced flows for both frequencies. A comparison of the forced PHI2 and 17% spread angles with the 1% PIV spread angle indicates  $Ao/A$  ratios of 0.70 and 0.36 respectively which are found to be similar but slightly less than the lateral spread  $Ao/A$  ratios obtained from liquid crystal and thermocouple measurements. Near the film cooling hole ( $<3$  diameters) the forced 1% flow is spread at approximately half the 17% spread angle from the PIV realizations.

Table 2 Mean Spread Angles  $x/d < 3$

Spread Angle	Blowing Ratio	Forced $Tu=1\%$	$Tu=1\%$	$Tu=17\%$
Mean PHI 1	0.5	29.5		
	0.7	34.3	22.2	29.2
	1.0	39		
Mean PHI 2	0.5	9.3		
	0.7	12.4	8.7	22.9
	1.0	13.1		

## 5. CONCLUSIONS

Short  $l/d$  film cooling holes significantly affect the flow by virtue of the film tube wall boundary layer. This film wall boundary layer remains a dominant driver in the development of the film coolant flow as evidenced by the reverse roll up seen in PIV realizations.

Turbine film cooling data from 35-mm film after digitization and from a 3060 x 2036 pixel CCD camera have been compared and found to have similar spatial resolutions. The CCD allowed optimization of seeding and laser-sheet intensity which resulted in higher vector densities. Hot-wire data and the average of more than 20 PIV frames at  $x/d = 1$  agreed favorably for these highly unsteady flows; however, direct use of mean values for these flows would require an average of more than the 30 samples used in this investigation.

Free stream turbulence of 17% results in attenuation of the cooling effectiveness by 50% at  $x/d=6$  and a 70% reduction at  $x/d=22$ . A linear relationship was observed between the instantaneous spread angle of the film, blowing ratio, and continuous free stream turbulence intensity. Periodic forcing and continuous free stream unsteadiness produce similar vertical jet spread at large  $x/d$ . The film jet spread angle, at small  $x/d$ , for periodic forcing with or without free stream turbulence is 57% less than continuous free stream turbulence. Periodic forcing exhibited film fluctuations at twice the forcing frequency. The film shear layer is dominated by Reynolds number over the hole and by blowing ratio and free stream turbulence after the hole.

PIV has proved to be extremely useful in obtaining additional information on the structure of turbine film-cooling flows such as jet spread, shear-layer growth, and shear-layer frequency. PIV also allows the computation of realizations of vorticity and dissipation for direct comparison with CFD data

## ACKNOWLEDGMENT

This work was performed under partial sponsorship of the Air Force Office of Scientific Research Project 2307BW, with Dr. James McMichael as program manager.

## REFERENCES

1. Adrain, R. J., 1991, "Particle Imaging Techniques for Experimental Fluid Mechanics," Annual Review of Fluid Mechanics, Vol 23 pp. 261-304.
2. Adrain, R. J., 1996, "Strategies for Imaging Flow Fields with PIV," AIAA 96-198, 27<sup>th</sup> AIAA Fluid Dynamics Conference, New Orleans, LA.
3. Bons, J., MacArthur, C., and Rivir, R., 1994, "The Effect of High Freestream Turbulence on Film Cooling Effectiveness," ASME 94-GT-51, 39th International Gas Turbine and Aeroengine Congress and Exposition, The Hague, Netherlands.
4. Bons, J., Rivir, R., Mac Arthur, C., and Pestian, D., 1995, "The Effect of Unsteadiness on Film Cooling Effectiveness," AIAA 95-0306, 33rd Aerospace Sciences Meeting and Exhibit, Reno NV.
5. Gogineni, S., Trump, D., Goss, L., Rivir, R., and Pestian, D., 1996a, "High Resolution Digital Two-color PIV (D2CPIV) and Its Application to High Freestream Turbulent Flows," 8th International Symposium on Applications of Laser Techniques to Fluid Mechanics, Lisbon, Portugal.
6. Gogineni, S., Rivir, R., Pestian, D., and Goss, L., 1996b, "PIV Measurements of Flat Plate Film Cooling Flows with High Free Stream Turbulence," AIAA 96-0617, 34th Aerospace Sciences Meeting and Exhibit, Reno NV.
7. Gogineni, S., Trump, D., Pestian, D., and Rivir, R., 1996c, "PIV Measurements of Periodically Forced Flat Plate Film Cooling Flows with High Free Stream Turbulence," 1996 ASME International Gas Turbine and Aeroengine Congress/Users Symposium and Exposition, Birmingham, UK. ASME 96-GT-236.
8. Gogineni, S., Rivir, R., Goss L., and Pestian, D., 1996d, "PIV Technology for Simulated Turbine Film Cooling Flows," The 6<sup>th</sup> International Symposium on Flow Modeling and Turbulence Measurements, Tallahassee FL.
9. Gogineni, S., Trump, D., Goss, L., Rivir, R., and Pestian, D., 1997, "High Resolution Digital Two-color Digital PIV Employing a Single CCD Camera," Experiments in Fluids, Revision in Progress.
10. Lorenzo, L. M., Krothapalli, A., and Smith, C. A., "Particle Image Velocimetry, Advances in Fluid Mechanics Measurements, (M. Gad-el-Hak, ed.) Springer-Verlag, Berlin, pp. 127-199.

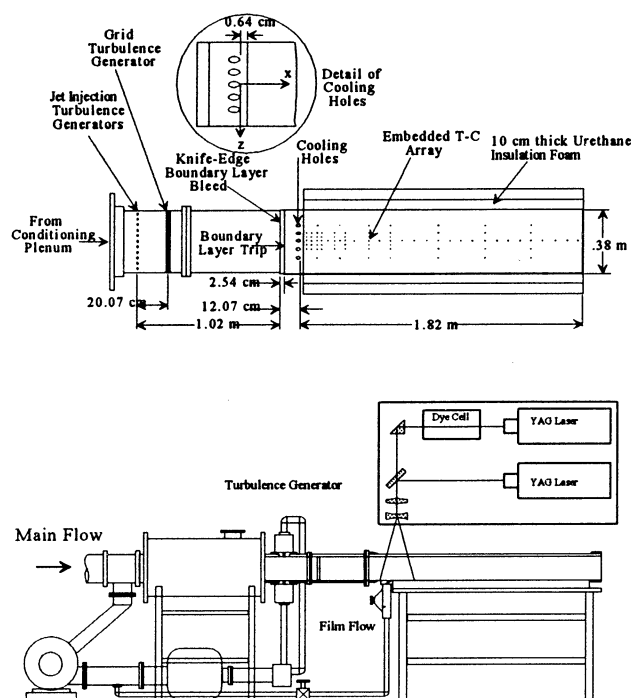


Figure 1. Schematic of the High Turbulence Film Cooling Facility with 2 Color PIV.

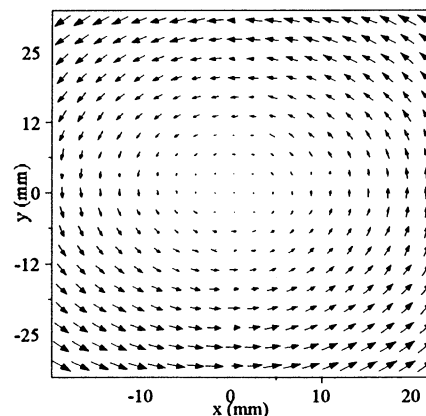


Figure 2a. Rotating Calibration Disk Velocity Vectors.

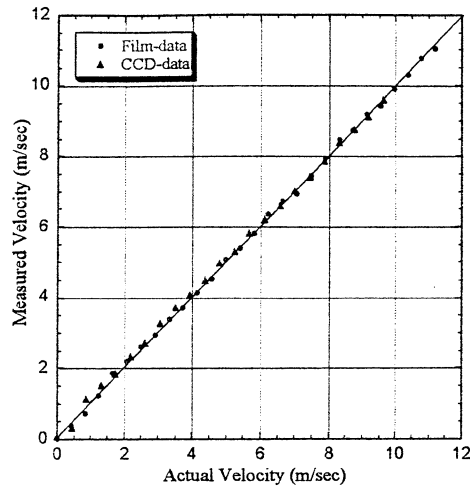


Figure 2b. Comparison of CCD and 35 mm Velocity Calibration.

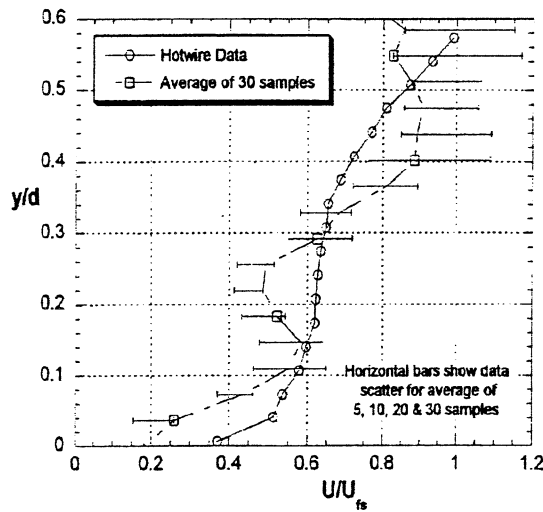


Figure 3a. Comparison of Hot Wire and PIV Velocity Profiles.

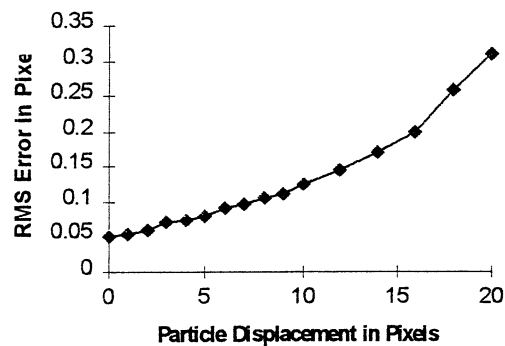


Figure 3b. RMS Error for Particle Displacement in Pixels

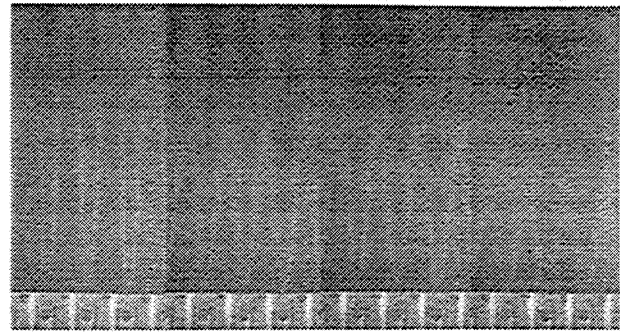


Figure 4. Liquid Crystal Measurement of Wall Film Spread Due to  $Tu=1\%$ ,  $6\%$ ,  $11\%$ ,  $17\%$ .

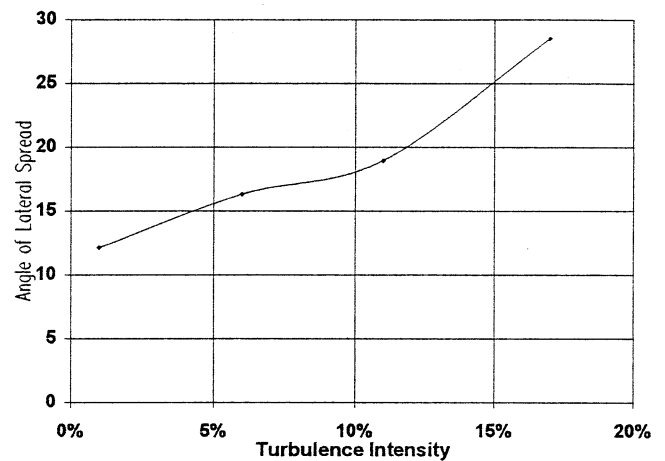


Figure 5. Liquid Crystal Measured Spread Angle at  $x/d=6.7$ , Due to  $Tu=1\%$ ,  $6\%$ ,  $11\%$ ,  $17\%$ .

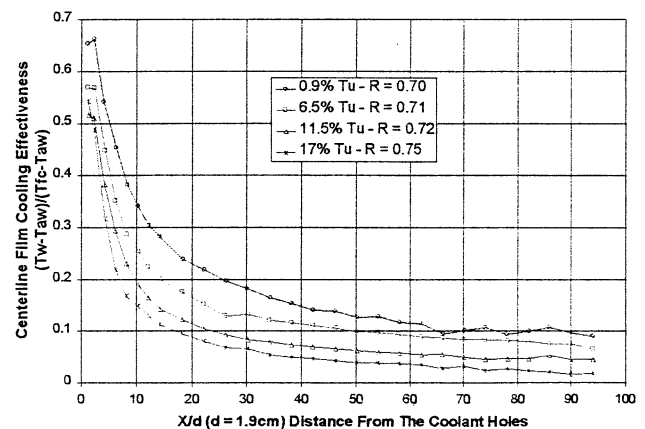


Figure 6. Centerline Film Cooling Effectiveness vs.  $x/d$  from Adiabatic Wall,  $Re=19,000$ ,  $z/d=0$ .

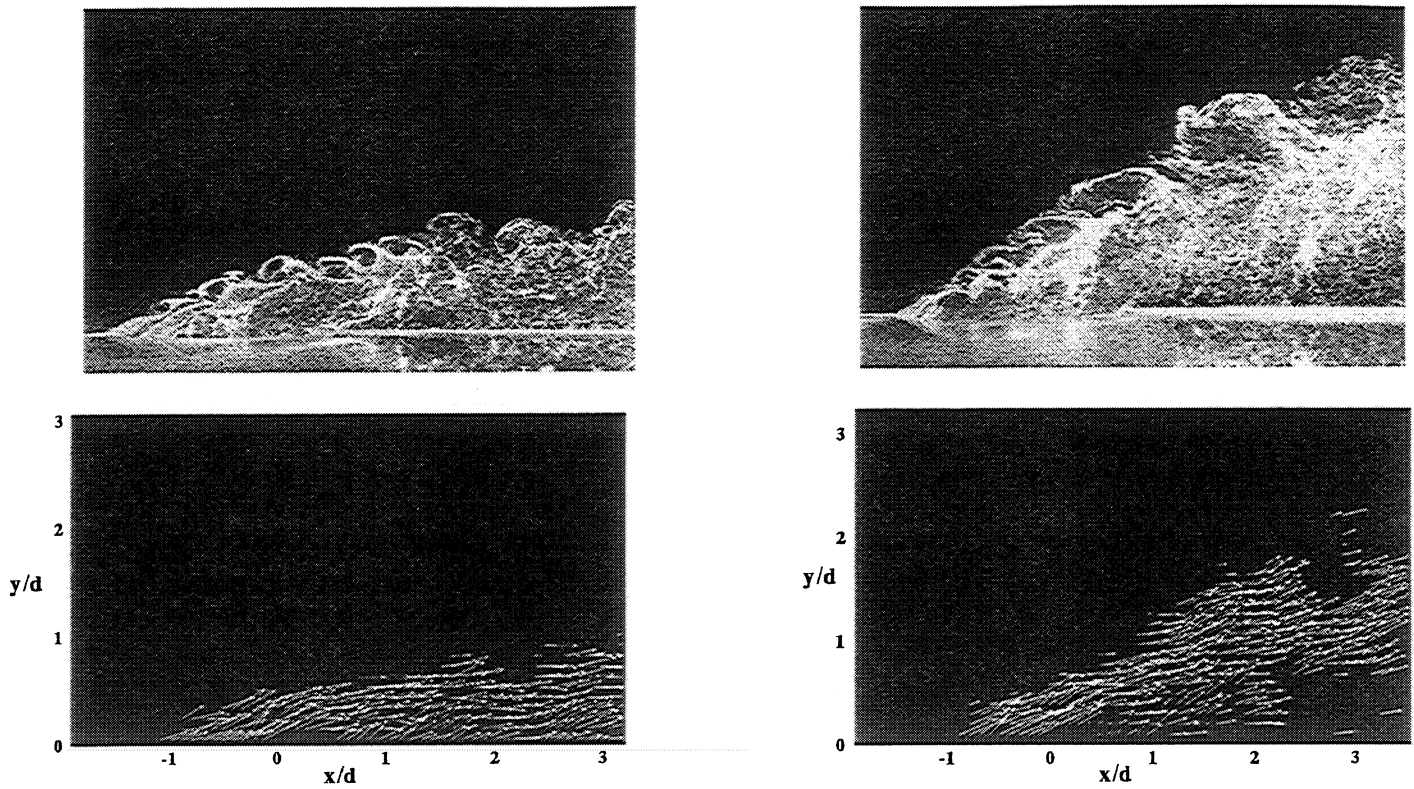


Figure 7. PIV Realizations and Vector Fields,  $Tu=1\%$  and  $17\%$ , for  $R=0.7$ , and  $Re=20,000$ .

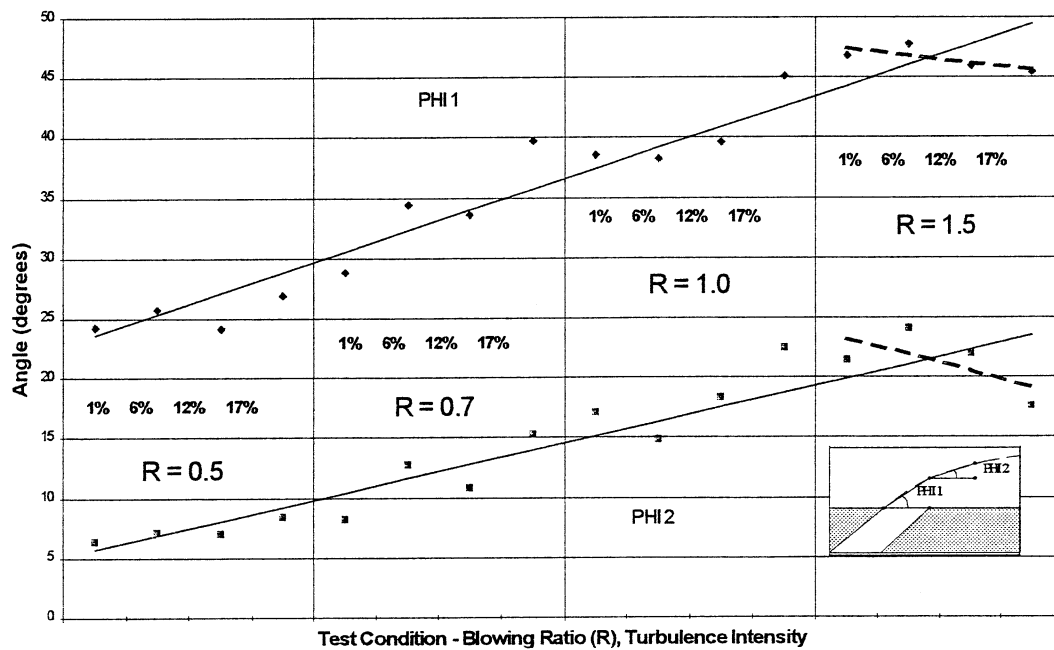


Figure 8. Film Cooling Spread Angles with  $Tu$  and Blowing Ratio,  $Re=20,000$ .



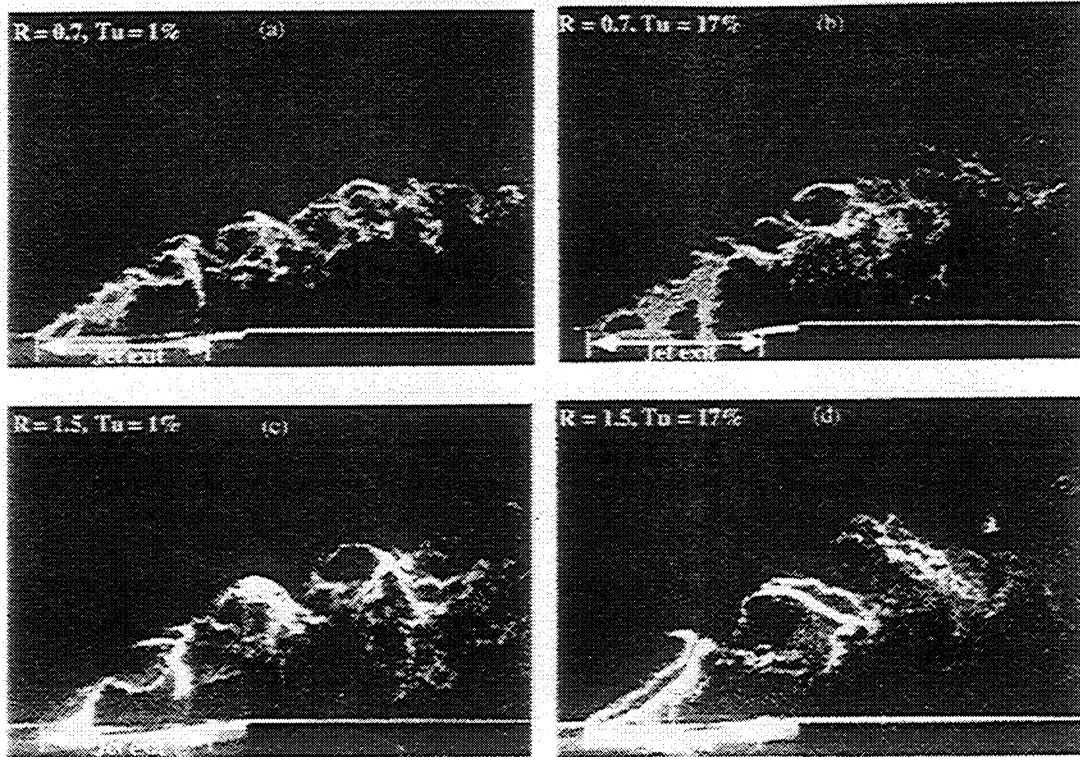


Figure 9a. Double Exposed PIV Images Using CCD Sensor ( $Re = 40,000$ )

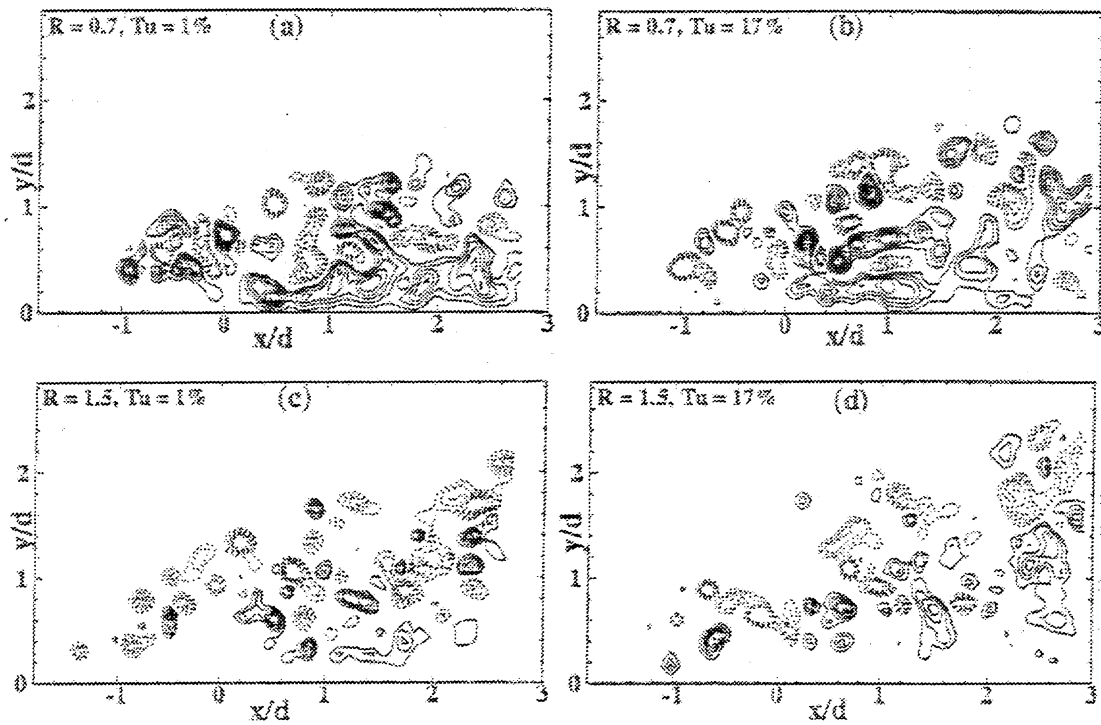
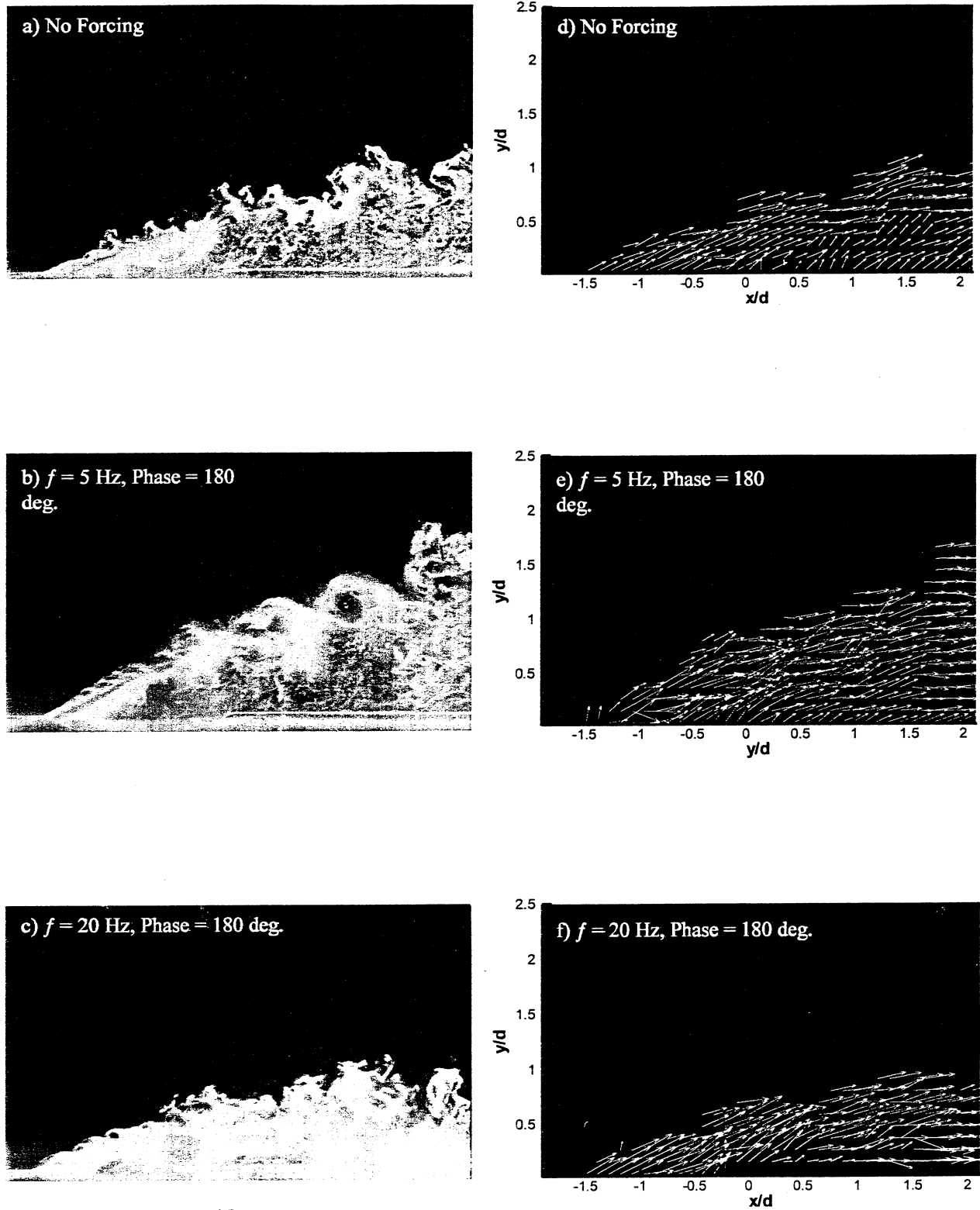


Figure 9b. Instantaneous Vorticity Distribution ( $Re = 40,000$ )



Double Exposed Images  
Instantaneous Velocity Distribution

Figure 10. Periodically Forced Film Cooling Flows

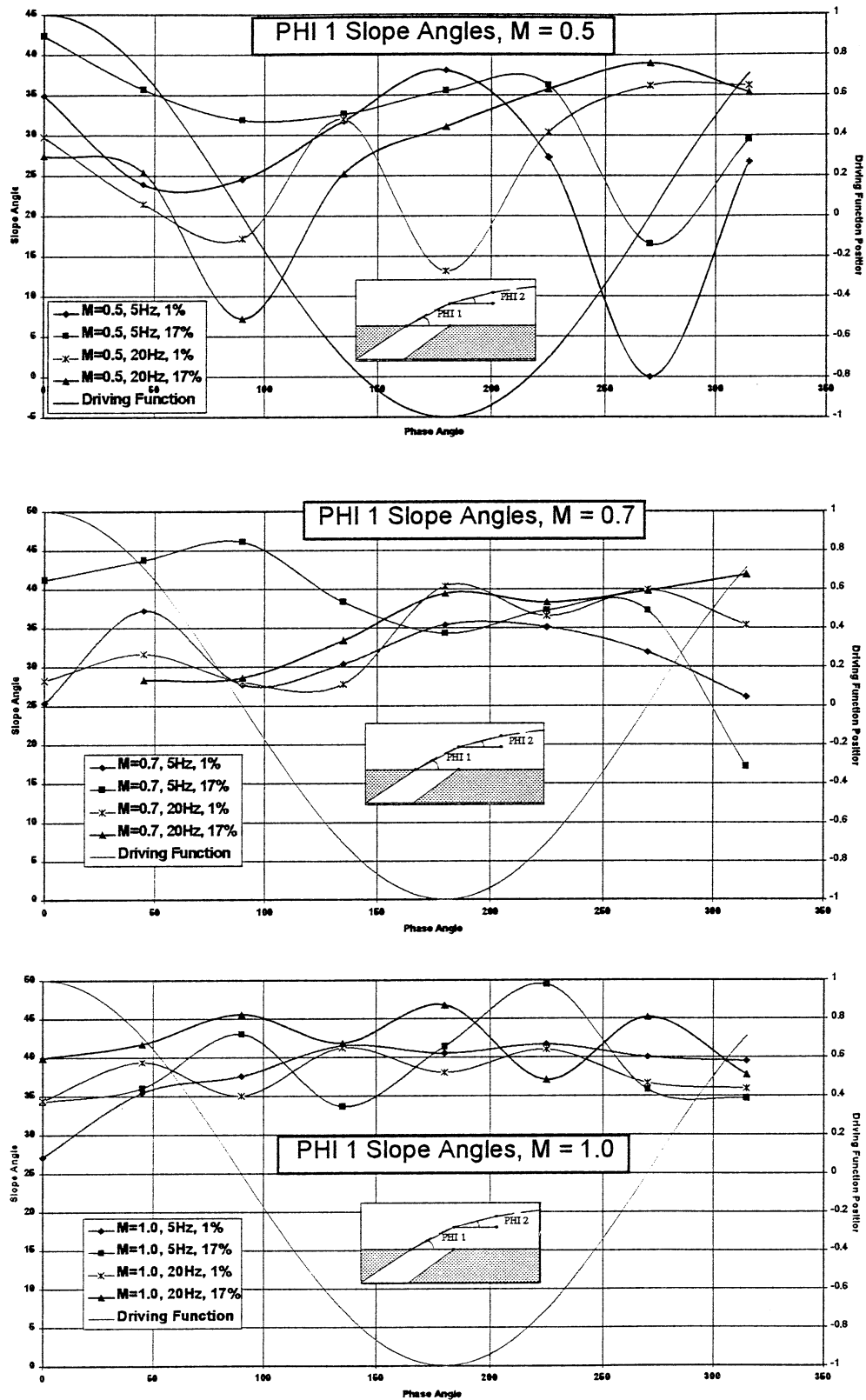


Figure 11. Phase locked Film Cooling Spread Angle Over the Film Cooling Hole.

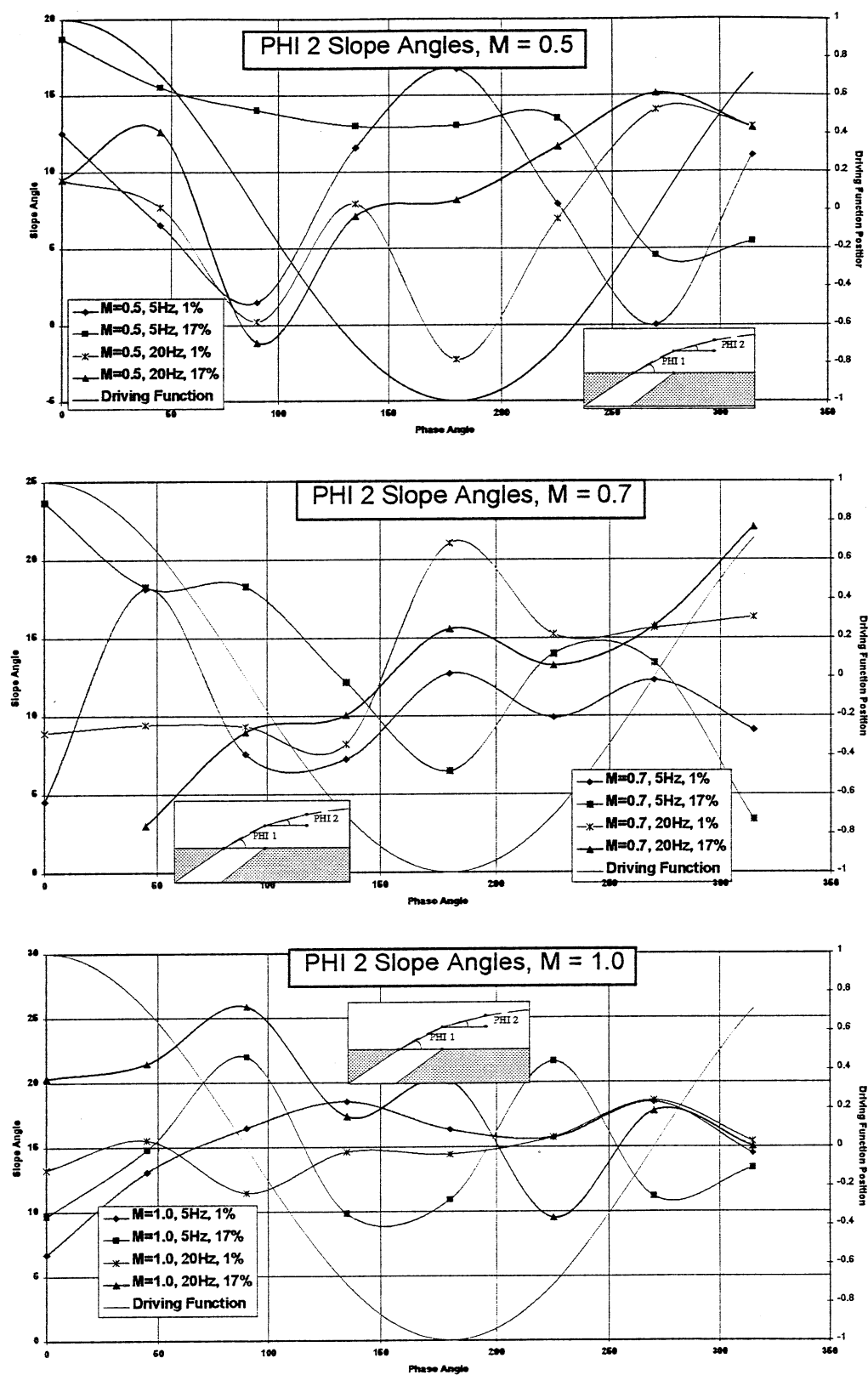


Figure 12. Phase locked Film Cooling Spread Angle After the Film Cooling Hole.

Paper 47  
Author: Rivir

Q: Warnack

How can the deviations between hot wire and PIV measurements (fig 3a) be explained?

A: The fluctuations in the film layer approach 20%, so the instantaneous variations in the PIV realisations would also be expected to approach 20%. Figure 3a shows that the average of the 30 PIV realisations falls within this envelope about the mean hot wire profile, as do nearly all of the smaller averages of PIV realisations.

Q: Schodl

When you study the film cooling flow development with PIV, did you seed only the cooling flow or also the main flow? Usually in mixing processes both should be seeded to get reliable results.

A: Only the film cooling flow has been seeded in what has been presented in this paper. We have independently seeded the primary flow but this is difficult to accomplish uniformly due to the large volume of seed and large area of distribution required. I agree that both flows must be seeded to show the total flow. We have in this paper emphasised the development of the film and its structures.



# Experimental investigation of the unsteady structure of a transitional plane wall jet

S. Gogineni, C. Shih

**Abstract** A laminar wall jet undergoing transition is investigated using the particle image velocimetry (PIV) technique. The plane wall jet is issued from a rectangular channel, with the jet-exit velocity profile being parabolic. The Reynolds number, based on the exit mean velocity and the channel width, is 1450. To aid the understanding of the global flow features, laser-sheet/smoke flow visualizations are performed along streamwise, spanwise, and cross-stream directions. Surface pressure measurements are made to correlate the instantaneous vorticity distribution with the surface pressure fluctuations. The instantaneous velocity and vorticity field measurements provide the basis for understanding the formation of the inner-region vortex and the subsequent interactions between the outer-region (free-shear-layer region) and inner-region (boundary-layer region) vortical structures. Results show that under the influence of the free-shear-layer vortex, the local boundary layer becomes detached from the surface and inviscidly unstable, and a vortex is formed in the inner region. Once this vortex has formed, the free-shear-layer vortex and the inner-region vortex form a vortex couple and convect downstream. The mutual interactions between these inner- and outer-region vortical structures dominate the transition process. Farther downstream, the emergence of the three-dimensional structure in the free shear layer initiates complete breakdown of the flow.

Received: 8 November 1995 / Accepted: 6 November 1996

S. Gogineni<sup>1</sup>  
Systems Research Laboratories  
2800 Indian Ripple Road  
Dayton, OH 45440-3696, USA

C. Shih  
FAMU-FSU College of Engineering  
Florida A&M and Florida State Universities  
Tallahassee, FL 32310, USA

Correspondence to: S. Gogineni

<sup>1</sup>Present address: Innovative Scientific Solutions, Inc. 3845 Woodhurst court, Beavercreek, OH 45430-1658 USA

This work was performed in the Fluid Mechanics Research Laboratory of Florida A&M and Florida State Universities, Tallahassee, Florida. The authors would like to thank Professors Krothapalli and Lourenco for their assistance during this research. The assistance of Mr. Zhong Ding with the data analysis is greatly appreciated as well as the editorial comments of Mrs. M. Whitaker (ISSI, Dayton, Ohio)

## 1 Introduction

### 1.1 Laminar and transitional wall jet

A plane wall jet is formed when a stream of fluid is blown tangentially along a plane wall. Its velocity profile consists of two distinct flow regimes – an inner region where the flow resembles that of the conventional boundary layer and an outer region where the flow is similar to that of a free shear layer. Since the early work of Glauert (1956), several experiments have been carried out on wall jets, with a view toward describing the structure of either laminar or turbulent wall jets via mean and r.m.s. velocity distributions. However, very few investigations of equal thoroughness have been conducted on transitional wall jets although many important practical problems such as film cooling on turbine blades involve such jets. The purpose of this investigation was to provide detailed knowledge of the unsteady flow structure of a laminar wall jet undergoing transition.

The behavior of a laminar wall jet was examined theoretically by Tetervin (1948) and Glauert (1956). Later several experimental and numerical investigations were carried out. Tsuji et al. (1977) investigated the stability characteristics of a two-dimensional wall jet and compared the results of the spatial analysis with experimental data; they observed the presence of double-row vortex structures with centers located in the inner and outer regions. Bajura and Catalano (1975) studied the two-dimensional plane wall jet under natural and forced conditions for exit Reynolds numbers ranging from 100 to 600. Based on their flow visualizations and hot-film studies, they described several stages in the transition process: 1) formation of discrete vortices in the free shear layer, 2) coalescence of adjacent vortices in the free shear layer, coupled with the vortices in the inner-region wall boundary layer, 3) eruption of the wall jet from a region near the surface of the flat plate into the ambient fluid, 4) dispersion of the organized flow pattern by three-dimensional turbulent motions, and 5) relaminarization of the upstream flow until vortex pairing occurs again. They concluded that the initial stages of transition are two-dimensional in nature and dominated by the mechanism of vortex pairing that is commonly observed in free shear layers. Horne (1981) also observed the presence of discrete vortices both in the free-shear-layer region and in the inner region of the wall jet. He concluded that the finite length of the wall has a significant effect on the formation and development of these vortices.

Mele et al. (1986) conducted a linear-stability analysis and confirmed the existence of a second neutral curve, enclosing a stable region for  $Re_\delta > Re_{\delta c}$  (where  $Re_\delta$  is the Reynolds number based on the exit velocity and the jet thickness,  $Re_{\delta c}$  is the critical Reynolds number). Their calculations showed the presence of two types of unstable eigen modes – the large- and small-scale disturbances having maximum values in the outer and inner regions, respectively. Recently Cohen et al. (1992) investigated the laminar-to-turbulent transition of wall-jet flows subjected to blowing and suction. Their linear-stability calculations clearly indicated the existence of two unstable modes: 1) an inviscid mode, representing the large-scale disturbances, that exhibits the highest amplitude in the free shear layer and 2) a viscous mode, describing the small-scale disturbances, that exhibits the highest amplitude near the wall. They also showed that the relative importance of each mode can be controlled by subjecting the wall jet to small amounts of blowing or suction. Zhou et al. (1992) studied the spatial amplification of the disturbances in the laminar wall jet both experimentally and theoretically. Their results indicate that the critical Reynolds number is 57, corresponding to a non-dimensional frequency of 0.565, and that the stable region exists between Reynolds numbers 377 and 456. The calculations of Chun and Schwarz (1967), however, showed the stable region to be between Reynolds numbers 370 and 750. Zhou et al. (1992) attributed this discrepancy to the small round-off errors in an interpolation subroutine with large increments in Reynolds numbers. They observed two closely coupled unstable eigen modes for a wide range of Reynolds numbers and frequencies. They also explored the effects of streamwise curvature on the relative importance of each mode in an attempt to provide better correlation between the coherent structures in the turbulent wall jet and the predominant instability modes. Hsiao and Sheu (1994) investigated the qualitative and quantitative behavior of double-row vortical structures in the near-field region of a plane wall jet using flow-visualization and hot-wire techniques.

## 1.2

### Vortex-induced boundary-layer separation

Vortex-induced boundary-layer separation occurs in a variety of flows (e.g., flows undergoing transition to turbulence) and is of interest in relation to the turbulent boundary layers where the regeneration process takes place. Harvey and Perry (1971), using total-head surveys in planes across the flow, demonstrated experimentally that a concentrated vortex near a wall induces a local boundary-layer separation that causes formation of a secondary vortex with sign opposite that of the main vortex. Walker (1978), using the computational results of the boundary-layer flow induced by a vortex above a plane wall, supported the interpretations of Harvey and Perry (1971). The experimental and theoretical studies of Walker et al. (1987) on the impact of a vortex ring on a wall showed that an unsteady separation develops in the boundary-layer flow in the form of a secondary ring attached to the wall.

Kaykayoglu and Rockwell (1986) investigated the unsteady jet-edge interaction and addressed the physical features of the flow in the near region of the edge, relating them to the instantaneous pressure fields on the edge surface. A model problem of the vortex-induced boundary-layer separation was

investigated by Peridier et al. (1991) in an attempt to understand the basic physical mechanism of vortex/viscous-layer interaction. Didden and Ho (1985) conducted detailed investigations on the unsteady separation in a boundary layer produced by an impinging jet; these studies revealed that as a consequence of the unsteady adverse pressure gradient induced by the primary vortex, the boundary layer becomes detached and a strong local shear layer is formed. This shear layer, when subjected to local instability, rolls up into a secondary vortex which triggers the total eruption of the flow.

An understanding of the unsteady flow characteristics associated with the dynamic behavior of vortices and their interactions can be gained only through the study of the instantaneous spatial vorticity distribution. Thus, the particle image velocimetry (PIV) technique was used in the present study to obtain the instantaneous, two-dimensional velocity and vorticity fields in a selected plane of the flowfield. A description of this technique has been given by Lourenco et al. (1989) and Adrian (1991).

The main parameters of the incompressible, transitional plane wall jet are Reynolds number (based on channel width and exit mean velocity), disturbance characteristics at the exit, aspect ratio of the channel, and length of the wall. In the present experiment, the Reynolds number was 1450; the exit mean velocity profile was parabolic; the aspect ratio of the channel was 20; and the wall extended to 60 widths downstream of the channel exit. A laminar, parabolic velocity profile at the exit is preferred since it has thicker boundary layers in both the inner and the outer regions of the jet where the velocity gradients are more gradual than those of a turbulent, top-hat exit-velocity profile and, as a result, the relative spatial resolution of the PIV data collected across the shear region is improved.

The goal of this experiment was to provide detailed knowledge of the instantaneous flow behavior of an unsteady laminar wall jet undergoing transition using the whole-flow-field PIV technique. Several laser-sheet/smoke flow-visualization pictures were acquired to obtain qualitative information on the flowfield. Surface pressure measurements were made to correlate the instantaneous vorticity distribution and the evolving surface pressure fluctuations.

## 2

### Experimental setup and procedures

#### 2.1

##### Jet facility

A schematic diagram of the experimental facility is shown in Fig. 1. The air flow is supplied to the settling chamber by a ring compressor. The rectangular settling chamber is 58 cm long, 21 cm wide, and 21 cm high; it contains a perforated plate, a honeycomb flow straightener, screens of progressively finer mesh size, and a section of porous foam to ensure a low turbulence level and to produce a uniform, smooth flow. A specially designed heat exchanger is installed between the ring compressor and the settling chamber to cool the heated air exiting the compressor and, thus, maintain the constant temperature that is essential for hot-wire measurements. A rectangular channel [0.5 cm wide ( $h$ ) and 52.7 cm long ( $L$ ), having a 10.0-cm span ( $S$ )], is connected to the settling

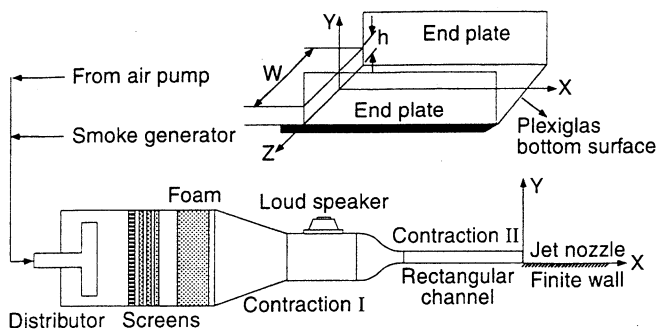


Fig. 1. Schematic of wall-jet facility

chamber by a two-stage contraction having an overall contraction-area ratio of 80. The aspect ratio ( $S/h$ ) of the channel is 20. A Cartesian coordinate system ( $x$ -axis in the streamwise direction,  $y$ -axis in the cross-stream direction, and  $z$ -axis in the spanwise direction) was chosen to describe the measurements of the velocity field. The wall surface attached to the channel exit is made of Plexiglas (10.0-cm span, 1.25 cm thick, and 60.0 cm long) and fitted with side walls (0.3 cm thick and 5.0 cm high) to minimize edge effects. This surface is also fitted with several pressure taps along the centerline for measuring surface pressure fluctuations. The use of Plexiglas is advantageous for PIV image recording since the laser sheet can be directed through the surface, which allows the flowfield to be free of optical obstructions.

## 2.2

### PIV system

The PIV image is obtained by illuminating the seeded flowfield with a thin laser-light sheet. In this case, the seed particles are oil-smoke droplets. The light scattered by the seed particles generates a pattern of the particle image that is recorded using a double/multiple-exposure photographic technique. The local fluid velocity is then obtained using optical and digital signal-processing techniques. A dual pulsed-laser system consisting of two Spectra-Physics DCR-11 Nd:YAG lasers is used to provide the double-illumination pulses, as shown in Fig. 2a. Each laser is equipped with a harmonic generator for producing the laser output at a wavelength of 532 nm. Each pulse produced by the laser has a pulse width of 6–7 ns, a pulse energy of 135 mJ, and a pulse-energy stability of 7%. The optimum pulse repetition rate is 10 Hz. A Bk-7 beam-combining cube along with an adjustable mirror is used to ensure the collinearity of the two laser beams – a very critical factor for correlation of the particle images. The combined laser beam is directed toward the test section to create the laser sheet in the selected plane using spherical and cylindrical lenses. The delay between the two laser pulses is controlled using a pulse generator and is dependent upon the maximum velocity, magnification of the recording optics, and the diameter of the interrogating beam. In the present experiment, a delay of  $\sim 15 \mu\text{s}$  was provided for a Reynolds number of 1450. The time delay between the pulses is measured in two ways: 1) recording the photomultiplier signal on an oscilloscope and 2) using a digital counter to measure directly the Q-switch synchronization of the laser power supplies. Because of the minimum-focus-distance limitation of the camera lens,

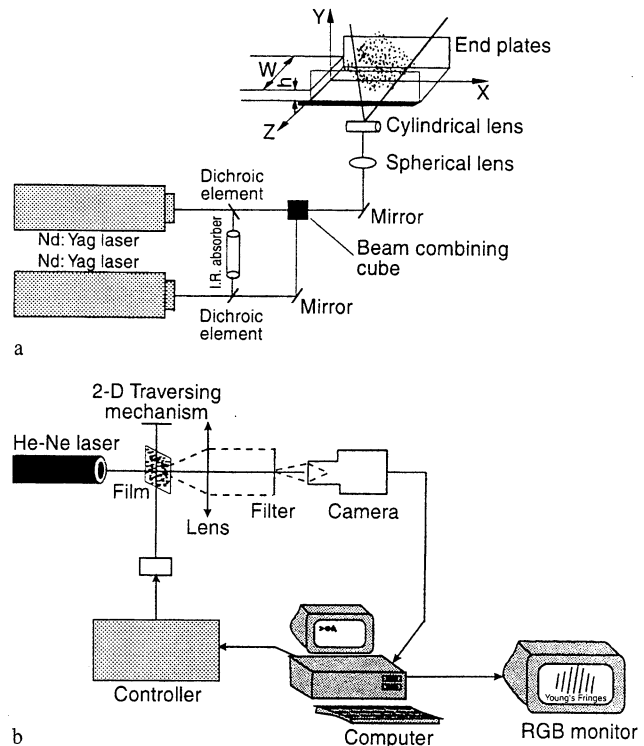


Fig. 2. a Schematic of PIV system; b schematic of interrogation system

the laser sheet is positioned 1 cm from the central  $x$ - $y$  plane. The laser sheet was 80 mm in width and  $< 1$  mm in thickness. A 35-mm camera (Nikon F3) with a 105-mm micro lens was used to record the flowfield; this lens allows an adequate stand-off distance between the camera system and the flowfield. The  $f$ -number has a significant effect on the mean exposure of an individual particle image; therefore, several tests were conducted and an  $f$ -number of 5.6 selected for optimal recording. For obtaining finer resolution of the flow-field, particularly near the wall region, the image was magnified 1.5 times. High-resolution film was chosen for recording the flowfield.

The jet was seeded with smoke particles produced by a smoke generator (Rosco Type 1500). The size of the smoke particles was assumed to be  $\sim 0.5 \mu\text{m}$ . The smoke and ambient air were mixed in a large tank (90 cm long and 45 cm in dia.). The entire apparatus was placed in a rectangular enclosure (1.5 m square) and covered with plastic sheets to minimize ambient disturbances. A second smoke generator of the same type was used to seed the ambient flow surrounding the jet.

The conventional PIV technique is limited by its inability to determine the direction of the velocity vector; therefore, an "image-shifting" or "velocity-bias" technique (Adrian 1986) was used. With this technique, the image field is shifted between the first and second exposures during the photographic recording; thus, all resulting image displacements are moving in one direction. This shift is selected based upon the estimate of the maximum-reversal velocity components. The true flowfield is recovered by removing this artificial shift during the processing phase. A scanning-mirror system (General Scanning Inc. Model CX-660) was used to provide the "image shift" in the present investigation.

The double-exposed photographic film was processed using the Young's fringe-analysis system shown schematically in Fig. 2b. The basis of this method and its limitations as well as comparisons of different systems have been discussed by Lourenco et al. (1989) and Adrian (1991). A He-Ne laser beam of 250- $\mu\text{m}$  dia. is directed toward the photographic film for interrogating the image. The Young's fringes are generated from the diffraction produced by the coherent illumination of the multiple images in the interrogation region, if a correlation exists among the particle images. These fringes have an orientation which is perpendicular to the local displacement and spacing which is inversely proportional to the displacement. A video camera interfaced to a personal computer digitizes the fringe pattern and computes its displacement via a FFT algorithm. A calibration test is performed to optimize the algorithm; the details have been given by Gogineni (1993) and Lourenco and Krothapalli (1995). The measurement error was found to be on the order of 1–2% of the full-scale range.

### 2.3

#### Surface pressure-fluctuation measurements

For correlating the instantaneous vorticity distribution and the evolving surface pressure fluctuations, pressure taps are provided at the bottom of the Plexiglas along the plane of interest. A digital manometer (Setra Systems) is used to obtain the signal from these taps. This signal is recorded using a spectrum analyzer (B&K Model 2032) and digitized using an ADC Board. Since the pressure-fluctuation signal is low in amplitude (on the order of a few millivolts), an amplifier (Tektronix AF501) is used. Placing the hot-wire probe in the outer region ( $y/h = 2$ ) and aligning it with the surface pressure tap allows the signals from the hot wire and the surface pressure tap to be recorded simultaneously and the instantaneous vorticity distribution and the pressure fluctuations to be correlated.

## 3

### Results and discussion

#### 3.1

##### Comparison of free jets and wall jets

Several qualitative images, as shown in Fig. 3, were obtained using the laser-sheet/smoke flow-visualization technique. These pictures cover the region from the channel exit to about 16 widths downstream for Reynolds numbers (based on exit mean velocity and channel width) between 300 and 4000. The jets are issued from a rectangular channel having an exit-velocity profile matching that of a fully developed channel flow. The upper half of each picture corresponds to the free jet and the lower half to the wall jet. The inclusion of the surface/boundary on one side of the free jet causes significant changes in the flow behavior such as reduction in growth rate and formation of vortices near the surface that are located out of phase with respect to the corresponding outer-region (free-shear-layer) vortices. These changes are directly related to the development of shear-layer instability inside the jet. For a free jet at a low Reynolds number ( $Re < 950$ ), the growth and interaction of the asymmetric shear-flow instability structures on either side of the jet dominate the flow development. By

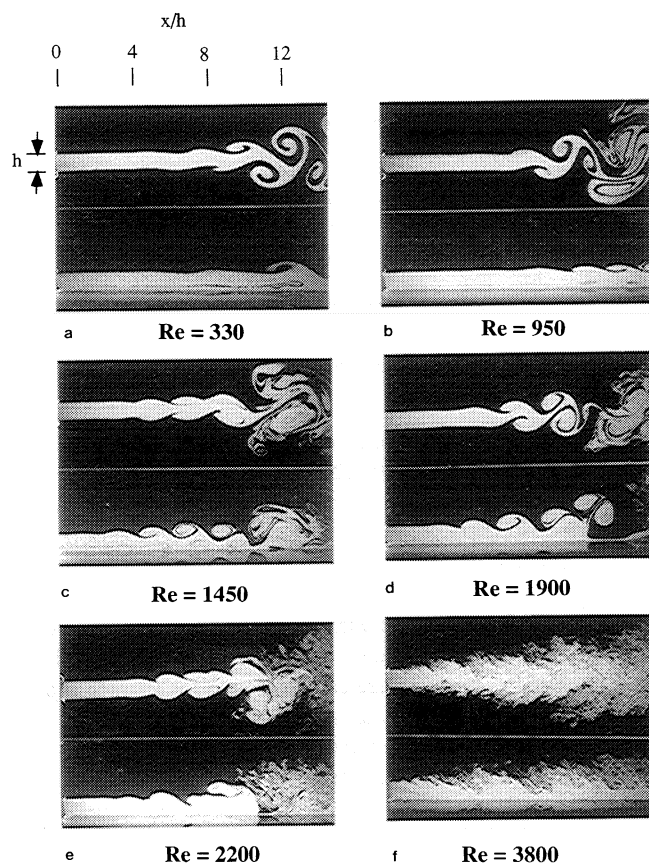


Fig. 3a–e. Comparison of transitional free jet and wall jet (parabolic velocity profile at the exit)

comparison, the presence of the solid surface totally suppresses the shear-layer instability activity on one side of the wall-jet flow. Consequently, the growth of the wall jet is significantly slower than that of the corresponding free jet (Fig. 3a and 3b) as a result of the lack of interaction of the shear-flow structures from the two sides of the jet. On the other hand, no appreciable difference in growth rate is apparent for the jets in the higher-Reynolds-number regime (Fig. 3c–3e). The outer-shear-layer vortices emerge nearer the nozzle and induce a set of counter-rotating vortical structures near the wall. The eruption of the inner vortices from the wall interrupts this double-row counter-rotating vortical-flow structure and triggers the breakdown of the jet. For higher Reynolds numbers, both the free jet and the wall jet become fully turbulent at the jet exit (Fig. 3f).

From these flow-visualization pictures, it is apparent that, in general, the behavior of wall-jet flows is similar; however, the location at which an event occurs varies with downstream distance and Reynolds number. Except for the highest-Reynolds-number case, all of these flows are initially of the laminar type and eventually become turbulent following the transition process.

#### 3.2

##### Flow visualization

The flow-visualization picture for a wall jet obtained in the  $x$ - $y$  plane is shown in Fig. 4. This photograph, covering the

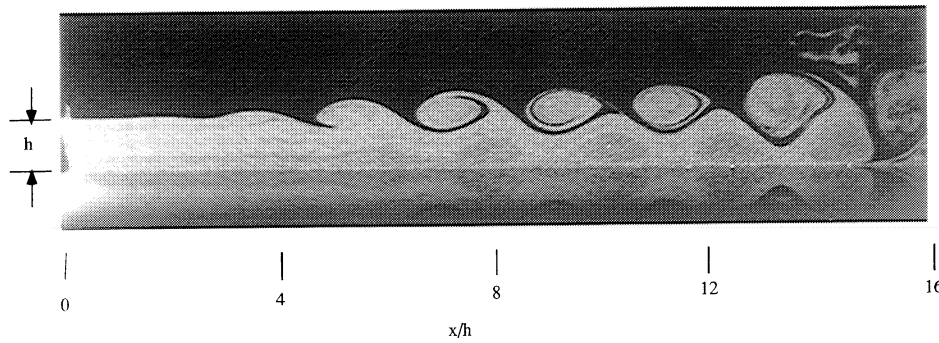


Fig. 4. Streamwise ( $x$ - $y$  plane) flow visualization

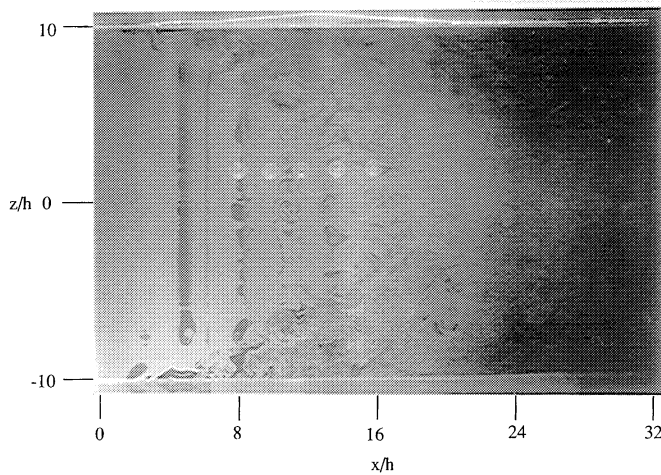


Fig. 5. Spanwise ( $x$ - $z$  plane) flow visualization

region from the jet exit to a location 16 widths downstream, clearly shows the emergence of discrete vortices in both the inner and the outer regions of the jet. In the outer region, Kelvin-Helmholtz-type instability waves grow and roll into discrete vortical structures. In the inner region, a boundary-layer flow structure consisting of discrete vortices that are out of phase with respect to the corresponding outer structures can be seen. The shear-layer vortices rotate in a counterclockwise direction, and the inner-region vortices rotate in a clockwise direction. This organized double-row vortex structure emerges near the nozzle exit and is convected downstream until the structures become indistinguishable at a location of about 20 widths (not shown in the picture). These structures were first predicted by Tsuji et al. (1977) who solved the Orr-Sommerfeld equation using a Glauert wall-jet profile. However, the five developmental stages of a wall jet observed by Bajura and Catalano (1975) are not apparent at this Reynolds number. To observe the two dimensionality of the flowfield, a spanwise flow visualization along the  $x$ - $z$  plane was conducted (Fig. 5). The circular holes represent the surface pressure taps on the Plexiglas plate. This photograph was taken inside the free-shear-layer region ( $y/h = 1.2$ ). The discrete dark bands across the span correspond to individual spanwise vortices. The emergence of streamwise secondary streaks that are superimposed on the spanwise primary structure can be observed between 10 and 14 widths downstream. Farther downstream, the flow becomes fully three dimensional.

For close examination of these streamwise structures, flow-visualization photographs were obtained in the  $y$ - $z$  plane and are shown in Fig. 6. These photographs cover the central portion along the spanwise direction up to 8.8 jet widths. Near the nozzle exit, the flow is uniform across the spanwise direction, indicating its two-dimensionality (Fig. 6a and 6b). The dark lines in the center of the photograph indicate entrainment of the smoke-free fluid into the jet that is caused by the folding and rolling up of the outer shear-layer vortices (Fig. 6c). Farther downstream at  $x/h = 11$ , the emergence of the counter-rotating streamwise vortices can be seen as mushroom-shaped protrusions on top of the outer shear layer (Fig. 6d). Since the jet suddenly narrows as compared to that shown in Fig. 6c, it is evident that this visualized region is located between two developed shear-layer vortices (Fig. 4). The strong stretching action imposed by two neighboring vortices strengthens the growth of these streamwise structures. Farther downstream, the continued development of these streamwise vortices in the free shear layer induces quasi-periodic spanwise modulations in the inner region of the wall jet (Fig. 6e). Eventually, the entire jet flow becomes fully three dimensional (Fig. 6f).

### 3.3

#### Instantaneous velocity and vorticity distributions

For examining the dynamics of the vortex interaction, the instantaneous velocity and associated vorticity fields were obtained using PIV. This technique is useful because it provides information on the whole flowfield near the wall region and in the outer region simultaneously. Since the recording camera has limitations, these flowfield data are taken at different instants of time. However, because of its quasi-periodic nature, flow evolution is fairly reproducible, and the sequence of data to be presented (Fig. 7a to 7d) can be considered to be a good representation of the transitional process of a wall jet.

Figure 7a shows the instantaneous velocity and vorticity field covering the region from the exit to about 6 widths downstream. The velocity information is obtained from PIV double-exposed images using the Young's-fringe method of interrogation. These negatives are digitized using a  $121 \times 81$  grid that produces 9801 vectors having a spatial resolution of 0.17 mm. The vorticity distribution is computed from the velocity field using a central-differencing scheme. The solid and dashed lines correspond to clockwise and counterclockwise vorticity, respectively. The clear distinction between the



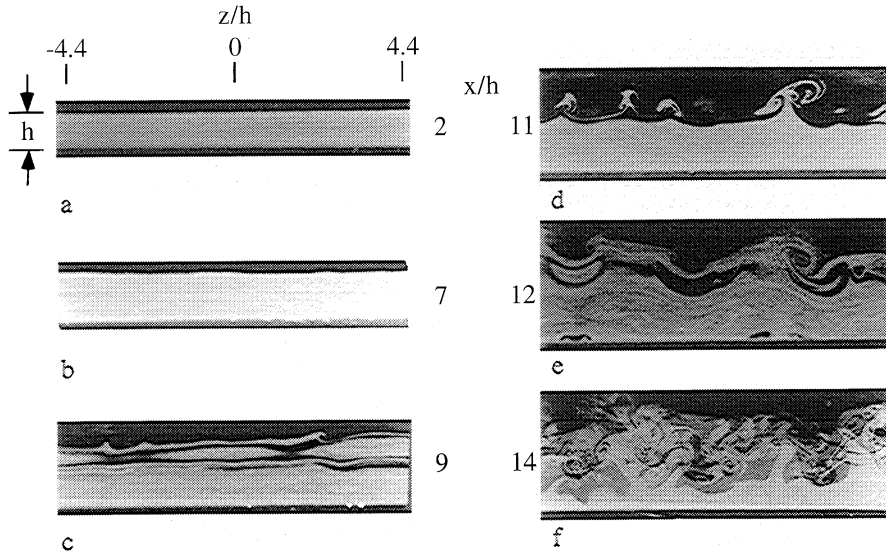


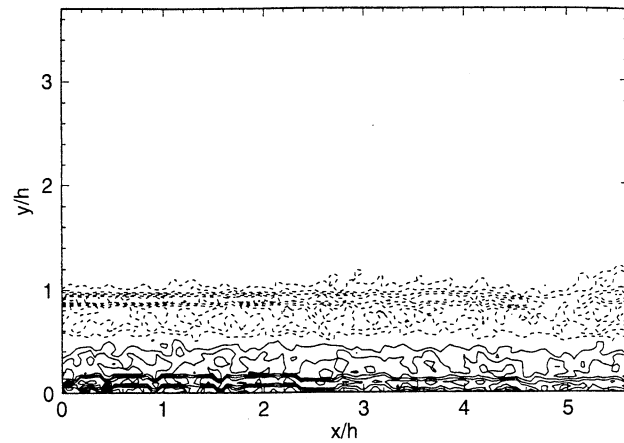
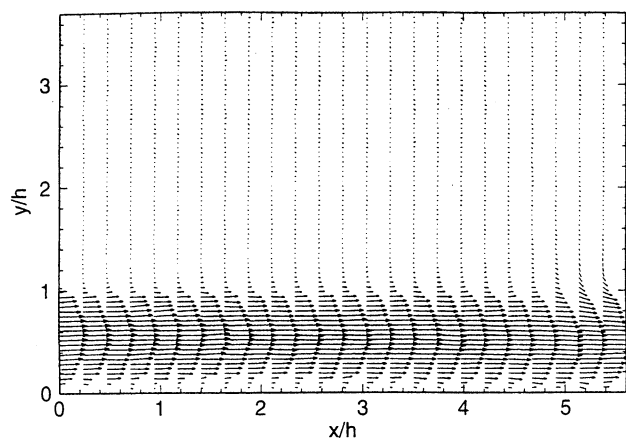
Fig. 6a-f. Cross-stream ( $y$ - $z$  plane) flow visualization

contours of positive and negative vorticity indicates that no appreciable interaction is taking place between the inner- and outer-region structures at this location. Figure 7b shows the instantaneous velocity and vorticity distributions covering locations from 5.8 to  $\sim 12$  widths downstream. In the region where the organized double-row vortical structures dominate, as shown by the flow-visualization results, a spatially quasi-periodic arrangement of both the inner and the outer vortices is observed. Discrete vortical structures emerge first in the outer shear layer at  $x/h=7$  and become distributed quasi-periodically downstream at  $x/h=9.4$  and  $11.6$ . The inner boundary layer appears to thicken under the influence of the shear-layer vortex ( $x/h=8$ ), but the first sign of the formation of the inner vortex is farther downstream at  $x/h=10.4$ . Nevertheless, no significant breakaway of the flow occurs in this region. From the velocity field (Fig. 7b), the primary-jet direction (can be identified as the maximum velocity vector near the central region) reveals two successive up-and-down flow patterns (one centered around  $x/h=8$  and the other around  $x/h=10.4$ ). Both locations correspond to the formation of boundary-layer structures, as shown in the iso-vorticity field (Fig. 7b). Close examination of the near-wall region in these locations reveals the existence of local flow-recirculation zones. The near-wall flow appears to exhibit a quasi-periodic pattern of detachment followed by reattachment. It is interesting to observe that as flow detachment is approached, the boundary-layer profile begins to change from a fuller parabolic-type profile to a shear-layer-type profile having a local inflection point. At the next location covering from  $11.6$  to  $\sim 18$  widths downstream (Fig. 7c), the interaction between the free shear layer and the corresponding inner-region vortices intensifies, and the inner-region vortices attempt a break away from the wall ( $x/h=13.5$  and  $16$ , for example). However, the two downstream free-shear-layer vortices ( $x/h=14.7$  and  $17.2$ ) are sufficiently strong to propel the boundary-layer vortices toward the wall through induction and, thus, prevent ejection. Therefore, the flow still undergoes quasi-periodic detachment and reattachment, as revealed by the velocity-vector plot (Fig. 7c). It is interesting to note that between  $x/h=14$  and  $15$ , the outer flow penetrates the inner region, which is consistent with

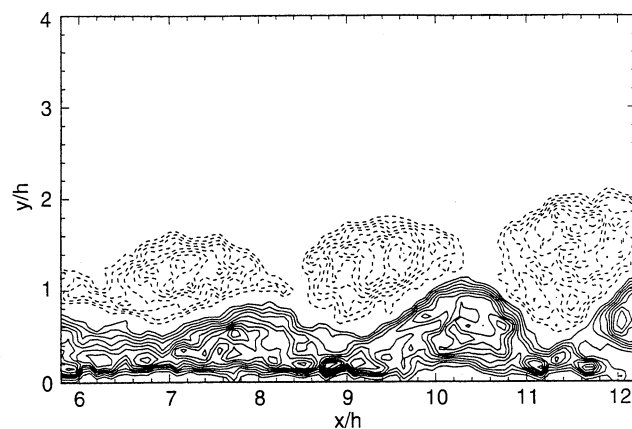
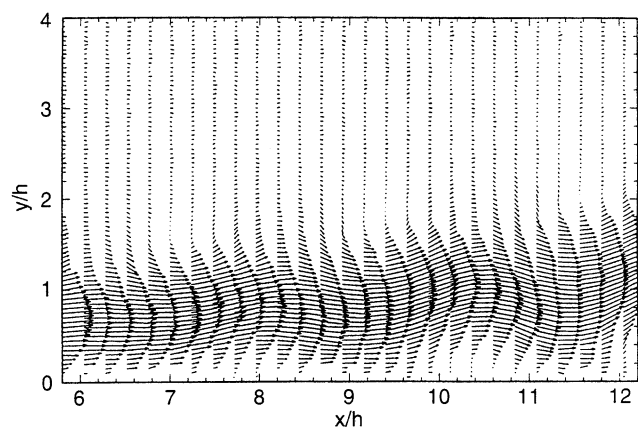
the cross-stream flow-visualization results (Fig. 6f). Farther downstream (Fig. 7d), because of the emergence of the three-dimensional instabilities, the spanwise vorticity in the shear-layer vortex is redistributed into a secondary structure aligned in the streamwise direction (Bernal and Roshko 1986). Consequently, the shear-layer vortex becomes weaker, and its stabilizing effect on the inner-boundary-layer vortex decreases. As a result, the inner-region vortex is ejected from the surface and penetrates deeply into the outer region of the wall jet. This ejection process is very explosive, as evidenced by the fact that the outer edge of the jet exceeds four nozzle heights in a very short downstream distance (Fig. 7d). Consequently, this ejection is accompanied by a complete breakdown of the flowfield. The highly irregular velocity distribution in this region indicates the emergence of strong three-dimensional flow during the transition process.

Simultaneous surface pressure fluctuation signals and hot-wire signals are recorded to correlate the instantaneous surface pressure fluctuations and the vorticity distribution (Fig. 8). The hot-wire probe is positioned away from the outer shear layer ( $y/h=2$ ) and aligned vertically with the corresponding surface pressure tap on the wall at  $x/h=8$ . The hot-wire measures flow fluctuations induced by the passage of the large-scale vortices inside the shear layer. It is well known that a counterclockwise vortex induces a negative (lower) velocity at its outer edge; this observation is confirmed by examining a sequence of instantaneous PIV velocity and vorticity data. Thus, a low hot-wire velocity can be interpreted as the passage of the shear-layer vortex. It is clear that these two signals are exactly in phase, confirming the fact that the passage of the shear-layer vortex (indicated by a low hot-wire velocity) induces local low pressure (pressure valley) on the surface. Farther downstream, the correlation of hot-wire and surface

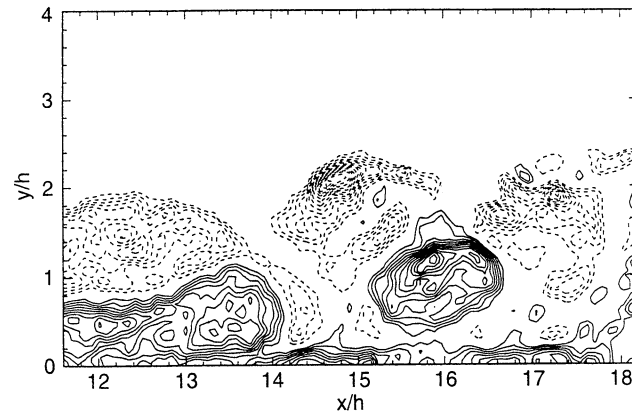
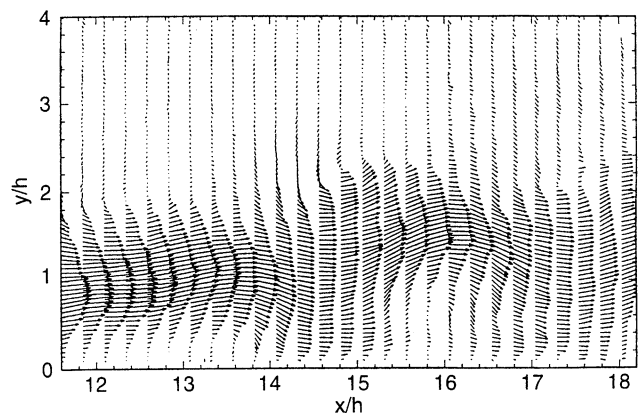
Fig. 7. a Instantaneous velocity and vorticity distribution ( $x/h=0-5.6$ ); b instantaneous velocity and vorticity distribution ( $x/h=5.8-12$ ); c instantaneous velocity and vorticity distribution ( $x/h=11.6-18$ ); d instantaneous velocity and vorticity distribution ( $x/h=14-20$ )



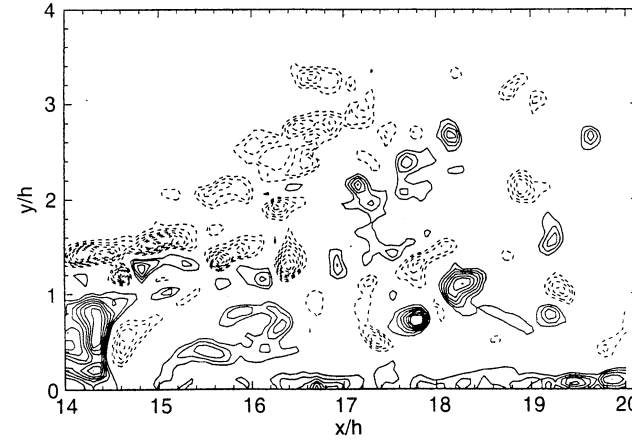
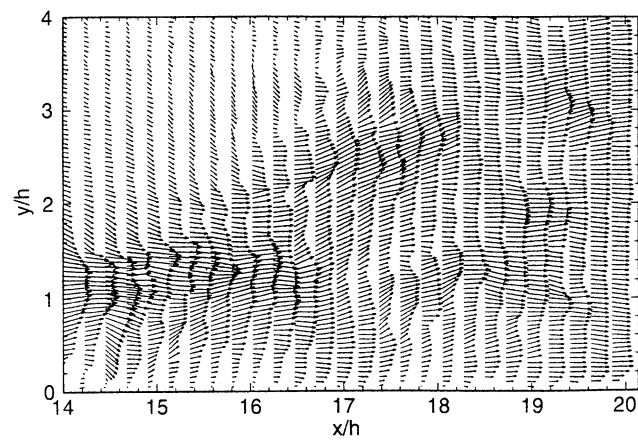
a



b



c



d

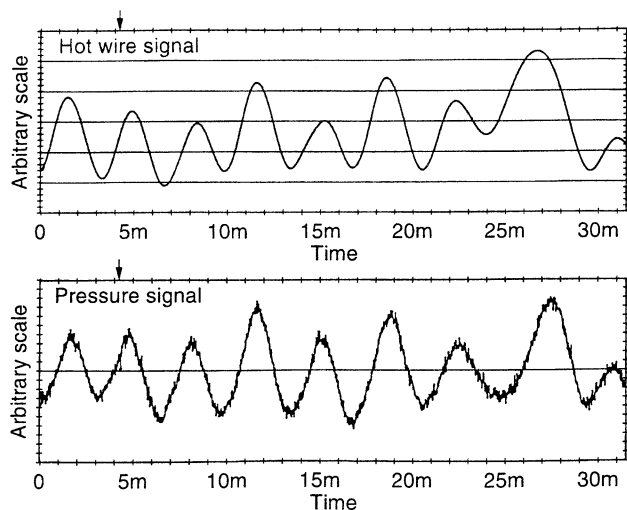


Fig. 8. Simultaneous recording of hot-wire and surface pressure signals

pressure signals is not so clear since the inner boundary layer also separates from the surface.

Based on the above data and other observations by Harvey and Perry (1971) and Didden and Ho (1985), formation of the boundary-layer vortex can be explained as follows: The rolling up of the free-shear-layer vortex causes the flow near the wall to accelerate; as a result a local low pressure is produced on the surface (Fig. 8). The alignment of peaks and valleys of the hot-wire and pressure signals clearly indicates that the passage of the shear-layer vortex induces a low (suction) pressure on the surface and that the pressure returns to a higher value as the vortex passes. Therefore, the resulting boundary-layer flow located directly beneath a vortex experiences an adverse pressure gradient in front and, at the same time, a favorable trailing pressure gradient (Fig. 9). The low-momentum fluid near the surface cannot negotiate this abruptly imposed pressure gradient and, as a result, the flow detaches from the wall. As the free-shear-layer vortex is convected downstream, the favorable pressure gradient following the adverse gradient tends to force the detached flow to reattach, forming a recirculation region. This region increases in size in the transverse direction and decreases in size in the streamwise direction as the vortex continues to move downstream (Gogineni 1993), pushing the boundary-layer flow farther from the wall. The separating boundary layer is, therefore, subjected to the inviscid instability usually experienced by a free shear

layer and coalesces into a vortex having positive (clockwise) vorticity in the inner region, commonly known as the inner-region vortex. Note that the free-shear-layer vortex has negative (counterclockwise) vorticity.

Once the inner-region vortex has formed, both the outer- and inner-region vortices couple and are convected downstream. As the inner-region vortex moves away from the surface into the center region of the jet, it encounters a higher convection jet stream and also stronger upward induction from the outer-region vortex. This induction propels the inner vortex ahead of the outer shear-layer vortex where it moves into a position approximately midway between the two neighboring shear-layer vortices. The downstream shear-layer vortex now has such increasing influence on the inner-region vortex that its downward induction prevents the complete ejection of the inner vortex from the wall and has a stabilizing effect on the jet flow. The neighboring vortices are found (Shih and Gogineni 1995) to have a profound effect on the stabilization and manipulation of wall-jet flow. Under the influence of the downstream vortex, the entire array of vortices, including several shear-layer and inner-region vortices, begins to move as a group (Figs. 4 and 7b). This arrangement persists downstream until the quasi-two-dimensional shear-layer vortex is weakened by the emergence of the three-dimensional structure (Fig. 6) and a rapid transition to turbulence (Fig. 7c). As a result, the stabilizing effect of the inner vortex decreases because of the downward induction from the downstream vortex, the inner vortex is ejected from the wall, and the entire jet breaks down (Fig. 7d).

From the analysis, it can be concluded that the transition process of a wall jet consists of formation and development of discrete vortices in both the inner and the outer regions in the initial stage and is dominated by the emergence of the three-dimensional structure at a later stage.

#### 4 Conclusions

Streamwise ( $x$ - $y$  plane) laser-sheet/smoke flow-visualization pictures have provided a global understanding of the flowfield. As expected, the wall-jet consists of discrete vortices in both the inner and the outer regions. The inner-region vortices are located out of phase with respect to the corresponding outer-region vortices. These vortices convect downstream until they become indistinguishable in the turbulent region. The spanwise ( $x$ - $z$  plane) flow-visualization pictures reveal that the

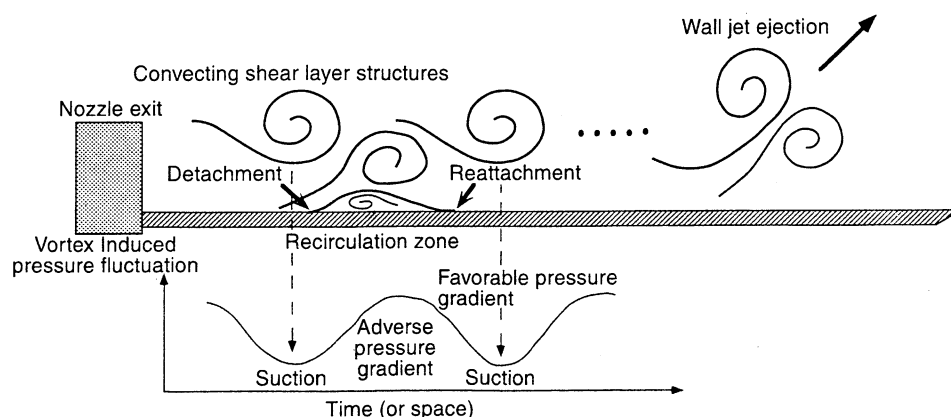


Fig. 9. Schematic of vortex/boundary-layer interaction

wall-jet flow is two-dimensional near the nozzle exit and that the streamwise streaks are superimposed on the spanwise vortices. The cross-stream ( $y$ - $z$  plane) flow-visualization pictures provide information concerning the formation and development of the counter-rotating streamwise vortices. The vortex-pairing mechanism identified by Bajura and Catalano (1979) in the lower-Reynolds-number range was not observed in the present investigation. The present observations are consistent with the Schlieren flow-visualization observations of Horne (1981) in the higher-Reynolds-number range. The transition process is dominated by the formation and development of discrete vortices in both the inner and the outer regions. The three-dimensionality is initiated in the outer region of the wall jet and then spreads to the inner region. The PIV technique has proved to be a valuable tool for exploring the flow features of unsteady flows – particularly very near the wall region – without disturbing the flowfield. The errors involved in this technique are estimated by comparing the data with those from numerical simulations (Gogineni 1993) and are shown to be on the order of 1–2% on the full-scale range.

PIV and surface-pressure results show that the boundary layer detaches from the wall as a result of the emergence of an adverse pressure gradient induced locally by the passage of the outer shear-layer vortex. This detachment leads to the formation of a local free shear layer. The detached boundary layer is inviscidly unstable, rapidly coalesces into a discrete vortex, and interacts strongly with the outer shear-layer vortex. The pairing of the outer and inner vortices of opposite sign forms a double-row vortical-structure pattern which dominates the initial development of the transitional wall jet. This pattern persists until the emergence of three-dimensional flow in the outer shear layer and complete ejection of the inner-region vortex into the outer region, which eventually leads to a rapid transition to turbulence.

This investigation can be extended to turbulent wall-jet flow to gain further understanding of the intricate interactions of the inner- and outer-region eddy structures. A quantitative comparison of transitional free jets and wall jets under different nozzle-exit conditions and for different Reynolds numbers would benefit the general understanding concerning their growth rates and the influence of the surface with regard to stability.

## References

- Adrian RJ (1986) An image shifting technique to resolve directional ambiguity in double pulsed laser velocimetry. *Appl Opt* 25: 3855–3858
- Adrian RJ (1991) Particle imaging techniques for experimental fluid mechanics. *Ann Rev Fluid Mech* 23: 261–304
- Bajura RA; Catalano MR (1975) Transition in a two-dimensional plane wall jet. *J Fluid Mech* 70: 773–799
- Bernal LP; Roshko A (1986) Stream wise vortex structure in plane mixing layers. *J Fluid Mech* 170: 499–525
- Chun DH; Schwarz WH (1967) Stability of the plane incompressible viscous wall jet subjected to small disturbances. *Phy Fluids* 10: 911–915
- Cohen J; Amitay M; Bayly BJ (1992) Laminar to turbulent transition of wall jet flows subjected to blowing and suction. *Phys Fluids A* 4: 283–289
- Didden N; Ho CM (1985) Unsteady separation in a boundary layer produced by an impinging jet. *J Fluid Mech* 160: 235–256
- Glauert MB (1956) The wall jet. *J Fluid Mech* 1: 625–643
- Gogineni S (1993) Particle image velocimetry study of two-dimensional transitional plane wall jet. Ph.D. Thesis. Tallahassee, Florida: Florida State University
- Harvey JK; Perry FJ (1971) Flow field produced by trailing vortices in the vicinity of the ground. *AIAA J* 9: 1659–1660
- Horne WC (1981) A study of the acoustic and flow fields of a rectangular jet. Ph.D. Thesis. Stanford, California: Stanford University
- Hsiao FB; Sheu SS (1994) Double row vortical structures in the near field region of a plane wall jet. *Exp Fluids* 17: 291–301
- Kaykayoglu R; Rockwell D (1986) Unstable jet-edge interaction. Part 1. Instantaneous pressure fields at a single frequency. *J Fluid Mech* 169: 125–149
- Lourenco L; Krothapalli A; Smith C (1989) Particle image velocimetry, In advances in fluid mechanics measurements (ed. Gad-el-Hak), Lecture Notes in Engineering, Vol. 45, Berlin: Springer
- Lourenco L; Krothapalli A (1995) On the accuracy of velocity and vorticity measurements with PIV. *Exp Fluids* 18: 421–428
- Mele P; Morganti M; Scibilla MF; Lasek A (1986) A behavior of wall jet in laminar to turbulent transition. *AIAA J* 24: 938–939
- Peridier VJ; Smith FT; Walker JDA (1991) Vortex induced boundary layer separation. Part I. The unsteady limit problem  $Re \rightarrow \infty$ . *J Fluid Mech* 232: 99–131
- Shih C; Gogineni S (1995) Experimental study of perturbed laminar wall jet. *AIAA J* 33: 559–561
- Tetervin N (1948) Laminar flow of a slightly viscous incompressible fluid that issues from a slit and passes over a flat plate. *NACA TN* 1644
- Tsuji Y; Morikawa Y; Nagatani T; Sakou M (1977) The stability of a two dimensional wall jet. *Aeronaut Qtrly* 28: 235–246
- Walker JDA (1978) The boundary layer due to a rectilinear vortex. *Proc Royal Soc (London)* A359: 167–188
- Walker JDA; Smith CA; Cerra AW; Doligalski TL (1987) The impact of a vortex ring on a wall. *J Fluid Mech* 181: 99–140
- Zhou MD; Rothstein J; Wagnanski I (1992) On the hydrodynamic stability of the wall jet. *Proc. 11th Australian Fluid Mechanics Conf.* Hobart, p 407

## VISUALIZATION AND DPIV MEASUREMENTS OF NON-CIRCULAR COAXIAL JET FLOWS

Sivaram Gogineni  
Innovative Scientific Solutions Inc.  
Dayton, OH 45430

Jason W. Biting  
Dimitris E. Nikitopoulos\*  
Mechanical Engineering Department  
Louisiana State University  
Baton Rouge, LA 70803

### ABSTRACT

Reactive Mie-scattering visualizations and Two-Color Digital Particle Image Velocimetry (DPIV) measurements of flows generated by coaxial, non-circular jets are presented. Geometry combinations employing square, triangular, lobed and circular nozzles have been examined. The outer-jet Reynolds number is 19k and the inner-to-outer jet velocity ratio is 0.3. Visualizations were carried out on cross-stream (horizontal) planes, using a pulsed laser sheet and  $\text{TiCl}_4$  seeding. High-resolution images (3kX2k) were recorded by a CCD camera. Time-averaged visualizations were used to qualitatively assess near-field shear-layer growth. Interesting interactions between inner and outer non-circular nozzle shear layers were observed. Large-scale, structures were observed in the inner wake-like region, but they were not as coherent as in low Reynolds number flows. Axis switching was not observed in any of the non-circular nozzle geometry combinations examined.

### INTRODUCTION

Several types of single non-circular nozzles, have been researched to date, including: Rectangular/Square, Triangular, Lobed, and Elliptic.

Rectangular and square nozzles produce square vortex rings at the exit which then deform and under certain conditions can lead to a switching of the jet axis. The axis switching is due largely to deformation and self-induction produced by the sharp corners of the nozzle and depends on the initial velocity profile characteristics. Quinn and Militzer<sup>1</sup> (1988) showed that for a square jet of the same hydraulic diameter as a circular jet, the square jet had a faster spreading rate at similar distances from the jet exit as compared to the circular jet. A detailed numerical simulation by Grinstein et al<sup>2</sup> 1995 followed by experimental investigation illustrated that the axis switching is due to self-induction governed by the Biot-Savart Law with hairpin vortices developing along the diagonals of the square jets. Triangular jets have also been investigated by Schadow et al<sup>3</sup> (1988). The process of self-induction in the corners of the

triangle produced enhanced mixing in that region. The flow results were different for depending on whether the jet emanated from a triangular orifice or a triangular pipe/nozzle emphasizing the importance of initial conditions. A numerical and experimental study by Koshigoe et al<sup>4</sup> (1988) explained the differences and formulated conditions for which axis switching occurs. Enhancement in the fine scale mixing and combustion stability in the corner regions of the triangular jet were verified by Schadow et al<sup>5</sup> (1990). Large scale mixing was accomplished on the flat sides with reduced pressure oscillations as compared to the circular jet. Elliptic jets have also been studied, and have exhibited the same axis switching and self-induction as found in triangular and rectangular jets. Gutmark and Ho<sup>6</sup> (1986) studied the elliptic jet. Axis switching was observed, resulting in entrainment rate of 8 times higher than a circular jet.

Although single non-circular nozzles have been shown to be promising in terms of improved mixing, coaxial configurations of such nozzles have hardly been studied. Recently Biting et al.<sup>7, 8</sup> (1997) presented some relevant flow visualization results. In this paper we have carried out a preliminary qualitative survey of the flows generated by a variety of non-circular (square, triangular, lobed) and circular coaxial nozzle combinations. This was done at a single co-flow Reynolds number and an inner-to-outer velocity ratio less than unity.

### EXPERIMENTAL SETUP AND METHODS

The test facility used for this study incorporates a modular design that allows easy exchange of inner and outer nozzles with different lip geometries. The test facility uses two independent air flow supplies. Four, 1" lines provide air to the inner nozzle while eight 1/4" lines provide air to the outer nozzle. On each main supply line an orifice flow meter is used to determine the air flow rate. Valved, bypass ports allow the use of part of the metered air streams for seeding purposes. The inner jet flow passes through a flow-straightening honeycomb screen prior to entering the jet contraction with a contraction ratio of approximately 19:1. The outer jet flow reaches the outer jet through an annular passage with a contraction ratio of approximately 8:1.

\*Author to whom all correspondence should be directed.  
Copyright © 2000 The American Institute of Aeronautics  
and Astronautics, Inc. All rights reserved

REPRINTED WITH PERMISSION



A circular coaxial nozzle with an inner diameter of 0.6 inches and an outer diameter of 1.5 inches has been used as the baseline nozzle. With the above dimensions, the hydraulic (effective) diameter of the inner jet and outer jet is  $d_i=0.6$  inches and  $d_o=0.75$  inches respectively. For the square nozzles, the hydraulic diameters are the same as for the circular jet. The inner-to-outer area ratio is preserved at 0.213.

Visualizations have been carried out using a pulsed laser sheet and seeding with  $TiCl_4$ , which upon reaction with moisture produces fine sub-micron  $TiO_2$  particles. Instantaneous and time averaged cuts have been made with a laser sheet from a Nd-YAG laser pulsing at 10 Hz. Short (10sec) exposures have been taken with a high-resolution Kodak CCD array (3000x2000) camera, to visualize the instantaneous structure of the jets, while long exposures (2 sec) have been used to provide a 20-realization average of the mixing regions.

Two-color, Digital Particle Image Velocimetry (DPIV) measurements have also been carried out on vertical planes for the axisymmetric and square II configurations. A Nd-YAG laser provided one color at 532nm and a

Sulforhodamine-640 dye laser pumped by a second Nd-YAG was used to provide the second color. The laser sheet thickness was 1mm and the laser pulse time separation was 20 $\mu$ sec. More details of the two-color DPIV system can be

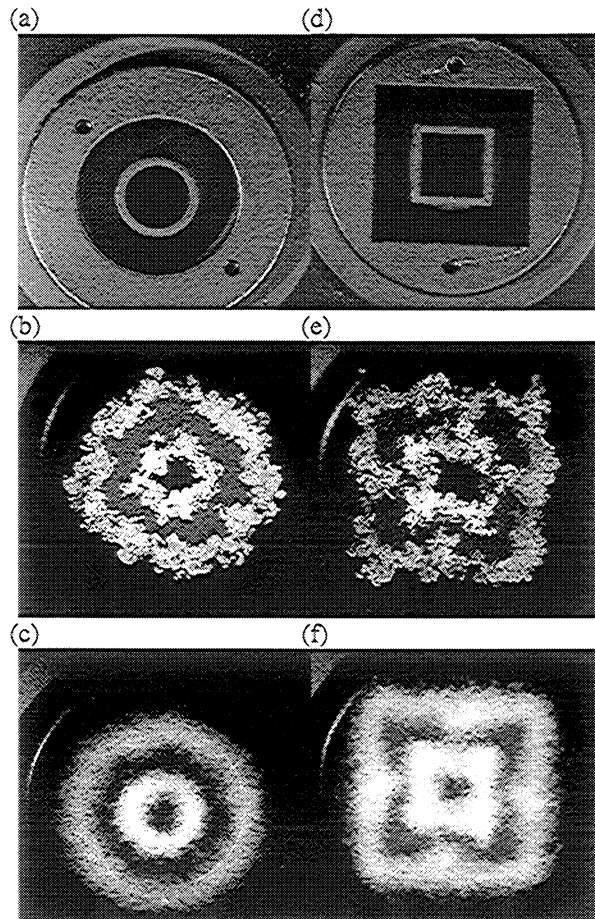


**Figure 1: Cross-stream visualizations of the mixing regions from circular and square coaxial nozzles at a distance of  $5/3D_i$  from the nozzle exit. (a, d) nozzle geometries, (b, e) instantaneous visualizations (c, f) averaged visualizations.**

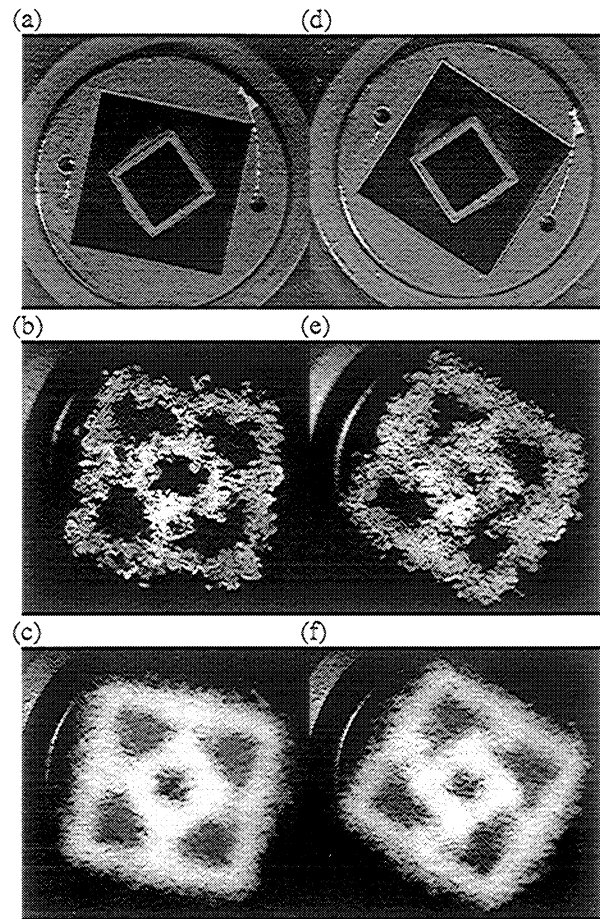


**Figure 2: Cross-stream visualizations of the mixing regions from two square coaxial nozzle configurations at a distance of  $5/3D_i$  from the nozzle exit. (a, d) nozzle geometries, (b, e) instantaneous visualizations (c, f) averaged visualizations.**

found in <sup>9</sup>Gogineni et al. (1997). Both nozzles were seeded with  $Al_2O_3$  particles for the DPIV measurements. The average diameter of the  $Al_2O_3$  particles was 1 micron, which provides for an adequate particle response time for the measurement of the flows at hand. The DPIV images were analyzed using ISSI's cross-correlation software (see <sup>9</sup>Gogineni et al. 1997) on a Macintosh Power PC. The interrogation window size was 64x64 pixels with 50% overlap between adjacent interrogation windows. The spatial resolution was 5%-of- $d_o$  in each direction on the laser sheet plane and 2.5%-of- $d_o$  across it. The displacement resolution for the velocity measurements was 1.2 microns (or 0.006%-of- $d_o$ ). Thus, the velocity resolution was 0.13 m/sec (or 1% of the co-flow average velocity). The latter was based on a sub-pixel resolution of 0.1 as per <sup>9</sup>Gogineni et al. (1997).

## RESULTS AND DISCUSSION

The results presented here give a preliminary overview of the flow structure resulting from various configurations of coaxial nozzles. Mie-scattering cross-stream visualizations of coaxial nozzle mixing regions are shown in Figures 1-4. The nozzle exit geometries are shown at the top of each figure followed by instantaneous and 20-image average visualizations. These visualizations were performed at a distance of  $1''$  or  $5/3$  of the inner nozzle hydraulic diameter. In all cases the Reynolds number based on the outer nozzle hydraulic diameter is 19,000 and the inner-to-outer nozzle velocity ratio based on average velocities is 0.3. Figure 1 shows the visualizations from the standard circular coaxial nozzle configuration and a square nozzle combination with parallel sides. At this elevation the unmixed regions in the core of the inner nozzle and between the inner and outer shear layers of the coaxial nozzle are to a great extent still present as it is evident from the averaged images in Figures 1(c) and

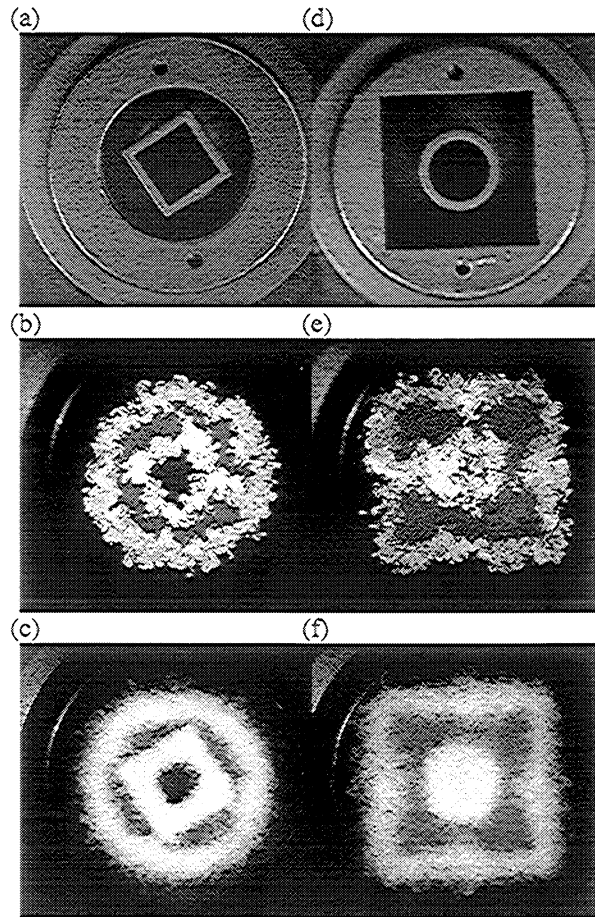


**Figure 3: Cross-stream visualizations of the mixing regions from two circular/square coaxial nozzle combinations at a distance of  $5/3D_i$  from the nozzle exit. (a, d) nozzle geometries, (b, e) instantaneous visualizations (c, f) averaged visualizations.**

1(f). Both instantaneous and averaged images indicate

significant localized interactions between the inner and outer shear layers. In the case of the square configuration (Figure 1(e) and 1(f)) these shear layers are almost fully connected, with the outer shear layer growing into the inner one. This is, largely, due to the shape of the mean velocity profile in the plane jet formed between the outer and inner square sides. Real-time observations during the visualization experiments indicated that the interaction between the inner and outer shear layers is intermittent in the near field of the jet. At one instant the seeded inner and outer shear layers would be fully connected, as in the case of the upper and right sides of the jet in Figure 1(e). At another instant the seeded inner and outer shear layers would be separated by an unmixed region as in the lower and left sides of the jet in Figure 1(e). In the other two square nozzle configurations, the visualizations of which are shown in Figure 2, the same type of interaction is observed between the outer shear layer and the corner flows of the inner jet. The outer shear layer, in general, maintains the square geometrical shape of its origin. There is no visible evidence, in any of the square nozzle cases, of distortion that

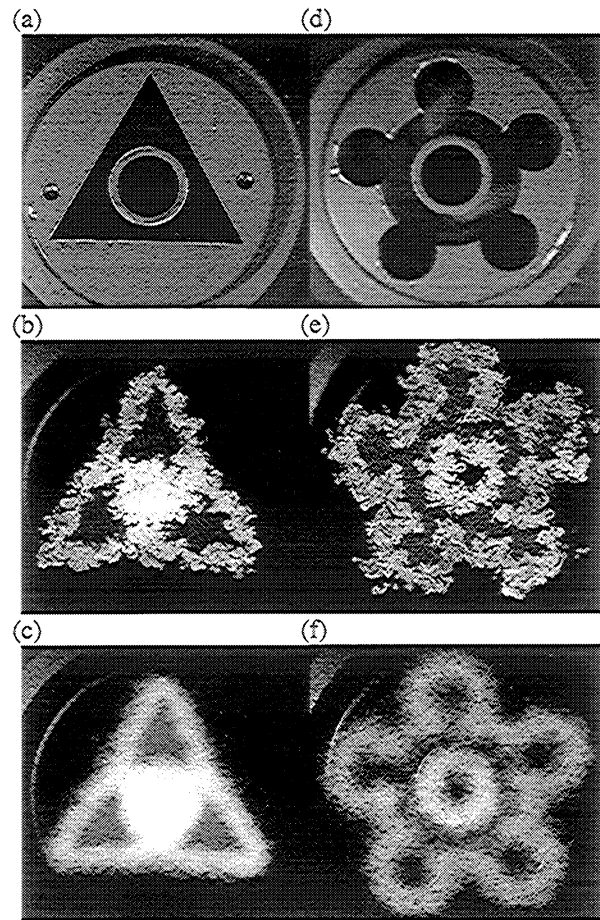


**Figure 4: Cross-stream visualizations of the mixing regions from triangular/circular and lobed/circular coaxial nozzle combinations at a distance of  $5/3D_i$  from the nozzle exit. (a, d) nozzle geometries, (b, e) instantaneous visualizations (c, f) averaged visualizations.**

could indicate that axis switching is in progress. The inner jet also maintains the geometrical shape of its origin although some distortion is observed. As shown by <sup>2</sup>Grinstein et al. (1995) the development of axis switching for single non-circular nozzles is strongly dependent on the initial flow conditions. Therefore, in addition to the presence of coaxial flow, which changes the shear stress on the inner jet and the physics considerably, it is possible that the initial conditions for the experiment do not promote this phenomenon. Local injection of small-scale "mushroom" shaped vortical structures from the mixing regions into the unmixed areas is clearly visible in all instantaneous images. The fine-grained structure of the shear layers in the instantaneous visualizations is indicative of a highly turbulent flow, which impairs the development of clearly defined (coherent) large-scale vortical structures at the exit of the jet. Bearing in mind the observations of <sup>2</sup>Grinstein et al. (1995), the highly turbulent shear layers generated at the exit of the square coaxial nozzles examined here, along with the low level of coherence of the associated large scale structures, may also be responsible for the apparent absence of axis switching.

Similar observations to those made for the square nozzle combinations are made for the remaining four coaxial geometries portrayed in Figures 3 and 4. The inner and outer shear layers maintain the shape of their origin and no evidence of axis switching is present. Intermittent interactions between inner and outer mixing layers are present in all cases. The inner unmixed core has disappeared at this level in the cases of the square/circular (Figure 3(f)) and the triangular/circular (Figure 4(c)).

Center plane DPIV results for four of the examined coaxial nozzle configurations are shown in Figures 5-8. In each of these figures, the plane of the measurement is indicated together with the raw seeded image and a superposition of the instantaneous velocity vector field on constant vorticity contours. The measurement of Figure 5 was obtained with smoke-seeding of the ambient environment combined with nozzle flow seeding in order to obtain valid data of the outer shear layer. The presence of a large-scale structure in the inner mixing layer is evident by the concentration of vorticity. Symmetry, indicative of an axisymmetric mode, is evident in the near field, while some asymmetry develops in the far field. This may be indicative of a varicose mode developing in the wake like region that forms as the lower speed unmixed core disappears. Vorticity concentrations are visible in the outer shear layer as well. However, the vortex structure is not at all coherent and it is unlikely attributed to shear layer instability. Similar features are revealed in Figure 6 where the inner square nozzle is rotated by 45° relative to the orientation of Figure 5. In the case of the triangular outer and circular inner nozzles shown in Figure 7, the inner mixing layer is asymmetric as are the associated concentrations of vorticity. This results from the mean flow asymmetry between the faster outer flow on the side of the triangle apex and the slower flow on the side of the triangle base. The flow on the latter side resembles that of a plane jet. Figure 8 shows the DPIV measurement on a symmetry plane of a lobed/circular nozzle configuration. Smoke seeding was also used here to obtain better data on the outer mixing layer. Again the inner mixing layer is asymmetric due to the asymmetry of the co-flow. The flow is faster on the side of the lobe and slower in the narrower

annular section. The inner and outer shear layers on the side of the annulus also have the structure of a plane jet. Concentrations of vorticity both in the inner and outer shear layers betray the presence of a large-scale structure.

## **ACKNOWLEDGEMENTS**

This work is supported by NASA the Louisiana Board of Regents LEQSF, and the AFOSR GSRP. The guidance and help of Dr. W. M. Roquemore of Wright Laboratory is gratefully acknowledged.

## **REFERENCES**

- <sup>1</sup>Quinn, W.R. and Militzer, J., (1988) "Experimental and Numerical Study of a Turbulent Free Square Jet," *Physics of Fluids*, Vol. 31, No. 5, pp. 1017-1025.
- <sup>2</sup>Grinstein, F. F., E. Gutmark, and T. Parr, (1995) "Near Field Dynamics of Subsonic Free Square Jets. A Computational and Experimental Study," *Physics of Fluids*, Vol. 7, No. 6, pp. 1483-1497.
- <sup>3</sup>Schadow, K.C., Gutmark, E., Parr, D.M., and Wilson, K.J. (1988) "Selective Control of Flow Coherence in Triangular Jets," *Experiments in Fluids*, Vol. 6, pp. 129-135.
- <sup>4</sup>Koshigoe, S., Gutmark, E., Schadow, K.C., and Tubis, A. (1988) "Wave Structures in Jets of Arbitrary Shape. III. Triangular Jets," *Physics of Fluids*, Vol. 31, No. 6, pp. 1410-1419.
- <sup>5</sup>Schadow, K.C., Gutmark, E., Wilson, K.J. and Smith, R.A. (1990) "Noncircular Inlet Duct Cross-Section to Reduce Combustion Instabilities," *Combustion Science and Technology*, Vol. 73, pp. 537-553.
- <sup>6</sup>Gutmark, E. and Ho, C. (1986) "Visualization of a Forced Elliptic Jet," *AIAA Journal*, Vol. 24, No. 4, pp. 684-685.
- <sup>7</sup>Bitting J. W., Nikitopoulos D. E., Gogineni S. P., and Gutmark E. J., (1997) "Visualization of Non-Circular, Coaxial Nozzle Flow Structure", *Bulletin of the American Physical Society*, Vol. 42, 50th Annual Meeting of the American Physical Society, San Francisco, CA, November 23-25, 1997.
- <sup>8</sup>Bitting J. W., Nikitopoulos D. E., (1997), "Visualization and two-color digital PIV measurements in circular and square coaxial nozzles", *Final Report, AFOSR GSRP, Wright Laboratory, Wright-Patterson AFB, August 1997.*
- <sup>9</sup>Gogineni, S., Goss, L., Pestian, D., and Rivir R., "Two-Color Digital PIV Employing a Single CCD Camera," *Experiments in Fluids* (in press).

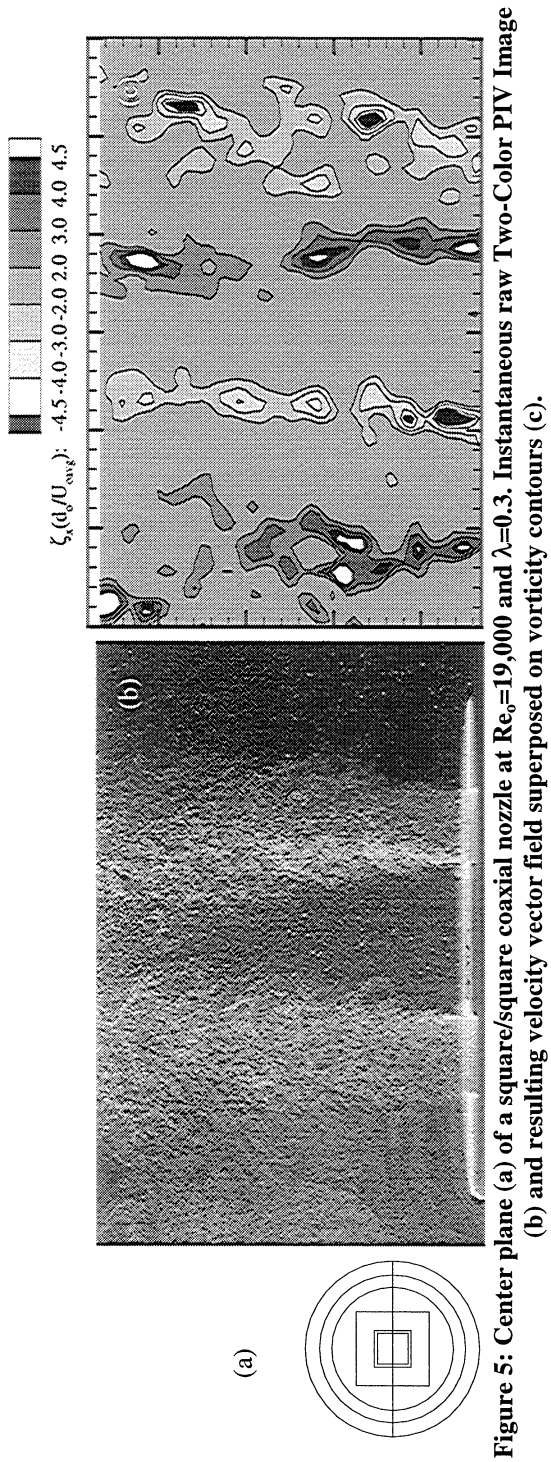


Figure 5: Center plane (a) of a square/square coaxial nozzle at  $Re_o=19,000$  and  $\lambda=0.3$ . Instantaneous raw Two-Color PIV Image (b) and resulting velocity vector field superposed on vorticity contours (c).

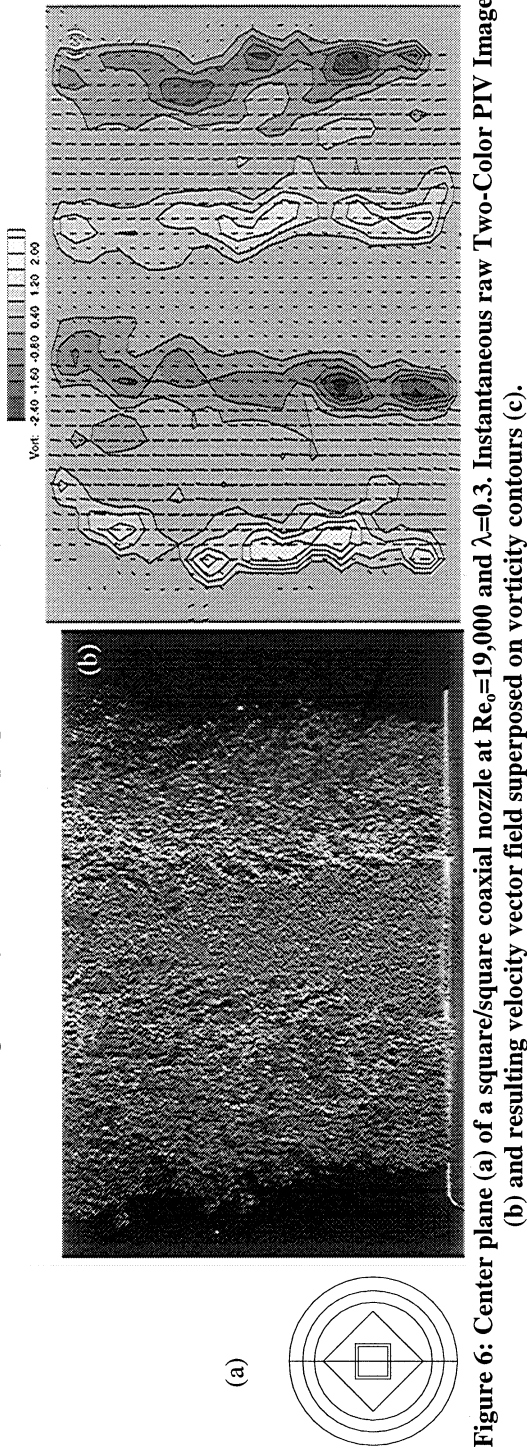


Figure 6: Center plane (a) of a square/square coaxial nozzle at  $Re_o=19,000$  and  $\lambda=0.3$ . Instantaneous raw Two-Color PIV Image (b) and resulting velocity vector field superposed on vorticity contours (c).



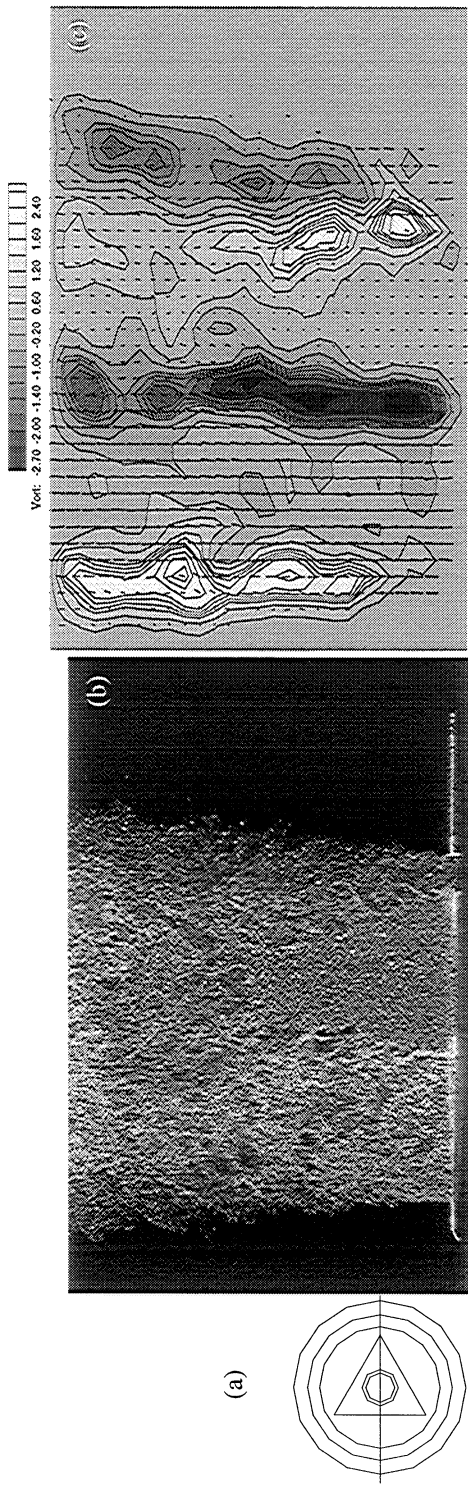


Figure 7: Center plane (a) of a triangular/circular coaxial nozzle at  $Re_0=19,000$  and  $\lambda=0.3$ . Instantaneous raw Two-Color PIV Image (b) and resulting velocity vector field superposed on vorticity contours (c).

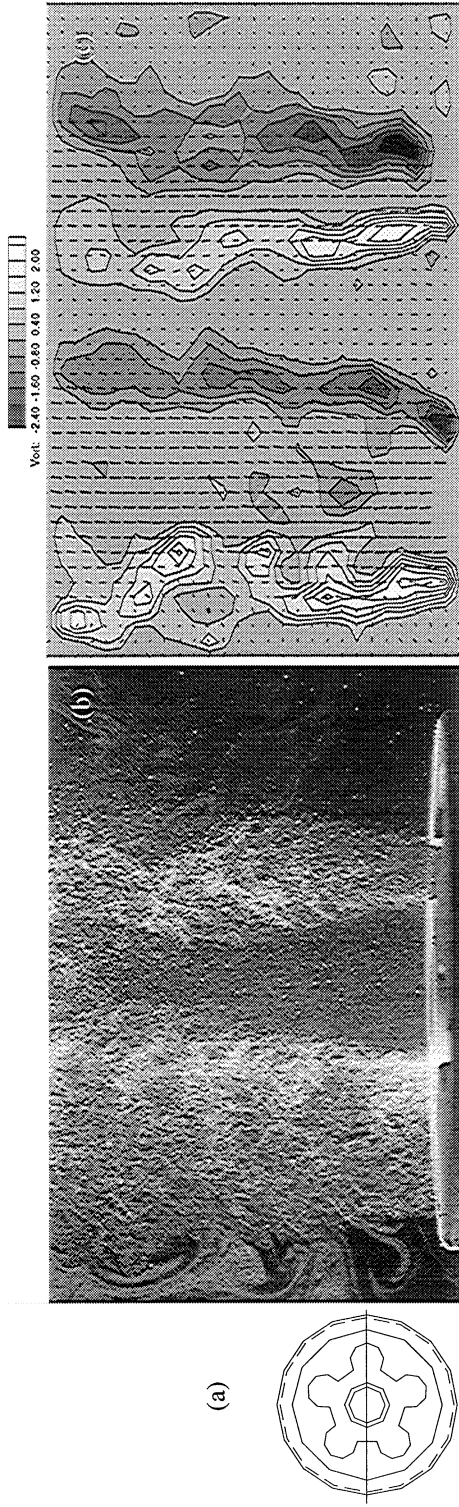


Figure 8: Center plane (a) of a lobed/circular coaxial nozzle at  $Re_0=19,000$  and  $\lambda=0.3$ . Instantaneous raw Two-Color PIV Image (b) and resulting velocity vector field superposed on vorticity contours (c).



## **VORTEX-FLAME INTERACTIONS IN HYDROGEN JET DIFFUSION FLAMES: A DPIV AND DNS INVESTIGATION**

**F. Schauer and R. Hancock**

Air Force Research Laboratory  
1790 Loop Road North  
Wright-Patterson AFB, OH 45433

**S. Gogineni**

Innovative Scientific Solutions, Inc.  
2786 Indian Ripple Road  
Dayton, OH 45440

**R. Lucht**

University of Illinois  
1206 West Green Street  
Urbana, IL 61801

### **ABSTRACT**

Vortex-flame interactions in a hydrogen jet diffusion flame are investigated with two-color Digital Particle Image Velocimetry (DPIV) and the results are compared with Direct Numerical Simulations (DNS). Driven-jet vortex-flame interactions are of particular interest because they are reproducible turbulent-like events that can be comprehensively investigated to gain insight into turbulent combustion. Previously, temperature and species concentration measurements were made in this flame, but a complete understanding of the vortex-flame interactions could not be gained without additional information concerning the flow field. The vortex structure of the combustng flow could not be reproduced using the hot-wire velocity data from cold flows. When the jet exit velocities from DPIV measurements were used as the driving profile for the DNS code, the resulting computations produced a vortex that matched the experimental vortex. The information obtained from DPIV and DNS provided insight into the complex reacting flows of vortex-flow interactions and aided the development of combustion modeling.

### **INTRODUCTION**

The fundamental building blocks of turbulent diffusion flames are the countless vortex-flame interactions that have length and time scales varying over several orders of magnitude. In hydrogen jet diffusion flames, the impact of vortex-flame interactions is being studied both computationally and experimentally.

Hancock, et al. [1-3], investigated these vortex-flame interactions using Coherent Anti-Stokes Raman Spectroscopy (CARS) and Laser-Induced Fluorescence (LIF) methods to measure gas-phase temperatures and concentrations. The experimental results were compared with Direct Numerical Simulations (DNS), and the model predictions were further

analyzed to investigate the physics and chemistry of the vortex-flame interactions.

The previous studies indicated that the vortex-flame interactions produce regions of positive and negative stretch in the flame surface. Within these stretched regions, the local flame temperature and NO concentration can vary significantly. The vortex-flame interaction impacts the flame structure through four complex phenomena: the local Lewis number (the heat/mass diffusion ratio), the Damköhler number (residence time over reaction time scale), flame stretch and curvature, and the gross velocity field (reactants and products can be swept into and out of the reaction zone) [4-6].

When a high-Damköhler-number hydrogen flame is stretched, the flame temperature changes; not because of incomplete chemical reactions but because of preferential diffusion resulting from the non-unity Lewis number. The fluid dynamics of high-Damköhler-number flames are sufficiently slow relative to diffusion rates that preferential diffusion competes with flame stretch.

Katta and Roquemore [7] found that when a vortex originates on the fuel-side of the flame front of a high-Damköhler-number flame, an outward bulge is produced and the temperature of the flame increases in the positively stretched regions of the flame and decreases in the negatively stretched (compressed) regions. This phenomenon is the opposite of what laminar flamelet theory would suggest. The diffusion of hydrogen to the flame zone is rapid, and the curvature of the flame toward the fuel in the positively stretched regions tends to focus and maintain the heat resulting from the reaction, producing super-equilibrium temperatures at these locations in the flame.

Previous studies provided information concerning the non-unity Lewis number effects of vortex-flame interactions; more detailed information about the velocity field of the vortex is required for investigation of the other three effects (Damköhler number, stretch, and gross flow). Thus, the aim of the present

paper was to obtain the velocity field employing particle image velocimetry (PIV) and use these data as input for the DNS code in an attempt to understand the vortex-flame interaction in a hydrogen jet diffusion flame.

This paper describes a combined experimental and computational study of the interaction of the induced fuel-side vortex with a diffusion flame sheet. In the experiment, a highly repetitive, vortex-flame interaction similar to a single turbulent event [8] was produced. The jet diffusion flame was stabilized on a 1-cm-diameter fuel nozzle surrounded by an annular co-flow of air. A fuel-side vortex was produced with a loudspeaker located in a chamber under the fuel tube. The axisymmetric vortex was mushroom-shaped and pushed outward on the flame surface, causing it to distort. Since this vortex-flame interaction was reproducible, the fuel jet velocity field could be measured quite accurately with a two-color Digital Particle Image Velocimetry (DPIV) technique during a variety of vortex-development phases.

The jet diffusion flame in this study was a mixture of hydrogen and nitrogen. Hydrogen was selected because its chemistry is fairly simple compared to that of other gaseous fuels; it departs significantly from unity-Lewis-number behavior and produces highly stable flames. Nitrogen is the gas species probed for CARS temperature measurements and is added to the jet fluid to move the stoichiometric contour closer to the shear layer. Driving the jet repeatedly with the loudspeaker forces the toroidal-shaped vortices to collide with the flame sheet, producing the vortex-flame interactions.

With velocity data obtained from the DPIV measurements, the time-dependent velocity profile at the jet exit was reproduced with the DNS model. The DNS results were then evaluated by comparing the vortex predictions and the experimental results.

## EXPERIMENTAL SYSTEMS

The apparatus for the driven jet diffusion flame experiment consisted of a 2.54-cm-diameter axisymmetric fuel tube that contracted to a 1-cm-diameter sharp-edged nozzle. The fuel tube was surrounded by a 15.24-cm-diameter co-flow of air at 0.48 m/s. The fuel jet was made up of 15.0 SLPM of hydrogen and 6.25 SLPM of nitrogen (0°C reference), resulting in a calculated average peak centerline axial velocity of 4.9 m/s at room temperature.

The jet and annular-air velocity profiles were also measured using a hot-wire anemometer and found to be nearly top-hat and within 5% of volume-based calculations over the center 8 mm of the jet. A periodically repeating vortex was formed inside the diffusion flame by passing the fuel over a pulsating loudspeaker located in a chamber directly below the fuel tube. The experimental facility is shown schematically in Fig. 1.

The loudspeaker was pulsed at 20 Hz, causing the fuel jet to experience periodic accelerations in velocity which, in turn, produced mushroom-shaped vortices that grew radially

outward. The loudspeaker driving pulse and the laser pulses were phase-locked to permit investigation of the vortex-flame interaction at a fixed phase of its development. Previous experiments indicated that the vortex and flame structures were reproducible to within  $\sim 100 \mu\text{m}$  from cycle to cycle over the axial region investigated [3].

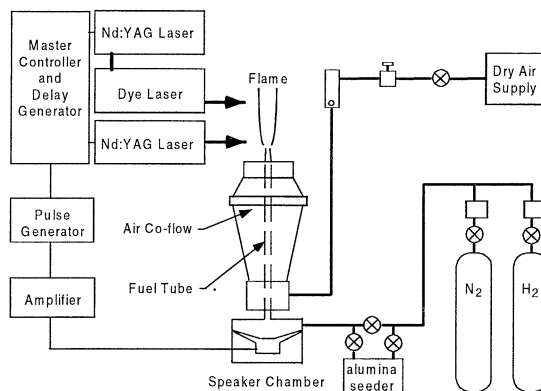


**Figure 1. Schematic of hydrogen jet diffusion flame burner and control system.**

## Two-Color DPIV System

The two-color DPIV system (Fig. 2) uses color for temporal marking of the seed particles in the flowfield. The green (532-nm) laser output from a frequency-doubled Nd:YAG laser and the red (640-nm) laser output from a Nd:YAG-pumped dye laser are combined by a dichroic beam splitter and directed through sheet-forming optics. The laser-sheet energy is typically 60 mJ/pulse, with a thickness of  $\sim 1 \text{ mm}$  at the test section. The temporal delay between the two lasers is a function of the gas velocity, optical magnification, and interrogation spot size. In the present experiment, the time delay between the two lasers was set at 21  $\mu\text{sec}$ . The flow is seeded with 1- $\mu\text{m}$  aluminum-oxide particles. The scattering from these seed particles is recorded on a CCD sensor (Kodak DCS 460c) which has a resolution of 3k x 2k pixels. This setup has been described by Gogineni, et al. [9].

Once the PIV image has been captured, the velocity field is obtained using a cross-correlation technique. The correlation function is calculated over small segments (interrogation domains) of the PIV image. The dimensions of each interrogation domain are dependent on particle density, estimated local velocity gradients, particle-image size, and desired spatial resolution. The maximum displacement of each particle must be less than one-half the interrogation spot.

In the present experiments, the interrogation domain measured 64 x 64 pixels, corresponding to 0.67 x 0.67 mm in the measured flow. For enhancing the overall resolution, the interrogation domains are overlapped by one-half the domain size. The peak of the correlation map corresponds to the average velocity displacement within the interrogation spot. An intensity-weighted peak-searching routine is used to determine

the exact location of the peak to sub-pixel accuracy. The number of particle pairs normally necessary to ensure a desirable signal-to-noise ratio is reduced to four or five pairs when the cross-correlation analysis is employed. The uncertainty and errors associated with the color sensor have been evaluated and the results were presented by Gogineni et al. [9].

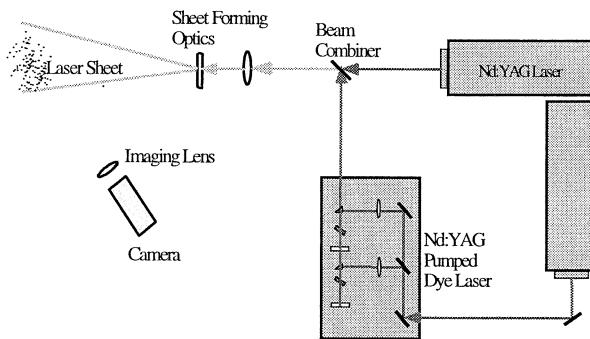


Figure 2. Schematic of two-color DPIV system.

## NUMERICAL MODEL

The direct numerical simulations of the diffusion flames were performed using a code developed by Katta, et al. [10], which has since been modified to incorporate the CHEMKIN chemistry model. Time-dependent, axisymmetric Navier-Stokes equations were solved along with species- and energy-conservation equations in the cylindrical coordinate system. Finite-difference forms of the momentum equations were obtained by an implicit QUICKEST scheme, and finite-difference forms of the species and energy equations were implemented with a hybrid scheme of upwind and central differencing using a  $151 \times 61$  mesh grid. The hydrogen/air chemical-kinetics model included 14 species and 54 reactions, and temperature and species-dependent properties were incorporated. The pressure field was calculated at every time step. Thermal diffusion of hydrogen was taken into account since it accentuates non-unity Lewis number effects in these flames [2]. The required inputs included mass fractions, boundary conditions, and the time-dependent jet velocity profile.

## RESULTS AND DISCUSSION

The raw DPIV image along with the processed vectors is shown in Fig. 3. In this image, only the jet flow is seeded. The fuel-side vortex is clearly evident from these images. Comparing multiple images at the same phase shows that the results are highly reproducible. The radial exit velocity profiles are nearly top-hat.

The co-flow was also seeded and a wide-angle image was captured for visualizing the entire burner, co-flow, and flame, as shown in Fig. 4. This image reveals the inner driven fuel-side vortex, the flame-zone where the seed density is low, and the larger flame zone structures above the fuel jet which are

produced both by buoyancy and by the periodically driven vortices. It is also evident that the co-flow is effective in producing laminar flow.

In contrast to the driven flame, the steady undriven flame (Fig. 5) has no inner vortex structure. Figure 5 depicts a classic jet diffusion flame. Although buoyant structure is evident in this image, it is much different than the driven flame of Fig. 4 which contains large structures in the flame zone much nearer the nozzle. Although not clearly visible in figures 4 and 5, a bulge in the flame zone is observed in the driven flame near the inner vortex. The contrasting images show the dramatic effect of the vortex-flame interaction on the overall flame structure.

Images were collected throughout the 20-Hz cycle of the vortex-flame interaction. The complete cycle is shown in Fig 6. Each DPIV image is for a different phase of the vortex. From these images the evolution of the vortex can be observed. As the speaker retracts, the fuel jet slows, drawing the flow radially inward as can be seen at  $t = 6$  and 12 msec. Then as the speaker pulses out, it drives the fuel jet into the slower moving fuel ahead of it. Consequently, the fuel moves radially outward, forcing it into the shear layer and forming the toroidal mushroom-shaped vortex as shown at  $t = 17$  and 21 msec. As the images show, the cycle is then repeated after the vortex has convected downstream ( $t = 24$  and 28 msec).

The centerline jet exit velocity can be extracted from these images. The DPIV results showed the radial variation of the exit velocity to be small; thus, a top-hat velocity profile could be used in the DNS models for the jet-nozzle boundary condition. The centerline jet exit velocity was employed to characterize the driving pulse and was used as the time-dependent boundary condition in the DNS model of the vortex-flame interaction. Accurate centerline jet exit velocity information was found to be extremely valuable in reproducing the vortex computationally [2].

A plot of centerline jet exit velocity as a function of time is shown in Fig. 7, along with hot-wire velocity data acquired previously. The hot-wire measurements were made in cold-flowing nitrogen, at the same flow rate as the fuel jet mixture. It is evident that hot wire measurements of cold nitrogen could not reproduce the actual driving velocity measurements in the fuel. It is suspected that replacing hydrogen with nitrogen resulted in changes in the momentum transfer of the driving speaker to the fuel. This hypothesis is supported by observations of stronger driving velocities when nitrogen was replaced with helium in other dilute hydrogen jet diffusion flame experiments [3]. The resolution of the hot wire measurements does not appear to be to blame as the temporal response of the hot wire was several thousand hertz. Hot wire data collected in the cold flowing nitrogen is insufficient to reproduce the driving velocity conditions of driven-vortex jet diffusion flames.

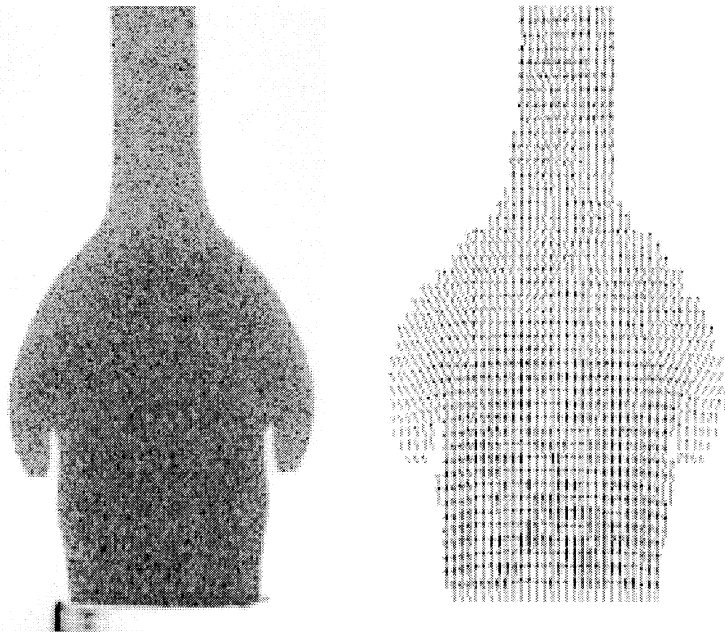


Figure 3. DPIV image and velocity vectors for driven-vortex hydrogen jet diffusion flame.



Figure 4. Flow visualization of driven-vortex hydrogen jet diffusion flame.

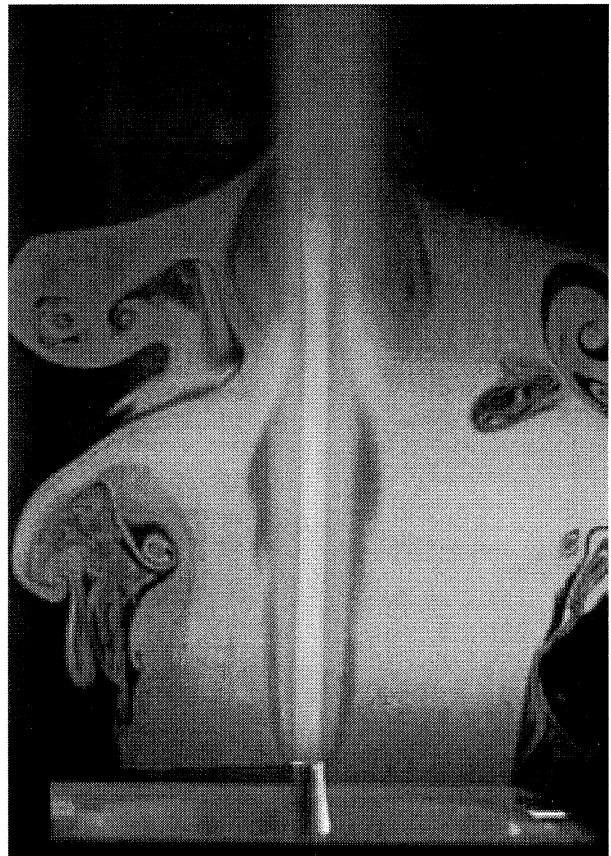


Figure 5. Flow visualization of undriven (steady) vortex hydrogen jet diffusion flame.

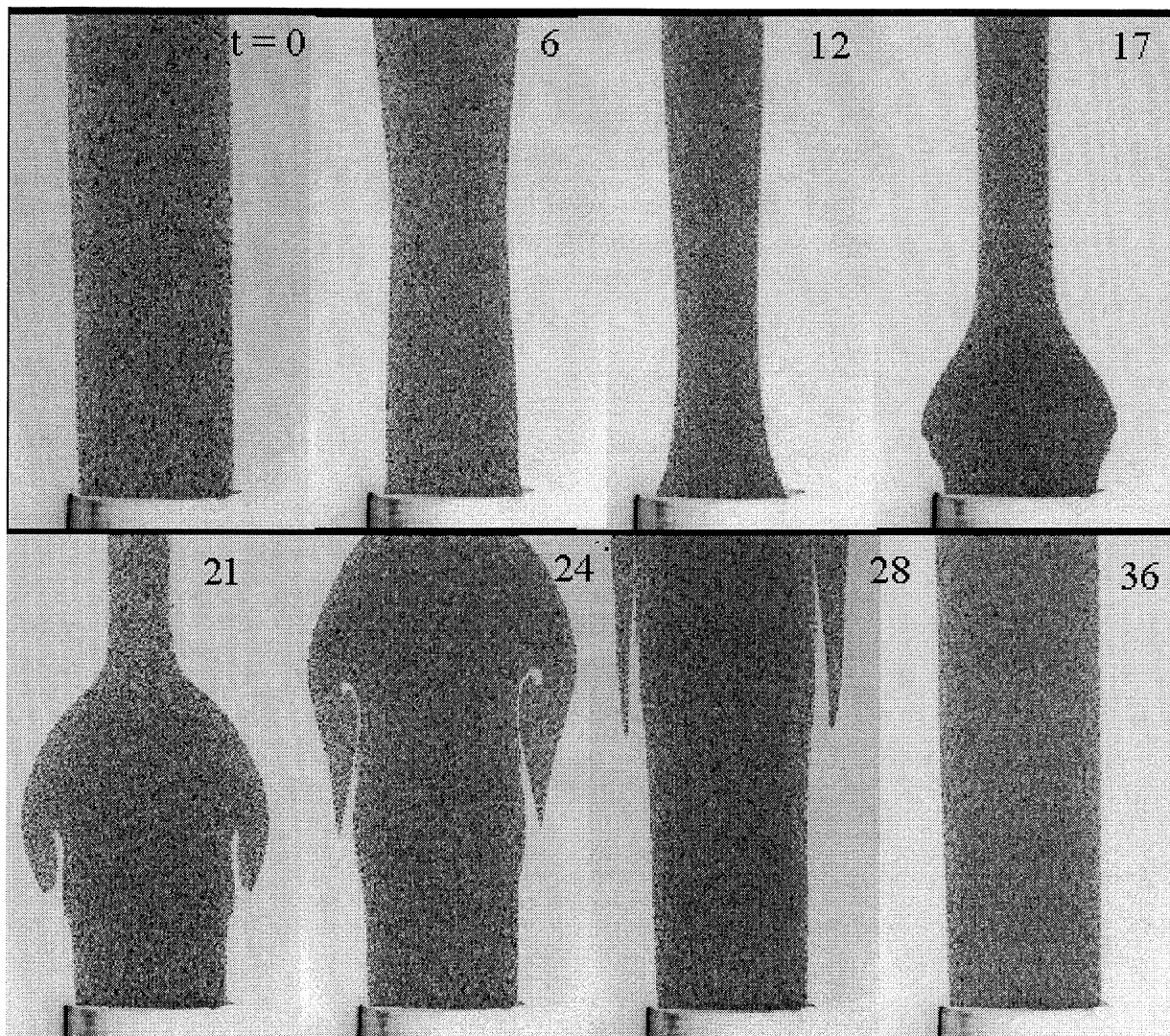


Figure 6. Development of vortex in driven hydrogen jet diffusion flame with time (times shown in msec).

When the DPIV exit velocities for each phase were used as input for the DNS driving profile, the vortex was reproduced computationally. Shown in Fig. 8 is a split experimental and computational image of the driven hydrogen/nitrogen flame. The left half is the DPIV image, and the right side is an image from the computational model. The DNS vortex is indicated using theoretical particle traces, and the peak flame temperature locations are represented by dots. This image shows the remarkable accuracy of the DNS in modeling the complex vortex-flame interaction.

From Fig. 8 it is evident that the vortex is generated when the faster moving fuel encounters slower moving fuel, forcing the fuel outward radially and causing a bulge in the flame zone. This can be seen in both the particle traces and the vectors in Fig. 3. The radially moving fuel compresses the flame zone, resulting in faster diffusion of hydrogen to the flame zone. In addition to this Lewis-number effect, the radially moving fluid decreases residence times, thus impacting the local Damköhler number.

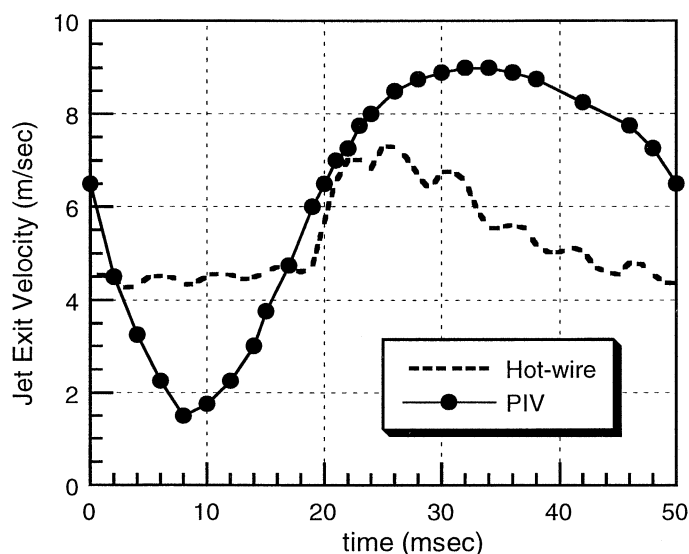


Figure 7. Plot of fuel jet exit velocity as a function of time.



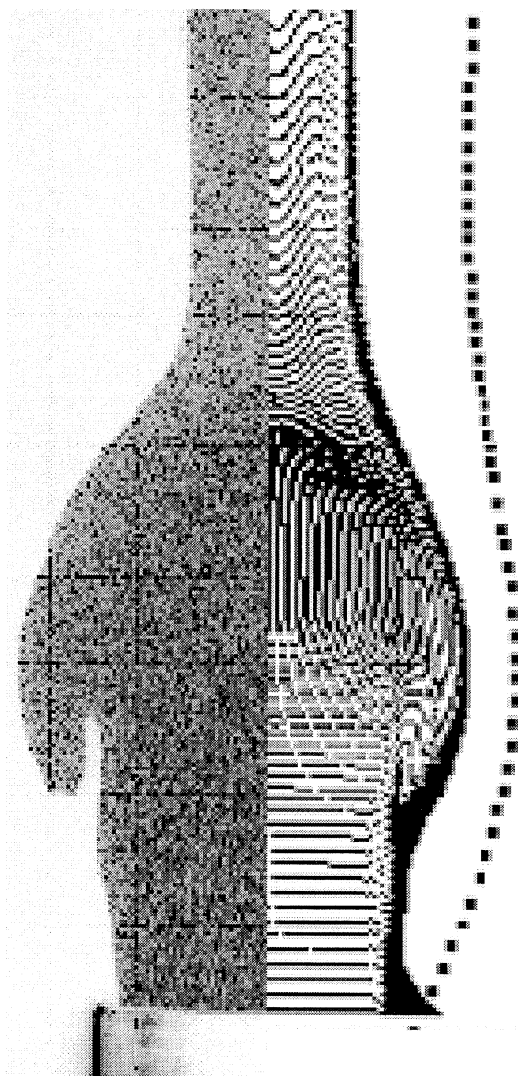


Figure 8. Split computational and experimental image of driven flame .

These images also indicate that the vortex produces areas of faster and slower flow, which stretches the flame front. Furthermore, the vortex produces a re-circulation zone and sweeps hot products back into the fuel side of the diffusion flame. The effects of these phenomena upon the flame structure are evident in the peak flame temperature.

Figure 9 is a plot of the peak flame temperatures as a function of axial location for the driven flame, comparing CARS temperature data and DNS predictions [2]. Both steady and driven flame results are shown. Remarkably similar (within ~1%) temperature profiles are observed for the CARS results and the numerical simulations. Both profiles exhibit a roughly 40-K temperature rise above the steady-state flame at the 15.24-mm axial location and a drop in the temperature of the flame farther downstream of the vortex in the negatively stretched region of the flame.

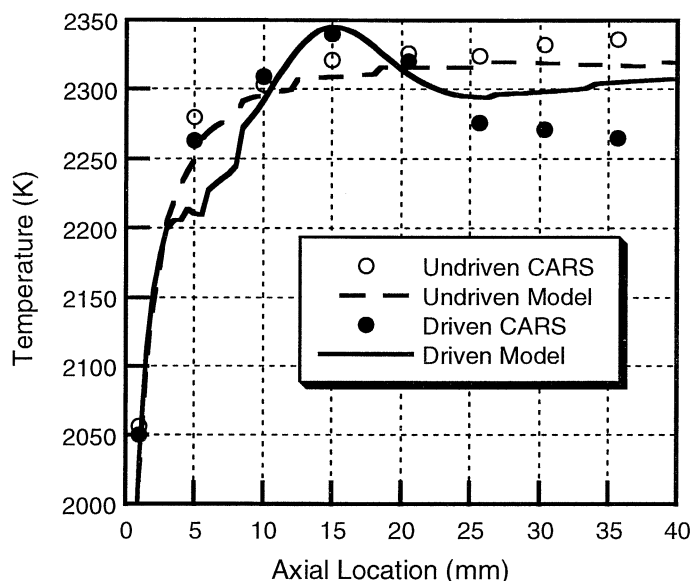


Figure 9. Comparison of calculated and measured peak flame temperatures as a function of axial location.

Figure 10 shows the computed axial flame stretch and peak flame temperatures versus axial location. The noisy flame stretch results below the 10 mm axial location are a product of very small displacements in the flame location in this region.

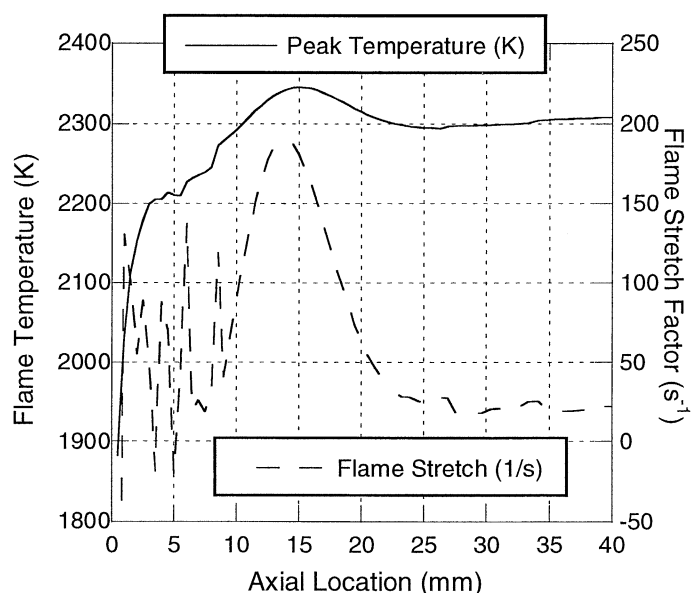


Figure 10. DNS calculation of axial variation of peak flame temperatures and flame stretch.

Katta and Roquemore [7] predicted the location of maximum positive stretch and maximum temperature to be just ahead of the vortex. They also observed a drop in temperature in the negatively stretched regions of the flame farther upstream and downstream of the vortex. For this particular flame the vortex center is at ~ 10 mm, and the peak stretch and



temperature occur farther downstream at 15 mm. These results directly support the argument that in the case of fuel-side vortices, the local temperature can actually rise above the steady-state flame temperature for regions of positive stretch and fall significantly below the steady-state flame temperature in regions of negative stretch.

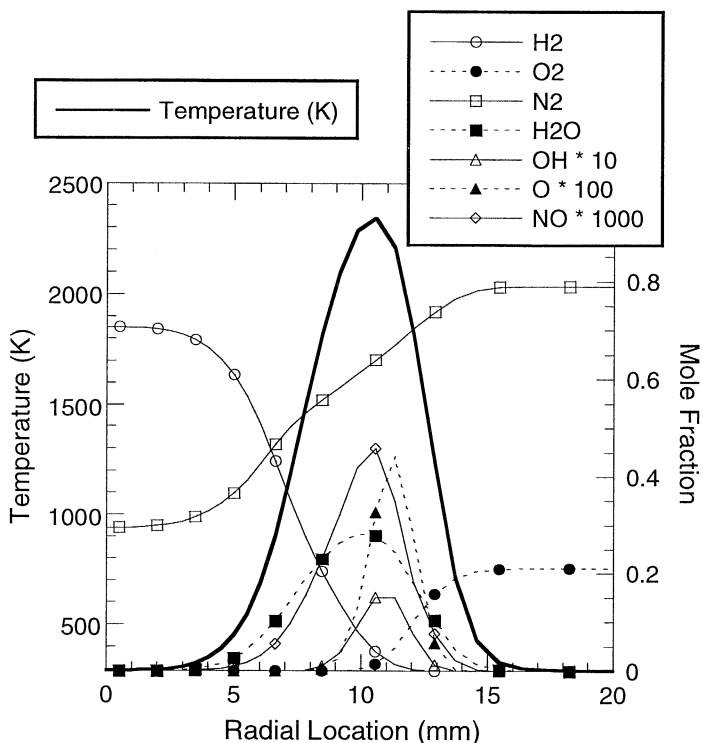


Figure 11. Temperature and mole fraction profiles for 2-Volt driving pulse at the 15.24 mm axial location for the stretched. These plots are produced from DNS data.

Figures 11 and 12 depict the computed radial variation of the temperature and species concentrations in the stretched and compressed regions of the driven-vortex flame interaction. The stretched region at the 15.24 mm axial location in Fig. 11 shows that the axial stretching acts to compress the flame zone, resulting in higher gradients. This increases the preferential diffusion of hydrogen to the flame zone, resulting in increased flame temperatures. At the axially compressed region at the 30.48 mm axial location, the combustion products spread out radially, resulting in cooler temperatures and increased product concentrations. The dramatic impact of the vortex-flame interaction upon the flame zone structure can be seen in in these two figures. In particular, the pollutant species NO can be seen to be significantly impacted by the vortex-flame interaction.

Another set of experiments was carried out to determine the effect of combustion on flow measurements. The flame was blown out, resulting in the DPIV images in Fig. 13 which is a comparison of the combustng flow and the cold flow. The dramatic difference in vortex structure demonstrates the

importance of performing these measurements in combustng flows.

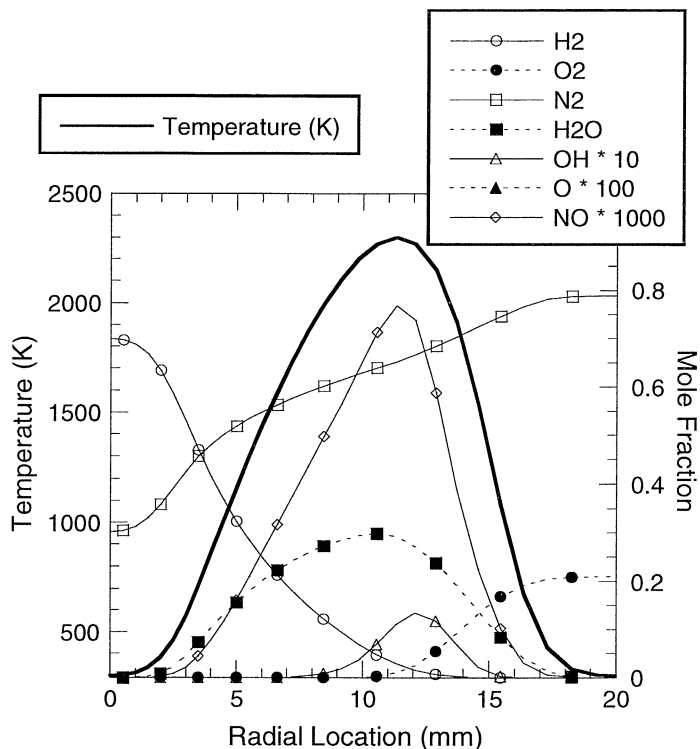


Figure 12. Temperature and mole fraction profiles for 2-Volt driving pulse at the 30.48 mm axial location for the compressed region. These plots are produced from DNS data.

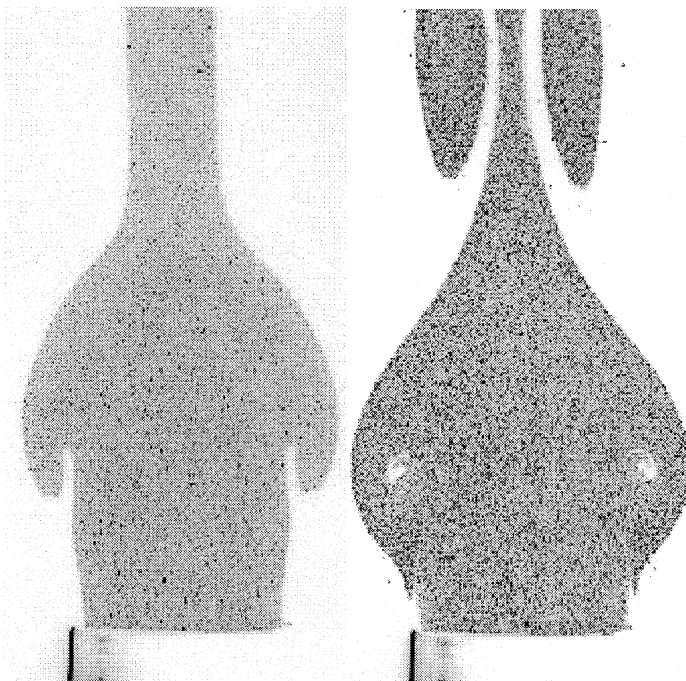


Figure 13. DPIV images for combustng (left) and cold flow with flame blown out (right).

## CONCLUSIONS

Vortex-flame interactions in a driven hydrogen jet diffusion flame were studied with two-color DPIV measurements and DNS modeling. The results demonstrate that DPIV is valuable in providing high spatial and temporal resolution velocity measurements in a harsh environment. It was found that velocity measurements must be made in the combustive flow if the flow field of vortex-flame interactions is to be studied accurately. When the jet exit velocities were used as the driving profile for the DNS code, the resulting computations produced a vortex that matched the experimental vortex. The results further validate the DNS code, which has performed well in predicting flame temperatures previously. The driven-vortex hydrogen jet diffusion flame provides insight into turbulent combustion by producing a single reproducible vortex-flame interaction. Stretched and compressed regions were observed in the flame surface when the vortex produced a bulge in the observed flame surface. These stretched and compressed regions impacted the resulting flame temperature and species concentrations, including NO emissions.

## ACKNOWLEDGMENTS

Financial support was provided by the Propulsion Directorate of the Air Force Research Laboratory (USAF) under Contract No. F33615-95-C-2507 and the Palace Knight Program (USAF).

## REFERENCES

1. Hancock, R. D., Schauer, F. R., Lucht, R. P., and Farrow, R. L., *Applied Optics*, Vol. 36, No. 15, 1997, pp. 3217-3226.
2. Hancock, R. D., Schauer, F. R., Lucht, R. P., Katta, V. R., and Hsu, K. Y., in *Twenty-Sixth Symposium (International) on Combustion*, (The Combustion Institute, Pittsburgh PA, 1996), pp. 1087-1093.
3. Hancock, R. D., *Laser Diagnostic Investigation of the Structure of Steady and Driven Hydrogen Jet Diffusion Flames*, Ph.D. Dissertation (University of Illinois, Urbana-Champaign, IL, 1996).
4. Peters, N., and Williams, F. A., *AIAA J.*, Vol. 21, No. 3, 1983, pp. 423-429.
5. Law, C. K., *Prog. Energy Comb. Sci.*, Vol. 10, 1984, pp. 295-318.
6. Williams, F. A., *Combustion Theory* (Addison-Wesley Publishing Company, Redwood City, CA, 1985).
7. Katta, V. R., and Roquemore, W. M., *Combust. Flame*, Vol. 100, 1995, pp. 61-70.
8. Hsu, K. Y., Chen, L. D., Katta, V. R., Goss, L. P., and Roquemore, W. M., AIAA Paper 93-0455, 31st Aerospace Sciences Meeting, Reno, NV.
9. Gogineni, S., Goss, L., River, R., and Pestian, D., "Two-Color Digital PIV Employing a Single CCD Camera," *Exp. Fluids* (in press).
10. Katta, V. R., Goss, L. P., and Roquemore, W. M., *Combust. Flame* Vol. 96, 1994, pp. 60-74.

## STRUCTURE OF A COMPRESSIBLE BOUNDARY LAYER OVER A CURVED WALL

Raymond C. Wier<sup>1</sup>

Munitions Directorate, Air Force Research Laboratory, Eglin AFB FL 32542

Rodney D. W. Bowersox<sup>2</sup>

University of Alabama, Department of Aerospace Engineering and Mechanics, Tuscaloosa, AL 35487

Diana D. Glawe<sup>3</sup>

Advanced Propulsion Division, Air Force Research Laboratory, WPAFB OH 45433-7251

Sivaram Gogineni<sup>4</sup>

Innovative Scientific Solutions, Inc., 3845 Woodhurst Court, Beavercreek, OH 45330.

An experimental analysis of a supersonic turbulent boundary layer distorted by streamwise pressure gradients was performed using particle image velocimetry (PIV) and hot-film anemometry. Four pressure gradients were examined; a zero pressure gradient ( $M = 2.8$ ), a favorable pressure gradient ( $M = 3.0$ ) an adverse pressure gradient ( $M = 2.7$ ), and a combined pressure gradient ( $M = 2.5$ ). Measurements included mean velocity, velocity turbulence intensity, mass flux turbulence intensity and energy spectra. Instantaneous (10 nsec) Mie scattering flow visualizations were also acquired. Qualitatively, the flow visualizations indicated that the turbulent flow structures were strongly affected by the pressure gradients. The PIV contours and the hot-wire profiles indicated that the boundary layer thickness increased 40% and decreased 30%, as compared to the zero pressure gradient, for the favorable and adverse pressure gradients, respectively. Further, the PIV and hot-wire data indicated that the axial turbulence intensity levels increased 22% for the adverse pressure gradient and combined pressure gradient, and decreased 25% for the favorable pressure gradient as compared to the zero pressure gradient. The energy spectra data indicated the pressure gradient (favorable or adverse) increased the energy transfer to the higher frequencies.

<u>Nomenclature</u>			
		x, y	wind tunnel coordinates
		$y^+$	Van Driest length scale
APG	Adverse pressure gradient	ZPG	Zero pressure gradient
CPG	Combined pressure gradient	$\beta$	Clauser's equilibrium factor
f	Frequency	$\delta$	Boundary layer thickness
FPG	Favorable pressure gradient	$\lambda$	Wavelength
h	Height	$\Pi$	Cole's wake function
k	Wave number ( $\equiv 2\pi f / U_\infty$ )	<u>Subscripts</u>	
LDV	Laser Doppler Velocimetry	1,2	Wind tunnel station
M	Mach number	e	Edge
MOHR	Multiple overheat ratios	t	Total
p	Static pressure	ts	Test section
P	Stagnation or total pressure	$\delta$	Boundary layer height
PIV	Particle Image Velocity	<u>Introduction</u>	
Re	Reynolds number	<p>Understanding the flow dynamics resulting from high-speed flow over complex shapes is essential in the design and analysis of advanced flight vehicles. However, the underlying physics of flow over many of the complex shapes encountered on the exterior surface of a vehicle and interior surface of an engine are not yet understood.<sup>1,2</sup> Thus, further experimental and related computational investigation is required to ascertain accurate predictions of the flow dynamics resulting from high-speed flow over complex shapes.</p> <p>Many experiments have been conducted to measure mean flow quantities for supersonic and</p>	
SOHR	Single overheat ratio		
T	Temperature		
TI	Turbulence intensity		
u	Axial velocity		
$u^*$	Van Driest friction velocity		
$u_{eff}^+$	Van Driest effective scaled velocity		

<sup>1</sup> Advanced Missile Design Engineer, Member AIAA<sup>2</sup> Assist Professor of Aerospace Engr, Senior Member AIAA<sup>3</sup> Experimental Research Engineer, Member AIAA<sup>4</sup> Senior Scientist, Member AIAA

This paper is declared a work of the U.S. Government and is not subject to copyright protection in the United States.

WL Wright Laboratories

hypersonic flows; however, most of these experiments focus on zero pressure gradient (ZPG) flow<sup>3,4,5,6</sup> and rarely measure turbulence quantities. Smith and Smits<sup>7</sup> offer the following explanation for this lack of data as “reliable and accurate measurements of turbulence properties are difficult to make in any supersonic flow, and the difficulties are usually more extreme in the presence of flow distortions”. For many studies where turbulence quantities are measured, the quality of the data was found to be flawed and unusable.<sup>8</sup> Settles and Dodson<sup>9</sup> echo this concern. They surveyed over one hundred shock/boundary layer interaction studies and only 19 met their exacting turbulence criteria.

Adverse pressure gradients (APG) have been found to destabilize the boundary layer. In other words, the fluctuating turbulent properties increase.<sup>10,11</sup> An APG can be created by a shock wave boundary layer interaction or by a concave curvature. Lewis and Gran<sup>12</sup> created an APG by shock wave boundary layer interaction. They found that turbulent results compare favorably with other low-speed results. Fernando and Smits<sup>13</sup> suggest that the turbulence quantities undergo an amplification while the mean flow structure remains unchanged.

Recall that an APG can be created by regions of concave curvature. Jayaram, Taylor and Smits<sup>14</sup> found that the turbulence levels increased due the combined effect of the pressure gradient, streamline curvature and bulk compression. Interestingly, they found, for two of their three APG models, the weak shock wave created had no effect on the turbulent quantities.

Few favorable pressure gradient (FPG) studies have been conducted. The few that do exist suggest that the FPG acts to damp out the turbulent fluctuations.<sup>15,16,17,18</sup> Bulk dilation and supersonic stream tube expansion provide the most likely explanations of this phenomena.<sup>16</sup>

The present paper describes the results from an experimental study that examines the effects of wall curvature on the structure of the turbulent boundary layer. PIV, hot-wire anemometry, and instantaneous flow visualizations were acquired to examine the turbulent structures and their energy content.

### Facilities and Instrumentation

The tests were performed in the Air Force Institute of Technology Mach 3.0 wind tunnel. Due to boundary layer growth, the freestream Mach number was reduced to 2.8 in the test section. The plenum chamber pressure ( $P_{t1}$ ) and temperature ( $T_{t1}$ ) were maintained at  $2.19 \times 10^5 \pm 11.8 \times 10^3$  Pa and  $295 \pm 2$  K during the tests, respectively. Two modular test sections, measuring 33

cm in length and 6.35 x 6.35 cm in cross-section, were mounted behind the nozzle. The aft test section was used for the present research.

### Coordinate System

A coordinate system was defined relative to the nozzle throat and wind tunnel ceiling. The x axis was positive in the streamwise direction with the origin placed at the nozzle throat. The y direction was defined as normal to the wind tunnel ceiling, positive down. A right-hand z axis (not used for this study) was defined to complete the right-hand coordinate system.

### Models

Three pressure gradient models were used in this study to produce four pressure gradients. The models were a ZPG model, a FPG model and an APG / combined pressure gradient (CPG) model (see Figure 1). The CPG was defined as a FPG following the APG. The surfaces of the pressure gradient models were defined by a cubic polynomial of the form  $\Delta h = a_0 + a_1\Delta x + a_2\Delta x^2 + a_3\Delta x^3$ .

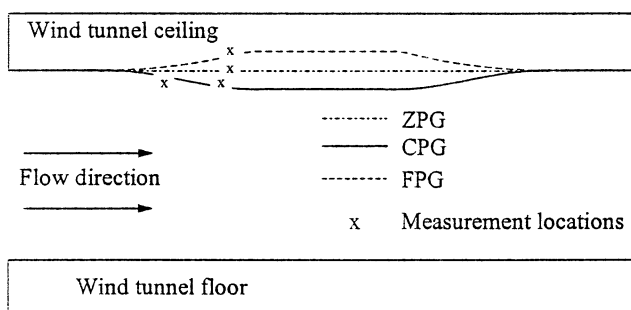


Figure 1: Schematic of pressure gradient models with measurement locations

$\Delta h$  was defined as the change in wind tunnel height in reference to the ZPG model height.  $\Delta x$  was the distance from the nozzle throat minus 60.0 cm. The model contours began at  $x = 65.1$  cm. Figure 1 contains a schematic of the pressure gradient models along with measurement locations. Table 1 contains the cubic polynomial coefficients. Measurements were obtained at  $x = 71.5$  cm on the ZPG and FPG models. Measurements were obtained at  $x = 68.0$  cm for the APG and at  $x = 70.0$  cm for the CPG on the APG / CPG model. All measurements were obtained along the tunnel centerline along the z-axis to minimize possible 3-D effects.

Table 1: Pressure gradient test section curve coefficients

Model	$a_0$	$a_1$	$a_2$	$a_3$
FPG	-0.2078	0.0897	-0.0095	-0.0360
APG / CPG	1.1858	-0.5410	0.0748	-0.0028

### Pressure and Hot-Film Instrumentation

Two types of hot-film probes were used in this experiment, a single hot-film (TSI model 1218-20) and a single hot-wire (TSI model 1218-T1.5). Each probe had a thickness of 51.0  $\mu\text{m}$ , sensing length of 1.0 mm, nominal resistance of 5.5 Ohms and a temperature coefficient of resistance of 0.24%. The hot-wire had a higher frequency response than the hot-film and was exclusively used for energy spectra data.

A TSI 100 Intelligent Flow Analyzer (IFA) constant temperature anemometer was used for this study. The IFA 100 is composed of the Model 150 anemometer and the Model 157 Signal Conditioner. The IFA 100 was operated in the 1:1 bridge mode. The external resistance and overheat ratio were set by a series of external resistors. The overheat ratios used ranged from 1.5 to 2.0. The bridge voltage output as measured by the TSI 100 was recorded at a sampling frequency of 25 KHz for velocity and total temperature data, and a frequency of 500 KHz for energy spectra data. Approximately 250,000 data points were collected for velocity/total temperature data and for frequency data. All hot-films were calibrated before acquiring data (minimum correlation coefficient  $\approx 0.99$ ). The hot-film probes were calibrated by increasing  $P_2$  while the probe was in the free-stream of the wind tunnel.

### PIV Instrumentation

A two laser PIV system was used for PIV measurement as well as for flow visualization. Two Continuum energy supplies Model SLI-10 were used to power the two Surlite Nd:YAG lasers. The Surlite lasers each produced two coherent laser beams with wavelengths ( $\lambda$ ) of 532 and 1,064 nm. The beam splitter was used to eliminate the higher  $\lambda$  beam. One beam passed through a Princeton Optics Model RC1000 Raman cell that contained  $\text{N}_2$  and  $\text{H}_2$  at a pressure of 65.6 MPa. By Raman scattering off the  $\text{N}_2$ , the  $\lambda = 532$  nm (green) beam was converted to a  $\lambda = 607$  nm (red) beam. The beams were combined and passed through a series of optics to form a laser sheet with a thickness  $< 1$  mm. The laser sheet was positioned on the spanwise centerline of the tunnel.

Each laser was pulsed at 10 Hz with a 10 nsec pulse width.<sup>19</sup> The time delay between the green and red pulse was adjusted by a Taitech Inc. PIV control box and monitored by a Gould Model 4074 oscilloscope. The nominal time delay was set at 300 ns and was recorded after each data run.

Images were recorded by a Kodak Model DCS 460C CCD camera (3060 x 2036 pixel array). The performance of this CCD sensor was evaluated by Gogineni et al.<sup>19</sup> and found that the data is an excellent agreement with the corresponding film data obtained under identical conditions. A Nikon N90 lens produced a magnification of approximately 71 pixels per millimeter. The lens aperture was set at a f-stop of 4.2 with an exposure time of 0.125 seconds. A maximum of three images were taken per data run.

A schematic of the PIV system is presented in Figure 2. For a complete description of the system, see Gogineni et al.<sup>19</sup>

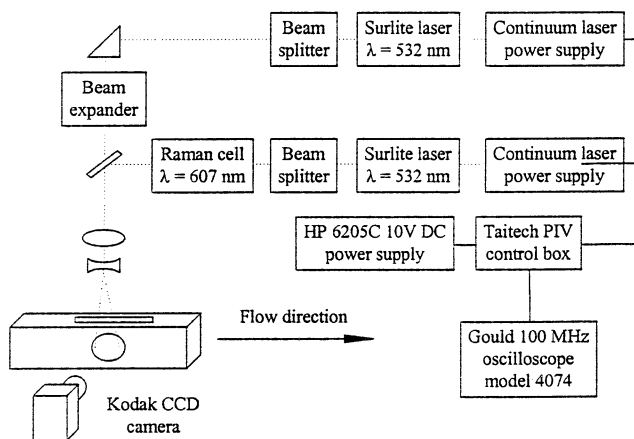


Figure 2: Schematic of the PIV System

### Results and Discussion

#### Flow Visualization

In order to understand the flow features qualitatively, Mie scattering images are obtained. Unlike traditional flow visualization techniques such as shadowgraph and schlieren, the Mie scattering images of PIV can be used both for flow visualization and for velocity measurements. These images offer the advantage of illuminating a single plane of view in the flow rather than an integrated view across the test section. Flow visualization images for the APG / CPG and FPG models are presented as Figures 3 and 4, respectively.

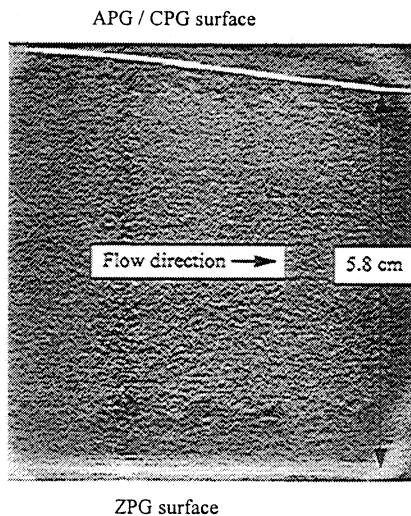


Figure 3: APG / CPG flow visualization

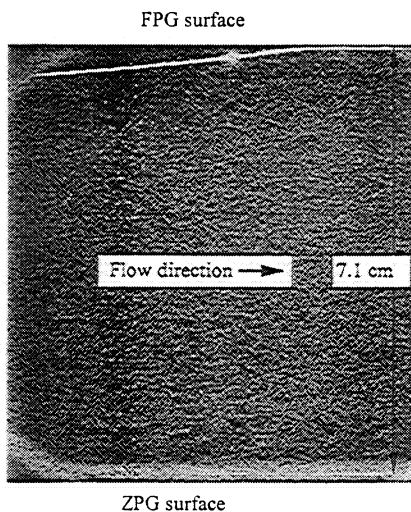


Figure 4: FPG flow visualization

Note in both figures, the ZPG boundary layer (along the tunnel floor) is uniform and the structures have an inclination of between  $45^\circ$  to  $60^\circ$ . This effect has been noted by Spina.<sup>20</sup> The ZPG flow structures span  $\sim \frac{1}{2}$  the boundary layer. Application of an APG / CPG (Figure 3) causes a decrease in the boundary layer thickness. Further, the APG / CPG structures have an inclination near  $20^\circ$  to  $30^\circ$ , and span nearly the entire boundary layer.

Figure 4 shows the comparison between the FPG and ZPG surfaces. As compared to the ZPG, the FPG boundary layer grows in the streamwise direction, as expected. More small scale structures are evident on the FPG boundary layer edge; however, the large scale structures are not clearly visible. This is consistent

with the theory that a FPG promotes the disassociation of large scale structures into small scale structures.<sup>16</sup>

Visual estimates of the boundary layer thickness can be ascertained from Figures 3 and 4. The measurements on the right hand side of figures 3 and 4 refer to the distance between the floor and the edge of the model surface. The estimated boundary layer thickness is 1.0 cm for the ZPG, 0.8 cm for the APG / CPG, and 1.1 cm for the FPG.

#### Mean Flow Profiles

Mean flow properties were evaluated by two different methods and compared to previous studies.<sup>11,17,18,21</sup> First, the hot-wire was used to measure the mass flux and total temperature. Second, PIV was used to provide velocity information. Data were normalized by their edge values and plotted versus  $y/\delta$  ( $\delta$  is the distance from the wall where  $u = 0.99 U_e$ ).

For mean flow data, the hot-film was traversed towards the wall until the probe struck the wall. Even though the probe struck the wall, the hot-film was undamaged. Then the probe was traversed back to its starting point. This allowed for accurate near wall data collection and for the wall position to be accurately located. Due to the thickness of the boundary layer and limitations on run time, data collection was only possible during the initial probe motion (traverse up) for the FPG. For the other pressure gradients, data was collected on the initial and final probe motion (traverse up & traverse down).

The ZPG data is presented in Figure 5. There is excellent agreement between data collected during the traverse up and the traverse down movement. The single overheat ratio (SOHR) data matches well with the multiple overheat ratio (MOHR) data implying that the total temperature variations were small. This is confirmed by the total temperature profiles which were reasonably constant across the boundary layer for both the traverse up and traverse down motions. For this case, the probe was traversed to only  $y/\delta \approx 1.2$ .

The FPG data is presented in Figure 6. Recall that data was only obtained during the traverse up movement. Again, the SOHR data matches the MOHR data. Aside from the expansion region in the freestream  $y/\delta > 1.3$ , the profiles were similar to the ZPG flow.

The APG data is presented in Figure 7. The largest value of mass flux does not occur in the freestream as in the ZPG or FPG. Instead, the largest value occurs near  $y/\delta \approx 1.0$ . This was the result of the



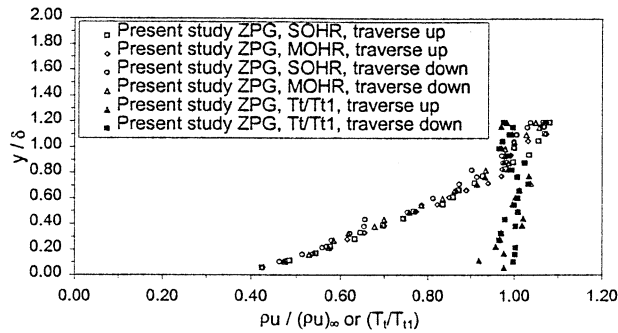


Figure 5: ZPG hot-film data

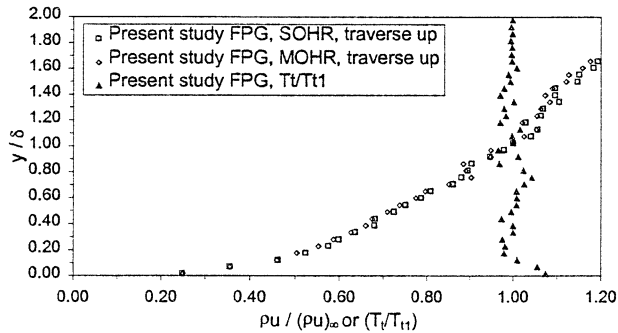


Figure 6: FPG hot-film data

compression wave formed off of the model surface. However, in the boundary layer region ( $y/\delta < 1.0$ ), the profile shape was very similar to the ZPG flow. The CPG data in Figure 8 has similarities to the FPG as well as the APG data. The shape of the mass flux curve does not have the elbow present in Figure 7.

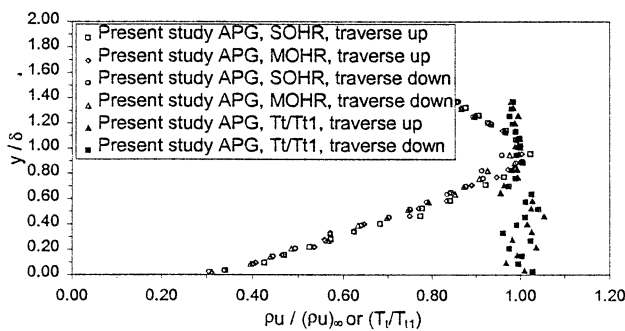


Figure 7: APG hot-film data

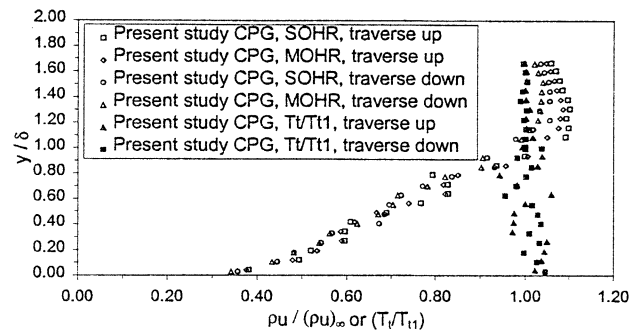


Figure 8: CPG hot-film data

Recall that PIV images (Figure 9 shows a representative plot) show the flow in the entire illuminated plane. The PIV images were averaged together and used to obtain mean and turbulent statistics. 25 images were averaged for the ZPG, 30 images were averaged for the APG/CPG and 25 or 93 images were averaged for the FPG. The two different data set sizes for the FPG case allowed a study of the effect of image sample size on flow field parameter convergence. For the present experimental set-up, 1 to 3 images per run were attainable. The images were analyzed using a custom developed software (ISSI) by overlapping 128 x 128 pixel interrogation block.

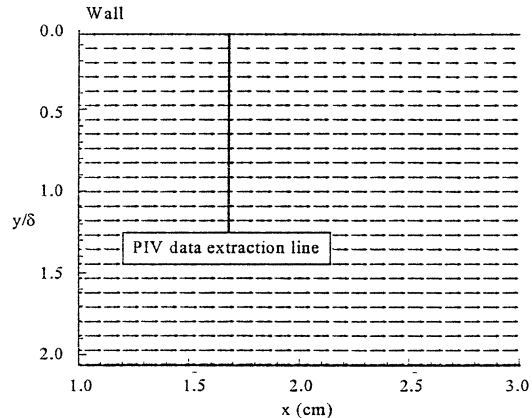


Figure 9: ZPG velocity vectors

The PIV velocity profiles were extracted at the same locations that the LDV data [16] were acquired. The velocity comparisons between LDV and PIV are presented as Figures 10 to 12 for the ZPG, FPG and APG / CPG, respectively.

Figure 10 presents the ZPG velocity comparisons. There is excellent agreement between the LDV and PIV data. This indicates that 25 images provides satisfactory mean flow data for the ZPG configuration.

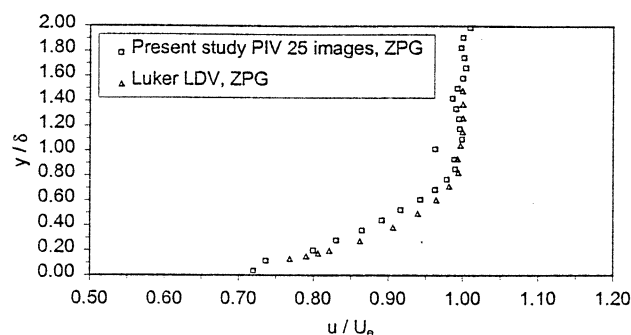


Figure 10: ZPG velocity comparison

Figure 11 presents the FPG data. Recall that the PIV FPG data was reduced with sample sizes of 25 and 93 images. The data for both sample sizes is in close agreement with the LDV data. Figure 12 presents the APG and CPG data. At both locations there is excellent agreement between the LDV and PIV data below  $y/\delta = 1.3$ . The non-dimensional boundary layer profiles in Figures 10 - 12 are similar (they all fall to within about 3 - 5 % of each other). Thus, the pressure gradients had little effect on the mean profiles.

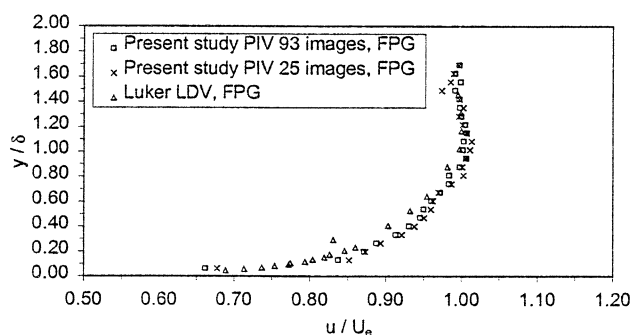


Figure 11: FPG velocity comparison

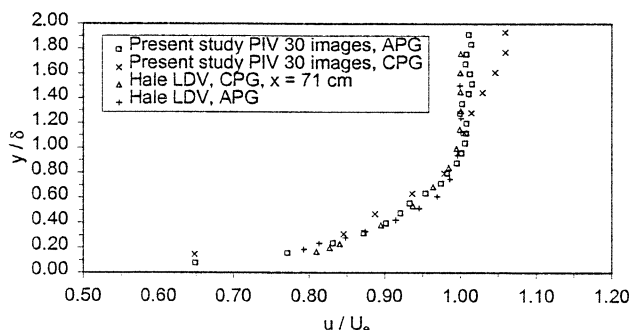


Figure 12: APG / CPG velocity comparison

### Van Driest Correlation

The PIV and hot-film data were compared to LDV data obtained by Luker et al.<sup>16</sup> and theoretical calculations based on the scaling laws proposed by Van Driest<sup>22</sup>. An Evan's correction factor<sup>23</sup> of 1.5% was used in the scaling law. The profiles for the ZPG are plotted in Figure 13 along with the theoretical flat plate values. For the flat plate, Clauser's parameter<sup>24</sup>,  $\beta$ , is approximately equal to zero. Setting  $\beta = 0$  leads to a Coles wake parameter<sup>25</sup>,  $\Pi$ , of 0.476. There is excellent agreement among the three data types and with the theory. The PIV data lie closer to the theoretical values than either the LDV or hot-film results. The difference between the LDV and hot-film results in Figure 13 is the estimate of  $\tau_w$ . Luker et al.<sup>17</sup> used the Couette flow assumption, while the present study used the Van Driest correlation. In addition, PIV allows for data to be collected nearer to the wall ( $y^+ \approx 31$ ) than LDV or the hot-film data. Note, in the outer region, the velocity profile estimated from the hot-wire shows a slight roll-off near the wall. It is expected that the probe experienced transonic effects in that region.

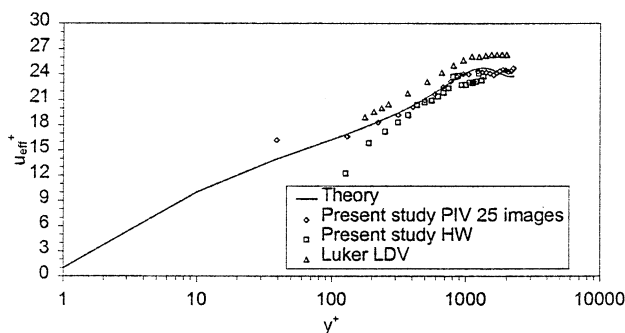


Figure 13: ZPG Van Driest velocity profile

### Turbulence Results

Hot-film anemometry and PIV were used to evaluate the fluctuating components of the fluid properties. Hot-film probes were used to evaluate the mass flux and total temperature fluctuations. Due to the higher frequency response (200 KHz vs. 100 KHz), hot-wire probes were used to obtain energy spectra. Energy spectra data was obtained by sampling at discrete locations in the boundary layer. The energy spectra data was also reduced for mass flux fluctuation data. Finally, PIV was used to evaluate velocity fluctuations where, as with the mean velocity profiles, were extracted from the 2D contour data.

The fluctuating mass flux profiles are given in Figures 14 to 17 for the ZPG, FPG, and APG / CPG combination, respectively. Figure 16 presents the ZPG mass flux turbulence intensity (TI). There is excellent agreement between the SOHR and MOHR methods as well as between the two different traversing methods. The discrete points from the spectra data also show excellent agreement with the traverse data. The data indicates that the probe just barely reached the freestream. The maximum TI occurs between  $y/\delta = 0.3$  and  $y/\delta = 0.5$  with a value of between 15% to 16%. These values are typical for a supersonic boundary layer.

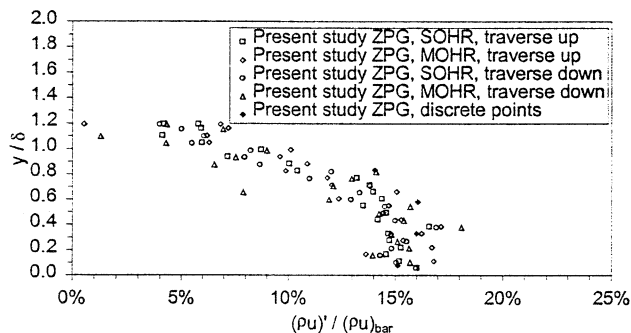


Figure 14: ZPG mass flux TI

Figure 15 presents the FPG mass flux TI. There is excellent agreement between the SOHR data, MOHR data and the discrete point data. The maximum turbulence intensity is 12% at a  $y/\delta$  of 0.5. Thus, the FPG reduced the maximum turbulence intensity by 25% as compared to the ZPG. Note that traversing the probe into the wall provides near wall data. These results confirmed that stabilizing effect of the combined wall curvature and FPG on the turbulent flow properties.

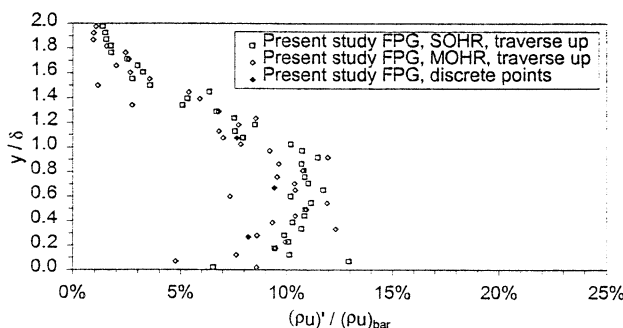


Figure 15: FPG mass flux TI

Figure 16 presents the APG mass flux TI. Again, there is excellent agreement between the discrete data points, the traversed MOHR and SOHR data. The maximum TI is approximately 20%, a 25% increase over the ZPG value, at  $y/\delta = 0.3$ . These results confirm the expected destabilizing effect of the wall curvature plus APG on the turbulent flow properties.

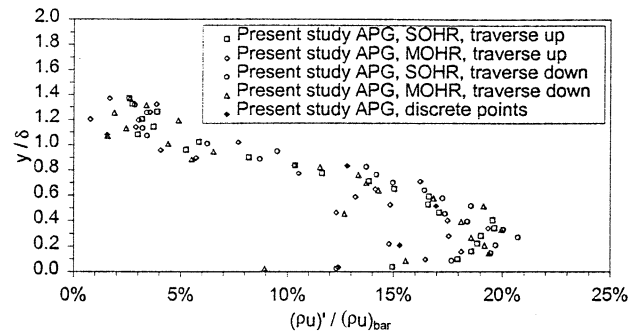


Figure 16: APG mass flux TI

Figure 17 presents the CPG mass flux TI. As with the ZPG and FPG, there is excellent agreement between the SOHR and MOHR data. The maximum TI is 22%. Unlike the results of the Smith and Smits<sup>7</sup>, these turbulence levels did not rapidly return to their upstream values.

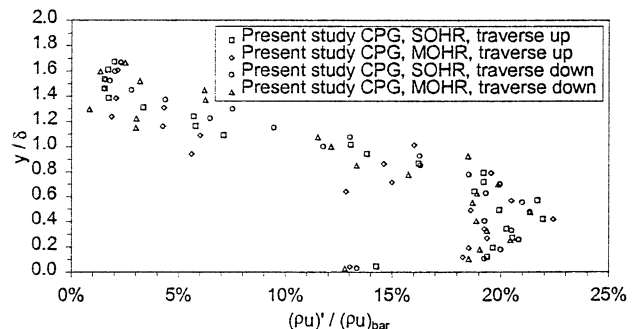


Figure 17: CPG mass flux TI

Hot-wires were used to interrogate the boundary layers to obtain energy spectra data. These results show the effect of the pressure gradient on the energy spectra. Figure 18 presents the energy spectra data for  $y/\delta = 0.33, 0.58$  &  $0.83$  for the ZPG flow. The data in Figure 18 indicates that the energy spectrum is relatively flat for frequencies less than about 20 KHz (i.e., corresponding to the larger scale eddies) at all 3 boundary layer locations. The near wall trace indicates a slightly higher dissipation rate in the 20 - 40 KHz range.

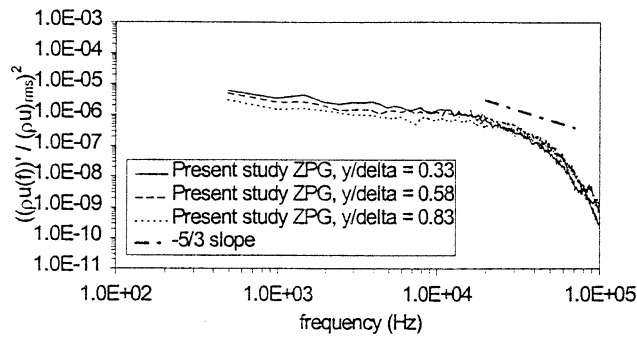


Figure 18: ZPG energy spectra data

Figure 19 presents the energy spectra for the FPG flow for  $y/\delta = 0.27$  and  $0.67$ . Overall, the large  $-dE/dk$  in the  $0.5 - 10$  KHz frequency range indicate that FPG/streamline curvature has increased the energy transfer rate to the smaller scales. This result is consistent with the observation for the PIV image (Figure 4), where it was noticed that the large scale structures were not apparent. If we consider what is happening from an impulse-particle point of view, the slower particles are exposed to the impulse (pressure gradient) for a longer period of time than the faster particles. Hence, the eddies thin in the streamwise direction. Clearly for the random shaped large scale structures, this results in a break down into smaller structures. If the expansion is strong and long enough the flow may relaminarize. This effect appears to be more profound at the lower frequencies for the  $y/\delta = 0.67$  trace where the  $dE/dk$  slope has a larger magnitude in the  $0.5 - 3$  KHz range as compared to the  $y/\delta = 0.27$  trace. On the other hand, at the higher frequencies, the eddies in the outer region contain more energy. This is the result of the increased transfer of energy from the large scales to the small scales in the outer region of the boundary layer. Nearer to the wall, the boundary layer is less populated with large scale structures, hence the “build up” of energy due to the FPG effects is less.

Figure 20 presents the energy spectra trace for the APG model for  $y/\delta = 0.21, 0.52$  and  $0.83$ . The most striking feature in these traces are at the low frequencies ( $\sim 0.5$  KHz), the relative energy levels are in order of magnitude higher than the ZPG flow. Also noting that  $(\rho u')^2_{rms}$  is roughly 40 - 50% larger for the APG as compared to the ZPG (see Figures 14 and 16), the amplification is even larger. This result is consistent with the destabilizing phenomena discussed in Spina et al.<sup>2</sup> It is insightful to consider the physics of the pressure gradient impulse on the turbulent eddy

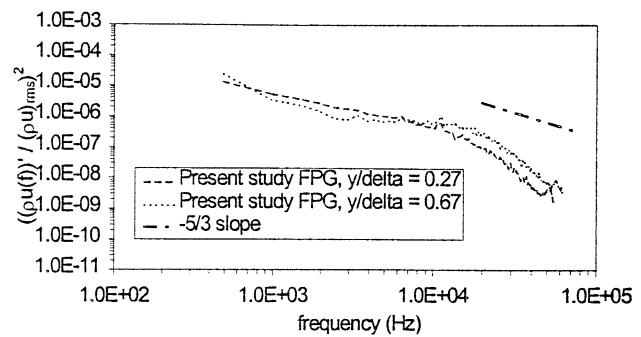
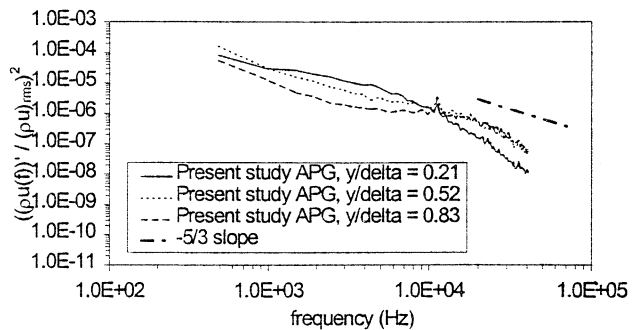


Figure 19: FPG energy spectra data

structures, where the slower particles are decelerated more due to their longer residence time within the impulse than the faster particles. Hence, the APG tends to “stretch” the eddy in the streamwise direction increasing turbulence fluctuations in that direction. These results are confirmed by the Mie image in Figure 3.

Like with the FPG flow, the magnitude of  $dE/dk$  is also increased across the boundary layer, where the outer region experiences the largest effect of the  $0.5 - 10$  KHz range and the near wall trace shows a larger decay rate in the high frequency range. At first when compared to Figure 19, these results seem counter intuitive. However, considering that the mean velocity profile was nearly unchanged for the APG flow as compared to the ZPG case (Figures 10 and 12), the trends in Figure 20 are more plausible. Specifically, the trends in Figure 20 and the unchanged nature of the velocity profiles indicate that increased low frequency turbulent energy is not being transferred back to the mean flow (otherwise, in a much fuller velocity profile would be expected). Thus, the viscous dissipation must increase. This conclusion is consistent with the increased heat transfer noticed for these flows (Spina et al).<sup>2</sup>

Figure 20: APG energy spectra data  
PIV Turbulence Results

The ZPG contour plot of TI is presented in Figure 21. The maximum TI is near the wall with a magnitude of 15%. This shows close agreement with the mass flux TI obtained via hot-film techniques (Figure 14). Regions of TI in excess of 20% in the freestream or near the wall are likely due to lack of seed resulting in insufficient data at those locations for some images. The TI gradient is resolved well throughout the boundary layer. The freestream TI is approximately 4%; this high value compared to the LDV or hot-film data is likely the result of the limited number of PIV images acquired.

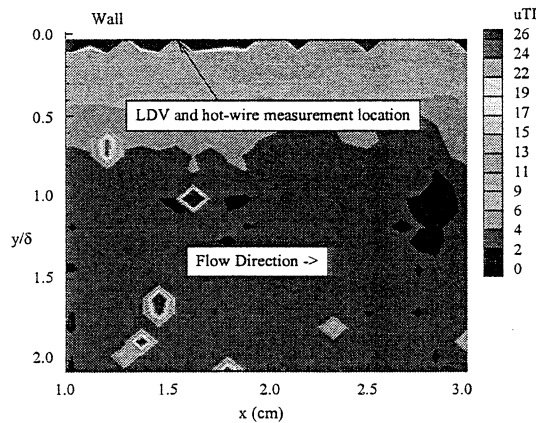


Figure 21: ZPG u TI contours (%)

Data were extracted from the PIV contour plots and compared to the present hot-film data (separated into velocities and density TIs with the Strong Reynolds Analogy and the assumption that  $p' \approx 0$ ). The LDV data of Luker [17] is also included. Klebanoff's [26] incompressible data is also included for comparative purposes. The line plot comparison is presented as Figure 22. In the boundary layer ( $y/\delta < 1.0$ ) there is close agreement between the LDV and PIV data. The hot-film, LDV and incompressible data all agree well. While the PIV data showed the same profile shape as the other sources of data, the TI levels were consistently 2 - 3% higher. The reasonable agreement demonstrated by the PIV data, considering the small sample size acquired, indicated that PIV could be used to examine planar TI trends.

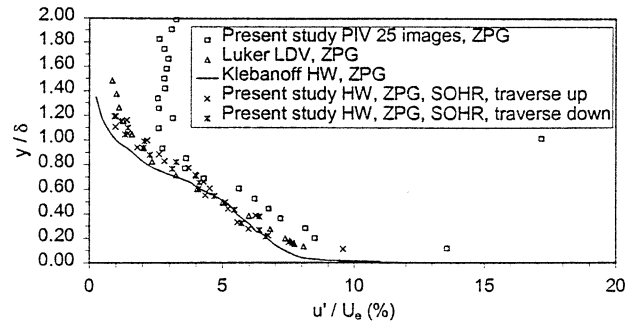


Figure 22: ZPG u TI profiles

Figures 23 and 24 presents the FPG, APG model TI contour plots. Although limited by the small sample sizes, the contours do confirm the trends discussed before. Before discussing those trends, the relatively high TI values in the freestream are the result of "holes" in the sample set due to window contamination or a lack of seed. The first trend that is readily visible in the contour plots is that the FPG model (Figure 23) boundary layer TI levels are consistently lower than the ZPG flow, for example, at the measurement location, the  $y/\delta = 0.4$  TI level was roughly 20% lower. On the other hand, for the APG measurement location (forward position indicated in Figure 24), the TI level @  $y/\delta = 0.4$  was roughly 25% higher than the ZPG flow. Hence, these data are in good agreement with the present hot-film data and the LDV data of Luker<sup>17</sup> and Hale.<sup>11</sup> Further, these data show that the boundary layer thickness increased for the FPG and decreased for the APG.

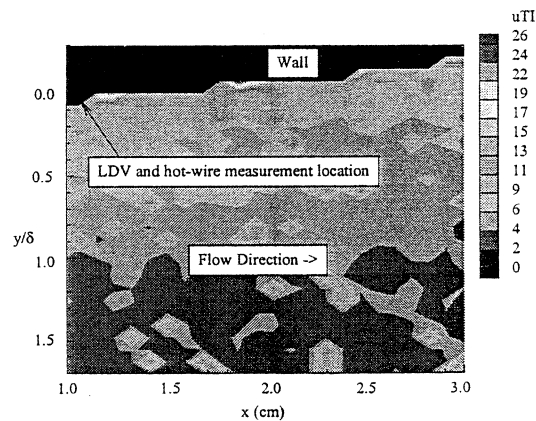


Figure 23: FPG u TI contours (%)

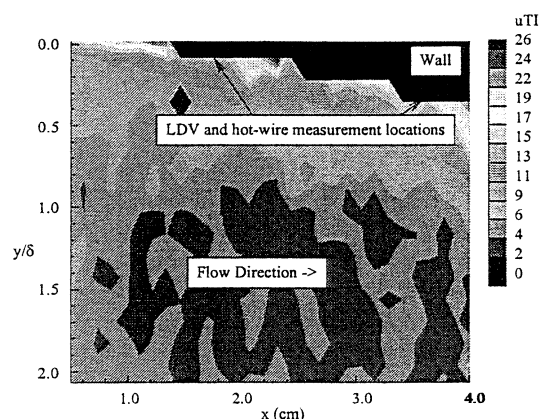


Figure 24: APG / CPG u TI contours (%)

### Conclusions

The main objective of this study was to examine the flow structure of supersonic boundary layers under the influence of pressure gradients. The objective was met by using a variety of measurement techniques (PIV, hot-wire, and Mie-scattering flow visualization) to provide empirical information. A secondary goal was the evaluation of digital two color PIV as a flow diagnostic tool for high-speed flows, where limited by sample size, the present study confirmed the accuracy of the PIV mean and first order turbulent statistics.

From the present data, a number of important conclusions about the influence of the wall curvature/pressure gradients on the turbulent flow structures were gleaned. First, the instantaneous (10 nsec) Mie scattering images indicated that the FPG boundary layer was thicker than the ZPG case, and the large scale structures clearly seen in the ZPG flow were not discernible. Conversely, the APG boundary layer was thinner, and the large scale structure angles were reduced (e.g., the structures "stretched" in the axial direction), where the structures spanned the entire boundary layer.

Both the PIV (velocity) and hot-film (mass-flux) axial turbulence intensity data showed the expected trends. The FPG was found to reduce the maximum mass flux TI by 25%, from 17% to 12.5%. The APG was found to increase the maximum mass flux TI 20% from the ZPG value. The CPG was found to increase the maximum mass flux TI 22% from the ZPG value. These results are consistent with the Mie scattering image observations. Although limited by a relatively small sample size, the PIV data confirmed that the trends seen in the profile data were consistent across the full curved wall regions.

Energy spectra measurements were taken for the three pressure gradient models with a hot-wire tuned to

give a high frequency response. Both curved wall models increased the rate of energy transfer from the large scales to the small scales (e.g.,  $dE/dk$  was greater with the FPG and APG than for the ZPG). This effect was found to depend on frequency and location in the boundary layer. For the present models, the outer region experienced the largest effect in the 0.5 - 10 KHz ( $k = 0.005 - 100$ ) range. The inner region experienced the largest effect in the high frequency region ( $k = 100 - 700$ ).

### Acknowledgments

The authors gratefully acknowledge Dr. James McMichael of the AFOSR for sponsoring this work. In addition, Dr. Abdollah Nejad (WL/POPT), Dr. Mark Gruber (WL/POPT), Dr. Larry Goss (ISSI) and Dr. Tzong Chen (Taitech Inc.) are acknowledged for providing the PIV equipment for these experiments.

### Uncertainty Analysis

The uncertainty estimates for hot-wire and PIV measurements are summarized in Table 2. The estimates account for uncertainties in hot-wire voltage and uncertainties in PIV signal to noise ratio.

Table 2: Uncertainty analysis results

Variable	Uncertainty Value
$\epsilon_{Me}$ (conventional probe)	0.60%
$\epsilon_{Til}$	5.1%
$\epsilon_y$	4.1%
$\epsilon_{\tau w}$ (Van Driest)	7.0%
$\epsilon_{(\rho u)}$ (hot-wire)	6.5%
$\epsilon_{(\rho u)'}'$ (hot-wire)	6.5%
$\epsilon_{p'}$ (hot-wire)	7.2%
$\epsilon_{u'}$ (hot-wire)	9.7%
$\epsilon_u$ (PIV)	3.0%
$\epsilon_{u'}$ (PIV)	3.0%

### Bibliography

<sup>1</sup>Bradshaw, P., "The Effect of Mean Compression or Dilation of the Turbulence Structure of Supersonic Boundary Layers," *Journal of Fluid Mechanics*, Vol. 63, Pt. 3, 1974, pp. 449 - 464.

<sup>2</sup>Spina, E. F., Smits, A. J., and Robinson, S. K., "The Physics of Supersonic Turbulent Boundary Layers," *Annual Review of Fluid Mechanics*, Vol. 26, 1994, pp. 287-319.



- <sup>3</sup>Robinson, S. K., Seegmiller, H. L., and Kussoy, M. I., "Hot-Wire and Laser Doppler Anemometry Measurements in a Supersonic Boundary Layer," AIAA-83-1723.
- <sup>4</sup>Johnson, Dennis A., and Rose, William C., "Laser Velocimeter and Hot-Wire Anemometer Comparison in a Supersonic Boundary Layer," *AIAA Journal*, Vol. 13, No. 4, April 1975, pp. 512-515.
- <sup>5</sup>Kistler, Alan J., "Fluctuation Measurements in a Supersonic Turbulent Boundary Layer," *The Physics of Fluids*, Volume 2, Number 3, May - June 1959, pp. 290-296.
- <sup>6</sup>Parrott, Tony L., Jones, Michael G., and Albertson, Cindy W., "Fluctuating Pressures Measured Beneath a High-Temperature, Turbulent Boundary Layer on a Flat Plate at a Mach Number of 5," NASA TP 2947, 1989.
- <sup>7</sup>Smith, D. R., and Smits, A. J., "The Effects of Streamline Curvature and Pressure Gradient on the Behavior of Turbulent Boundary Layers in Supersonic Flow," AIAA-94-2227.
- <sup>8</sup>Bradshaw, P., and Ferriss, D. H., "Calculation Boundary-Layer Development Using the Turbulent Energy Equation: Compressible Flow on Adiabatic Walls," *Journal of Fluid Mechanics*, Vol. 46, 1971, pp. 83 - 110.
- <sup>9</sup>Settles, Gary S., and Dodson, Lori, J., "Supersonic and Hypersonic Shock/Boundary-Layer Interaction Database," *AIAA Journal*, Vol. 32, No. 7, July 1994, pp. 1377 -1383.
- <sup>10</sup>Glawe D. D., Goss, L. P., Gogineni, S. P., Bowersox, R. D. W., Terry, W. F., and Dasgupta, S., "Digital Two-Color PIV Measurements in a Mach 2.8 Boundary Layer," AIAA paper 96-2799, 1996.
- <sup>11</sup>Hale, C. S. *Experimental Investigation of a Supersonic Boundary Layer Flow With Adverse Pressure Gradients*. MS Thesis. School of Engineering, Air Force Institute of Technology (AU), Wright-Patterson AFB OH, December 1995.
- <sup>12</sup>Lewis, J. E., Gran, R. L., and Kubota, T., "An Experiment on the Adiabatic Compressible Turbulent Boundary Layer in Adverse and Favorable Pressure Gradients," *Journal of Fluid Mechanics*, Volume 51, 1992, pp. 657-672.
- <sup>13</sup>Fernando, Emerick M., and Smits, Alexander J., "A Supersonic Turbulent Boundary Layer in an Adverse Pressure Gradient," *Journal of Fluid Mechanics*, Vol. 211, 1990, pp. 285 - 307.
- <sup>14</sup>Jayaram, M., Taylor, M. W., and Smits, A. J., "The Response of a Compressible Turbulent Boundary Layer to Short Regions of Concave Surface Curvature," *Journal of Fluid Mechanics*, Vol. 175, 1985, pp. 343-362.
- <sup>15</sup>Arnette, S. A., Samimy, M., and Elliot, G. S., "Structure of Supersonic Turbulent Boundary Layer After Expansion Regions," *AIAA Journal*, Vol. 33, No. 3, March 1995, pp. 430-438.
- <sup>16</sup>Luker, J. J., Hale, C. S., Bowersox, R. D. W., "Experimental Analysis of the Turbulent Shear Stresses for Distorted Supersonic Boundary Layers," AIAA paper 97-0426, 1997.
- <sup>17</sup>Luker, J. *Compressible Turbulence Measurements in a Supersonic Flow with Favorable Pressure Gradient*. MS Thesis. School of Engineering, Air Force Institute of Technology (AU), Wright-Patterson AFB OH, December 1995.
- <sup>18</sup>Miller, R. S. *Compressible Turbulence Measurements in a Supersonic Flow with Favorable Pressure Gradient*. MS Thesis. School of Engineering, Air Force Institute of Technology (AU), Wright-Patterson AFB OH, December 1994.
- <sup>19</sup>Gogineni, S., Goss, L., Glawe D., Bowersox, R., and Wier, R., "Digital Two-Color PIV and Flow Visualization Studies for Complex Supersonic Flows," ASME Fluids Engineering Division summer meeting, Vancouver, British Columbia, Canada, June 22 - 26, 1997.
- <sup>20</sup>Spina, E. F., *Organized Structures in a Supersonic Turbulent Boundary Layer*. Ph.D. dissertation, Princeton University, Princeton, New Jersey, 1988.
- <sup>21</sup>Dotter, J. W., *Compressible Turbulence Measurements in a Supersonic Flow with Adverse Pressure Gradients*. MS Thesis. School of Engineering, Air Force Institute of Technology (AU), Wright-Patterson AFB OH, December 1994.
- <sup>22</sup>Van Driest, E. R., "Turbulent Boundary Layer in Compressible Flows," *Journal of the Aeronautical Sciences*, Vol. 18, March 1951, pp. 145-160.
- <sup>23</sup>Evans, R. L., "Freestream Turbulence Effects on Turbulent Boundary Layers in an Adverse Pressure Gradient," *AIAA Journal*, Vol., 23, No. 11, November 1985, pp. 1814-1816.
- <sup>24</sup>Clauser, F. H., "Turbulent Boundary Layers in the Adverse Pressure Gradients," *Journal of the Aeronautical Sciences*, Vol. 21., Feb. 1954, pp. 91-108.
- <sup>25</sup>Coles, D. E., "The Wall of the Wake in the Turbulent Boundary Layer," *Journal of Fluid Mechanics*, Vol. 1, 1956, pp. 191-226.
- <sup>26</sup>Klebanoff, P. S., "Characteristics of Turbulence in a Boundary Layer With Zero Pressure Gradient," NASA TN 3178, July 1954.

### **2.1.7 Pressure-Sensitive-Paint Technique**

Pressure-sensitive-paint (PSP) development in this program focused on turbomachinery applications; this required the development of robust high-temperature and high-pressure paints capable of withstanding extremely adverse environments. The paper entitled “Sol-Gel-Based Pressure-Sensitive Paint Development” (see pp. 137-146) discusses the development of a new series of pressure paints especially designed for harsh conditions. Improvements were also required in the analysis of data from PSP images. The publication entitled “Data Analysis Methods for the Development and Deployment of Pressure-Sensitive Paints” (see pp. 147-158) discusses improved approaches to image registration during data analysis. The results of pressure and temperature measurements on the suction surface of a first-stage rotor are reported in the paper entitled “Optical Measurements of Surface Pressure and Temperature in Turbomachinery” (see pp. 159-171). Application of the PSP technique to supersonic flowfields is discussed in the publication entitled “Effects of Mach Number on Supersonic Wraparound Fin Aerodynamics” (see pp. 172-178).

## SOL-GEL-BASED PRESSURE-SENSITIVE PAINT DEVELOPMENT

Jeffrey D. Jordan,\* A. Neal Watkins,\* William L. Weaver,\* AFRL  
Innovative Scientific Solutions, Inc. (ISSI), Dayton, OH 45440-3638

Gary A. Dale,† AFRL/VAAA and Kelly R. Navarra,† AFRL/PRTF  
Wright-Patterson Air Force Base, OH 45433-7251

### Abstract

This paper describes recent advances in the development of sol-gel-based pressure-sensitive paints (PSPs) for the investigation of low-speed-flow aerodynamics. Sol-gel-based materials are an attractive PSP binder matrix because of their robust material characteristics and compatibility with optical measurements. Preparation and application techniques have been developed to adapt the advantages of sol-gel thin-film technology to the development of pressure-sensitive coatings. Sol-gel-based PSPs have been produced that exhibit satisfactory sensitivity for small changes in pressure about ambient ( $\leq 6\%/psi$  for  $14.7 \pm 2$  psia) and low temperature sensitivity ( $\sim 0.80\%/^{\circ}C$ , for  $-10 \leq T \leq 100^{\circ}C$ ). Sol-gel PSP platforms have demonstrated stability and sensitivity at temperatures ranging from  $-123$  to  $+150^{\circ}C$ . Bi-luminophore self-referencing paints (SRP) are under development that eliminate the need to acquire wind-off images, greatly minimizing wind-tunnel downtime. The temporal response of the sol-gel-based PSPs has been determined using a newly developed instrument. In this paper, we present an introduction to sol-gel-processed materials and outline their application in two low-speed wind-tunnel tests.

### Introduction

The ability to make an accurate determination of pressure and temperature distributions over an aerodynamic surface based on the emitted luminescence signal from a coating has attracted much attention in the aerospace community.<sup>1-13</sup> PSP measurements exploit the oxygen ( $O_2$ ) sensitivity of luminescence probe molecules dispersed within gas-permeable binder materials. The mechanism for temperature-sensitive paint (TSP) sensitivity is based on thermal-deactivation processes inherent in the probe species, and temperature-dependent viscosity changes of the binder.<sup>14</sup>

In the design of PSP coatings, the polymeric support dictates the thermal and mechanical stability, adherence characteristics, and surface roughness, while contributing to the pressure and temperature sensitivity and temporal response. Control of these parameters would allow the formation of PSP systems ideally suited for particular test conditions (P, T) of interest. Recently, the development of PSPs has been complemented by sol-gel technology.<sup>13</sup> The sol-gel process allows the formation of controlled-pore glasses under ambient conditions of temperature and pressure.<sup>13, 15-17</sup> Sol-gel processing involves the transition of a solution phase into a gel; this is followed by densification and loss of solvent, ultimately resulting in a solid, optically transparent glass. In a generic sense, sol-gel-processing chemistry is represented by the five-step process, shown in Figure 1.

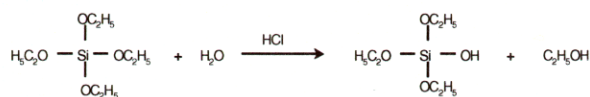
---

\* Analytical Chemist, AIAA Member

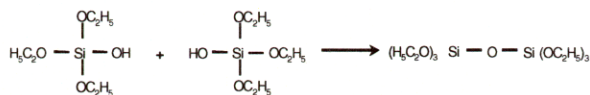
† Mechanical Engineer, AIAA Member

This paper is declared a work of the U.S.  
Government and is not subject to copyright  
protection in the United States.

*Hydrolysis* TEOS, tetraethylorthosilicate



*Condensation*



*Polycondensation*

Formation of 3D matrix

*Aging/Drying*

Expulsion of solvent  
Composite strength increased

**Figure 1. Sol-gel-processing chemistry.**

The process is initiated by the acid or base-catalyzed hydrolysis of a metal or semi-metal alkoxide such as tetraethylorthosilicate (TEOS) to form the hydrated product. Condensation of these moieties results in the formation of metal-oxygen-metal bonds (Si-O-Si) and a colloidal mixture termed a sol. Polycondensation of these species results in the formation of a three-dimensional network and macroscopic solid, as defined by the gelation point. Subsequent aging and drying of the composite film causes the expulsion of solvent from the matrix, which increases the composite strength. Host composites for chemical-sensing applications can be easily produced in this manner by incorporating recognition elements (RE, e.g., probe molecules) directly into the sol-gel-precursor solution, followed by thin-film deposition. In this manner, the RE is entrapped within the porous matrix, and a significant population remains accessible to the external analyte. In addition, the molar ratio of sol-gel precursors, hydrolysis time and temperature, and aging and drying conditions affect the sol-gel-processing chemistry and, thus, the physicochemical properties of the final composite (e.g., porosity, polarity).<sup>13, 15-17</sup>

Conventional methods of sol-gel thin-film formation include dip-coating and spin-coating techniques in which a test substrate is submerged within a sol-gel solution or mechanically rotated to coat a surface via centrifugal force. Both methods require large volumes of coating solution (paint), the majority of which is wasted in the coating process. Moreover, neither technique is amenable to uniform thin-film formation on test articles of irregular geometry such as aerodynamic test models. Therefore, it became clear that new methods for the formation of thin, uniform films were required for full exploitation of the advantages of sol-gel-processed materials for PSP development. To this end, we developed a pressure-based aerosol deposition technique for the formation of thin, uniform sol-gel-derived PSPs. Previous work<sup>13</sup> has shown that the deposition approach employed can

dramatically affect sensor performance in addition to macroscopic material properties. For example, scanning electron microscopy (SEM) and surface-profile experiments were performed for both aerosol-generated and spin-coated sol-gel-processed films, and the results are shown in Figure 2.

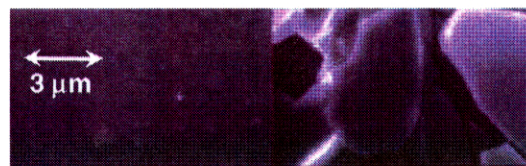


**Figure 2. Scanning electron micrographs of sol-gel-derived thin films formed using aerosol deposition (left) and spin coating (right).**

The films shown above were 2.0 μm in thickness. It is clear that the aerosol-deposition approach (left image) produced a thin, uniform surface with very low surface roughness (< 0.1 μm). In contrast, the conventional spin-coating technique (right image) produced an unstable, highly cracked film unsuitable for PSP applications.

The use of sol-gel-derived composite coatings as platforms for chemical and biological sensors has been demonstrated.<sup>13, 15-17</sup> Typically, successful applications of these coatings involve deposition onto silicon substrates such as glass or quartz. Adaptation of this technology for commercial and military wind-tunnel applications that employ test models made from various metallic and ceramic materials introduces two additional challenges associated with coating adherence and substrate-induced quenching of the entrapped probe species via phonon coupling to the surface. To overcome these difficulties, we identified a suitable commercially available white base-coat material. The base coat simultaneously improves sol-gel adherence to the surface, eliminates substrate-induced quenching of the sol-gel-entrapped probe, increases PSP output signal (multiple reflections), maintains pressure sensitivity, and masks test-surface irregularities.

Application of sol-gel-derived composites to PSP technology offers several attractive features. First, sol-gel-derived coatings are characterized by high thermal stability and, therefore, exhibit very low temperature-dependent viscosity changes. Second, the aerosol-based deposition technique allows the formation of thin, uniform films that are optically transparent, robust, and smooth.<sup>13</sup> Furthermore, these coatings can be easily removed by destabilizing the base coat with a mild solvent (e.g., alcohol, acetone), leaving the test surface unaffected. Third, sol-gel thin films exhibit excellent loading capabilities, allowing multiple probe species to be incorporated into the same film at higher



concentration for increasing output signals. Finally, novel thin-film architectures have been designed that provide a convenient means of optimizing the sensitivity of these composite coatings for the specific pressure and temperature regimes of interest.

## Applications

### Extending Temperature Capabilities

The temperature capability of PSPs is dominated by the probe and binder thermal stability, the temperature dependence of the binder viscosity, and the robustness to temperature cycling. The low viscosity vs. temperature dependence of sol-gel-based composites coupled with their high-temperature stability (can be sintered at  $> 1000^{\circ}\text{C}$ ) makes these materials attractive candidates for extreme-temperature applications. Figure 3 shows pressure-sensitivity data for a sol-gel-based PSP incorporating a ruthenium bathophenanthroline (RB) pressure probe.

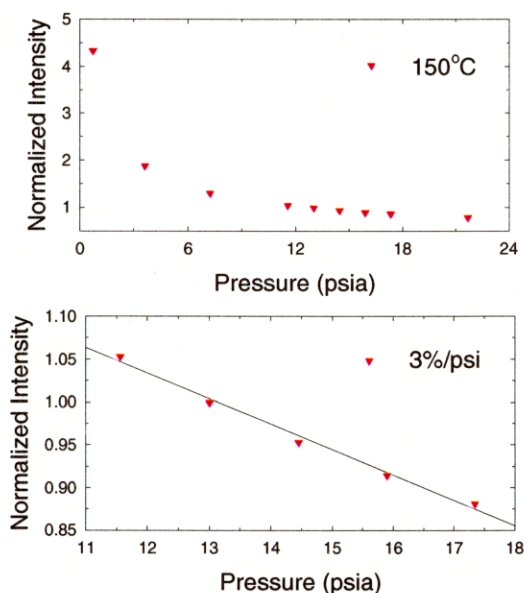


**Figure 3. Pressure sensitivity of a RB-doped sol-gel PSP at  $150^{\circ}\text{C}$ .**

These data illustrate the utility of sol-gel-based PSPs for probing surface-pressure distributions to at least  $150^{\circ}\text{C}$ . This temperature represents a limitation of our current calibration cell; a higher temperature ( $250^{\circ}\text{C}$ ) and pressure (100-psia) calibration chamber is under construction.

High-Reynolds-number facilities such as the 0.3-m transonic cryogenic wind tunnel (0.3-m WT) and the National Transonic Facility at NASA Langley Research Center require PSPs exhibiting cryogenic stability and pressure sensitivity over a broad temperature range

( $\sim -170$  to  $+30^{\circ}\text{C}$ ).<sup>5-7</sup> Toward that end, we have pursued the development of sol-gel PSPs for cryogenic applications. Figure 4 shows pressure-calibration data acquired at Purdue University in the laboratory of Professor John Sullivan at temperatures ranging from  $-173$  to  $-50^{\circ}\text{C}$ .

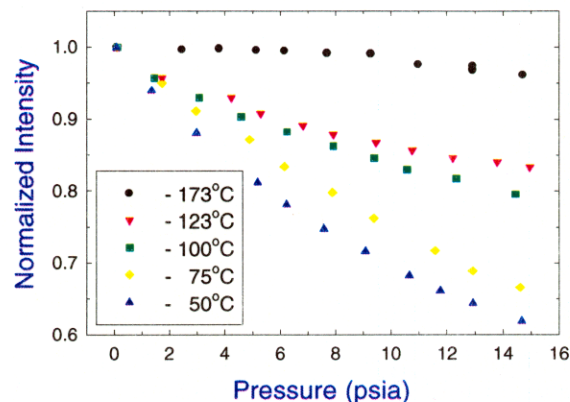


**Figure 4. Pressure sensitivity of a Pt(TfPP)-based sol-gel PSP at cryogenic conditions.**

The data show relatively low sensitivity down to  $-123^{\circ}\text{C}$  ( $\sim 1\%/\text{psi}$ ), diminishing to the negligible response observed at  $-173^{\circ}\text{C}$ ; however, the potential of sol-gel-derived materials as cryogenic PSP platforms is evident.

The dependence of pressure on PSP temperature sensitivity is an important issue for the correction of PSP data using the in situ calibration method.<sup>3</sup> Figure 5 shows normalized intensity ( $T = 20^{\circ}\text{C}$ ) vs. temperature data at near-vacuum (1.4 psia) and ambient (14.7 psia) pressure conditions.

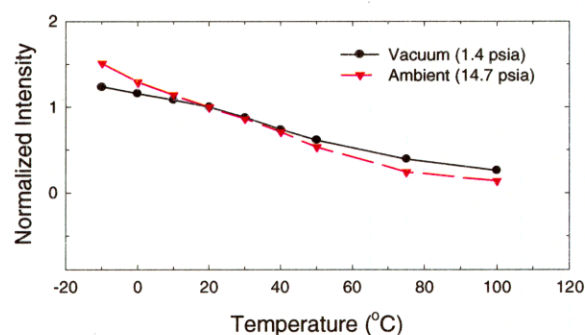


**Figure 5. Pressure dependence of PSP temperature sensitivity.**

The data show that the temperature sensitivity is independent of pressure over the temperature range  $10$  -  $40^{\circ}\text{C}$ . This is indicated by the convergence of the low- and high-pressure data to the same slope over the



temperature range encountered under low-speed flow conditions (10 - 40°C).

### Low-Speed Aerodynamics

For most low-speed flow applications, the critical issues are PSP low signal output and sensitivity at near-ambient pressure ( $14.7 \pm 2$  psia).<sup>8,9</sup> The key issues governing pressure sensitivity include the probe luminescence lifetime ( $\tau$ ), quantum efficiency ( $\phi_e$ ), and accessibility to molecular oxygen ( $O_2$ ).<sup>14</sup> Lifetime and quantum-efficiency characteristics of a PSP are dominated by the photophysics of the luminescent species. Probe accessibility to  $O_2$  determines the efficiency of the quenching process and is modulated by the porosity or void volume of the polymeric support matrix.

In general, higher PSP luminescence output can be obtained by increasing the concentration of probe species in the binder. The upper limit of this loading capability is dictated by the characteristics of the polymeric binder and its ability to maintain probe separation. In this way self-absorption phenomena that result in decreased luminescence output can be avoided.<sup>14</sup> The porous network within sol-gel composites serves to maintain separation between probe species, supporting probe loadings as high as 4 mg/mL.

Sol-gel processing also provides a mechanism for increasing the pressure sensitivity for small changes in pressure about ambient. Figure 6 shows pressure-sensitivity data for a series of sol-gel formulations (F1 – F6) incorporating the pressure probe Platinum meso-Tetra(pentafluorophenyl) porphine (PtTfPP).

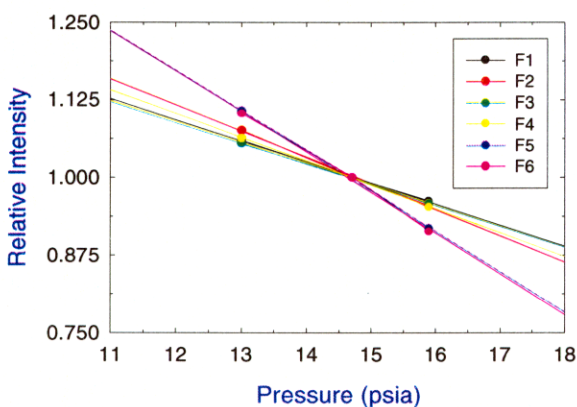


**Figure 6. Increasing near-ambient PSP pressure sensitivity via sol-gel processing.**

These data illustrate the utility of sol-gel processing as a means of tailoring PSP performance

characteristics by controlling the porosity of the support matrix. For example, manipulation of the sol-gel processing variables (e.g., hydrolysis time, temperature, precursor identity) increased the near-ambient pressure sensitivity of the resulting PSPs by a factor of two.

PSP tests were performed in the 5-ft low-speed wind tunnel at Wright-Patterson AFB in collaboration with the Air Force Institute of Technology (AFIT). This closed-loop facility is driven by two DC motors with current top speed of ~ Mach 0.15.

The test article under investigation was a model laser-communication turret for a T39 aircraft with two fairing configurations for reduced drag. The photographs shown in Figure 7 depict the unpainted (upper left) and painted (lower left) test article, a member of the ISSI PSP team prepping and painting the model (upper right), and an upstream view of the model under nine blue- (460-nm) LED illumination sources.

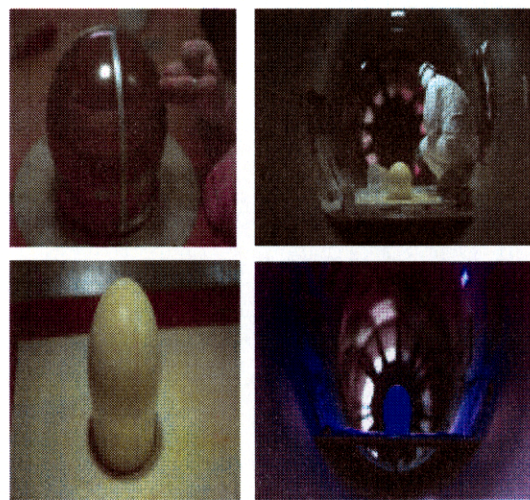


**Figure 7. PSP test on a T39 laser-communication turret in the 5-ft low-speed wind tunnel at Wright-Patterson AFB.**

For this test, the turret, the ground plane, and two fairings were coated with a RB-based sol-gel PSP, which appears yellow and emits red-orange (~ 610-nm) luminescence under the appropriate illumination.

Conventional wind-off/wind-on referencing was performed and data acquired as a function of air speed and fairing configuration. Preliminary data for the fairing-on configuration are shown in Figure 8.



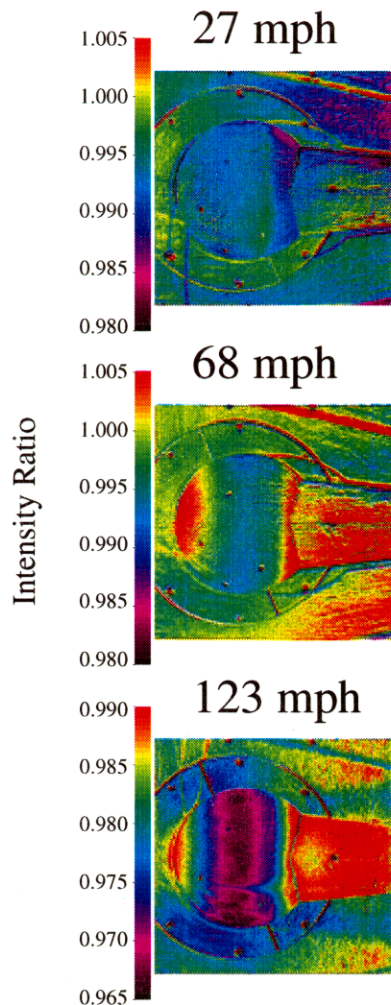


**Figure 8. Preliminary PSP intensity-ratio image of a T39 laser-communication turret at three velocities.**

Pressure-tap data was acquired during these tests, and is currently being employed for in situ calibration by Air Force personnel using the Greenboot™ software. Temperature-corrected pressure data is forthcoming.

The intensity output and near-ambient pressure sensitivity of the sol-gel-based PSPs, coupled with the stability of LED lamps, provided adequate signal-to-noise (S/N) for the recovery of surface-pressure measurements at wind speeds as low as 27 mph.

Recently, we had the opportunity to run sol-gel PSPs in the 0.3-m WT, which is used for testing two-dimensional airfoil sections and other models at high Reynolds numbers. This test was run under ambient-temperature air at low speed. The model was a supercritical airfoil designated SC3. A Pt(TfPP)-based sol-gel low-speed PSP was applied to a portion of the model, with nine registration marks subsequently being drawn on the paint with permanent marker, as shown in Figure 9.

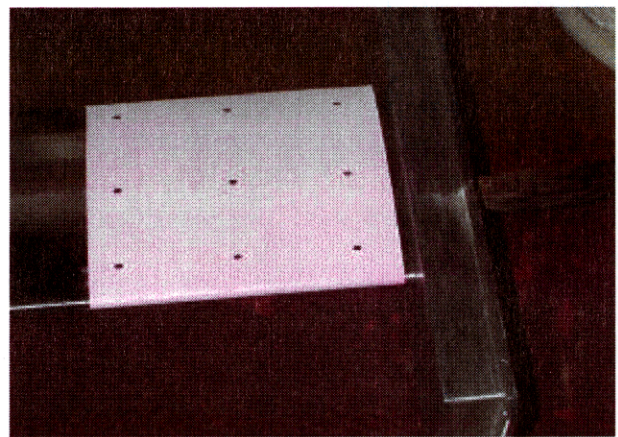


**Figure 9. Pt(TfPP)-based sol-gel PSP applied to SC3 model in the 0.3-m TCT at NASA Langley.**

Images were acquired using a 512 x 512 14-bit CCD camera with the model at 10° alpha under wind-off conditions and at Mach numbers of 0.15, 0.25, and 0.50 (ambient air). The data were analyzed by Langley personnel using the Greenboot™ software and the in situ calibration method; the results are shown in Figure 10.



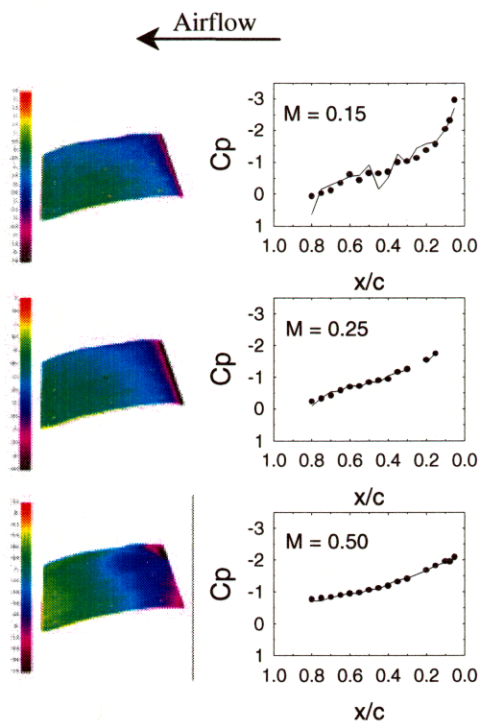


**Figure 10. Pressure distribution across chord of SC3 model at three velocities.**

The plots to the right of each image show a comparison of the pressure coefficient ( $C_p$ ) recovered from the pressure-tap (points) and PSP data (line). Good correlation was observed at  $M = 0.25$  and  $0.50$ , with slight deviation at the lowest velocity investigated ( $M = 0.15$ ), demonstrating the capability of PSP-based techniques for the measurement of 2D surface-pressure distributions at low velocity.

### **Self-Referencing Paints**

Self-referencing paint (SRP) systems provide a convenient means of eliminating the wind-off reference image. In these schemes a reference image is acquired at condition and ratioed with the pressure image. At a minimum, SRPs require a luminescent species sensitive to pressure and a probe insensitive to both pressure and temperature. In this fashion, the reference signal corrects for nonuniformities in the illumination field and coating application, provided both probes are homogeneously distributed throughout the same layer. Therefore, the critical features governing SRP development include the spectral and temporal emission

characteristics of the pressure and reference probes, energy-transfer concerns, and matrix effects.

For SRP development, overlap of the absorbance and emission spectral profiles of the pressure and reference probes provides a means of radiative energy transfer, the effect being the pumping of the absorbance band of one species by the emission band of the other. For most systems, this type of energy transfer will be unavoidable. Therefore, it is clear that selection of the spectral properties of component luminescent species is critical to successful SRP design. Moreover, the direction of the energy-transfer process can directly bias the intensity measurement. Consider, for example, a system consisting of a PSP deposited over an insensitive reference paint (ISP), where energy transfer from the higher-energy (blue-shifted) ISP emission to the lower-energy PSP absorbance occurs. In this case illumination of the SRP would excite both the ISP and PSP directly and would initiate energy transfer, resulting in a decrease in ISP signal and concomitant increase in PSP signal. For the reverse case, it is clear that energy transfer from PSP to ISP would result in pressure-dependent excitation of the ISP, eliminating the utility of the reference signal.

PSP/ISP systems allow illumination nonuniformities to be taken into account through image ratioing. Because the ISP and PSP are applied as individual layers, signal ratioing will not account for coating heterogeneity. In fact, coating error is compounded because of the need for two paint applications. Thus, the advantage of single-layer biluminophore SRP systems becomes evident.

In single-layer SRP coatings, intermolecular effects between pressure and reference probes must be considered in addition to spectral-overlap concerns. Sol-gel-derived films have been shown to exhibit excellent loading capabilities due to the ability of the microporous network to isolate dopant species.<sup>13, 15-17</sup> This feature minimizes intermolecular aggregation and clustering that can result in self-quenching and self-absorption phenomena, leading to decreased performance.

We have produced a series of sol-gel-based SRPs using Pt(TfPP) and RB as the pressure probe and a series of Coumarin laser dyes as the reference. Figure 11 shows typical pressure- and temperature-sensitivity calibration data for biluminophore RB-based SRP coatings using LD466, Diethylaminocoumarin (DAC), and Coumarin 500 (C500).



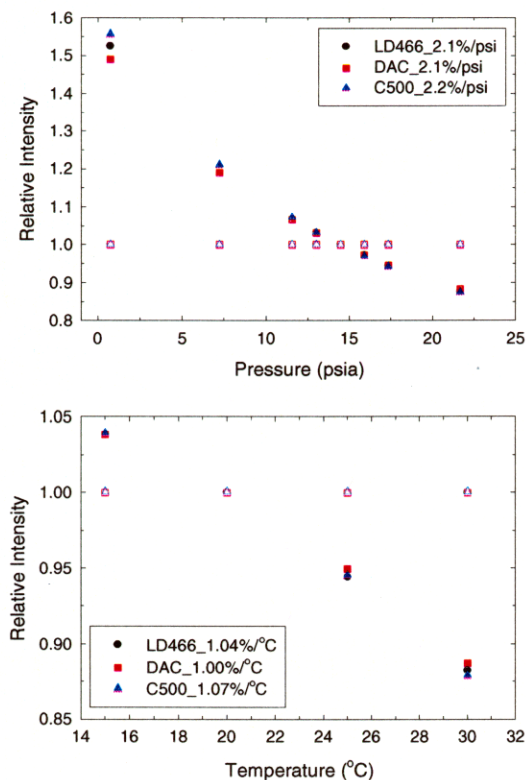


**Figure 11. Pressure-sensitivity calibration data for sol-gel-based biluminophore SRP.**

The RB-based SRPs exhibit  $\sim 2.1\%$  intensity change per psi for small changes in pressure about ambient ( $14.7 \pm 2$  psia), with low temperature sensitivity ( $\sim 1\%/^{\circ}\text{C}$ ). Reference signals from the three probes (open symbols) investigated were independent of pressure and temperature.

To test the self-referencing capabilities of the RB-based SRPs, a low-speed air jet was positioned  $\sim 80^{\circ}$  relative to a RB/LD466-based SRP-coated coupon. Sample illumination was provided by the output of a blue-LED array and images acquired using a  $512 \times 512$ , 16-bit CCD camera. The pressure and reference signals were acquired through  $600 \pm 50$  nm and  $500 \pm 50$  nm band-pass filters, respectively. Pressure and reference images were acquired with and without the impinging jet. To simulate changes in the illumination field between the wind-off and wind-on measurements, the LED lamp was pulled back from the sample and rotated with respect to the sample surface to produce a glare prior to jet initiation. Conventional ratiometric (wind off/wind on) analysis was performed for the same illumination configuration and compared to a “ratio-of-ratios” methodology. In the latter approach, pressure (P) and reference (R) images were acquired under

wind-off (off) and wind-on (on) conditions employing the different illumination configurations denoted by the subscripts 1 – 3 in the cartoon (Figure 12, upper panels). The pressure image at each condition was divided by the corresponding reference image and the ratio of ratios manifest as the quotient of the “off” ( $[P_{\text{off}}/R_{\text{off}}]_1$ ) and “on” ( $[P_{\text{on}}/R_{\text{on}}]_2$ ) terms, as shown in Figure 12.

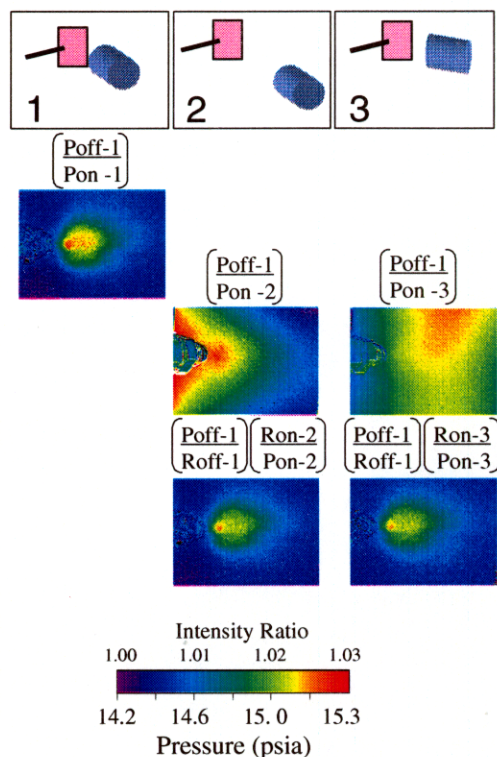


**Figure 12. Low-speed (< 1 psig) air jet impinging on a sol-gel SRP coating. Cartoon depicting various illumination configurations (top). Ratioed wind-off, position 1/wind-on at position 1 (upper) image, and positions 2 and 3 images (middle). Self-referenced images (lower).**

The intensity-ratio image (Figure 12, upper image) is the experimental control since wind-off and wind-on images were acquired under the same illumination field. If the wind-off pressure image under configuration 1 (Poff-1) is ratioed with the pressure image at conditions 2 and 3 (Pon-2,3), the middle images result. The deviation in the illumination field resulted in a loss of the jet profile. The ratio-of-ratios results (Figure 12, lower images) demonstrate the utility of the reference signal for correcting illumination nonuniformities between the pressure wind-off and wind-on conditions.



Similar results were observed for the RuB SRPs incorporating DAC and C500.

One disadvantage of the ratio-of-ratios technique is the error associated with the additional coordinate-mapping steps. A more attractive approach would eliminate the need to acquire any wind-off images. The primary challenge in this regard is the difference in quantum efficiency (QE) of the pressure and reference probes. For example, QE data for PtTfPP and the reference probe Coumarin 540 (C540) are shown in Figure 13.

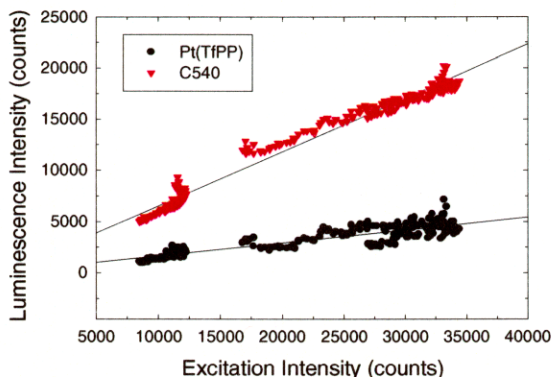


**Figure 13. Recovered luminescence intensity for PtTfPP (●) and C540 (●) as a function of excitation intensity.**

In this experiment, the excitation intensity was acquired by imaging an SRP-coated sample through a band-pass filter (450 nm) coincident with the spectral profile of the source. The luminescence intensity values of the Pt(TfPP) and C540 were determined using 650-nm and 550-nm band-pass filters, respectively. These data show the effect of excitation intensity on the luminescence output of the pressure (PtTfPP) and reference (C540) signals. The difference in slope is due to the higher QE of the C540 and illustrates why direct ratioing of reference and pressure images at condition does not correct for non-uniformity in the illumination field. In other words, the intensity ratio of the C540 to Pt(TfPP) signals is not constant as a function of excitation intensity. However, if the transform between the reference and pressure intensities is determined a priori for a given SRP, then a pressure “wind-off” image can be generated from the reference data acquired at condition on a pixel-by-pixel basis. If this process is successful, the result will be an analysis technique that does not require the acquisition of wind-off images. In addition, minimal image registration/resection will be required to align the pressure and reference images since both are acquired

at the same condition with the model under the same aerodynamic load. Investigation of this approach is continuing.

### **High-Frequency Response**

Characterizing the transient response of PSPs to unsteady pressure flows is a critical aspect in assessing the capabilities of a given formulation. Carroll, *et al.*<sup>10,11</sup> previously developed an apparatus capable of delivering a step change in pressure and reported response times (on the order of 1 s) for proprietary PSP formulations tested. Sub-millisecond response times have also been measured using an instrument and post-processing software developed by Baron, *et al.*<sup>12</sup> In previous studies conducted by our group,<sup>13</sup> a pressure-jump apparatus was constructed and used to measure PSP response times on the order of 1 ms.

To quantify the dynamic-response characteristics of the sol-gel-based PSP formulations, we constructed a high-frequency PSP instrument that allows periodic changes in the pressure at frequencies ( $\nu$ ) from 20 Hz to a few hundred kilohertz (kHz). [ $\Delta P \leq 1$  psi for  $\nu \leq 1$  kilohertz (kHz);  $\Delta P \leq 0.01$  psi for  $\nu \geq 1$  kHz]. The system is depicted in Figure 14.

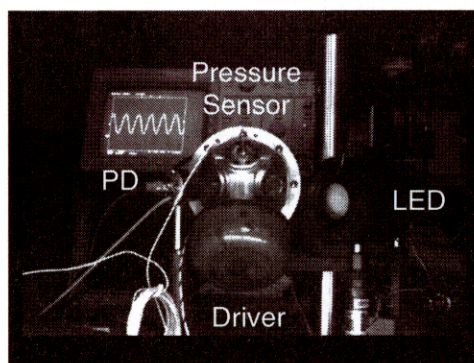


**Figure 14. High-frequency calibration rig.**

A PSP-coated sample coupon is rigidly fixed within a four-port pyramidal pressure cell. Excitation of the sample is provided through one port by an LED array (LED), and luminescence detection is accomplished by a photodiode (PD). The speaker driver (Driver) is attached to one of the ports of the chamber and supplies the oscillating pressure waves. A Kistler® piezoresistive pressure sensor, capable of measuring pressure changes up to a few tens of kHz, is used to measure pressure oscillations in the cell. Data are collected using a dual-phase lock-in amplifier. The amplifier is employed to detect very small AC signals and is especially useful for measuring signals that are obscured by large amounts of noise—it detects the



response at a given frequency and discriminates against all other responses outside a very small bandwidth about the target frequency.

In our experiments, the lock-in amplifier is used as both the excitation source and the detector. The output of the internal oscillator of the lock-in is used to drive the speaker amplifier at a given frequency (the lock-in can generate and measure frequencies from 1 mHz to 102 kHz), which also acts as the center of the band-pass frequency for measurement. The output of the photodiode or pressure transducer is sent to the lock-in, which amplifies the response about the reference signal, thus attenuating most of the noise in the measurement. The lock-in then measures both a DC signal that is proportional to the amplitude of the incoming signal and the phase lag between the incoming signal and the reference frequency.

To make data collection both easy and rapid, the lock-in amplifier was interfaced to a computer via its internal GPIB card. The data-acquisition program was written in LabWindows®/CVI™. The lock-in amplifier is used to collect the photodiode response both with and without illumination (to account for any background effects) as well as the pressure-transducer response (to determine the pressure fluctuation at each frequency). The phase of each response was also determined. The amplitude and phase of each result was then saved to a file for post-processing. An aluminum coupon coated with a RB-based sol-gel PSP (~ 2- $\mu$ m thick) was investigated using the lock-in to acquire frequency-response data. The response of the RB-based PSP at 600 Hz is shown in Figure 15.

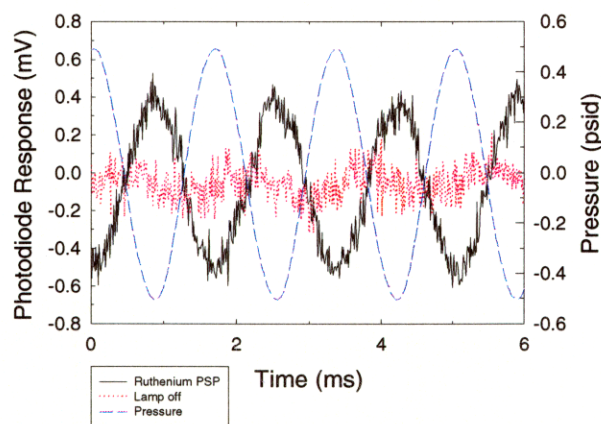


**Figure 15. Temporal response of PSPs to oscillating pressure fields.**

The data reveal feedback occurring at the higher frequencies, as evidenced by the oscillation observed in the photodiode signal at 600 Hz with the lamp off (smallest signal). Analysis of the amplitude of the data

was accomplished by subtracting the lamp-off data from the PSP response to account for electromechanical interference. The amplitude was then divided by the amplitude of the pressure-sensor response curve to account for differences in pressure between experiments. The response of the RB-based PSP is shown in Figure 16.

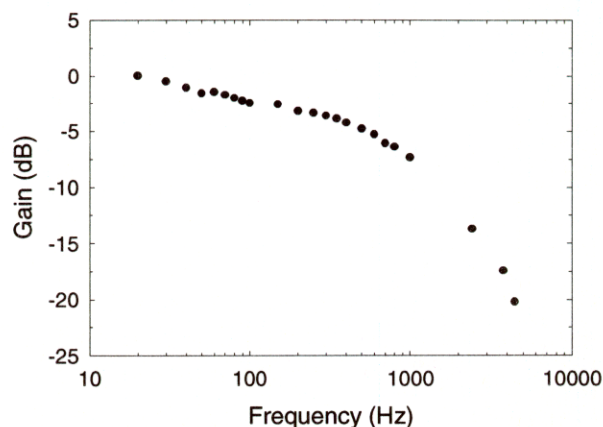


**Figure 16. Amplitude response of the RB-based PSPs to oscillating pressure fields.**

The RB-based PSP exhibits response to at least 1 kHz, with measurable AC signals extending past 5 kHz. In the current embodiment, a siren driver is used to generate unsteady pressure modulations in the range 20 – 1000 Hz. To access frequencies greater than 1 kHz, a piezoelectric driver is used. The high frequency (> 1 kHz) sensitivity is currently limited by the low output of the piezoelectric speaker driver ( $\sim 14.7 \pm 0.01$  psia). High-frequency drivers that provide higher-pressure output are being sought.

### Summary

Sol-gel-based PSP platforms have been developed that are suitable for a range of aerodynamic testing applications. Pressure sensitivity from ca. -150 to +150°C has been demonstrated. The high loading capabilities of the sol-gel composites have been exploited to produce PSPs with high intensity and sensitivity at ambient pressure. Sol-gel PSPs have been successfully deployed in low-speed wind-tunnel tests, recovering surface-pressure distributions at speeds as low as 27 mph. Self-referencing paints have been developed by the incorporation of pressure and reference probe species within the same sol-gel film to produce bi-luminophore coatings suitable for providing reference data at condition and minimizing wind-tunnel downtime. High-frequency response to small pressure modulations about ambient have been observed for the

sol-gel coatings using a newly developed calibration instrument. Current efforts focus on 1) improving existing SRP platforms through optimization of the data-reduction algorithm and inclusion of internal temperature compensation, 2) increasing the pressure sensitivity under extreme-temperature conditions, and 3) increasing the high-frequency response.

### References

1. Kavandi, J. Callis, J. Gouterman, M. Khalil, G., Wright, D., Green, E., Burns D., and McLachlan, B., "Luminescence Barometry in Wind Tunnels," *Reviews of Scientific Instrumentation*. 61(11), 3340 – 3349, 1990.
2. Morris, M. J., Donovan, J. F., Kegelman, J. T., Schwab, S. D., Levy, R.L., and Crites, R. C. "Aerodynamic Applications of Pressure Sensitive Paint," AIAA Paper 92-0264, 1992.
3. McLachlan, B. G., and Bell, J. H., "Pressure-Sensitive Paint in Aerodynamic Testing," *Experimental Thermal and Fluid Science*, Vol. 10, 470 - 485, 1995.
4. Liu, T., Campbell, B. T., Burns, S. P., and Sullivan, J. P., "Temperature- and Pressure-Sensitive Luminescent Paints in Aerodynamics," *Applied Mechanics Reviews*, 50(4), 227 – 246, 1997.
5. Erausquin, R. Jr., Cunningham, C., Sullivan, J. P., Asai, K., Kanda, H., Kunimasu, T., and Iijima, Y., "Cryogenic Pressure Sensitive Fluorescent Paint Systems," AIAA Paper 98-0588, 1998.
6. Asai, K. Kanda, H., and Kunimasu, T., "Detection of Boundary-Layer Transition in a Cryogenic Wind Tunnel by Using Luminescent Paint," AIAA Paper 96-2185, 1996.
7. Asai, K., Kanda, H., Cunningham, C., Erausquin, R., Sullivan, J., "Surface Pressure Measurement in a Cryogenic Wind Tunnel by Using Luminescent Coating," ICIASF, Monterey, CA, 1997.
8. Shimbo, Y., Mehta, R. D., Cantwell, B. J., Vortical Flow Field Investigation Using the Pressure Sensitive Paint Technique at Low Speed," AIAA Paper 97-0388, 1997.
9. Torgerson, S. D., Liu, T., Sullivan, J. P., "Use of Pressure Sensitive Paints in Low Speed Flows," AIAA Paper 96-2184, 1996.
10. Carroll, B., Abbitt, J., Lukas, E., and Morris, M., "Pressure Sensitive Paint Response to a Step Pressure Change," AIAA Paper 95-0483, 1995.
11. Winslow, N. A.; Carroll, B. F.; Setzer, F. M., "Frequency response of pressure sensitive paints," AIAA Paper 96-1967, 1996.
12. Baron, A. E., Danielson, J. D., Gouterman, M., Wan, J., Callis, J. B., and McLachlan, B., "Submillisecond Response Times of Oxygen-Quenched Luminescent Coatings," *Reviews of Scientific Instrumentation* 64(12), 3394-3402, 1993.
13. Jordan, J. D. "Development and Application of Sol-Gel-Derived Platforms for Chemical and Biological Sensing," Ph.D. Dissertation, State University of New York at Buffalo, NY, May 1997, and references therein.
14. Lakowicz, J. R. *Principles of Fluorescence Spectroscopy*, Plenum Press, New York, 1983.
15. *Chemical Processing of Advanced Materials*, (L. L. Hench and J. K. West, Eds.), Wiley, New York, 1992.
16. Paul, A. *Chemistry of Glasses*, 2nd ed., Chapman and Hall, New York, 1990.
17. Brinker, C. G. and Scherer, G. W., *Sol-Gel Science*, Academic Press, New York, 1989.

### Acknowledgments

The authors thank Mr. Darryl D. Trump, Mr. Benjamin Sarka, and Dr. Larry P. Goss of ISSI for their insight, ideas, and support, Mr. Gary A. Clinehens of SelectTech Corporation for his LED lamp expertise, and Mr. Nate Lachendro from Purdue University for his cryogenic calibration efforts. This work was generously supported by the U.S. Air Force under Contracts F33615-95-C-2507 and F33615-98-C-3012 and by NASA Ames Research Center (NAS2-13605).





**AIAA 99-0565**

**Data Analysis Methods for the Development  
and Deployment of Pressure-Sensitive  
Paints**

W. L. Weaver and J. D. Jordan  
Innovative Scientific Solutions, Inc. (ISSI)  
Dayton, OH

G. A. Dale and K. R. Navarra  
Air Force Research Laboratory  
Wright-Patterson AFB, OH

**37th AIAA Aerospace Sciences  
Meeting and Exhibit  
January 11-14, 1999 / Reno, NV**

# DATA ANALYSIS METHODS FOR THE DEVELOPMENT AND DEPLOYMENT OF PRESSURE SENSITIVE PAINTS

William L. Weaver<sup>\*</sup> and Jeffrey D. Jordan<sup>\*</sup>  
Innovative Scientific Solutions, Inc. (ISSI)  
Dayton, Ohio 45440-3638 USA

and

Gary A. Dale<sup>†</sup> and Kelley R. Navarra<sup>†</sup>  
Air Force Research Laboratory  
Wright-Patterson AFB, Ohio 45433-7251 USA

## Abstract

An automated calibration instrument has been assembled for the measurement of PSP response to controlled values of pressure and temperature. The PSP luminescence is excited using pulsed excitation, thereby permitting the concomitant acquisition of the time-resolved and time-integrated luminescence intensity response. The calibration data is analyzed in both time-resolved and time-integrated intensity-parameter spaces using rearranged-Stern-Volmer and traditional-Stern-Volmer analyses. Uncertainties in all extracted values are available for review and confidence intervals between replicate measurements are calculated. CCD camera calibration is performed by collecting images of the PSP sample under continuous-wave illumination over a range of static temperature and pressure conditions. Intensity statistics on a pixel-by-pixel basis are calculated to investigate the effects of non-uniformity in the illumination, coating thickness, and test article temperature on the determination of pressure.

As a supplement to published coordinate-mapping image registration techniques used to account for model movement and deformation, an automated image registration technique based on identifiable features in the PSP coating is under development. These features are identified algorithmically and used to generate a transformation matrix that is tolerant of the independent displacement of disparate model surfaces. The transformation matrix also represents a quantitative measurement of model-surface displacement.

<sup>\*</sup>Analytical Chemist, Member AIAA

<sup>†</sup>Mechanical Engineer, Member AIAA

This paper is declared a work of the U.S. Government and it not subject to copyright protection in the United States

## Introduction

As the utility of pressure-sensitive paint (PSP) as a method for the quantitative visualization of surface pressure has increased, so to has the need for the development of new and varied PSP formulations and sensor platforms. These innovations are targeted for PSP deployment over a broad range of test article conditions ranging in temperature from low (cryogenic) to high (> 250°C) and air velocities from low (< 40 ft/s) to high (hypersonic), and the PSP may be required to exhibit fast (>1 kHz) response times. The performance of each new PSP formulation is measured over a range of conditions to assess PSP efficacy and to elucidate pathways for further optimization.

## Calibration Model

Pressure-sensitive paint is sensitive to pressure by means of its response to the concentration of molecular oxygen ( $[O_2]$ ) over the instrumented surface. The PSP oxygen-concentration sensitivity is exhibited as a modulation of PSP luminescence intensity and is described qualitatively by the relationship in Equation 1. The intensity ( $I$ ) represents the steady-state

$$I \propto \frac{1}{[O_2]} \quad (1)$$

luminescence intensity of the active luminophore in the PSP while under constant illumination or the time-integrated luminescence intensity emitted after exposure to a short pulse of excitation light. This relationship is demonstrated experimentally in Figure 1, wherein, the luminescence intensity from a dilute solution of pyrene in cyclohexane is displayed as a function of time after excitation from a short pulse of 337-nm laser light. Mixtures of nitrogen and air are bubbled through the solution to obtain concentrations of

dissolved molecular oxygen ranging from 0 ppm to 72 ppm. The lifetime of the luminescence decay and the time-integrated intensity decrease concomitantly with increased concentration of dissolved molecular oxygen. This behavior is modeled quantitatively by the Stern-Volmer relationship appearing in Equation 2 (lifetime) and Equation 3 (time-integrated intensity). In the

$$\frac{\tau_0}{\tau} = 1 + K_{SV} [O_2] \quad (2)$$

$$\frac{I_0}{I} = 1 + K_{SV} [O_2] \quad (3)$$

lifetime relationship, the ratio of the luminescence-decay lifetime observed in the absence of oxygen ( $\tau_0$ ) to the values observed in the presence of oxygen ( $\tau$ ) is a linear function of oxygen concentration with a y-intercept of 1 and a slope of  $K_{SV}$ , the Stern-Volmer constant which is obtained for an individual PSP formulation. The time-integrated intensity model can be used for both pulsed-excitation and steady-state applications and follows the same functional form, wherein,  $I_0$  and  $I$  are the observed intensity at zero and non-zero oxygen concentration, respectively.

The PSP luminescence lifetime is independent of excitation intensity or detector-collection efficiency and therefore values of oxygen concentration (pressure) over the test article can be obtained directly from the calibration curve. As the absolute value of the time-integrated and steady-state luminescence intensity are affected by both excitation intensity and detector efficiency, the reference value of  $I_0$  is not a constant for a given PSP coating and must be measured *in-situ*. Since it is very rarely feasible to remove all of the oxygen in contact with the painted model during the actual test, the intensity recorded at any convenient, known, isobaric condition ( $P_{ref}$ ) is collected and the calibration curve is recast with the substitution of this "wind-off" reference intensity ( $I_{ref}$ ) for the  $I_0$  value. The intensity ( $I$ ) collected at an unknown pressure ( $P$ ) "wind-on" condition is related to the reference values using a calibration relationship having the same functional form as the Stern-Volmer relationship and appears in Equation 4. This calibration curve is created from calibration values recorded in the laboratory after the value of  $P_{ref}$  is obtained during the test.

$$\frac{I_{ref}}{I} = A + B \frac{P}{P_{ref}} \quad (4)$$

### Laboratory Calibration

The performance of new oxygen-sensitive luminescent molecules, binder formations, preparation methodologies, and platform structures (collectively termed PSP formulations) are evaluated for their sensitivity to oxygen at known conditions of pressure and temperature. The calibration instrument (Figure 2) is based on a modified 4-way cross pressure chamber with optical access on all four sides. Typically only two right-angle windows are used during calibration. The pulsed laser light illuminates the PSP sample and the emitted luminescence is focused onto a PMT and recorded by a digital oscilloscope. The recorded intensity decay is transferred to the controlling computer and stored for offline data analysis. The pressure and temperature conditions are adjusted under computer control using a digital pressure controller and a thermo-electric heater/cooler. The time-resolved intensity-decay traces obtained from a full calibration (5-200 kPa, 0 - 120°C) are stored in a master file/sub-file system, such that the master file contains references to the decay files and condition information for each acquisition.

The data collected from the pressure-temperature calibration instrument is analyzed by a separate utility program. A screen capture of the program interface appears as Figure 3. This program analyzes the sensitivity of the PSP formulation to pressure at each value of temperature. At a given temperature and pressure setting, the intensity decay is read into computer memory and fit to a time-resolved single-exponential decay using the Marquardt-Levenberg nonlinear error minimization algorithm. The fitted value of decay lifetime ( $\tau$ ), its uncertainty ( $\sigma_\tau$ ), and the error in the fit are extracted from the time-resolved intensity decay traces. The time-integrated intensity ( $I$ ) of the decay is obtained by summing the intensity values across the decay. The calculation of lifetime and time-integrated intensity is performed on all pressure values at a given temperature.

The values of  $\tau$  and  $I$  are then plotted as a function of pressure. These curves are subsequently fit to models based on a rearranged version of the Stern-Volmer relationship. The lifetime ( $\tau$ ) model and the intensity ( $I$ ) model appear as Equations 5 and 6, respectively. The parameter of  $k_q$  appearing in Equation 5 is the oxygen quenching rate coefficient and is determined along with the value of  $\tau_0$  in the nonlinear fitting algorithm. Since the value of  $\tau_0$  is obtained through curve fitting methods, it is not necessary to insure that the calibration apparatus be capable of

$$\tau = \frac{\tau_0}{1 + k_q \tau_0 [O_2]} \quad (5)$$

$$I = \frac{I_0}{1 + K_{SV} [O_2]} \quad (6)$$

achieving a value near absolute vacuum. This same method is used to calculate the value of  $I_0$  in Equation 6. Since the time-integrated intensity analysis does not provide a method for the determination of  $\tau_0$ , the Stern-Volmer constant for the paint is calculated instead of the value of  $k_q$  ( $K_{SV} = k_q \tau_0$ ).

After the values of  $\tau_0$  and  $I_0$  and their uncertainty are obtained using the rearranged-Stern-Volmer analysis, the traditional, linear-Stern-Volmer values of  $\tau_0/\tau$  and  $I_0/I$  are calculated and plotted as a function of pressure. These values are then fit to the models in Equation 2 and Equation 3 and the fitted value of  $K_{SV}$  with uncertainty is extracted for each curve. All fitted values and their associated uncertainty can be reviewed graphically and exported to an ASCII data file for further analysis. An example plot of PSP intensity as a function of pressure and temperature is shown in Figure 4.

#### Two-Dimensional PSP Calibration

In order to evaluate the uniformity of the PSP sensitivity to pressure across the surface of a painted calibration coupon, the single-point PMT detector is replaced by a two-dimensional CCD detector and the pulsed light source is replaced by a stable, continuous-wave LED lamp. The paint coupon is placed in the calibration chamber and the pressure and temperature are varied as described above. Individual CCD images are recorded at each pressure and temperature condition and analyzed by a utility program written to perform steady-state-intensity-Stern-Volmer analysis in two disparate modes. In the first mode of operation, the utility program calculates the average pixel intensity within a user-defined region of interest (ROI). These average intensity values are calculated for a family of CCD images acquired over a range of pressures at a single temperature. The individual values of average intensity are fit to the modified-Stern-Volmer model shown in Equation 6. The fitted values of  $I_0$  and  $K_{SV}$  obtained from this analysis can be compared to the values obtained by the PMT calibration.

The second mode of operation analyzes the CCD images on a pixel-by-pixel basis. Using the same ROI that was defined for the average intensity analysis, the intensity values of a given pixel on the CCD image

collected over the pressure range at a given temperature are gathered and fit to the modified-Stern-Volmer model shown in Equation 6. The resulting fitted values of  $K_{SV}$  are saved as a matrix of values for display as an image of  $K_{SV}$  values across the PSP coupon.

The  $K_{SV}$  values relate directly the sensitivity of the PSP to changes in pressure. Although the intensity ratio of wind-off to wind-on accounts for variation in excitation intensity, it does not account for concentration non-uniformity in the PSP coating that contributes to a modulation of  $K_{SV}$  values across the surface. A 50 by 50 pixel ROI extracted from the image of a PSP coupon under conditions of 10 kPa and 100 kPa appear Figure 5. In these images, there is an intensity distribution across the coupon that decreases from left to right. The illumination intensity is also low compared to the full digitization range of the 16-bit CCD camera (6000 max counts out of 65000 counts). Although the illumination pattern on the LED lamp does not have internal structure, the non-uniformity of the PSP coating is manifest as areas of local increased intensity or hot-spots in the images. A pixel-by-pixel  $K_{SV}$  analysis of the coupon was performed and the results appear in Figure 6 (left image) along with the pixel-by-pixel pressure values obtained by applying the resulting calibration to the intensity values (right image). Although the intensity images in Figure 5 display an overall intensity gradient from left to right across the coupon, the images in Figure 6 display a  $K_{SV}$  and pressure gradient from top to bottom across the coupon. This top-to-bottom-distribution is attributed to non-uniformity of the PSP concentration. The local areas of greater intensity in Figure 5 exhibit a larger sensitivity to pressure than the surrounding areas of lesser intensity. The distribution of  $K_{SV}$  values for this sample has a relative standard deviation (rsd) of 4.1%. This is manifest as an rsd of 5.7% in the calibrated pressure values obtained for a calibration chamber pressure of 10 kPa. The areas of increased pressure sensitivity (higher  $K_{SV}$  values) skew the average pressure value to lower than actual, resulting in an average calibrated pressure value of 6.7 kPa. This is a deviation from the actual mean (dfm) of -33%. This large amount of error is due to the high sensitivity of the PSP at low pressures. In a pressure region where the PSP sensitivity is smaller (high pressure, 150 kPa) the dfm is 2.8%.

To investigate the effect of local temperature distribution, a higher amount of excitation intensity was used to illuminate a PSP coupon in the calibration chamber. The PSP intensity was recorded by the CCD over the range of 10 kPa to 150 kPa at a temperature of

20°C. The TE cooler/heater platform is not large enough to be in contact with the entire calibration coupon. The intensity from a 50 by 50 pixel ROI of that portion of the coupon which is not in direct thermal contact with the TE appears in Figure 7 for values of 10 kPa (left image) and 100 kPa (right image). The intensity distribution across the coupon varies from a CCD count value of 50000 to 10000 from the upper left to the lower right of the coupon. A pixel-by-pixel calibration of  $K_{SV}$  was performed and appears in Figure 8 (left image). In this case, the variation of  $K_{SV}$  does track with the intensity distribution, indicating that the amount of light on the coupon is heating the coupon. An rsd of 6.5% in the KSV values is manifest as an rsd of 5.7% in the calibrated pressure values for the coupon at 10 kPa and the average pressure value is skewed to a dfm of +14% (Figure 8 – right image).

Methods of compensation for both PSP non-uniformity and temperature distribution across the PSP surface are currently under development. The compensation strategy is in the form of multi-luminophore paints. This strategy would incorporate a pressure-insensitive, temperature-sensitive component and a pressure- and temperature-insensitive component with the existing pressure- and temperature-sensitive luminophore. This would provide pixel-by-pixel correction for PSP concentration and temperature non-uniformity.

### PSP Image Registration

Image registration is an area of active research in the PSP community. Currently-deployed PSP systems require that intensity ( $I$ ) images collected at condition (wind-on) be ratioed to images collected at an isobaric (wind-off) condition ( $I_{(wind-off)} / I_{(wind-on)}$ ). Model deflection and warping between the wind-on condition and wind-off condition result in systematic errors in the calculated intensity ratio. Identical image locations on the model rather than identical CCD camera pixel locations must be ratioed.

In practice, image processing for paint-sensor systems falls into two categories -- image registration and image resection. Image registration is concerned with the effects of model movement and deformation on the calculation of the  $I_{(wind-off)}/I_{(wind-on)}$  ratio, and image resection involves the accurate placement of the resulting two-dimensional image of pressure values on a three-dimensional wire-mesh model grid for spatial quantitative visualization. Algorithms for image registration and image resection in the area of pressure-sensitive paint appear in the published literature.<sup>1,2</sup> For

simple image translation,  $x$  and  $y$  coordinates of a given pixel in the wind-on image are related to the pixel coordinates of the identical model location in the wind-off image ( $x'$  and  $y'$ ) through the transforms in Equation 7 below, where  $m$  is a magnification factor and  $s_x$  and  $s_y$

$$x = R_x(x', y') = mx' + s_x \quad (7a)$$

$$y = R_y(x', y') = my' + s_y \quad (7b)$$

represent the  $x$  and  $y$  components of the shift, respectively. To account for model bending, Equation 7 is extended to a set of second-order equations appearing in Equation 8. The coefficients  $a_{ij}$  and  $b_{ij}$

$$x = \sum_{i,j=0}^2 a_{i,j} x'^i y'^j \quad (i+j \leq 2) \quad (8a)$$

$$y = \sum_{i,j=0}^2 b_{i,j} x'^i y'^j \quad (i+j \leq 2) \quad (8b)$$

can be determined by using at least six pairs of known image locations in the wind-off and wind-on images  $[(x,y),(x',y')]$  pairs and solving for the coefficients using a least-squares fitting algorithm. These image locations are typically well-defined model features or registration marks placed on the model. After the coefficients are determined, the shifted  $x$  and  $y$  pixel coordinates are calculated, and the pixel values of the registered wind-on image are calculated by linear interpolation of the pixel intensities in the actual wind-on image. The intensity ratio of the  $I_{(wind-off)}$  to the registered  $I_{(wind-on)}$  yields the corrected values.

The process of image resection has its basis in the area of photogrammetry.<sup>3-6</sup> Image resection is the process of recovering the three-dimensional coordinates of a surface from a two-dimensional image of the surface and is used in the PSP technique for accurate placement of the calculated pressure values on a three-dimensional wire-mesh model of the test article to extract three-dimensional quantitative surface-pressure information. Bell and McLachlan<sup>2</sup> have demonstrated the utility of the Direct Linear Transform<sup>6</sup> (DLT) formulation for the process of image resection. The  $x$  and  $y$  coordinates of the two-dimensional CCD camera image are translated into  $X$ ,  $Y$ , and  $Z$  model coordinates via Equation 9.

The 11 DLT unknown coefficients in Equation 9 can be determined using the same six pairs of registration marks that were used for image registration. Information required from the six pairs is the  $X$ ,  $Y$ , and  $Z$  coordinates of the registration marks in model space and the two-dimensional  $x$ ,  $y$  coordinates of the

$$x = \frac{L_1 X + L_2 Y + L_3 Z + L_4}{L_9 X + L_{10} Y + L_{11} Z + 1} \quad (9a)$$

$$y = \frac{L_5 X + L_6 Y + L_7 Z + L_8}{L_9 X + L_{10} Y + L_{11} Z + 1} \quad (9b)$$

registration marks in the CCD camera image. The location of the x, y pixel coordinates is obtained from inspection of the CCD camera image. The X, Y, Z model coordinates are obtained independently using a three-dimensional coordinate-mapping instrument. Armed with the six registration marks of known 2-D and 3-D coordinates, the coefficients in Equation 9 can be uniquely determined by solving the resulting system of linear algebraic equations.

#### Development of QPED Registration Method

The effort described in this paper is currently investigating the development of new algorithms to aid in the image registration process. The investigation involves evaluating the utility of automated image-registration techniques that have potential for performing image registration in an unattended and non-user-assisted algorithm. The algorithm under development is called Quantum Pixel Energy Distribution (QPED). This algorithm is based on the discrete pixel-based architecture of the CCD camera and is aimed at augmenting the linear-interpolation algorithm used for fractional-pixel image shifting. Figure 9 displays the image-shifting paradigms for (a) linear-interpolation and (b) the QPED algorithm. The linear-interpolation algorithm operates on the pixel pattern depicted in Figure 9(a). The intensity values of pixels A, B, and C in the wind-on image are used to calculate the new "shifted" pixel intensity at pixel D. The coefficients for the linear interpolation are calculated using the known x and y coordinates of registration marks in both the wind-on and the wind-off image. The QPED algorithm is based on the paradigm in Figure 9(b), wherein an individual pixel located in the original image is assigned individual values of x-shift and y-shift. These values are tabulated in the QPED matrix. When the original image is transformed through the QPED matrix, the resulting QPED image represents the properly registered original image. The values of x-shift and y-shift contain a whole-pixel shift portion and a fractional-pixel shift portion. In the example shown in Figure 9(b), the energy (measured intensity) of the source pixel is shifted with the value of x-shift = 0.5 and y-shift = 0.0. The pixel in the resulting QPED image appears to have grown in size;

however, the total pixel energy of the single pixel in the original image has simply been distributed to the original pixel and the neighboring pixel, resulting in 50% remaining in the original x, y pixel location and 50% "spilling" over into the adjacent pixel located at  $x = x' + 1$ . When both x-shift and y-shift have non-zero fractional values, then the pixel energy is distributed to four pixels, as in Figure 10. The integer portion of the shift values is 2 in this example. This value can be varied to any size as long as the same model locations are still in the field of view of the CCD camera for both wind-off and wind-on conditions.

The QPED process is used as the foundation for an optimizing search algorithm. In this algorithm the QPED matrix values for each pixel in a wind-off image are adjusted on a pixel by pixel basis. The resulting QPED image is ratioed with the wind-on image, and the quality of the resulting intensity-ratio image is assessed. The QPED matrix values are adjusted until the optimal condition is found. This algorithm has been applied in the laboratory to a set of wind-off/wind-on images of a 3 in x 3 in aluminum PSP painted coupon. When the coupons were cut from a larger piece of material, they became bowed. The material used to affix the bowed coupon to the support was not sufficiently rugged to prevent the coupon from flexing under the influence of a jet of air used to create the wind-on condition. The coupon deflection resulted in PSP intensity-ratio images that were of very poor quality. Since the need for registration marks during this laboratory test was not anticipated, registration marks were not applied.

Spatial anomalies in the base coat used for these jet tests resulted in the noisy intensity-ratio image shown in Figure 11(a). The wind-off and wind-on images were submitted to the QPED registration algorithm, and the values for the QPED matrix were optimized and are shown in Figure 11(b). The resulting QPED image was ratioed with the wind-on image and is shown in Figure 11(c). The QPED registration was accomplished without the placement of additional registration marks and executed without the need for a trained program operator.

#### Development of Embedded Registration Marks

The QPED algorithm relies on spatial anomalies in the base coat application for the registration of the images in Figure 11. As base coat formulations and deployment methods improve, the density of spatial anomalies decreases. To provide the QPED algorithm with a more repeatable and uniform placement of intensity differences, an aerosol mist of gray paint is



applied over the dry base coat before the application of the pressure-sensitive top layer. This layer of diffuse registration marks is being called the "raspberry coat," as the spray pattern is similar to that obtained by vibrating the tongue between the lips while blowing, which is known colloquially as a "raspberry".

The intensity pattern from a PSP that has been prepared with a raspberry base coat appears in Figure 12. The raspberry coat results in a uniform but irregular placement of many registration marks. Being applied below the PSP top layer, the raspberry coat does not effect the sensitivity of the PSP to changes in pressure. The wind-off to wind-on ratio of a raspberry based-coated PSP coupon with an impinging flow of nitrogen appears in Figure 13. Since the presence of the raspberry coat does not effect the value of  $K_{SV}$  for the PSP, the intensity modulation imparted by the raspberry coat is ratioed out and the resulting intensity-ratio image does not indicate the presence of the raspberry base coat. The PSP coupon in Figure 13 was then translated to the left by the use of a laboratory translation stage. The wind-off to wind-on ratio was recalculated under the same flow conditions of nitrogen and resulted in the Figure 14. Since the intensity modulation imparted by the raspberry base coat is no longer divided by the same image location, the intensity modulation is very evident in the ratioed image. The wind-on and wind-off images used to obtain the intensity ratio in Figure 14 were submitted to the QPED algorithm for registration. The resulting QPED matrix reported a coupon displacement 1.6 pixels. The corrected QPED image was then ratioed with the wind-on image to produce the corrected image in Figure 15. This figure shows that the areas of the coupon that are not affected by the nitrogen jet have been correctly calculated to be a ratio of 1.0, as reported by the intensity ratio calculated before the coupon was translated, Figure 13. Additional development of the QPED algorithm and investigation of the performance of the raspberry base coat is continuing.

### Conclusions

The process of PSP calibration permits the qualitative relationship given in Equation 1 to be applied to the analysis of images acquired during the deployment of the PSP technique under test conditions for the extraction of quantitative values of pressure on the painted surface. Several factors that are quantified in order to increase the accuracy of the PSP measurement include the quantitation of the PSP pressure sensitivity ( $K_{SV}$ ), the PSP temperature

sensitivity, the amount of model surface displacement and deformation, the non-uniformity of PSP concentration across the model surface, the temperature of the painted surface during the test, and a method for the accurate correlation between the corrected pressure distributions and locations on the test article. Continued research in all of these areas will continue to move pressure-sensitive-paint to a reliable, repeatable, and cost-effective method for the quantitative determination of surface pressure.

### Acknowledgments

This effort is funded through a United States Air Force research contract, F33615-95-C-2507-15, and a United States Air Force-sponsored STTR program, F33615-98-C-3012.

### References

1. J. F. Donovan, M. J. Morris, A. Pal, M. E. Benne, and R. C. Crites, "Data Analysis Techniques for Pressure- and Temperature-Sensitive Paint," **AIAA Paper No. 93-0176**, 31<sup>st</sup> Aerospace Sciences Meeting and Exhibit, Reno, NV, January 11-14, 1993.
2. J. H. Bell and B. G. McLachlan, "Image Registration for Luminescent Paint Sensors," **AIAA Paper No. 93-0178**, 31<sup>st</sup> Aerospace Sciences Meeting and Exhibit, Reno, NV, January 11-14, 1993.
3. C. C. Slama, Ed., *Manual of Photogrammetry*, 4th Ed., (American Society of Photogrammetry, Falls Church, VA, 1980).
4. P. R. Wolf, *Elements of Photogrammetry*, (McGraw Hill, New York, 1974).
5. G. T. Marzan and H. M. Karara, "A Computer Program for Direct Linear Transformation Solution of the Collinearity Condition, and Some Applications of It," in *Proc. ASP Symp. on Close-Range Photogrammetric Systems*, Urbana, Illinois, p. 420 (1975).
6. Y. I. Abdel-Aziz and H. M. Karara, "Direct Linear Transformation From Comparator Coordinates into Object Space Coordinates", in *Proc. ASP/UI Symp. on Close-Range Photogrammetric Systems*, Urbana, Illinois, p. 1 (1971).

Figures

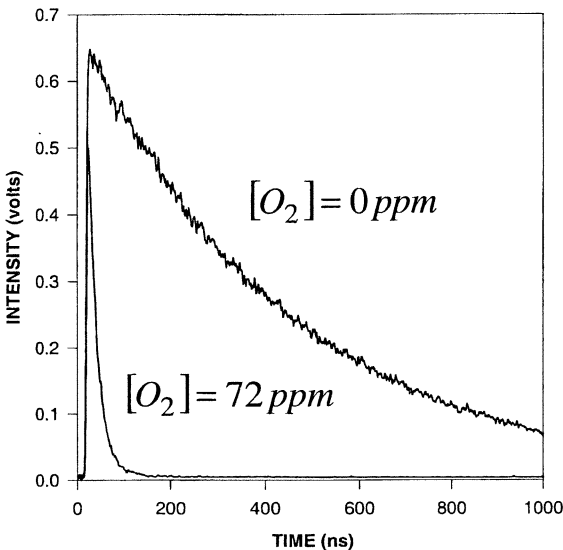


Figure 1. Time-resolved luminescence intensity obtained from a solution of pyrene in cyclohexane under two values of dissolved oxygen concentration.

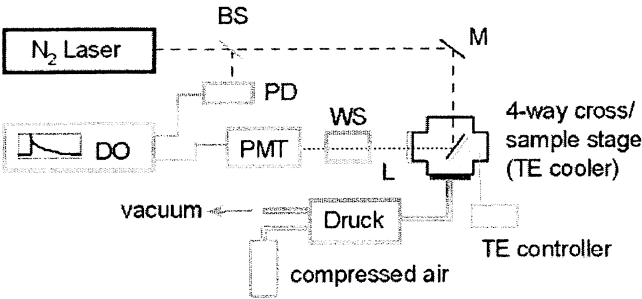


Figure 2. Block diagram of calibration instrument. N2 laser – Pulsed nitrogen laser; BS – Beam Splitter; M – Mirror; TE – Thermo-electric; Druck – Druck pressure controller; L – Lens; WS – Wavelength selector (filter or monochrometer); PMT – Photomultiplier tube; PD – Photodiode; DO – Digital Oscilloscope.

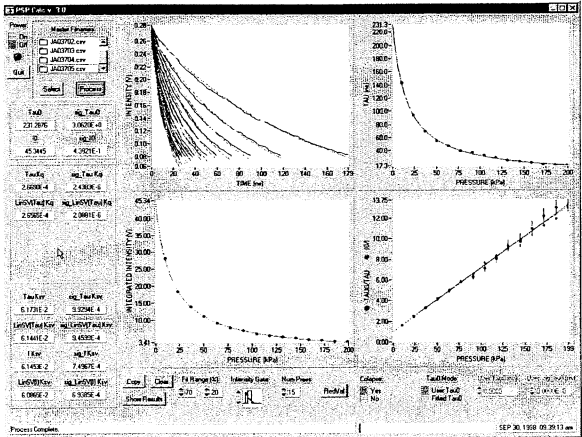


Figure 3. Screen capture of time-resolved and time-integrated intensity analysis program.

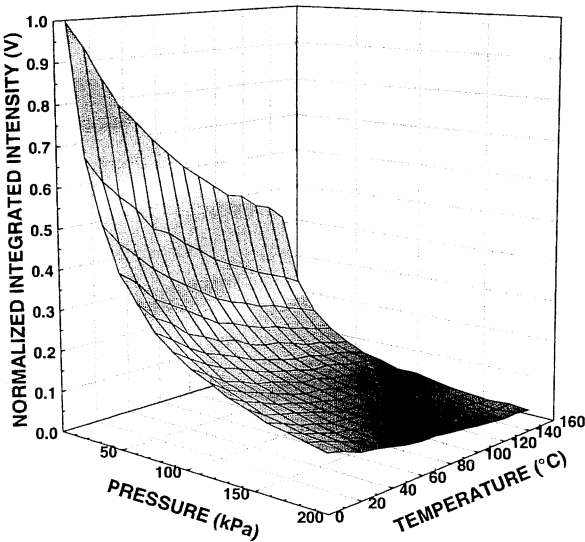


Figure 4. Normalized integrated-intensity as a function of pressure and temperature for PSP formulation of pyrene in RTV.

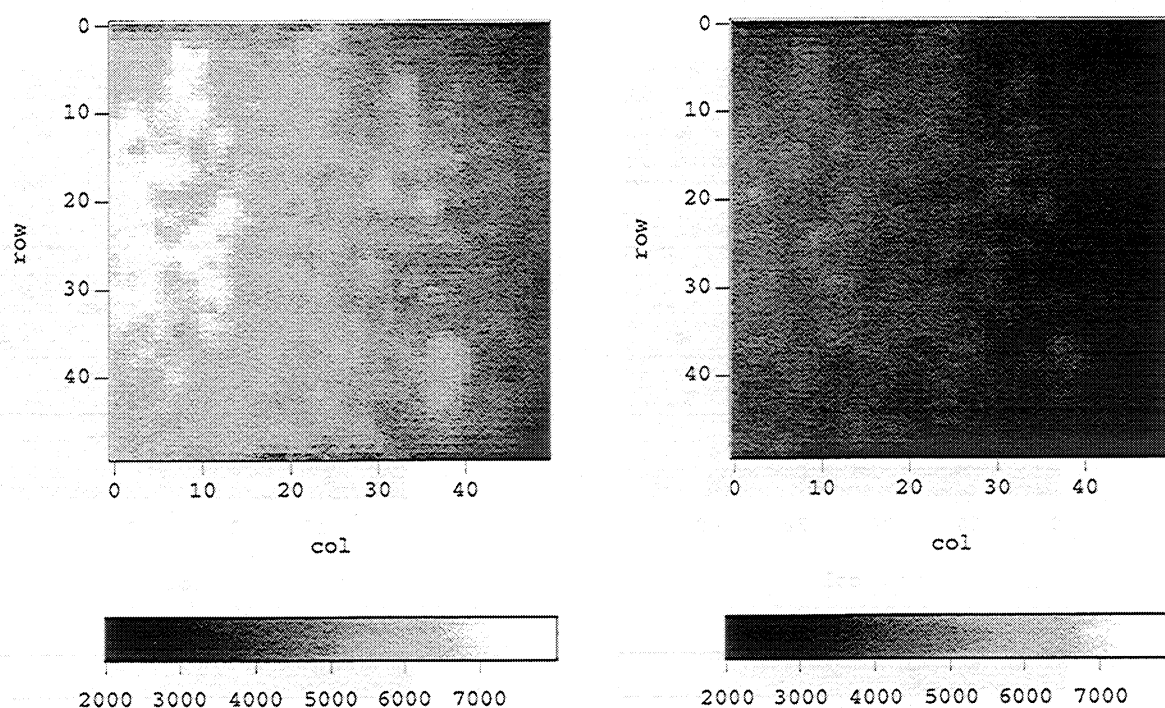


Figure 5. CCD intensity images of 50 x 50 pixel region of interest. Left – calibration chamber at 10 kPa; Right – calibration chamber at 100 kPa. Scales are in units of CCD intensity counts.

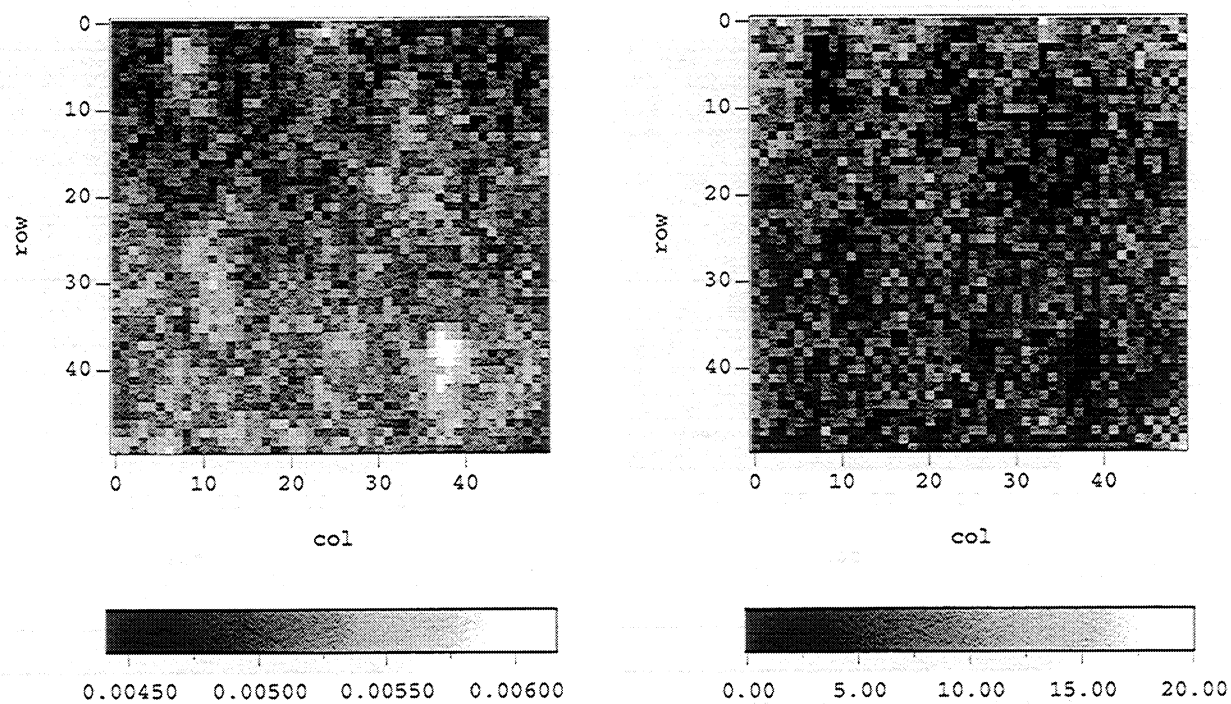


Figure 6. Distribution of KSV values (left) and distribution of calibrated pressure values in units of kPa at a calibration pressure of 10 kPa (right).

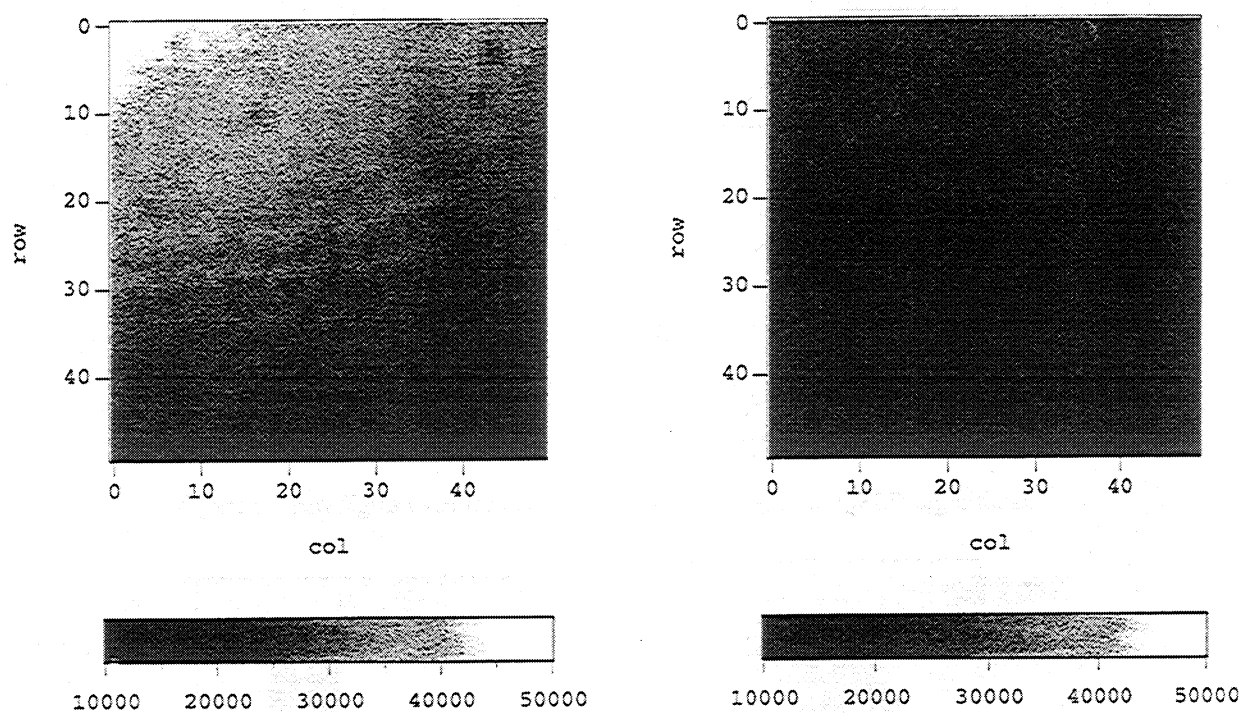


Figure 7. CCD intensity images of 50 x 50 pixel region of interest. Left – calibration chamber at 10 kPa; Right – calibration chamber at 100 kPa. Scales are in units of CCD intensity counts.

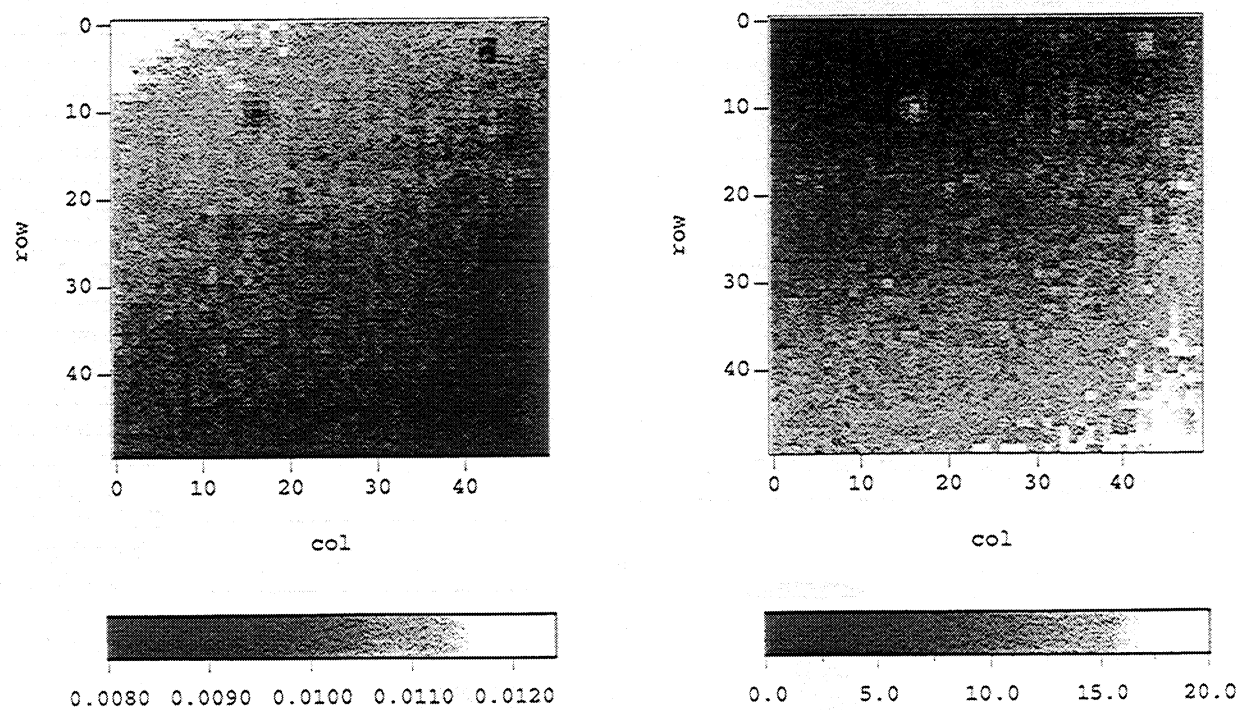


Figure 8. Distribution of KSV values (left) and distribution of calibrated pressure values in units of kPa at a calibration pressure of 10 kPa (right).

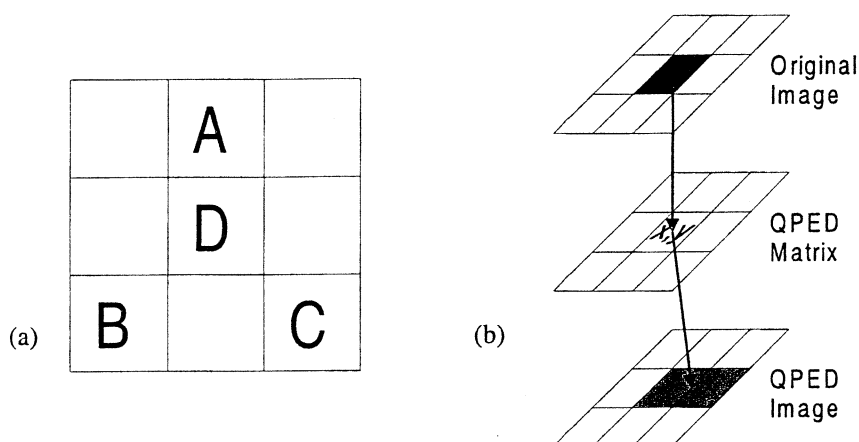


Figure 9. Paradigms used for (a) linear interpolation and (b) QPED algorithms.

Figure 10. Single-pixel QPED processing with shift values of  $x = 2.5$  and  $y = 2.5$ . Resulting pixel energy is distributed to four pixels in the registered QPED image. The integer portion of the shift values is 2 in this example. This value can be varied to any size as long as the same model locations are still in the field of view of the CCD camera for both wind-off and wind-on conditions.

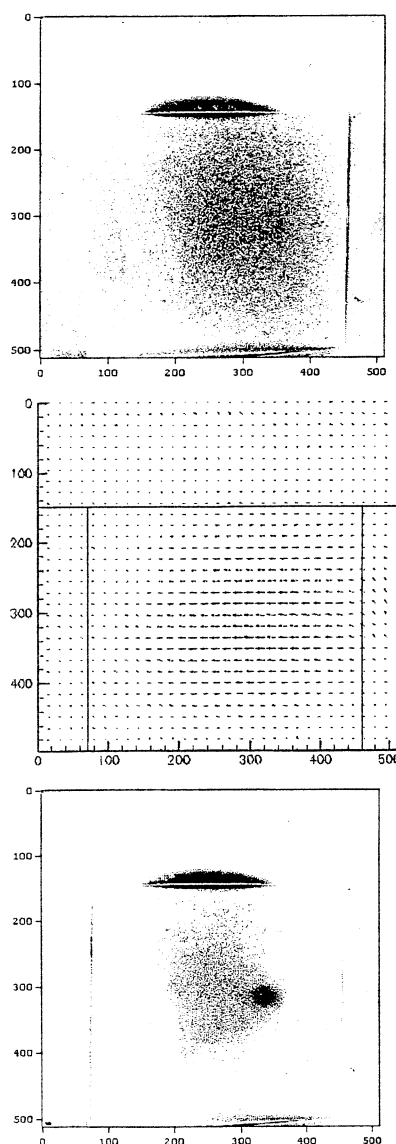
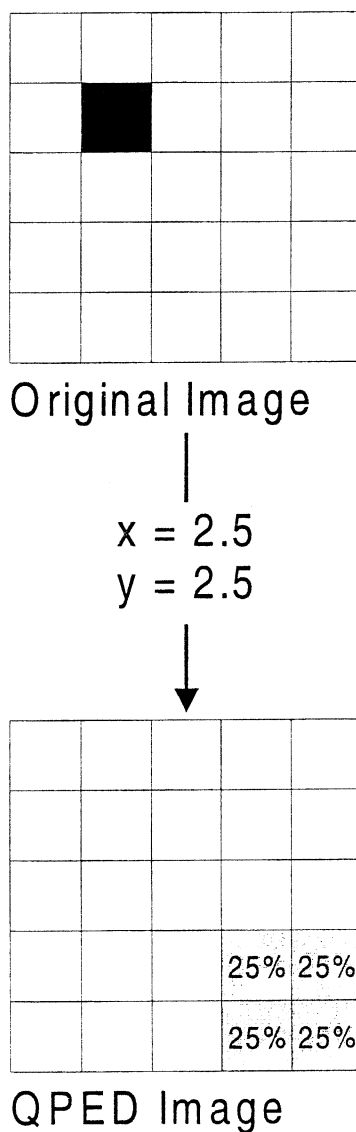


Figure 11. PSP coupon used for jet test. (a-Top) Original intensity ratio without image registration. (b-Middle) Vector plot of resulting optimized pixel-shift values used by QPED Matrix. (c-bottom) Intensity ratio of registered QPED image to wind-on image. The air jet is impinging from right-to-left across the vertical center of the coupon.

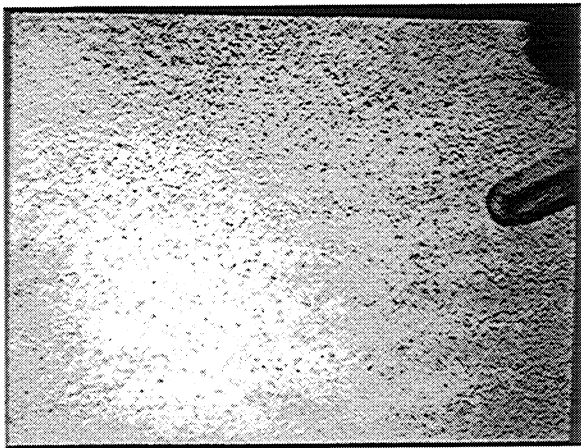


Figure 12. Intensity image of PSP coating with raspberry base coat.

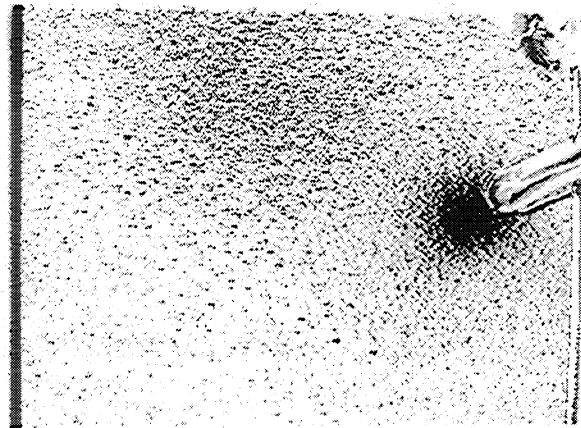


Figure 14. Wind-off to wind-on intensity ratio image of PSP with raspberry base coat and a coupon translation of ca. 1.6 pixels.

#### Appendix: QPED Development and Applications

The QPED algorithm for image registration in PSP applications is in the earliest stages of development. Generation of the registered QPED image using the QPED matrix of optimized pixel-energy-shift values is implemented sequentially in first the x- and then y-shift directions. Since the x- and y-axes are defined by the orientation of the 2D optical sensor, their orthogonality is guaranteed regardless of model position. The search for optimal values for the QPED matrix is time-consuming and optimizations are under development. It is conceptually feasible to generate a library of expected QPED deformation matrices for a particular model *a priori* and search for the optimal entire QPED

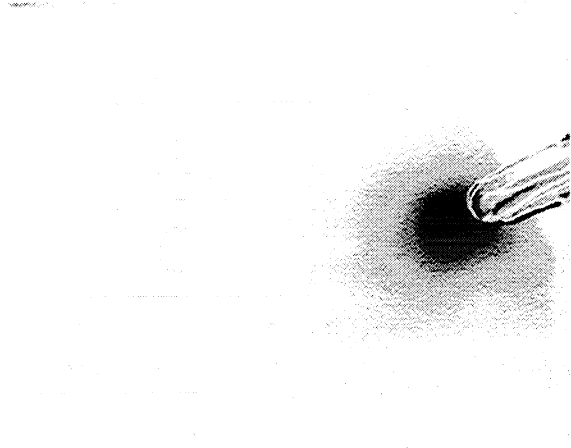


Figure 13. Wind-off to wind-on intensity ratio image of PSP with raspberry base coat and no coupon translation.

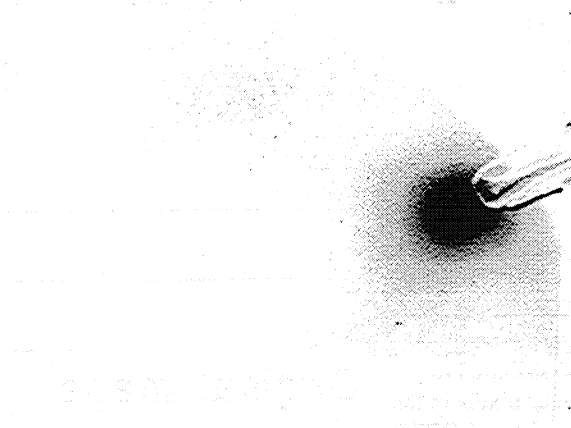


Figure 15. Wind-off to wind-on intensity ratio image of PSP with raspberry base coat and a coupon translation of ca. 1.6 pixels after images have been corrected for translation by QPED algorithm.

matrix rather than for the individual pixel-energy-shift values on a pixel-by-pixel basis.

The QPED algorithm is applicable to diagnostics other than PSP in which there is object movement between two images. For example, ISSI is currently applying the QPED algorithm to the processing of Particle Imaging Velocimetry (PIV) and Planar Doppler Velocimetry (PDV) data. The QPED paradigm can also serve as the basis of an optical technique for the direct quantitative measurement of component deformation. This new diagnostic would provide full-field measurements of strain as a complement to the current use of strain-gauges in the same manor in which PSP measurements augment the use of pressure taps.



## Optical Measurements of Surface Pressure and Temperature in Turbomachinery

Kelly Navarra  
Larry Goss  
Jeffery Jordan

ISS Inc., 3845 Woodhust Court  
Beavercreek, Ohio 45430-1658, USA

Doug Rabe  
Jim Gord  
David Car

Aero-Propulsion and Power Directorate  
WL/POTE, Bldg 18D  
Wright-Patterson AFB, Cleveland OH 45433, USA

### 1.0 SUMMARY

A new pressure-measurement technique which employs the tools of molecular spectroscopy has recently received considerable attention in the aerospace community. Measurements are made via oxygen-sensitive molecules attached to the surface of interest as a coating, or paint. The pressure-sensitive-paint (PSP) technique is now commonly used in stationary wind-tunnel tests; this paper presents extension of the technique to advanced turbomachinery applications. New pressure- and temperature-sensitive paints (TSPs) have been developed for application to a state-of-the-art transonic compressor where pressures up to 2 atm and surface temperatures to 140°C are expected for the first-stage rotor. PSP and TSP data images have been acquired from the suction surface of the first-stage rotor at 85% of the correct design speed for the compressor peak-efficiency condition. The shock structure is clearly visible in the pressure image, and visual comparison to the corresponding computer prediction shows quantitative pressures similar to the PSP data. The measurement error is estimated to range from 0.36 kPa in low-pressure regions to 4 kPa in high-pressure regions. The errors were significantly increased by a failure mode of the camera which will be described.

### 2.0 INTRODUCTION

The turbomachinery community is continually striving to improve the performance of gas turbine engines. The engine performance depends upon the compressor pressure ratio and efficiency where the stage pressure ratio is a function of the work, inlet total temperature, and stage efficiency. The turning of the flow which creates work is induced by the pressure profile over the suction and pressure surfaces of the blade. Because the pressure is rising through the rotor passage the amount of turning is limited by blade-surface and end-wall

boundary layer behavior. Boundary layers in an adverse pressure gradient tend to separate, which can cause a loss of efficiency and prevent any further increase in the pressure ratio. Currently, the stage pressure ratio and stage efficiency is determined experimentally by measuring the inlet and exit total pressure and temperature of the stage. Because of the complex flow interactions which occur in a rotor, it would be most beneficial to also know the pressure profile of the blade surface.

Early surface pressure measurements of a subsonic rotor were made by Sexton, O'Brien, and Moses in 1973 where blade-mounted pressure transducers and a multi-channel radio telemetry system were used<sup>1</sup>. Still today, blade-mounted pressure transducers are the only means to measure surface pressure on rotors. Unfortunately, such transducers cover a limited region (< 5%) of the blade surface, result in some compromise to the structural integrity of the blade and to the flow integrity, and have limited reliability in full-scale transonic turbomachinery environments. For these reasons, improved blade-surface pressure-measurement techniques are needed to aid the understanding of flow behavior in turbomachinery components.

A relatively new technique that employs the tools of molecular spectroscopy to measure pressures by optical means is the subject of this paper. Measurements are made via photoluminescent oxygen-sensitive molecules attached to the surface of interest as a coating, or paint; hence, the technology is referred to as pressure-sensitive paint (PSP). The objective of this research effort was to develop a PSP suitable for the harsh turbomachinery environment and to demonstrate the measurement technique for turbomachinery applications.

### 3.0 MEASUREMENT CONCEPT

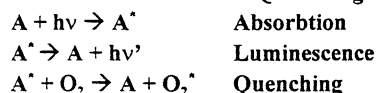
Table 3.1 summarizes the typical pressure-measurement concept. In this scheme, a photoluminescent species (A) absorbs light of appropriate energy ( $h\nu$ ) and is promoted to an excited electronic state ( $A^*$ ). The excited-state molecules then return to the ground electronic state either by some radiative-decay process involving the emission of a photon (fluorescence or phosphorescence) or by a non-radiative pathway such as dynamic quenching. Dynamic quenching is the non-radiative phenomenon in which the excess energy is transferred to the motion of the quencher, which in this case is oxygen. Because of the effective competition between the luminescence and oxygen quenching, the luminescence can be used to quantify the local oxygen concentration. Oxygen quenching is usually modeled by some variation of the Stern-Volmer relation. In its simplest form, the relation is given by

$$I = \frac{I_0}{1 + K_o P_{O_2}} = \frac{I_0}{1 + k_q \tau_o P_{O_2}} \quad (1)$$

where  $I$  is the luminescence,  $I_0$  the luminescence in the absence of oxygen,  $P_{O_2}$  the partial pressure of oxygen, and  $K_o$  the Stern-Volmer constant. The Stern-Volmer constant is a product of the bimolecular quenching rate,  $k_q$ , and the lifetime of the molecule at a vacuum,  $\tau_o$ . Unfortunately, the pressure-sensitive probe molecules have other mechanisms by which they can return to the ground state which are manifested in a sensitivity to temperature<sup>2-4</sup>. As a result, development has begun on compatible temperature-sensitive paints<sup>5-7</sup>. As with pressure-sensitive coatings, the luminescence of temperature-sensitive coatings can be related to the surface temperature and can be measured with essentially the same instrumentation. For capitalizing on this compatibility, efforts are underway to combine both temperature and pressure probe molecules in the same layer of paint.

**Table 3.1** Pressure-measurement concept based upon  $O_2$  quenching of photoluminescent probe molecules.

#### Photoluminescence and Quenching Process:



#### Temporal Behavior of Photoluminescence:

$$\begin{aligned} d[A^*]/dt &= -k_t[A^*] \\ k_t &= k_1 + k_q[O_2] \\ [A^*]_t/[A^*]_0 &= \exp(-k_t t) \end{aligned}$$

To acquire surface pressure measurements in a wind tunnel test intensity fields are commonly measured because of the simplicity of the data acquisition procedure. To apply a Stern-Volmer model, the luminescence intensity at a reference

pressure level,  $I_{ref}$ , must be divided by the luminescence intensity at some test condition,  $I$ , over the area of interest. For this method, the ratio of luminescence intensities is calibrated to indicate the surface pressure. The intensities are generally sampled over the surface of interest by a detector array such as a charge-coupled device (CCD) camera. With today's CCD cameras having a million or more pixels, PSP can provide continuous surface pressure measurement at an unequaled spatial resolution. The output of the CCD array can be visually represented as a two-dimensional image, with the luminescence corresponding to a gray scale.

### 4.0 PAINT DEVELOPMENT

The basic pressure-sensitive paint is diagrammed in Fig. 4.1. A binder material which is oxygen-permeable (typically silicone-based) is used to suspend luminescent probe molecules whose emission is effectively quenched by a collision with molecular oxygen. The probe molecules can either be fluorescent (short lifetime  $< 300$  ns) or phosphorescent (long lifetime  $> 100$   $\mu$ s). The luminosity or lifetime of the excited paint is related to the oxygen concentration by the Stern-Volmer relations previously presented.

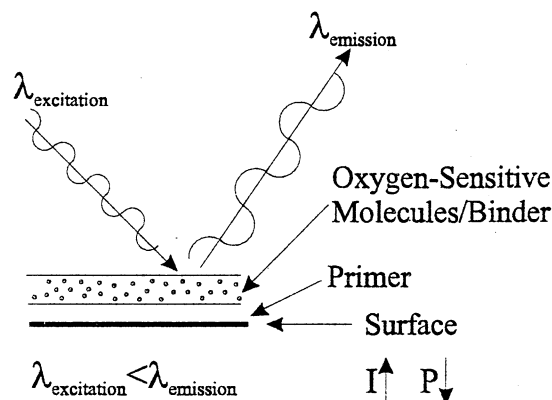


**Figure 4.1** Basic PSP structure.

Given an oxygen-sensitive molecule, there are three primary factors involved in fabricating a suitable PSP. First, the binding medium used to attach the probe to a surface must be oxygen permeable in order to permit oxygen quenching. Second, the binding medium must be compatible with the probe molecule. For example, if the polymer is highly polar and the probe molecule is non-polar, the resulting paint could be completely insensitive to pressure. Finally, the binding medium must provide a stable environment for the probe. Often, significant variations in paint performance over time results from continued reorganization of the polymer system. Thus, it is beneficial to

use a polymer which cures quickly near room temperature. The first two factors can effectively be satisfied through the appropriate selection of probes and polymers. The final factor is the most difficult to achieve, the primary obstacle being a result of temperature effects.

The sensitivity of pressure paints to temperature involves both the vibrational activity of the probe molecule itself and the binding medium. However, the temperature-sensitivity effects are currently dominated by the binder. The Stern-Volmer constant of the pressure paint can be expressed as a function of temperature and binder viscosity by

$$K_o = 8RT/3000\eta \quad (2)$$

where  $R$  is the gas constant, and  $\eta$  is the viscosity of the binder. Another effect of temperature on paint performance involves the solubility of oxygen in the paint binder. The solubility of oxygen in a silicone binder is given by Henry's Law

$$[O_2(T)] = [O_2]_0 \exp(-\Delta H / RT) \quad (3)$$

where  $\Delta H$  is the enthalpy of solution (-3.0 kcal/mole for silicone). Therefore, the paint performance is inconsistent throughout the paint layer where temperature variations exist. As a result, care must be taken in designing the correct binder, both for homogeneous performance and compatibility with the probe molecule.

#### 4.1 Paint Performance

After screening numerous molecular probes/binder combinations, one prototype paint was selected for demonstration in a state-of-the-art transonic rotor. The selected paint utilized a derivative form of pyrene (1-pyreneacetic acid) in a white RTV (GE 734). While ordinary pyrene in RTV typically yields satisfactory surface pressure measurements<sup>8</sup>, the pyrene could not withstand the elevated temperatures of a transonic compressor<sup>9</sup>. For the rotor under study the suction surface blade temperatures and pressure were expected to approach 140 °C and 2 atm, respectively<sup>9</sup>. By using a derivative form of pyrene, which has a higher boiling point compared to pyrene, a paint which survived the extreme temperature was developed. The temperature survivability was, however, obtained at the expense of some pressure sensitivity. As presented in Figure 4.2, the Stern-Volmer calibration of the 1-pyreneacetic acid (PA) paint at room temperature shows a decrease in pressure sensitivity of ~ 15% as compared to pyrene. Pyrene, on the other hand, vaporizes at ~80 °C<sup>9</sup>. The calibration of the PA paint over pressure and temperature is presented in Fig. 4.3. Figure 4.4 presents the calibration of five

independently painted samples representing the sample to sample repeatability.

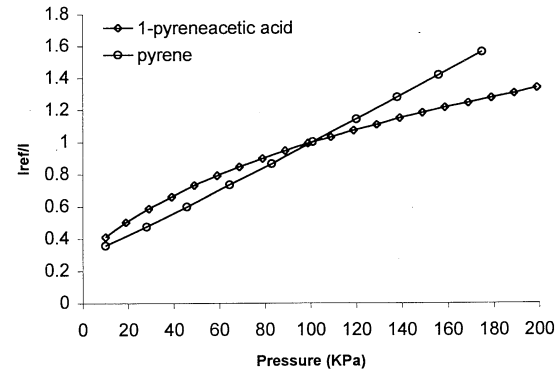


Figure 4.1 Calibration comparison of pyrene and 1-pyreneacetic acid (room temperature).

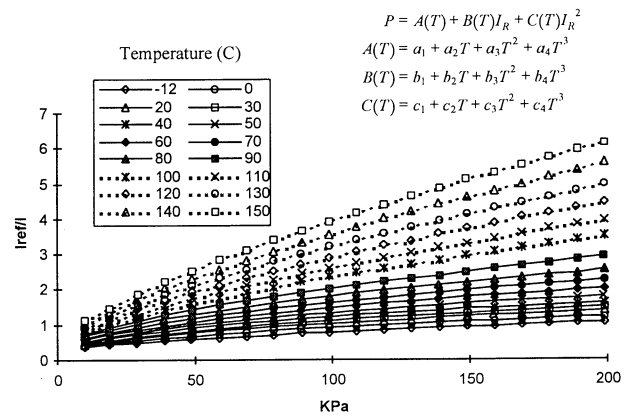
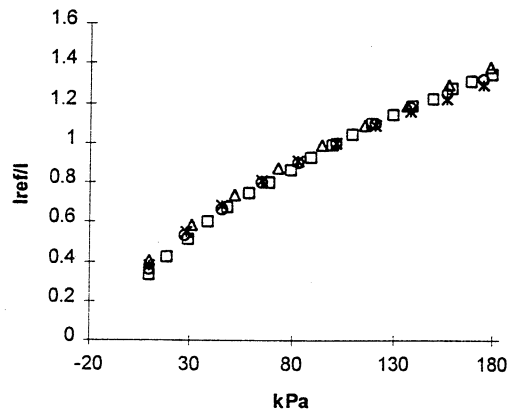
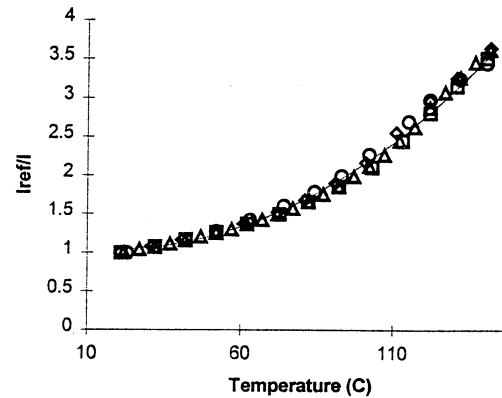


Figure 4.3 Performance of PSP developed for turbomachinery.



**Figure 4.4** Calibration variation of four independent PSP samples at room temperature. (final data will be of 5 data sets)

As can be seen in Figure 4.3, despite efforts to minimize temperature sensitivity the PSP remains quite sensitive to temperature. In order to correct for the temperature-sensitivity of the PSP, a temperature-sensitive paint was also developed. Thus, in a rotor test, two blades would be painted and surface pressure and temperature measurements could be obtained sequentially. The design of a temperature sensitive paint is similar to that of a PSP with the exception that the selected binding medium was impermeable to oxygen. For the TSP a fluorescent laser dye (1,3-bis(1 pyrene)propane) was suspended in a marine caulk (Bostick). The Stern-Volmer Calibration for the TSP is presented in Fig. 4.5.



**Figure 4.5** Performance of TSP developed for turbomachinery.

#### 4.2 Paint Photodegradation

All luminescence-based paints display a common characteristic referred to as photodegradation, whereby the paint-intensity signal deteriorates as a function of time with continued exposure of the paint to visible light. Figures 4.6 and 4.7 show the photodegradation results of the PSP and TSP as a function of input energy. (These plots will later be combined into one) The paint photodegradation is expressed in terms of percent of the initial intensity. In general, the PSP displayed a higher rate of degradation than the TSP and absorbed a larger amount of input energy before the rate started to decline. At 30 mJ of total energy delivered to the paint the PSP degraded ~ 6.6% while the TSP degraded ~ 1.3%. The rate of photodegradation circumvents the advantage of using increased illumination power to improve signal levels. Hence, the effect of photodegradation must be considered when designing a PSP experiment.

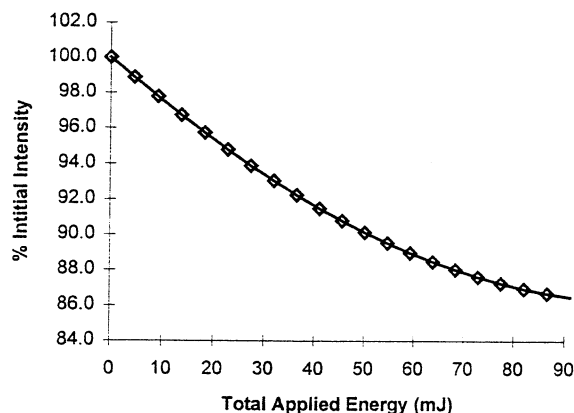


Figure 4.6 PSP rate of photodegradation as a function of total energy delivered to the paint.

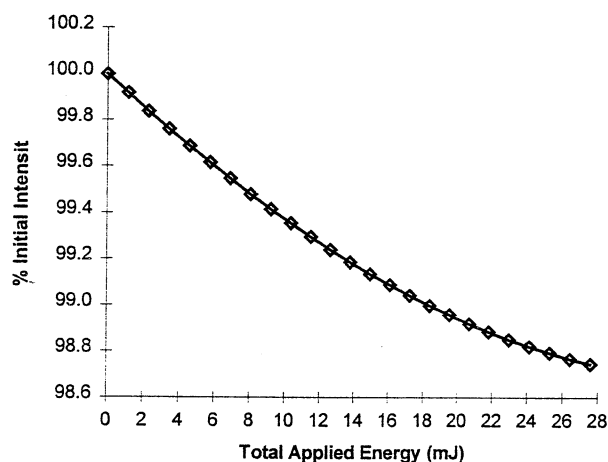


Figure 4.7 TSP rate of photodegradation as a function of total energy delivered to the paint.

#### 4.3 Paint Pressure Sensitivity

A PSP image of a jet impinging on a flat plate will be presented. Figure 4.8 will present an image of the pressure gradient created by the jet and Figure 4.9 will show a cross section comparing PSP data with transducer data. Examples of these figures are attached. Final figures will include error bars etc.

## 5.0 TEST ARTICLE DESCRIPTION

For application demonstration, the selected pressure-sensitive paints were applied to a state-of-the-art transonic compressor. The compressor test was conducted from September 1996 to January 1997 at the Turbine Engine Research Center (TERC) located at Wright-Patterson Air Force Base. The primary objective of this test was to obtain quantitative pressure measurements from the suction surface of the first stage rotor. The following paragraphs describe the test article description, test set up, and data acquisition procedure. The two-stage test compressor is presented schematically in Figure 5.1. The general airfoil geometry for this rotor is described in Table 5.1. At the aerodynamic design point, the relative Mach number was supersonic over 75% of the blade span. Table 5.2 presents the demonstrated baseline performance of this rotor at the design condition where the rotor speed is 13,288 rpm.

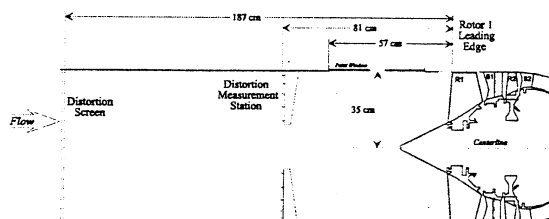


Figure 5.1. Profile Schematic of Test Compressor.

Table 5.1. Airfoil Geometry Parameters for Rotor 1.

Parameter	Value
Number of Blades	16
Average Aspect Ratio	1.22
Rotor Tip Radius, cm	35.24
Inlet Radius Ratio	0.33
Average Radius Ratio	0.47
Tip Solidity	1.5
Max. Thickness/Chord	0.028

Table 5.2 Rotor 1 Performance at 98.6% Speed, Design Pressure Ratio and Flow.



Parameter	Value
Total Adiabatic Efficiency, %	88.9
Total Pressure Ratio	2.5
Total Temperature Ratio	1.3
Corrected Tip Speed, m/s	480.7
Corrected Mass Flow, kg/s	71.8
Average Tip Clearance, mm	0.96
Tip Clearance to Actual Chord, %	0.46

In this study, PSP and TSP data at peak efficiency (PE) operating point at 85% corrected speed were obtained. Peak efficiency at 85% speed was the overall peak efficiency of the compressor<sup>10</sup>. Therefore, the first stage rotor was at least moderately loaded for the peak efficiency condition used in this demonstration.

### 5.1 Test Setup

The rotor test setup is shown in Fig. 5.2. A 305 x 25 mm window was placed ~260 mm upstream of the rotor leading edge. A 16-bit Princeton Instruments intensified charge-coupled device (ICCD) camera (576 x 384-pixel Thompson chip), fitted with a 50-mm *f*/1.2 lens, was located ~0.5 m upstream of the rotor. The camera viewed the blades across the flow path and was angled ~5 deg below the centerline to avoid viewing the bullet nose. A 2-mJ nitrogen pulsed laser beam (337 nm, 1-ns pulse) was launched into a fiber which was mounted adjacent to the camera. The laser was used in the pulse-on-demand mode—the laser only fired when the command was given to the ICCD to acquire an image. The beam (measured at 0.4  $\mu$ J at the exit of the fiber) was expanded to illuminate the visible suction surface of the first-stage rotor. With the presented viewing angle, the adjacent blade prevented viewing beyond 52% chord at the tip, and the image size restricted viewing inboard of 62% span.

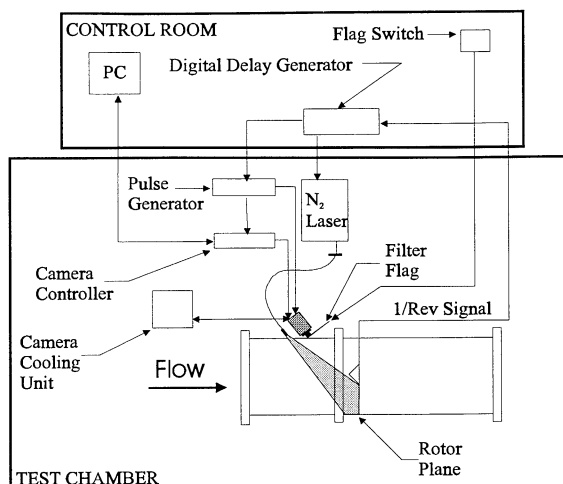


Figure 5.2 PSP Test Set Up.

The Princeton Instruments detection system included the ICCD, an ST-138 camera controller for image acquisition and readout via the personal computer, and an FG-100 pulse generator for triggering the camera. The camera system and laser were mounted on an optical table inside the test chamber. A Neslab cooling unit was used to maintain the ICCD chip at -20° C to minimize readout noise. The camera and nitrogen laser were remotely controlled from an adjacent room. As mentioned previously, TSP requires a blue filter on the detector while PSP does not. A filter arm (flag) was configured with a switch to allow remote positioning of the blue filter. When switched on, the current in the flag created a magnetic field which attracted the flag towards another magnet mounted on the optical table. Thus, the switch could be used to move the filter in and out of the camera path.

The following procedure was used to image the blade and acquire data images. Once the operator sends the command to initiate image acquisition, the CCD camera was charged, and the once-per-revolution pulse (1/rev) from the test article was used to initiate the timing sequence. The 1/rev signal was delayed by the amount,  $\Delta t_{\text{delay}}$ , required to rotate the desired painted blade into the image plane. A Stanford Research DG535 delay generator, triggered by the 1/rev, was used to send out two pulses—the first to trigger the pulse generator, which in turn triggered the camera, and the second to trigger the laser. The second pulse trailed the first by 13  $\mu$ s to take into account the time required for the camera electronics to respond to the trigger. This allowed synchronization of the arrival of the laser light at the blade surface and the activation of the camera intensifier for collecting the resulting fluorescence emission. The period of operation of the intensifier (gate time) was

determined by the laser pulse width and subsequent fluorescence emission of the paint. For this test a 1-ns laser pulse was used, and the maximum fluorescence lifetime was determined from calibration to be 323.5 ns (at vacuum and room temperature). The gate time was selected to be 10  $\mu$ s to take into account laser jitter on the order of 1  $\mu$ s. Therefore, the timing required to image the blade ( $< 2 \mu$ s) was achieved by the combination of the short laser pulse and the short-lived fluorescence of the paint--not by the gate of the intensifier. The camera "shutter," or charge time, was preset to a minimum of one rotor revolution. After the shutter closed, the acquisition of another image could not be initiated until the CCD downloaded the data to the computer. The readout time of the 221,184-pixel CCD chip was 234 ms. This limits this particular camera to steady state measurements since another image can not be acquired until the readout is complete.

### 5.2 Data Acquisition Procedure

Four types of images were required in PSP and TSP measurements: a wind-off reference image, a wind-on test image, a black image, and a white image. The black images were taken with the lens cap on to define the thermal noise of the CCD array. The white image was taken of a uniformly illuminated surface of arbitrary intensity. This image provided a flat-field correction for the "honeycomb" pattern on each image which results from the "minifier"--the tapered fiber-optic coupling between the photocathode and the CCD chip. Both the black and white images were only camera-dependent and could be taken either before or after the test. Thus, during a scheduled testing period, only the wind-off and wind-on images were acquired.

Wind-off images were acquired both before and after each test; pre- and post-test wind-off images could be compared to determine whether oil might be present in the compressor and to check for paint photodegradation. For acquiring the wind-off images, the rotor rotated 150 rpm where the pressure gradient was well below the current resolving capability of the paints. This approach provided valid reference images while allowing the timing circuitry to be used for accurate positioning of the blade images. For acquiring the wind-off images, the camera shutter was set to 400 ms. Sequential images were acquired using various timing delays until the desired painted blade appeared in the image. Care was taken to determine the delays required to place the TSP and PSP blades in the same location. The locations were determined by the image pixel coordinates of the blade leading edge. The delay and coordinates of each blade were recorded. Fifty wind-off images were acquired for each paint for steady-state averaging.

Once the wind-off images were acquired, the compressor was throttled to a desired test speed and condition. For the wind-on images, the camera shutter was reduced to 50 ms. To provide a

constant background noise from image to image, the shutter value remained constant for all of the wind-on images, regardless of the rotational speed. From the coordinates previously recorded during the acquisition of the wind-off images, the delays required to superimpose the TSP and PSP blades were determined, and the corresponding wind-on images were acquired. Fifty wind-on images were acquired from each blade at each test condition for averaging.

### 6.0 IMAGE PROCESSING

The post-processing was carried out mainly using PAINTCP, a program developed for NASA Ames by Sterling Software, Inc.<sup>11</sup>. This package is used in PSP image analysis for wind-tunnel aircraft model tests. For the purposes of this experiment, many of the functions within the code were not required; however, the program was used for its ability to register the alignment marks in each image and transform the wind-off image to align it with the wind-on image. A separate computer program was used to perform basic functions such as image averaging, subtraction, and division.

Each image captured by the ICCD camera can be described as a product of camera sensitivity,  $S(x,y)$ , illumination power,  $P(x,y)$ , and the paint emission,  $E(x,y)$ , plus thermal background noise,  $B(x,y)$ , as follows:

$$I(x, y) = S(x, y)P(x, y)E(x, y) + B(x, y) \quad (4)$$

where each parameter varies spatially. As a result of equation 4, two corrections were required for the wind-off and wind-on images prior to division and conversion to quantitative temperature or pressure data: 1) a background correction to take into account the thermal noise on the ICCD chip, and 2) a flat-field correction to take into account the spatial variations in camera sensitivity and illumination (attenuation). The thermal noise was removed by subtracting the background image, which only contained  $B(x,y)$ , from the wind-off and wind-on images. Removal of the camera attenuation was more difficult. A flat-field correction was used to remove the attenuation caused by the minifier--which results in a honeycomb pattern on the data image. This pattern--a mechanical effect of the camera--was fixed in all images; therefore, manipulation of the wind-on image to align it with the wind-off image would skew this pattern relative to the wind-on image, adding unnecessary pattern noise to the final image, as illustrated in Fig. 6.1.

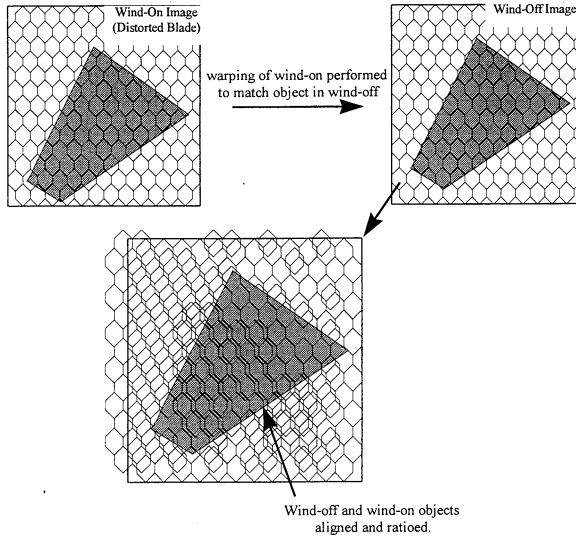


**Figure 6.1** Honeycomb-pattern noise caused by ICCD minifier.

To remove the honeycomb pattern caused by the ICCD minifier prior to using PAINTCP, both the background-corrected wind-off and wind-on images were divided by a white image--which was also background corrected. The process is depicted by equation 5:

$$\begin{aligned}
 I_{x_{\text{corrected}}} &= \frac{I_x - I_{\text{black}}}{I_{\text{white}} - I_{\text{black}}} \\
 &= \frac{\{S(x,y)P(x,y)E(x,y) + B(x,y)\} - \{B(x,y)\}}{\{S(x,y)P(x,y)E_o(x,y) + B(x,y)\} - \{B(x,y)\}} \\
 &= \frac{E(x,y)}{E_o(x,y)} \quad (5)
 \end{aligned}$$

where  $x$  represents either the wind-off or wind-on condition and the white image records the sensitivity, illumination power, and a reference emission,  $E_o(x,y)$ . All of the images (white, wind-off, and wind-on) were corrected for thermal noise,  $B(x,y)$ , by subtracting the background image,  $I_{\text{black}}$ . Dividing the wind-off and wind-on images by a white image should effectively remove  $S(x,y)$  and  $P(x,y)$ , leaving only the ratio of the paint emission,  $E(x,y)$ , and the reference emission used to create the white image,  $E_o(x,y)$ . Therefore, the final images should be free of the thermal noise caused by the CCD and the honeycomb pattern caused by the fiber-optic coupler of the camera. The reference emission,  $E_o(x,y)$ , cancels later in post processing

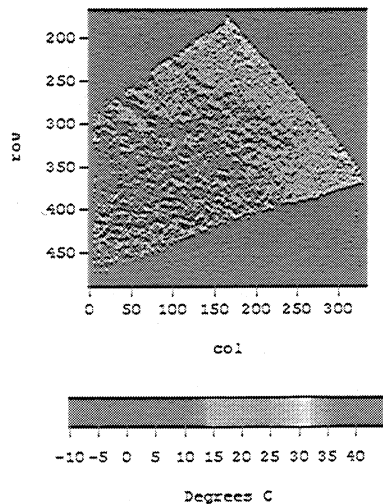
when the corrected wind-off image is divided by the corrected wind-on image.

Once the wind-off and wind-on images were corrected, the PAINTCP program was used to locate the alignment marks on the corrected images and the program was used to "warp" the corrected wind-on image to match the pattern of alignment marks in the corrected wind-off image. The wind-off image was then divided by the properly aligned wind-on image, and the final-image ratio is written to an IEEE floating binary file. This procedure was performed twice for each test condition--once for the TSP data and once for the PSP data. In order to temperature-correct the PSP data, the TSP image was also aligned with the PSP image. Therefore, all of the pressure and temperature images were aligned to the same wind-off PSP image.

The output from the PAINTCP program was read into a software package which allowed simple matrix and image manipulation. The equation determined from the paint calibration for the TSP was applied to the temperature matrix to convert the intensity ratio to surface temperatures (in °C). These results were output to a new matrix. Because the temperature image was aligned with the pressure image using PAINTCP, the temperature image could be used to calibrate the pressure image directly. The surface-temperature information and the intensity-ratio data from the PSP image were input into the calibration equation for the PSP, and the resulting surface-pressure information was output to a second matrix. The final temperature image and temperature-corrected pressure image were scaled and plotted with false-color.

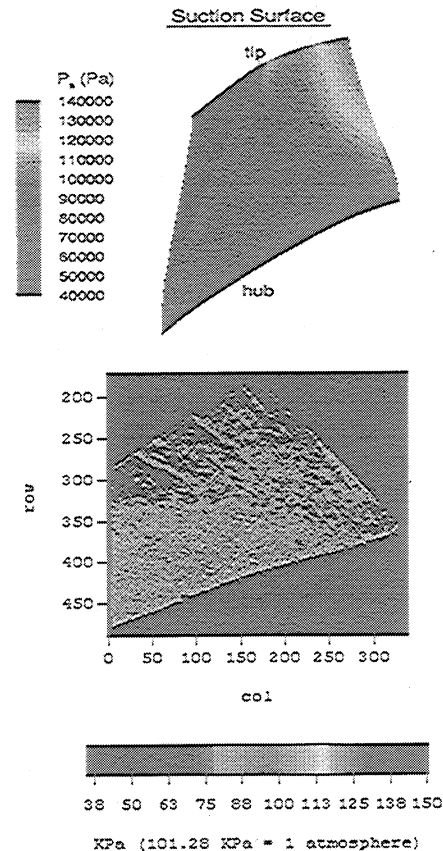
## 7.0 TRANSONIC ROTOR RESULTS

Figure 7.1 depicts the area of the blade where temperature and pressure data were acquired. The lines are used to outline the physical image region of the blade because the photograph of the blade was taken at a different point-of-view than the data acquired from the paints. The approximate dimensions of the viewable area of the blade where data were acquired are from 0-52% chord at the tip and from 62-100% span at the leading edge. Approximately 61,500 pixels were focused on the blade for P/TSP measurements. Accounting for pixel blur, the actual spatial resolution obtained was 1.2 mm in the direction of rotation and 0.4 mm radially. Therefore, the PSP offers a measurement point ~ 27% of the size of a 1.5-mm diameter transducer. While the spatial resolution was maintained in the radial direction, only 1/3 of the



**Figure 7.2** Calibrated TSP image at 85% Nc, peak-efficiency operating condition.

The average of fifteen TSP and 15 PSP images obtained at the 85% Nc, peak-efficiency condition were processed as described previously. Figure 7.2 presents the final TSP results. The surface temperatures at the leading edge ranged from 25° C at ~62% span to 50° C at the tip. At ~52% chord the temperatures ranged from 0° C at ~62% span to 50° C at the tip. Figure 7.3 shows the final PSP data corrected for temperature using the TSP data. The two chordwise streaks are the result of some oil present in the test article. The oil contamination was visible in the wind-off TSP image. Because the oil was present in only one image it was not ratioed out. Furthermore, since the oil affected the TSP image, the streaks were propagated into the PSP data when the data was corrected for temperature. Figure 7.3 also shows the CFD prediction for 85% Nc for qualitative comparison. The CFD code used was developed by NASA Lewis<sup>12</sup>. The shock location in the PSP agrees with the prediction.



**Figure 7.3** CFD prediction and temperature-corrected PSP image, 85% Nc, peak-efficiency operating condition.

## 9.0 DISCUSSION

-prototype paints successfully endured environment and adequately demonstrated the technology potential.

-paints need to be improved. "Off-the-shelf" RTVs are not the binder of choice. It is very difficult to engineer crosslinked polymers (RTV's) to get desired binder performance (e.g. temperature stability, oxygen permeability). Paint development will continue using sol-gels and synthesized polymers.

## ACKNOWLEDGEMENTS

The authors would like to thank all the employees of the Turbine Engine Research Center (TERC), Wright Laboratory, for their support during the compressor test. We would like to thank Dr. Chunill Hah of NASA Lewis Research Center for providing the CFD code used for qualitative comparison to the

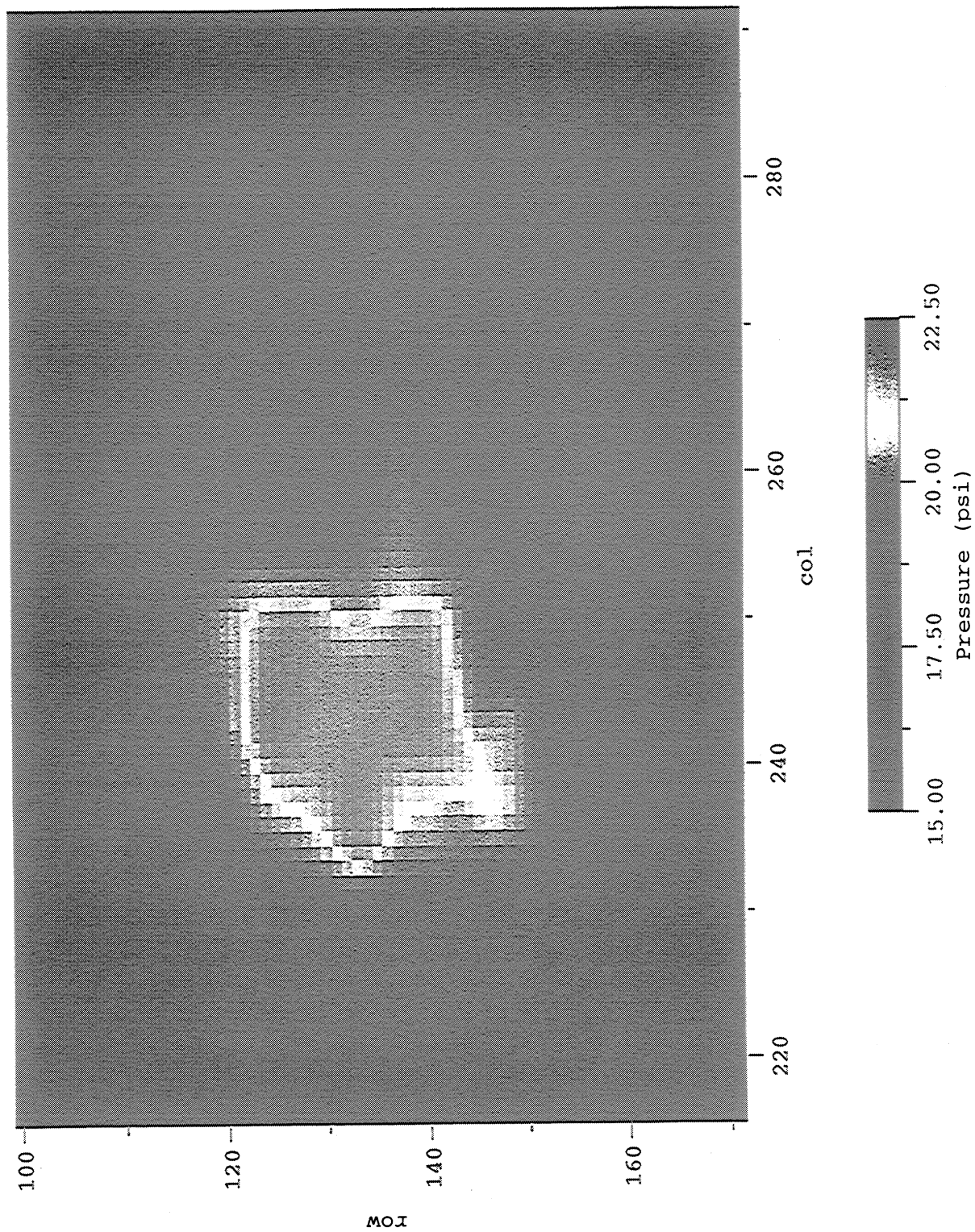
PSP data and Dr. James Bell of NASA Ames Research Center for providing the PAINTCP code used for image processing.

# REFERENCES

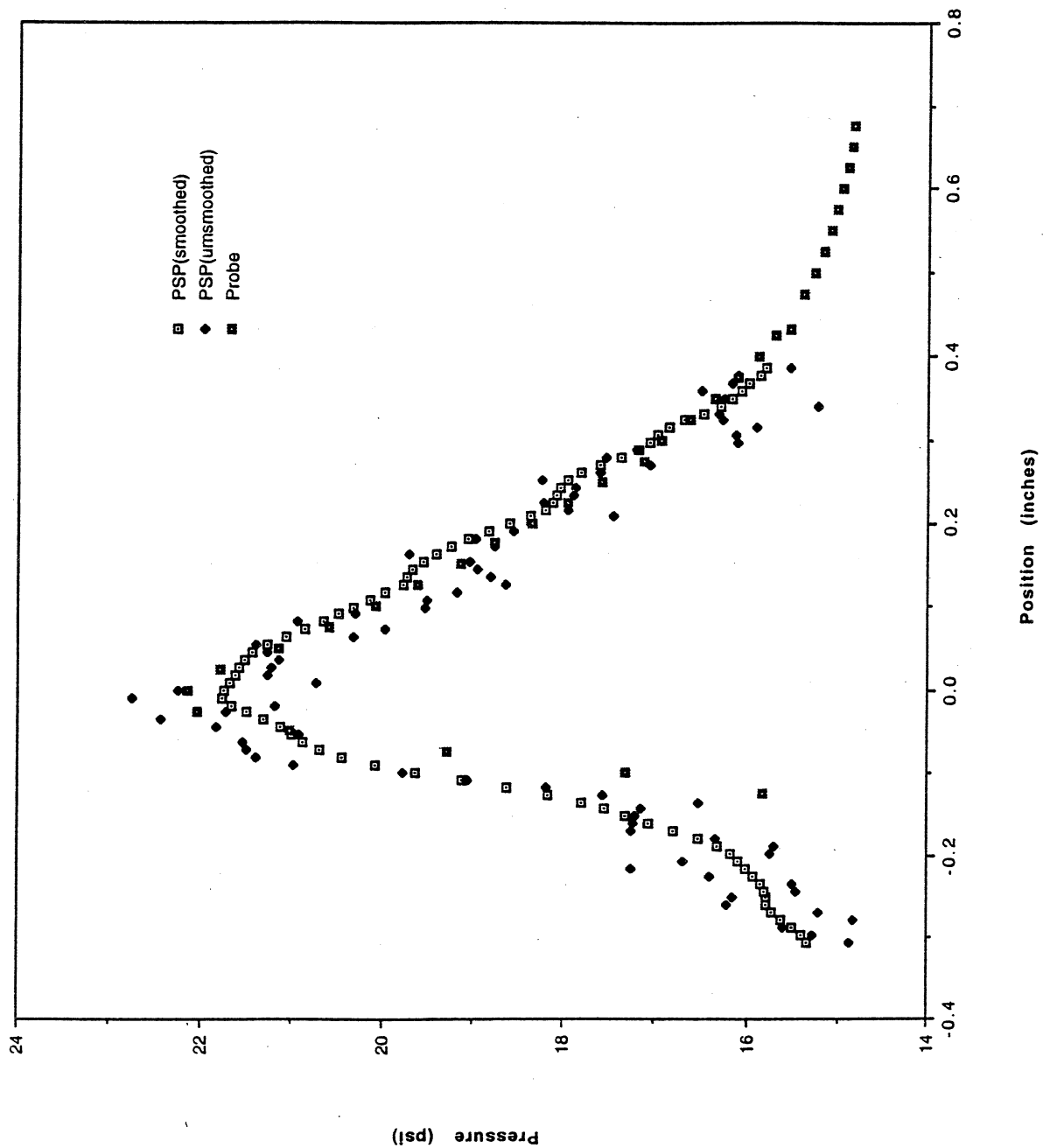
- (1) Sexton, M. R., O'Brien, W. F., and Moses, H. L., "An On-Rotor Investigation of Rotating Stall in an Axial Compressor," Defense Technical Information Center (DTIC) Technical Report, Cameron Station, Alexandria, VA, pp. 33.1-10, 1973.
- (2) Kavandi, J., Callis, J., Gouternam, M., Khalil, G., Wright, D., Green, E., Burns, D., and McLachlan, B., "Luminescent Barometry in Wind Tunnels," *Rev. Sci. Instrum.*, Vol. 61, No. 11, pp. 3340-3347, 1990.
- (3) Sabroske, K. R., Rabe, D. C., and Williams, C., "Pressure-Sensitive Paint Investigation for Application in Turbomachinery," ASME Paper No. 95-GT-92, ASME International Gas Turbine and Aeroengine Congress and Exposition, Houston, Texas, 1995.
- (4) Lepicovsky, J., Bencic, T. C., and Bruckner, R. J., "Application of Pressure-Sensitive Paint to Confined Flow at Mach Number 2.5", AIAA- Paper No. 97-3214, AIAA/ASME/SAE/ASEE Joint Propulsion Conference and Exhibit, Seattle, WA, 1997.
- (5) Hamner, M., B. Campbell, T. Liu, and J. Sullivan, "A Scanning Laser System for Temperature and Pressure-Sensitive Paint," AIAA- Paper No. 94-0728, AIAA 32nd Aerospace Sciences Meeting and Exhibit, Reno, NV, 1994.
- (6) Morris, M. J., and Donovan, J. F., "Application of Pressure- and Temperature-Sensitive Paints to High-Speed Flows", AIAA- Paper No. 94-2231, AIAA 32nd Aerospace Sciences Meeting and Exhibit, Reno, NV, 1994.
- (7) Liu, T., Johnston, R., Torgerson, S., Fleeter, S., and Sullivan, J., "Rotor Blade Pressure Measurement in a High Speed Axial Compressor using Pressure and Temperature Sensitive Paints," AIAA Paper No. 97-0162, AIAA 35th Aerospace Sciences Meeting and Exhibit, Reno, NV, 1997.
- (8) Gruber, M. R., Nejad, A. S., and Goss, L. P., "Surface Pressure Measurements in Supersonic Transverse Injection Flowfields," AIAA Paper No. 97-3254, 33rd AIAA/ASME/SAE/ASEE Joint Propulsion Conference and Exhibit, Seattle, WA, 1997.
- (9) Navarra, K. R., "Development of the Pressure-Sensitive-Paint Technique for Turbomachinery Applications", Master's Thesis, Virginia Polytechnic Institute and State University, Blacksburg, VA, May, 1997.
- (10) Russler, P., Rabe, D., Cybyk, B., and Hah, C., "Tip Flow Fields in a Low Aspect Ratio Transonic Compressor," ASME Paper No. 95-GT-089, ASME International Gas Turbine and Aeroengine Congress and Exposition, Houston, Texas, 1995.
- (11) *PaintCp V2.2 User's Guide*, Sterling Software Technical Note TN-93-8006-000-48, 1994.
- (12) Copenhaver, W. W., Hah, C., and Puterbaugh, S. L., "Three-Dimensional Flow Phenomena in a Transonic, High-Through-Flow, Axial-Flow Compressor Stage," *J. Turbomachinery*, Vol. 115, No. 2, pp. 240-248, 1993.



## Jet - Plate Experiment



## Wall-Jet Experiment



Paper 18  
Author: Navarra

Q: Voigt

Since the honeycomb is a consistent pattern in the images that have been taken with an intensified CCD-camera, it should be possible to suppress the effect in the frequency domain, where the pattern will appear as a peak at a certain spatial frequency. Did you try this ?

A: No, this was not attempted but, it is believed that this would not be sufficient to correct the data because of the noise.

Q: Versluis

Referring to the poor quality of the images (in your paper attributed to the ICCD camera). Are you sure these effects are not caused by pulse-to-pulse fluctuations of the pulsed  $N_2$  - laser ?

A: No, the pulse-to-pulse fluctuation of the laser is  $\sim 1\%$  and therefore was not a concern. Again, the major noise source was from the intensified CCD camera.

Q:

Did you observe or have to correct for any self-illumination effects in your work within the confined spaces in turbomachinery ?

A: No, the painted blades were not adjacent, they were sufficiently spaced such that self-illumination was not an issue.

# Effects of Mach Number on Supersonic Wraparound Fin Aerodynamics

Thomas C. McIntyre\*

*U.S. Air Force Institute of Technology, Wright–Patterson Air Force Base, Ohio 45433-7765*

Rodney D. W. Bowersox†

*University of Alabama, Tuscaloosa, Alabama 35487-0280*

and

Larry P. Goss‡

*Innovative Scientific Solutions, Inc., Dayton, Ohio 45440-3638*

An experimental Mach number parametric ( $M \in [2.15, 3.83]$ ) study was conducted to investigate the apparent rolling-moment reduction with increasing Mach number noted in flight-test experiments. The aerodynamic loading and the surface flow in the fin region of wraparound fin missiles in high-Reynolds-number ( $Re_C \in 0.3 \times 10^6$  to  $0.9 \times 10^6$ ) supersonic cross streams were investigated using photoluminescent pressure-sensitive paint and surface oil-flow visualizations with fluorescent pigment as the seeding medium. Schlieren photography was used to characterize the fin-generated shock structures. Two curved-fin missiles were tested, one having a solid fin and the other a slotted fin. The fin pressures were integrated for rolling moments; these data confirm the solid-fin missile reduction in rolling moment with increasing Mach number. The slotted-fin missile exhibited a similar rolling-moment Mach number dependence. Analysis of the pressure distributions, surface streamlines, and shock structures indicated that the flowfields experienced very strong and complicated inviscid–viscous interactions and that these interactions had a significant impact on the aerodynamic loading of the fins. Finally, the slotted-fin missile demonstrated the potential for increased roll stability and reduced wave drag.

## Nomenclature

$A$	= missile cross-sectional area, mm <sup>2</sup>
$C_L$	= $L/(q_\infty Ad)$
$d$	= missile diameter, mm
$I_0/I$	= pixel luminescence ratio ( $I_0$ = ambient reference intensity)
$K_q$	= Stern–Volmer constant
$L$	= rolling-moment, N-m
$P_{O_2}$	= partial pressure of oxygen
$p$	= static pressure, atm
$p_{t\infty}$	= freestream total pressure, atm
$q_\infty$	= freestream dynamic pressure, atm
$Re_C$	= Reynolds number based on fin chord length

## Introduction

WRAPAROUND fins (WAFs; Fig. 1) have been used on tube-launched missiles and dispenser-launched projectiles. Modern advances in stealth technology have made the use of missiles equipped with WAFs desirable because they can be stowed to reduce the radar cross section of the aircraft. Recent studies have identified several roll- and pitch-moment instabilities.<sup>1</sup> The roll reversal at transonic conditions is the most recognized instability. The rolling moment of the WAF is positive at subsonic velocities (defined here to mean that the missile rolls toward the concave side of the fin). A roll reversal occurs at Mach 1.0. Range tests<sup>1–4</sup> have indicated that the magnitude of the rolling moment decreases with increasing Mach number and that a second rolling-moment reversal may occur at high supersonic speeds ( $M \sim 4.5$ – $4.7$ ). Abate<sup>5</sup> postulated that the

loss of static stability at high supersonic Mach numbers is related to the complex shock structure in the fin region.

Tilman et al.<sup>6</sup> and Tilman and Bowersox<sup>7</sup> examined experimentally and numerically the flow structure in the vicinity of a single fin mounted onto a blended cylindrical-body wind-tunnel wall model at Mach 3.0 and 5.0. Those studies indicated that the flowfield was highly asymmetric about the WAF, with a stronger bow-shock structure on the concave side of the fin. The viscous computational fluid dynamics (CFD) solutions indicated that, on the concave side of the fin, the shock is focused, creating a very high-pressure region between the fin and its center of curvature, which resulted in relatively high surface pressures near the midspan of the fin. In contrast, on the convex side of the fin, surface pressure is relatively independent of location along the span. In addition to the shock-structure asymmetries, a juncture vortex on the concave side of the fin was identified. This viscous structure also was found to influence asymmetrically the pressure loading of the curved fin. The numerical viscous solutions did predict a reduction in rolling moment at Mach 5.0 as compared to Mach 3.0. However, a roll reversal was not observed.

The primary purpose of the present study is to examine experimentally the Mach number dependence of the aerodynamic loading and viscous surface flow in the fin region of the WAF projectiles. Two full axisymmetric four-fin missile models were tested. One model was equipped with solid fins, and the other had slotted fins. The purpose of the slot was to provide pressure relief, thereby reducing the Mach number dependence of the rolling moment. Pressure-sensitive paint (PSP), surface oil-flow visualizations, and schlieren photography were used to analyze the fin pressure loading, viscous streamline structure, and shock structure, respectively. A high-Reynolds-number Mach number parametric study was performed, where the Mach number was varied over the range 2.15–3.83. In addition to the Mach number parametric investigation, the single-fin configuration from Refs. 6 and 7 was examined using the same PSP apparatus. A comparison of the experimental results to the CFD predictions of Refs. 6 and 7 was performed.

## Experimental Facilities

The two four-fin models used for testing are shown in Figs. 1 and 2 (side and rear views). The projectile diameter was used to

Received March 27, 1998; revision received May 26, 1998; accepted for publication May 27, 1998. This paper is declared a work of the U.S. Government and is not subject to copyright protection in the United States.

\*Graduate Research Assistant; 2nd Lieutenant; currently Project Officer, Launch Programs, Space and Missile Systems Center, Medium Launch Vehicle Office (Delta II). Member AIAA.

†Assistant Professor, Department of Aerospace Engineering and Mechanics. Senior Member AIAA.

‡Research Scientist and President, 2786 Indian Ripple Road. Senior Member AIAA.

Table 1 Nominal test conditions

Mach no.	$p_{\infty}$ , atm	$Re_C$ , $\times 10^6$	$L$ , N-m	
			Solid fin	Slotted fin
2.15	2.8	0.33	-0.046	-0.052
2.15	6.1	0.72	-0.048	-0.050
2.15	7.0	0.83	-0.052	-0.042
2.41	3.9	0.40	-0.032	-0.057
2.41	7.1	0.74	-0.036	-0.047
2.41	8.6	0.90	-0.041	-0.073
2.86 <sup>a</sup>	2.1	0.37	—	—
2.86	5.8	0.48	-0.031	-0.062
2.86	8.2	0.68	-0.028	-0.020
2.86	9.8	0.81	-0.032	-0.052
3.25	8.9	0.60	-0.016	-0.041
3.25	10.4	0.70	-0.032	-0.055
3.50	8.7	0.52	-0.017	-0.061
3.50	10.0	0.60	-0.024	-0.039
3.50	11.3	0.68	-0.025	-0.055
3.83	11.5	0.58	-0.022	—
3.83	12.1	0.61	-0.016	—

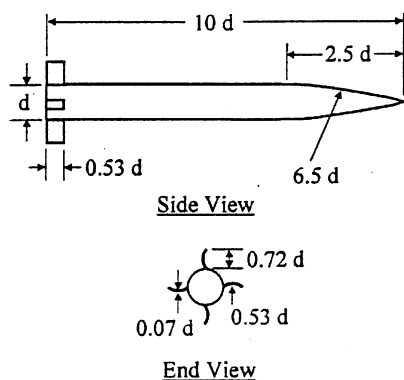
<sup>a</sup>Single-fin experiments.

Fig. 1 Schematic of solid-fin model (not drawn to scale).

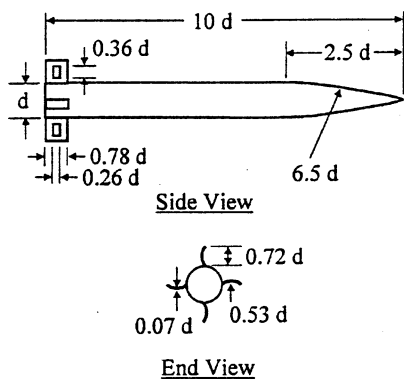


Fig. 2 Schematic of slotted-fin model (not drawn to scale).

scale the major physical features of the models. Both models had a diameter of 1.91 cm. The slotted-fin model had 28.6% more surface area than the solid-fin model, when viewed from the side.

A variable-Mach supersonic blowdown wind tunnel located at Wright-Patterson Air Force Base was used for testing the missile models shown in Figs. 1 and 2. The wind tunnel provided a uniform Mach number distribution across the test section to within 2.0%. The test-section static pressure, total pressure, and total temperature were recorded during each run. The total temperature was 295 K for all runs. The expected uncertainties are described in the Uncertainty Analysis section. The nominal flow conditions for each test condition are summarized in Table 1. The test-section dimension of this tunnel ( $15.24 \times 15.24$  cm) limited the lowest Mach number to 2.15. For Mach numbers lower than this, the missile nose shock reflections off the tunnel walls intersected with the tail of the missile.

PSP tests also were conducted on the single-fin model described in Refs. 6 and 7. A schematic of this model is presented in Fig. 3.

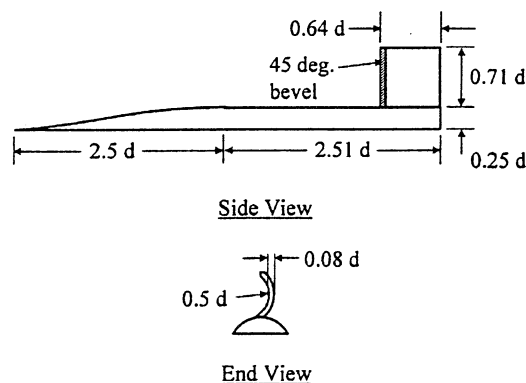


Fig. 3 Schematic of single-fin model (not drawn to scale).

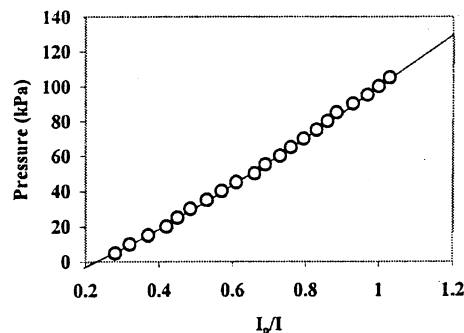


Fig. 4 PtOEP pressure calibration.

The Mach 3 pressure-vacuum wind tunnel described in Ref. 6 was used for the single-fin model testing.

## Experimental Techniques

### PSP

PSP was used to analyze fin pressures. This nonintrusive method provided continuous pressure data on the missile body and fins. Because the fins are the source of rolling moment due to pressure forces, the pressure measurements were concentrated in the fin region.

PSP technology has been documented extensively.<sup>8-10</sup> Measurements are based on the phenomenon of photoluminescence. A probe molecule absorbs a photon of specific energy, exciting it to a higher state. The molecule then returns to the ground state by emitting a photon of lower energy. However, if an oxygen molecule is present, the excess energy of the probe molecule will be transmitted to the oxygen during a collisional deactivation. The oxygen-quenching phenomenon can be modeled with the Stern-Volmer relationship:

$$I_0/I = 1 + K_q P_{O_2} \quad (1)$$

Variations in temperature affect  $I_0$  and  $K_q$ , causing temperature sensitivities. In the present study, short test times (<30 s) and 30-min reservoir recharge periods resulted in the missile surface remaining at room temperature (295 K).

The Stern-Volmer equation was applied by taking images at a reference pressure condition (ambient pressure) and at the test condition. The ambient pressure intensity  $I_0$  then was divided by the test intensity  $I$ . The ratio of intensities was calibrated at room temperature. The calibration curve obtained is shown in Fig. 4. The correlation coefficient for the curve fit was 0.999.

The pressure-sensitive material applied to the WAF missiles was developed at the Arnold Engineering Development Center (AEDC).<sup>11</sup> The probe molecule consisted of platinum octaethylporphyrin (PtOEP) diluted in toluene and sprayed over a white Krylon titanium dioxide primer layer of paint. This primer removed intensity variations in the metallic construction of the missile fins and body. The maximum excitation wavelengths of the PtOEP paint are at 380 and 540 nm, with emissions at 650 nm. A scientific-grade Pixel Vision charge-coupled device (CCD) camera recorded photographs, using a  $516 \times 516$  pixel monochrome CCD and 50-mm lens.



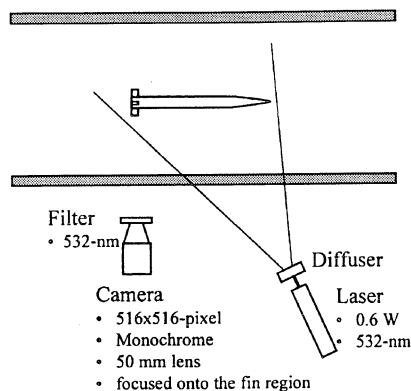


Fig. 5 Top-view schematic of the PSP experimental setup.

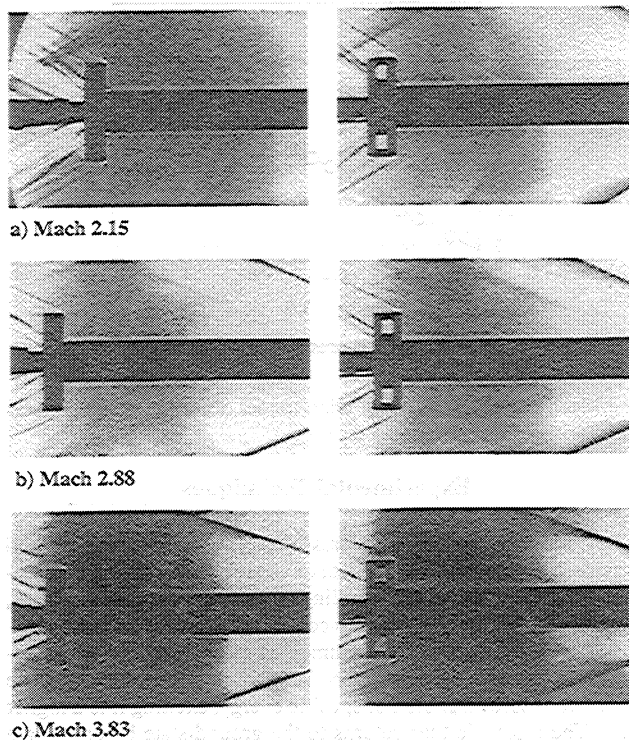


Fig. 6 Solid- and slotted-fin schlieren images (vertical knife edge).

The paint was excited with a Spectra-Physics Millennia continuous-wave laser at 532 nm. The 0.6-W laser light was diffused by a plate of packed ground glass and shined on the test subject. A red filter was placed over the camera lens to ensure that only paint emissions would be captured on the CCD. Figure 5 is a schematic of the setup. Ten air-off images were taken and averaged to remove systematic ambient nonuniformities.

#### Surface Oil-Flow and Schlieren Photography

To obtain surface streamlines, a fluorescent powdered yellow dye was diluted into 200 cS of silicon oil. During the tunnel run, the dye was illuminated with two 115-V Black-Ray B-100A ultraviolet lamps. Schlieren photography, with a continuous mercury-vapor light source, was used to characterize the shock structures. A vertical knife-edge arrangement was used to improve the definition of the shock/boundary-layer interactions. For both the surface oil flow and the schlieren photography, images were acquired with a Kodak DCS 420 color digital camera (ISO setting of 200 and shutter speed of 1/30th s).

### Experimental Results

#### Schlieren Imaging

Presented in Fig. 6 are representative schlieren photographs for the solid- and slotted-fin missiles for Mach numbers 2.15, 2.88,

and 3.83. These images highlight the complex nature of the present flowfield near the fin regions of the missiles. Important details are revealed about shock locations. A slightly detached bow shock is visible just upstream of the fin. When this shock interacted with the fuselage boundary layer, a lambda shock was formed, which appeared just upstream of the base of the fin leading edge. Also noticeable in the schlieren images are oblique shock-wave structures exiting the fin region. The angle and vertical extent up the fin decreased with decreasing Mach number. These shock waves were produced by viscous phenomena near the fin-fuselage juncture—a vortex on the convex side and a flow separation on the concave side (these features are discussed in detail in the next section).

#### Surface Oil-Flow Visualizations

As mentioned in the Introduction, one of the purposes of the study was to examine the effects of Mach number on the surface flow. To that end, Fig. 7 shows the surface oil-flow visualization results for the solid- and slotted-fin missiles for  $M = 2.15$ , 2.88, and 3.83. The convex fin is on the top and the concave fin is on the bottom. Qualitatively, the fin surface streaklines are very similar to those of the single-fin numerical solutions of Tilmann et al.<sup>6</sup>

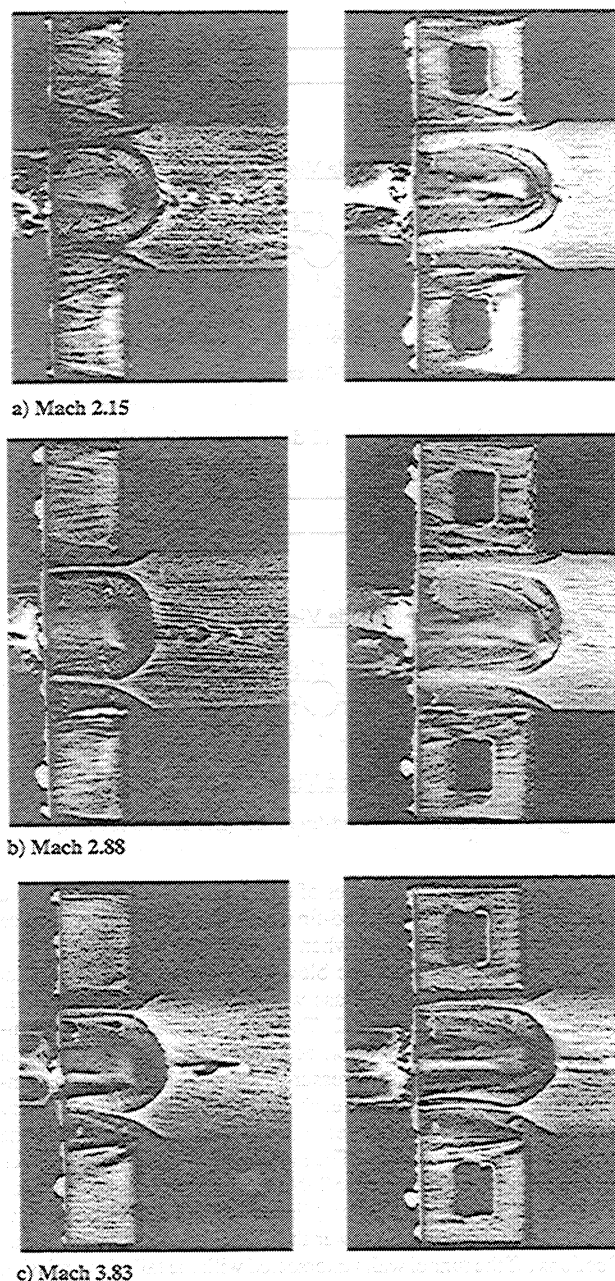


Fig. 7 Solid- and slotted-fin surface oil-flow visualizations.

However, the missile body streamlines did not compare well because the multiple fins in the present configuration created shock-induced compressions in the oil flow between the two fins. Examination of these images reveals the Mach number dependence on the salient flowfield features described in detail in Ref. 6.

Concentrating first on the surface phenomena on the concave side of the solid fin (bottom fin in Fig. 7), the flow near the fin root was characterized by a vortex embedded in the juncture of the fin and fuselage. The relatively large accumulation of oil that began near the fin leading-edge root region and progressed downstream at an angle relative to the fuselage provided an indication of the size and shape of the vortex. The size of the dark regions above and below the vortex, which indicate streamline divergence toward the vortex, also provided an indication of the vortex strength, i.e., the strength of the entrainment process. At Mach 2.15, the secondary flow motion influenced a relatively large (compared to the higher Mach numbers) portion of the fin. At Mach 3.83, the vortex was confined to a very small region. However, the strength of the vortex appears to have increased with increasing Mach number, where a large portion of the flow, as indicated by the strong divergence of streaklines (dark region just outward of the juncture vortex) over the fin has been entrained into the vortex. Tilmann et al.<sup>6</sup> have suggested that this viscous phenomenon may, in part, be responsible for the reduced rolling moment at the high Mach numbers.

The surface oil-flow visualizations also highlight the flow pattern near the outer tip of the fin. The dark wedge-structure oil pattern, which emanated from the leading-edge tip region, provided evidence for a slight leakage or separation from the fin, which, like the juncture vortex, was more prominent at the low Mach number. For the higher-Mach-number experiments ( $\geq 2.41$ ), the flow over the main region of the fin, away from the juncture-vortex and the tip, was relatively orderly. For the Mach 2.15 case, a large disturbance is noticeable emanating from the leading-edge root and proceeding to the trailing-edge midfin height. It is thought that this feature created a region of relatively low pressure and thus had a strong impact on the rolling moment.

On the concave side of the fin (top fin in Fig. 7), the juncture region was characterized by a separation, indicated by the wedge-like region near the root that is void of oil. As the Mach number was increased, the size of the separation region decreased dramatically. The oil patterns near the tip suggest that the flow diverged slightly out toward the fin bevel. As on the convex side, the flow over a large region of the fin (away from the root separation) was reasonably well ordered, with a slight divergence near the aft region of the fin.

The surface oil-flow visualizations in Fig. 7 also highlight the fuselage flow. Progressing in the flow direction, i.e., from right to left, the asymmetric lambda-shock separation line is the first surface disturbance. As expected, as the Mach number was increased, the shock structure became more oblique. The lambda shock was slightly more normal on the convex side and slightly more oblique on the concave side of the fin. The next line of separation indicates the location of the fin-fuselage horseshoe-vortex system. Like the shock structure, the horseshoe vortex was also asymmetric around the fin. As the Mach number was increased from 2.15 to 3.83, the horseshoe vortex moved closer to the fin on the concave side. However, on the convex side of the fin, the horseshoe-vortex position remained fixed as the Mach number was varied.

The slotted-fin surface oil-flow visualizations indicate that the presence of the slot dramatically changed the surface flowfield. Concentrating on the convex side of the fin (bottom fin in Fig. 7) at Mach 2.15, the juncture vortex described earlier was present upstream of the slot. However, the vortex intersected the slot region of the fin, and the strength of the vortex was reduced aft of the slot. This slot interaction effect was observed to diminish with increasing Mach number; this occurred because the vortex region became more confined to the fuselage as the Mach number was increased. Furthermore, the slot appears to have eliminated the tip leakage separation near the fin tips.

The slots also had a significant impact on the fuselage flow patterns. First, at  $M = 2.15$ , the extent around the fin of the lambda shock was greatly reduced, which indicated that the pressure relief

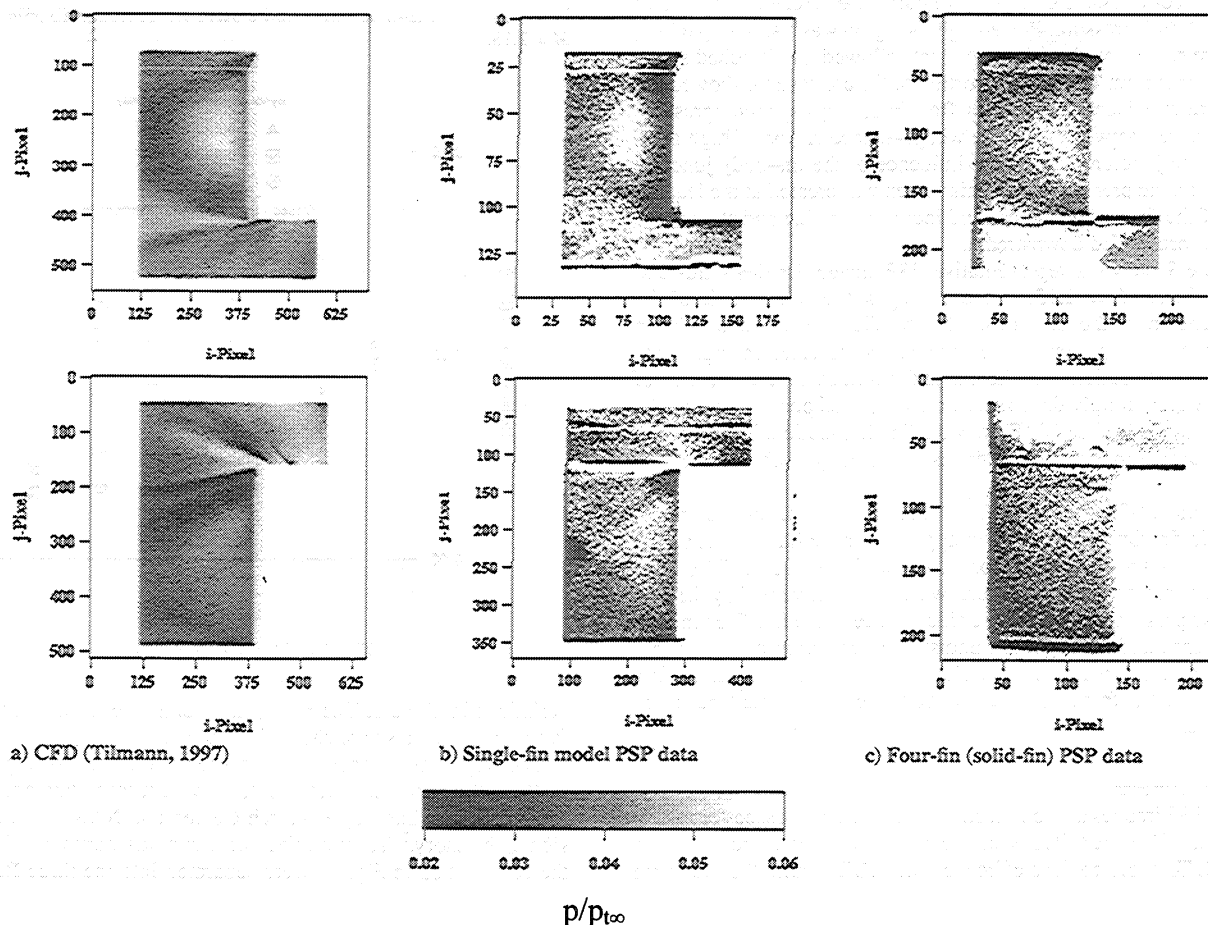


Fig. 8 Comparison of pressure fields at Mach 2.9 (convex side of fin on the top, and concave side of fin on the bottom).

provided by the slot reduced the apparent blockage of the fin. This pressure relief translates into potential wave drag reduction; this effect was so strong that a relatively large region of undisturbed flow existed between the shock structures generated by adjacent fins. This region of undisturbed flow was not present for any of the solid-fin experiments. Interestingly, as the Mach number was increased past 2.88, the shock structure upstream of the fin became more symmetrical and somewhat independent of Mach number. As the Mach number was increased, the adjacent fin-generated shock structure interactions became more severe and the undisturbed region diminished in size. On the concave side of the fin, at Mach 3.83, the undisturbed region was no longer present, and the shocks appear to have interacted with the horseshoe vortex, creating a complex flow region.

### PSP

PSP was applied to the wall-mounted, single-fin model of Ref. 6 and the four-fin models (Figs. 1 and 2) for validation and flowfield analysis purposes, respectively. Figure 8 compares viscous CFD results<sup>6</sup> for the single-fin configuration to present PSP measurements for both the single-fin and four-fin models. A reasonable degree of dynamic similarity existed among the CFD calculations, the single-fin model, and the axisymmetric four-fin model, where the Mach numbers were matched to within the measurement uncertainty and the Reynolds numbers based on fin chord were reasonably consistent. The flow conditions and fin geometry for the single-fin CFD calculations<sup>6</sup> were chosen to match the single-fin experimental test case ( $M = 2.88$  and  $Re_c = 3.7 \times 10^5$ ). For the four-fin model, the Mach number was set to 2.88 and the Reynolds number for the data shown in Fig. 8 was somewhat higher at  $4.8 \times 10^5$ . As the data in Fig. 8 indicate, good qualitative and quantitative agreement was observed between the single- and four-fin models and the CFD solution. The black spot in the aft, middle portion of the convex fin (Fig. 8b) resulted from an accumulation of Krylon primer, which flawed the data in this location.

The solid-fin images in Fig. 8 show high pressures along the leading edge of the fin. These strong stagnation pressures were expected for the relatively blunt fins in this study. On the concave side fin surface, the compressive effects of fin curvature<sup>6</sup> created a triangular region of high pressure. Preceding this region was a small lip of low pressure caused by the expansion that followed the detached shock in front of the fin. The bottom portion of the concave fin showed another pressure increase, resulting from boundary-layer compression that occurred between fins. The wedge-shaped region of high pressure in the juncture depicts the influence of the fin-body juncture vortex<sup>6</sup> on the pressure field. This vortex was created at the leading edge of the fin-body juncture and increased in size and strength as the flow proceeded downstream.

Figure 9 shows a representative PSP image for the solid- and slotted-fin at  $M = 2.15$ . In these images, the convex side of the fin is shown at the bottom of the missile, the concave side on the top, and a top view in the middle. As indicated in Fig. 9, the pressure distributions on the fin and fuselage in the vicinity of the fin were strongly dependent on the viscous phenomena, as described in the Surface Oil-Flow Visualization section. The detached shock formed in front of the fins is also clearly visible in the PSP images.

The slotted-fin images in Fig. 9 display many of the features of the solid fin. On the fin, the slot appears to have little effect on the pressure distribution, except for the slot walls themselves. The same triangular region of high pressure, which was interrupted by the slot, was also present on the concave side surface of the fin. The juncture vortex appeared to have been undisturbed upstream of the slot but disappeared downstream of the slot. It is likely that momentum flux through the slot from the concave side of the fin dispersed the vortex structure.

### Rolling Moments

The PSP images at each Mach number were processed for rolling moments. The magnitudes of the rolling moments are shown in Fig. 10. To avoid cooling effects on the PtOEP paint, the first three photographs at each flow condition were used. During this 12-s period, the total pressure varied, resulting in the Reynolds number

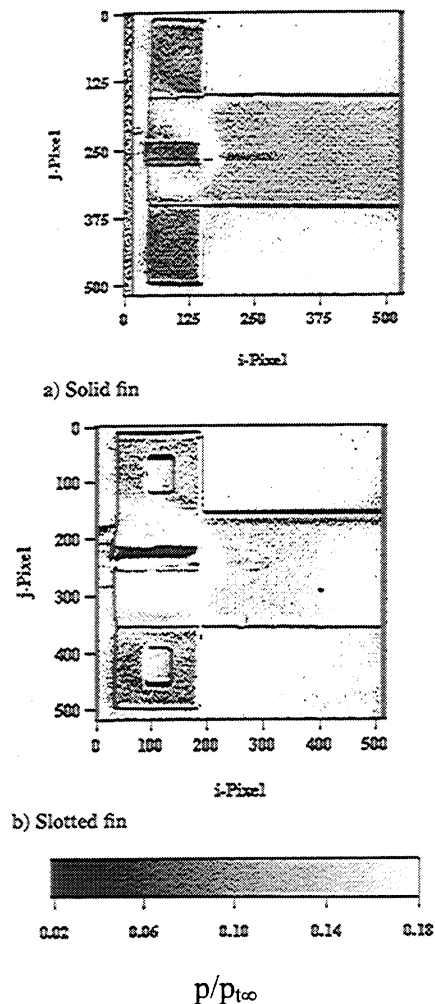


Fig. 9 Comparison of solid- and slotted-fin pressure distributions at  $M = 2.15$ .

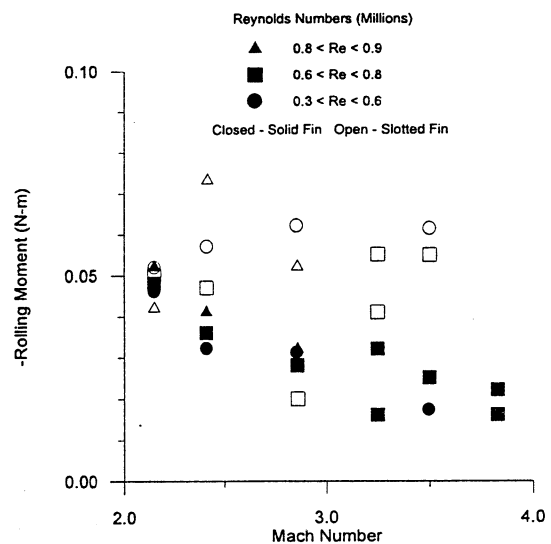


Fig. 10 Rolling moments.

variations in Table 1. The rolling moments at each flow condition for both models also are shown in Table 1.

The Reynolds number has been shown to have a strong impact on the rolling-moment coefficient, as evident from data obtained at AEDC, NASA Langley Research Center, and NASA's Jet Propulsion Laboratory.<sup>7</sup> To minimize the Reynolds number influences, the data plotted in Fig. 10 were separated into the three Reynolds number ranges as annotated. As indicated, the Reynolds number variations did produce increased scatter of the data. However, all

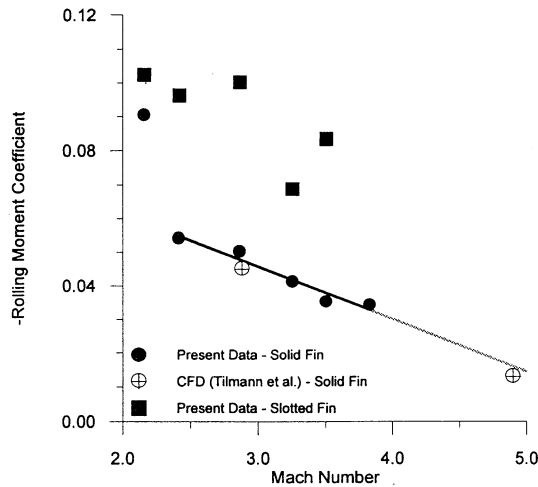


Fig. 11 Rolling-moment coefficients.

of the data suggest a strong reduction in the rolling moment with increased Mach number. This result confirms the test-range trend described by Abate.<sup>5</sup>

The slotted-fin rolling moments also are plotted in Fig. 10. The rolling-moment scatter of the slotted fin was higher because of the increased uncertainty associated with locating the slot in the data reduction procedure. This effect, coupled with the aforementioned Reynolds number variations, obscured the Mach number trends. This shortcoming is discussed in the remainder of this section.

The rolling-moment coefficients are plotted in Fig. 11. To reduce the apparent experimental scatter, the data shown in Fig. 11 correspond to a Reynolds number of nominally  $0.6 \times 10^6$  ( $\pm 10\%$ ) and a dynamic pressure of 100 kPa ( $\pm 10\%$ ). However, for the Mach 2.15 and 2.41 cases, the plotted data correspond to Reynolds numbers of 0.33 and 0.40, respectively. For the Mach numbers with more than one data point within the 10% range, those values were averaged into the single points plotted in Fig. 11. The expected uncertainties are described in the Uncertainty Analysis section. Also shown in Fig. 11, for comparison purposes, are the rolling-moment CFD predictions (the dynamic pressures were 40 and 99 kPa at  $M = 2.9$  and 4.9, respectively) of Tilman et al.<sup>6</sup> Considering the relatively large uncertainty associated with the experimental data (see the next section) and the slightly different fin models, the agreement between the CFD predictions and experimental data is considered to be rather fortuitous. The solid-fin data confirmed the previously observed rolling-moment coefficient reduction with increasing Mach number. The dark line indicates a linear curve fit for  $M \in [2.41, 3.83]$ , and the light line is an extrapolation to Mach 5. As indicated, the CFD predictions followed this extrapolation. The Mach 2.15 data point did not follow this trend. The large flow disturbance across the fin described in the Oil-Flow Visualization section is likely the cause of this discrepancy. Limited PSP experiments also were performed at Mach 2.28, and the corresponding rolling moment was well above the linear trend (similar in magnitude to the  $M = 2.15$  data). If the linear trend were to persist to higher Mach numbers, then the rolling moment would reach zero at  $M = 5.9$ .

The slotted-fin rolling-moment coefficients calculated as described in the preceding paragraph also are given in Fig. 11. In general, the rolling-moment coefficients were roughly twice those of the solid fin, and, as discussed earlier, the scatter in the data was larger. However, these data also suggest a decrease in the rolling-moment coefficient with increasing Mach number.

### Uncertainty Analysis

Taking into account transducer uncertainties, the freestream flow-condition uncertainties were estimated as  $\pm 0.3\%$ ,  $2.5\%$ , and  $2.0\%$  for the Mach number, dynamic pressure, and Reynolds number, respectively. The calibration curve used for PSP measurements resulted in an uncertainty of  $\pm 2.068$  kPa, which, coupled with the transducer calibration uncertainties, produced  $p/p_{\infty}$  uncertainties of  $\pm 0.009$ . The normalization procedure was used to minimize the uncertainties introduced by the light source and camera; hence

those errors were neglected. Also, because the model temperature did not deviate substantially from room temperature, the surface-temperature-induced effects also were assumed to be negligible. The pressure data were used to determine rolling moments, which, coupled with the pixel resolution, resulted in a rolling-moment uncertainty of  $\pm 0.0053$  N-m for the solid fin and  $\pm 0.0064$  N-m for the slotted fin. This error contribution, along with wind-tunnel errors, resulted in an average rolling-moment coefficient error of  $\pm 0.0066$  for the solid fin and  $\pm 0.0077$  for the slotted fin.

In addition to the inherent random uncertainties of the measurement techniques, two other sources of bias error influenced the rolling-moment data. First, the leading-edge data of the missile fins were neglected in the rolling-moment calculations. These high stagnation pressures were outside the calibration range of the PtOEP paint. Thus, only pressure data on the sides and tips were used to compute a rolling moment. To quantify the error involved in this negligence, the CFD pressure images from Ref. 6 were processed with the same software used for the experimental data. It was found that neglecting the leading-edge contributions to the rolling moment resulted in an underprediction of the rolling-moment coefficient by nominally 2%. Second, the effects of shear stress on the rolling moment also were neglected. The CFD pressure images were again processed using the entire fin. Comparison to the CFD rolling-moment calculations that included the rolling moments indicated that neglecting the shear-stress forces resulted in rolling-moment coefficients that were overestimated by nominally 5%.

### Conclusions

The complex viscous flowfield features in the vicinity of the fin for two WAF missiles are characterized as a function of Mach number ( $M \in [2.15, 3.83]$ ) using PSP, surface oil-flow visualizations, and schlieren photography. A complete flowfield description is provided. In summary, the Mach number is found to have a profound impact on both the viscous phenomena and fin loading. The rolling moment decreases rapidly (almost discontinuously) by a factor of nearly 2 between the Mach numbers of 2.15 and 2.41. For Mach numbers of 2.41 and above, the rolling moment decreases almost linearly with increasing Mach number. This trend confirms observed flight-test anomalies.

Adding a slot to the fin for pressure relief was found to dramatically reduce the strength of the shock structure produced by the fin at low Mach numbers. This finding could translate into reduced wave drag. In addition, the rolling-moment magnitudes for the slotted fin, which had a 28.6% larger wetted surface area, were nearly double those of the solid fin. However, a decreasing rolling-moment trend with Mach number also was noticed for the slotted fin.

### Acknowledgments

The authors acknowledge Gregg Abate, U.S. Air Force Research Laboratory, Armament Directorate, for providing funding for this project under U.S. Air Force Contract F33610-90-C-2507. The authors also thank Carl Tilman for providing the computational fluid dynamics data. Alan Forlines, Ben Sarka, Kelly Navarra, and Gary Dale are acknowledged for providing suggestions in support of this research. Finally, the efforts of Andy Pitts, Dave Driscoll (deceased), and Mike Suggs also are gratefully acknowledged.

### References

- Abate, G. L., and Winchenbach, G. L., "Aerodynamics of Missiles with Slotted Fin Configurations," AIAA Paper 91-0676, Jan. 1991.
- Abate, G. L., and Winchenbach, G., "Analysis of Wrap-Around Fin and Alternative Deployable Fin Systems for Missiles," AGARD Flight Vehicle Integration Conf., Ankara, Turkey, Oct. 1995.
- Abate, G. L., Swenson, M. N., and Whyte, R. H., "Aerodynamic Test and Analysis of Wrap-Around Fins at Supersonic Mach Numbers Utilizing Design of Experiments," AIAA Paper 94-0200, Jan. 1994.
- Dahlke, C. W., "The Aerodynamic Characteristics of Wrap-Around Fins at Mach Numbers of 0.3 to 3.0," U.S. Army Missile Command, TR RD-77-4, Redstone Arsenal, AL, Oct. 1976.
- Abate, G., "Aerodynamic Research of Wrap Around Fin Missile Configurations and Alternate Wrap Around Fin Designs," U.S. Air Force Wright Lab., WL-TR-94-7015, Eglin AFB, FL, Feb. 1994.
- Tilman, C. P., Huffman, R. E., Jr., Buter, T. A., and Bowersox, R. D. W., "Experimental Investigation of the Flow Structure Near a Single

Wraparound Fin," *Journal of Spacecraft and Rockets*, Vol. 34, No. 6, 1997, pp. 729-736.

<sup>7</sup>Tilman, C., and Bowersox, R., "Characterization of the Flowfield Near a Wrap-Around Fin at Mach 4.9," AIAA Paper 98-0684, Jan. 1998.

<sup>8</sup>Morris, M. J., Donovan, J. F., Kegelmann, J. T., Schwab, S. D., and Levy, R. L., "Aerodynamic Applications of Pressure-Sensitive Paint," AIAA Paper 92-0264, Jan. 1992.

<sup>9</sup>Morris, M. J., and Donovan, J. F., "Application of Pressure- and Temperature-Sensitive Paints to High-Speed Flows," AIAA Paper 94-2231, June 1994.

<sup>10</sup>Goss, L. P., Gruber, M. R., and Nejad, A. S., "Surface Pressure Measurements in Supersonic Transverse Injection Flowfields," AIAA Paper 97-3254, July 1997.

<sup>11</sup>Sellers, M. E., "A Comparison of an AEDC and a Russian Developed Pressure Sensitive Paint in the AEDC Propulsion Wind Tunnel 16T," AEDC-TR-95-18, Arnold Engineering Development Center, TN, Dec. 1995.

J. R. Maus  
*Associate Editor*



## **2.2 FUEL DIAGNOSTICS**

### **2.2.1 Overview**

In modern high-performance aircraft, the fuel serves two essential functions--it provides the energy for propulsion and acts as the coolant for onboard heat sources. As a result, the fuel is exposed to temperatures at which oxidative and pyrolytic reactions occur. The ultimate products of these reactions are gums and particulates that can severely affect the safe and efficient operation of the aircraft. To improve the thermal stability of the fuel and, thereby, enhance the capabilities of future high-performance aircraft, a thorough understanding of the chemical and physical processes that occur in fuels at high temperatures and pressures is required. Obtaining this knowledge requires diagnostic techniques capable of measuring important fuel parameters. The diagnostic techniques developed during this program emphasized the characterization of fuel particle size, dissolved-oxygen concentration, and surface mass deposition. Other techniques explored included picosecond pump/probe diagnostics and spectroscopic approaches. These approaches are summarized in the publications outlined below.

### **2.2.2 Particle-Sizing, Oxygen-Concentration, and Mass-Deposition Methods**

The initial diagnostic development during this portion of the program was focused on techniques for monitoring the effects of thermal stressing of jet fuels. In particular, photon correlation spectroscopy (particle sizing), fluorescence quenching (oxygen concentration), and quartz crystal microbalance (mass deposition) were developed. The publications entitled "Simultaneous Measurement of Particle Size, Mass Rate of Deposition, and Oxygen Concentration in Thermally Stressed Jet Fuel" (see pp. 180-187) and "Application of Photon-Correlation Spectroscopy and Quartz-Crystal Microbalance to the Study of Thermally Stressed Jet Fuel" discuss integration of the three techniques for quantitative measurement of the effects of thermal stressing of jet fuels. The latter paper, co-authored by V. Vilimpoc and B. Sarka, was published in *Industrial and Engineering Chemistry Research*, Vol. 36, pp. 451-457 (1997). A patent was granted for an oxygen-monitoring technique based upon fluorescence quenching; the patent is entitled "Optical Method for Quantitating Dissolved Oxygen in Fuel" (see pp. 188-195).

Presented at the ASME Forum on Measurement Techniques in Multiphase Flows, ASME Winter Annual Meeting, November 1995, San Francisco

PUBLISHED WITH PERMISSION

**SIMULTANEOUS MEASUREMENT OF PARTICLE SIZE, MASS RATE  
OF DEPOSITION, AND OXYGEN CONCENTRATION  
IN THERMALLY STRESSED JET FUEL**

**V. Vilimpoc, B. Sarka, and W. L. Weaver**  
Systems Research Laboratories, Inc.  
A Division of Space Industries International, Inc.  
Dayton, OH 45440-3696

**J. R. Gord**  
Wright Laboratory, Aero Propulsion and Power Directorate  
Wright-Patterson Air Force Base, OH 45433-7103

**ABSTRACT**

Three techniques integrated into a single instrumented platform allow simultaneous measurement in real time of particle size and growth rate, surface mass-deposition rate, and concentration of dissolved oxygen in thermally stressed jet fuel. Particle growth rate is studied using Photon Correlation Spectroscopy (PCS); surface mass-deposition rate is measured with a Quartz Crystal Microbalance (QCM); and dissolved oxygen concentration is monitored by Pyrene Fluorescence Quenching (PFQ).

**INTRODUCTION**

Fuels are used as the coolant for avionics and hydraulic systems in modern aircraft. Exposure of fuels to high temperature results in formation of particulates and deposits that clog valves and filters and degrade injection-nozzle performance. Several studies have shown that the auto-oxidation of hydrocarbons is the main reaction leading to formation of insoluble products and deposits (Katta and Roquemore, 1992; Krazinski et al., 1990; Anderson et al., 1994; Jones et al., 1995; Jones and Balster, 1995; Chin and Katta, 1995). Efforts to develop highly stable jet fuels would benefit from an understanding of the relationship among particle size and growth rate, rate of particle deposition on a surface, and dissolved-oxygen concentration resulting from thermally induced degradation of jet fuel. No single analytical technique exists that can provide all the required information. Therefore, integration of existing applicable techniques into a single instrumented platform where all the required parameters can be measured simultaneously and in-situ would be highly desirable. In this paper progress on such an effort is reported.

**EXPERIMENTAL TECHNIQUES**

PCS is a dynamic light-scattering technique capable of measuring particle size in the range  $10^{-8}$  to  $10^{-6}$  m. Laser light incident on a sample of particles undergoing Brownian motion will be scattered with different phases, depending on the position of each particle in the laser beam and on the distance between the particle and the detector. Thus, the composite light scattered from the group of particles in the scattering volume will form an interference pattern at the detector. As the particles randomly diffuse through the solution, the pattern produced will be modulated by the particle motion. The intensity fluctuations associated with the interference pattern at the detector, although random, will be more rapid for small, rapidly diffusing particles than for larger, more slowly diffusing ones. The random-noise signal produced by the detector as a result of the scattered light can be characterized by its autocorrelation function,  $g(t)$ , defined by

$$g(t) = \langle I[T] I[T+t] \rangle \quad (1)$$

where  $I[T]$  is the intensity at the detector at time  $T$  and the angular brackets denote a time average over  $T$ . The autocorrelation function is a measure of the similarity, or correlation, between the configuration of particles contributing to an intensity  $I$  at  $T$  and that at a later time  $T+t$ . At short  $t$  the configuration of the particles within the scattering volume will remain essentially unchanged, and the correlation with the configuration at  $T$  will be high. At longer  $t$  the particles will have diffused such that their new positions will be statistically uncorrelated with their former ones. For a system of particles of uniform size and

shape undergoing Brownian motion, the autocorrelation function will be a decaying exponential:

$$g(\tau) = A e^{-2\Gamma\tau} + B \quad (2)$$

where  $\Gamma$  is a decay constant characteristic of particles of that size and  $A$  and  $B$  are experimental constants dependent on the geometry, optical collection efficiency, and counting efficiency of the electronics.  $1/\Gamma$  is the decay time of the Brownian motion, i.e., the time required for any particular configuration of particles within the scattering volume to become uncorrelated with its former configuration. The decay constant is related to the diffusion constant of the particles and to the geometry of the experiment through

$$\Gamma = q^2 D; \quad q = 4\pi n \sin(\theta/2)/\lambda \quad (3)$$

where  $q$  is the magnitude of the scattering vector,  $D$  the diffusion constant of the particles,  $n$  the refractive index of the fluid,  $\theta$  the scattering angle, and  $\lambda$  the laser wavelength. For spherical particles, the diffusion constant is related to the particle diameter through the Stokes-Einstein equation

$$D = kT/3\pi\eta d \quad (4)$$

where  $k$  is the Boltzman constant,  $T$  the absolute temperature,  $\eta$  the fluid viscosity, and  $d$  the particle diameter.

When the sample contains particles of different sizes, the autocorrelation function will be the sum of decaying exponentials weighted by the intensity of light scattered from particles of each characteristic size, and the autocorrelation function can be described by

$$g(\tau) = \int_a^b X(s) e^{-\Gamma(s)\tau} ds \quad (5)$$

where the index,  $s$ , denotes the size of the particles and  $X(s)$  is the particle-size distribution, which yields the relative proportion of scattering from particles of size  $s$ . The constants  $a$  and  $b$  are the lower and upper limits of particle size. This integral equation must be numerically inverted to extract the size distribution,  $X(s)$ , from the measured autocorrelation function (Bott, 1987). CONTIN (Provencher, 1979, 1982), a widely used FORTRAN program for this type of data analysis, was employed.

QCM is a technique for measuring extremely small mass accumulation on a quartz-crystal surface. It is designed around a piezoelectric wafer, sliced from a single crystal of quartz. The quartz wafer is sandwiched between two gold electrodes bonded to the wafer surface. As a piezoelectric material, the quartz deforms slightly in the electric field applied between the two electrodes. The oscillating electric field perpendicular to the wafer surface induces mechanical oscillation, in the form of a standing wave, in the bulk of the quartz wafer. In the QCM, an AT-cut quartz wafer

efficiently produces mechanical shear oscillation with displacement parallel to the wafer surface. A resonant oscillation is usually achieved by including the wafer in an appropriately designed oscillator circuit. Sandia National Laboratories (Martin et al., 1991) developed the oscillator circuit used in this study. In such a circuit, the electrical and mechanical oscillation centers at a characteristic fundamental frequency. Mechanical oscillation of the crystal is at a maximum where the electrodes overlap and diminishes rapidly in areas where they do not. Thus, the QCM is most useful when probing processes that occur uniformly across the QCM surface--processes that can be represented as a change in mass per unit area. The oscillation frequency depends on several factors: 1) factors that are normally constant include the physical properties of the quartz wafer (thickness, density, and shear modulus); 2) factors that normally are held constant include the density and viscosity of the phases in contact with the QCM wafer and the pressure and temperature differences across the wafer. The theory relating the measured frequency changes to the surface mass deposition has been presented previously (O'Hern, 1993) and is given by

$$\Delta f \approx -2f^2/N(\mu_q \rho_q)^{1/2} [\Delta \rho_s + (\rho \eta/4\pi f)^{1/2}] \quad (6)$$

where  $\Delta f$  is the change in oscillation frequency,  $f$  the unperturbed resonant frequency,  $N$  the overtone mode number,  $\mu_q$  the quartz shear modulus ( $2.947 \times 10^{11} \text{ g cm}^{-1} \text{ s}^{-2}$ ),  $\rho_q$  the density of quartz ( $2.648 \text{ g cm}^{-3}$ ),  $\rho_s$  the surface mass density, and  $\rho$  and  $\eta$  the liquid density and viscosity, respectively. The first term in Eq. (6) relates the change in surface mass density to the change in frequency, and the second relates the change in fluid properties to that in oscillation frequency. When all other factors are held constant, the variation in mass of an adsorbate or thin film attached to the electrode can be determined from the change in frequency. Under such conditions the change in surface mass deposition can be related to the change in the fundamental resonant frequency by

$$\Delta \rho_s = -[2.21 \times 10^5 (\text{g/cm}^2 \text{ s})] \Delta f/f^2 \quad (7)$$

PFQ is based on determination of the fluorescence lifetime of pyrene doped in the fuel at the parts-per-million level. Spectroscopically, molecular oxygen is difficult to study in solution (Herzberg, 1945). It does not absorb in the infrared, and its electronic transitions lie far in the ultraviolet where fuel components absorb strongly. Oxygen has a Raman-allowed transition, but Raman spectroscopy is not the technique of choice for trace analysis. Oxygen also has a unique ESR (electron-spin-resonance) signature, but the expense and limited sensitivity of this technique prohibit its use for this application. An alternative optical approach involves quantitating dissolved oxygen indirectly through its influence on the fluorescence of a probe molecule (Cox, 1985) such as pyrene. Oxygen

efficiently and reproducibly quenches the fluorescence of pyrene as a result of the energy match between the singlet-triplet gap in oxygen and the energy of the first excited singlet state of pyrene (Lakowicz, 1983). This process provides the basis for a spectroscopic technique for quantitating dissolved molecular oxygen. The technique is based on the propensity of dissolved molecular oxygen to quench probe-molecule fluorescence excited with a pulsed nitrogen laser. Linear calibration curves based on Stern-Volmer kinetics are generated through measurement of the time-resolved fluorescence signal produced by pyrene.

Collisions between photoexcited pyrene and oxygen molecules result in the non-radiative transfer of energy from pyrene to oxygen because of the energy match between the singlet-triplet gap in oxygen and the energy of the first excited singlet state of pyrene. At a given temperature, a decrease in the dissolved-oxygen concentration reduces the oxygen-pyrene collision frequency, resulting in an increase in both the total fluorescence quantum yield and the lifetime of the excited state of pyrene. Instrumentally, it is a simpler task to measure the total fluorescence intensity, which may be converted to a quantum yield. However, previous work has shown this approach to be intractable for quantitating dissolved oxygen during fuel-thermal-stability studies since the amount of pyrene doped into the fuel must be precisely controlled. If pyrene is consumed (or produced) during oxidation of the fuel, the total fluorescence intensity will vary, independent of the presence of oxygen. However, the lifetime of the excited state of pyrene is independent of pyrene concentration (within certain limits). Thus, the pyrene fluorescence lifetime is a reliable and reproducible indicator of the dissolved-oxygen concentration at a given fuel temperature. After photoexcitation of an ensemble of pyrene molecules, the excited species return to their ground states, producing an observed fluorescence signal that can be described by the single exponential decay in

$$\Phi_f(t) = \Phi_f^0 \exp(-k_f t) \quad (8)$$

where  $\Phi_f^0$  is the fluorescence radiant power immediately following excitation. The fluorescence power decays with an overall rate constant,  $k_f$ , that contains contributions from the first-order (natural or radiative) decay rate constant,  $k_r$ , and a second-order rate constant for dynamic quenching with oxygen,  $k_q$ , as shown in

$$k_f = k_r + k_q[\text{O}_2] \quad (9)$$

Using the relationship between the rate constant ( $k$ ) and the lifetime ( $\tau$ ) of a single exponential decay ( $k=1/\tau$ ), Eq. (9) can be written in terms of the fluorescence lifetime, as in the Stern-Volmer Equation,

$$\tau_0/\tau_f = 1 + \tau_0 k_q [\text{O}_2] \quad (10)$$

where  $\tau_f$  is the measured lifetime of the observed fluo-

rescence (Dynamically Quenched Fluorescence Lifetime, DQFL) and  $\tau_0$  is the measured lifetime of the observed fluorescence in the absence of quenching. By measuring  $\tau_0$  at  $[\text{O}_2] = 0$  and the DQFL at known values of  $[\text{O}_2]$ , a linear calibration curve can be constructed that relates the lifetime of the observed pyrene fluorescence to the concentration of dissolved oxygen (as measured by existing gas-chromatographic and electrochemical methods).

## EXPERIMENTAL SETUP AND PROCEDURES

The experimental setup is as shown in Fig. 1. Light from a 35-mW HeNe laser beam is focused into a quartz optical cell from above, while the time-varying light scattered from particles is collected at a fixed angle in the horizontal plane by a photomultiplier. The time-varying signal from the photomultiplier is converted into pulse trains by an amplifier/discriminator whose output is processed by a digital correlator (Langley Ford Instrument Correlator Model 1096). The outputs from the correlator (exponential decay curve for each run) are stored and later processed off-line on a workstation to yield size data. A  $\text{N}_2$  laser beam is directed into the test cell from below to occupy the same probe volume as the PCS HeNe laser beam. A small portion of the  $\text{N}_2$  laser beam is split off with a flat glass into a photodiode. The output of the photodiode initiates data acquisition by a LeCroy 9354 digital storage oscilloscope. Fluorescence from the pyrene is collected by an RCA 931A photomultiplier tube. For each data set, 100 fluorescence decay curves were averaged. Typical fluorescence decays have time constants of 20 - 300 nsec.

The experimental test cell is a cylindrical block, 56 mm in diam and 64 mm long, made of 304 stainless-steel; into this block four 3.2-mm-diam holes are drilled symmetrically. Two sections of these blocks are connected and surrounded by cylindrical heating jackets. The entire apparatus is wrapped with fiberglass insulation to minimize temperature fluctuation. The fuel is pumped through the test cell by an HPLC syringe pump (ISCO 500D). All tests in this study were conducted with a JET-A fuel (POSF2827). Typical flow rates to obtain 1 - 20 min of residence time are in the range 4.212 - 0.211 cc/min. Either an optical quartz cell or a QCM cell (or both) can be attached to the end of the reactor to obtain *in-situ* size and mass rate data. At high temperature the PCS signal-to-noise ratio was observed to be low; therefore, some experiments were conducted by pumping fuel through the reactor into the QCM cell (maintained at the test-cell temperature) and then through a 0.15-mm-od stainless-steel tube immersed in a water bath into a 4-mm-square optical quartz cell at room temperature.

## RESULTS AND DISCUSSION

The mechanism of particulate formation during thermal degradation of jet fuel remains a mystery. Do particles

form as a result of physical processes when there is a change in the physical or chemical properties of the fuel, for example, by condensation due to differences in solubility between the solvent and solute phases (Oswald ripening) or by agglomeration resulting from collisions and sticking together of small particles? Or do particles form and grow as a result of chemical reaction?

In-situ measurement while particles are being formed would answer this question unambiguously. A typical result from a number of attempts to make an in-situ particle-size measurement at 185°C is shown in Fig. 2. A complication in conducting an in-situ PCS experiment is that at high temperature, particles move in and out of the probe volume very rapidly because of its large Brownian motion. These fast movements that result in low signal-to-noise ratio necessitate the use of small time bins to capture the rapid exponential decays that are typical of small particles. The consequence is obvious from examination of Fig. 2; at short residence times, the small size and the small number of particles generated do not scatter sufficient light (scattered-light intensity is proportional to particle number density and particle size) to permit meaningful correlation by the PCS system. As particles grow in size, move more slowly, and are produced in larger quantities at longer residence times, they become detectable by the PCS system. Unfortunately, beyond the detection threshold, these particles are no longer growing in size with increasing residence time, although they are produced and deposited in ever-increasing quantities. The poor signal-to-noise ratio is reflected in the large uncertainty in particle size at short residence times. No attempt was made to measure in-situ oxygen concentration with PFQ at high temperature because small changes in very short fluorescence decay times cannot be measured accurately.

For ascertaining the effect of temperature changes on particle size, fuel was heated at a long residence time to generate particles sufficiently large for detection; then fuel flow to the test cell and power to the heater were shut off. PCS was used for continuous monitoring of particle size as the fuel cooled down to obtain data on particle size as a function of temperature. The result is shown in Fig. 3. As can be seen from the figure, the particle size increases continuously, while the scattered-light intensity increases to a maximum and then slowly decreases. The scattered-light intensity is a function of particle residence time in the probe volume, particle number density, and particle size. A plausible explanation for the observed profiles is that as temperature decreases, the average-particle Brownian motion also decreases, resulting in longer residence times for particles in the probe volume and, thus, more scattered light per unit time during the first 10 min of elapsed time. Although the particles are becoming larger, beyond 10 min the scattered-light intensity is decreasing. The increase in particle size is probably due to agglomeration which would account for the reduction of scattered-light intensity. This result indicates that growth in particle size by a physical process is slow compared to that by chemical kinetics.

For obtaining the particle-size growth rate as a function of exposure time to high temperature, fuel thermally stressed for different lengths of time was quenched to room temperature and studied with PCS and PFQ, while mass-deposition rates were monitored in-situ with QCM. At the start of an experiment, a computer commands the syringe pump (ISCO 500D) to begin pumping fuel through the test cell at a predetermined flow rate to achieve a given exposure time. The computer then monitors the volume of fuel flow and the fuel temperature in the QCM cell. The quartz-crystal oscillation frequency is a function of both the temperature and the amount of mass deposit on the crystal surface; therefore, the QCM temperature must remain relatively constant when mass-deposition-rate data are being obtained. When at least two reactor volumes (30 cc) of fuel have been purged through the reactor-QCM cell and the fuel temperature in the QCM cell has remained constant to within 0.1°C for 16 min, then the computer begins taking PCS and QCM data for subsequent processing. At each flow rate 20 PCS and QCM data points and five PFQ fluorescence decay times are taken at 2-min intervals. Therefore, the rates of mass deposition are measured over a period of 40 min. When sufficient data are collected, the pump is commanded to pump at a new flow rate, and the entire process is repeated. Because of the large thermal mass of the reactor-QCM cell, ~ 2 hr is required to achieve a steady-state temperature from initial room temperature; however, once steady state is reached, the temperature remains very stable.

Typical results for a fuel thermally stressed for different exposure times at 165 and 195°C are shown in Figures 4 and 5, respectively. In these figures, scattered-light intensity and oxygen concentration are normalized to minimum and maximum particle size to ensure that they will be on the same scale for demonstrating the relationships among the variables. At 165°C, particle size and scattered-light intensity increase with increasing residence time but at decreasing rates, while oxygen concentration decreases in a reciprocal manner. Particle size and scattered-light intensity begin to level off at a 20-min residence time, while the rate of mass deposition peaks at 14 min. In comparison, at 195°C the mass-deposition rates and scattered-light intensity reach their maxima at about 3.5 min, while the particle-size growth profile does not level off for about 10 min. Note the similarity between the scattered-light intensity, which represents the total number density of particles, and the rate of mass deposition. Both profiles show progressively longer residence times required to reach a maximum, from 3 - 4 min at 195°C to 15 - 20 min at 165 °C. This result clearly suggests that particulates are formed and deposited as a result of chemical reactions. The higher the temperature, the larger the quantity of particles formed and the faster they are formed as a function of fuel-exposure time to temperature. Particle-diameter profiles in the range 165 - 195°C as a function of residence time are shown for comparison in Fig. 6. Figures 7 and 8 show scattered-light-intensity and mass-deposition-rate profiles, respec-



tively. Comparison of the scattered-light-intensity profiles in Figs. 2 and 7 shows a striking difference between in-situ and post-test quenched experiments. In Fig. 2, the scattered-light-intensity profiles increase slowly toward a plateau for long residence times, while in Fig. 7 the profiles reach a peak at about a 3-min residence time and then decrease.

One plausible explanation for the scattered-light-intensity profiles decreasing after peaking in the post-test experiments is competition between different mechanisms. A larger quantity of particles and larger particles are produced as the residence time increases; therefore, the scattered-light intensity increases. However, flow velocity is lower for longer residence times, thus permitting particle-removal processes such as settling or agglomeration to take place in the quench line between the test cell and the optical cell; this results in decreasing scattered-light intensity for longer residence times. The quantity of particles removed by settling and agglomeration will be proportional to the length of time available for the processes and, therefore, inversely proportional to the flow velocity of the fuel. PCS and QCM measurements were made by pumping fuel at different flow rates through the test cell to obtain different residence times; therefore, if the scattered-light intensity and mass-deposition rates are normalized by the flow rates, the results will be somewhat independent of the influence of flow velocity. The results of such normalization are shown in Figs. 9 and 10, respectively. The normalized scattered-light intensity can now be thought of, to a first approximation, as concentration of particles per cubic centimeter of fuel and the rate of mass deposition in units of micrograms of deposit per square centimeter of quartz crystal surface per cubic centimeter of fuel flow over the surface. From a comparison of the profiles at 195 and 165°C, it is obvious that the 165°C profiles from 2 to 20 min residence time mimic those at 195°C from 1 to 5 min residence time--but at a much lower particle number density and mass deposition rate and at a much slower pace. The normalized profiles suggest the existence of two mechanisms in the particle formation and deposition rates. The initial rates are fast and exhibit an S-shaped curve characteristic of autocatalytic reaction, while the rates for longer residence times are slow and linear. Both regimes exhibit decreasing rates with decreasing temperature, suggesting a dependence on reaction mechanisms as the primary cause.

Figure 11 contains oxygen-concentration profiles at different temperatures. Dissolved oxygen is almost depleted at 195°C after about a 5-min residence time in the reactor, while ~ 50% of the oxygen remains after 20 min at 165°C. Many particles are generated during the first 5 min of reaction time at 195°C; therefore, little oxygen remains to fuel further particle production at longer residence times. The result is a large rate decrease. At 165°C the rate of particle production is much slower; therefore, some oxygen remains at long residence times and the rate decrease is small. Obviously at lower temperature the rate of particle growth, mass deposition, and oxygen consumption will be slow;

therefore, more dissolved oxygen will remain in the fuel and, as a result, reaction can proceed for a longer time at a lower temperature. The rates of particle growth and mass deposition as a function of temperature seem to be closely tied to the concentration of dissolved oxygen.

## CONCLUSION

The combination of three techniques has provided insight into the relationship among particle size, growth rate, mass-deposition rate, and oxygen concentration. Scattered-light-intensity profiles for in-situ and post-test quenched experiments do not exhibit the same shape, suggesting that settling or agglomeration, in addition to reaction kinetics, may play a role in determining the size and quantity of particles formed. Further experiments are required to delineate the differences in the observed scattered-light-intensity profiles.

## ACKNOWLEDGMENT

This study was performed at and supported by Wright Laboratory, Aero Propulsion and Power Directorate, Wright-Patterson Air Force Base, OH, in part, under USAF Contract No. F33615-90-C-2033.

## REFERENCES

- Anderson, S. D., Jones, E. G., Goss, L. P., and Balster, W. J., 1994, "The Effect of Additives on the Formation of Insolubles in a Jet A Fuel," Presented at the 5th International Conference on Stability and Handling of Liquid Fuels, 3-7 October, Rotterdam, The Netherlands.
- Bott, S. E., 1987, "Submicrometer Particle Sizing by Photon Correlation Spectroscopy: Use of Multiple-Angle Detection," *Particle Size Distribution - Assessment and Characterization*, ACS Symposium Series 332, T. Provder, ed., American Chemical Society, Washington, D. C., pp. 74-88.
- Chin, L. P., and Katta, V. R., 1995, "Numerical Modeling of Deposition in Fuel-Injection Nozzles," AIAA Paper No. 95-0497.
- Cox, M. E., and Dunn, B., 1985, *Applied Optics*, Vol. 24, p. 2114.
- Herzberg, G., 1945, *Infrared and Raman Spectra of Polyatomic Molecules*, Van Nostrand, New York.
- Jones, E. G., and Balster, W. J., 1995, "Surface Fouling in Aviation Fuel: Short- vs Long-Term Isothermal Tests," Accepted for publication in *Energy and Fuels*.
- Jones, E. G., Balster, W. J., and Post, M. E., 1995, *Journal of Energy for Gas Turbines and Power*, Vol. 117, p. 125.
- Katta, V. R., and Roquemore, W. M., 1992, "A Numerical Method for Simulating the Fluid-Dynamic and Heat-Transfer Changes in a Jet Engine Injector Feed-Arm due to Fouling," AIAA Paper No. 92-0768.

Krazinski, J. L., Vanka, S. P., Pearce, J. A., and Roquemore, W. M., 1990, "A Computational Fluid Dynamics and Chemistry Model for Jet Fuel Thermal Stability," Presented at the 35th ASME International Gas Turbine and Aeroengine Congress and Exposition, 11-14 June, Brussels, Belgium.

Lakowicz, J. R., 1983, *Principles of Fluorescence Spectroscopy*, Plenum Press, New York.

Martin, S. J., Granstaff, V. E., and Frye, G. C., 1991, *Analytical Chemistry*, Vol. 63, p. 2272.

O'Hern, T. J., Trott, W. M., Martin, S. J., and Klavetter, E. A., 1993, "Advanced Diagnostics for In Situ Measurement of Particle Formation and Deposition in Thermally Stressed Jet Fuels," AIAA Paper No. 93-0363.

Provencher, S. W., 1979, *Makromolecular Chemistry*, Vol. 180, p. 201.

Provencher, S. W., 1982, *Computer Physics Communications*, Vol. 27, p. 229.

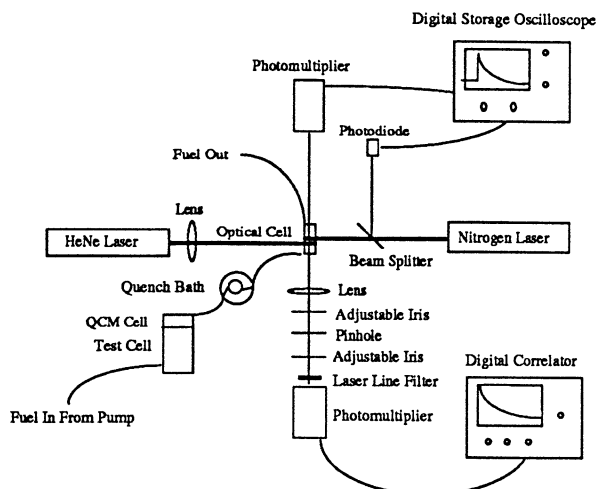


Fig. 1. Diagram of Experimental Setup.

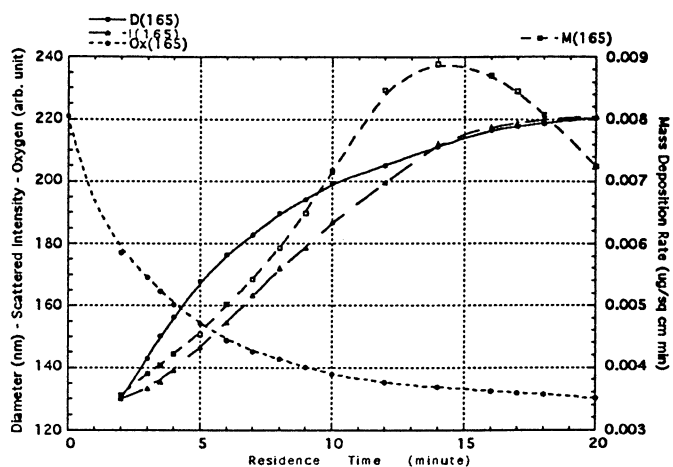


Fig. 4. Post-Test Quenched Results at 165°C.

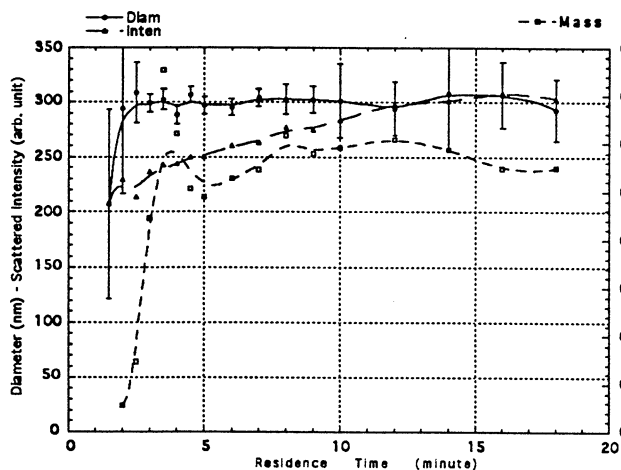


Fig. 2. In-situ Experimental Results.

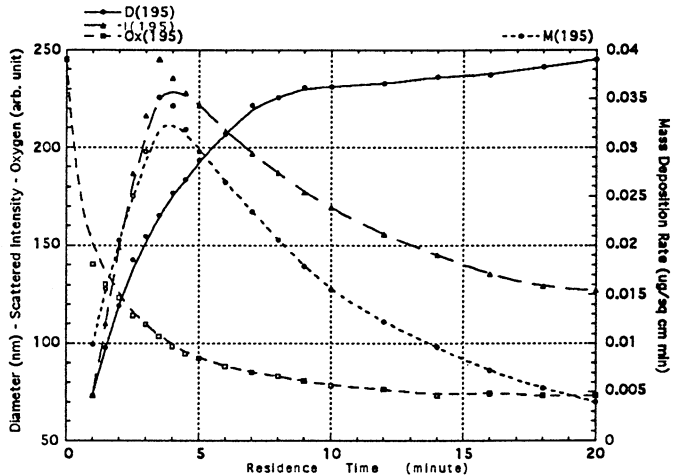


Fig. 5. Post-Test Quenched Results at 195°C.

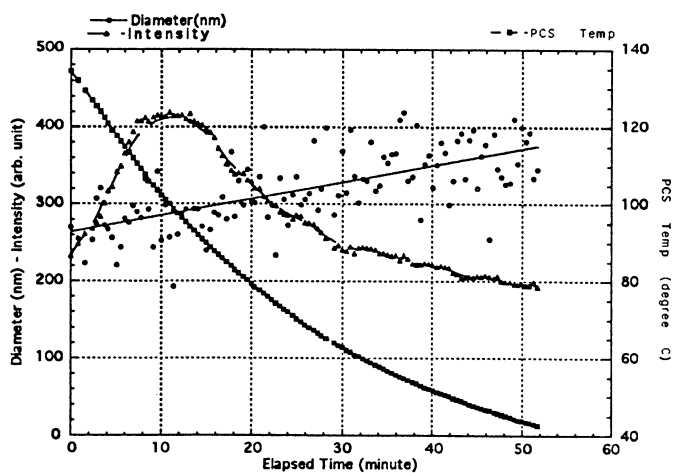


Fig. 3. In-situ Cooling Results.

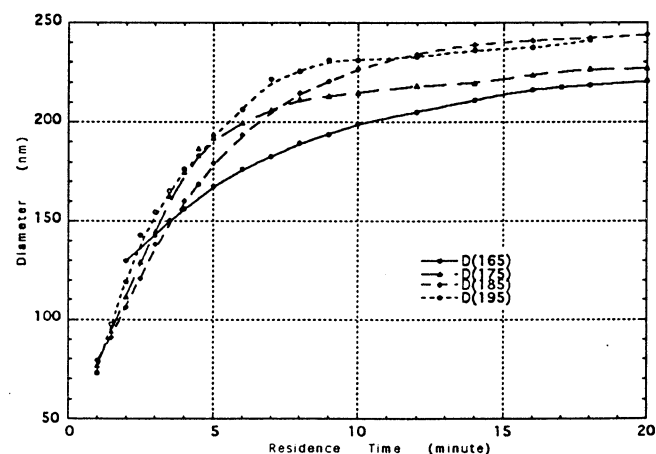


Fig. 6. Post-Test Quenched Diameter Profiles.

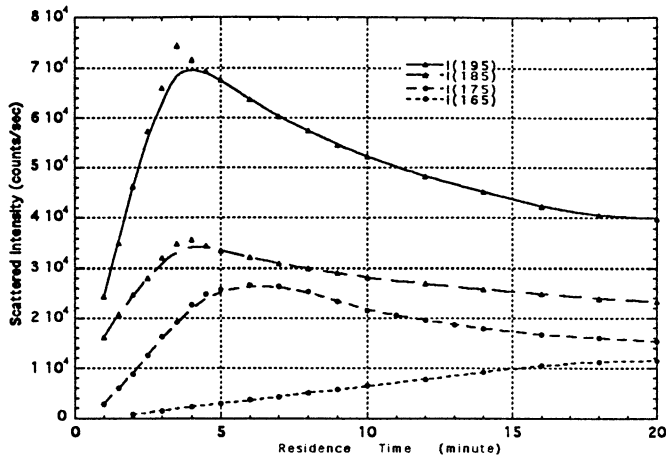


Fig. 7. Post-Test Quenched Scattered-Light Intensity.

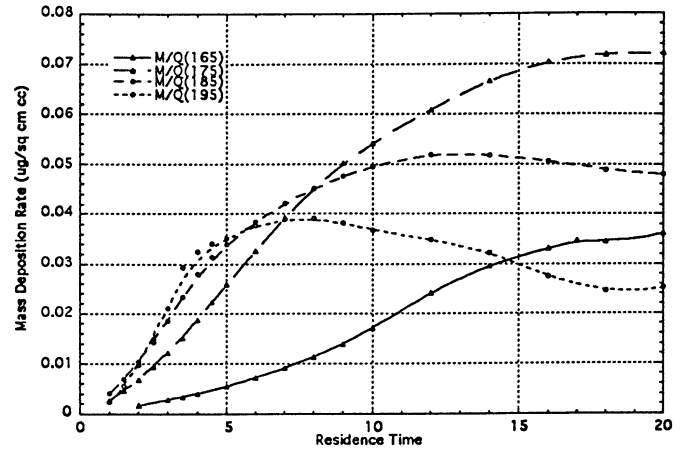


Fig. 10. Normalized Mass-Deposition Rates.

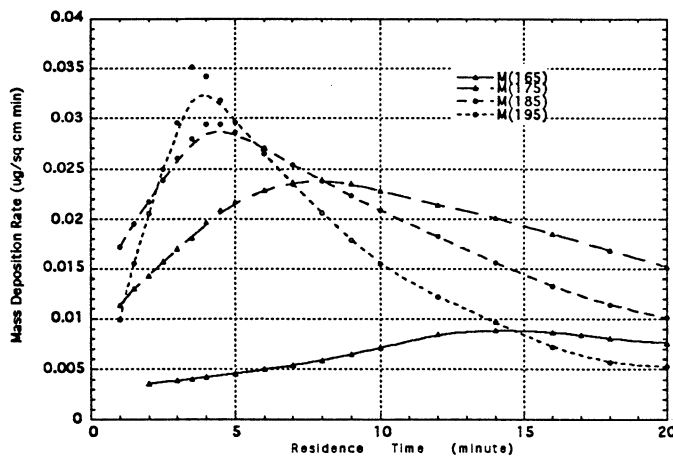


Fig. 8. Post-Test Quenched Mass-Deposition Rates.

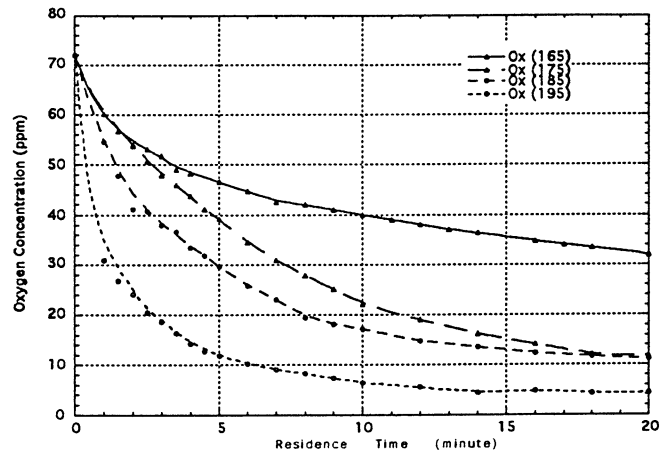


Fig. 11. Post-Test Quenched Oxygen Concentration.

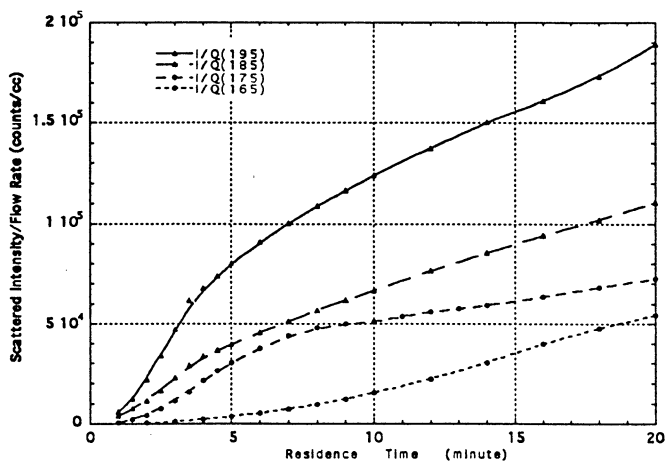


Fig. 9. Normalized Scattered-Light Intensity.



US005919710A

**United States Patent** [19][11] **Patent Number:** **5,919,710****Gord et al.** PUBLISHED WITH PERMISSION[45] **Date of Patent:** **Jul. 6, 1999**[54] **OPTICAL METHOD FOR QUANTITATING DISSOLVED OXYGEN IN FUEL**[75] **Inventors:** **James R. Gord**, Beavercreek, Ohio;  
**Steven W. Buckner**, Columbus, Ga.;  
**William L. Weaver**; **Keith D. Grinstead, Jr.**, both of Beavercreek, Ohio[73] **Assignee:** **The United States of America as represented by the Secretary of the Air Force**, Washington, D.C.[21] **Appl. No.:** **08/920,350**[22] **Filed:** **Jul. 16, 1997****Related U.S. Application Data**[60] **Provisional application No.** 60/022,226, Jul. 18, 1996.[51] **Int. Cl.**<sup>6</sup> ..... **G01N 21/64**[52] **U.S. Cl.** ..... **436/127; 436/27; 436/28; 436/29; 436/30; 436/56; 436/136; 436/138; 436/140; 422/82.05; 422/82.08; 250/458.1; 250/459.1; 250/461.1; 356/317; 356/318; 356/417**[58] **Field of Search** ..... **436/27, 28, 29, 436/30, 127, 136, 138, 56, 140, 172; 422/82.05, 82.08; 250/458.1, 459.1, 461.1; 356/317, 318, 417**[56] **References Cited****U.S. PATENT DOCUMENTS**

3,612,866	10/1971	Stevens	250/71
4,580,059	4/1986	Wolfbeis et al.	250/459.1
4,775,514	10/1988	Barnikol et al.	422/68
4,810,655	3/1989	Khalil et al.	436/138
5,043,285	8/1991	Surgi	436/136
5,108,932	4/1992	Wolfbeis	436/124

**FOREIGN PATENT DOCUMENTS**

568558	10/1975	Switzerland
9212424	7/1992	WIPO

**OTHER PUBLICATIONS**

Draxler et al. "Time-resolved fluorescence spectroscopy for chemical sensors". Appl. Opt. (1996), 35(21), 4117-4123 Abstract only.

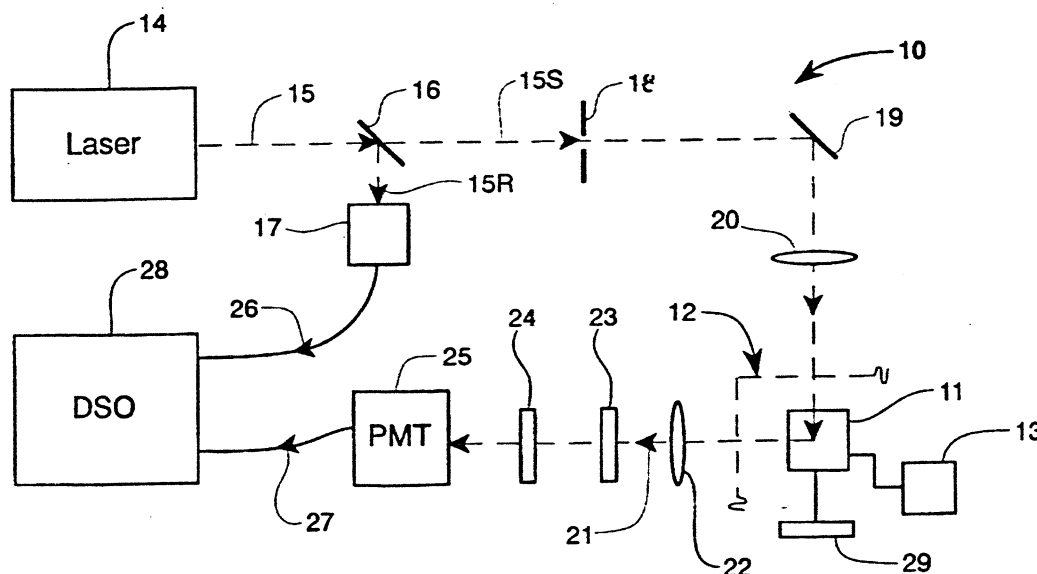
Viiimpoc et al. "Simultaneous measurement of particle size, mass rate of deposition, &amp; oxygen concentration in thermally stressed jet fuel".

HTD CAM. Soc. Mech. Eng.) (1995, 321 (Proceedings of the ASME Heat Transfer and Fluids Engineering Divisions, 1995) pp. 343-350. Abstract only.

"Dissolved Oxygen Quantitation in Fuel Through Measurements of Dynamically Quenched Fluorescence Lifetimes." by Gord et al. IEEE Publication 95CH3482-7, pp. 39.1-39.6 (Jul. 1995).

**Primary Examiner**—Jeffrey Snay**Assistant Examiner**—S. Carrillo**Attorney, Agent, or Firm**—Bobby D. Searce; Thomas L. Kundert[57] **ABSTRACT**

A method for the quantitative determination of dissolved oxygen in a liquid fuel includes the steps of doping a sample of the fuel with a preselected concentration of a probe material including a luminophor which exhibits luminescence of wavelength which is quenched by oxygen dissolved in the fuel, illuminating the fuel with light from a coherent light source, such as a laser, of a wavelength which induces the luminescence in the luminophor, and thereafter measuring the change with time of the luminescence from the luminophor in the fuel and determining from the change with time of the luminescence the concentration of oxygen in the fuel.

**6 Claims, 4 Drawing Sheets**



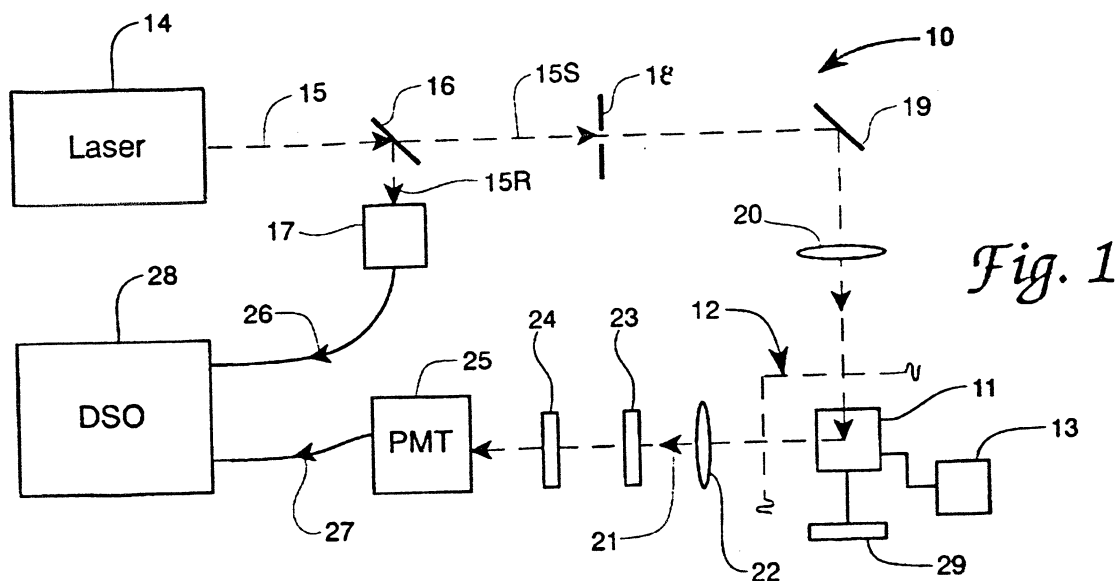
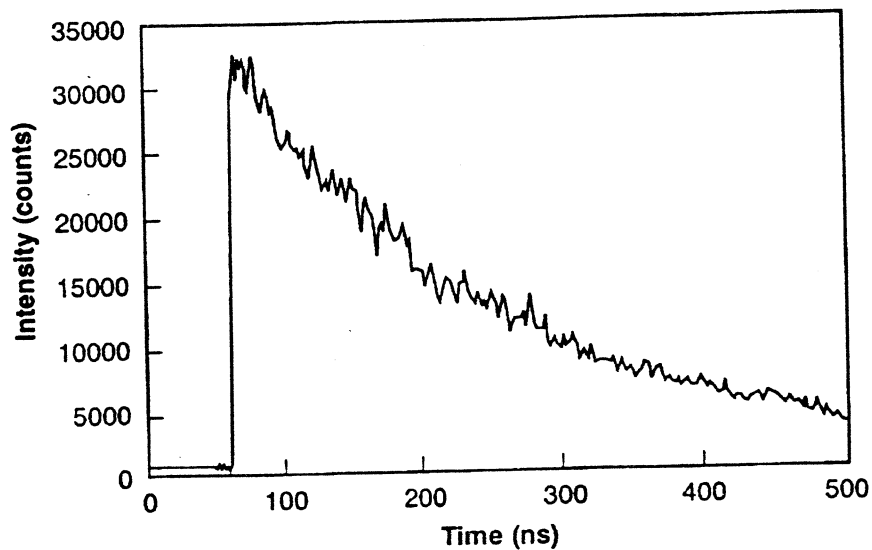
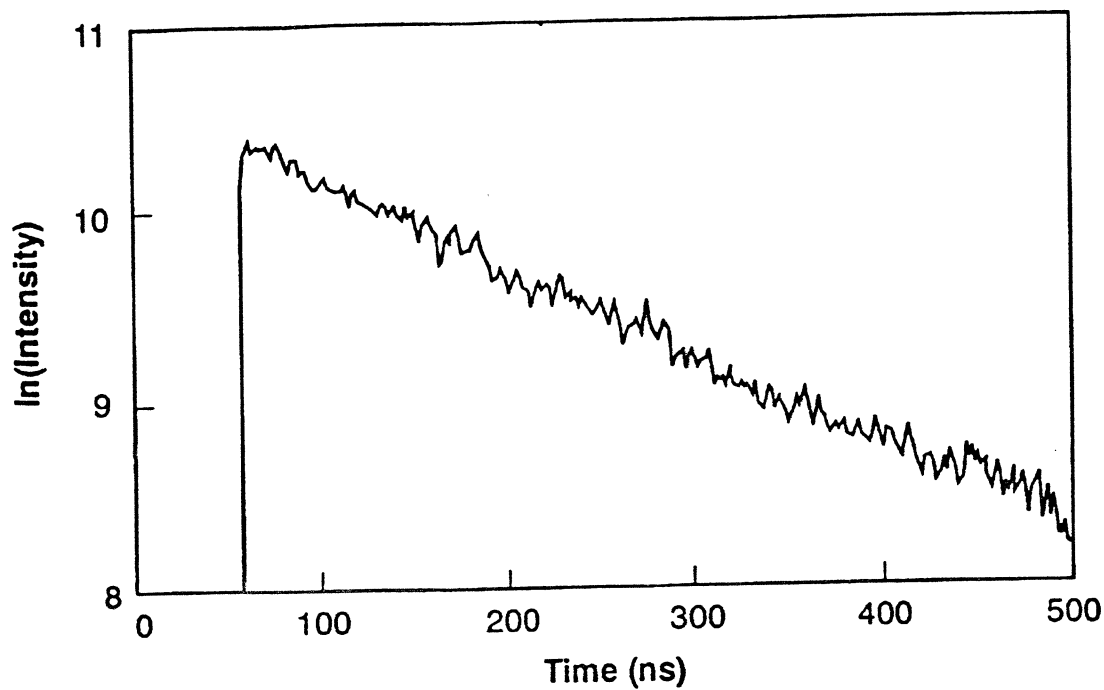
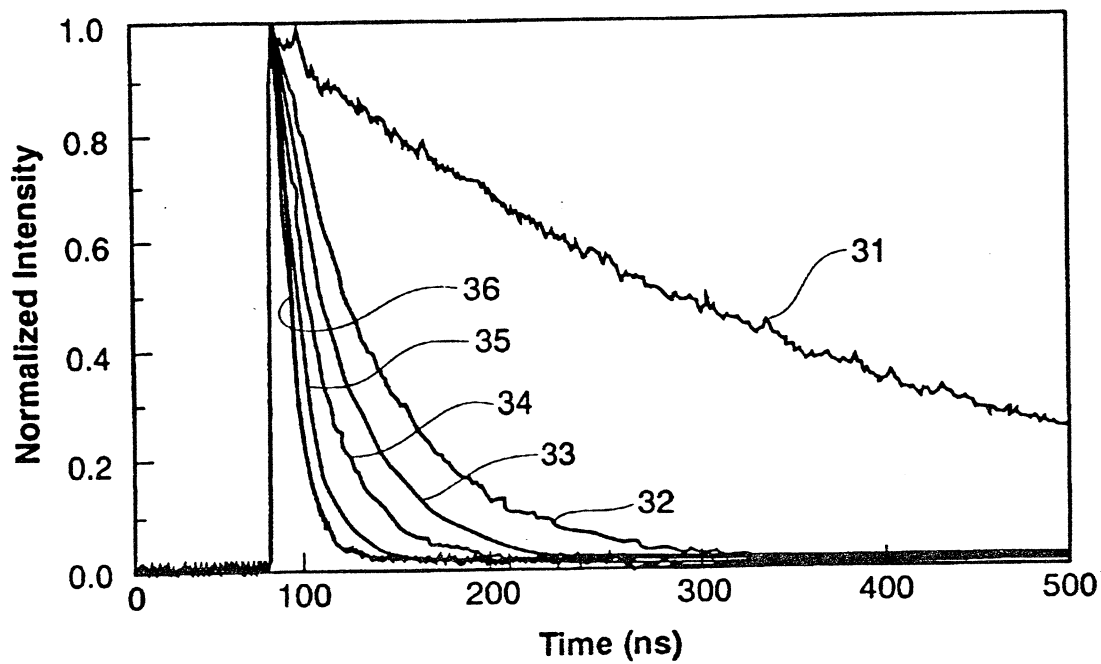
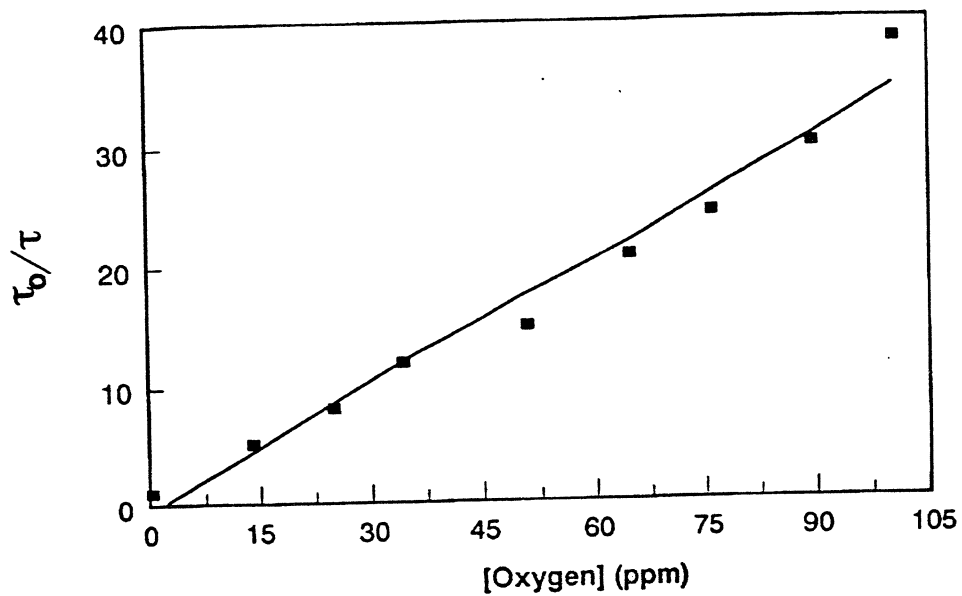
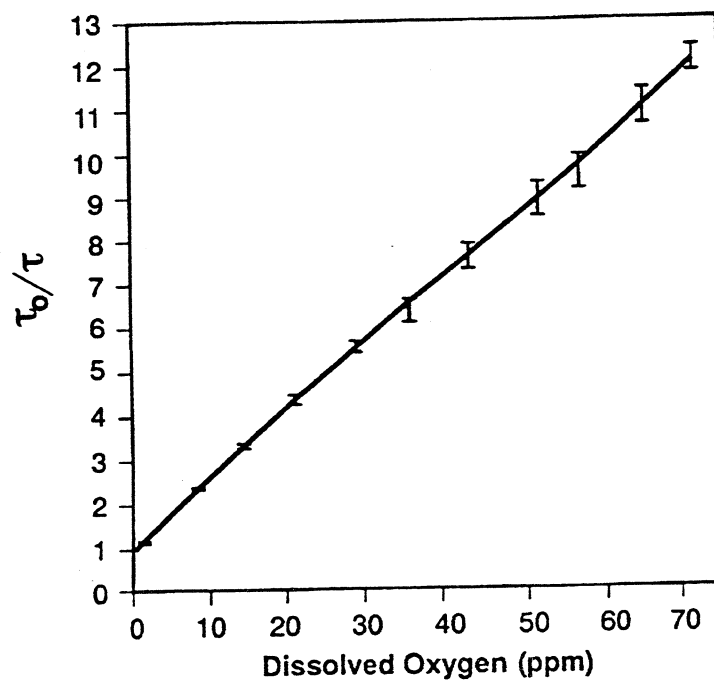
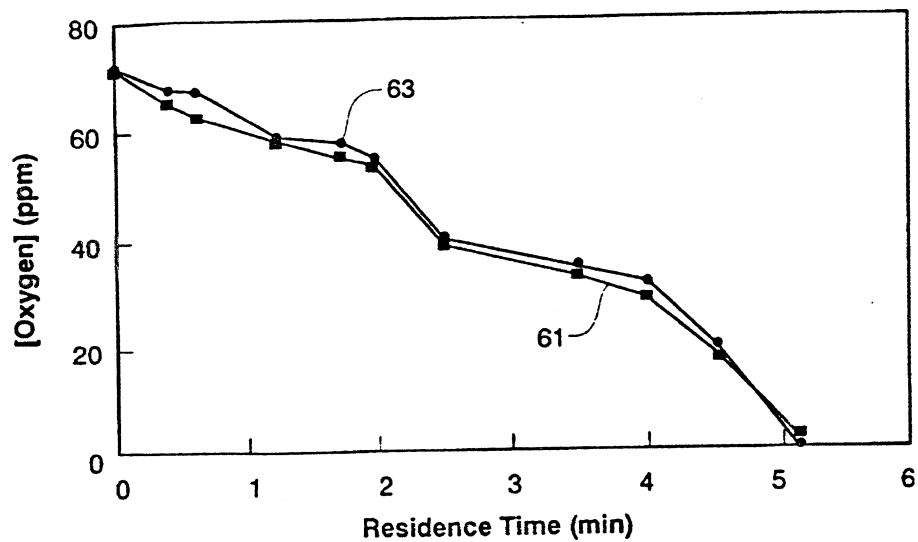
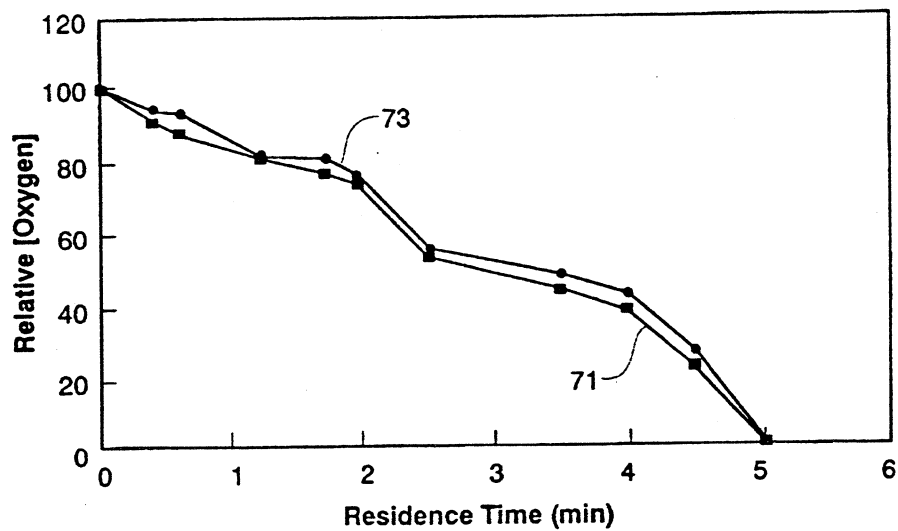


Fig. 2a



*Fig. 2b**Fig. 3*

*Fig. 4**Fig. 5*

*Fig. 6**Fig. 7*

1

## OPTICAL METHOD FOR QUANTITATING DISSOLVED OXYGEN IN FUEL

This application claims the benefit of Provisional Application Ser. No. 60/022.226 filed Jul. 18, 1996.

### RIGHTS OF THE GOVERNMENT

The invention described herein may be manufactured and used by or for the Government of the United States for all governmental purposes without the payment of any royalty.

### BACKGROUND OF THE INVENTION

The present invention relates generally to systems and methods for the quantitative determination of oxygen in liquid fuels, and more particularly to system and method for quantitation of dissolved molecular oxygen ( $O_2$ ) in fuel by observing the quenching by dissolved oxygen of the fluorescence of a laser excited probe molecule in the fuel.

Prior art methods for determining dissolved oxygen concentration in liquid fuel are cumbersome and time-consuming as to be rendered substantially useless for many measurements. For example, methods based on gas chromatography (GC) and combined GC and mass spectrometry (MS) are sensitive to at least a few parts per million (ppm)  $O_2$  and give results with fairly high precision. However, in the GC based method, the oxygen must be separated from the fuel prior to introduction to the GC column and, because any fuel in the GC sample degrades column efficiency, the column must be run through a heating cycle regularly to remove small amounts of fuel; GC is relatively slow and does not allow study of rapidly time-varying signals and is performed off-line which prevents in-situ and spatially resolved sample measurements; and GC based methods, and GC/MS based methods in particular, are relatively expensive to perform.

Electrochemical methods, such as potentiometry and voltammetry, can be used for analysis of oxygen. Oxygen is a reducible species detectable with high sensitivity by polarography in aviation fuel because of a paucity of other reducible species in the fuel; this method is relatively inexpensive and requires no separation of the oxygen from the fuel prior to measurement, but the interface between the fuel and the electrochemical cell is cumbersome and the measurement is slow, which substantially prevents use of the method for rapidly time-varying signals, and cannot be performed non-invasively. Oxygen is difficult to measure spectroscopically in organic solutions because  $O_2$  does not absorb in the infrared and has electronic transitions in the far ultraviolet where organic solutions absorb strongly. Although  $O_2$  has a Raman allowed transition and unique electron spin resonance, methods based on these attributes have low sensitivity, high cost and experimental complexity.

The invention solves or substantially reduces in critical importance problems with prior art methods as just described by providing an optical method for determining dissolved oxygen in fuel using the oxygen concentration dependence of the luminescence lifetime of an appropriate probe molecule doped in the fuel. The method of the invention is rapid, in that a single measurement can be made on a microsecond timescale and a signal comprising the average of 30 decays may be made in one second. The method is highly sensitive, non-intrusive, non-destructive, insensitive to thermal stressing of the fuel, less expensive than existing methods, and may be designed to obtain spatially-resolved profiling of oxygen concentration in fuel lines.

2

It is therefore a principal object of the invention to provide a method for determining dissolved oxygen in liquid fuel.

It is a further object of the invention to provide an optical method for the quantitative determination of dissolved oxygen in liquid fuel.

It is yet another object of the invention to provide a non-invasive method for determination of dissolved oxygen in liquid fuel.

It is a further object of the invention to provide a highly sensitive method for quantitatively determining the concentration of dissolved oxygen in liquid fuel by observing the laser excited fluorescence of a probe molecule in the fuel.

These and other objects of the invention will become apparent as a detailed description of representative embodiments proceeds.

### SUMMARY OF THE INVENTION

In accordance with the foregoing principles and objects of the invention, a method for the quantitative determination of dissolved oxygen in a liquid fuel is described which in a preferred embodiment comprises the steps of doping a sample of the fuel with a preselected concentration of a probe material including a luminophor which exhibits luminescence of wavelength which is quenched by oxygen dissolved in the fuel, illuminating the fuel with light from a coherent light source, such as a laser, of a wavelength which induces the luminescence in the luminophor, and thereafter measuring the change with time of the luminescence from the luminophor in the fuel and determining from the change with time of the luminescence the concentration of oxygen in the fuel.

### DESCRIPTION OF THE DRAWINGS

The invention will be more clearly understood from the following detailed description of representative embodiments thereof read on conjunction with the accompanying drawings wherein:

FIG. 1 is a schematic block diagram of a representative system useful in the practice of the method of the invention;

FIGS. 2a and 2b are plots of luminescence intensity of pyrene in cyclohexane and the natural logarithm of luminescence of pyrene in cyclohexane, respectively, versus time;

FIG. 3 is a plot of decay of pyrene luminophor probe luminescence intensity in isooctane versus time for varying oxygen concentrations;

FIG. 4 is a calibration curve for oxygen concentration in isooctane using pyrene as a probe;

FIG. 5 is a calibration curve for oxygen concentration in jet-A fuel using pyrene as a probe;

FIG. 6 is a plot of oxygen concentration versus residence time showing absolute oxygen concentration during aviation fuel thermal stress tests comparing the luminescence method of the invention to the GC method; and

FIG. 7 is a plot of oxygen concentration versus residence time showing relative oxygen concentration during aviation fuel thermal stress tests comparing the luminescence method of the invention to the GC method.

### DETAILED DESCRIPTION

Theoretical considerations and experimental procedures for the quantitative determination of dissolved oxygen in liquid fuels according to the invention are described in Gord et al. "Dissolved Oxygen Quantitation in Fuel Through



Measurements of Dynamically Quenched Fluorescence Lifetimes." IEEE Publication 95CH3482-7, pp 39.1-39.6 (Jul. 1995), the entire teachings of which are incorporated by reference herein.

In accordance with a governing principle of the invention, the oxygen molecule ( $O_2$ ) efficiently quenches the luminescence of a variety of luminophors in fuels as a result of an energy match between the single-triplet gap in  $O_2$  and the energies of the first excited state of many polycyclic aromatic hydrocarbons and of many metal complexes. Luminophors of interest in the practice of the invention exhibiting luminescence which is quenched by  $O_2$  include pyrene, anthracene and naphthalene and the derivatives thereof, or others as would occur to the skilled artisan practicing the invention. Variations in oxygen concentration will result in variations in the collision rate between oxygen and a luminophor (probe) present in a solution. Both the quantum yield and lifetime of the luminescence of the probe exhibit an inverse oxygen concentration dependence.

The principle of the invention may be illustrated by considering the photoexcitation of probe molecule A, the excited state  $A^*$  which decays by luminescence with rate constant  $k_L$  or is quenched by  $O_2$  with a rate constant  $k_q(Q)$ :



The overall first order rate constant  $k_r$  for Eq (1) is given by:

$$k_r = k_L + k_q(Q) \quad (2)$$

The integrated rate expression for the decay of the excited states of A is:

$$A_r = A_0 \exp(-k_r t) \quad (3)$$

A single excited state will show a simple exponential decay. Eq (2) shows that determination of the rate constant for the decay of the excited state at a series of oxygen concentrations yields a straight line. For the best operating mode in the invention the lifetime  $\tau$  for the decay of the excited state equals  $1/k$ . Eq (2) can be expressed using the lifetime of the unquenched excited state  $\tau_0$  and the lifetime of the excited state at a concentration Q of quencher  $\tau_q$  as:

$$Q \tau_0 / \tau_q + 1 = \tau_0 / \tau_s \quad (4)$$

where

$$1/\tau_s = k_s \quad (5)$$

Eq (4) is the Stern-Volmer equation (see Lakowica, *Principles of Fluorescence Spectroscopy*, Plenum Press, NY (1983), incorporated by reference herein), and can be used as a calibration equation with  $\tau_0/\tau_s$  plotted versus  $O_2$  concentration.

Referring now to the drawings, FIG. 1 is a schematic block diagram of representative system 10 useful in the determination of  $O_2$  concentration in a liquid fuel according to the method of the invention. In system 10, a liquid fuel sample 11 to be tested is disposed within a sample region 12, which may include a cuvette, flask, cell, flowing fuel line, or other suitable disposition occurring to the skilled artisan practicing the invention. Sample 11 comprises a liquid fuel such as cyclohexane, isooctane, Jet-A, hexane, heptane, nonane, decane, kerosene, oil or other fuel the oxygen content of which is sought. Sample 11 is doped with a known concentration of a probe 13 molecule selected from the class of luminophors known in the art as suitable for the intended purpose, including those listed above. A coherent light

source such as laser source 14 provides light beam 15 for exciting probe 13 in sample 11. Sources 14 suitable for use in the method of the invention include pulsed nitrogen, Eximer, Nd:YAG, Nd:YLF, Ti:sapphire, and Nd:YVO<sub>4</sub> lasers, or other source as would occur to the skilled artisan practicing the invention. Beam 15 is split by beamsplitter 16 into reference beam portion 15R directed onto detector 17 (such as a photodiode, photomultiplier, external trigger or other equivalent purpose detector) and sample beam portion 15S directed onto sample 11. Beam 15S may be directed onto sample 11 through any suitable number and type of optical elements comprising an optical train such as that suggested in FIG. 1 as including iris 18, mirror 19 and lens 20. Luminescence from the probe molecules within sample 11 in the form of beam 21 is directed through a second optical train (such as lens 22, neutral density filter 23 and color filter 24 illustrated in the non-limiting system 10 embodiment) onto a second detector 25 (in the form of photomultiplier tube, photomultiplier, micro-channel plate, or photodiode). Signals 26, 27 respectively from detectors 17, 25 are directed into suitable electronic data storage means represented in FIG. 1 by digital storage oscilloscope 28. Signal 27 defines the luminescence output from probe 13 in sample 11. The purpose of beam portion 15R directed onto detector 17 is to provide an output signal 26 from detector 17 to initiate data acquisition from oscilloscope 28. It is noted, however, that data acquisition may be triggered directly by signal 27 from probe 13. Excess beam 15S energy passing through sample 11 may be absorbed by beam dump 29.

In demonstration of the method of the invention, cyclohexane and isooctane liquid fuels were tested for  $O_2$  using pyrene as a luminophor probe. FIG. 2a shows decay of luminescence intensity of the excited pyrene as a function of time for a 9 ppm solution of pyrene in cyclohexane after sparging with nitrogen. FIG. 2b shows the data of FIG. 2a displayed as the natural logarithm of pyrene luminescence versus time. The lifetime of the luminescence may be obtained by directly fitting the exponential decays or by linearizing the data to determine lifetime using least squares. FIG. 2b shows the linearity of the logarithm of intensity decay over at least two orders of magnitude.

FIG. 3 is a plot of pyrene probe luminescence intensity decay in isooctane versus time for various oxygen concentrations illustrating the effect of luminescence quenching by oxygen. Curve 31 represents the longest luminescence lifetime for oxygen-free isooctane (0 ppm  $O_2$  concentration). Curves 32, 33, 34, 35, 36 are luminescence decay traces of pyrene in isooctane, respectively, for  $O_2$  concentrations of 16 ppm, 30 ppm, 40 ppm, 67 ppm and 101 ppm. Pyrene lifetime in isooctane clearly decreases with increased  $O_2$  concentration in predictable fashion according to the principal teaching of the invention. FIG. 4 is a Stern-Volmer plot for  $O_2$  quenching in the pyrene-isooctane system showing good linear dependence. FIG. 4 or the equivalent plot for other luminophor-liquid fuel systems may be used as a calibration curve for  $O_2$  determination in the fuel.

The method of the invention was demonstrated on actual fuel samples in order to illustrate the best mode of operation of the invention. FIG. 5 shows a calibration curve for determination of  $O_2$  concentration in Jet-A fuel at room temperature containing 10 ppm pyrene as the probe. The natural logarithm of the decay of luminescence intensity with time is linear. The lifetimes show a broad range from air saturated to fully unquenched giving good precision to the results. The pyrene could be decreased in concentration to the 1 ppm level without significantly diminishing the

5

quality of results. All data were collected with a neutral density filter which reflects about 99% of the luminescence intensity.

The method of the invention was also demonstrated with flowing heptane fuel pumped through a heated tube simulating a jet fuel line. Pyrene at 0.1 to 100 ppm levels were added to the fuel in separate runs. The fuel reacts with the initially dissolved  $O_2$ , but system tightness prevents further absorption of  $O_2$  into the fuel. By varying fuel flow rate through the tube the residence time of the fuel in the tube and hence the reaction time at high temperature may be varied. Oxygen concentration as a function of flow rate was measured to yield an  $O_2$  consumption plot. Measurements using the method of the invention were compared against GC. The validity of the luminescence method of the invention was cross-checked by inserting an optical cell in-line with the GC. The fuel was returned to room temperature prior to the luminescence and GC measurements. It must be noted that the luminescence lifetime is temperature dependent, and control of temperature during comparative testing is therefore important.

FIG. 6 is a plot of  $O_2$  concentration versus residence time showing absolute  $O_2$  concentration during aviation fuel thermal stress tests comparing the method of the invention to GC. FIG. 7 is the corresponding plot of relative  $O_2$  concentration versus residence time. In FIGS. 6 and 7, plots 61, 71 (defined by squares indicia) define measurements using the luminescence method of the invention and two-point calibration. Plots 63, 73 (defined by circle indicia) define measurement results using GC. Accuracy and reproducibility of measurements using the method of the invention is apparent, including the structure of the decay curves, which reflects passivation effects characteristic of the heated simulated fuel line. Stern-Volmer plots of  $\tau_0/\tau_q$  (see FIG. 5 supra) were used as calibration curves for data in FIG. 6. However, two point calibration can also be used. All generated Stern-Volmer plots were linear so that accurate measurement of the air-saturated and fully unquenched measurements were sufficient to define the calibration curves. Measurements of luminescence lifetime in the fuel at the slowest flow rate (at which all oxygen is consumed) and of the luminance lifetime of air-saturated fuel produces an accurate two-point calibration curve as illustrated in FIG. 7.

The luminescence lifetime may be obtained using a frequency-resolved rather than a time-resolved analysis as suggested in Gord et al. supra. The frequency-resolved method has lower cost and greater instrumental simplicity, but the time-resolved method gives better separation of background fuel luminescence from the probe luminescence.

6

The invention therefore provides a method for quantitatively determining dissolved oxygen in fuel. It is understood that modifications to the invention may be made as might occur to one with skill in the field of the invention within the scope of the appended claims. All embodiments contemplated hereunder which achieve the objects of the invention have therefore not been shown in complete detail. Other embodiments may be developed without departing from the spirit of the invention or from the scope of the appended claims.

We claim:

1. A method for quantitating dissolved oxygen in liquid fuel, comprising the steps of:

- (a) providing a sample of liquid fuel disposed within a sample region;
- (b) doping said liquid fuel with a preselected concentration of a probe material comprising a luminophor which exhibits a luminescence which is quenched by oxygen dissolved in said liquid fuel;
- (c) providing a source of light having a wavelength which induces said luminescence in said luminophor;
- (d) illuminating said sample of liquid fuel with light from said source;
- (e) measuring the change with time of said luminescence from said luminophor in said sample of liquid fuel; and
- (f) determining from said change with time of said luminescence the concentration of dissolved oxygen in said liquid fuel.

2. The method of claim 1 wherein said luminophor is a polycyclic aromatic hydrocarbon or a metal complex which when illuminated with light of a particular wavelength exhibits luminescence which is quenched by oxygen dissolved in said liquid fuel.

3. The method of claim 2 wherein said luminophor is selected from the group consisting of pyrene, anthracene and naphthalene.

4. The method of claim 1 wherein said liquid fuel is selected from the group consisting of cyclohexane, isooctane, hexane, heptane, nonane, decane, kerosene and oil.

5. The method of claim 1 wherein said source is a coherent light source.

6. The method of claim 5 wherein said coherent light source is selected from the group consisting of a pulsed nitrogen laser, Eximer laser, Nd:YAG laser, Nd:YLF laser, Ti:sapphire laser, and Nd:YVO<sub>4</sub> laser.

\* \* \* \* \*

### **2.2.3 Picosecond Pump/Probe Diagnostics**

In an effort to develop picosecond pump/probe diagnostics, the rate-equation formalism originally used to model pump/probe interactions was extended to molecules and used to estimate new detection limits for various species. The results of this effort were summarized in the invited review article entitled “Developments in Picosecond Pump/Probe Diagnostics” (see pp. 197-212).



**AIAA 98-0306**

**Developments in Picosecond Pump/Probe  
Diagnostics**

M. Linne and T. Settersten  
Center for Combustion and Environmental Research  
Colorado School of Mines  
Golden, Colorado

J. Gord, Wright Laboratory,  
Aero Power and Propulsion Directorate,  
Wright Patterson AFB, Ohio

G. Fiechtner,  
Innovative Scientific Solutions, Inc.  
Dayton, Ohio

**36th Aerospace Sciences  
Meeting & Exhibit**  
January 12–15, 1998 / Reno, NV

## DEVELOPMENTS IN PICOSECOND PUMP/PROBE DIAGNOSTICS

M. Linne and T. Settersten  
Center for Combustion and Environmental Research  
Colorado School of Mines, Golden, CO

J. Gord  
Wright Laboratories, Wright Patterson AFB, OH

G. Fiechtner  
Innovative Scientific Solutions Inc., Dayton, OH

**Abstract**

This paper describes further developments in picosecond pump/probe combustion diagnostics. The rate equation formalism originally used to model pump/probe has been extended to molecules, and it has been used to estimate new detection limits for various species of importance to combustion. In practice, we typically use 2 ps or 60 ps pulses, an interaction for which the rate equation limit is not entirely appropriate. The bulk of this paper describes a new non-perturbative density matrix model that more exactly describes the pump/probe interaction and briefly compares it to the rate equation formalism.

**Introduction**

We have demonstrated in previous work<sup>1</sup> that picosecond pump/probe is a combustion diagnostic offering an absolute determination of number density. In the rate equation limit, the measurement does not require calibrations or corrections<sup>2</sup>. It is, essentially, a spatially resolved absorption measurement. Even molecules with poor fluorescence yield can be observed with pump/probe. We expect that pump/probe measurements will be insensitive to the collisional environment, because it's possible to make the measurement in time scales much smaller than normal collisional times. Moreover, the transform-limited bandwidth of picosecond pulses is broader than single linewidths, so pressure effects on linewidth do not propagate to the signal.

For a laser source, we prefer to use mode-locked cw lasers because cw laser diagnostics are capable of

recovering all the relevant frequency spectrum information in turbulent flames, power spectral densities (psd's) for example. Psd's require up to 10 kHz bandwidth. Cw lasers also allow continuous monitoring of rapid events, such as ignition. It is important to note, however, that the overall instrumentation bandwidth is controlled somewhat by the detection limits required of the measurement. Pump/probe is a linear technique that scales with pump pulse energy, so the detection limit can be lowered with amplification. The pulses emitted by a mode-locked Ti:sapphire laser oscillator have energy on the order of 20 nJ at the peak of the fundamental (giving peak power in the kilowatt regime). With amplification, pulse energies can reach 0.01 mJ at 50 kHz, and 1 mJ at 1 kHz. While amplification can reduce the instrumentation bandwidth, it provides significant pulse energy, and this is a trade-off that must be considered.

In what follows, we briefly describe a rate equation model for pump/probe as it would be applied to molecules, and we quote expected detection limits for CH, as one example. The rate equations are not fully appropriate for a picosecond interaction, so we describe the development of a non-perturbative, 2-level density matrix model for the pump/probe interaction. Here we, include a discussion of the numerical approach used. We then present some results of the model and briefly compare it to rate equation results for the potassium atom. We then conclude by discussing future directions.

**Pump/Probe**

In Pump/Probe spectroscopy, the output from the laser is tuned to a transition of interest and the beam is split into two portions. The pump beam (typically much stronger) is directed through a modulator, and is crossed with the probe beam (typically much weaker) in the

Copyright © 1997 by the American Institute of Aeronautics and Astronautics, Inc. All rights reserved.

REPRINTED WITH PERMISSION

flame. This beam crossing forms a sample volume within the flame (see Fig. 1). The pump modulation is impressed upon the resonant molecules in the sample volume because the populations of the ground and excited state are modified by the presence of the pump beam. These populations then modulate the probe beam at the intersection via absorption and stimulated emission, changing the probe irradiance at the modulation rate. This change in irradiance is defined as the modulation depth, expressed as a fraction of the total probe irradiance. After the flame, the pump beam reaches a beam stop, and the probe beam is detected. The detector signal is then synchronously demodulated using a lock-in amplifier. The measured probe modulation depth is proportional to the concentration of molecules. For optically thin conditions, the modulation depth will be at most a few percent. Nevertheless, for mode-locked lasers<sup>3</sup>, the minimum detectable modulation depth is approximately  $10^{-8}$ .

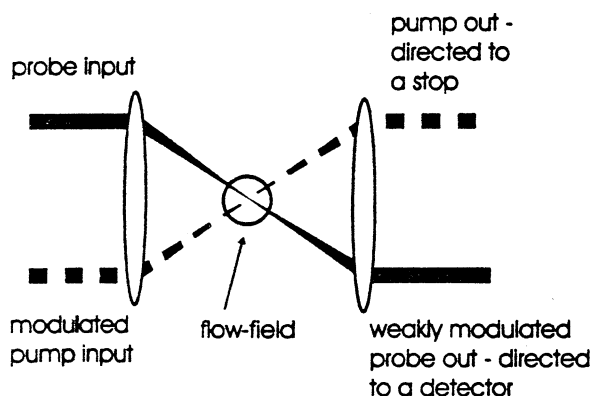


Figure 1. Schematic of single-point Pump/Probe interaction in the flow-field.

We use a Spectra-Physics regeneratively mode-locked Ti:sapphire laser, equipped with both a 2 ps and a 60 ps Gires-Tournois interferometer (Kafka *et al.*, 1992). This laser produces about 1.8 W of output when pumped with 8 W from an intra-cavity doubled, diode-pumped Nd:YVO<sub>4</sub> laser, with autocorrelation pulse-widths around 1.4 ps in the 2 ps configuration. The transform-limited bandwidth is about 0.2 nm. This radiation can then be frequency doubled in 6 mm of LBO to give up to 500 mW of 400 nm radiation. The laser wavelength is monitored several ways: first the laser is tuned using a Burleigh WA 4500 wavemeter, then the flame is ignited and we observe fluorescence. Finally, when signals had been established, the laser is tuned to maximize the signal.

## Rate Equation Models

In the interest of preserving space for a discussion of the density matrix model, we discuss rate equation models only briefly. Further details can be found in the work by Fiechtner *et al.*<sup>2</sup> and by Settersten and Linne<sup>4</sup>.

In our experiments, both the pump and probe are in resonance with the same transition. For a two-level atom, the rate equations then give a modulation depth described by<sup>2</sup>:

$$\alpha_{\text{mod}} = \left( \ln \left( \frac{1}{\sqrt{2}-1} \right) \right)^2 \frac{c^4 P_{\text{AVE}}^{\text{PUMP}} N_T L}{16\pi^3 D^2 h f^L (\Delta \nu_{1/2}^L)^2} \cdot \left[ \frac{A_{21}^2 g_2}{\nu_{12}^5 g_1} \left( 1 + \frac{g_2}{g_1} \right) \right] \quad (1)$$

where :

- $g_i$  = degeneracy of level  $i = 1$  or  $2$ ,
- $D$  = focal diameter,
- $L$  = beam interaction length,
- $f^L$  = laser repetition rate,
- $\nu_{12}$  = transition frequency,
- $\Delta \nu_{1/2}^L$  = laser bandwidth,
- $P_{\text{AVE}}^{\text{PUMP}}$  = average power of the pump beam,
- $A_{21}$  = Einstein coefficient for spontaneous emission,
- $N_T$  = absolute number density of absorber.

Here the modulation resides on a large intensity carrier (typically  $10^4$  to  $10^7$  larger than the modulated portion of the signal). The model assumes an optically thin analyte, the linear absorption regime, a 2-level system, a temporal top-hat pulse profile and broad bandwidth with respect to the absorption linewidth. The modulation depth ( $\alpha_{\text{MOD}}$ ) is easy to measure, and this is related directly to the number density ( $N_T$ ). The other terms in equation (1) are usually known or can be measured.

We have demonstrated that Pump/Probe is an absolute determination of number density when this equation was applied to our Potassium measurements and then compared to atomic absorption spectroscopy using a Tungsten filament lamp<sup>1</sup>.

Equation (1) represents several approximations, and applies only to a 2-level spectroscopic system. It's easy to use the equation, however, to infer the effect of variables (e.g. pump pulse energy) on the signal, and this is the real utility of the expression. We have recently developed an extended rate equation model for a molecular pump/probe interaction by accounting for numerous ro/vibrational levels, including: the individual Boltzmann fractions, Einstein rate constants for each



line, line broadening and overlap between the laser linewidth and the individual lines pumped by the laser. It was simply assumed that the interaction could be represented by a summation over a number of distinct 2-level resonances. In doing so, the term in square braces in equation (1) becomes:

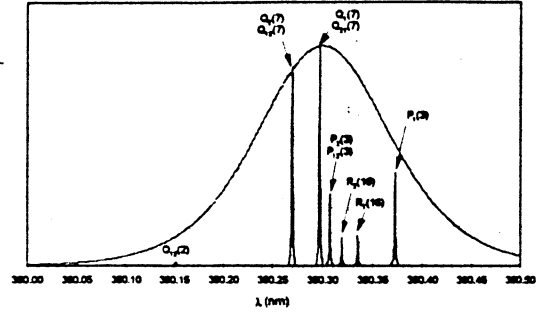
$$\left[ \sum_i A_{21,i}^2 \lambda_{21,i}^5 f_{\text{Boltzmann},i} \eta_i \frac{g_{2,i}}{g_{1,i}} \left( 1 + \frac{g_{2,i}}{g_{1,i}} \right) \right] \quad (2)$$

The two additional terms in this expression are the Boltzmann fraction  $f_{\text{Boltzmann},i}$  and an laser interaction efficiency  $\eta_i$ . The laser interaction efficiency simply has the form of the normalized laser spectral profile. Resonance lines that do not fall on line center will have  $\eta < 1$ . We assume that energy re-distribution within the upper manifold is negligible within the 10 ps time frame spanning the pump and probe interactions. As before, we assume a top-hat temporal pulse profile. We use the model to computationally tune the laser and maximize the P/P signal. The current optics set in our Ti:sapphire oscillator will allow us to reach the CH B  $\rightarrow$  X electronic transition, which is of particular interest to us. The tuning shown in Figure 2 maximizes the pump/probe signal for the B  $\rightarrow$  X electronic transition, for a 2 ps and 60 ps pulse. Further details can be found in the work of Settersten and Linne<sup>5</sup>. That work makes extensive use of the spectroscopic data of Luque and Crosley<sup>6,7,8</sup> and Zachwieja<sup>9</sup>.

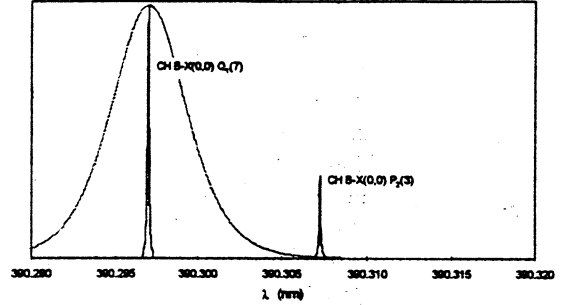
The model just described, when used with conservative numbers (e.g. we assume 200 mW average pump power at about 400 nm when we have routinely reached 300 mW at the experiment), indicates that we can achieve the detection limits contained in Table 1, where the detection limit is written in terms of the following:

$$N (\text{lower limit}) = \beta \times \alpha_{\text{MOD}} (\text{lower limit}).$$

We write it this way because the limit of detection is clearly linked to the lowest modulation depth detectable by the electronics. To detect peak levels of CH in a 2500 K CH<sub>4</sub>-O<sub>2</sub> flame (roughly  $10^{14} \text{ cm}^{-3}$ ), our current pump/probe detection system (for the CH B  $\rightarrow$  X transition and a 2 ps pulse) must see a signal level of  $5 \times 10^{-7}$ . CH has many energy levels at about the same term value, which produces fairly low Boltzmann fractions for individual lines, and this is the major limitation. Our former Ar:Ion laser pumped Ti:sapphire system generated unusually large amounts of 1/f noise in the probe beam. When this was coupled with a mechanical chopper (at 4 kHz), a modulation depth of  $10^{-7}$  was impossible to measure. These issues lead us to



a.



b.

Figure 2. Example : a. Overlap between part of the CH B  $\rightarrow$  X (0,0) band (mixed P,Q & R-branch lines) and the laser emission linewidth at 2 ps - this laser tuning gives maximum P/P signal, b. Similar overlap for 60 ps.

**Table 1**

Estimated Detection Limits for Standard Pump/Probe

Molecule/Transition	$\lambda(\text{nm})$	$\beta (\text{cm}^{-3})$	pulsewidth(ps)
CH B $\rightarrow$ X	390.29	$5.0 \times 10^{-21}$	2
CH B $\rightarrow$ X	390.30	$2.0 \times 10^{-19}$	60
CH A $\rightarrow$ X	431.24	$5.0 \times 10^{-21}$	2
CH A $\rightarrow$ X	430.98	$1.2 \times 10^{-19}$	60

The following parameters were used : average cw laser power = 200 mW, laser rep rate = 82 MHz, beam focus diam. = 100  $\mu\text{m}$ , interaction length = 100  $\mu\text{m}$ , laser bandwidth =  $3.15 \times 10^{11} \text{ Hz} \rightarrow 0.16 \text{ nm}$  (at 390 nm).

investigate the 60 ps case. For the 60 ps case, we would need to reach  $2 \times 10^{-5}$  modulation depth (a routine measurement) if the same average power were available. Unfortunately, doubling efficiency falls rapidly as one goes to 60 ps in the fundamental, where we achieve only a few mW in the blue, increasing the detection limit by the ratio of power levels.

We can improve the basic cw experiment in a straightforward way. We are currently installing a 10 W intra-cavity doubled, diode-pumped Nd:YVO<sub>4</sub> pump laser. This will reduce the noise in the Ti:sapphire significantly. The manufacturer's data show an order of

magnitude lower noise for this pump laser when compared to a properly operating Ar:Ion laser. This new laser system will be used with an E/O modulator and lock-in extender (both operating at  $> 100$  kHz, beyond the  $1/f$  noise spectrum for this laser). It is not clear at this point what lower limit of modulation we can reach with this system. Work continues in this 82 MHz regime, but amplifiers are another approach for reducing the detection limit.

Wright Laboratories has recently installed a 50 kHz Ti:sapphire regenerative amplifier that produces 0.01 mJ/pulse in the red. This will easily give pump energies near 2  $\mu$ J/pulse at 2 ps and 400 nm. The values for  $\beta$  in Table 1 will then be decreased by a factor of about  $10^2$ . In the amplified case, to detect the same peak levels of CH B  $\rightarrow$  X in the 2500 K CH<sub>4</sub>-O<sub>2</sub> flame at 2 ps, the detection system would need to see a signal level of  $10^{-3}$ , which is trivial.

The group at CSM has recently ordered a complimentary 1 kHz regenerative amplifier, generating 1 mJ in the red. This will easily give pump energies near 200  $\mu$ J/pulse at 2 ps and 400 nm. The values for  $\beta$  in Table 1 will then be decreased by a factor of about  $10^4$ . In the amplified case, to detect the same peak levels of CH B  $\rightarrow$  X in the 2500 K CH<sub>4</sub>-O<sub>2</sub> flame at 2 ps, the detection system would only need to see a signal level of 1%. Another way to state the same fact is that the detection limit will be reduced by a factor of  $10^4$ , at the price of instrumentation bandwidth. The group at CSM is interested in using pump/probe for imaging, however, requiring that the pump beam be spread into a sheet. Clearly, extra pump pulse energy is required in order to accomplish this.

### Density Matrix Model

As stated in the introduction, we expect that pump/probe measurements will be insensitive to the collisional environment, because it's possible to make the measurement in time scales much smaller than normal collisional times. Our pulsewidths are typically 2 ps long, and the probe pulse is adjusted to trail the pump pulse by only a few pulsewidths. These time frames are significantly shorter than the collision times, coherence lifetimes, and the excited state lifetimes of molecules in flames. This necessarily means that the probe pulse will sample the coherences created by the pump pulse. As such, it is not accurate to use the rate equations to describe the pump/probe interaction.

For this reason, we have developed a non-perturbative model that is based upon semi-classical theory. It combines the time-dependent density matrix equations with Maxwell's equations to describe the propagation of the pump and probe pulses. Our goal is

to discover how well the rate equation model approximates the pump/probe interaction, when it occurs within the rate equation limits, or to find a similarly simple expression. Failing that, we plan to find some other way to relate the experimentally measured modulation depth to number density. We also plan to define the limits of applicability of such expressions, and then to explore other sensing possibilities offered by departures from the rate equation limits.

This model combines three formalisms to self-consistently describe pulse propagation. First, the density matrix formalism of Quantum Mechanics describes the microscopic response of resonant and near-resonant atoms immersed in the laser field. Secondly, Statistical Physics describes how the individual atomic responses add up to produce a net induced polarization on the macroscopic level. This statistical averaging takes into account the Doppler broadening of the resonance. Lastly, from Classical Electrodynamics, we obtain the one-dimensional wave equation that describes the propagation of the laser pulse. Each of these topics will be discussed in three sections to follow. Prior to that, we will set the stage for those sections by introducing the formalism used to represent the laser pulses.

### Pulse Representation

The pump and probe pulses will be described as plane waves traveling in the  $\hat{e}_z$ -direction with a linear electric field polarization in the  $\hat{e}_x$ -direction. The model described here, therefore, does not assume the crossed beam geometry shown in Figure 1, but instead a collinear geometry. The electric field of a pulse can be expressed as the product of a slowly varying envelope function and a rapidly varying phase, both of which are functions of the spatial coordinate  $z$  and the time  $t$ :

$$\vec{E}(z,t) = \hat{e}_z \mathcal{E}(z,t) \left( e^{-i[\omega_0 t - k_0 z + \phi(z,t)]} + c.c. \right) \quad (3).$$

Both the angular frequency  $\omega_0$  and the propagation constant  $k_0$  are considered constants, while the slowly varying phase term  $\phi(z,t)$  allows for dispersive effects. With no loss of generality,  $\phi(z,t)$  can be incorporated into the envelope function, resulting in a complex envelope function with real and imaginary components  $\mathcal{E}^R$  and  $\mathcal{E}^I$ :

$$\vec{E}(z,t) = \hat{e}_z \left( \tilde{\mathcal{E}}(z,t) e^{-i[\omega_0 t - k_0 z]} + c.c. \right) \quad (4).$$

This transformation allows us to describe the propagation of a pulse solely in terms of the propagation of a complex envelope since the rapidly varying phase term cannot change form. We describe the net induced polarization of the sample in an analogous way:

$$\bar{P}(z,t) = \hat{e}_z \left( \bar{p}(z,t) e^{-i[\omega_0 t - k_z z]} + c.c. \right) \quad (5).$$

Since the pump and probe pulses are produced from the same laser by using a beam splitter, their envelope functions have the same functional form with the same initial phase  $\phi$ , but they can have different magnitudes. Also, when describing both pulses in the same coordinate system, a spatial transformation must be applied to the probe pulse. This is due to the fact that the pump and probe pulses travel through different pathlengths on their way to the interaction volume. If the probe pathlength is a distance  $\Delta z$  longer than that of the pump, the necessary spatial transform is  $z \rightarrow z + \Delta z$ . Since the beams are collinear through the interaction volume, the superposition principle can be used to describe the total field due to both pulses. Assuming that both pulses have the same electric field polarization, the total electric field is equal to the sum of the two fields. If the pump and probe pulses are each expressed as in equation (3), the total electric field takes the form of Equation (4) where the real and imaginary parts of the total envelope function are given by the following expressions.

$$\begin{aligned} \varepsilon^R(z,t) &= \varepsilon_1(z,t) \cos \phi \\ &+ \varepsilon_2(z + \Delta z, t) \begin{bmatrix} \cos \phi \cos k_o \Delta z \\ + \sin \phi \sin k_o \Delta z \end{bmatrix} \end{aligned} \quad (6a)$$

$$\begin{aligned} \varepsilon^I(z,t) &= -\varepsilon_1(z,t) \sin \phi \\ &+ \varepsilon_2(z + \Delta z, t) \begin{bmatrix} \cos \phi \sin k_o \Delta z \\ - \sin \phi \cos k_o \Delta z \end{bmatrix} \end{aligned} \quad (6b)$$

An example of an envelope function used to describe a pump and a probe pulse in this manner is shown in Figure 6 in the "Results" section.

### Density Matrix Equations

We use the density matrix formalism to describe the response of resonant or near-resonant atoms to the electric field of a laser pulse. Definition of the density matrix, discussion of its properties, and derivations of the density matrix equations are found in most graduate quantum mechanics texts<sup>10</sup>. Additionally, we have found several books that contain useful introductions to this formalism with particular emphasis on laser-matter interaction<sup>11,12,13</sup>.

For the purposes of this study, we will model a resonant atom or molecule as a closed two-level system. This simplification can be justified in cases where the resonance is isolated and where transfer rates between

the resonant energy levels and other energy levels are negligible on the time scales considered by the model.

The two-level system that will be considered is shown in Figure 3. The combined spontaneous emission and collisional de-excitation rates are given by  $\Gamma_{21}$ . The collisional dephasing rate  $\gamma_{21}$  accounts for collisional broadening. Collisional excitation rates are considered negligible.

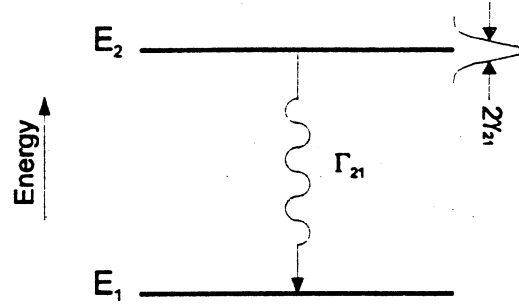


Figure 3. Energy level diagram for a closed two-level system. Also depicted in the figure are collisional/radiative de-excitation (with a rate  $\Gamma_{21}$ ), and collisional broadening (characterized by the coherence dephasing rate  $\gamma_{21}$ ).

The density matrix  $\rho$  for an atom contains all necessary information about this quantum system. For a two-level atom, the diagonal elements  $\rho_{11}$  and  $\rho_{22}$  are the probabilities that the atom is in state 1 or 2, respectively. For a closed two-level system, the trace of the density matrix must be equal to one, since the atom must be in one state or the other. The off-diagonal elements are the coherences between the states with the property that  $\rho_{21} = \rho_{12}^*$ .

When a resonant electric field is applied to an atom, the interaction Hamiltonian, denoted by  $V$ , is introduced into the Schrödinger equation. In the electric dipole approximation, the off-diagonal elements of the interaction Hamiltonian are given by:

$$\begin{aligned} V_{21}(t) &= -\mu_{21} E(t) \\ V_{12}(t) &= -\mu_{12} E(t) \end{aligned} \quad (7).$$

In general, the off-diagonal elements are complex conjugates. However, the dipole matrix elements  $\mu_{12}$  and  $\mu_{21}$  can be made purely real and equal, with no loss of generality, if the basis vectors describing the energy eigenstates 1 and 2 are judiciously chosen. In that case, the interaction Hamiltonian is also purely real, and  $V_{21} = V_{12}$ .

The density matrix equations are a set of coupled ordinary differential equations that describe the time evolution of the density matrix elements in response to an interaction Hamiltonian. With the relaxation rates defined earlier, the density matrix equations for a 2-level system are given by<sup>12</sup>:

$$\frac{d}{dt} \rho_{11} = \Gamma_{21} \rho_{22} + \frac{i}{\hbar} (V_{21} \rho_{12} - \rho_{21} V_{12}) \quad (8a),$$

$$\frac{d}{dt} \rho_{21} = -(i\omega_{21} + \gamma_{21}) \rho_{21} + \frac{i}{\hbar} V_{21} (\rho_{22} - \rho_{11}) \quad (8b).$$

When the laser electric field is applied, the system responds at the optical frequency  $\omega_o$ . As such, it stands to reason that the coherence can be written in terms of the product of a slowly varying complex envelope and the same rapidly varying phase term, as in equation (4):

$$\rho_{21} = \tilde{\sigma}_{21} e^{-i[\omega_o t - k_o z]} \quad (9).$$

The envelope function for the coherence has real and imaginary parts  $\sigma_{21}^R$  and  $\sigma_{21}^I$ , respectively.

When the interaction Hamiltonian is expressed explicitly, and equation (9) is substituted into the differential equations (8a) and (8b), the following two equations result:

$$\frac{d}{dt} \rho_{11} = \Gamma_{21} \rho_{22} + \frac{i\mu_{21}}{\hbar} \left( \begin{array}{l} -\tilde{\epsilon} \tilde{\sigma}_{21}^* + \tilde{\epsilon}^* \tilde{\sigma}_{21} \\ + \left[ \tilde{\epsilon} \tilde{\sigma}_{21} e^{-2i(\omega_o t - k_o z)} \right] \\ - c.c. \end{array} \right) \quad (10a),$$

$$\frac{d}{dt} \tilde{\sigma}_{21} = -[i(\omega_{21} - \omega_o) + \gamma_{21}] \tilde{\sigma}_{21} - \frac{i\mu_{21}}{\hbar} (\rho_{22} - \rho_{11}) (\tilde{\epsilon} + \tilde{\epsilon}^* e^{2i(\omega_o t - k_o z)}) \quad (10b).$$

Both of these equations have terms that are slowly varying and terms that oscillate at twice the optical frequency  $\omega_o$ . In the rotating wave approximation, the rapidly varying terms are neglected. Furthermore, these equations can be expressed in terms of the complex and real parts of the envelope functions for the electric field and for the coherences. This results in three real equations:

$$\frac{d}{dt} \rho_{11} = \Gamma_{21} (1 - \rho_{11}) + \frac{2\mu_{21}}{\hbar} (\epsilon^I \sigma_{21}^R - \epsilon^R \sigma_{21}^I) \quad (11a),$$

$$\begin{aligned} \frac{d}{dt} \sigma_{21}^R &= -\gamma_{21} \sigma_{21}^R + (\omega_{21} - \omega_o) \sigma_{21}^I \\ &+ \frac{\mu_{21}}{\hbar} \epsilon^I (1 - 2\rho_{11}) \end{aligned} \quad (11b),$$

$$\begin{aligned} \frac{d}{dt} \sigma_{21}^I &= -\gamma_{21} \sigma_{21}^I - (\omega_{21} - \omega_o) \sigma_{21}^R \\ &- \frac{\mu_{21}}{\hbar} \epsilon^R (1 - 2\rho_{11}) \end{aligned} \quad (11c).$$

Given an initial electric field envelope function ( $\epsilon$ ), these three equations can be directly integrated to produce the time evolution of the coherence.

The coherence is then used to calculate the atomic response, given by the expectation value of the atomic dipole moment. Using the formalism of Quantum Mechanics, the expectation value of any operator is given by the trace of the matrix resulting from the density matrix acting on the operator. For the dipole moment operator, which has non-zero elements only off-diagonal, the expectation value is simply:

$$\begin{aligned} \langle \mu \rangle &= \rho_{12} \mu_{21} + \rho_{21} \mu_{12} \\ &= \mu_{21} (\tilde{\sigma}_{21} e^{-i(\omega_o t - k_o z)} + c.c.) \end{aligned} \quad (12).$$

### Statistical Averaging

The net induced polarization is a macroscopic property that results from the sum of the microscopic responses of individual atoms, given by equation (12). The macroscopic polarization in a volume  $V$  is the volume average of the atomic dipole moments of all  $M$  atoms in  $V$ :

$$P(z, t) = \frac{1}{V} \sum_{i=1}^M \langle \mu \rangle_i \quad (13).$$

The atomic dipole moments in this problem can be parameterized by the atomic velocity component  $u$  along the optical axis  $\hat{e}_z$ . Atoms traveling with different velocities along that axis will respond to the laser excitation at an optical frequency that is Doppler shifted. With this in mind, we introduce a more explicit notation that emphasizes this parameterization. A partial polarization  $P(z, t; u)$  is defined as the time-dependent expectation value of the dipole moment of an atom at position  $z$  with a velocity component  $u$ :

$$P(z, t; u) = \langle \mu(z, t; u) \rangle \quad (14).$$

The summation in Equation (13) is treated in statistical physics by introduction of the velocity distribution function. For this analysis, we consider a

steady-state and spatially-uniform Maxwellian velocity distribution, which is only a function of the velocity component  $u$ . In this case, the probability that an atom has a velocity component  $u$  in the interval  $(u, u+du)$  is given by:

$$f(u)du = \left( \frac{m}{2\pi k_B T} \right)^{\frac{1}{2}} e^{-\frac{mu^2}{2k_B T}} du \quad (15),$$

where:

$$\begin{aligned} m &= \text{Mass of Atom,} \\ k_B &= \text{Boltzmann Constant,} \\ T &= \text{Translational Temperature.} \end{aligned}$$

Using this distribution function, Equation (13) becomes the following integral, where  $N_{\text{TOT}}$  is the total number density of the resonant atomic species:

$$P(z,t) = N_{\text{TOT}} \int_{-\infty}^{+\infty} P(z,t;u) f(u) du \quad (16).$$

The partial polarization can be written in terms of the coherence envelope function. In the notation of Equation (5), the envelope function for the net polarization is:

$$\tilde{p}(z,t) = N_{\text{TOT}} \mu_{21} \int_{-\infty}^{+\infty} \tilde{\sigma}_{21}(z,t;u) f(u) du \quad (17).$$

### One-Dimensional Wave Equation

The one-dimensional wave equation is derived from Maxwell's Equations, and it has the following form in MKS units (to switch to Gaussian (CGS) units, simply replace  $1/\epsilon_0$  with  $4\pi$ ):

$$\left[ \frac{\partial^2}{\partial z^2} - \frac{1}{c^2} \frac{\partial^2}{\partial t^2} \right] E(z,t) = \frac{1}{\epsilon_0 c^2} \frac{\partial^2}{\partial t^2} P(z,t) \quad (18).$$

It is desirable to reduce the second order wave equation to a first order differential equation. This reduction is possible using an important approximation and a small bit of algebra. First, equations (4) and (5) are substituted into the wave equation. Next, invoking the slowly varying envelope approximation (SVEA), second order derivatives of the slowly varying functions  $\epsilon(z,t)$  and  $p(z,t)$  are neglected. Furthermore, time derivatives of  $p(z,t)$  can also be ignored with respect to the other terms in the equation. Finally, writing the wave equation in terms of the real and imaginary parts of the envelope functions, the following two real differential equations result for terms that are in phase and in quadrature with the optical phase:

$$\left[ \frac{\partial}{\partial z} + \frac{1}{c} \frac{\partial}{\partial t} \right] \epsilon^R(z,t) = -\frac{k_0}{2\epsilon_0} p^I(z,t) \quad (19a),$$

$$\left[ \frac{\partial}{\partial z} + \frac{1}{c} \frac{\partial}{\partial t} \right] \epsilon^I(z,t) = \frac{k_0}{2\epsilon_0} p^R(z,t) \quad (19b).$$

A further simplification results by invoking the retarded time transformation:  $t \rightarrow \tau = t - z/c$ . This change of variables transforms the wave equations from partial differential equations to two ordinary differential equations that can be directly numerically integrated:

$$\frac{\partial}{\partial z} \epsilon^R(z,\tau) = -\frac{k_0}{2\epsilon_0} p^I(z,\tau) \quad (20a),$$

$$\frac{\partial}{\partial z} \epsilon^I(z,\tau) = \frac{k_0}{2\epsilon_0} p^R(z,\tau) \quad (20b).$$

### Pump/Probe Model

The complete model employs a quantum-mechanically-correct description of the interaction of intense laser pulses with resonant or near-resonant two-level atoms. The resulting density matrix equations characterize the individual atomic responses to the applied laser field for atoms at a particular position in space and with a particular velocity component along the optical axis. Assuming a Maxwellian velocity distribution for the target atoms, the individual atomic responses are statistically averaged, resulting in the net induced polarization at that position. The induced polarization determines how the laser pulse propagates in space according to the one-dimensional wave equation. The model invokes the slowly varying envelope approximation (SVEA) and the rotating wave approximation (RWA) to reduce the description to a set of three coupled ordinary differential equations (ODE) in time and two ODE's in space. The input field envelope is defined such that it includes both the pump and probe pulses, and the model calculates the attenuation/gain of the envelope as the pulses propagate through the sample volume.

The five differential equations describing this system are given in equations (11) and (20). These are repeated below using explicit notation for the dependencies of the variables:

$$\begin{aligned} \frac{\partial}{\partial \tau} \rho_{11}(z,\tau;u) &= \Gamma_{21} [1 - \rho_{11}(z,\tau;u)] \\ &+ \frac{2\mu_{21}}{\hbar} \left[ \epsilon^I(z,\tau) \sigma_{21}^R(z,\tau;u) \right. \\ &\quad \left. - \epsilon^R(z,\tau) \sigma_{21}^I(z,\tau;u) \right] \end{aligned} \quad (21a),$$

$$\begin{aligned} \frac{\partial}{\partial \tau} \sigma_{21}^R(z, \tau; u) &= -\gamma_{21} \sigma_{21}^R(z, \tau; u) \\ &+ [\omega_{21} - \omega(u)] \sigma_{21}^I(z, \tau; u) \\ &+ \frac{\mu_{21}}{\hbar} \mathcal{E}^I(z, \tau) [1 - 2\rho_{11}(z, \tau; u)] \end{aligned} \quad (21b),$$

$$\begin{aligned} \frac{\partial}{\partial \tau} \sigma_{21}^I(z, \tau; u) &= -\gamma_{21} \sigma_{21}^I(z, \tau; u) \\ &- [\omega_{21} - \omega(u)] \sigma_{21}^R(z, \tau; u) \\ &- \frac{\mu_{21}}{\hbar} \mathcal{E}^R(z, \tau) [1 - 2\rho_{11}(z, \tau; u)] \end{aligned} \quad (21c),$$

$$\frac{\partial}{\partial z} \mathcal{E}^R(z, \tau) = -\frac{k_z}{2\epsilon_0} p^I(z, \tau) \quad (21d),$$

$$\frac{\partial}{\partial z} \mathcal{E}^I(z, \tau) = \frac{k_z}{2\epsilon_0} p^R(z, \tau) \quad (21e).$$

The first three differential equations describe the time evolution of the density matrix at a particular spatial location for an atom with a particular velocity component. The atoms addressed by these equations will see a Doppler shifted laser frequency, and as such, the apparent laser frequency  $\omega$  is shown to have a velocity dependence. The Doppler-shifted frequency is:

$$\omega(u) = \omega_0 - k_z u \quad (22).$$

The last two differential equations relate the spatial gradient of the electric field to the induced polarization. The induced polarization envelope functions are directly related to the coherence envelope functions as follows:

$$\begin{aligned} p^R(z, \tau) &= N_{\text{TOT}} \mu_{21} \left( \frac{m}{2\pi k_B T} \right)^{\frac{1}{2}} \\ &\bullet \int_{-\infty}^{+\infty} \sigma_{21}^R(z, \tau; u) e^{-\frac{mu^2}{2k_B T}} du \end{aligned} \quad (23a),$$

$$\begin{aligned} p^I(z, \tau) &= N_{\text{TOT}} \mu_{21} \left( \frac{m}{2\pi k_B T} \right)^{\frac{1}{2}} \\ &\bullet \int_{-\infty}^{+\infty} \sigma_{21}^I(z, \tau; u) e^{-\frac{mu^2}{2k_B T}} du \end{aligned} \quad (23b).$$

### Numerical Solution

In order to numerically solve these equations, a spatial-temporal grid is set up as shown in Figure 4.

The interaction volume starts at  $z_1=0$ , and it is discretized into  $I$  positions with a uniform spacing  $h_z$ . At each position  $z_i$ , the electric field is solved on a temporal grid that starts at the retarded time  $\tau_1=0$ , ends at time  $\tau_j$ , and has a uniform spacing  $h_\tau$ . At each position, the atomic response is calculated for velocity groups  $u_k$  where  $k=1, 2, \dots, K$ .

We assume that prior to the interaction region ( $z \leq 0$ ), the electric field has not had any resonant interactions with matter. The electric field envelope is assigned a particular functional form that depends upon experimental conditions such as the laser power, the beam splitter ratio, and the pump-probe pulse delay. The electric field is then specified on the  $\tau$ -axis as shown in Figure 4. To indicate that the values of the electric field envelopes are known at these grid points, the left side of each grid point is blackened.

We define the electric field to be zero for  $\tau \leq 0$  at  $z=0$ . Since information cannot travel faster than the speed of light, this constraint forces the electric field to be zero for  $\tau \leq 0$  at all  $z$ . Therefore, the resonant atoms are at equilibrium for these conditions, and the density matrix assumes equilibrium values at grid points along the  $z$ -axis in Figure 4. To indicate that the values of the density matrix elements, and therefore, the polarization envelope functions, are known at these grid points, the right half of each has been blackened.

The density matrix equations (21a-c), form a set of coupled ODE's at a position  $z_i$ . If the values of the electric field envelope functions are known for all  $\tau_j$  at  $z_i$ , and the density matrix elements are known for  $\tau=0$  at  $z_i$ , this set of ODE's takes the form of an initial value problem (IVP). In other words, the equations can be directly integrated by marching forward in time from  $\tau=0$ . This is the case for the  $\tau$ -axis in Figure 4. A rectangle has been drawn around these grid points to indicate that the density matrix equations can be solved for these points when the initial conditions are specified. The integration is performed using a Bulirsch-Stoer adaptive step-sizing routine<sup>15</sup>. This integrator solves for  $\rho_{11}$ ,  $\sigma_{21}^R$ , and  $\sigma_{21}^I$  at each time grid point. However, since it is an adaptively stepping algorithm, it requires



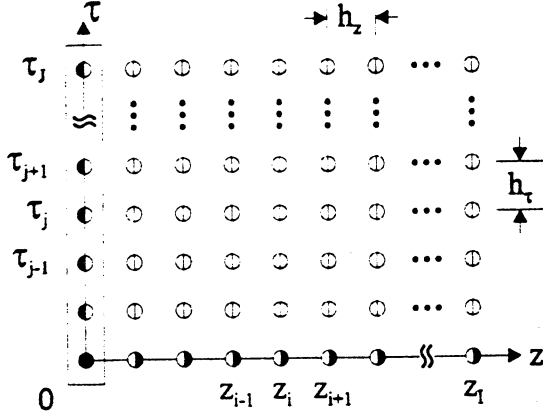


Figure 4. The spatial-temporal grid on which the pulse propagation equations are solved. The state shown in the figure corresponds to initial conditions. A circle with the right half blackened indicates that the values of  $p^R$  and  $p^I$  are known at that grid point. A darkened left half indicates that the values of  $\epsilon^R$  and  $\epsilon^I$  are known.

values of  $\epsilon^R$  and  $\epsilon^I$  between the grid points. When such an evaluation is necessary, cubic spline interpolation is used.

To obtain the induced polarization envelope functions at position  $z_i$ , the density matrix equations must be solved for each velocity group,  $u_k$ . The results are averaged at each grid point as specified by the integrals in equations (23a) and (23b). These integrals have the form of  $g(x)\exp(-x^2)dx$ , and as such, they are efficiently computed using Gauss-Hermite integration<sup>15</sup>. For a  $K^{\text{th}}$ -order Gauss-Hermite integration, the values of  $u_k$  are chosen so that they correspond to the zeros of the  $K^{\text{th}}$ -order Hermitian polynomial  $x_k$ :

$$u_k = \sqrt{\frac{2k_B T}{m}} x_k ; \quad k = 1..K \quad (24).$$

Using weight functions  $w_k$ , defined in reference [15], the integrals are approximated as follows:

$$\begin{aligned} & \int_{-\infty}^{+\infty} \sigma_{21}(z_i, \tau_j; u) e^{-\frac{mu^2}{2k_B T}} du \\ & \approx \frac{1}{\sqrt{\pi}} \sum_{k=1}^K \sigma_{21}(z_i, \tau_j; u_k) w_k \end{aligned} \quad (25)$$

After these integrals have been computed for all  $\tau_j$  at  $z_1$ , both the electric field and the induced polarization are known at  $z_1$ . This state is shown in Figure 5a, where the grid points along the  $\tau$ -axis are completely filled-in.

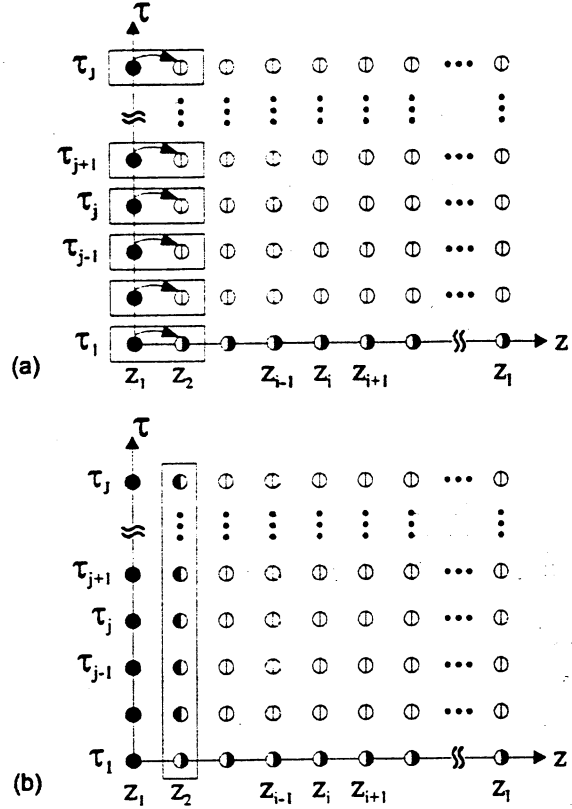


Figure 5. (a) Euler method is used to compute  $\epsilon^R$  and  $\epsilon^I$  at  $z_2$ . (b) The induced polarization envelopes,  $p^R(z_2, \tau_j)$  and  $p^I(z_2, \tau_j)$ , are calculated by integrating the density matrix equations and statistical averaging the atomic responses at  $z_2$ .

The propagation of the electric field is determined by equations (21d-e). These equations are numerically integrated between  $z_1$  and  $z_2$  using the simple Euler method at each time  $\tau_j$ . These steps are symbolically shown in Figure 5a. The 2J equations used to compute the electric field envelope functions are:

$$\epsilon^R(z_2, \tau_j) = -h_z \left[ \frac{k_o}{2\epsilon_o} p^I(z_1, \tau_j) \right] ; \quad j = 1..J \quad (26a),$$

$$\epsilon^I(z_2, \tau_j) = h_z \left[ \frac{k_o}{2\epsilon_o} p^R(z_1, \tau_j) \right] ; \quad j = 1..J \quad (26b).$$

As a result of these integrations, all of the initial conditions necessary to integrate the density matrix equations at position  $z_2$  are now known. By integrating equations (21a-c) for each of the  $K$  velocity groups, and statistically averaging the atomic responses at each time as dictated by equation (25), the induced polarization at  $z_2$  is calculated. This step involves the grid points within the rectangle in Figure 5b.

At this point, values of the electric field and induced polarization envelopes are known for all  $\tau_j$  at the first two positions. With this information, a simple predictor-corrector scheme is used to calculate the electric field envelopes at the next position. For each time  $\tau_j$ , prediction of the electric field envelope functions are made by taking symmetric Euler steps from  $z_0$  to  $z_2$  using the value of the polarization at the central grid point. In general, the predictor step is given below, where the subscript "p" on the electric field denotes a *predicted* value.

$$\begin{aligned} \varepsilon_p^R(z_{i+1}, \tau_j) &= \varepsilon^R(z_{i-1}, \tau_j) \\ &- 2h_z \left[ \frac{k_z}{2\varepsilon_0} p^I(z_i, \tau_j) \right]; j = 1..J \end{aligned} \quad (27a)$$

$$\begin{aligned} \varepsilon_p^I(z_{i+1}, \tau_j) &= \varepsilon^I(z_{i-1}, \tau_j) \\ &+ 2h_z \left[ \frac{k_z}{2\varepsilon_0} p^R(z_i, \tau_j) \right]; j = 1..J \end{aligned} \quad (27b)$$

The density matrix equations and statistical summations are computed at position  $z_{i+1}$  using the predicted values of the electric field. This results in predicted values of the polarization at  $z_{i+1}$ . Finally, corrected values for the electric field at  $z_{i+1}$  are computed by taking an Euler step from  $z_i$  to  $z_{i+1}$  using the average of the polarization at  $z_i$  and the predicted polarization at  $z_{i+1}$ . The *corrector* step is given by the following equations:

$$\begin{aligned} \varepsilon^R(z_{i+1}, \tau_j) &= \varepsilon_p^R(z_{i+1}, \tau_j) \\ &- \frac{1}{2} h_z \frac{k_z}{\varepsilon_0} \left[ p^I(z_i, \tau_j) + p_p^I(z_{i+1}, \tau_j) \right]; j = 1..J \end{aligned} \quad (28a)$$

$$\begin{aligned} \varepsilon^I(z_{i+1}, \tau_j) &= \varepsilon_p^I(z_{i+1}, \tau_j) \\ &+ \frac{1}{2} h_z \frac{k_z}{\varepsilon_0} \left[ p^R(z_i, \tau_j) + p_p^R(z_{i+1}, \tau_j) \right]; j = 1..J \end{aligned} \quad (28b)$$

After each corrector step, the integral of the square of the electric field envelope is computed using Romberg integration<sup>15</sup>. Like the Bulirsch-Stoer algorithm, this is an extrapolative method that requires function evaluation between grid points. Once again, cubic spline interpolation is used for these evaluations. The limits of integration are set to contain only the probe pulse so that the result is proportional to the total probe pulse energy. By normalizing this result to that for position  $z_1$ , one obtains the pulse-averaged probe attenuation at position  $z_i$ .

Repeating this predictor-corrector scheme, the electric field and induced polarization is determined at all grid points.

## Density Matrix Model Results

We now present some preliminary results for pulse propagation in pump/probe experiments with potassium. We are focusing on potassium because we wish to validate our model results experimentally, and we are well-suited to carry out potassium pump/probe experiments. Potassium has several advantages which make it ideal for this characterization. First, it has two strong ground state transitions in the fundamental tuning range of Ti:Sapphire. Secondly, for these resonances, potassium is completely described by a three-level model. Therefore, we can be certain that our model accurately describes the physical interaction. Although our current model uses the two-level density matrix equations, we will implement a three-level model soon. The following simulations use parameters typical to proposed experimental conditions.

### Experimental Parameters

The proposed experiments will employ the Spectra Physics regeneratively mode-locked Ti:Sapphire laser system described earlier. The beam diameter is approximately 100  $\mu\text{m}$  at the sample volume. Assuming a  $\text{sech}^2$  intensity profile, the electric field magnitude at the sample is approximately  $1.5 \times 10^7$  V/m for the 2-ps pulses, and  $2.8 \times 10^6$  V/m for the 60-ps pulses. The transform-limited spectral FWHM of a 2-ps pulse is  $\Delta\omega_{2ps} = 0.99 \text{ ps}^{-1}$ , while that of a 60-ps pulse is  $\Delta\omega_{60ps} = 3.3 \times 10^{-2} \text{ ps}^{-1}$ .

The laser will be tuned to the  $4^2S_{1/2} - 4^2P_{1/2}$  transition of atomic potassium at 769.9 nm. Both the ground state and the excited state have a degeneracy of 2, so the density matrix model does not need to explicitly account for degeneracy of states. Fiechtner and Linne<sup>1</sup> probed the  $4^2S_{1/2} - 4^2P_{3/2}$  transition (766.5 nm) in prior pump/probe experiments, but to properly model that transition, the density matrix equations would need to explicitly account for the different degeneracies of the two states. For the conditions of their experiments, it was determined that to avoid saturation the pump and probe beam powers had to be kept below 4 mW (49 pJ per pulse) and 5 mW (61 pJ/pulse), respectively<sup>16</sup>.

The spontaneous emission coefficient for the  $4^2S_{1/2} - 4^2P_{1/2}$  transition<sup>17</sup> is approximately  $0.382 \times 10^8 \text{ s}^{-1}$ . This value corresponds to a dipole moment of  $2.5 \times 10^{-29} \text{ C} \cdot \text{m}$ . For atmospheric flame conditions, we assume that the collisional dephasing rate  $\gamma_{21}$  and the de-excitation rate  $\Gamma_{21}$  are both equal to  $5 \times 10^9 \text{ s}^{-1}$ .

A Winefordner-style aspirating burner will be used to seed the potassium into an atmospheric methane/air flame. We assume an equilibrium temperature of approximately 2000 K, which corresponds to a FWHM

of the potassium velocity distribution of 922 m/s. The corresponding Doppler broadening of the atomic line is  $\Delta\omega_{\text{Doppler}} = 7.5 \times 10^{-3} \text{ ps}^{-1}$ .

For simulations involving 2-ps pulses, the temporal discretization is typically set to 0.05 ps so that 40 grid points span one intensity FWHM. All simulations shown here use 2 mm interaction region, and the spatial discretization is chosen so that the difference between the predictor (27) and the corrector step (28) is kept within a 5% tolerance. When Doppler broadening is explicitly included in the simulations, 19 velocity groups are used in the integrations defined by equation (25).

### Initial Conditions

We assume that when unperturbed, all atoms are in the ground state. Furthermore, the coherences must be zero when no coherent excitation is present. These initial conditions are summarized as follows.

$$\left. \begin{aligned} \rho_{11}(z_i, 0; u_k) &= 1 \\ \sigma_{21}^R(z_i, 0; u_k) &= \sigma_{21}^I(z_i, 0; u_k) = 0 \end{aligned} \right\} \quad (28)$$

$$i = 1..I, k = 1..K$$

We further assume that the mode-locked laser pulses are described by hyperbolic secant envelope functions. The envelope function for the pump has a magnitude  $\varepsilon_1$ , and it peaks at  $\tau = \tau_1$ . The probe envelope has a magnitude  $\varepsilon_2$ , and it peaks at  $\tau = \tau_2$ . The pulses are spatially separated by  $\Delta z = c(\tau_2 - \tau_1)$ . Each pulse has the same intensity full width at half-maximum (FWHM) which is denoted by  $\Delta\tau_{\text{FWHM}}$ . Using (6), the electric field envelope is specified at  $z=0$  by the following two functions.

$$\begin{aligned} \varepsilon^R(0, \tau) &= \varepsilon_1 \operatorname{sech} \left[ \frac{-2 \ln(\sqrt{2}-1)}{\Delta\tau_{\text{FWHM}}} (\tau - \tau_1) \right] \cos \varphi \\ &+ \varepsilon_2 \operatorname{sech} \left[ \frac{-2 \ln(\sqrt{2}-1)}{\Delta\tau_{\text{FWHM}}} (\tau - \tau_2) \right] \\ &[\cos \varphi \cos k_o \Delta z + \sin \varphi \sin k_o \Delta z] \end{aligned} \quad (30a)$$

$$\begin{aligned} \varepsilon^I(0, \tau) &= -\varepsilon_1 \operatorname{sech} \left[ \frac{-2 \ln(\sqrt{2}-1)}{\Delta\tau_{\text{FWHM}}} (\tau - \tau_1) \right] \sin \varphi \\ &+ \varepsilon_2 \operatorname{sech} \left[ \frac{-2 \ln(\sqrt{2}-1)}{\Delta\tau_{\text{FWHM}}} (\tau - \tau_2) \right] \\ &[\cos \varphi \sin k_o \Delta z - \sin \varphi \cos k_o \Delta z] \end{aligned} \quad (30b)$$

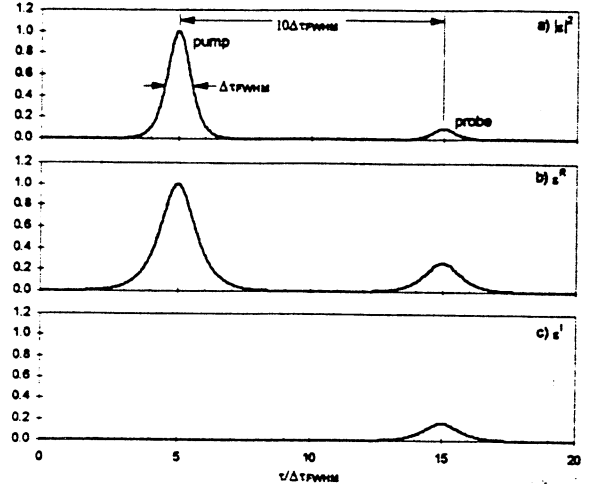


Figure 6. Example of the electric field envelope for  $z=0$ . The square of the magnitude of the envelope function is shown in part a). Part b) show the real part of the complex envelope function, and part c) shows the imaginary part of the envelope function.

Figure 6a depicts the modulus squared for a pump/probe envelope. In this example, the phase is set so that the pump envelope is purely real at  $z=0$  ( $\varphi(0, \tau)=0$  in Equation (3)). The probe intensity is 10% of the pump intensity. The peak of the pump pulse occurs at  $\tau_1 = 5\Delta\tau_{\text{FWHM}}$ , and the probe pulse peaks at  $\tau_2 = \tau_1 + 10\Delta\tau_{\text{FWHM}}$ . For the numerical integration, it is important to truncate the envelope functions, so that the laser electric field is always zero for  $\tau \leq 0$ . A further restriction is placed on the functions to distinctly separate the pump and probe pulses. This is accomplished by setting the electric field for each pulse to zero for  $|\tau - \tau_{\text{peak}}| > 4\Delta\tau_{\text{FWHM}}$ .

Figures 6b) and 6c) show the real and imaginary parts of the envelope function as determined from (30). When considered independently, the pump and probe pulses were taken to be purely real. However, when the envelope function for both pulses is calculated, the imaginary part is non-zero due to the phase  $k_o \Delta z$  introduced by the pump-probe delay.

An important point to be made here is that very slight changes in  $\Delta z$ , on the order of a fraction of an optical wavelength, can dramatically change the envelope function. For example, if  $\Delta z$  is set so that the envelope is purely real, coherences due to the pump pulse are exactly in phase with the probe pulse. If  $\Delta z$  is then shifted one-half of an optical wavelength, the pump and probe are exactly out of phase. Shifts of this magnitude will most definitely occur in an experiment. Therefore, future improvements to the model will include handling of these as well as other typical fluctuations.

## Doppler Effects

The model includes Doppler effects by averaging atomic responses over a Maxwellian distribution. However, for potassium, under atmospheric flame conditions, Doppler broadening is negligible with respect to the spectral bandwidth of a 2-ps pulse. At 2000 K, the Doppler width for potassium is two orders of magnitude smaller than the laser spectral bandwidth. Therefore, atomic responses vary little for velocity groups within the Maxwellian distribution, and the average atomic response turns out to be the response that is calculated for stationary atoms. Therefore, the remaining simulations do not carry out the statistical average explicitly.

## Probe Pulse Propagation - No Pump

The following figure shows the excited state population that results after a single pulse interaction. For these simulations, the pulse is propagated through an interaction length of 2 mm, with a total potassium number density of  $10^{11} \text{ cm}^{-3}$ .

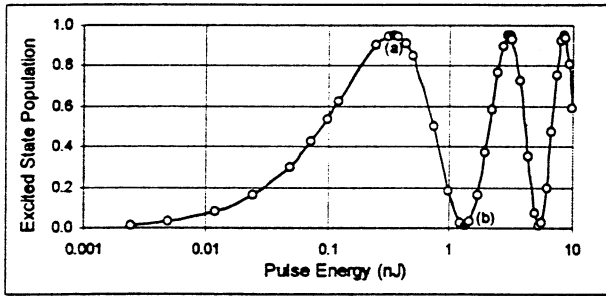


Figure 7. The excited state population of potassium is plotted as a function of pulse energy. Circles indicate that the data point is a simulation result. The connecting lines are not actual simulation data, but only included to aid in visualization.

Initially, the excited state population scales linearly with pulse energy. This is the result predicted by the rate equations. However, as the energy increases, the excited state population does not saturate at a value of 0.5 as predicted by the rate equations. Instead, at 0.34 nJ (indicated by point (a) in the figure), almost all of the population is in the excited state. If the pulse energy is increased still further, the population is stimulated back towards the ground state. At point (b), almost all of the population is back in the ground state. The excited state population and the laser attenuation for a pulse with energy (b) are both plotted as a function of time in Figure 8. Since little collisional relaxation occurs on

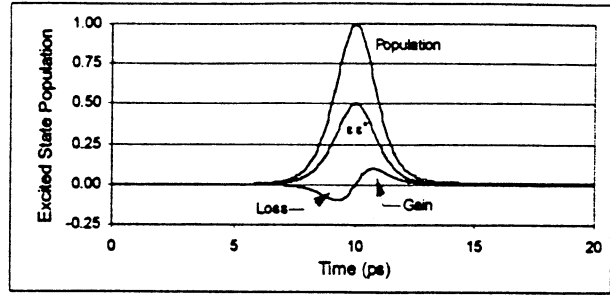


Figure 8. The time history of the excited state population and the pulse gain are shown for a 1.3 nJ pulse after propagating through 2 mm of potassium at  $10^{11} \text{ cm}^{-3}$ . This corresponds to point (b) in Figure 7.

these short time scales, conservation of energy dictates that this pulse sees very little integrated attenuation. This is shown in the figure, where the first half of the pulse is attenuated, and the second half experiences gain. The time-integrated gain is approximately zero. This behavior has been extensively studied, and is termed "self-induced transparency." McCall and Hahn<sup>18</sup> wrote the definitive paper on this subject in 1969.

An interesting phenomena occurs as the pulse energy is increased beyond point (a) in Figure 7. The population then flops back and forth during the pulse. If the electric field of the pulse is constant, these oscillations occur at a fixed frequency, the Rabi frequency ( $\Omega_{\text{Rabi}}$ ). In general, the Rabi frequency is time-dependent and is related to the electric field envelope by

$$\Omega_{\text{Rabi}} = \frac{\mu_{21} \mathcal{E}(t)}{\hbar} \quad (31)$$

Figure 9 shows the Rabi oscillation corresponding to the maximum pulse we can produce with our unamplified

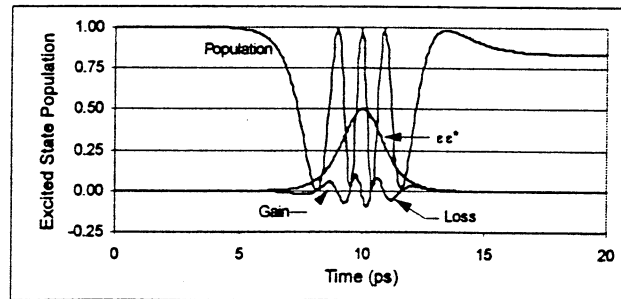


Figure 9. The time history of the excited state population and the pulse gain are shown for a 22.6 nJ pulse after propagating through 2 mm of potassium at  $10^{11} \text{ cm}^{-3}$ . This corresponds to the maximum pulse energy for our unamplified Ti:sapphire laser.

Ti:sapphire laser. The pulse energy is 22.6 nJ. Although this phenomena is interesting, for our purposes, it is undesirable to operate in this regime. The state of the atomic population following a pulse that induces Rabi oscillations is highly sensitive to pulse shape, height, and duration. Slight laser fluctuations result in very unpredictable behavior, and this makes correct characterization of the pump/probe experiment not possible.

### Pump/Probe Propagation

The previous results, shown in Figure 7, suggest that potassium pump/probe will most likely be linear when pulse energies are less than 0.1 nJ. For preliminary investigation, we decided to consider a probe energy of 1.2 pJ (100  $\mu$ W average power). We varied the pump energies from 1.2 pJ to 122 pJ. We have simulation results for these pump and pulse energies with the product of the total number density and the interaction length,  $N_{TOT}L$ , varying from  $2 \times 10^9$  to  $2 \times 10^{12}$  mm cm<sup>-3</sup>. Currently, numerical errors prevent us from obtaining results with  $N_{TOT}L < 2 \times 10^9$  mm cm<sup>-3</sup>. This issue will be addressed in a future version of the code.

We are looking for a linear relationship between modulation depth and the  $N_{TOT}L$  product, such as:

$$\alpha_{MOD} = C N_{TOT} L \quad (32)$$

To determine if such a relationship exists, we solved equation (32) for  $C$ , and plotted that result in Figure 10. As an example, when the pump pulse energy is 24 pJ, the constant in equation (32) is approximately  $-0.5 \times 10^{-14}$ , where  $N_{TOT}$  is given in cm<sup>-3</sup>, and  $L$  is given in mm. This relationship holds provided that the  $N_{TOT}L$  product does not exceed  $3 \times 10^{11}$  mm cm<sup>-3</sup>. Similar limits can be defined for other pump energies.

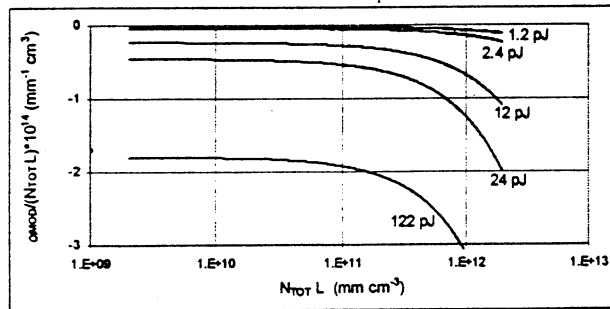


Figure 10. Linearity of pump/probe modulation depth with  $N_{TOT}L$  for several values of pump pulse energy. The probe pulse energy is 1.2 pJ.

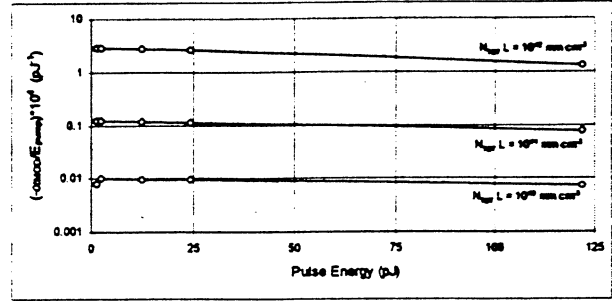


Figure 11. Linearity of pump/probe modulation depth with pulse energy for several values of  $N_{TOT}L$ . The probe pulse energy is 1.2 pJ. Circles indicate the data point is a simulation result. The connecting lines are not actual simulation data, but only included to aid in visualization of departure from linearity.

A similar presentation of the data can be made to check for linearity of the pump/probe signal with pump pulse energy. In this case we assume the following relationship.

$$\alpha_{MOD} = K E_{PUMP} \quad (33)$$

Figure 11 plots  $K$  as a function of the pulse energies shown in Figure 10. Clearly, for pump energies less than 25 pJ, this relationship applies fairly well. However, it does not hold between 25 pJ and 122 pJ.

We conclude, therefore, that it will be possible to perform picosecond pump/probe experiments within well-defined rate equation limits, which are in agreement with the limits originally set by Fiechtner *et al.*<sup>2</sup>. Whether the density matrix formalism predicts the same modulation depth as the rate equations is another question.

### Comparison Between the Rate Equation and Density Matrix Formalisms

We find that, when realistic numbers are used in both the rate equation and the density matrix formalisms, the two approaches always agree to within an order of magnitude - when we remain within the rate equation limit. Indeed, it is possible to force complete agreement by adjusting the phase shift between the pump and probe pulses in the density matrix model. This is a reflection of a point we have already made - very slight changes in  $\Delta z$ , on the order of a fraction of an optical wavelength, can dramatically change the pulse envelope function. For example, if  $\Delta z$  is set so that the envelope is purely real, coherences due to the pump pulse are exactly in phase with the probe pulse. If  $\Delta z$  is then shifted one-half of an optical wavelength, the pump and probe are exactly out of phase. These seemingly minor

phase shifts can significantly change the modulation depth predicted by the model. Shifts of this magnitude will most definitely occur in an experiment. At this point in time, encouraging rough agreement has been found. In order to explore this question accurately, however, it will be necessary to average the modulation depth predicted by the density matrix model over the phase shifts one should encounter in a real experiment. That work is ongoing.

### Conclusions

This paper presents a basic discussion of both rate equation and a density matrix models that we are currently developing to study pulse propagation in pump/probe experiments. The non-perturbative density matrix model does not use any simplifying assumptions with regards to pulse intensities, and treats the atomic response with a quantum-mechanically-correct formalism. This model is being developed in an attempt to either validate the rate equation-based model or to identify a similar kind of relationship. Furthermore, the model can be used to maximize signal while staying within the experimental limits of applicability of this relationship.

Preliminary simulation results were presented to demonstrate qualitative behavior as a function of both pump pulse energy and total number density. Experimental parameters for a potassium pump/probe experiment were used, and the simulations demonstrated linear behavior in the weak interaction limit. However, a departure from this linearity was observed as the interaction strength was increased. When the laser pulses are sufficiently strong to cause Rabi oscillations in the atomic populations, it is no longer possible to characterize the experiment with simple expressions. In this regime, subtle changes in pulse amplitude and shape can result in dramatically different modulation depths.

In order to accurately compare the rate equation and density matrix formalisms, it will be necessary to average the modulation depth predicted by the density matrix model over the phase shifts one should encounter in a real experiment. Future work will also include the implementation of multi-level models for the atomic resonance. A fully accurate potassium model requires that the three-level density matrix equations are used, although the Potassium D lines are sufficiently separated that the two-level model contains most of the important physics. Following some basic improvements to the numerical code, we will simulate potassium pump/probe propagation, and thoroughly characterize the parameter space. This will involve careful experimentation, including real-time pump/probe and line-of-sight absorption measurements over the range of

concentrations and laser intensities of interest. Measurements will then be compared to the predictions of the density matrix and rate equation formalisms.

### Acknowledgments

This research has been supported by the National Science Foundation through grants CTS-9411391, CTS-9711889, and DGE-9554559, and by the US Air Force Wright Laboratories through grant number F33615-96-C-2632.

### References

1. G.J. Fiechtner and M.A. Linne, "Absolute Concentrations of Potassium by Picosecond Pump/Probe Absorption in Fluctuating, Atmospheric Flames", *Combust. Sci. and Tech.*, Vol. 100, 11-27, (1994).
2. G.J. Fiechtner, G.B. King, and N.M. Laurendeau, "Rate-equation model for quantitative concentration measurements in flames with picosecond pump-probe absorption spectroscopy", *Appl. Opt.*, Vol. 34, No. 6, 1108-116, (1995).
3. J. P. Heritage, "Picosecond nonlinear spectroscopy of silver microstructures and surface adsorbates", in B.A. Gartez and J.R. Lombardi (Ed), *Advances in Laser Spectroscopy 2*, John Wiley & Sons Ltd., New York, NY, 207-224, (1983).
4. T. Settersten and M. Linne, "Two-Level Rate Equation Based Model for Single-Point Picosecond Pump/Probe Measurements of Molecular Populations", technical note # CCER97-002, Center for Combustion and Environmental Research, Colorado School of Mines, (1997).
5. T. Settersten and M. Linne, "Two-Level Rate Equation Based Model Results for Single-Point Picosecond Pump/Probe Measurements of CH", technical note # CCER97-003, Center for Combustion and Environmental Research, Colorado School of Mines, (1997).
6. J. Luque and D.R. Crosley, "LIFBASE: Database and Spectral Simulation program (Version 1.0)", SRI Internal Report MP 96-001, (1996).
7. J. Luque and D.R. Crosley, "Electronic transition moment and rotational transition probabilities in the CH A-X system", *J. Chem. Phys.*, 104, 2146, (1996).
8. J. Luque and D.R. Crosley, "Electronic transition moment and rotational transition probabilities in the CH B-X system", *J. Chem. Phys.*, 104, 3907, (1996).
9. M. Zachwieja, "New investigations of the A-X band system in the CH radical and a new reduction



- of the vibration-rotation spectrum from ATMOS spectra", *J. Mol. Spectros.*, **170**, 285, (1995).
10. J.J. Sakurai, *Modern Quantum Mechanics*, Addison-Wesley Publishing Company, Inc., New York, NY, (1985).
  11. J.R. Lalanne, A. Ducasse, and S. Kielich, *Laser-Molecule Interaction: Laser Physics and Molecular Nonlinear Optics* (John Wiley & Sons, Inc., New York, NY, 1996).
  12. R.W. Boyd, *Nonlinear Optics*, Academic Press, San Diego, CA, (1992).
  13. J.T. Verdeyen, *Laser Electronics*, Third Edition, Prentice Hall, Englewood Cliffs, NJ, (1995).
  14. Ref. 7, p. 195.
  15. W.H. Press, S.A. Teukolsky, W.T. Vetterling, and B.P. Flannery, *Numerical Recipes in C: the Art of Scientific Computing, Second Edition* (Cambridge University Press, New York, NY, 1992), pp. 707.
  16. G.J. Fiechtner, Quantitative Concentration Measurements in Atmospheric-Pressure Flames by Picosecond Pump/Probe Absorption Spectroscopy, Ph.D. dissertation, Purdue University (1992).
  17. W.L. Wiese, M.W. Smith, and B.M. Glennon, *Atomic Transition Probabilities (Na through Ca - A Critical Data Compilation)*, National Standard Reference Series, National Bureau of Standards 22, Volume II, U.S. Government Printing Office, Washington D.C. (1966).
  18. S.L. McCall and E.L. Hahn, "Self-Induced Transparency," *Phys. Rev.* **183**(2), 457, (1969)

#### **2.2.4 Spectroscopic Techniques**

Significant interest has been focused on obtaining an understanding of the critical physical and chemical process of fuel thermal stability; however, many of the techniques employed to date have been applied only to the study of fuel cooled to room temperature following thermal stressing. Characterizing the fuel in situ while at room temperature and pressure during stressing should yield an improved understanding of the fouling process and provide superior solutions to thermal management. Optical spectroscopic methods were applied to the study of the chemical and physical processes that occur in aviation fuels under high-temperature, high-pressure conditions. The results of this study were documented in the paper entitled “Spectroscopic Investigations of High-Temperature, High-Pressure Model Aviation Fuels” (see pp. 214-217).

Symposium on Structure of Jet Fuels V  
Presented Before the Division of Petroleum Chemistry, Inc.  
216th National Meeting, American Chemical Society  
Boston, MA, August 23-27, 1998

## Spectroscopic Investigations of High-Temperature, High-Pressure Model Aviation Fuels

*Christopher E. Bunker and James R. Gord*  
*Propulsion Sciences & Advanced Concepts Division*  
*Air Force Research Laboratory*  
*Wright-Patterson Air Force Base, OH 45433-7103*

*Keith D. Grinstead, Jr.*  
*Innovative Scientific Solutions, Inc.*  
*2786 Indian Ripple Rd.*  
*Dayton, OH 45440-3638*

### INTRODUCTION

In modern high-performance aircraft, the fuel serves two essential functions: It provides the energy for propulsion and acts as the coolant for on-board heat sources. As a result, the fuel is exposed to temperatures at which oxidative and pyrolytic reactions occur (1). The ultimate products of these reactions are gums and particles that can severely affect the safe and efficient operation of the aircraft. To improve the thermal stability of the fuel and thereby enhance the capabilities of future high-performance aircraft, a thorough understanding of the chemical and physical processes that occur in fuels at high temperatures and pressures is required. A great deal of interest has been focused on obtaining this understanding (1-4); however, many of the techniques employed to date have been applied only to the study of fuel cooled to room temperature following thermal stressing. While the information gained has produced significant improvements in the thermal stability of some fuels (5) — primarily through the incorporation of fuel additives designed to mitigate certain aspects of the fouling process — there are still significant issues to be addressed. For example, does the understanding achieved by studying post-stress fuel samples at ambient conditions adequately describe the processes underway during stressing at high temperature and pressure, or does the process of cooling and depressurizing the sample under study obscure essential features of the fouling chemistry and physics? Characterizing the fuel while at temperature and pressure during stressing will no doubt yield an improved understanding of the fouling process and provide superior thermal management solutions. Unfortunately, the complications associated with in situ measurements have restricted all but a few researchers (6-8) to off-line analyses of post-stress samples at room temperature and pressure.

This paper describes progress in applying optical spectroscopic methods to the study of the chemical and physical processes that occur in aviation fuels under high-temperature, high-pressure conditions. Optical spectroscopy offers a number of potential advantages over other forms of analysis. Optical measurements can be achieved through the simple incorporation of an optical port into a fuel analysis rig, while off-line techniques require extractive sampling of hot, high-pressure fuels, and mass spectrometric analysis requires differential pumping to accommodate high gas loads. When accomplished with modest excitation, optical measurements are non-invasive and non-destructive, impacting neither the chemistry nor the fluid dynamics of the system under study. Finally, the techniques of optical spectroscopy can offer high sensitivity and selectivity and often provide detailed, chemically specific information. Efforts to exploit these advantages of optical spectroscopy through the development of a suitable optical sampling interface for high-temperature, high-pressure studies of aviation fuels are described, and preliminary measurements obtained in supercritical hexane ( $T_c=234^\circ\text{C}$ ,  $P_c=498$  psi) with spontaneous Raman scattering and fluorescence emission methods are presented.

### EXPERIMENTAL

The high-temperature, high-pressure fuel system includes a stainless steel optical cell constructed in-house (vide infra), a syringe pump (High Pressure Equipment Co.) and pressure gauge (Matheson Gas Com-

pany, 200-3000 psi) for controlling cell pressure, and a 120-V, 300-W band heater (Watlow Electric Manufacturing Co.) and Digi-Sense Model 89000 temperature controller (Cole Parmer Instrument Co.) for controlling cell temperature. Raman spectra were acquired by using a Millennia V diode-pumped Nd:YVO<sub>4</sub> laser (Spectra-Physics Lasers, Inc.) for excitation at 532 nm, an HR460 spectrograph and Spectrum-1 CCD detector (Spex Industries, Inc.) for scattered light collection, and a 532-nm holographic notch filter (Kaiser Optical Systems, Inc.) for rejection of the excitation light. Fluorescence spectra were recorded using a Fluorolog 3 spectrofluorometer (Spex Industries, Inc.) with excitation and emission monochromator slits set to 5.0 mm. During both the Raman and the fluorescence measurements, the optical cell was configured in a right-angle excitation/emission geometry. All fluorescence spectra were corrected for the non-linear response of the detection system.

A first-generation high-temperature, high-pressure optical cell was constructed from a cylindrical, stainless steel vessel equipped with a high-pressure fitting on one end and a flange cap on the other. The flange cap was bolted to the cylindrical assembly to secure a quartz or sapphire window using graphite gaskets to make the seal. In an effort to ensure a safe system, the unsupported region of the 5/8"-diameter window was limited to a 3/8"-diameter circular area defined by a hole in the flange cap. To

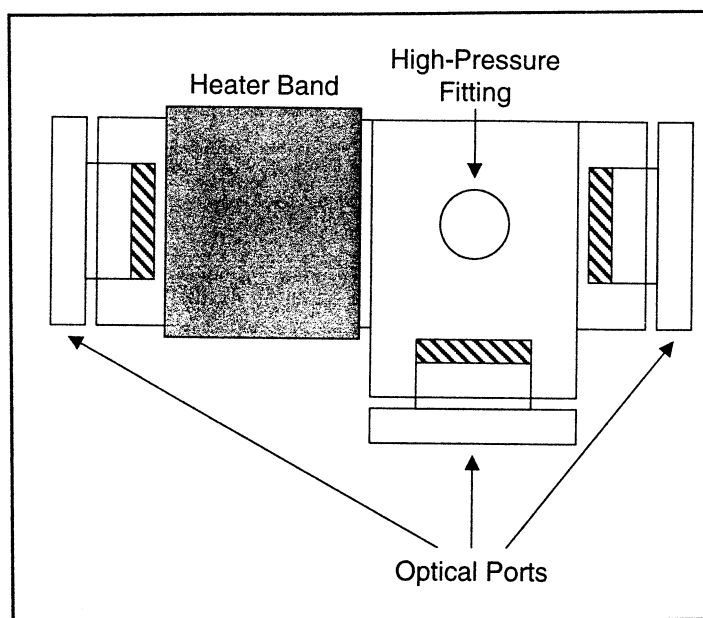


Figure 1. Planform of the high-temperature, high-pressure optical cell.

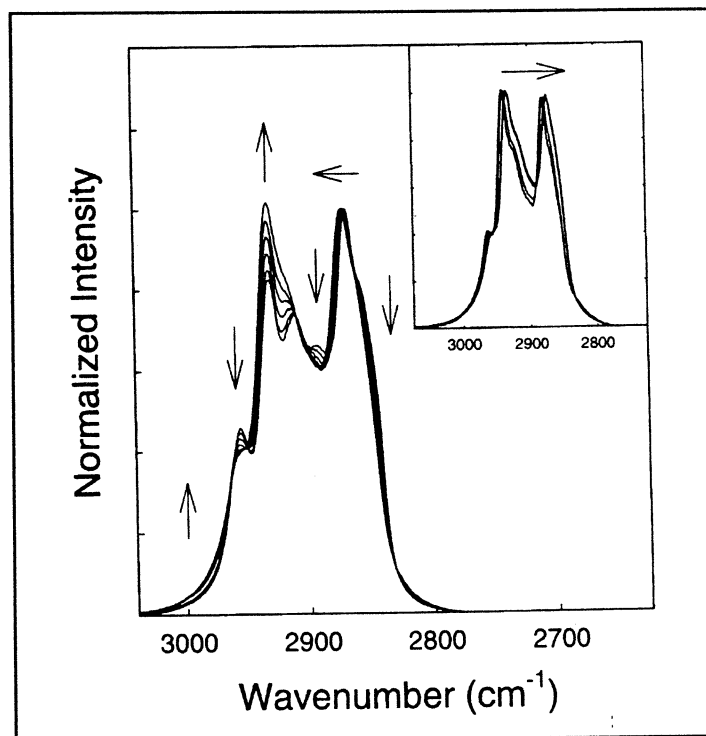


Figure 2. Raman spectra of hexane acquired at room temperature ( $\sim 23^\circ\text{C}$ ), 50, 100, 150, 200, and  $250^\circ\text{C}$ . The arrows indicate the direction of change with increasing temperature. Inset, Raman spectra of hexane at  $250^\circ\text{C}$  and pressures of 250, 550, 1100, and 2500 psi. The arrow indicates the direction of change with increasing pressure.

heat the cell, a circular band heater was attached around the cylindrical cell assembly. This configuration, which was tested to a temperature of  $600^\circ\text{C}$  and a pressure of 2000 psi, achieves the conditions necessary for characterizing aviation fuel fouling; however, optical experiments with

this cell are limited by its restricted optical access and its front-surface geometry.

A second-generation cell expanded to include two additional optical ports is depicted in Figure 1. This cell includes a window at each end of the cell and a third at  $90^\circ$  with respect to these two. To accommodate this optical geometry, the high-pressure fitting was located on the top of the cell. This second-generation cell, which permits operation at desired temperatures and pressures, is ideally configured for absorption, luminescence, and scattering experiments.

## RESULTS AND DISCUSSION

Using the second-generation optical cell, spontaneous Raman spectra were recorded for neat hexane as a function of temperature and pressure. The temperature-dependent spectra for the hexane C-H stretch are depicted in Figure 2. The arrows in the figure indicate the direction of spectral changes for the indicated features with increasing temperature. The observed temperature-dependent spectral changes are reversible: The original room-temperature Raman spectrum is recovered following cooling to room temperature from elevated temperatures as high as  $250^\circ\text{C}$ , the highest temperature explored in this phase of the study. Excellent agreement between the original room-temperature spectrum and that obtained after cooling from  $250^\circ\text{C}$  suggests that no observable thermal decomposition of the fuel is occurring under these experi-

mental conditions. Because the observed Raman spectrum in this region is composed of many individual vibrational transitions, the changes with temperature reflect the combined temperature-dependence of these individual transitions. For example, the transition responsible for the feature at  $\sim 2870\text{ cm}^{-1}$  shows a shift to higher energies with increasing temperature.

To explore the effects of pressure on the high-temperature Raman spectrum, measurements were accomplished at  $250^\circ\text{C}$  over the range of pressures 250–2500 psi. Hexane at  $250^\circ\text{C}$  is above its critical temperature ( $T_c=234.2^\circ\text{C}$ ); consequently, it exists as one phase within the cell regardless of pressure. Raman features in the C-H region shift to lower energy with increasing pressure as depicted in the Figure 2 inset. This behavior may arise from increased stabilization of the excited vibrational state at high fluid densities, suggesting that the C-H stretch region might serve as a sensitive probe of the local (averaged) fluid environment.

The same series of experiments was performed to explore the C-C aliphatic stretch and bending region ( $\sim 1600$  to  $200\text{ cm}^{-1}$ ). Unlike the C-H region, the C-C region exhibits no significant pressure dependence and no temperature dependence other than broadening of the transitions with increasing temperature.

In addition to these Raman experiments, fluorescence spectra were recorded with the second-generation cell to evaluate the effects of pressure on the behavior of the environment-sensitive probe ethyl *p*-(*N,N*-diethylamino)benzoate (DEAEB) in supercritical hexane at  $260^\circ\text{C}$ . DEAEB is characterized by dual fluorescence

with emission from a locally excited (LE) state and from a twisted intramolecular charge-transfer (TICT) state (9). The TICT emission band is highly sensitive to solvent polarity, shifting to lower energies with increasing polarity due to increased stabilization of the TICT state. In relatively non-polar fluids, the intensity of the TICT emission band increases with increasing polarity relative to that of the LE emission band due to TICT-state stabilization. Both the position and the intensity of the TICT emission band can be employed to characterize local solvent polarity.

Depicted in Figure 3 are the fluorescence spectra of DEAEB at a temperature of  $260^\circ\text{C}$  and pressures of 700, 950, 1250, and 1750 psi. Replicate measurements accomplished at each pressure suggest no thermal decomposition or photochemical reaction of DEAEB under these conditions. As the system pressure is increased through the addition of hexane, fluorescence emission in the red region of the spectrum increases. This observa-

tion is in good agreement with the established behavior of DEAEB and other TICT-state molecules studied in supercritical fluids with near-ambient critical parameters (10, 11). A thorough study of DEAEB fluorescence in hexane promises to reveal quantitative details of local solvent polarity important for understanding the fuel fouling process.

## CONCLUSIONS

A highly functional optical cell capable of operation at high temperatures and pressures has been constructed enabling the detailed investigation of aviation fuels, fuel surrogates, and fuel additives under thermal-stressing conditions. The utility of this cell has been demonstrated through the acquisition of temperature- and pressure-dependent Raman and fluorescence spectra. These preliminary studies suggest that the solvent-dependent characteristics of selected environment-sensitive probe molecules can be exploited to explore the chemical and physical processes responsible for fuel fouling.

## ACKNOWLEDGMENTS

Support for CEB is provided by the Propulsion Sciences & Advanced Concepts Division, Air Force Research Laboratory, through a National Research Council Postdoctoral Associateship. The authors acknowledge Dr. Tim Edwards and Mr. Steve Anderson of the Fuels Branch for stimulating discussions and thank Drs. DeLyle Eastwood, Jeff Martin, and Larry Burggraf of the Air Force Institute of Technology for access to their Spex Fluorolog 3 spectrofluorometer. JRG gratefully acknowledges Dr. Julian Tishkoff and the Air Force Office of Scientific Research (AFOSR) for continuing sup-

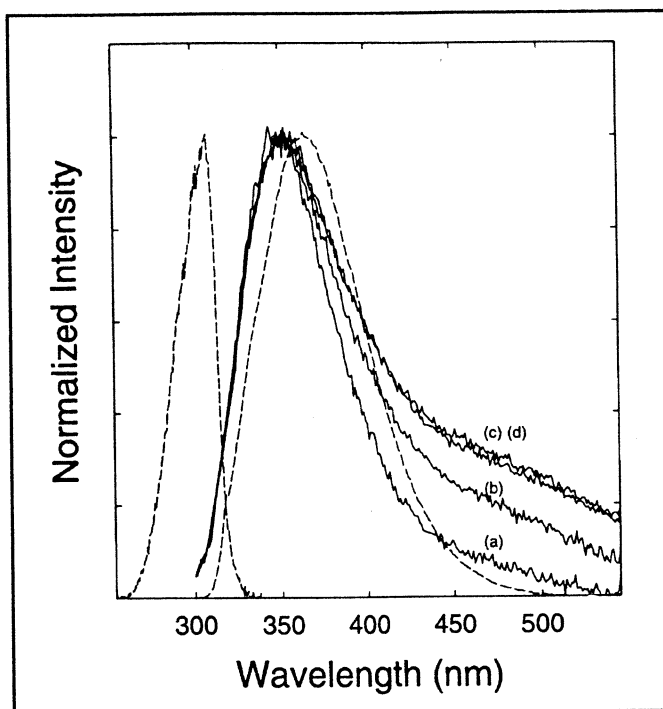


**Figure 3.** Fluorescence spectra of DEAEB in hexane at  $260^\circ\text{C}$  and (a) 700 psi, (b) 950 psi, (c) 1250 psi, and (d) 1750 psi. The fluorescence excitation and emission spectra of DEAEB in room-temperature hexane (---) are included for comparison.

port of advanced supercritical fuels research.

#### LITERATURE CITED

- (1) Edwards, T., Atria, J. V., ASME 97-GT-143, ASME International Gas Turbine and Aeroengine Congress, Orlando, FL, June 2-5, 1997.
- (2) Edwards, T., Zabarnick, S., Ind. Eng. Chem. Res., 32, 3117 (1993).
- (3) Selvaraj, L., Sobkowiak, M., Coleman, M. M., PREPRINTS, Am. Chem. Soc., Div. of Petrol. Chem., 37(2), 451 (1992).
- (4) Yu, J., Eser, S., Ind. Eng. Chem. Res., 36, 574 (1997).
- (5) Heneghan, S. P., Zabarnick, S., Ballal, D. R., Harrison, W. E. III, Trans. ASME, 118, 170 (1996).
- (6) Serio, M. A., Pines, D. S., Kroo, E., Knight, K. S., Solomon, P. R., Bonanno, A. S., SPIE Proceedings Series, 2069, 20 (1993).
- (7) Parker, T. E., Fooutter, R. R., Rawlins, W. T., Ind. Eng. Chem. Res., 31, 2243 (1992).
- (8) Acker, W. P., Hahn, R. T., Mach, T. J., Sung, R. L., PREPRINTS, Div. of Petrol. Chem., ACS, 37(2), 433 (1992).
- (9) Sun, Y.-P., Bowen, T. L., Bunker, C. E., J. Phys. Chem., 98(48), 12486 (1994).
- (10) Sun, Y.-P., Bunker, C. E., Chem. Comm., 1, 5 (1994).
- (11) Sun, Y.-P., Bunker, C. E., Ber. Bunsen-Ges. Phys. Chem., 99(7), 976 (1995).





